Structural and Functional Studies of c-type Cytochromes from Anaerobic Ammonium-Oxidizing Bacteria

Dissertation

Ruprecht-Karls-Universität
Heidelberg, Germany

Mohd Akram
Heidelberg, 2018

Dissertation
submitted to the
Combined Faculties for the Natural Sciences and for Mathematics
of the Ruperto Carola University of Heidelberg, Germany
for the degree of
Doctor of Natural Sciences

presented by

Mohd Akram, M.Sc.
born in Tundla, India

Oral examination: 08. June 2018

Structural and Functional Studies of c-type Cytochromes from Anaerobic Ammonium-Oxidizing Bacteria

Referees: Prof. Dr. Ilme Schlichting
Dr. Thomas Barends

“Exploratory research is really like working in a fog.
You don't know where you're going. You're just groping.
Then people learn about it afterwards and think how straightforward it was.”

“If you want to understand function, study structure.”

Francis Crick
(1916-2004)

Table of contents

Acknowledgements

During the course of my PhD work, several people supported me in many different ways. Without the help of these people, this thesis would not have been possible.

First of all, I would like to thank my supervisor Dr. Thomas Barends for the continuous support of my PhD study, his scientific input, constructive criticism, the freedom to follow my own ideas and for helping me to overcome obstacles in crystallography. I really enjoyed learning and gathering experiences in the fields of X-ray crystallography, biophysics and biochemistry.

I would like to thank Prof. Dr. Ilme Schlichting for giving me the chance to work in her department, for her support and for being my first referee.
Dr. Thomas Barends is thanked for reviewing this thesis and to be my second referee.

I would like to thank the entire staff of the department of Biomolecular Mechanisms (BMM) for their continuous support and the nice atmosphere. I particularly would like to acknowledge:

- Melanie Müller for performing protein mass spectrometric analyses
- Ulrike "Ulli" Mersdorf for preparing all of the great negative stain electron micrographs of HDH
- Sabine Zimmermann for excellent technical supportand as well as for her advice on work related problems.
- Dr. Andreas Dietl for productive discussions, practical support and for carefully correcting the manuscript
- Josephine Bock (B.Sc.) who worked as a lab rotation student on the characterization of Kustc0562
- Chris Roome and the IT group for excellent hard- and software support
- Martina Blochmann for her continous support regarding all administrative issues.
- The staff of the cleaning and media kitchens who provided us with cleaned glassware and cell culture media

For X-ray data collection I am grateful to the SLS-team of the MPI for Medical Research as well as the staff at the Swiss Light Source. Ingrid Vetter (MPI Dortmund) is greatly acknowledged for providing us with crystallographic analysis software.

Dr. Kristian Parey and Simone Prinz (MPI of Biophysics, Frankfurt/Main, Germany) are grately acknowledged for preparing cryo-EM samples, image acquisitions and structure determination of HDH. Dr. Thomas Hackl (now at MIT Boston, MA, USA) is thanked for his help with mapping *Kuenenia stuttgartiensis* transcriptome data. I am grateful to Manuel Oehlke from the Abwasserzweckverband Heidelberg for providing us with DEMON® granular sludge.

I especially like to thank the people of our collaborating group at the Microbiology Department at Radboud Universiteit, Nijmegen, the Netherlands and its head Prof. Dr. Mike S. M. Jetten for providing us with protein preparations from *Kuenenia stuttgartiensis* and discussing our scientific results. In particular, these are Dr. Joachim Reimann, who purified *Ks*HDH and *Ks*NaxLS, as well as Dr. Wouter Maalcke, Dr. Christina Ferousi, Dr. Naomi de Almeida, Dr. Laura van Niftrik, Dr. Jan Keltjens, Dr. Huub Op den Camp and Dr. Boran Kartal.

I would like to thank all former and present members of the BMM department for providing a pleasant and productive atmosphere at the institute, for discussing ideas and problems and for sharing knowledge and materials in the lab. In addition to the people mentioned above I would also like to thank Madeleine, Felix, Jule, Egle, Iris, Gabriela, Mirek, Andrea, Matthias, Kristina, Tiia, Veronika, Alexa, Elisabeth, Sabine, Kazuhiro, Clara, Kerstin, Karol, Martine, Sarah, Monica, Sophie, Alexander Gorel, Alexander Christiansen, Marie, Miriam, Susanne, Ali, Bruce, Abdul, Tatiana, Diana, Bob, Toni, Rob, Max, Jochen and Jolanta.

I am grateful to all the teachers in my life who guided me through the journey so far.
My special thanks are to my parents, brothers and my sister who always encouraged me and supported me during my life. I would like to thank all my friends in Heidelberg and around the World who played a significant part in my life. Finally, I especially thank my wife for being a great life partner and being present in all situations.

Conference presentations and posters

Poster: “A unique heterodimeric cytochrome c complex
from the anammox bacterium *Kuenenia stuttgartiensis*“
Annual Conference of the Association for General and Applied Microbiology (VAAM),
Marburg, Germany, 01.–04. Mar 2015

Poster: “A unique heterodimeric cytochrome c complex
from the anammox bacterium *Kuenenia stuttgartiensis*”
66. Mosbacher Kolloquium der Gesellschaft für Biochemie und Molekularbiologie,
Mosbach, Germany, 26.–28. Mar 2015

Poster: “Towards the Structure of an Anammox Nitrite Oxidase Complex“
Annual Conference of the Association for General and Applied Microbiology (VAAM),
Jena, Germany, 13.–16. Mar 2016

Poster: “A unique heterodimeric cytochrome c complex
from the anammox bacterium *Kuenenia stuttgartiensis*”
13th European Biological Inorganic Chemistry Conference (EuroBIC 13),
Budapest, Hungary, 28. Aug – 01. Sep 2016

Poster: “Straightforward Purification of Anammox Proteins from Granular Sludge“
Annual Conference of the Association for General and Applied Microbiology (VAAM),
Würzburg, Germany, 05.–08. Mar 2017

Short talk: “Structure of the 1.7 MDa Hydrazine Dehydrogenase Complex
from Anammox Bacteria“
Annual Conference of the Association for General and Applied Microbiology (VAAM),
Wolfsburg, Germany, 15.–18. Apr 2018

Publications

Tahseen Q., Akram M., Mustaqim M., Ahlawat S., 2014. Descriptions of *Pelodera scrofulata sp. nov*. and *Pelodera aligarhensis sp. nov.* (Nematoda: Rhabditidae) with supplementary information on *Pelodera teres* (Schneider, 1866). *Journal of Natural History* **48** (17-18): 1027–1053.

Abstract

Anaerobic **amm**onium **ox**idation (anammox) is a microbial process in the Earth's nitrogen cycle with both major ecological and technical significance. The anammox process is carried out by unique, slowly growing bacteria belonging to the phylum of *Planctomycetes*. These bacteria are indeed estimated to contribute to almost 50 % of dinitrogen (N_2) release from the oceans into the atmosphere (Arrigo 2005; Lam 2011) and are increasingly being applied in environmentally friendly waste water treatment procedures. The cells of anammox bacteria are characterized by the presence of a large intracellular compartment called "anammoxosome" which is the location of their unique metabolic pathway. Anammox bacteria use the oxidation power of nitrite (NO_2^-) to anaerobically oxidize ammonium (NH_4^+) to dinitrogen gas and water *via* two highly unusual intermediates namely nitric oxide (NO) and hydrazine (N_2H_4). The final step of this metabolic pathway, the oxidation of hydrazine to N_2, is catalyzed by an octaheme c-type cytochrome called hydrazine dehydrogenase (HDH). The electron transport between the various enzyme complexes involved in this metabolism is believed to be carried out by small c-type cytochromes, numerously present in anammox bacteria.

In this thesis work, the molecular structures of HDH and several small c-type cytochromes were determined by X-ray crystallography in order to elucidate their mechanism of action. Moreover, these proteins were also characterized by various biophysical and biochemical methods.

The first part of this work (chapter 3) describes the investigation of hydrazine dehydrogenase (HDH). This enzyme is related to octaheme hydroxylamine oxidoreductases (HAO) and forms covalently crosslinked trimers (α_3) which were previously shown to associate into higher oligomers in solution namely 24mers $(\alpha_3)_8$ and 30mers $(\alpha_3)_{10}$ with molecular masses of 1.6 and 2.0 MDa, respectively (Maalcke 2016). In the current study, the crystal structure of a 24meric hydrazine dehydrogenase complex purified from the anammox organism *Kuenenia stuttgartiensis* (*Ks*HDH) was determined at 2.8 Å resolution. This intriguing complex is composed of eight conically shaped HDH trimers that are positioned at the corners of a cube pointing their apexes outwards. This assembly enables the interaction of 24 c-type hemes from each trimer to form an astonishing network of 192 hemes. In addition, 12 molecules of an unanticipated ~10 kDa protein identified as the gene product of kustc1130 were found at each edge of the cubic assembly between two neighboring HDH trimers. This complex has an overall molecular mass of 1.7 MDa.

Interestingly, an additional covalent crosslink between a conserved cysteine residue and the active site heme P460 was discovered which might contributed to the specificity of HDH towards hydrazine. This work was complemented by structural studies of both 24mer and 30mer HDH assemblies by cryo-electron microscopy (cryo-EM) by Dr. Kristian Parey. The *Ks*HDH 24mer crystal structure could be well superimposed with the molecular model of an HDH 24mer determined by cryo-EM, which was, however, lacking the small binding partner protein Kustc1130. Various biophysical methods showed that oligomerization of HDH trimers to both 24mers and 30mers was promoted at high ionic strength (>100 mM). Moreover, the presence of Kustc1130 preferably induced the formation of the 24mer assembly independent of ionic strength. HDH was found to be most active with its binding partner at 100-150 mM ionic strength. Therefore, it can be proposed that the 24mer HDH assembly with 12 molecules of its binding partner is the physiologically relevant oligomeric state of HDH.

The next part (chapter 4) describes the investigation of small c-type cytochromes namely the *Ks*NaxLS complex and the monoheme cytochrome c Kustc0563 and its paralogue Kustc0562. *Ks*NaxL and *Ks*NaxS are the gene products of kusta0087 and kusta0088, respectively, and were purified as a stable complex from *K. stuttgartiensis*. The X-ray structure of the *Ks*NaxLS complex was determined at 1.7 Å resolution and showed a single heterodimeric assembly in the asymmetric unit. The molecular model of *Ks*NaxL shows a four-helix bundle fold typical for class II cytochromes c, whereas *Ks*NaxS displays a typical class I cytochrome c structure. Importantly, *Ks*NaxLS represents the first structure of a complex between class I and II monoheme c-type cytochromes. The heme iron in each subunit is coordinated by a rare cysteine ligand at its distal side. Biophysical investigations of *Ks*NaxLS resulted in a molecular mass of approximately 24 kDa which is consistent with a heterodimer in solution. Moreover, the complex could be reconstituted *in vitro* from its individual subunits that were heterologously expressed in *Shewanella oneidensis* MR-1. UV-Vis spectroscopy revealed that the complex and its components possess a Soret band maximum at around 420 nm showing a unique blue shift upon reduction. Further UV-Vis spectroscopic analyses indicated binding of nitric oxide (NO) and carbon monoxide (CO) to the hemes in the *Ks*NaxLS complex and its individual subunits. The obtained spectroscopic features match with those of CO-sensing as well as NO-scavenging and -shuttling hemoproteins. Finally, a pull-down assay indicated that *Ks*NaxLS might interact with the hydrazine synthase (HZS) complex. Based on these results, one can propose a role of

*Ks*NaxLS as an NO-scavenger which binds free nitric oxide in the anammoxosome which would otherwise inhibit the activity of HDH. In addition, NaxLS might shuttle NO to HZS which uses this compound as a substrate.

The highly expressed class I monoheme c-type cytochrome Kustc0563 was the very first protein purified from the anammox bacterium *K. stuttgartiensis* (Cirpus 2005). In this study, the X-ray structure of heterologously expressed Kustc0563 was determined at 1.9 Å resolution. Biochemical studies showed that this protein can act as redox partner in hydroxylamine oxidation assays by hydroxylamine oxidase (HOX) and also in hydrazine oxidation by HDH. Interestingly, hydroxylamine oxidation activity was 6-7 times higher with Kustc0563 than with bovine cytochrome c as redox partner. On the contrary, Kustc0562, a paralogue of Kustc0563 possessing a similar redox potential, did not show redox activity with HOX, but displayed comparable activity to Kustc0563 in assays with HDH. Although the 3.3 Å resolution crystal structure of Kustc0562 was highly similar to Kustc0563, it revealed highly diverse surface electrostatics which might explain the different redox activities of the two proteins.

Eventually, chapter 5 describes the purification and characterization of anammox proteins from granular sludge collected from a DEamMONification (DEMON®) reactor at a local waste water treatment plant. Phylogenetic analyses showed that the sampled biomass contained *Brocadia fulgida* as the sole representative anammox species. In addition, aerobic ammonium-oxidizing bacteria (AOB), represented by the genus *Nitrosomonas* could also be detected. Key metabolic enzymes from the anammox bacterium *B. fulgida* such as HZS, HDH as well as HOX could be purified from the biomass using anion exchange-, hydroxyapatite- and gel filtration chromatography. The identity of the isolated proteins was confirmed by mass spectrometry. All purified proteins showed characteristic UV-Vis spectra in their as-isolated, reduced and substrate-bound states. HDH and HOX were shown to be optimally active and were of sufficient quality for crystallization. Finally, the 3.0 Å resolution X-ray structure of *B. fulgida* HOX was determined which shows high similarity to *K. stuttgartiensis* HOX. This work proves the possibility of using granular sludge from large scale anammox reactors at waste water treatment plants as a convenient source for the purification of anammox proteins as well as their biochemical, biophysical and structural characterization.

Zusammenfassung

Die **an**aerobe **Amm**onium**ox**idation (Anammox) ist ein mikrobieller Prozess im Stickstoffkreislauf der Erde von sowohl großer ökologischer als auch technischer Bedeutung. Der Anammox-Prozess wird von einzigartigen, langsam wachsenden Bakterien durchgeführt, die zum Stamm der *Planctomyceten* gehören. Diese Bakterien tragen tatsächlich zu geschätzten ca. 50 % des aus den Ozeanen in die Atmosphäre freigesetzten Distickstoffs (N_2) bei (Arrigo 2005; Lam 2011) und werden zunehmend in umweltfreundlichen Abwasserbehandlungsverfahren angewendet. Die Zellen von Anammox-Bakterien sind durch das Vorhandensein eines großen intrazellulären Kompartiments gekennzeichnet, das "Anammoxosom" genannt wird, welches der Ort ihres einzigartigen Stoffwechselweges ist. Anammox-Bakterien nutzen die Oxidationskraft von Nitrit (NO_2^-) zur anaeroben Oxidation von Ammonium (NH_4^+) zu Distickstoffgas und Wasser über zwei sehr ungewöhnliche Zwischenprodukte, nämlich Stickstoffmonoxid (NO) und Hydrazin (N_2H_4). Der letzte Schritt dieses Stoffwechselweges, die Oxidation von Hydrazin zu N_2, wird durch ein Octahäm C-typ Cytochrom, der Hydrazin-Dehydrogenase (HDH), katalysiert. Es wird angenommen, dass der Elektronentransport zwischen den verschiedenen Enzymkomplexen, die an diesem Metabolismus beteiligt sind, durch kleine C-typ Cytochrome ausgeführt wird, welche zahlreich in Anammox-Bakterien vorhanden sind.

In dieser Arbeit wurden die molekularen Strukturen von HDH und einigen kleinen C-typ Cytochromen mittels Röntgenkristallographie untersucht, um deren Wirkmechanismus aufzuklären. Darüber hinaus wurden diese Proteine auch durch verschiedene biophysikalische und biochemische Methoden charakterisiert.

Der erste Teil dieser Arbeit (Kapitel 3) beschreibt die Untersuchung der Hydrazin-Dehydrogenase (HDH). Dieses Enzym ist verwandt mit Octahäm Hydroxylamin-Oxidoreduktasen (HAO) und bildet kovalent verknüpfte Trimere (α_3), von denen zuvor gezeigt wurde, dass sie in Lösung zu höheren Oligomeren assoziieren, nämlich 24meren $(\alpha_3)_8$ und 30meren $(\alpha_3)_{10}$ mit Molekularmassen von 1.6 bzw. 2.0 MDa (Maalcke 2016). In der vorliegenden Arbeit wurde die Kristallstruktur eines 24meren Hydrazin-Dehydrogenase-Komplexes aus dem Anammox-Organismus *Kuenenia stuttgartiensis* (*Ks*HDH) mit einer Auflösung von 2.8 Å bestimmt. Dieser faszinierende Komplex besteht aus acht konisch geformten HDH-Trimern, die an den Ecken eines Würfels positioniert sind und ihre Spitzen nach außen zeigen. Diese Anordnung ermöglicht die Wechselwirkung von 24 C-typ Häm Kofaktoren von jedem Trimer, um ein erstaunliches Netzwerk von 192 Häm Molekülen zu

bilden. Zusätzlich wurden 12 Moleküle eines unerwarteten ~10 kDa Proteins gefunden, welches als das Genprodukt von kustc1130 identifiziert wurde, und sich an jeder Kante der kubischen Anordnung zwischen zwei benachbarten HDH Trimeren befindet. Dieser Komplex hat eine Gesamtmolekularmasse von 1.7 MDa. Interessanterweise wurde eine zusätzliche kovalente Verknüpfung zwischen einem konservierten Cysteinrest und dem P460 Häm im aktiven Zentrum entdeckt, welche die Spezifität von HDH gegenüber Hydrazin erklären könnte. Diese Arbeit wurde durch Strukturuntersuchungen von 24meren und 30meren HDH-Anordnungen durch Kryo-Elektronenmikroskopie (Kryo-EM) ergänzt. Die Kristallstruktur des *Ks*HDH 24mers konnte gut mit dem molekularen Modell des HDH 24mers überlagert werden, das durch Kryo-EM bestimmt wurde. Letzterem fehlte jedoch das kleine Bindungspartnerprotein Kustc1130. Verschiedene biophysikalische Methoden zeigten, dass die Oligomerisierung von HDH-Trimeren zu 24meren als auch zu 30meren bei hoher Ionenstärke (> 100 mM) gefördert wurde. Darüber hinaus induzierte die Anwesenheit von Kustc1130 vorzugsweise die Bildung der 24mer-Anordnung unabhängig von der Ionenstärke. HDH erwies sich als am aktivsten zusammen mit seinem Bindungspartner bei 100-150 mM Ionenstärke. Man kann daher vorschlagen, dass die 24mere HDH-Anordnung mit 12 Molekülen seines Bindungspartners der physiologisch relevante oligomere Zustand von HDH ist.

Der nächste Teil (Kapitel 4) beschreibt die Untersuchung von kleinen C-typ Cytochromen, nämlich des *Ks*NaxLS-Komplexes und des Monohäm-Cytochroms c Kustc0563 und seines Paralogs Kustc0562. *Ks*NaxL und *Ks*NaxS sind die Genprodukte von kusta0087 bzw. kusta0088 und wurden als ein stabiler Komplex aus *K. stuttgartiensis* gereinigt. Die Röntgenstruktur des *Ks*NaxLS-Komplexes wurde mit einer Auflösung von 1.7 Å bestimmt und zeigt ein einzelnes Heterodimer in der asymmetrischen Einheit. Das molekulare Modell von *Ks*NaxL zeigt eine für Cytochrome der Klasse II typische Vier-Helix-Bündelfaltung, während *Ks*NaxS eine typische Cytochrom-c-Struktur der Klasse I aufweist. *Ks*NaxLS stellt bedeutender Weise die erste Struktur eines Komplexes zwischen Monohäm C-Typ Cytochromen der Klassen I und II dar. In jeder Untereinheit wird das Häm-Eisen von einem seltenen Cysteinliganden an seiner distalen Seite koordiniert. Biophysikalische Untersuchungen von *Ks*NaxLS ergaben eine Molekülmasse von ca. 24 kDa, was mit einem Heterodimer in Lösung übereinstimmt. Darüber hinaus konnte der Komplex *in vitro* aus seinen individuellen Untereinheiten, die in *Shewanella oneidensis* MR-1 heterolog exprimiert wurden, rekonstituiert werden.

UV-Vis-Spektroskopie zeigte, dass der Komplex und seine Komponenten ein Maximum der Soret-Bande bei etwa 420 nm aufweisen, welche bei Reduktion eine einzigartige Blauverschiebung zeigte. Weitere UV-Vis-spektroskopische Analysen zeigten eine Bindung von Stickstoffmonoxid (NO) und Kohlenmonoxid (CO) an die Häm-Kofaktoren im *Ks*NaxLS-Komplex und seinen einzelnen Untereinheiten. Die erhaltenen spektroskopischen Merkmale stimmen mit denen von CO-detektierenden sowie NO-bindenden und NO-transportierenden Hämoproteinen überein. Schließlich zeigte ein Pull-down-Assay, dass *Ks*NaxLS mit dem Hydrazinsynthase (HZS)-Komplex interagieren könnte. Basierend auf diesen Ergebnissen kann man eine Rolle von *Ks*NaxLS als NO-Scavanger vorschlagen, der freies Stickstoffmonoxid im Anammoxosom bindet, das ansonsten die Aktivität von HDH inhibieren würde. Zusätzlich könnte NaxLS NO zu HZS transportieren, welches diese Verbindung als ein Substrat verwendet.

Das stark exprimierte Klasse-I Monohäm-Cytochrom Kustc0563 war das allererste Protein, das aus dem Anammox-Bakterium *K. stuttgartiensis* gereinigt wurde (Cirpus 2005). In dieser Studie wurde die Röntgenstruktur von Kustc0563 mit einer Auflösung von 1.9 Å bestimmt. Biochemische Studien haben gezeigt, dass dieses Protein als Redoxpartner in Hydroxylaminoxidationsassays durch Hydroxylaminoxidase (HOX) und auch in der Hydrazinoxidation durch HDH fungieren kann. Interessanterweise war die Hydroxylamin-oxidationsaktivität mit Kustc0563 6-7 mal höher als mit Rindercytochrom c als Redoxpartner. Im Gegensatz dazu zeigte Kustc0562, ein Paralog von Kustc0563, das ein ähnliches Redoxpotential besitzt, keine Redoxaktivität mit HOX, wies aber in Tests mit HDH eine vergleichbare Aktivität wie Kustc0563 auf. Obwohl die Kristallstruktur von Kustc0562 bei 3.3 Å Auflösung große Ähnlichkeit mit Kustc0563 aufweist, zeigt sie eine sehr unterschiedliche elektrostatische Oberfläche, welche die unterschiedlichen Redoxaktivitäten der beiden Proteine erklären könnte.

Schließlich beschreibt Kapitel 5 die Reinigung und Charakterisierung von Anammox-Proteinen aus granulösem Schlamm, welcher aus einem DEamMONifikations (DEMON®) Reaktor einer lokalen Kläranlage erhalten wurde. Phylogenetische Analysen zeigten, dass die Biomasseprobe *Brocadia fulgida* als einzige repräsentative Anammox-Spezies enthielt. Zusätzlich konnten aerobe Ammonium-oxidierende Bakterien (AOB), repräsentiert durch die Gattung *Nitrosomonas*, nachgewiesen werden. Wichtige Stoffwechselenzyme aus dem Anammox-Bakterium *B. fulgida* wie HZS, HDH sowie HOX konnten mittels Anionenaustausch-, Hydroxylapatit- und Gelfiltrationschromatographie aus der Biomasse

gereinigt werden. Die Identität der isolierten Proteine wurde durch Massenspektrometrie bestätigt. Alle gereinigten Proteine zeigten charakteristische UV-Vis-Spektren in ihren isolierten, reduzierten und substratgebundenen Zuständen. HDH und HOX erwiesen sich als optimal aktiv und waren von ausreichender Qualität für ihre Kristallisation. Schließlich wurde die Röntgenstruktur von *B. fulgida* HOX bei 3.0 Å Auflösung bestimmt, welche eine hohe Ähnlichkeit mit *K. stuttgartiensis* HOX aufweist. Diese Arbeit beweist, dass granulöser Schlamm von Anammox-Großreaktoren aus Kläranlagen eine geeignete Quelle für die Reinigung von Anammox-Proteinen sowie deren biochemische, biophysikalische und strukturelle Charakterisierung darstellt.

Chapter 1

Introduction

1. Introduction

1.1 The Biogeochemical Nitrogen Cycle

The chemical element nitrogen is an important building block of essential biological macromolecules such as proteins and nucleic acids. Although it is highly abundant in the Earth's atmosphere (~78 %), the strong N≡N triple bond makes molecular nitrogen (N_2) highly inert such that it is unavailable for living systems (Holleman 2007). However, more reactive nitrogen species such as ammonium (NH_4^+), nitrite (NO_2^-) or nitrate (NO_3^-) can easily be assimilated by organisms. In a process called "nitrogen fixation" N_2 is converted to ammonium. This is the starting point of the so-called "nitrogen cycle" which includes oxidative reactions of ammonium towards more oxidized N-species (NO_2^- , NO_3^- and N_2O) as well as their back reaction into N_2 (Fig 1.1). These chemical conversions are primarily carried out by microorganisms which gain energy for their metabolism from them. In addition to these biological processes, geological activities such as volcanic release of nitrogen dissolved in the Earth's mantle or atmospheric nitrogen fixation by lightning contribute marginally. Nowadays, the Haber-Bosch process and other anthropogenic activities contribute to about ~45 % of the total nitrogen fixation on Earth (Canfield 2010).

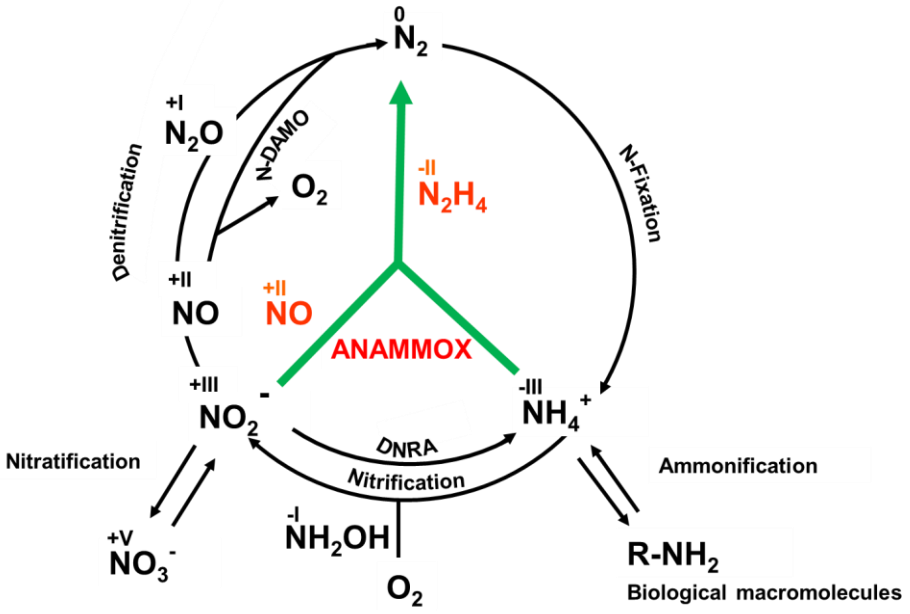

Figure 1.1 Representation of the nitrogen cycle
Nitrogen cycles through different chemical species with their oxidation states being indicated in roman numerals. DNRA: dissimilatory nitrite/nitrate reduction to ammonium, N-DAMO: nitrite-driven anaerobic methane oxidation, Anammox: anaerobic ammonium oxidation.

Since nitrogen in its compounds exists in a large variety of oxidation states (-III to +V), there is a great diversity of microorganisms dealing with these distinct chemicals species. The N-cycle consists of three major anabolic steps namely nitrogen fixation, ammonium assimilation and assimilatory nitrate reduction as well as seven catabolic processes which are nitrification, nitratification, denitrification, dissimilatory nitrate/nitrite reduction to ammonium (DNRA), nitrite-driven anaerobic methane oxidation (N-DAMO), anaerobic ammonium oxidation (anammox) and ammonification. All these steps can be performed by designated bacteria (Jetten 2009). Although the individual processes of the nitrogen cycle have been studied for more than 100 years, even today this topic remains interesting with surprising discoveries being made regularly. This is mainly due to recent advances in molecular biology tools which have enabled the identification of further microbial players in the N-cycle that would otherwise be difficult and sometimes even impossible to detect using classical culture-based methods. Such new findings include aerobic ammonium-oxidizing archaea (AOA) that were found in both marine (Könneke 2005) and terrestrial ecosystems (Tourna 2011; Stieglmeier 2014) as well as nitrite-driven anaerobic methane oxidation (N-DAMO) (Ettwig 2008; Ettwig 2010) and ammonium oxidation coupled to iron (III) reduction ("feammox") (Sawayama 2006; Yang 2012). Fairly recently, members of the genus *Nitrospira* were discovered which can oxidize ammonium *via* hydroxylamine and nitrite directly to nitrate, a process termed as "complete ammonia oxidation" or "comammox" (van Kessel 2015; Daims 2015). They connect nitrification and nitrite oxidation that are otherwise commonly found in two separate groups of bacteria in one organism.

1.2 Anaerobic Ammonium Oxidation (Anammox)

Already in 1932, during anaerobic fermentation of sediments from Lake Mendota (Wisconsin, USA) the generation of unusually high amounts of dinitrogen gas (N_2) was reported that could not be explained (Allgeier 1932). In 1965, Richards reported the disappearance of ammonium during anaerobic remineralization of organic matter, which could not be accounted by known denitrifier activity (Richards 1965). As there was no explanation for this loss based on known biological processes of ammonium oxidation, this field saw very little attention. However, four decades ago Engelbert Broda predicted two kinds of missing autotrophs in nature based on thermodynamic calculations (Broda 1977). These included chemolithotrophic anaerobic ammonium oxidizers which produce N_2 using nitrate (NO_3^-) or nitrite (NO_2^-) as the oxidant. In the early 1990s, Arnold Mulder made similar observations as had been done by Richards. In their anoxic denitrifying pilot reactor, ammonium disappeared at the expense of nitrate to

produce dinitrogen gas. Even before understanding the mechanism of this process people already realized its applications in removal of unwanted ammonium from waste water. Therefore, Mulder made no delay in filing a patent (Mulder 1992). Further experimental studies provided further evidence for this anaerobic ammonium oxidation ("anammox", (Mulder 1995) and that it is indeed a microbial process (van de Graaf 1995). Isotopic labeling experiments with $^{15}NH_4^+$ in combination with $^{14}NO_3^-$ showed that $^{14\text{-}15}N_2$ was the dominant product making up to 98.2 % of total labeled N_2 (van de Graaf 1995). Later, mass balance studies confirmed that the responsible microorganisms use the oxidizing power of NO_2^- for ammonium oxidation rather than NO_3^- (van de Graaf 1996) (Figure 1.1, eq.1.1).

$$NO_2^- + NH_4^+ \longrightarrow N_2 + 2\,H_2O \qquad \Delta_rG_m° = -357\ kJ/mol \quad (eq.\ 1.1)$$

The basal medium included ammonium and nitrite, bicarbonate as sole carbon source, minerals and trace metals to support essential cellular functions and the cultures were sparged with argon to maintain anaerobicity (van de Graaf 1996). Under these conditions, an activity of 2.4 kg N $m^{-3}day^{-1}$ was achieved. Continuous bioreactor-based culture techniques allowed the enrichment of anammox bacteria (Strous 1998) and the first anammox species "*Candidatus* Brocadia anammoxidans" was finally identified (Strous 1999) as a member of the eubacterial phylum *Planctomycetes.* Anammox bacteria grow very slowly with generation times of 1-3 weeks (Strous 1999) such that growing them in pure cultures has failed so far (therefore anammox species still possess the status of a "*Candidatus*"). Anammox turned out to be crucial in understanding the global nitrogen cycle since it is estimated to contribute to almost 50 % of dinitrogen production from the oceans (Arrigo 2005; Lam 2011).

Recent times have seen the anammox process being applied in waste water treatment as a cost effective and environmentally friendly alternative to conventional nitrogen removal systems (Kartal 2010; Ali 2015a). Many species of anammox bacteria have been enriched from waste water treatment plants (WWTPs) such as *Ca.* Scalindua brodae, *Ca.* S. wagneri (Schmid 2003), *Ca.* B. fulgida (Kartal 2008), *Ca.* Brocadia caroliniensis (Park 2017) and *Ca.* B. sinica (Oshiki 2011). In waste water treatment processes nitrification and anammox are combined either in two-reactor systems *e.g.* the **S**ingle reactor system for **H**igh activity **A**mmonium **R**emoval **O**ver **N**itrite (SHARON)-ANAMMOX® (van Dongen 2001) or one-reactor systems such as the **C**ompletely **A**utotrophic **N**itrogen removal **O**ver **N**itrite process (CANON®; (Third 2001)), **S**ingle stage **N**itrogen removal using **A**nammox and **P**artial nitritation (SNAP®;(Furukawa 2006)) or **DE**am**MON**ification (DEMON®; (Wett 2006)).

1.3 Habitats and Phylogeny of Anammox Bacteria

The enrichment and characterization of the first anammox bacteria enabled the design of molecular biological tools to detect these organisms in their natural habitats (Neef 1998; Schmid 2001; Schmid 2005). Based on 16S rRNA gene detection or anammox-specific molecular markers, anammox bacteria were found in virtually all possible environments. So far six genera of anammox bacteria have been identified. All of them still hold the title "*Candidatus"* as they have not been obtained in pure culture. These include "*Ca.* Kuenenia" (Schmid 2000), "*Ca.* Brocadia" (Kartal 2008; Strous 1999), "*Ca.* Anammoxoglobus" (Kartal 2007b), "*Ca.* Jettenia" (Quan 2008), "*Ca.* Scalindua" (Schmid 2003; Schmid 2007) and "*Ca.* Anammoximicrobium" (Khramenkov 2013). The species belonging to the genus *Ca.* Kuenenia, *Ca.* Brocadia and *Ca.* Jettenia were identified in sewage treatment plants (Strous 1999; Schmid 2000; Kartal 2008; Quan 2008; Oshiki 2011; Ali 2015b). Members of the genus *Ca*. Scalindua seem to occur in a wider range of habitats from marine to fresh water systems. These include *Ca.* Scalindua sorokinii in the Black Sea (Kuypers 2003) or *Ca.* Scalindua profunda which was discovered in the Swedish Gullmar fjord (van de Vossenberg 2008). Members of the genus *Scalindua* are also responsible for significant nitrogen losses in oxygen minimum zones at the Namibian (Kuypers 2005; Woebken 2007) and Peruvian coasts (Hamersley 2007). They were also reported in fresh water ecosystems such as the African Tanganyika Lake (Schubert 2006) and even permafrost soils (Penton 2006). Recent biodiversity analyses of different parts of Lake Superior (USA) indicated the presence of a wide range of unexplored fresh water anammox bacteria (Crowe 2017). Moreover, anammox bacteria are also present in extreme environments such as hydrothermal vents (Byrne 2009), hot springs (Jaeschke 2009), cold seeps (Russ 2013) and marine hypersaline basins (Borin 2013). Such a broad diversity of habitats raises the question how anammox bacteria can adapt to such divers environments while keeping their central energy metabolism intact.

Currently, about nineteen named anammox species are known. But this number could be just the tip of the iceberg since more than 2,500 16S rRNA gene sequences from anammox bacteria have been deposited at Genbank (https://www.ncbi.nlm.nih.gov/genbank/). These might belong to different species, subspecies or strains representing a wide variety of specific ecological niches in different habitats (Kartal 2013).

Based on 16S rRNA gene sequence identity, the deposited anammox sequences are all assigned to the phylum of *Planctomycetes* (Fuerst 2011). *Planctomycetes* form a distinct phylum of the eubacterial domain of life (Figure 1.2 a). Unlike members from other bacterial phyla they possess several unusual features such as intracellular compartmentalization, the presence of a highly condensed nucleoid and reproduction *via* budding instead of binary fission (Fuerst 2011, 2013). Within the *Planctomycetes*, anammox bacteria form a deeply branched monophyletic clade (Fig 1.2 b). This phylogenetic position together with a wide range of physiological, cellular and molecular traits entitle anammox bacteria to be grouped into their own order *Brocadiales* (family *Brocadiaceae*) (Noel 2010) (Figure 1.2 b).

a

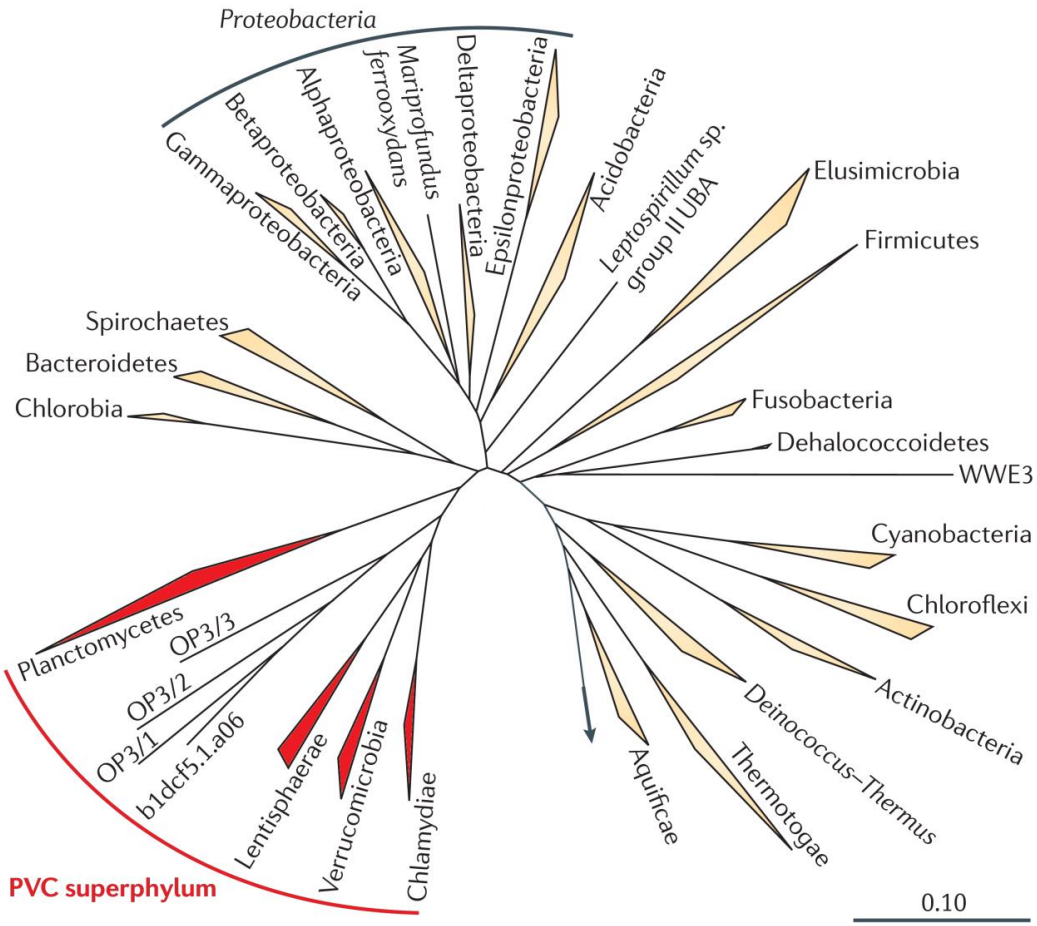

b

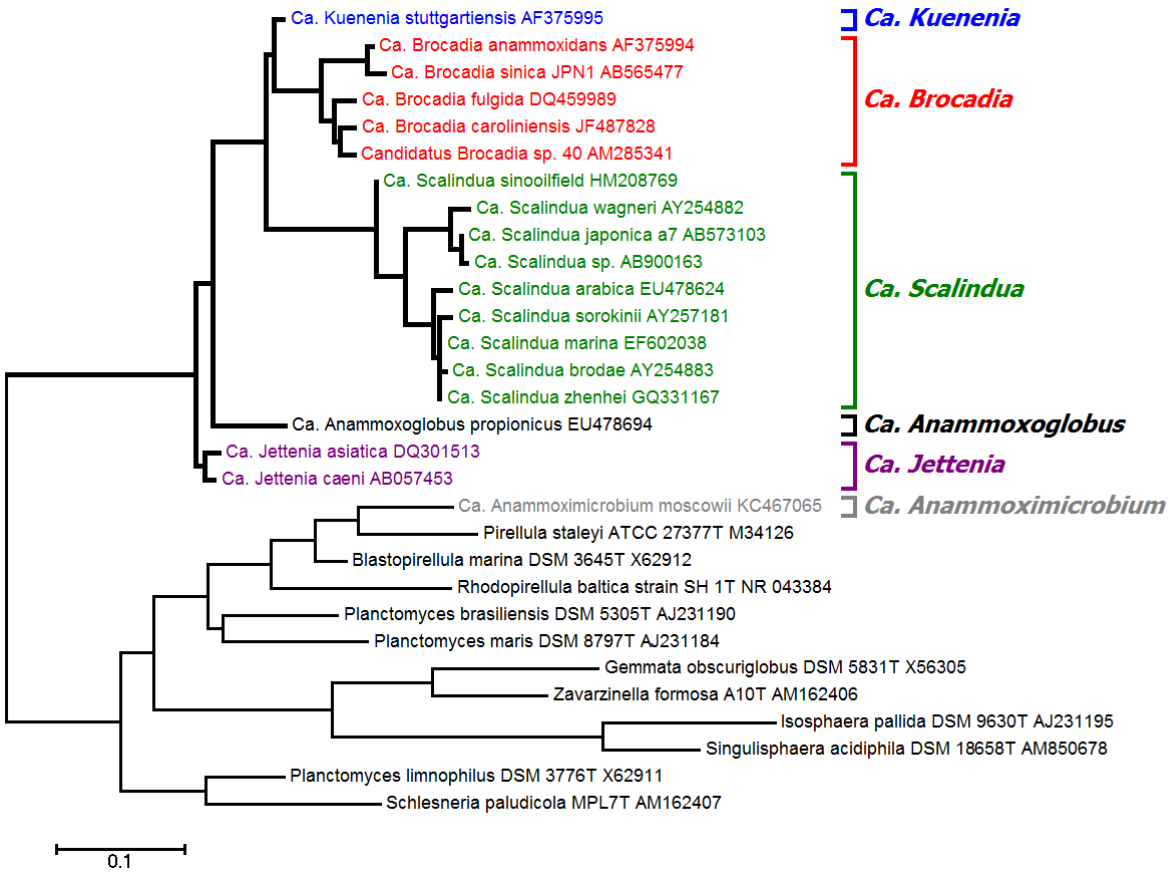

Figure 1.2 Phylogeny of anammox bacteria.
a) 23S ribosomal RNA gene tree showing the phylogenetic position of the *Planctomycetes* within the *Planctomycetes–Verrucomicrobia–Chlamydiae* (PVC) superphylum (shown in red) when compared with a selection of other bacterial phyla. The arrow next to the *Aquificae* indicates the outgroup *i.e.* the domains Archaea and Eukarya. The scale bar represents 0.1 substitutions per nucleotide position. Figure adapted from (Fuerst 2011).
b) 16S rRNA phylogenetic tree illustrating the relationships of different genera of anaerobic ammonium-oxidizing (anammox) bacteria within the *Planctomycetes*. Each species name is followed by the NCBI accession code of its 16S rDNA sequence. All genera of anammox bacteria (except *Anammoximicrobium*) cluster within the order of *Brocadiales* (Noel 2010) in the single family of the *Brocadiaceae* (branches shown in bold). The order of *Planctomycetales* with its single family *Planctomycetaceae* comprises the genera *Pirellula*, *Planctomyces*, *Isosphaera* and *Gemmata*. Figure adapted from (Dietl 2016).

1.4 Anammox Cell Biology

An intriguing hallmark of members belonging to the phylum *Planctomycetes* is their high degree of intracellular compartmentalization (Fuerst 2011, 2013). Moreover, the species *Gemmata obiscuriglobus* has been believed to possess a membrane-bound nucleoid (Sagulenko 2014) and to form endocytic vesicles that are able to internalize high molecular weight macromolecules such as proteins (Lonhienne 2010). Based on these observations, *Planctomycetes* have initially been considered as early evolutionary forms related to eukaryotes, justifying a distinct nomenclature of their cellular architecture (Fuerst 2011).

Several recent studies, however, took this into question and suggested that their cellular structure rather represents a variant of the Gram-negative bacterial cell plan. For instance, it has been found that *Planctomycetes* do possess an intact peptidoglycan layer (van Teeseling 2015; Jeske 2015) as well as an asymmetric outer membrane containing porin proteins and a lipid insertion complex (Speth 2012b; van Teeseling 2018) . Moreover, more advanced microscopy techniques revealed that invaginations of the cytoplasmic membrane were mistaken for endocytic vesicles in *Gemmata* (Boedeker 2017).

Based on these findings the cellular structure of *Planctomycetes* is now defined according to Gram-negative bacteria generally consisting of two compartments. The inner compartment, called "riboplasm" in the initial nomenclature, is the bacterial cytoplasm which is surrounded by the cytoplasmic membrane (previously known as "intracytoplasmic membrane"). The cytoplasm contains the bacterial genomic DNA appearing as a condensed nucleoid as well as the machinery for transcription and translation. The other compartment is the periplasm (previously known as "paryphoplasm") which contains a peptidoglycan layer and is surrounded by the outer membrane (previously denoted as "cytoplasmic membrane").

Unlike other *Planctomycetes*, anammox bacteria possess an additional very large compartment located inside of their cytoplasm, the so-called "anammoxosome", which is surrounded by the anammoxosomal membrane (Fig 1.3 a and b).

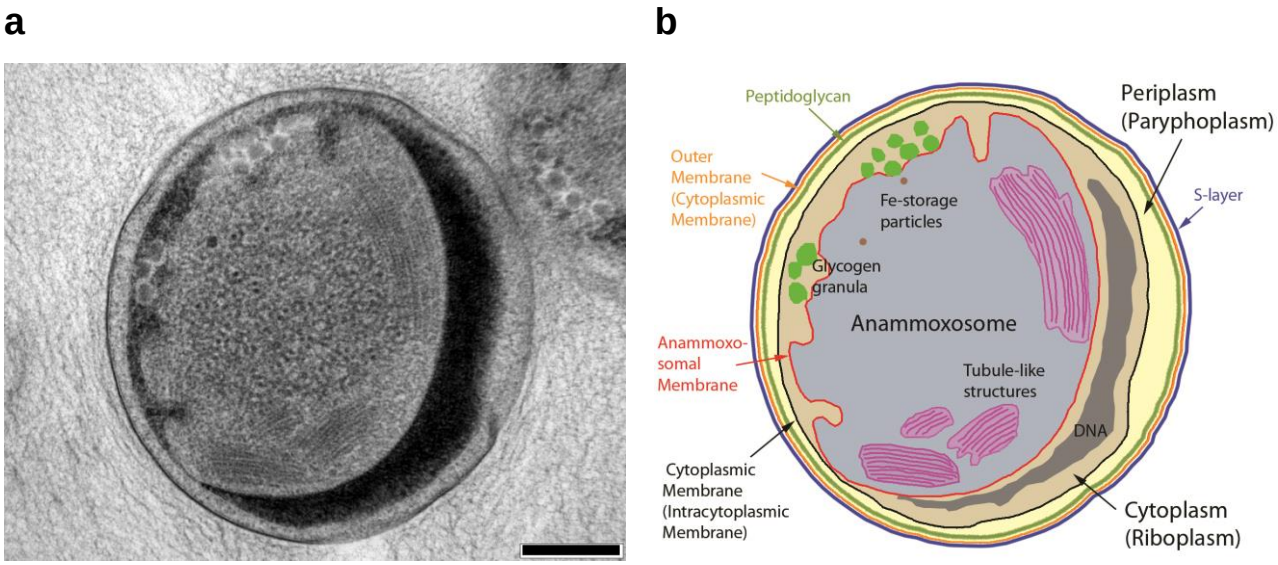

Figure 1.3 Overall Architecture of the Anammox Bacterial Cell
a) Transmission electron micrograph (TEM) of a section of a cryo-fixed, freeze-substituted and Epon-embedded "*Ca.* Kuenenia stuttgartiensis" cell. The scale bar is 200 nm. Image courtesy of Laura van Niftrik, Radboud University, Nijmegen. **b)** Schematic representation of the general cell architecture of an anammox cell based on the outline and inner structures observed in the TEM image in a). The names of cellular features according to the classical *Planctomycetes* cell concept are given in brackets in addition to the terms of the Gram-negative bacterial cell plan. The image is used with the permission of Andreas Dietl.

In the following, a detailed description of the anammox cell architecture from the outside to its inside is presented. Pili or flagella have not been observed in case of the genus *Kuenenia, Brocadia, Anammoxoglobus* (van Niftrik 2008a) and *Jettenia* (Ali 2015b). However, genes responsible for their formation are at least present in the genome of *K. stuttgartiensis* (Strous 2006). Interestingly, pili-like appendages were observed in some *Scalindua* species (van Niftrik 2008a; van de Vossenberg 2008) and possibly also flagella (Russ 2015). Therefore, it is quite possible that these cell appendages are expressed under certain environmental conditions (van Teeseling 2013).

In *K. stuttgartiensis,* the presence of a proteinaceous outer S-layer has been shown (van Teeseling 2014). This layer contains hexagonal units of a protein encoded by kustd1514 and was shown to be highly glycosylated *via O*-linkages (van Teeseling 2016). Pores of about 4 nm through the S-layer were reported which might enable free diffusion of small molecules. The distance between the S-layer and the underlying membrane was determined to be 10-15 nm. It seems that an S-layer is also present in *Brocadia sinica* as its genome encodes a Kustd1514 homolog (BROSI_A1236) with 44 % sequence identity (Oshiki 2015). However, a corresponding homologue is lacking in other known genera.

As mentioned before, the identity of a "true" Gram-negative bacterial outer membrane in *Planctomycetes* has been a matter of debate. Particularly in anammox bacteria, an F-type ATPase was detected in the outer membrane using immunogold labelling (van Niftrik 2010) which is usually absent in Gram-negative bacteria. Moreover, a putative cell division ring made up by the protein Kustd1438 was also seen at the outer membrane (van Niftrik 2009). In addition, the periplasm (initially called "paryphoplasm") was defined as a more cytoplasm-like compartment due to the presence of RNA (despite the absence of DNA and ribosomes) (Lindsay 2001) and the lack of c-type cytochromes (van Niftrik 2008b). Conversely, several outer membrane porins (OMPs) and a lipid insertion complex were detected in case of *Scalindua profunda* both at the genomic and proteomic level (Speth 2012b). In *K. stuttgartiensis*, the abundant 55 kDa protein Kustd1878 was co-purified with the S-layer protein (van Teeseling 2014). Recent results showed that Kustd1878, which was predicted to be a β-barrel OMP belonging to the alginate family, can act as a moderately cation-selective channel (van Teeseling 2018). Homologs of Kustd1878 were also detected in *Jettenia caeni* (Hira 2012), *B. sinica* (Oshiki 2015), *B. fulgida* (Ferousi 2013) and *S. brodae* (Speth 2012b). Moreover, a later study on the localization of F-type ATPases suggests that they are only present at the anammoxosomal membrane (Karlsson 2014), which is corroborated by previous sub-proteomic predictions (Medema 2010). As a result, it is now believed that the previously postulated "outer cytoplasmic membrane" could indeed be a true Gram-negative bacterial outer membrane.

For a long time the absence of a peptidoglycan layer in *Planctomycetes* was assumed due to the lack of muramic acid and their resistance against beta-lactam antibiotics (König 1984). However, more recently it was observed that penicillin G inhibits growth and lysozyme causes lysis of anammox cells which gave first hints for the presence of peptidoglycan (Hu 2013). Lately, the presence of all genes necessary for peptidoglycan synthesis has been shown. Moreover, biochemical and morphological studies (Jeske 2015; van Teeseling 2015) revealed 4.5-6 nm thick peptidoglycan layers.

As in other Gram-negative bacteria, the cytoplasm (previously called "riboplasm") contains the genomic DNA and ribosomes (Lindsay 2001). In addition, glycogen granules were found in this compartment (van Niftrik 2008b).

The anammoxosome is the biggest, innermost compartment in anammox cells which makes up 51-66 % of the total cell volume (van Niftrik 2008b). The anammoxosome membrane is highly curved but remains intact also during binary fission of the cell (van Niftrik 2008b; van Niftrik 2008c; van Niftrik 2009). Isolated anammoxosomes were shown to perform the anammox pathway independently (Neumann 2014). This fact ascertains the anammoxosome as a genuine bacterial organelle. C-type cytochromes have been shown to be localized at the inner face of the anammoxosomal membrane (van Niftrik 2008b). The enzymes that are central to the anammox pathway such as hydrazine synthase, hydrazine dehydrogenase and others were shown to be localized throughout the anammoxosome (Almeida 2015). Tubule-like structures associated with the nitrite:nitrate oxidoreductase (Nxr) were also observed (van Niftrik 2008c; Almeida 2015) along with electron-dense iron storage particles (van Niftrik 2008c). An F-type ATPase specifically located within the anammoxosome membrane (van Niftrik 2010), suggests that the organelle is responsible for energy conversion, providing ATP to metabolic reactions in the cytoplasm.

Another unique feature of anammox bacteria is the presence of unusual lipids called "ladderane lipids" in their membranes (Sinninghe Damsté 2002). These phopholipids consist of three to five fused cyclobutane rings which are linked to a glycerol backbone *via* both ester and ether bonds (Fig 1.4) within the same lipid molecule (Sinninghe Damsté 2004). Initially it was thought that ladderane lipids are only present in the anammoxosome membrane (Sinninghe Damsté 2002) but they were recently identified in the other membranes of the anammox cell, too (Neumann 2014). The exact role of ladderane lipids in the membranes of anammox bacteria and their biosynthesis is still unclear. Initially it was assumed that the densely packed membranes formed by these lipids (Sinninghe Damsté 2002; Boumann 2009a) might prevent the diffusion of toxic intermediates of the anammox metabolism (hydrazine and nitric oxide) as suggested by their impermeability to certain fluorophores (Sinninghe Damsté 2002). However, molecular dynamics simulations (Chaban 2014) as well as experiments on isolated anammoxosomes (Neumann 2014) showed that small molecules like hydrazine can indeed pass through such membranes. Other proposed functions of ladderane lipids are free-radical scavenging (Nouri 2012) or to prevent the dissipation of the proton gradient along the membrane. The latter proposal appears more likely since the anammox metabolism is slow and generates only a moderate proton gradient such that proton leakage would be detrimental.

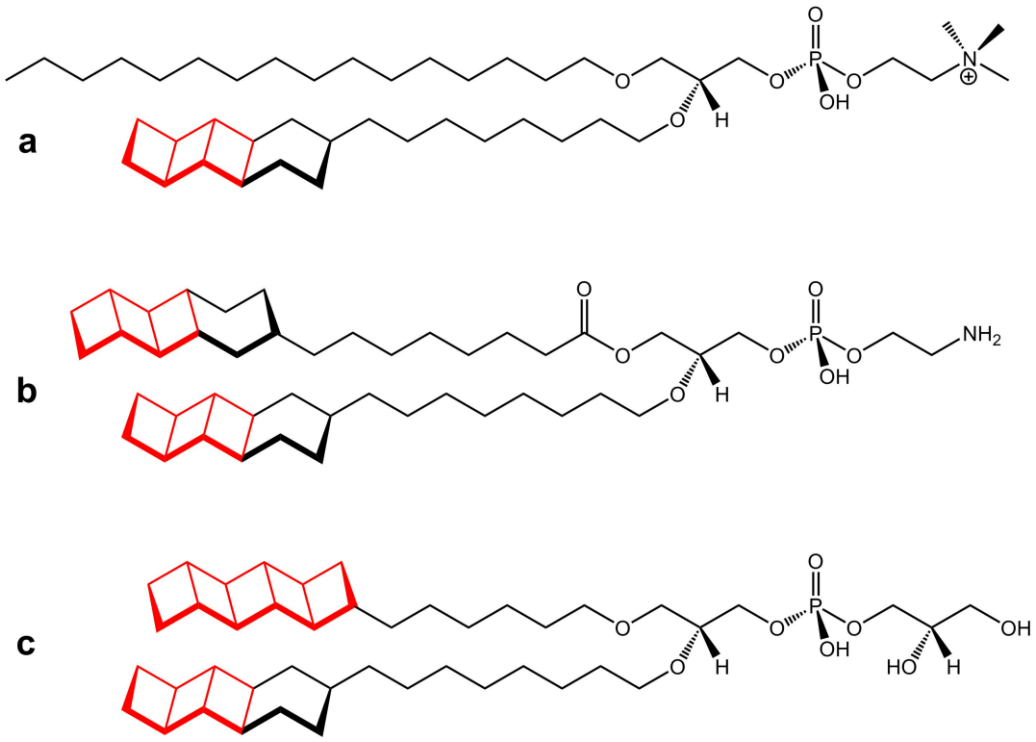

Figure 1.4 Few examples of ladderane lipids.
Several structural variants have been reported which are either ester- or ether-linked to a glycerol backbone. The ladderane moieties consist of three or five linearly fused cyclobutane rings (highlighted in red), forming pleated sheet-like structures that are designated as [3]- and [5]-ladderanes, respectively. [3]-ladderanes are fused to an additional cyclohexane ring. The ladderane moieties are connected *via* C_6- or C_8-alkyl chains to the glycerol backbone. Major polar headgroups of ladderane lipids are phosphoethanolamine (PE), phosphocholine (PC) and phosphoglycerol (PG). Figure adapted from (Boumann 2009b).
a) 1-hexadecanyl-2-(8-[3]-ladderane-octanyl)-*sn*-glycerophosphocholine
b) 1-(8-[3]-ladderane-octanoyl)-2-(8-[3]-ladderane-octanyl)-*sn*-glycerophosphoethanolamine
c) 1-(6-[5]-ladderane-hexanyl)-2-(8-[3]-ladderane-octanyl)-*sn*-glycero-3-phospho-(1′-*sn*-glycerol)

1.5 Anammox Genomes

The first anammox genome was obtained from the fresh water anammox bacterium *Ca.* Kuenenia stuttgartiensis (Strous 2006). Its 4.2 Mb genome comprises five contigs (from kust-a to kust-e). In total 4,663 open reading frames (ORFs) were annotated out of which only ~30 % were assigned to a function indicating that anammox bacteria possess a large genetic repertoire waiting to be unraveled. Later, it was found that the anammox reactor providing the sequenced genetic material indeed contained two slightly different *Kuenenia* strains (Speth 2012a). Most recently, the fully closed genome of the dominating strain MBR1 was deciphered using Single-Molecule Real-Time (SMRT) sequencing techniques (Frank 2018). These sequencing data also include the first genome-wide methylation profile from an anammox species.

So far, nine anammox genomes have been sequenced and we have already obtained several surprising insights into anammox biology from these information. In addition to the first *Kuenenia* genome, genomic data from *Brocadia fulgida* (Gori 2011; Ferousi 2013), *Scalindua profunda* (van de Vossenberg 2013), *Jettenia caeni* (previously called anammox strain KSU-1) (Hira 2012), *Brocadia sinica* (Oshiki 2015), *Scalindua brodae* (Speth 2015), *Brocadia* sp. 40 (Ali 2016), *Scalindua rubra* (Speth 2017) and *Scalindua japonica* (Oshiki 2017) are also available. Interestingly, there are unexpected differences in the genomes not only "among" but also "within" different genera. For example, in *S. profunda* out of the total 4,664 annotated ORFs only 693 genes had significant BLASTN hits with *K. stuttgartiensis* (van de Vossenberg 2013). BLASTP gave more results (2,016 hits), although the averaged identity of the ORFs was only 48.6 %. Moreover, 2,187 ORFs in the *K. stuttgartiensis* genome did not match with any ORF in the genome of *S. profunda* (reviewed by Kartal 2013). There are several examples to justify differences between genomes from different species belonging to the same genus. The genome size of *Brocadia* sp. 40, for instance, is 2.93 Mb (Ali 2016) which is significantly smaller than that of its close phylogenetic neighbour *Brocadia fulgida* (genome size 3.55 Mb), probably providing a growth advantage to *Brocadia* sp. 40 (Ali 2016; Kurokawa 2016).

Further indications of genetic hence physiological diversity within a single genus were established from comparative genome analyses between *S. japonica, S. rubra and S. profunda*, where it was shown that one third of the total genes present in *S. japonica* are not present in its two counterparts (Oshiki 2017). In fact, *S. rubra* has also been shown to share only 94 % of genome identity to *S. profunda* and *Scalindua brodae* (Speth 2017). One more intriguing feature unique to *S. rubra* is the presence of eleven gas vesicle forming genes (Speth 2017). It has been hypothesized that these gas vesicles may help the bacteria to position within the Red Sea brine-seawater interface (BSI) where the material used for metagenome sequencing was sampled. If the bacteria otherwise moved within the BSI they would suffer cellular stress from steep gradients in salinity or temperature. This example provides a clue of genetic versatility of these organisms in response to environmental conditions.

Several genes are dedicated particularly to energy metabolism. They redundantly code for key systems such as complex I, the bc_1 complex and ATP synthase. Altogether, in *K. stuttgartiensis*, for example, 200 genes are dedicated to energy metabolism (reviewed by Kartal 2013). Astonishingly, all anammox genera known so far encode a high number of c-

type cytochromes. There are 63 encoded by the *K. stuttgartiensis* genome (Strous 2006; Kartal 2011) and even 85 in the genome of *S. profunda* (van de Vossenberg 2013). These numbers exceed the number of c-type cytochromes encoded by S*hewanella oneidensis* (total 41; Gao 2010) which is renowned for its ability to utilize a wide range of electron acceptors.

1.6 The Anammox Metabolism

1.6.1 Catabolic Pathways

The first boost to understanding anammox catabolism was provided by van de Graaf and colleagues (1997). They discovered a transient accumulation of a compound with a molecular weight of 32 Da when they incubated an anammox culture in the presence of hydroxylamine (Fig 1.5). The formed compound was unambiguously identified as hydrazine (N_2H_4). Since then, many studies have applied the same experiment to diagnose the presence of anammox bacteria (Strous 1997; Schalk 2000; Kartal 2008; van der Star 2008a). Based on this observation, van de Graaf *et al.* put forward a three step model. The first step is the four-electron reduction of nitrite to hydroxylamine (NH_2OH) (eq. 1.2). In the second step hydroxylamine and ammonium (NH_4^+) are converted to hydrazine (N_2H_4) (eq. 1.3) and finally the four-electron oxidation of hydrazine yields dinitrogen (N_2) (eq. 1.4). However, the availability of the first anammox genome nine years later put the first two steps in this proposed scheme into question. The genome of *K. stuttgartiensis* codes for a c*d*$_1$ nitrite reductase (NirS) and its accessory proteins (Strous 2006) which might be involved in the reduction of nitrite to nitric oxide (NO).

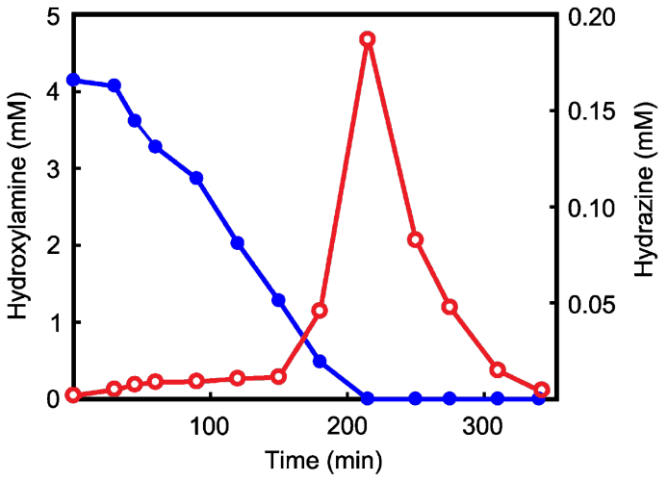

Figure 1.5 Transient accumulation of hydrazine (red line, open circles) after the addition of hydroxylamine (blue line, filled circles) to a culture of *Brocadia fulgida* (adapted from Kartal, 2008)

	$\Delta_r G_m°$ [kJ mol^{-1}]	E°' [V]	
$NO_2^- + 5\ H^+ + 4\ e^- \longrightarrow NH_2OH + H_2O$	-222.63	+0.059	(eq. 1.2)
$NH_2OH + NH_4^+ \longrightarrow N_2H_4 + H_2O + H^+$	-7.02	0	(eq. 1.3)
$N_2H_4 \longrightarrow N_2 + 4\ H^+ + 4\ e^-$	-128.10	-0.746	(eq. 1.4)
$NO_2^- + NH_4^+ \longrightarrow N_2 + 2\ H_2O$	-357.75		(eq. 1.1)

Based on genome analysis and physiological experiments, Strous *et al.* put forward an alternative three-step model which also takes account of energy conservation and involves nitric oxide (NO) as intermediate (Strous 2006). The first step here is the one-electron reduction of nitrite to nitric oxide (eq. 1.5) catalyzed by the nitrite reductase (NirS and its associated proteins, Kuste4136–4140). The second step would involve a novel enzyme which condenses nitric oxide with ammonium to form hydrazine (eq.1.6). This step was proposed to be catalyzed by a complex of the gene products of kuste2859-2861 termed hydrazine synthase (HZS). The final step involves the oxidation of hydrazine to finally form dinitrogen gas (eq. 1.7) catalyzed by an octaheme c-type cytochrome called hydrazine dehydrogenase (HDH, two paralogs are present in *K. stuttgartiensis* namely Kustc0694 and Kustd1340).

	$\Delta_r G_m°$ [kJ mol^{-1}]	E°' [V]	
$NO_2^- + 2\ H^+ + e^- \longrightarrow NO + H_2O$	-113.38	+0.347	(eq. 1.5)
$NO + NH_4^+ + 2\ H^+ + 3e^- \longrightarrow N_2H_4 + H_2O$	-116.27	+0.126	(eq. 1.6)
$N_2H_4 \longrightarrow N_2 + 4\ H^+ + 4\ e^-$	-128.10	-0.746	(eq. 1.4)
$NO_2^- + NH_4^+ \longrightarrow N_2 + 2\ H_2O$	-357.75		(eq. 1.1)

For the pathway to be productive, the electrons have to be replenished. This is due to the fact that anammox bacteria are chemolithotrophic and the only way they can convert chemical energy is by a chemiosmotic mechanism. For that reason, the four electrons produced in the final step of the pathway are proposed to cycle through a membrane-bound electron transport chain that results in a proton gradient across the anammoxosome membrane which is finally used for ATP generation (Fig 1.6). Indeed, three candidate gene clusters in the *Kuenenia stuttgartiensis* genome were annotated as putative bc_1 complexes (kustd1480–85, kustd4569–74 and kuste3096–97). The genome also possesses gene clusters encoding for four different ATP synthases. One of them is V-type (kuste3864–71) and three are F_oF_1-type (kuste3787–

96, kuste4592–4600 and kustc0572–79). In fact, one of these ATPases (Kuste3787–96) could be localized at both the cytoplasmic and anammoxosomal membranes by immunogold-labelling (van Niftrik 2010). In figure 1.6, the electron flow to and from the electron transport chain is shown, though the identity of the redox partners that mediate electron transfer from the membrane proteins to the soluble catalytic cytochrome complexes is so far unknown. It is speculated that small c-type cytochrome could perform this task as nearly all of them are targeted to the anammoxosome and several of them are expressed at above average levels as shown by transcriptomic and proteomic studies (Kartal 2011).

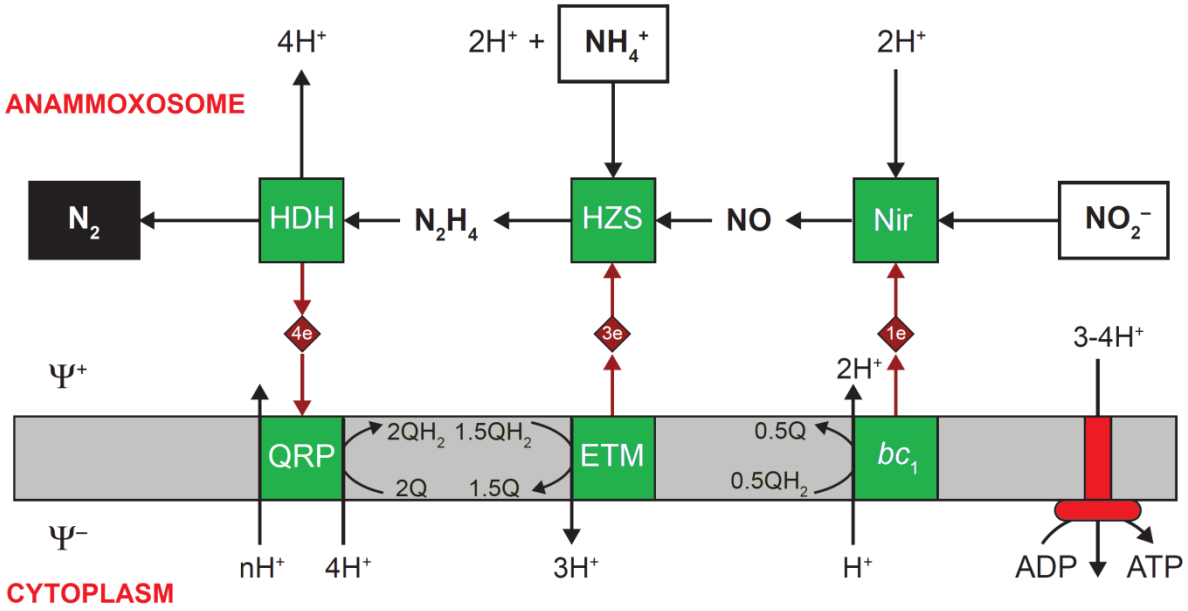

Figure 1.6 Proposed Model for the Central Anammox Pathway and ATP generation
Nitrite (NO_2^-) is converted to nitric oxide (NO) by a nitrite reductase (Nir). NO is condensed with ammonium (NH_4^+) to form hydrazine (N_2H_4) by hydrazine synthase (HZS). N_2H_4 is finally oxidized to dinitrogen (N_2) by hydrazine dehydrogenase (HDH) producing four electrons (e). The red diamonds show cytochrome c proteins that might act as electron transporters between the soluble and membrane-anchored enzyme complexes with the number of electrons also represented. QRP: hypothetical complex that transfers electrons from the cytochrome to the quinol pool. bc_1 represents quinol:cytochrome c oxidoreductase (bc_1, complex III), ETM represents an electron transfer module providing electrons to hydrazine synthase HZS. Ψ^+, Ψ^- indicate the positive (anammoxosome) and negative side (cytoplasm), respectively, of the electrochemical gradient along the anammoxosomal membrane. Figure adapted from (Kartal 2013).

Kartal and colleagues (2011) validated the hypothesis made by Strous *et al.* (2006). The results were obtained by complementary techniques involving physiological and biochemical experiments including whole cell based transcriptomics and proteomics. Metabolizing cells were grown in the presence of unlabelled (^{14}N) hydrazine or ammonium and ^{15}N-labelled nitrite. It was shown that hydrazine with a mixed isotopic nitrogen composition ($H_2{}^{14}N$-$^{15}NH_2$) formed at the expense of nitrite and ammonium. The presence of nitric oxide (NO) as intermediate was established by inhibition studies and by incubation with a dye that

fluoresces inside the anammox cells in the presence of NO. Furthermore, they also reported the identification and purification of enzymes involved in hydrazine synthesis (Kuste2859-2860-2861) and oxidation (Kustc0964) (Kartal 2011). Recently, the molecular structure of the hydrazine synthase complex was determined by our group (Dietl 2015). HZS forms a dimer of heterotrimers consisting of the two diheme c-type cytochromes Kuste2861 (α-subunit) and Kuste2860 (γ-subunit) as well as the non-heme β-barrel protein Kuste2859 (β-subunit). The complex contains two unique c-type heme active centres and one redox interaction site in each heterotrimer. A system of tunnels has been shown to connect these proposed active sites. A two-step model of hydrazine synthesis has been proposed based on these structural features. In the first step, a three-electron reduction of nitric oxide yields hydroxylamine, which passes through the major tunnel to the second active centre where hydroxylamine is condensed with ammonia to form hydrazine (Dietl 2015).

Hydrazine has been known as an alternative substrate for hydroxylamine oxidoreductases (HAOs) from aerobic ammonium oxidizers (Hooper 1965; Hooper 1997). These enzymes catalyze the conversion of hydroxylamine to nitrite. Several of these enzymes have been well characterized (Igarashi 1997; Arp 2002; Klotz 2008). Strikingly, *K. stuttgartiensis* possesses ten paralogous members of the HAO family. Six of them have been shown to be highly expressed at transcriptomic and proteomic levels, belonging to the "type II" class of hydrazine/hydroxylamine oxidoreductases (Kartal 2011). Among them, two have been purified and characterized. The first purified HAO-like enzyme, Kustc1061, termed as hydroxylamine oxidase (HOX), has been shown to catalyze the three-electron oxidation of hydroxylamine to nitric oxide (eq. 1.7) (Maalcke 2014).

$$NH_2OH \longrightarrow NO + 3\,H^+ + 3\,e^- \qquad \Delta_rG_m^\circ = +109.25\ kJ\ mol^{-1} \quad E^{\circ\prime} = -0.037\ V \quad \text{(eq. 1.7)}$$

This protein has also been characterized structurally possessing a typical HAO-like fold. It forms a covalently linked trimer *via* bonds between tyrosine residues and the active site hemes from adjacent subunits, the so-called P460 cofactor. It is proposed to be indirectly involved in the central anammox pathway as it might function as a clean-up system for hydroxylamine, which might leak from HZS and acts as a strong HDH inhibitor. Moreover, HOX turns hydroxylamine back into NO, which can be directly used as a substrate for HZS (Kartal 2011; Maalcke 2014). The second HAO purified was Kustc0694 which has been identified as hydrazine dehydrogenase (HDH) (Kartal 2011; Maalcke 2016). The paralogue of Kustc0694, Kustd1340, showed much lower expression levels. Kustc0694 has been shown to

be a genuine HDH as it has a high catalytic efficiency for N_2H_4, while NO and NH_2OH act as competitive inhibitors (Maalcke 2016). Interestingly, Kustc1061 can also oxidize N_2H_4 but with lower rates. Although both enzymes presumably possess a similar overall architecture and active sites with the typical tyrosine crosslink, HDH shows strict specificity for N_2H_4.

1.6.2 Anabolic Pathways

Since anammox bacteria are chemolithoautotrophs, they assimilate carbon dioxide (CO_2) to support their growth. *K. stuttgartiensis* has been shown to possess all genes of the acetyl-CoA (Wood-Ljungdahl) pathway for CO_2 fixation (Strous 2006). All of these genes were also shown to be expressed (Kartal 2011). The activity of the key enzyme acetyl-CoA synthase was demonstrated (Strous 2006) along with stable carbon isotope fractionation studies of lipids (Schouten 2004) indicating that indeed the acetyl-CoA pathway is responsible for carbon fixation. This pathway proceeds with the reduction of one molecule of CO_2 to carbon monoxide (CO). A second molecule of CO_2 is reduced to a cobalamine-bound methyl group. Both chemical species are condensed to acetyl-CoA, the precursor for sugar or fatty acid synthesis. The reduction of CO_2 requires low redox potential electrons which gives rise to the question from where those electrons are derived. Although several possibilities have been reviewed by Kartal *et al.* (2013), the observation that the growth of anammox bacteria is associated with the formation of nitrate strongly indicates that the required electrons are derived from the oxidation of nitrite to nitrate by a dedicated nitrite:nitrate oxidoreductase (Nxr) (Fig 1.7; eq. 1.8 and 1.9).

$$CO_2 + 2\,NO_2^- + H_2O \longrightarrow <CH_2O> + 2\,NO_3^- \quad \text{(eq. 1.8)}$$

$$NO_2^- + H_2O \longrightarrow NO_3^- + 2\,H^+ + 2\,e^- \quad \Delta_rG_m^\circ = +165.59\ \text{kJ mol}^{-1} \quad E^{\circ\prime} = +0.444\ \text{V} \quad \text{(eq. 1.9)}$$

NarGHI has been described as a canonical heterotrimeric nitrate reductase whose structure has been determined (Bertero 2003) and resembles the structure of formate dehydrogenase (Jormakka 2002). In *K. stuttgartiensis,* Nxr is also a heterotrimer encoded by Kustd1700 (NxrA, homologue of NarG), Kustd1703 (NxrB, homologue of NarH) and a third subunit Kustd1704 (NxrC) which does not match with NarI. Instead it shows 24 % sequence identity with the gamma subunit (EbdC) of ethylbenzene dehydrogenase (EBDH) (Kloer 2006). The alpha subunits of these enzyme complexes (NxrA, NarG, EbdA) are members of the molybdenum *bis*-molybdopterin-guanine dinucleotide (Mo-*bis*MGD) cofactor-containing protein family (Johnson 2001; Kloer 2006). Nxr resides exclusively in the anammoxosome and has been observed to be associated with tubule-like structures (Almeida 2015).

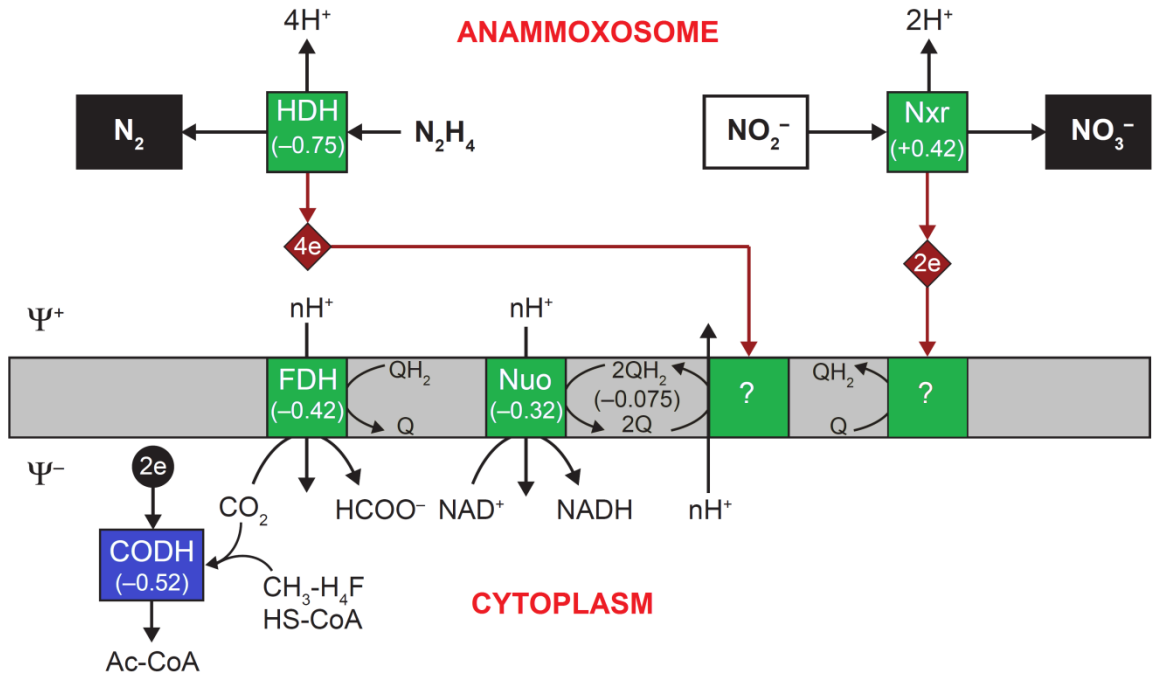

Figure 1.7 Electrons used in the acetyl-CoA pathway are compensated from nitrite oxidation. Standard redox potentials (in V) of the different redox processes are given in parentheses. CODH: CO dehydrogenase/acetyl-CoA (Ac-CoA) synthase, FDH: formate dehydrogenase, HDH: hydrazine dehydrogenase, Nuo: NADH:quinone (Q) oxidoreductase (complex I), Nxr: nitrite:nitrate oxidoreductase, CH_3-H_4F: methyltetrahydrofolate. Question marks (?) represent a hypothetical system that feed electrons from hydrazine and nitrite oxidation into the quinone pool.

The loss of electrons due to the leakage of reaction intermediates such as hydrazine and NO from the cells (Neumann 2014) prompts anammox bacteria to replenish them from different organic and inorganic sources. Besides the described core catabolic pathway, anammox bacteria can use a variety of organic compounds such as formate, acetate, propionate, mono- and dimethylamine as electron donors (Strous 2006; Kartal 2008; Kartal 2007a). Strikingly, they do not directly incorporate organic carbon from such compounds into their biomass, but rather oxidize them to CO_2. The obtained electrons are then fed into the central anammox pathway while they maintain their strictly chemolithoautotrophic life style with CO_2. It has been shown that different species of anammox bacteria can be more efficient in metabolizing one organic compound or another. For example, *B. fulgida* outcompetes other species when grown on acetate, whereas *A. propionicus* has a growth advantage in the presence of propionate (Kartal 2007b). However, the rates of oxidation were only 4-6 % to that of ammonium oxidation.

Anammox bacteria can also act as "disguised" denitrifiers when growing exclusively on nitrate. In this case nitrate is fully converted to nitrite. Half of the formed NO_2^- is then turned into ammonium. NH_4^+ and the other half of nitrite are then both fed to the central anammox pathway (Kartal 2007a). The six-electron reduction of nitrite to ammonium resembles a key step in the dissimilatory nitrite reduction to ammonium (DNRA) where it is carried out by the pentaheme nitrite:ammonium oxidoreductase NrfA (Simon 2002; Smith 2007). The identity of such enzyme(s), however, remains elusive in anammox bacteria.

Apart from organic compounds, inorganic substances such as Fe(II) can also act as electron donors and Fe(III), Mn(IV) and nitrate as electron acceptors (Strous 2006). A complete set of Ni-Fe hydrogenase genes are present in the *K. stuttgartiensis* genome indicating that hydrogen can also be used as electron acceptor. Besides formate dehydrogenase and nitrate reductase, *K. stuttgartiensis* also possesses three other members of the Mo-*bis*MGD family (Kustc0484, Kustc0546 and Kuste4466) indicating that this organism can extract electrons from a variety of metal rich environments. All these metabolic features make anammox bacteria truly novel and versatile.

1.7 C-type Cytochromes in Anammox Bacteria

Cytochromes are proteins containing the heme cofactor which is an iron-protoporphyrin IX ring system. The iron-protoporphyring IX ring is made up of four pyrrole subunits which are interconnected at their α-carbon atoms by methine bridges (=CH−). The interconnected tetrapyrrole moieties coordinate a central iron ion (Fe^{2+} or Fe^{3+}) through their nitrogen atoms. The protoporphyrin IX ring contains 26 delocalized π electrons (which fits to Hueckel's law of aromaticity *i.e.* 4n+2; n=6) and is therefore aromatic in nature which forces the system to be planar. Because of the highly conjugated π electron system, porphyrins absorb strongly in the visible spectral region which cause them to appear in intense colors. Hemoproteins possess characteristic UV-visible spectra with several diagnostics bands. The most pronounced band is the so-called Soret- or B-band between 390 and 430 nm ($\varepsilon = 10^4$–10^5 M^{-1} cm^{-1}), which is based on doubly degenerate π-π* transitions of the porphyrin. Less prominent bands are the Δ- or N-bands between 300 and 380 nm ($\varepsilon = 10^3$–10^4 M^{-1} cm^{-1}, porphyrin π-π* transitions) and the Q-bands between 510 and 580 nm ($\varepsilon = 10^4$ M^{-1} cm^{-1}). The lower-energy band (*i.e.* at longer wavelength) of these is called α-band and the band at higher energy (*i.e.* at shorter wavelength) is called β-band (Myer 1978).

Heme proteins can be divided into several categories depending on the nature of substituent groups on their porphyrin macrocycle. The most common heme types are heme b and heme c. Heme b binds to the protein non-covalently, whereas heme c is characterized by the presence of two (rarely one) covalent thioether bonds between cysteine Sγ and the heme's vinyl groups at position 3 and 8. There are other less common types of hemes present such as heme d_1 (present in cytochrome cd_1 nitrite reductase), heme a, which is found in cytochrome c oxidase and the related heme o, found in some bacterial oxidases (reviewed by Bowman 2008).

As discussed, c-type hemes bind to the protein *via* two cysteines. These are derived from a canonical heme binding motif CXXCH, where X can be any amino acid except Cys. Remarkably, the attachment to the heme occurs with a conserved stereochemistry. The vinyl groups at positions 3 and 8 are connected to the N- and C-terminal Cys of the CXXCH motif, respectively. The face of heme where the CXXCH sequence is located is called proximal side while the other side is called distal side. Therefore, the histidine residue in the CXXCH motif which coordinates to the heme iron is called "proximal ligand". There are other types of rare binding motifs reported such as the CX_3CH motif in diheme cytochrome c_3 (Aragao 2003), CX_4CH in tetraheme cytochrome c_3 (Simoes 1998) and even $CX_{15}CH$ in the octaheme c-type cytochrome MccA from *Wolinella succinogenes* (Hermann 2015). There are also examples where a covalent attachment to only one Cys was reported for example in the cytochromes c and c_1 from mitochondria of *Euglena*, *Trypanosoma* and *Leishmania* species which have AXXCH and FXXCH motifs (Bowman 2008). The distal side of the heme can be ligated either by small molecules such as water or protein-derived ligands such as histidine coordinated *via* Nε (rarely Nδ), cysteine Sγ, methionine Sδ, tyrosine Oη and lysine Nζ side chains. Some cytochromes also contain the amino function at the N-terminus as the distal ligand. They are referred as cytochrome *f*.

Cytochromes c can be further divided into four major classes. Class I includes rather small soluble cytochromes (8-12 kDa) with His/Met heme axial ligation. They are low spin with their heme binding motif located near their N-terminus and their distal ligand being a residue present close to their C-terminus. Class II cytochromes c contain usually high spin (rarely also low spin) c-type hemes bound to heme-binding motifs close to their C-terminus with their distal ligand provided by an amino acid side chain located close to their N-terminus. They typically possess a four-helix bundle fold. Class III c-type cytochromes are multiheme proteins with *bis*-His heme axial ligation. They usually possess very low redox potential

hemes. Finally, class IV comprises high molecular mass (~40 kDa) tetraheme cytochromes, with either *bis*-His or His/Met heme axial ligation systems.

C-type cytochromes are involved in a variety of functions such as electron transfer (cytochrome c), oxygen transport and storage (hemoglobin and myoglobin), catalysis (peroxidases, catalase, hydroxylamine oxidoreductase *etc*.), gas sensing and gene regulation. However, the most prevalent function of c-type cytochromes is electron transport. They transfer electrons in a wide variety of energy transduction processes including photosynthesis, various pathways of respiration and processes involved in the nitrogen and sulfur cycles. This ability seems to be related to the wide range of redox potentials which c-type cytochromes can exhibit. *Bis*-His ligated hemes *b,* for instance, possess standard reduction potentials of -150 to +380 mV whereas c-type hemes are ranging from -450 to +380 mV *vs*. SHE (reviewed by Bowman 2008). The diverse range of redox potentials is supposed to be achieved by conformational distortions of the porphyrin plane ("ruffling") as well as polarizing effects of adjacent residues from the heme-binding motif on the proximal histidine. The latter effects modulate the histidine-iron bond strength. The redox potential also depends on the ligand field of the His, which can be present in its neutral (histidine) or anionic (histidinate) states tuned through interactions with residues from its neighborhood. As already mentioned, 65 and 85 c-type cytochromes are encoded by the genomes of *K. stuttgartiensis* and *S. profunda*, respectively. All of these c-type cytochromes contain N-terminal signal peptides to target them to the anammoxosome (Kartal 2011; Almeida 2015). Moreover, several of these cytochromes are subunits of multienzyme complexes which were shown to be involved in the central anammox pathway (Kartal 2011; Maalcke 2016; Maalcke 2014; Dietl 2015). Other small c-type cytochromes might work as redox partners of these enzyme complexes.

1.8 Aims of this thesis

As discussed, the first anammox genome sequencing led to a conceptualization of the anammox pathway (Strous 2006), which was later corroborated by experimental studies (Kartal 2011). Several interesting questions are related to the biochemistry of the enzymes involved in the central anammox pathway including the mechanism by which hydrazine is synthesized and then further oxidized to dinitrogen. In this pursuit, our group has achieved important milestones. Most importantly we determined the structure of the hydrazine synthase (HZS) complex (Dietl 2015) which provided a concept for a unique two-step mechanism leading to the formation of nature's most powerful reductant hydrazine (a compound used also as rocket fuel).

In the same lines, my thesis project focused on the biochemical and structural characterization of central enzymes complexes involved in the anammox pathway as well as their small candidate redox partners. The project was pursued in close collaborations with the research group of Mike Jetten (Radboud University, Nijmegen, the Netherlands) and with Kristian Parey (MPI of Biophysics, Frankfurt, Germany). The principle techniques used were X-ray crystallography alongside with several biophysical and biochemical methods.

The particular objectives of this project were:

- The structural, biophysical and biochemical characterization of hydrazine dehydrogenase (HDH, Kustc0694) and its binding partner Kustc1130. HDH oxidizes hydrazine to dinitrogen, hence the final step in the anammox pathway. This will be described in chapter 3.
- The heterologous expression, structural, and biophysical characterization of the unique heterodimeric *Ks*NaxLS complex (Kusta0087/88) consisting of class I and II monoheme cytochromes will described in chapter 4. Moreover, two small, highly expressed class I c-type cytochromes (Kustc0562 and Kustc0563) will be structurally and biochemically characterized in order to determine their abilities to act as redox partners to several anammox enzyme complexes.
- Finally, the possibility of using anammox bacterial biomass from a waste water treatment plant for anammox research will be explored in chapter 5. This includes the determination of the microbial biodiversity found in the sampled biomass, purification of anammox key enzymes as well as their biochemical, biophysical and structural characterization.

Chapter 2

Materials and Methods

2. Materials and Methods

2.1 Materials

2.1.1 Chemicals and Consumables

If not indicated otherwise all used chemicals were purchased from the companies Sigma-Aldrich (Schnelldorf, Germany), Fluka (Schnelldorf, Germany), Merck (Darmstadt, Germany), AppliChem (Darmstadt, Germany) or Carl Roth (Karlsruhe, Germany) in analytical grade purity. All buffers and solutions were prepared from de-ionized water obtained from an ELGA-Purelab ultra system (ELGA LabWater, Celle, Germany). Compressed pure gases were purchased from Air Liquide GmbH (Ludwigshafen, Germany).

96-well sitting-drop trays (Greiner XTL low-profile)	Greiner Bio One, Frickenhausen, Germany
Amicon ultra centrifugal dialysis units	Millipore Bioscience, Schwalbach, Germany
Baysilone Paste, mittelviskos	Bayer AG, Leverkusen, Germany
BD Plastipak disposable syringes with Luer lock	Becton Dickinson, Heidelberg, Germany
Centrifugal tubes (“Falcon tubes”) 15 mL and 50 mL	Sarstedt, Nümbrecht, Germany
Cover slips, diameter 22 mm	Carl Roth, Karlsruhe, Germany
EM copper grids with graphite-coated formvar	Plano GmbH, Wetzlar, Germany
Gel filtration standard	Bio-Rad, Hercules, CA, USA
GelRed™ Nucleic Acid Gel Stain	Biotium Inc., Hayward, CA, USA
Gene Ruler™ 1 kb DNA ladder	MBI Fermentas, St. Leon-Rot, Germany
illustra NAP-5 columns	GE Healthcare, Uppsala, Sweden
InstantBlue™ Colloidal Coomassie blue solution	Expedeon Ltd., Cambridge, UK
Linbro 24-well plates	ICN Biomedicals Inc., Aurora, Ohio, USA
Low Molecular Weight Protein Marker	GE Healthcare, Uppsala, Sweden
Mini-PROTEAN® TGX® Precast Gels 4-20%	Bio-Rad, Hercules, USA
PageRuler™ Prestained Protein Ladder	MBI Fermentas, St. Leon-Rot, Germany
Parafilm M	Bemis NA, Neenah, WI, USA
PCR cups (0.2 mL)	Biozym Scientific GmbH, Hess. Oldendorf, Germany
PD-10 desalting columns	GE Healthcare, Uppsala, Sweden
pH indicator strips	Merck, Darmstadt, Germany
Phusion® High-Fidelity DNA Polymerase	New England Biolabs**,** Schwalbach, Germany
Polystyrene half-micro cuvettes	Sarstedt, Nümbrecht, Germany
Polyvinylidene difluoride (PVDF) membrane	Roche, Indianapolis, USA
PowerSoil® DNA Isolation Kit	MO BIO Laboratories Inc., Carlsbad, CA, USA
ProtoGel (30 % acrylamide, 0.8 % bis-acrylamide)	National Diagnostics, Atlanta, USA
Quantifoil R 2/2 holey carbon grids	Quantifoil Micro Tools GmbH, Jena, Germany
Quick T4 DNA Ligase	New England Biolabs, Schwalbach, Germany
Reaction tubes 0.5 mL, 1.5 mL and 2.0 mL	Carl Roth, Karlsruhe, Germany
Restriction Enzymes	New England Biolabs**,** Schwalbach, Germany
Steri Top Filters (0.22 µm)	Millipore Bioscience, Schwalbach, Germany
Syringe Filters (0.22 µm, 0.45 µm)	TPP Techno Plastic Products, Trasadingen, CH
Vivaspin ultra centrifugal dialysis units	Sartorius, Göttingen, Germany
Whatman paper	GE Healthcare, Buckinghamshire, UK
Wizard® *Plus* SV Minipreps DNA Purification System	Promega Corp., Madison, WI, USA
Wizard® SV Gel and PCR Clean-Up System	Promega Corp., Madison, WI, USA
Zero Blunt® TOPO® PCR Cloning Kit	Invitrogen, Carlsbad, CA, USA

2.1.2 Chromatography

Superdex 200 (10/300 GL)	GE Healthcare, Uppsala, Sweden
Superdex 200 increase (10/300 GL)	
Superdex 75 (10/300 GL)	
Superose 6 (10/300 GL)	
Superose 6 increase (10/300 GL)	
Ni-NTA Agarose	Qiagen, Hilden, Germany
Ni-IDA Profinity beads	Bio-Rad laboratories GmbH, Munich, Germany
Q-Sepharose (50 mL)	Merck KGaA, Darmstadt, Germany
Ceramic hydroxyapatite (5 mL)	Bio-Rad, Hercules, USA

2.1.3 Crystallization Screens

JCSG Core I, II, III and IV Suite	Qiagen, Hilden, Germany
PEG Suite	
Classics Suite	
Ammoniumsulfate Suite	
Protein Complex Suite	
Wizard I and II	Emerald, Bainbridge Island, WA, USA
Additive Screens 1, 2 and 3	Hampton Research, Alison Viejo, CA, USA
Detergent Screens 1, 2 and 3	
PGA screen	Molecular Dimensions, Suffolk, UK
MemGold HT-96	
MemGold2	

2.1.4 General Equipment

1260 Infinity II HPLC system	Agilent Inc., Santa Clara, CA, USA
700 series Cryostream Cooler	Oxford Cryosystems Ltd., Long Hanborough, UK
Äkta Purifier FPLC System	GE Healthcare, Uppsala, Sweden
An-60 Ti rotor	Beckman Coulter Inc., Palo Alto, USA
BRANSON Sonifier 250 and W-450	G. Heinemann Ultraschall- und Labortechnik, Schwäbisch Gmünd, Germany
Centrifuges and rotors	Eppendorf, Hamburg, Germany Beckman Coulter Inc., Palo Alto, USA Sorvall/Kendro Laboratory Products, Langenselbold, Germany
ChemiDoc™ MP CCD detection system	Bio-Rad, Hercules, CA, USA
Cryo-holder for TEM specimen	Gatan GmbH, Munich, Germany
CrystalCap Magnetic Ported Mounted Cryo Loops	Hampton Research, Alison Viejo, CA, USA
DAWN 8+ Heleos II® multi-angle scattered light photometer	Wyatt Technology, Santa Barbara, CA, USA
ELGA-Purelab ultra system	ELGA LabWater, Celle, Germany
FEI Tecnai G2 T20 Twin transmission electron microscope	FEI NanoPort, Eindhoven, the Netherlands
Flow-through 12 mm centrepiece assembly with sapphire windows	Beckman Coulter Inc., Palo Alto, USA
Gel casting stand GMTV2	cti GmbH, Idstein, Germany
Gene Pulser II	Bio-Rad, Hercules, CA, USA
Glove box including microscope box and Dewar port	Belle Technology Ltd., Weymouth, UK
Heraeus B6 microbial incubator	Kendro laboratory products, Newtown, CT, USA
INFORS Multitron Pro Shakers	INFORS HT, Bottmingen, Switzerland
Keithley 2450 source measure unit	Tektronix Inc., Beaverton, OR, USA

Mar345 image plate detector	MarResearch, Norderstedt, Germany
maXis ESI-TOF Mass Spectrometer	Bruker Daltonik GmbH**,** Bremen, Germany
Microfluidizer M110-S	Microfluidics, Newton, MA, USA
Mini-Twin vertical electrophoresis chamber MTV1	cti GmbH, Idstein, Germany
Modular Flake-Ice Machine MF36	Scotsman Europe, Pogliano, Italy
Mosquito nanolitre pipettor	TTP LabTech Ltd., Melbourne, UK
ND-1000 Spectrophotometer	PEQLAB Biotechnologie, Erlangen, Germany
Olympus CX 41 microscope	Olympus Deutschland GmbH, Hamburg, Germany
Optilab T-Rex refractive index detector	Wyatt Technology, Santa Barbara, CA, USA
Orbital shaker DOS-10L	neoLab Migge GmbH, Heidelberg, Germany
Peristaltic pump P-1	GE Healthcare, Uppsala, Sweden
Pipetman P pipettes (P2, P10, P20, P100, P200, P1000)	Gilson, Limburg-Offheim, Germany
Power Pac 300 electrophoresis power supply	Bio-Rad, Hercules, CA, USA
ProgResR C3 microscope camera	Jenoptik AG, Jena, Germany
Proteome-LabXL-I analytical ultracentrifuge	Beckman Coulter Inc., Palo Alto, USA
PTC-200 DNA Engine® thermocycler	MJ Research Inc., Waltham, MA, USA
Quartz micro-cuvettes	Hellma GmbH, Müllheim, Germany
Rigaku MicroMax 007 HF microfocus X-ray generator	Rigaku, Kemsing, UK
Rock Imager	Formulatrix, Bradford, USA
Shimadzu Biotech Axima TOF^2 Performance Mass Spectrometer	Shimadzu, Duisburg, Germany
SPD-M20A photodiode array detector	Shimadzu, Duisburg, Germany
Stereomicroscope Leica MZ 16	Leica Mikrosysteme GmbH, Wetzlar, Germany
Thermomixer	Eppendorf GmBH, Wesseling-Berzdorf, Germany
Thermostat	Haake/Thermo Electron GmbH, Karlsruhe, Germany
V-650 and V-760 UV-Vis spectrophotometer	Jasco GmbH, Gross-Umstadt, Germany
Viscotek 802 DLS	Viscotek Corporation, Houston, USA
Vitrobot^{TM} Mark IV	NanoPort, Eindhoven, the Netherlands

2.1.5 Bacterial strains

Shewanella oneidensis MR-1 wildtype as well as strain S2095 (MR-1 ΔendA; deletion of the SO_0833 gene; Heun 2012) and a ΔendA, ΔexeM, ΔexeS nuclease triple knock-out strain (unpublished) were kindly provided by Prof. Dr. Kai Thormann (Justus-Liebig-Universität Gießen, Germany).

The following *Escherichia coli* strains were used:

Strain	Genotype	Source
BL21 [DE3]	*E. coli* str. B F$^-$ *ompT gal dcm lon hsdS$_B$*($r_B^-m_B^-$) λ(DE3 [*lacI lacUV5-T7 gene 1 ind1 sam7 nin5*]) [*malB*$^+$]$_{K\text{-}12}$(λ^S)	Novagen Inc. (Madison, WI, USA) (Studier 1986)
DH5α	F$^-$ *endA1 glnV44 thi-1 recA1 relA1 gyrA96 deoR nupG purB20* φ80d*lacZ*ΔM15 Δ(*lacZYA-argF*)U169, hsdR17($r_K^-m_K^+$), λ$^-$	(Taylor 1993)
XL1-Blue	*endA1 gyrA96(nal^R) thi-1 recA1 relA1 lac glnV44* F'[::Tn10 proAB$^+$ lacI^q Δ(lacZ)M15] hsdR17(r_K^- m_K^+)	Stratagene Inc.

2.1.6 Plasmids

The following vectors for protein expression were used:

Name	Description	Expression host	Producer
pET24d	Inducible *E. coli* expression vector controlled by a T7 promotor; encoding C-terminal 6x His Tag; Kanamycin resistance	*E. coli* BL21 [DE3]	Novagen Inc. (Madison, WI USA)
pET24d_Kustc1130	pET24d vector harboring the kustc1130 gene	*E. coli* BL21 [DE3]	This work (see Appendix 1)
pET24d_Broful02728	pET24d vector harboring the BROFUL_02728 gene	*E. coli* BL21 [DE3]	This work (see Appendix 1)
pUC19kan2	pUC19 derivative for constitutive expression in *S. oneidensis* MR-1, lac promotor; encoding N-terminal signal sequence of the small tetraheme cytochrome (STC) and C-terminal 6x His Tag; Kanamycin resistance	*S. oneidensis* MR-1	Andreas Dietl
pUC19kan2a	pUC19kan2 derivative, engineered NotI restriction site	*S. oneidensis* MR-1	Andreas Dietl
pUC19kan3	pUC19 derivative for constitutive expression in *S. oneidensis* MR-1; lac promotor; encoding N-terminal signal sequence of the small tetraheme cytochrome (STC), N-terminal 6x His-Tag and TEV cleavage site; Kanamycin resistance	*S. oneidensis* MR-1	Andreas Dietl
pUC19kan2_A0087	pUC19kan2 vector harboring the kusta0087 gene without its endogenous signal peptide	*S. oneidensis* MR-1	This work (see Appendix 1)
pUC19kan2_A0088	pUC19kan2 vector harboring the kusta0088 gene without its endogenous signal peptide	*S. oneidensis* MR-1	This work (see Appendix 1)
pUC19kan3_A0088	pUC19kan3 vector harboring the kusta0088 gene without its endogenous signal peptide	*S. oneidensis* MR-1	This work (see Appendix 1)
pUC19Kan2a_KustA87-88	pUC19kan2a vector harboring kusta0087 and Kusta0088 genes as bicistron	*S. oneidensis* MR-1	This work (see Appendix 1)
pUC19Kan3_KustC0563	pUC19kan3 vector harboring the kustc0563 gene without its endogenous signal peptide	*S. oneidensis* MR-1	This work (see Appendix 1)
pUC19Kan2a_C0563	pUC19kan2a vector harboring the kustc0563 gene without its endogenous signal peptide	*S. oneidensis* MR-1	This work (see Appendix 1)
pUC19Kan3_KustC0562	pUC19kan3 vector harboring the kustc0562 gene without its endogenous signal peptide	*S. oneidensis* MR-1	This work (see Appendix 1)
pUC19kan2a_C0562	pUC19kan2a vector harboring the kustc0562 gene without its endogenous signal peptide	*S. oneidensis* MR-1	This work (see Appendix 1)

2.2 Methods

2.2.1 Microbiological Methods

2.2.1.1 Growth Media

Liquid cultures of *Escherichia coli* and *Shewanella oneidensis* MR-1 were generally grown in lysogeny broth (LB) (Sambrook 2001). Single colonies were obtained by streaking on standard-I-nutrient (STI) agar plates. Both LB medium and STI-agar plates were routinely provided by the media kitchen of the Max Planck Institute for Medical Research.

Depending on the plasmids and strains used, media were supplemented with different antibiotics as selection markers (added from 1000× stock solutions) to reach final concentrations of 50 µg/mL kanamycin sulfate, 100 µg/mL ampicillin or 30 µg/mL chloramphenicol. Cultures were generally inoculated with overnight pre-cultures in a dilution of 1:100 (10 mL/L).

Medium Components

LB medium
10 g/L Bacto tryptone
5 g/L Bacto yeast extract
10 g/L NaCl
Adjusted to pH 7.0 with NaOH
and autoclaved at 121 °C

STI-agar plates
25 g/L Standard-I-nutrient-broth
15 g/L Bacto agar
Autoclaved at 121 °C

2.2.1.2 Preparation of chemically competent *E. coli* cells

Chemically competent *E. coli* BL21 (DE3), DH5α and XL1-blue cells were prepared by inoculating 200 mL LB medium. Cells were grown until they reached an OD_{600} of ~0.5. Subsequently, the cells were incubated on ice for 15 min and harvested by centrifugation for 10 min at 5,500×g at 4 °C. The supernatant was discarded and the cell pellets were washed with 4 × 10 mL of TFB-1 on ice. Finally, cells were centrifuged again (5,000×g, 4 °C, 10 min), the supernatant was discarded and the cell pellets were resuspended in a total volume of 4 mL TFB-2 on ice. 80 × 50 µL aliquots were prepared in pre-cooled 1.5 mL Eppendorf tubes placed on ice and then flash-frozen in liquid nitrogen. Competent cells were stored at -80 °C until further use.

TFB-1	M [g/mol]	mass [g]
30 mM Potassium acetate	98.15	1.472
50 mM $MnCl_2$	197.91 (·$4H_2O$)	4.95
100 mM RbCl	120.92	6.05
10 mM $CaCl_2$	147.02 (·$2H_2O$)	0.735
15 % (v/v) glycerol		75 mL (94.5 g)

Potassium acetate was dissolved in 80 mL H_2O and the pH was adjusted with conc. HCl (1 drop) to 5.8. Then the other ingredients were added, the solution was filled up to 500 mL and sterile filtered.

TFB-2	M [g/mol]	mass [g]
10 mM MOPS (pH 7.0)	209.26	0.209
10 mM RbCl	120.92	0.121
75 mM $CaCl_2$	147.02 (·$2H_2O$)	1.103
15 % (v/v) glycerol		15 mL (18.9 g)

MOPS was dissolved in in 80 mL H_2O and the pH was adjusted to 7.0 with 5 M NaOH (few drops). Then the other ingredients were added, the solution was filled up to 100 mL and sterile filtered.

2.2.1.3 Transformation of chemically competent *E. coli* cells

Chemically competent *E. coli* cells were transformed with plasmid DNA using the heat shock method. 50 µL cells were thawed on ice and subsequently incubated with 50-100 ng plasmid DNA on ice for 10 min. The heat shock was performed for 40 s at 42 °C. Then 500 µL LB medium were added and the cells were shaken for 1 h at 37 °C. The cells were streaked on STI agar plates supplemented with the respective antibiotics and incubated over night at 37 °C.

2.2.2 Molecular Biology Methods

2.2.2.1 Genomic and plasmid DNA purification

Bacterial genomic DNA was isolated from *Kuenenia stuttgartiensis* and *Scalindua brodae* using a modified protocol of (Wilson 2001) by Andreas Dietl (Dietl 2016). Total genomic DNA from DEMON® granules was extracted using the PowerSoil® DNA Isolation Kit (MO BIO Laboratories Inc., Carlsbad, CA, USA). Bacterial plasmid DNA from *E. coli* was purified according to the alkaline lysis protocol (Sambrook 2001). 7 mL LB medium supplemented with the appropriate antibiotics were inoculated with a single colony and grown at 37 °C, 140 rpm overnight (14–18 h). The cells were harvested by centrifugation (5,000×g, 10 min, 4 °C) and plasmid DNA was isolated using the Wizard® Plus SV Minipreps DNA Purification System (Promega Corp., Madison, WI, USA).

The concentration and purity of isolated DNA was determined using a NanoDrop™ ND-1000 spectrophotometer (PEQLAB Biotechnologie, Erlangen, Germany) by measuring the absorbance at 260 nm (assuming that $A_{260}^{1\ cm} = 1$ corresponds to 50 ng/µL double-stranded DNA). The purity was assessed from the $A_{260/280}$ ratio (≥ 1.8 for pure DNA).

2.2.2.2 Agarose gel electrophoresis

Agarose gel solutions were prepared by dissolving 1 % (w/v) agarose (Serva GmbH, Heidelberg, Germany) in 200 mL 1 × TAE buffer using microwave heating and were kept in a 60 °C incubator for long time uses. To 50 mL liquid agarose solution, 5 µL GelRed™ Nucleic Acid Gel Stain (Biotium Inc., Hayward, CA, USA) were added and the mixture was poured into a casting tray containing a comb. Prior to loading of the DNA samples on the solidified gel, DNA loading dye was added to the DNA samples. DNA separation was performed at 100-110 V in 1 × TAE buffer until the desired separation was obtained. DNA bands were visualized on a ChemiDoc™ MP CCD detection system (Bio-Rad, Hercules, CA, USA) using UV transillumination.

50x TAE buffer
242 g Tris
57.1 mL glacial acetic acid
100 mL 0.5 M EDTA/NaOH (pH 8)
ad 1 L ddH2O

10x DNA loading dye
40 % (w/v) sucrose
0.25 % (w/v) Orange G

2.2.2.3 Gene cloning

The gene of interest for cloning was amplified using PCR from template DNA (genomic or plasmid DNA) in 0.2 mL PCR cups (Biozyme Scientific GmbH, Hess. Oldendorf, Germany) using a PTC-200 DNA Engine® thermocycler (MJ Research Inc., Waltham, MA, USA). The PCR reaction mixture contained the thermostable Phusion® High-Fidelity DNA Polymerase (New England Biolabs, Schwalbach, Germany). The oligonucleotide primers (~20-45 bp) were designed using the GENtle software (http://gentle.magnusmanske.de). The size and purity of the amplified PCR products were assessed by agarose gel electrophoresis.

Components	**1x Reaction**	**Final concentrations**
5x HF-Phusion HF Buffer	10 µL	1x
10 mM dNTPs*	1 µL	200 µM each
Forward Primer (10 pmol/µL)	2.5 µL	0.5 µM
Reverse Primer (10 pmol/µL)	2.5 µL	0.5 µM
Template DNA	0.5 µL	< 250 ng
Phusion DNA Polymerase (2 U/µL)	0.5 µL	1 Unit
ddH_2O (autoclaved)	33 µL	
Total	50 µL	

* Mixture of 2'-desoxynucleosidetriphosphates containing 10 mM dATP, dCTP, dGTP and dTTP each

Thermocycling Program:

98 °C	1 min	
98 °C	10 s	30 cycles
T annealing	30 s	
72 °C	30–60 s/kb, at least 1 min	
72 °C	10 min	
10 °C	∞	

T annealing = Tm (lower Tm primer) + 3 °C
Tm was automatically calculated by the GENtle software using the nearest neighbor method.

Plasmid DNA and PCR products were digested in 0.2 mL PCR cups (Biozym Scientific GmbH, Hess. Oldendorf, Germany) at 37 °C for 3 h to overnight. Restriction enzymes, buffers and bovine serum albumin (BSA) were obtained from New England Biolabs (Schwalbach, Germany). Digested PCR fragments were purified directly using the Wizard® SV Gel and PCR Clean-Up System (Promega Corp., Madison, WI, USA). Digested vectors were separated by agarose gel electrophoresis and the desired fragment was purified by gel extraction again using the Wizard® SV Gel and PCR Clean-Up System.

Standard digestion protocol

Purified PCR product or vector (100–500 ng/µL)	10–20 µL
H_2O	10–20 µL
10x buffer	4 µL
10x BSA	4 µL
Restriction enzyme 1 (20 U/µL)	1 µL
Restriction enzyme 2 (20 U/µL)	1 µL
Total	40 µL

Digested and purified PCR products and plasmids were ligated using Quick T4 DNA Ligase (New England Biolabs, Schwalbach, Germany). The ligation reaction was performed at room temperature for 5-30 min. 5 µL of the reaction mixture was used to transform chemically competent *E. coli* DH5α or XL-blue cells (heat shock protocol described in 2.2.1.3).

Digested vector	1–2 µL (ca. 100 ng)
Digested PCR product	3–4 µL (ca. 200–500 ng)
H_2O	x µL
2x Quick Ligation buffer*	5 µL
Quick T4 Ligase (2,000 U/µL)	0.5 µL
Total	10 µL

*****1x Quick Ligation Reaction Buffer contains: 66 mM TrisCl, 10 mM $MgCl_2$, 1 mM dithiothreitol, 1 mM ATP, 7.5 % Polyethylene glycol (PEG 6000), pH 7.6.

2.2.2.4 Screening for positive clones

Single colonies from transformed *E. coli* cells were picked and grown in LB medium overnight. Plasmid DNA was purified from overnight cultures as described in section 2.2.2.1. Plasmids were digested in order to cut out the cloned gene (section 2.2.2.3) using appropriate restriction enzymes. The digested fragments were separated by agarose gel electrophoresis and visualized to look for fragments with the desired size (section 2.2.2.2). Around 20 µL plasmid DNA with concentrations between 50-100 ng/µL were sent for sequencing to GATC Biotech (Konstanz, Germany). All genes were sequenced using T7 promoter, T7 terminator, M13F or M13R primers.

2.2.2.5 Site directed mutagenesis

Site directed DNA mutagenesis was carried out using the QuikChange® Site Directed Mutagenesis protocol (Stratagene, La Jolla, CA, USA) with few modifications. The mutagenic primers contained the mutation in the middle of the sequence and were designed using the GENtle software (http://gentle.magnusmanske.de). The length of the primers used was 30-45 bp. Their melting temperature (Tm) was calculated using PrimerX (http://www.bioinformatics.org/primerx/cgi-bin/primer.cgi) and primers with a Tm ≥78 °C were chosen. The PCR reactions were carried using PfuUltra™ II DNA polymerase (Agilent, Santa Clara, CA, USA) or Phusion® High-Fidelity DNA Polymerase (New England Biolabs, Schwalbach, Germany).

10x PfuUltra II Buffer	5 µL
10 mM dNTPs*	1 µL
Forward Primer (10 pmol/ µL)	1 µL
Reverse Primer (10 pmol/ µL)	1 µL
1:10 plasmid dilution (ca. 50 ng)	2 µL
PfuUltra II DNA polymerase (2.5 U/µL)	1 µL
ddH_2O (autoclaved)	39 µL
Total	50 µL

OR

5x Phusion® Buffer	10 µL
10 mM dNTPs*	1 µL
Forward Primer (10 pmol/ µL)	1 µL
Reverse Primer (10 pmol/ µL)	1 µL
1:10 plasmid dilution (ca. 50 ng)	2 µL
Phusion DNA polymerase (2.5 U/µL)	1 µL
ddH_2O (autoclaved)	34 µL
Total	50 µL

* Mixture of dNTPs containing 10 mM dATP, dCTP, dGTP and dTTP each

Program

95 °C	30 s	
95 °C	30 s	16 cycles
55 °C	1 min	
68 °C	1.5 min/kb	
68 °C	10 min	
10 °C	Hold	

After the PCR, the parental plasmid DNA was digested using 1 µL DpnI (20 U/µL, New England Biolabs Schwalbach, Germany) for 3 hours at 37 °C. DpnI eliminates the methylated parental DNA such that only the non-methylated PCR-amplified plasmid DNA containing the mutation will be used for transformation of chemically competent *E. coli* DH5α or XL-blue cells. The desired mutant clones were verified by DNA sequencing by GATC Biotech.

2.2.2.6 Microbial diversity analysis of DEMON® granules

To determine the microbial diversity in the sampled DEMON® biomass, fragments of both 16S rDNA and functional genes were amplified by PCR using Phusion® High-Fidelity DNA Polymerase (New England Biolabs, Schwalbach, Germany). Degenerate primers for amplification of 16S rRNA gene fragments from *Planctomycetes* (Pla46F/1392R; Neef 1998; van der Star 2008b) as well as hydrazine synthase alpha subunit (hzsA526F/1829R) (Harhangi 2012) and hydroxylamine oxidoreductase (hao) were applied. Primer sequences and PCR conditions are given in the appendix 2.

After assessing the presence and size of the desired amplicons by agarose gel (1 % w/v) electrophoresis, the PCR products were cloned using the Zero Blunt® TOPO® PCR Cloning Kit (Invitrogen, Carlsbad, CA, USA) following the manufacturer's instructions. Plasmid DNA was isolated with the Wizard® Plus SV Minipreps DNA Purification System (Promega Corp., Madison, WI, USA). Plasmids were screened for inserts of the expected size by agarose gel (1 % w/v) electrophoresis after EcoRI digestion. The inserts of positive clones were sequenced by the Sanger method (GATC Biotech AG, Konstanz, Germany) using SP6 and M13 forward primers. The obtained raw sequences were aligned and edited using the freeware program SEQULATOR (http://sequlator.com/index.html). Alignments of multiple DNA or protein sequences were performed using Clustal Omega (http://www.ebi.ac.uk/Tools/msa/clustalo/) (Sievers 2011) applying default settings. Phylogenetic tree reconstruction was performed by the Phylogeny.fr server (http://www.phylogeny.fr/; Dereeper 2008) based on multiple sequence alignment in MUSCLE (Edgar 2004), alignment refinement in Gblocks (Castresana 2000) and tree reconstruction by the maximum-likelihood method in PhyML (Guindon 2010). Phylogenetic trees were rendered using the MEGA 6.0 software (Tamura 2013).

2.2.3 Protein Expression and Purification

2.2.3.1 Cytochrome c expression in *Shewanella oneidensis* MR-1

Shewanella oneidensis MR-1 is a gram-negative facultative anaerobic γ-proteobacterium which is rod-shaped, 2-3 µm in length and 0.4-0.7 µm in diameter. Its genome encodes 42 c-type cytochromes so that the cells appear red (Heidelberg 2002). Its codon usage is similar to that of *E. coli*. The optimum cell growth temperature is ~30 °C and the doubling time is similar to that of *E. coli.* Vectors containing ampicillin resistance cannot be used for selection as *S. oneidensis* expresses β-lactamases (Poirel 2004). However, kanamycin- and chloramphenicol resistance gene containing vectors can be applied. *S. oneidensis* can be transformed by electroporation with many vectors available for *E. coli* (pUC and p15A origins of replication) though the transformation efficiency is much lower (Myers 1997). In this study an endA nuclease deficient strain (*S. oneidensis* MR-1 ΔendA) (Heun 2012) as well as a nuclease triple mutant (ΔendA, ΔexeM, ΔexeS; unpublished) was used. Since both strains do not secrete the endA nuclease into the medium their transformation efficiency is increased. It was observed that vectors encoding a lacI gene have very poor transformation efficiency for unknown reasons (observation by Andreas Dietl). Therefore, none of the vectors used to transform *S. oneidensis* MR-1 in this study had expression regulation.

Transformations of *S. oneidensis* were done as follows. *S. oneidensis* from a glycerol stock was streaked on standard-I-nutrient (STI) agar plates without any antibiotics and grown for two days at 30 °C. A single red colony was picked to inoculate 5 mL LB pre-culture and grown overnight at 30 °C. A 50 mL final LB culture was prepared and inoculated with 1 % (v/v) of pre-culture. The bacteria were grown to an OD_{600} of 0.3-0.4 at 30 °C and 200 rpm. 30 mL of the culture were harvested in 50 mL Falcon tubes at 5,000×g, 10 min and 4 °C. The pellet was then resuspended in 2.5 mL 1 M sorbitol and divided into several aliquots of 300 µL in 1.5 mL Eppendorf tubes. Each aliquot was again centrifuged for 1 min at 12,000×g at RT. The supernatant was removed and the pellet resuspended in 40 µL of 1 M sorbitol. 200-500 ng of desired plasmid DNA were added to each tube and incubated for up to 15 min on ice. Then, the DNA and *S. oneidensis* cells mixtures were pipetted into pre-chilled electroporation cuvettes (0.1 cm gap). Electroporation was done at 0.55 kV, 25 µF, 200 Ω using a Gene Pulser II (Bio-Rad, Hercules, CA, USA) after which 500 µL of LB were added to the electroporation cuvettes immediately and the suspension was transferred to 1.5 mL Eppendorf tubes. Afterwards, the cells were incubated at 30 °C, 800 rpm in a thermomixer for

~ 2 h. The cells were then centrifuged at 13,000 rpm at RT. 400 µL supernatant was removed, the cells were resuspended in the residual supernatant and plated on semi-dry STI-agar plates containing kanamycin or chloramphenicol. The cells were grown further for two days at 30 °C. Reddish bacterial colonies became visible after two days.

For large scale purification of c-type cytochromes, 6-10 L of LB medium were supplemented with 50 µg/mL kanamycin and inoculated with 1 % (v/v) of *S. oneidensis* MR-1 overnight culture harboring the desired expression vector. Initially, large scale cultures were grown in 2-liter unbaffled Erlenmeyer flasks at 30 °C and 100 rpm for 5-6 hours, after which the OD_{600} reached 0.6-0.8. After that, the temperature was lowered to 20 °C and the cultures were shaken at 60 rpm for further 60-70 hours. After the expression, the cells were harvested by centrifugation at 6,000 rpm, 4 °C for 10 min in a Fiberlite™ F9-6 x1000 LEX rotor (Thermo Scientific, Darmstadt, Germany). Pellet yield was ~20 g (wet-weight) per 6 L culture. Pellets were either directly used for purification or frozen in liquid nitrogen and stored at -80 °C.

2.2.3.2 Cytochrome c purification

All expressed c-type cytochromes had either a cleavable N-terminal or a non-cleavable C-terminal 6xHis tag. Thus, Ni-affinity chromatography was used to purify the proteins followed by gel filtration chromatography.

The following buffers were used:

Wash/ Lysis Buffer (WB)
300 mM NaCl
50 mM Tris-Cl, pH 8.0
10 mM imidazole

Elution Buffer (EB)
300 mM NaCl
50 mM Tris-Cl, pH 8.0
250 mM imidazole

TEV Digest Buffer (TDB)
150 mM NaCl
20 mM Tris-Cl, pH 8.0
2 mM TCEP, pH 7.0

Gel filtration Buffer (GFB)
150 mM NaCl
50 mM Tris-Cl, pH 8.0

Storage Buffer (SB)
25 mM KCl
25 mM HEPES (KOH), pH 7.5

The pellet from the expression was resuspended in WB at a 1:4 ratio of pellet wet-weight in gram to WB volume in mL. The suspension was stirred in a cold room for 30-40 min to homogenize the mixture. Cell lysis was performed on ice by sonication using a Branson W-450 sonifier (G. Heinemann, Schwäbisch Gmünd, Germany) at 50 % amplitude, 0.5 s bursts and 10 minutes total *on* time. The lysate was cleared by ultracentrifugation at 158,420×g for 45 min at 4 °C in a Ti-45 rotor (Beckman Coulter, Krefeld, Germany). Immobilized metal ion affinity chromatography (IMAC) was performed using 2-3 mL Ni-NTA agarose beads (Qiagen, Hilden, Germany) pre-equilibrated with ~20 column volumes (CV) of WB. The bound protein was washed again with 20 CV of WB. Finally, the protein was eluted from the column using EB in 1 mL fractions. The purity of the fractions was assessed using 15 % SDS-PAGE. Most pure and red fractions were pooled together. If the purity was poor, IMAC was repeated again with 1 mL Ni-IDA Profinity beads (Bio-Rad laboratories GmbH, Munich, Germany) in a similar way as described for Ni-NTA. Pure fractions of C-terminally His-tagged cytochromes were concentrated to 0.5-1 mL using 3 kDa cut-off Amicon concentrators (Millipore Bioscience, Schwalbach, Germany) and used for gel filtration chromatography. Gel filtration was performed using a Superdex 75 (10/300 GL) column connected to an Äkta Purifier FPLC system (GE Healthcare, Uppsala, Sweden). The purification progress was monitored using the absorbance at 280 nm, 410 nm and 260 nm. 0.5 mL fractions were collected at a flow rate of 0.5 mL/min. Fractions corresponding to peaks in the 280 nm and 410 nm absorbance channels were assessed on 15 % SDS-PAGE and purest fractions were pooled, buffer exchanged to SB and concentrated up to an $A_{280}^{1\ cm}$ of 10. After that, the protein was either used directly for crystallization or flash frozen in liquid nitrogen and stored at -80 °C. In the case of N-terminally cleavable 6×His-tagged proteins, additional steps had to follow to remove the His-tag. The concentrated protein after affinity chromatography with Ni-NTA or Ni-IDA (see above) was buffer exchanged to TDB using a PD-10 column (GE Healthcare, Uppsala, Sweden). To the eluate, His-tagged TEV protease was added at a 1:100 ratio of A_{280} of TEV protease to protein. The mixture was incubated at 4 °C overnight. The next day, the cleaved protein was separated from uncleaved protein and TEV protease using Ni-NTA affinity chromatography in essentially the same way as described above, except that this time only the flow-through was collected containing the cleaved protein. The cleaved cytochrome was concentrated and further purified using gel filtration chromatography and later steps as described before.

2.2.3.3 Hydrazine Synthase (HZS), Hydroxylamine Oxidase (HOX) and Hydrazine Dehydrogenase (HDH) Purification from DEMON® Granules

Approximately 200 g of frozen DEMON® granules were resuspended in 600 mL buffer A (50 mM TrisCl pH 8.0) and stirred in a cold room to loosen the granules. The granular material was then homogenized in 30-50 mL portions in a 100 mL Dounce homogenizer with a motor-driven Teflon pestle at 1,000–1,400 rpm. The homogenized material was centrifuged for 20 minutes at 8,000×g and 4 °C and then resuspended in 600 mL buffer A. Lysozyme (0.25 mg/mL), DNaseI (0.05 mg/mL) and Complete™ protease inhibitor cocktail tablets (Roche Applied Science, Mannheim, Germany; 2 tablets per 100 mL) were added and the mixture was stirred for 30–60 min. All steps were performed in a cold room at 8 °C. Cell lysis was done by sonication in 100 mL portions on ice using a Branson W-450 sonifier (G. Heinemann, Schwäbisch Gmünd, Germany) at 50 % amplitude, 0.5 s. bursts and 10 minutes total *on* time. Phenylmethylsulphonyl fluoride (PMSF) was added to each portion prior to sonication to a final concentration of 100 µM from a 100 mM stock in isopropanol. The lysate was then cleared by ultracentrifugation in a Beckmann Ti-45 rotor at 45,000 rpm (158,420×g) for 1 hour at 4 °C.

The cleared lysate was loaded onto a 50 mL Q-Sepharose column (Merck, Darmstadt, Germany) using a 150 mL Superloop on an Äkta purifier FPLC system (GE Healthcare, Uppsala, Sweden) while monitoring the absorbance at 280 nm, 410 nm and 260 nm wavelengths. After loading the lysate, the column was washed until the absorbance stabilized, after which a gradient from 0 to 800 mM NaCl was applied over 10 column volumes. HZS eluted between 320 and 390 mM NaCl whereas the octaheme cytochromes c HDH and HOX eluted between 440 and 530 mM NaCl. The HZS and octaheme cytochrome c (OCC) fractions were pooled separately, buffer-exchanged to 20 mM potassium phosphate pH 7.0 and concentrated to final volumes of 1 mL for HZS and 10 mL for the OCCs. HZS and OCC pools were separately loaded onto a 5 mL ceramic hydroxyapatite column (Bio-Rad, Hercules, CA, USA) pre-equilibrated in 20 mM potassium phosphate buffer. In each case, the column was washed until the baseline became stable. A gradient of 20 mM to 250 mM potassium phosphate (KPi) pH 7.0 was then applied over 10 column volumes for HZS and from 20 to 500 mM KPi over 20 column volumes for the OCCs. HZS eluted around 150 mM KPi and octaheme cytochromes eluted in two peaks, the first one eluting at 180 mM KPi was dominated by HOX and the second one at 250 mM was dominated by HDH. As a final step, all the peaks from the hydroxyapatite column were concentrated separately to the minimal

possible volume and further purified by gel filtration on a Superpose 6 (10/300 GL) column (GE Healthcare, Uppsala, Sweden). HZS eluted at around 15.9 mL, whereas trimeric HOX and HDH both eluted at 16.2 mL. The high-molecular weight [$(a_3)_8$ and $(a_3)_{10}$] assemblies of HDH (Maalcke 2016) eluted at 11.3 mL. All fractions of HZS, HOX and HDH were pooled separately, after which the buffer was exchanged to storage buffer (25 mM HEPES pH 7.5 (KOH), 25 mM KCl) by ultrafiltration. The samples were then concentrated to an $A_{280}^{1\ cm}$ of 45 for HZS and 20 for both HDH and HOX, flash-frozen in liquid nitrogen and finally stored at -80 °C.

2.2.3.4 Cloning, heterologous expression and purification of Kustc1130 and its homologue Broful02728

Both kustc1130 and broful02728 genes were cloned into the pET24d vector using NcoI/XhoI restriction sites including the sequences coding for their endogenous N-terminal signal peptides and C-terminal hexa-histidine tags (the primers used are given in appendix 1). Each plasmid was transformed into chemically competent *E. coli* BL21 (DE3) cells as expression host. For each construct, 3 x 2 L LB medium supplemented with 50 µg/mL kanamycin were inoculated with 10 mL/L overnight pre-cultures and were grown at 37 °C while shaking at 120 rpm. When the OD_{600} reached ~0.6, the temperature was set to 20 °C. At this temperature protein expression was induced with 500 µM IPTG at an OD_{600} of 0.8-1.0. After induction, the bacterial cultures were further grown at 20 °C, 120 rpm for 18-20 hours.

Kustc1130_CHis and Broful02728_CHis were purified according to the same protocol. The bacterial cells containing expressed proteins were harvested by centrifugation at 10,000×g, 10 min and 4 °C. The cell pellets were resuspended in buffer WB (50 mM TrisCl pH 8.0, 300 mM NaCl and 10 mM imidazole pH 8.0). The cells were disrupted by using a Microfluidizer (Microfluidics) operated at a pressure of 0.7 MPa and the lysate was clarified by centrifugation at 43,456 × g for 20 min at 4 °C. The cleared lysate was loaded twice onto a column containing 2 mL of Ni-NTA agarose pre-equilibrated with buffer WB. The column was further washed with 20 mL of buffer WB. The individual proteins were eluted using buffer EB (same as buffer WB but with 250 mM imidazole pH 8.0) and collected in 1 mL fractions. Fractions containing the desired proteins in decent purity were pooled and concentrated using 10 kDa cut-off Amicon concentrators (Millipore Bioscience, Schwalbach, Germany). The concentrated proteins were further purified using gel filtration chromatography on a Superdex 75 (10/300 GL) column (GE healthcare, Uppsala, Sweden) in GFB buffer (50 mM HEPES/KOH pH 7.5 and 50 mM NaCl). The peaks eluting around 14

mL corresponding to either Kustc1130_CHis or Broful02728_CHis were collected. Both proteins were concentrated and buffer-exchanged to storage buffer SB (25 mM HEPES/KOH pH 7.5 and 25 mM KCl) using 10 kDa cut-off Amicon concentrators. Both proteins were flash-frozen in small aliquots in liquid nitrogen and stored at -80 °C until further use.

2.2.4 Biochemical Methods

2.2.4.1 Sodium Dodecyl Sulphate Polyacrylamide Gel Electrophoresis (SDS-PAGE)

To evaluate the purity of protein preparations, proteins were separated according to their electrophoretic mobility by denaturating SDS-PAGE (Laemmli 1970). Protein samples were mixed with 4 x SDS sample buffer and heated to 95 °C for 5-10 min. Electrophoresis was performed in SDS-PAGE 1 x running buffer using 10 %, 12 %, 15 % or 20 % gels and a constant current of 40 mA. The gels consisting of an upper stacking gel and a lower separating gel were prepared manually and the polymerization reaction was initiated by APS and TEMED. When required, gradient SDS-PAGE with concentrations from 4-20 % were cast using a gradient gel maker or were used from a commercially available source (Mini-PROTEAN® TGX® Precast Gels; Bio-Rad, Hercules, USA). In normal SDS-PAGE described above, glycine is used as trailing ion. To separate small molecular weight proteins Tricine SDS-PAGE was applied (Schägger 1987).

The composition of Tris-glycine SDS-PAGE was as follows:

stacking gel	**separating gel**
125 mM Tris / HCl pH 6.8	375 mM Tris / HCl pH 8.8
4.5 % acrylamide / bis-acrylamide	10-20 % acrylamide / bis-acrylamide
0.1 % SDS	0.1 % SDS
2.2 mM APS[1)]	1.5 mM APS[1)]
0.1 % TEMED[2)]	0.05 % TEMED[2)]

[1)] APS: Ammoniumperoxodisulfate ($(NH_4)_2S_2O_8$)
[2)] TEMED: N,N,N',N'-Tetramethylethylenediamine

	Final concentrations	Preparation
10x Running Buffer	0.25 M Tris 1.0 M Glycine 1 % (w/v) SDS	30.28 g Tris 144.14 g glycine 10 g SDS ad 1,000 mL ddH_2O
4x Sample Buffer	200 mM TrisCl pH 6.8 8 % (w/v) SDS 400 mM DTE** 40 % (v/v) glycerol 0.01 % (w/v) bromophenolblue	4 mL 4x Stacking Gel Buffer 0.8 g SDS 0.62 g DTE** 4 mL glycerol 1 mg bromophenolblue ad 10 mL ddH_2O

*) pH of the Tris buffer was adjusted with concentrated hydrochloric acid, SDS was added afterwards
**) DTE was omitted in case of non-reducing sample buffer.
2x sample buffer containing 100 mM TCEP was prepared by mixing 0.8 mL 250 mM TCEP hydrochloride/NaOH (pH 7.0) with 1 mL 4x non-reducing sample buffer and 0.2 mL ddH_2O.

The composition of Tris-tricine SDS-PAGE was as follows:

Components	stacking gel		separating gel	
	Total 5 mL	Total 15 mL	10 %	12 %
3x Buffer	1,250 µL	3,750	10,000	10,000
Acrylamide 40 % (29:1)	500 µL	1,500	7,500	9,000
Glycerol 70 % (v/v)	---	---	4,000	4,000
H_2O	3,090 µL	9,270	8,200	6,700
10 % APS (w/v)	80 µL	240	150	150
10 % TEMED (v/v)	80 µL	240	150	150

The 3x Buffer contained 3 M Tris-Cl pH 8.45 and 0.3 % SDS. The 10 x cathodes Buffer (or upper buffer) contained 1 M Tris, 1 M Tricine and 1 % SDS pH 8.25. The anode buffer was made up of 2.1 M Tris pH 8.9.

2.2.4.2 Coomassie staining

Ready for use colloidal Coomassie blue solution (InstantBlue™ ; Expedeon Ltd., Cambridge, UK) was used to stain the protein bands on SDS-PAGE gels. InstantBlue™ was first shaken well and 10-20 mL was used for staining the gels from 15 min to 1 hour. Protein bands were usually visible after 15 min but further incubation with InstantBlue™ intensified them. Gels were destained by shaking them in de-ionized water overnight.

2.2.4.3 Heme staining

C-type cytochromes possess one or more heme moieties covalently bound to the polypeptide chain *via* two thioether bonds with cysteines. Therefore, even after denaturation with SDS, the heme moiety keeps some catalytic activity in reacting with peroxide which is used to visualize c-type cytochrome bands in gels. A fast and cheap chemiluminescent (CL) method for heme staining was developed by Andreas Dietl (PhD thesis, 2016) as described here. C-type cytochromes were resolved using SDS-PAGE. The sample buffer contained 50 mM tris(2-carboxyethyl)phosphine (TCEP), as thiol-reducing agents since DTE or β-mercaptoethanol cannot be used because these reagents strongly reduce CL intensity. Gels were first fixed in 40 % (v/v) ethanol for 10 min and then soaked in 20 mL CL solution without hydrogen peroxide (H_2O_2) for 15 min. After that 6 µL of 30 % (w/w) H_2O_2 was added and incubated for 5 min. The gel was then briefly rinsed with de-ionized water and placed inside a plastic bag. The pre-stained marker bands were marked by green phosphorescent acrylic paint (Lukas Acryl-Paint effect, Dr. Fr. Schoenfeld GmbH, Düsseldorf, Germany) on the outside of the plastic bag and the chemiluminescent signals were detected using a ChemiDoc^{TM} MP CCD detection system (Bio-Rad, Hercules, CA, USA) exposing for 10, 20 or 30 seconds.

Chemiluminescent (CL) heme staining solution for 1–2 gels

Luminol is first dissolved in 1 M CAPS/NaOH, pH 11 and *p*-coumaric acid (in ethanol) and then filled up to 20 mL with water.

Final concentrations	Preparation
0.25 mg/mL luminol	5 mg luminol
0.1 mg/mL *p*-coumaric acid	2 mL *p*-coumaric acid (1 mg/mL in ethanol)
100 mM CAPS/NaOH, pH 11	2 mL 1 M CAPS (N-cyclohexyl-3-aminopropanesulfonic acid)/NaOH, pH 11
	ad 20 mL ddH_2O

2.2.4.4 Blotting and Edman's N-terminal Sequencing

Natively purified HDH from *Kuenenia stuttgartiensis* showed a prominent band around 10 kDa when analyzed by 15 % SDS-PAGE (section 2.2.4.1). In order to identify this protein, the band was transferred onto a polyvinylidene difluoride (PVDF) membrane (Roche, Indianapolis, USA) and subjected to Edman's N-terminal sequencing as follows. A rectangular piece (approximately 100 x 80 mm) of PVDF membrane was cut along with several pieces of Whatman paper (GE Healthcare, Buckinghamshire, UK) with similar shape and size. The PVDF membrane was activated by incubating in absolute ethanol for 10 min at room temperature.

The activated PVDF membrane, the SDS-gel and pieces of Whatman paper were soaked in transfer buffer (20 % v/v ethanol in 1x SDS-PAGE running buffer; section 2.2.4.1) for 5 min. Afterwards, a semi-dry blot was assembled by placing three layers of Whatman paper at the cathode side (bottom) of a semidry-blotter followed by the gel, PVDF membrane and finally three more layers of Whatman papers on top (at the anode side). Excess liquid was removed by rolling with a Pasteur pipette. The transfer was carried out at 40 mA for approximately 1.5 hours. After complete transfer of the desired band, as judged from the transfer of the bands from the pre-stained protein marker, the PVDF membrane was stained using a solution containing 0.1 % (w/v) Coomassie brilliant blue R250 (Serva GmbH, Heidelberg, Germany), 10 % (v/v) acetic acid and 40 % (v/v) methanol in de-ionized water. The PVDF membrane was destained by incubation in de-ionized water while shaking for 1 hour. This destaining procedure was repeated for three times with exchanges of the de-ionized water. The membrane was dried, the ~10 kDa protein band was cut out and sent for N-terminal sequencing by Edman's degradation method involving stepwise cleavage by automated phenylisothiocyanate chemistry (Proteome Factory, Berlin, Germany).

2.2.4.5 Pull-Down Assay

Pull-down assays have been traditionally used to identify interacting proteins partners (Louche 2017). These assays involve immobilization of an affinity-tagged protein used as "bait". Examples of affinity-tags include polyhistidine and biotin tags which can be immobilized on Ni^{2+}- and streptavidin-containing matrices, respectively. The immobilized "bait" protein is usually incubated with cell lysate or even a purified protein that is a predicted interacting partner, called "pray". This step is followed by extensive washing to remove non-specifically binding proteins. Finally, complexes between bait and pray proteins are eluted and analyzed by SDS-PAGE followed by identification of the binding partners by mass spectrometry.

C-terminally hexahistidine-tagged *Ks*NaxLS, its individual subunits as well as Kustc0563 were used as bait by immobilizing them on Ni-IDA Profinity beads (Bio-Rad, Munich, Germany) which were pre-equilibrated with wash buffer (150 mM NaCl, 50 mM HEPES/NaOH pH 7.5). For the preparation of a cell lysate from *K. stuttgartiensis* biomass, 180-200 mg of cell pellet was resuspended in 1 mL of lysis buffer (25 mM HEPES, pH 7.5, 150 mM NaCl and 0.4 % v/v Triton X-100). The cells were disrupted by sonication using a Branson 250 sonifier (G. Heinemann, Schwäbisch Gmünd, Germany) equipped with a sonication microtip at 50 % amplitude, 0.5 s bursts and total 20 pulses which was repeated for three times. The lysate was incubated for 15 min while rotating in a cold room at 8 °C. Then the lysate was cleared by centrifugation at 16,000 × g, 15-20 min at 4 °C. 50 µL Ni-IDA beads loaded with the individual immobilized bait proteins were incubated with 100 µL *K. stuttgartiensis* cell lysate in 2 mL Eppendorf tubes while rotating at 8 °C for 60 min. In parallel, another set of bait-loaded Ni-IDA beads (50 µL) was incubated with 100 µL purified *Ks*HZS protein solution (A_{280}^{1cm}=1.0). Moreover, both cleared cell lysate and *Ks*HZS protein solutions were incubated with Ni-IDA beads without any bait as a control.

The excess lysate and protein solution were removed by centrifugation afterwards and the beads were washed thrice with 1 mL wash buffer. The proteins were eluted using 50 µL elution buffer (50 mM TrisCl pH 8.0, 300 mM NaCl and 250 mM imidazole). The eluted samples were analyzed by 15 % SDS-PAGE. The protein bands of interest were subjected to peptide mass finger printing by MALDI mass spectrometry (see section 2.2.5.5) for their identification.

2.2.4.6 Protein concentration determination

Protein concentrations were routinely assayed spectrophotometrically using an ND-1000 Nanodrop spectrophotometer (PEQLAB, Erlangen, Germany) with a sample volume of 2 µL. Samples were measured after appropriate dilution in the respective buffer (absorbance between 0.05 and 1.2) at two wavelengths in case of c-type cytochromes (A_{280} and Soret band maximum).

Since the extinction coefficient of c-type cytochromes at 280 nm is strongly influenced by the absorption of the heme cofactors, the concentrations of the studied c-type cytochromes are rather documented as absorbance values at 280 nm (A_{280}) without further calculating the concentration based on Lambert-Beer's law. However, for use in activity assays the concentration was determined using the Bradford method (Bradford 1976). 1 µL of samples were mixed with 999 µL of Bradford reagent (Bio-Rad, Munich, Germany). After incubation for 5 min at RT the absorbance at 595 nm was measured. Protein concentrations were calculated using a concentration standard curve with known concentrations of bovine serum albumin (BSA).

2.2.4.7 HDH and HOX activity assays

Activity assays for HOX and HDH were performed essentially as described by Maalcke *et al.* 2014 and Maalcke *et al.* 2016, respectively, with some modifications. Basically, the reduction of bovine heart cytochrome c (cyt c) by the respective octaheme cytochrome was followed by monitoring the increase in absorbance at 550 nm ($\Delta\varepsilon$=19,600 M^{-1} cm^{-1}, Yonetani 1965). To this end, 1 mL reaction mixtures containing 50 µM cyt c and 1 µg enzyme (HOX or HDH) in 25 mM HEPES/KOH, pH 7.5 were analyzed in polystyrene cuvettes (Sarstedt AG, Nümbrecht, Germany). The absorbance at 550 nm was recorded for 1 minute using a Jasco V-650 spectrophotometer (Jasco GmbH, Gross-Umstadt, Germany) at 37 °C after which the reaction was started by adding an appropriate amount of substrate (hydroxylamine for HOX and hydrazine for HDH). A similar procedure was followed to compare the activities of HOX and HDH in the presence of other small cytochromes such as Kustc0563 and Kustc0562. To check whether hydroxylamine inhibited HDH activity, 1 mM of hydroxylamine (as hydroxylammonium chloride, pH 7.0) was added to the reaction mixture prior to starting the reaction. Initial rates were fitted by non-linear regression in GraphPad Prism (GraphPad Software Inc., La Jolla, CA, USA) applying the Michaelis-Menten equation.

2.2.5 Biophysical Methods

2.2.5.1 UV-Vis Spectroscopy

Spectra in the ultraviolet and visible range (200 to 700 nm, scan speed 400 nm/min) were recorded in 200 µL quartz micro-cuvettes with 1.0 cm path length (Hellma GmbH, Müllheim, Germany) at 0.5 nm bandwidth using JASCO V-650 or V-760 spectrophotometers (Jasco GmbH, Gross-Umstadt, Germany) at room temperature. The data were processed using the Jasco32 software.

For qualitative spectra, cytochrome samples were diluted in 25 mM KCl, 25 mM HEPES/KOH pH 7.5. Routine spectra of the reduced proteins were recorded after addition of a few grains of solid sodium dithionite ($Na_2S_2O_4$) to the samples. Spectra of the ferric proteins were also recorded in the presence of 10 mM hydroxylamine (NH_2OH, as hydrochloride), hydrazine (N_2H_4, as hydrochloride), phenylhydrazine (C_6H_5-N_2H_3), methylhydrazine (CH_3-N_2H_3) and hydroxyethylhydrazine (HO-C_2H_4-N_2H_3). These reagents were supplied by dilution from 200 mM stock solutions (pH adjusted to 7.0 with 1 M NaOH or 1 M HCl as required).

Samples of the oxygen sensitive ferrous proteins were prepared in a nitrogen-filled glove box (Belle Technology Ltd., Weymouth, UK, < 10 ppm O_2) using thoroughly degassed and argon-saturated buffers. 145 µL of *Ks*NaxLS samples (A_{280}^{1cm} = 0.25-0.5) were reduced by adding 10 mM Ti (III) citrate (about 1 mM final concentration, freshly prepared) in a buffer containing 25 mM KCl, 25 mM HEPES/KOH pH 7.5. Other cytochromes were reduced accordingly but using sodium dithionite. The reduced samples were transferred in stoppered quartz micro-cuvettes outside of the glove box for measuring the reduced spectrum. Afterwards, the cuvette was opened and the sample was gently bubbled with 10 mL air supplied from a syringe to obtain the re-oxidized protein by oxygen.

Nitric oxide (NO) was freshly prepared by mixing 5 mL of 1.2 M ferrous sulfate in 1.8 M H_2SO_4 (solution A) with 3 mL of 1.2 M sodium nitrite (solution B) in a syringe inside of the glove box (eq. 2.1), followed by washing of the resulting colorless gas by 1 M anoxic NaOH to remove NO_2 impurities.

$$2\ NaNO_2 + 2\ FeSO_4 + 3\ H_2SO_4 \longrightarrow 2\ NO\uparrow + Fe_2(SO_4)_3 + 2\ NaHSO_4 + 2\ H_2O \quad \text{(eq. 2.1)}$$

Carbon monoxide (CO) was transferred from a lecture bottle (Air Liquide, Ludwigshafen, Germany) into a balloon which was transferred into the glove box for further use.

In order to obtain qualitative spectra of CO or NO bound cytochromes, 1 mL buffer (25 mM KCl, 25 mM HEPES/KOH pH 7.5) was sparged with either 20-30 mL CO or NO and used for diluting cytochrome samples immediately.

2.2.5.2 Dynamic light scattering (DLS)

Dynamic light scattering (DLS) is a convenient method to determine the homogeneity of protein samples. It is based on the determination of the hydrodynamic radius of molecules depending on their Brownian motion in a solvent system. The hydrodynamic radius is derived from the translational diffusion coefficient based on the Stokes-Einstein equation (eq. 2.2). The fluctuations of the scattered light intensity are used to determine the diffusion coefficient *via* fitting of an autocorrelation function.

$$r_h = \frac{kT}{6\pi\eta D} \quad \text{(eq. 2.2)}$$

Where, r_h = hydrodynamic radius; D = translational diffusion coefficient; k = Boltzmann's constant; T = absolute temperature and η= viscosity of the solution.

DLS was used to determine the conditions under which hydrazine dehydrogenase (HDH) is either present as trimers or forms octamers/decamers thereof. HDH at a final concentration of ~2 µM was mixed with a buffer containing 25 mM HEPES pH 7.5 (KOH) and supplemented with appropriate concentrations of different chemical compounds to study their effect on HDH oligomerization. As a control, 50 mM HEPES pH 7.5 and 300 mM KCl was used where HDH preferably exists as octamers/decamers of trimers. Samples were first centrifuged at 15,000 × g for 20 min at 4 °C. 20 µL of the supernatants were then gently pipetted into DLS cuvettes (Hellma GmbH, Müllheim, Germany). Data were acquired and analyzed using a Viscotek 802 DLS instrument and the OmniSIZE software (Viscotek Corporation, Houston, USA). All measurements were performed at 20 °C.

2.2.5.3 Analytical size exclusion chromatography coupled to multi-angle static light scattering (SEC-MALS)

Multi-angle static light scattering (MALS) was performed to determine the molecular mass of proteins and protein complexes in a shape-independent manner (reviewed by Wyatt 1993). Molecular masses were determined according to the *Debye-Zimm* formalism (eq. 2.3) of the *Rayleigh-Gans-Debye* theory assuming a refractive index increment (dn/dc) of 0.185 mL/g.

$$M = \frac{R}{K\,c} \quad \text{(eq. 2.3)}$$

with K experimental constant: $K = 4\pi^2\, n_0^2 (dn/dc)^2\, \lambda_0^{-4} N_A^{-1}$
n_0 refractive index of solvent, dn/dc refractive index increment of the solute,
λ_0 wavelength of the incident light, N_A Avogadro constant

c solute concentration (determined from the refractive index of the solution)

R excess Rayleigh ratio $R = \frac{(I - I_{solvent})\, r^2}{I_0 V}$

I ($I_{solvent}$) intensity of scattered light by solute (solvent), I_0 intensity of the incident beam, V scattering volume, r distance scattering volume to detector

M weight averaged molecular mass

Protein samples were separated by analytical size exclusion chromatography (SEC) on Superdex 75, Superdex 200 or Superose 6 increase (10/300 GL) gel filtration columns (GE Healthcare, Uppsala, Sweden). Analyses were performed using a 1260 Infinity II HPLC system (Agilent Inc., Santa Clara, CA, USA) equipped with a photodiode array detector SPD-M20A (Shimadzu, Duisburg, Germany). Static light scattering analyses were performed *in line* using a DAWN 8+ Heleos II® multi-angle scattered light photometer (Wyatt Technology, Santa Barbara, CA, USA) combined with a refractive index detector Optilab T-rEX (Wyatt Technology, Santa Barbara, CA, USA).

The system was equilibrated with a buffer containing 50 mM HEPES pH 7.5 and 150 mM KCl. A flow rate of 0.5 mL min^{-1} was used. To calibrate the gel filtration column a standard (Bio-Rad, Hercules, CA, USA) containing thyroglobulin (670 kDa), γ-globulin (158 kDa), ovalbumin (44 kDa), myoglobin (17 kDa) and vitamin B_{12} (1.35 kDa) was used. 40 µL of each sample with concentrations ranging from 20-100 µM were injected using an autosampler. Data analysis was performed using the *ASTRA 7.1.2* software (Wyatt Technology, Santa Barbara, CA, USA), providing weight-averaged molar masses of the eluting species.

2.2.5.4 Analytical ultracentrifugation (AUC)

Analytical ultracentrifugation is a powerful technique to determine the oligomeric state and molecular mass of proteins over a wide range. This technique can be applied to any kind of macromolecule such as nucleic acids, proteins, carbohydrates, lipids or even viruses (Ralston 1993). It analyses the hydrodynamic properties of particles in dilute solutions by determining the sedimentation behavior in the centrifugal field of the centrifuge. While traveling through the solvent, the particle experiences three forces namely centrifugal, buoyant and frictional force. These three forces determine the sedimentation coefficient of the particle described by the Svedberg equation (eq. 2.4).

$$s = \frac{M(1-\rho\overline{\upsilon})}{N_A f} = \frac{u}{\omega^2 r} \quad \text{(eq. 2.4)}$$

Where s = the sedimentation coefficient; r = the distance of the particle from the rotation axis; u = the terminal velocity of the particle; ω = the angular velocity; M = the molar mass; N_A = the Avogadro constant; $\overline{\nu}$ = the partial specific volume; ρ = the density of the solvent and f = the frictional coefficient.

The sedimentation coefficient depends on the properties of the particle. In particular, it is proportional to the buoyant effective molecular weight (M) of the particle and inversely proportional to the frictional coefficient (f) according to eq. 2.4. The sedimentation coefficient has the dimension of *seconds.* The Svedberg unit (S) is defined as 10^{-13} seconds (1 S = 10^{-13} seconds). $S_{w,\,20}$ is an extrapolated value of the sedimentation coefficient to water and 20 °C and is therefore independent of temperature and buffer composition.

A perfectly spherical particle would possess a minimal frictional coefficient (f_{min}) and therefore a maximum sedimentation coefficient (S_{max}) which can be calculated as $S_{\max} \approx 0.00361 \times M^{2/3}$ (M is the molar mass in g/mol) (Erickson 2009). Therefore, the $S_{max}/S = f/f_{min}$ ratio contains information on the anisotropy of a molecule. The sedimentation velocity (SV) method was used to determine the sedimentation coefficients of different protein species present in solution in order to obtain information on their molecular shape and their oligomeric states. Exact molecular masses of proteins were determined using sedimentation equilibrium (SE) analyses.

For the SV method, protein stocks were first dissolved in 25 mM KCl, 25 mM HEPES (KOH) pH 7.5 and the buffer was equilibrated *via* repeated buffer exchange in 10, 30 or 100 kDa MWCO Amicon tubes (Millipore, Schwalbach, Germany) depending on the size of the protein. The final protein concentration was kept at an absorbance of 0.5 at the scanning wavelength (280 nm, 409 nm or 420 nm) for 1.2 cm path length according to the suitability and availability of the protein(s). The measurement cells (Beckman Coulter Inc., Palo Alto, USA) were assembled according to the manufacturer's instructions. The cells were filled with 400 µL protein sample and 420 µL of buffer in two different windows of the cell. For HDH, samples were sedimented at 20,000 rpm and for other proteins at 30,000 rpm for 24 hours at 20 °C in an An-60 Ti rotor (Beckman Coulter Inc., Palo Alto, USA). Absorbance scans were recorded at 280 nm, 409 nm or 420 nm wavelength using the Beckman XL-A/XL-1 data analysis software. The initial 150 scans were processed using SEDFIT (Schuck 2000) which includes the determination of sedimentation coefficient distributions c(S), $S_{20,w}$ (sedimentation coefficients corrected to pure water) and molecular masses assuming a fixed frictional ratio (f/f_{min}) of 1.2. Sednterp (Hayes D.B. et al., New Hampshire, USA) was used to calculate the density and viscosity of the buffer. A partial specific volume of 0.73 mL/g for the proteins was used to fit the data (Erickson 2009).

SE measurements were performed in the same cells with 200 µL sample and 220 µL buffer. Three speeds (8,000; 12,000 and 15,000 rpm) were used to equilibrate the samples. Five photometric scans were taken at each speed after 22 hours equilibration at 20 °C. SE data were processed using SEDPHAT (Schuck 2000).

2.2.5.5 Mass spectrometric analyses

All protein mass spectrometric analyses were kindly performed by Melanie Mueller and Marion Gradl of our department.

The identity of native or heterologously expressed proteins was determined or confirmed by peptide mass fingerprinting (PMF) using Matrix-Assisted-Laser-Desorption/Ionisation-Time-Of-Flight (MALDI-TOF) mass spectrometry. For this purpose, gel slices of specific bands were cut from SDS-PAGE gels. In-gel tryptic digests and analyses on an Axima TOF^2 Performance MALDI-TOF mass spectrometer (Shimadzu Biotech, Duisburg, Germany) were performed according to published procedures (Shevchenko 2006). Peptide mass searches were carried out using the MASCOT software (Matrix Science Inc., MA, USA).

Total molecular masses of proteins in solution were determined either by MALDI-TOF or by Electrospray ionization (ESI) mass spectrometry. ESI-MS data were recorded on a maXis spectrometer (Bruker Daltonik GmbH, Bremen, Germany) and analyzed using the Compass software, vers. 4.0 (Bruker Daltonik GmbH, Bremen, Germany). If required, N-terminal sequencing was performed using the MALDI-TOF in-source decay (ISD) or ESI-MS electron transfer dissociation (ETD) methods.

2.2.5.6 Negative stain Transmission Electron Microscopy (TEM)

All TEM sample preparations, image acquisitions and analyses were kindly performed by Ulrike Mersdorf (MPImf).

In order to visualize protein particles, negative stain TEM was performed. HDH and HOX were first diluted to A_{280}^{1cm} = 1.0-3.0 in buffer (25 mM HEPES (KOH) pH 7.5, 25 mM KCl). To analyze the effect of KCl and Kustc1130 on *Ks*HDH (or Broful02728 on *Bf*HDH) oligomerization, the protein solution was diluted to a final absorbance of $A_{280}^{1cm} \approx 1.0$ using a buffer containing 25 mM HEPES (KOH) pH 7.5 supplemented with an appropriate amount of KCl the small binding partner proteins or both.

Samples were pipetted onto glow-discharged copper grids with carbon-coated formvar (Plano GmbH, Wetzlar, Germany) and stained with either aqueous 1 % (w/v) uranyl acetate (pH 4.2-4.5) or methylamine tungstate (pH 6-7) solution. Stained EM grids were inserted into the vacuum port of a FEI Tecnai G2 T20 Twin transmission electron microscope (FEI NanoPort, Eindhoven, the Netherlands) running at 200 kV accelerating voltage and electron micrographs were recorded using a FEI Eagle 4k HS, 200 kV CCD camera.

2.2.5.7 Cryo-Electron Microscopy

All cryoEM sample preparations, image acquisitions and analyses were performed by Ulrike Mersdorf (MPImf) as well as Simone Prinz and Kristian Parey (MPI of Biophysics, Frankfurt/Main, Germany).

Glutaraldehyde crosslinked *Ks*HDH was prepared as described before (Maalcke 2016) and diluted to a final concentration of $A_{280}^{1\ cm} \approx 4$ in 25 mM HEPES/KOH, pH 7.5, 25 mM KCl. High salt conditions were achieved by adding 25 mM HEPES/KOH, pH 7.5 and 300 mM KCl to a *Ks*HDH sample with a concentration of $A_{280}^{1\ cm}$=32 in a ratio of 9:1. 2.5 µL of each sample was applied to Quantifoil R2/2 holey carbon grids (Quantifoil Micro Tools, Germany). The grids were automatically blotted (blot time 4 s, drain and wait time 0 s, blot

force 4 a.u.) using a FEI Vitrobot^{TM} Mark IV (FEI NanoPort, the Netherlands) plunge-freezer. Cryo-EM images were recorded on a FEI Tecnai Polara transmission electron microscope operating at 300 kV equipped with a Gatan K2 back-thinned direct detector operating in movie mode. Images were collected manually at a nominal magnification of 200,000 × corresponding to a sampling density of 1.08 Å pixel^{-1}. Videos were collected for 6 s with a total of 30 frames with a calibrated dose of about 0.5 e^-/ Å^2 per frame, at defocus values between -0.75 and -2.75 µm.

The image processing was done as follows. A set of 452 and 151 micrographs of crosslinked and high salt *Ks*HDH particles was collected and the frames were aligned using the algorithm developed by (Li 2013). Particles were picked using Autopick within the RELION workflow (Scheres 2012) and the semi-automatic procedure of EMAN Boxer (Ludtke 1999). The micrograph-based CTF was determined with gctf (Zhang 2016). The initial dataset contained a total of 10,332 and 5,866 particle images (extracted using a box of 350 pixels) for the crosslinked and high salt conditions, respectively. The particles were subjected to an initial reference-free two-dimensional (2D) classification in RELION (Scheres 2012) to discard imperfect particles (7,557 and 2,256 particles, respectively). Visual selection of particle classes with interpretable features resulted in a dataset of the crosslinked (4,235 for the octamer and 2,071 particle images for the decamer) and high salt (3,246 particle images) samples for 3D consensus refinement. Cryo-EM maps of the octamer and decamer based on the particular initial 3D classes were low-pass filtered to 50 Å and used as initial models for the 3D gold standard refinement in RELION. The post-processing procedure implemented in RELION was applied to the final maps for B-factor sharpening and resolution validation (Chen 2013). The local resolution of the map was estimated with the ResMap software (available at http://resmap.sourceforge.net) (Kucukelbir 2014). Figure illustration and rigid body fitting with the model of the crystal structure from *Ks*HDH was performed using Chimera (Pettersen 2004). The structure was refined by PHENIX real space refinement followed by manual rebuilding in COOT (Emsley 2004).

2.2.5.8 Spectroelectrochemical Analyses

Spectropotentiometric titrations of wild type Kustc0562 and Kustc0563 were performed at room temperature in a custom-built optically transparent thin-layer electrochemical (OTTLE) cell (designed and manufactured by Andreas Dietl) connected to a Keithley model 2450 source measure unit (SMU; Tektronix Inc., Beaverton, OR, USA) operated as a potentiostat. The electrochemical cell was based on a 26 × 76 mm glass slide. Ultrathin gold electrode connections (< 1 µm thickness) were prepared by spray coating with gold paint ("Glanzgold" GG B 15/M; Heraeus, Hanau, Germany) followed by heating to 520 °C. A silver/silver chloride reference electrode patch was prepared using Ag/AgCl ink (ALS Co., Ltd, Tokyo, Japan). A gold mesh (500 wires/inch, 60 % open area, 10 µm thickness; Goodfellow Ltd., Huntingdon, UK) was used as working electrode. The gold mesh was modified by incubation for > 1 h in a solution of 20 mM 4,4'-dithiodipyridine (DTP) in 160 mM TrisCl, pH 8.0 and 20 % (v/v) ethanol. 15 µL of Kustc0562 or Kustc0563 ($A_{280}^{1\ cm} \approx 12$) in 10 mM MOPS/KOH (pH 7.0), 100 mM KCl was loaded onto the DTP-modified gold mesh in the pre-assembled cell. In case of Kustc0563 the sample was supplemented with a mediator mix containing ten redox mediators at a final concentration of 10 µM each (Collins 1993, Table 2.1).

Afterwards the cell was closed with a 22 × 22 mm glass cover slip, excess liquid was carefully removed and the cell was sealed with parafilm. The cell setup is shown in figure 2.1. The experiment started with a reductive pre-poise at -300 mV *vs.* Ag/AgCl/100 mM KCl for 10 min. The following titrations were performed in oxidative and reductive directions in steps of 50 mV and 20 mV distant and close to the midpoint potential, respectively. The applied potential was automatically changed using a TSP script running on the SMU once the measured current stopped changing *i.e.* the system reached redox equilibrium. Spectra in the visible range (350 to 700 nm, scan speed 400 nm/min, 0.5 nm bandwidth) were recorded using JASCO V-650 and V-760 spectrophotometers (Jasco GmbH, Gross-Umstadt, Germany). Spectra measurements were automatically triggered using the SMU and a custom-built mouse interface.

a

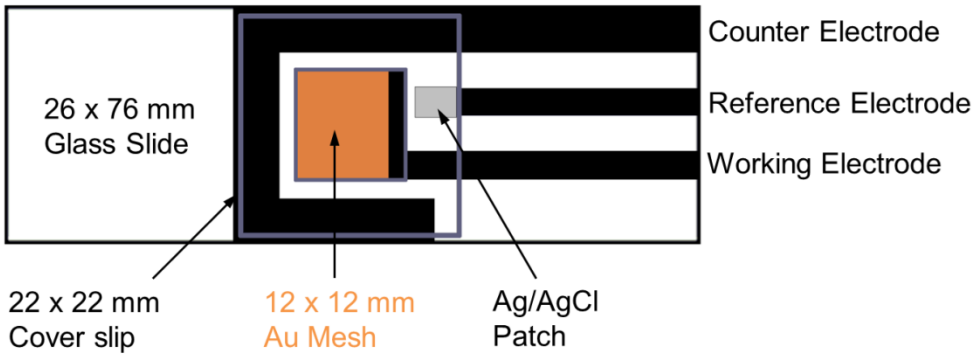

b

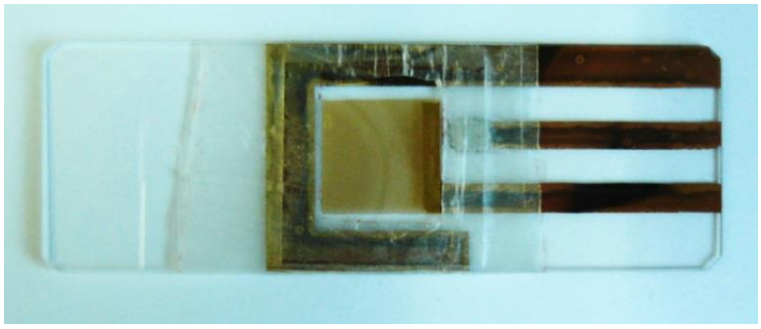

c

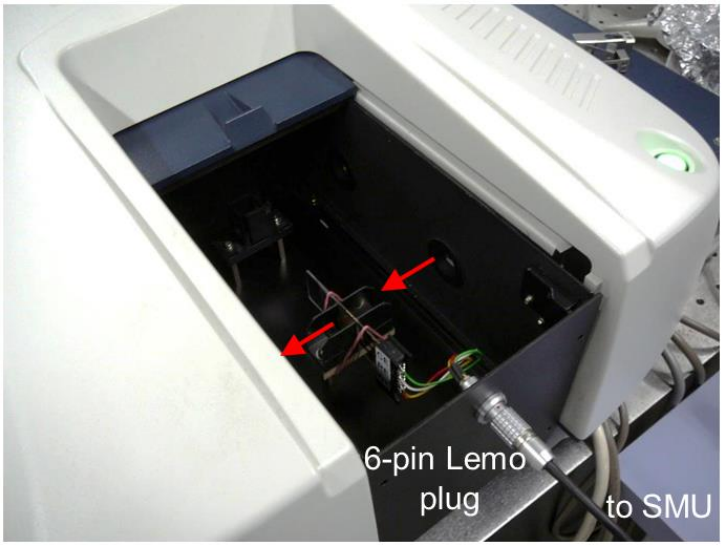

Figure 2.1 Spectroelectrochemical Setup to determine Redox Potentials
a) Schematic cell setup. **b)** Photo of the assembled cell. **c)** Cell mounted in a Jasco V-650 spectrophotometer. The light path is indicated by arrows.

Raw spectrum data were processed using the Jasco32 software. Absorbance values at 420 nm (Soret band) and 550 nm (α-band) were fitted to a single Nernstian function (eq. 2.5) using non-linear least square minimization in Microsoft Excel in order to determine the midpoint potential (E_m).

$$Y = A - A_{ox} = \frac{a}{\exp\left(\frac{nF}{RT}\left(E - E_m\right)\right) + 1} \qquad \text{(eq. 2.5)}$$

A: absorbance, A_{ox}: absorbance of fully oxidized state, a: amplitude, E: potential, E_m: midpoint potential, n: number of electrons (n=1), F: Faraday constant (96,485.34 J V^{-1} mol^{-1}), T: absolute temperature (in K), R: ideal gas constant (8.3145 $Jmol^{-1}K^{-1}$)

Compound	E° *vs* SHE (mV)	Mw (g/mol)
K-Ferricyanide	430	329.24
N,N,N',N'-tetramethyl-phenylenediamine (TMPD)	275	164.25
Dichlorophenolindophenol (Na salt)	215	290.08
Phenazine methosulfate	80	306.34
Gallocyanine	20	336.73
Indigo carmine	-125	466.35
Janus green B	-220	511.06
Safranine T	-290	350.84
Benzyl viologen dichloride	-350	409.35
Methyl viologen dichloride	-430	257.16

Table 4.1 Redox mediators used in the spectropotentiometric Titration of Kustc0563
Each redox mediator was diluted to a final concentration of 20 mM in water (TMPD in ethanol). The stock solutions were mixed and diluted to a final concentration of 100 µM of each compound in 10 mM MOPS/KOH (pH 7.0), 100 mM KCl. Prior to the measurement 13.5 µL cytochrome solution (buffer exchanged to 10 mM MOPS/KOH (pH 7.0), 100 mM KCl) and 1.5 µL of the redox mediator solution (100 µM of each mediator) were mxed.

In order to correct the potential against the standard hydrogen electrode (SHE), the voltage between the Ag/AgCl patch in a drop of 10 mM MOPS/KOH (pH 7.0), 100 mM KCl and a commercial Ag/AgCl/4 M KCl reference electrode (Pine Research Instrumentation, Durham, NC, USA; E°= + 200 mV *vs* SHE) was measured.

2.2.6 Bioinformatics

2.2.6.1 Signal Peptide Prediction

Proteins destined for the anammoxosome (such as c-type cytochromes) possess a signal peptide at their N-terminus. This N-terminal signal peptide is recognized and translocated by the Sec-type machinery similar to *E. coli* for periplasmic or secretory proteins (Ferousi 2013). N-terminal signal peptides of anammoxosomal proteins were predicted using the SignalP 3.0 server (http://www.cbs.dtu.dk/services/SignalP-3.0) (Bendtsen 2004). Both Hidden Markov Model (HMM) as well as the Neural Network Models (NNM) for Gram-negative bacteria were applied. Predictions from HMM turned out to be more reliable.

2.2.6.2 Protein Properties Predictions

The properties of proteins such as theoretical molecular mass, isoelectric point (pI), amino acid composition and absorption extinction coefficient at 280 nm were predicted using the ProtParam module of the ExPASy server (http://web.expasy.org/protparam; Swiss Institute of Bioinformatics Lausanne, Switzerland).

2.2.6.3 Homology Searches

Sequences were retrieved from the National Centre for Biotechnology Information (NCBI; https://www.ncbi.nlm.nih.gov) database. Queries for similar protein or nucleic acid sequences were performed using NCBI-BLAST (BLASTp or BLASTn) against bacteria (Taxonomy ID: 2) using a non-redundant database search (https://blast.ncbi.nlm.nih.gov/Blast.cgi). Structures with similar protein sequences were searched again using BLASTp but in PDB database search mode.

2.2.6.4 Sequence Alignments and Phylogenetic Analyses

Sequence alignments of proteins or nucleic acids were performed using the Clustal Omega server (http://www.ebi.ac.uk/Tools/msa/clustalo) (Sievers 2011) applying default settings. Phylogenetic tree reconstruction was performed by the Phylogeny.fr server (http://www.phylogeny.fr/; Dereeper 2008) based on multiple sequence alignment in MUSCLE (Edgar 2004), alignment refinement in Gblocks (Castresana 2000) and tree reconstruction by the maximum-likelihood method in PhyML (Guindon 2010). Phylogenetic trees were rendered using the MEGA 6.0 software (Tamura 2013).

2.2.6.5 Transcriptomics

Illumina reads from a *K. stuttgartiensis* metatranscriptome dataset SRR037687 (Kartal 2011) were mapped against the reference genome (CT030148, CT573071–4) using the Burrows-Wheeler Aligner (Li 2009; http://bio-bwa.sourceforge.net/) by Thomas Hackl. The mRNA read coverage (logarithmic scale) was plotted against the length of the gene clusters using the Integrative Genomics Viewer (Thorvaldsdottir 2013). Putative promotor sites were predicted using BPROM (http://linux1.softberry.com/all.htm; Solovyev 2011).

2.2.7 Crystallographic methods

2.2.7.1 Crystallization

Initial crystallization screening was performed using the sitting drop vapour diffusion method. 100 nL of concentrated proteins were screened against 100 nL precipitant solutions from commercial crystallization screens pre-pipetted into 96-well sitting drop trays (Greiner XTL low-profile, Greiner Bio One, Frickenhausen, Germany) using a Mosquito crystallization robot (TTP Labtech Ltd., Melbourne, UK) at 20 °C. The setups were observed using a Rock imager 100 (Formulatrix Inc, Bedford, USA). Identified crystallization hit conditions were used to prepare bigger crystallization setups in 24-well hanging drop Linbro plates (ICN Biomedicals Inc., Aurora, Ohio, USA). 800 µL of precipitant solution was used in the wells, while the drops contained 1-2 µL of protein solution mixed with 1-2 µL of precipitant solution. Crystals were grown for up to several days at 20 °C.

2.2.7.2 Protein Crystal Mounting, Soaking and Cryo Cooling

To transfer and mount protein crystals appropriately sized (0.1, 0.2, 0.3 or 0.4 mm) nylon fiber loops (Hampton Research, Aliso Viejo, CA, USA) were used. If appropriate, crystals were soaked into cryo-protectant solution containing appropriate chemicals such as substrates, inhibitors or heavy metals. In order to prevent ice formation, protein crystals were incubated in cryo protecting agents such as 20-30 % (v/v) glycerol or 20-25 % (v/v) ethylene glycol in mother liquor for 1-10 min prior to being flash-frozen in liquid nitrogen.

2.2.7.3 In-house Diffraction Quality Testing

Cryo-protected protein crystals were tested for their diffraction quality using a wavelength of 1.5418 Å (Cu Kα) generated by a rotating copper anode X-ray source (MicroMax 007 HF, Rigaku, Kemsing, UK). Crystals were exposed to X-rays for 10 min on a MarDTB diffractometer with the crystals kept at 100 K by a nitrogen cryostream (Oxford Cryosystems Ltd., Long Hanborough, UK). Diffraction images were collected using a Mar345 image plate (Mar Research, Norderstedt, Germany).

2.2.7.4 Data Collection

High resolution native data and high-redundancy single-wavelength anomalous dispersion (SAD) data were collected by members of the Department of Biomolecular Mechanisms of the MPI for Medical Research at beamline X10SA at the Swiss Light Source (SLS) of the Paul-Scherrer-Institute (Villigen, Switzerland). Diffraction data sets were collected using the rotation method with oscillation ranges of 0.1–0.2° (fine-slicing) while the crystals were kept at 100 K. Diffraction images were recorded using a PILATUS 6M detector (Dectris, Baden, Switzerland).

2.2.7.5 Structure Determination

Diffraction data were processed using XDS (Kabsch 2010). Experimental phases using data from SAD experiments were obtained using AutoSHARP 2.0 (Global Phasing Ltd, Cambridge, UK) or PHENIX AutoSol (Terwilliger 2009). PHASER (McCoy 2007) was used to determine phases by the molecular replacement (MR) method against an appropriate crystallographic structure of a homologous protein. When required density modification was performed using DM (Cowton 1994) with application of non-crystallographic symmetry operations. Structural models were iteratively built using COOT (Emsley 2004) and refined using REFMAC (Murshudov 1997) or PHENIX refine (Afonine 2012). Structure validation was performed using validation tools in COOT or the MolProbity server (http://molprobity.biochem.duke.edu/). Figures were prepared using PyMOL (Schrödinger LLC) or UCSF Chimera (Pettersen 2004).

2.2.7.6 Structure Analyses

Structural assemblies were calculated from the atomic coordinates of the molecules in the asymmetric unit using the Protein Interfaces, Surfaces and Assemblies service (PDBePISA) at the European Bioinformatics Institute (http://www.ebi.ac.uk/pdbe/prot_int/pistart.html, Krissinel & Henrick, 2007). Structurally similar proteins were searched against the protein data bank (PDB) using the Dali server (http://ekhidna.biocentre.helsinki.fi/dali_server/; (Holm 2010).

Hydrodynamic properties such as sedimentation coefficients $S_{20,w}$ or radii of gyration r_g were calculated from molecular models using bead-modelling methodologies by the program WinHYDROPRO (vers. 10; Ortega 2011). In the calculations the following parameters were used: solvent viscosity η = 0.010194 g cm^{-1} s^{-1}, solvent density ρ = 1.00135 g cm^{-3} at a temperature of 20 °C, partial specific volume of the protein of 0.7300 mL/g.

Chapter 3

Structural, Biophysical and Biochemical Characterization of the Hydrazine Dehydrogenase (HDH) Enzyme Complex

3. Structural, Biophysical and Biochemical Characterization of the Hydrazine Dehydrogenase (HDH) Enzyme Complex

3.1 Introduction

Bacterial multiheme c-type cytochromes form a large group of evolutionarily related heme proteins, which are involved in the global biogeochemical nitrogen and sulphur cycles (Simon 2011; Kartal 2013). Representative examples of this family are pentaheme c-type cytochrome nitrite reductases (NrfA) which perform the six-electron reduction of nitrite to ammonium and octaheme c-type cytochromes (OCCs). The latter class includes MccA (or SirA), which catalyzes the six-electron reduction of sulfite to sulfide but also has a slight nitrite reductase activity (Hermann 2015) and more importantly hydroxylamine oxidoreductases (HAOs) and hydrazine dehydrogenases (HDHs) from aerobic and anaerobic ammonium oxidizers (Igarashi 1997; Maalcke 2014; Maalcke 2016). Despite often low sequence identities, remarkable structural similarities were noted when comparing the positions of the hemes among different OCCs (Fig 3.1; reviewed by Kartal 2016). It has also been postulated that OCCs have evolved from NrfA as the positions of hemes 1-5 of NrfA can be superimposed with hemes 4-8 in HAOs (Kartal 2016), which might imply that OCCs evolved by genetic fusion of an NrfA-like protein and a triheme c-type cytochrome (Fig 3.1) (Klotz 2008).

(Figure on next page)

Figure 3.1 Structural Features of Multiheme C-type Cytochromes involved in Nitrogen and Sulphur cycles
The left column shows structures of the monomers which are rendered as cartoons in rainbow colouring from the N-terminal part (blue) to the C-terminus (red). The middle column shows the arrangement of the heme cofactors with the central iron atoms as orange spheres. The quaternary structures are shown in a molecular surface representation on the right. The hemes' numbering indicates the order of the c-type heme binding motifs in the protein sequence. Catalytic hemes are circled in red. Blue circles indicate the heme cofactors that constitute electron entry or exit points. Hemes circled green are at the contact site with a neighboring subunit. The heme arrangement among all these examples is highly conserved despite significant differences in their overall structures and protein sequences.
a) Homotrimeric hydroxylamine oxidase from *Kuenenia stuttgartiensis* (*Ks*HOX; PDB id: 4N4J) (Maalcke 2014).
b) Ammonium-forming homodimeric pentaheme nitrite reductase (NrfA) from *Sulfurospirillum deleyianum* (PDB id: 1QDB) (Einsle 1999).
c) Hexameric octaheme nitrite reductase (ONR) from *Thioalkalivibrio nitratireducens* (PDB id: 2OT4) (Polyakov 2009).
d) Homotrimeric octaheme sulfite reductase MccA from *Wolinella succinogenes* (PDB id: 4RKM) (Hermann 2015).
e) Monomeric octaheme tetrathionate reductase from *Shewanella oneidensis* (PDB id: 1SP3) (Mowat 2004). The figure is adapted from (Kartal 2016).

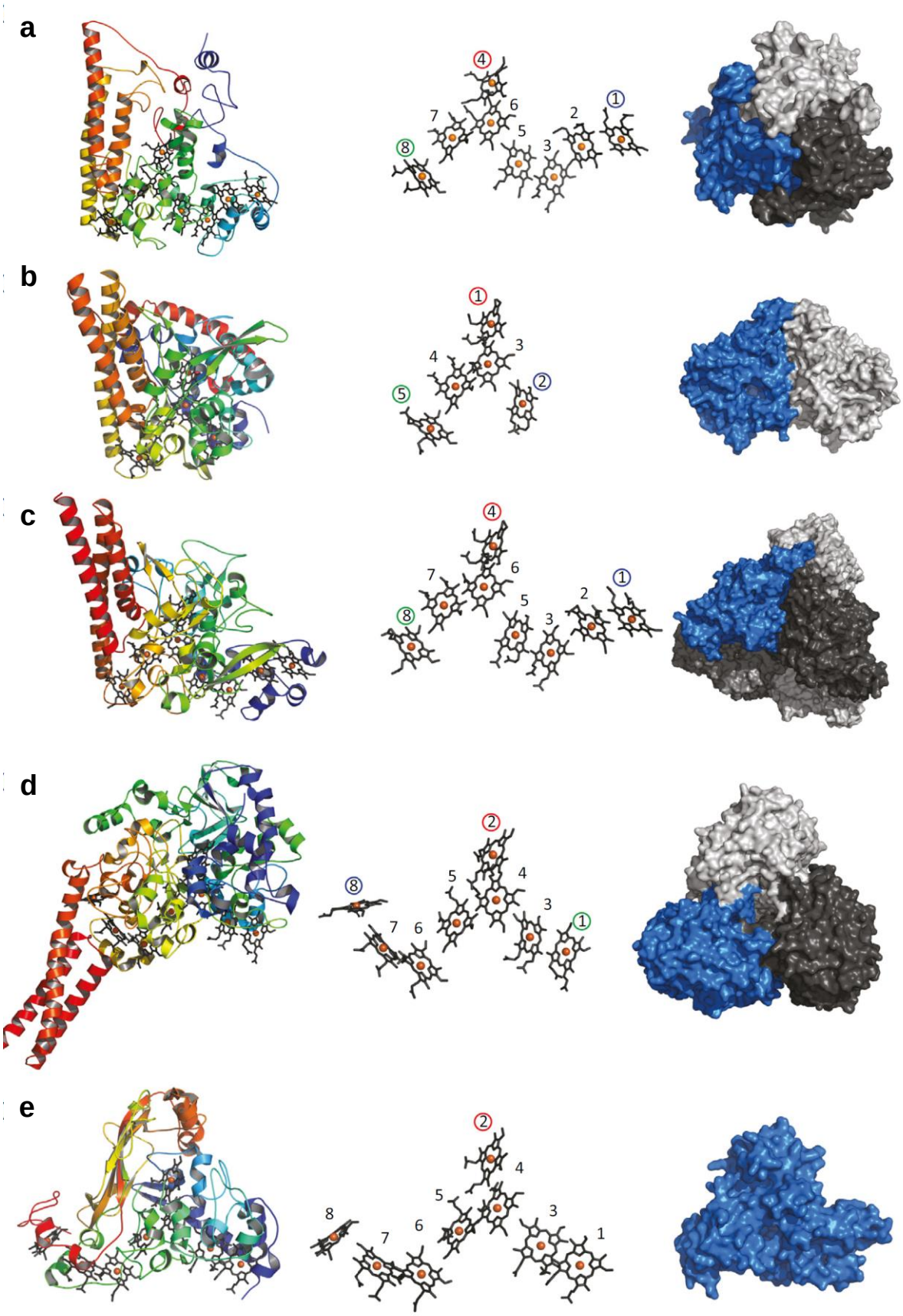
a
b
c
d
e

OCCs such as MccA (Hermann 2015), octaheme nitrite reductases (ONRs) (Polyakov 2009; Klotz 2008) or octaheme tetrathionate reductases (OTRs) (Mowat 2004; Atkinson 2007) all perform reactions in the direction of the reduction of their substrates only. On the contrary, some HAOs exclusively catalyze the oxidation of their substrates but do not work in the reductive direction under physiological conditions (Klotz 2008). This OCC family includes *Ne*HAO from *Nitrosomonas europaea* which catalyzes the four-electron oxidation of hydroxylamine to nitrite (Igarashi 1997; Cedervall 2013; Maalcke 2014), hydroxylamine oxidase from *Kuenenia stuttgartiensis* (*Ks*HOX, catalyzes the three-electron oxidation of hydroxylamine to nitric oxide; Maalcke 2014) and hydrazine dehydrogenase (HDH, catalyzes the four-electron oxidation of hydrazine to dinitrogen (Maalcke 2016; Shimamura 2007). Tuning of these HAOs to oxidative catalysis results from the covalent attachment of a tyrosine residue from a neighboring chain to the catalytic heme *via* two bonds described in figure 3.2. The involved tyrosine is proposed to temporarily store one electron derived from substrate oxidation. This tyrosine-heme crosslink causes pronounced heme ruffling and can be diagnosed by the presence of a characteristic band at around 460 nm in the UV-Vis spectrum upon reduction, hence the name P460 cofactor was conferred to this active site heme. The distal side of the P460 cofactor has a vacant coordination site were substrate molecules bind during the reaction. It has been observed that these HAOs can perform oxidation reactions of compounds other than their *in vivo* substrates (Maalcke 2014). Hydroxylamine, for instance, is the physiological substrate of *Ne*HAO and *Ks*HOX, but it has been shown that they can catalyze the oxidation of hydrazine as well (Maalcke 2014). Apart from the active site heme P460, there are seven other hemes which are *bis*-His coordinated and are involved in electrons transfer.

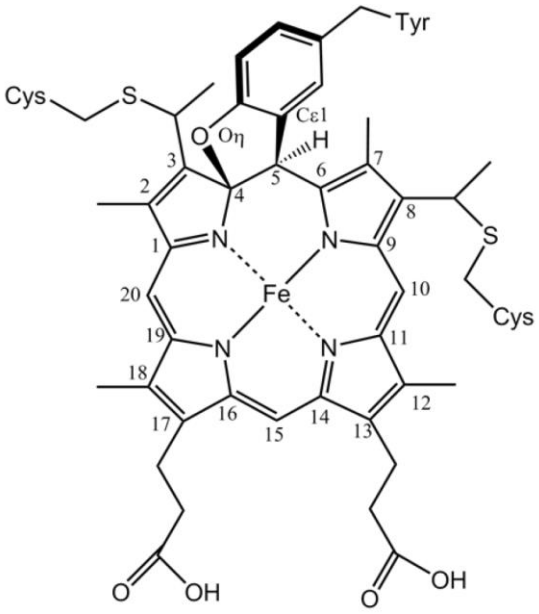

Figure 3.2 The tyrosine crosslink to the active site P460 heme.
Structure of the P460 cofactor with two bonds: one between Oη and C4 another between Cε1 and C5 of a conserved tyrosine residue and the heme macrocycle, respectively. The figure is adapted from Andreas Dietl's PhD thesis (Dietl 2016) and also described in (Maalcke 2014; Cedervall 2013).

The *Kuenenia stuttgartiensis* genome contains ten paralogues of HAO-like proteins (Kartal 2011) and *Scalindua japonica* codes for even eleven HAOs (Oshiki 2017) which are highly conserved among the sequenced genomes so far. Variable degrees of expression were reported for these paralogues (Fig 3.3 a) (Kartal 2011). Transcriptomic analyses indicated that apparently Kustc0694 shows the highest expression level followed by Kustc1061 (hydroxylamine oxidase or *Ks*HOX). Kustc0694 and its homologue from *Jettenia caeni* (KSU1_D0435) has been shown to be the genuine hydrazine dehydrogenase (HDH), based on their high hydrazine oxidation activities, whereas hydroxylamine (NH_2OH) and nitric oxide (NO) act as inhibitors (Kartal 2011; Maalcke 2016; Shimamura 2007). On the contrary, *Ks*HOX has been shown to perform the three-electron oxidation of NH_2OH to NO. Additionally, it can also catalyze the oxidation of hydrazine to nitrogen but with lower specificity (Maalcke 2014).

Despite having only 30 % sequence identity, the structures of *Ks*HOX and *Ne*HAO are both fully superimposable homotrimers (structural rmsd of 1.64 Å for 358 residues, Fig 3.3 b). Except few residues, the active sites of these two enzymes are similar possessing the typical tyrosine-heme crosslink and a highly conserved His-Asp pair (Fig 3.3 c). The ring-like arrangement of the hemes in homotrimeric *Ks*HOX is also conserved in *Ne*HAO, with heme 4 serving as active site and heme 1 as electron exit site (Fig 3.3 d). The most important

difference is the substitution of tyrosine 358 (in *Ne*HAO) to methionine 323 (in *Ks*HOX), which is proposed to contribute to their product specificities (Maalcke 2014). The tyrosine side chain in *Ne*HAO is proposed to position a water molecule which provides an additional oxygen atom during the last oxidation step of a heme-bound NO-intermediate that forms during the oxidation of hydroxylamine (NH_2OH) to nitrite (NO_2^-, eq. 3.1). The methionine in *Ks*HOX, however, would hinder water molecules from binding in the distal pocket of the active site heme, such that hydroxylamine oxidation would stop at the level of nitric oxide (NO; eq. 3.2). However, both *Ks*HOX and *Ne*HAO have been shown to catalyze the oxidation of hydrazine (Maalcke 2014), but with lower specificities in case of *Ks*HOX. Surprisingly, *Ne*HAO shows a significantly higher activity for hydrazine oxidation, even more than that of *Ks*HDH (Maalcke 2016). Based on protein sequence analyses, the trimeric structure of HDH was also expected to be similar to that of *Ks*HOX with conserved positions of the hemes. However, several differences are also expected which result in the fact that HDH oxidizes hydrazine with higher specificity than HOX whereas hydroxylamine and NO act by inhibiting hydrazine oxidation activity of HDH (eq. 3.3) (Maalcke 2016).

(Figure on next page)

Figure 3.3 Overview of hydroxylamine oxidoreductase (HAO)-like c-type octaheme proteins in *Kuenenia stuttgartiensis*. **a)** HAO-like proteins in the *K. stuttgartiensis* (kust) genome. Most closely related proteins at sequence level are boxed by broken lines. The lengths of the polypeptides are drawn to scale of amino acids (aa). The homologous heme sites are vertically aligned. In the "Redox partners" column "putative" electron transfer partners are listed based on their position in the same gene cluster. Expression values are given as n-fold coverage of Solexa RNA sequencing of the *K. stuttgartiensis* transcriptome (Strous 2006; Kartal 2011). Structural motifs: TMH, transmembrane-spanning helix; cleavage site, N-terminal signal peptide cleavage site; multi-copper oxidase, multi-copper oxidase domain; catalytic heme; CXXCH, heme c-binding motif; CXXXXCH, unusual heme c-binding motif in hydrazine dehydrogenases (kustc0694 and kustd1340); Tyrosine crosslink, tyrosine covalently linking subunits; laminin, laminin sequence. Remarkably, these HAO-like proteins are conserved in all sequenced genomes of anammox bacteria, except for kustd2021.**b)** Overall architecture of the homotrimeric hydroxylamine oxidase from *K. stuttgartiensis* (*Ks*HOX) (PDB ID: 4N4L) (Maalcke 2014). Its three subunits are displayed in different colors. The localization of the catalytic site is indicated by the square. **c)** X-ray structure of the heme 4 (P460) catalytic center of *Ks*HOX soaked with hydrazine seen from the same axis as in b). A putative diazene (HN=NH) (blue) is seen on top of the heme. **d)** The ring-like arrangement of the c-type hemes in homotrimeric hydroxylamine oxidase from *K. stuttgartiensis* (*Ks*HOX). The figure shows the outline of the structure of trimeric *Ks*HOX (PDB ID: 4N4J) seen from the bottom along the three-fold symmetry axis featuring the 24 hemes (eight hemes per monomer). The substrate oxidation at the catalytic site (heme 4) followed by transfer of electrons towards the exit site heme 1 (indicated by arrows). The spatial arrangement of these hemes is fully conserved in hydroxylamine oxidoreductase from *Nitrosomonas europaea* (*Ne*HAO) (Maalcke 2014; Kartal 2016). Figure adapted from Kartal *et al.* (2016).

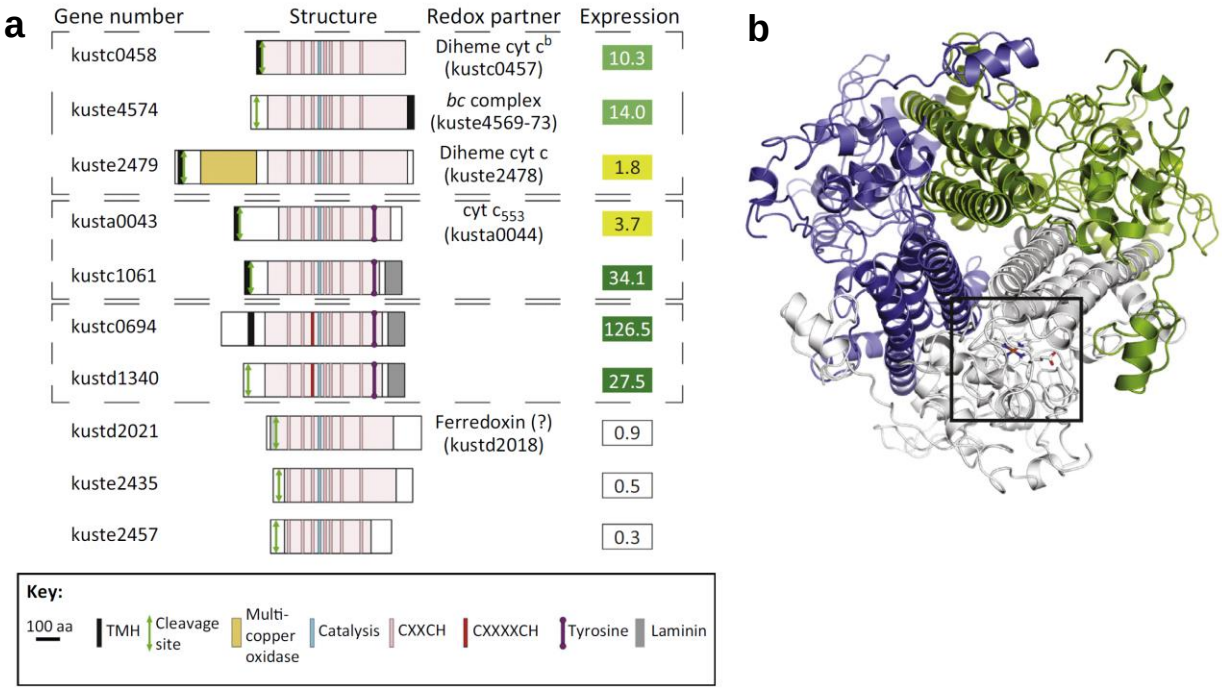
a
Gene number
Structure
Redox partner
Expression
kustc0458
Diheme cyt c^b (kustc0457)
10.3
kuste4574
bc complex (kuste4569-73)
14.0
kuste2479
Diheme cyt c (kuste2478)
1.8
kusta0043
cyt c553 (kusta0044)
3.7
kustc1061
34.1
kustc0694
126.5
kustd1340
27.5
kustd2021
Ferredoxin (?) (kustd2018)
0.9
kuste2435
0.5
kuste2457
0.3
Key:
100 aa
TMH
Cleavage site
Multi-copper oxidase
Catalysis
CXXCH
CXXXXCH
Tyrosine
Laminin

b

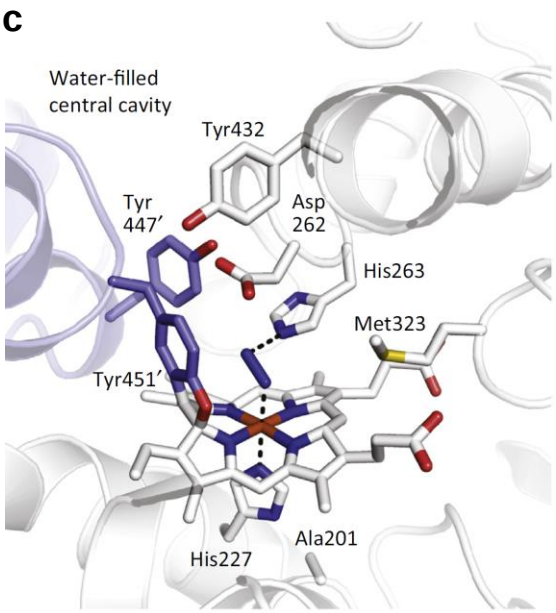
c
Water-filled central cavity
Tyr432
Tyr 447′
Asp 262
His263
Met323
Tyr451′
Ala201
His227

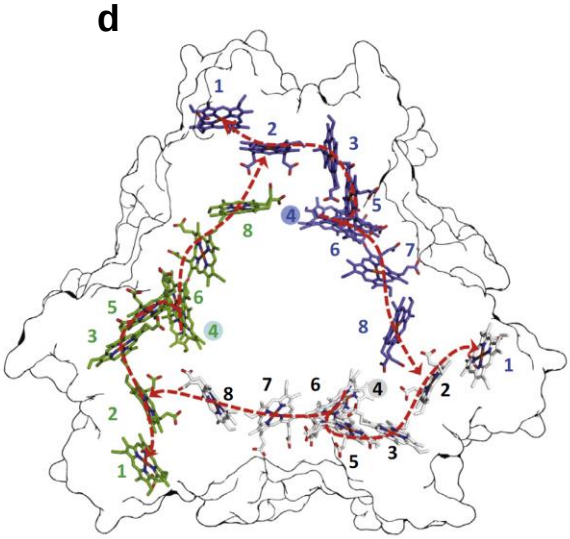
d

$$NH_2OH + H_2O \longrightarrow NO_2^- + 5\,H^+ + 4\,e^- \quad \text{(eq. 3.1)}$$

$$NH_2OH \longrightarrow NO + 3\,H^+ + 3\,e^- \quad \text{(eq. 3.2)}$$

$$N_2H_4 \longrightarrow N_2 + 4\,H^+ + 4\,e^- \quad \text{(eq. 3.3)}$$

Kustc0694 has a close paralogue (Kustd1340) with >98 % sequence identity, hence, it could have evolved by gene duplication as a second copy of HDH. Kustd1340, however, has been detected in relatively low quantities (at both mRNA- and protein levels) and only under stress conditions (Maalcke 2016; Kartal 2016). Therefore, it is possible that Kustd1340 plays some special role under certain environmental conditions. In all other known genomes there are also two copies of HDH (Maalcke 2016; Kartal 2016; Oshiki 2017; Ali 2015b; Shimamura 2007). The unique feature by which HDH can be identified is the presence of an unusual CX_4CH motif at the heme 3 binding site (Fig 3.3 a). Recently, Oshiki *et al.* (2017) showed by transcriptomic and proteomic studies that both copies of HDH in the anammox bacterium *Scalindua japonica* are abundant when compared to other proteins. However, one copy of HDH (SCALIN_C45_0044) which is located downstream of the hydrazine synthase (HZS) gene cluster, shows significantly higher expression while the other one (SCALIN_C38_0043) is found in lower quantity (approximately half of SCALIN_C45_0044), however still slightly higher than other prominent proteins such as the hydrazine synthase beta and gamma subunits (HZSβγ; Fig 3.4). It should be noted that *S. japonica* is a marine anammox bacterium while *K. stuttgartiensis* lives in fresh water. Therefore, the difference in the environment might well be responsible for different expression levels of the second copy of HDH, as it was also pointed out in case of *K. stuttgartiensis* (Maalcke 2016). Surprisingly, another copy of a HAO-like protein containing a CX_4CH motif at heme 3 was also detected, however with significantly lower expression (nearly 40 times less than SCALIN_C38_0043 and 90 times less than SCALIN_C45_0044) (Oshiki 2017).

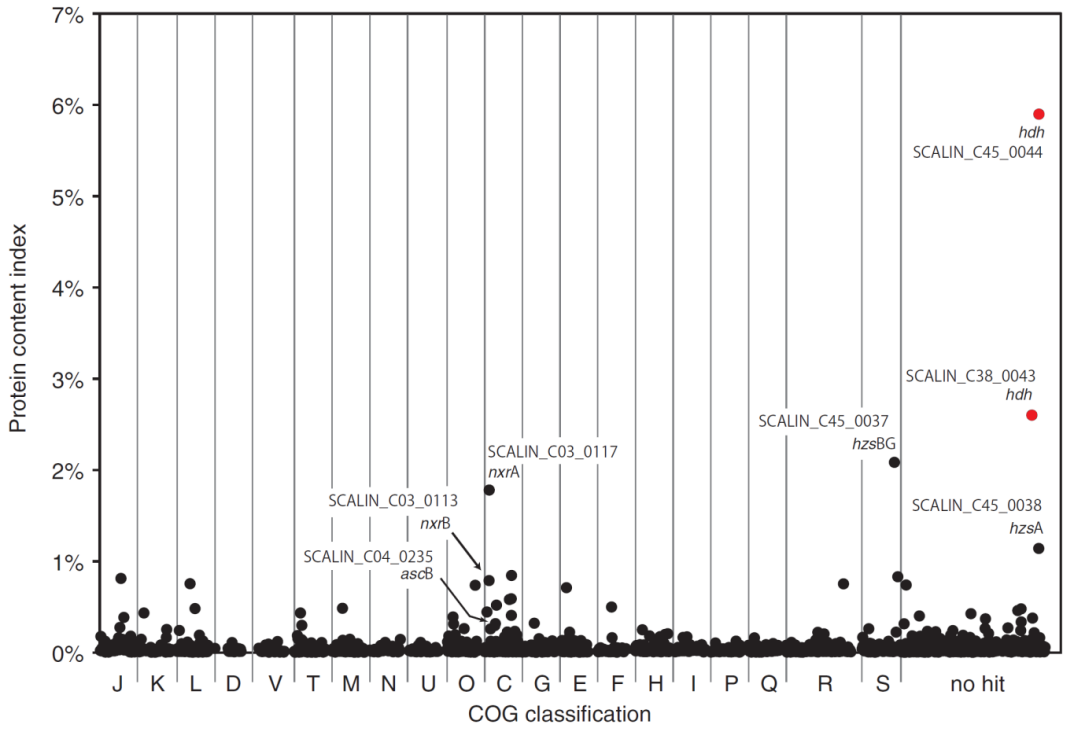

Figure 3.4 Abundance of proteins detected in *Scalindua japonica* cells
Extracted total proteins were separated by sodium dodecyl sulphate polyacrylamide gel electrophoresis (SDS-PAGE) and identified by nanoscale liquid chromatography coupled with tandem mass spectrometry (nano LCMS/MS) followed by MASCOT search (Perkins 1999). Abundance of the identified proteins in the cells of *S. japonica* is given as protein content indices calculated from the exponentially modified protein abundance index (emPAI). Descriptions of clusters of orthologous groups (COG) functional categories are as follows: [J] translation, ribosomal structure and biogenesis; [K] transcription; [L] replication, recombination and repair; [D] cell cycle control, cell division and chromosome partitioning; [V] defense mechanisms; [T] signal transduction mechanisms; [M] cell wall/membrane/envelope biogenesis; [N] cell motility; [U] intracellular trafficking, secretion and vesicular transport; [O] post-translational modification, protein turnover and chaperones; [C] energy production and conversion; [G] carbohydrate transport and metabolism; [E] amino acid transport and metabolism; [F] nucleotide transport and metabolism; [H] coenzyme transport and metabolism; [I] lipid transport and metabolism; [P] inorganic ion transport and metabolism; [Q] secondary-metabolite biosynthesis, transport and catabolism; [R] general function prediction only; and [S] function unknown. Category 'no hit' contains proteins that are not assigned to any COG functional category. Note that both copies of HDH (SCALIN_C38_0043 and SCALIN_C45_0044) are highly abundant (red dots). Figure is adapted from Oshiki *et al.* (2017).

As mentioned earlier, HDH can only oxidize hydrazine, while hydroxylamine and NO act as inhibitors leading to the important question what causes its substrate specificity and the mechanism of inhibition. Moreover, a previous study reported the presence of higher oligomeric states namely octamers of covalently linked HDH trimers (*i.e.* 24mers, $(\alpha_3)_8$) and even decamers of trimers (*i.e.* 30mers, $(\alpha_3)_{10}$) as inferred by biophysical analyses in solution and negative stain transmission electron microscopy (TEM) (Maalcke 2016). These findings raise the question how HDH trimers arrange to higher oligomeric forms and whether these oligomers are physiologically relevant.

In order to answer these questions, this chapter describes a detailed structural analysis of the *Ks*HDH 24-mer by means of X-ray crystallography. This work is complemented by the 3D reconstruction of *Ks*HDH 24- and 30-mers by cryo-transmission electron microscopy (cryo-TEM) performed in collaboration (Kristian Parey, MPI of Biophysics, Frankfurt). Further biophysical studies by analytical ultracentrifugation (AUC), analytical size exclusion chromatography coupled with multi-angle static light scattering (SEC-MALS) and negative stain TEM were performed to analyze the formation of higher HDH oligomers under different conditions. Finally, the influence of oligomer formation on HDH activity was investigated by biochemical assays. Several investigations described in this chapter were performed in parallel on the hydrazine dehydrogenases from both *Kuenenia stuttgartiensis* and *Brocadia fulgida* (Broful01550-51, see chapter 5). In all further sections of the current chapter, Kustc0694 will be referred as *Ks*HDH, Broful01550-51 as *Bf*HDH and Kustc1061 as *Ks*HOX.

3.2 Results

3.2.1 Crystallization of *Ks*HDH

Initial crystallization hits were obtained from 96-well sitting drop vapor diffusion setups using commercially available crystallization screens (Molecular dimensions, UK). 12 % (w/v) PEG 4000, 0.34 M $(NH_4)_2SO_4$ and 0.1 M sodium citrate (pH 5.5) was used as the starting condition for further optimization of the crystallization by the hanging drop vapor diffusion method in 24-well plates at 20 °C. While no effect of the applied concentration of $(NH_4)_2SO_4$ (0.2-0.3 M) was seen, increasing PEG concentrations affected the morphology of the crystals. At lower PEG concentrations (8-9 %) crystals grew in 3-4 days, yielding smooth, thick, elongated hexagonal blocks with a length of up to 200-400 µm (Fig 3.5 a). At higher PEG concentrations, however, crystals grew within a few hours, looked more intergrown and diffracted to lower resolution (Fig 3.5 b). The obtained HDH crystals tended to dissolve when being exposed after opening the setup during crystal fishing, however, could be stabilized for several hours by adding mother liquor with added cryoprotectant (25 % v/v glycerol or ethylene glycol) to the crystallization droplet. Although ethylene glycol promoted longer stability of the crystals, glycerol resulted in better diffraction and was therefore used as cryoprotectant (however, no statistically significant studies were conducted).

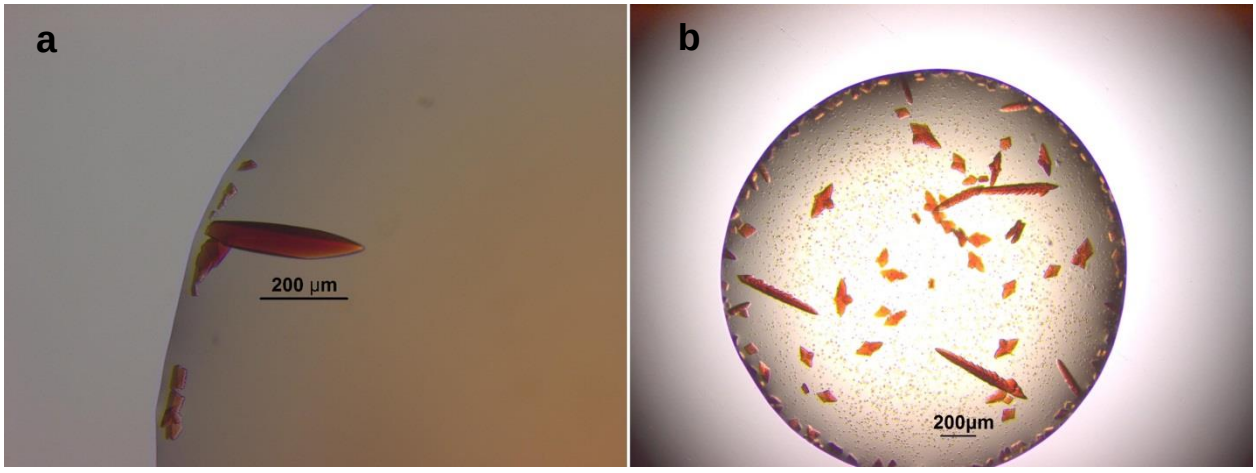

Figure 3.5 Crystals of *Ks*HDH
Crystals were grown in 24-well hanging drop vapor diffusion setups at 20 °C. Droplets of 1 µL *Ks*HDH stock (A_{280}^{1cm} = 20 and A_{408}^{1cm} = 76, stored in 25 mM HEPES/KOH pH 7.5, 25 mM KCl) were mixed with 1 µL precipitant solution on cover slips, which were placed over reservoir wells containing 800 µL of precipitant solution. **a)** A big (~400 µm) crystal grown at low PEG 4000 concentration (8-9 % w/v) and 250 mM ammonium sulfate. **b)** Crystals grown at higher PEG 4000 concentration (≥ 10% w/v PEG) and 250 mM ammonium sulphate.

3.2.2 Structure Determination and Refinement of *Ks*HDH

A dataset with a resolution limit of 3.0 Å was collected using an X-ray wavelength of 1.698 Å and raw data were processed with XDS (Kabsch 2010). The crystals showed $P3_1$ space group symmetry with very large unit cell dimensions of $a=b=212$ Å, $c=397$ Å; $\alpha=\beta=90°$, $\gamma=120°$.

The phases were solved by molecular replacement (MR) using PHASER (McCoy 2007), with the structure of the *Ks*HOX trimer (Kustc1061; PDB id: 4N4J) as search model. As discussed earlier, the structural positions of the hemes remain conserved in related OCCs despite moderate overall sequence identity (*Ks*HOX shares ~37 % sequence identity with *Ks*HDH). Therefore, the positions of the iron atoms in the hemes were explicitly included in the search model which turned out to be beneficial in solving the structure of *Ks*HDH as evidenced by the lack of model bias. The *Ks*HOX sequence in the initial model was replaced with conserved parts in the *Ks*HDH sequence using MOLREP (Vagin 1997), and later the gaps were built manually using COOT (Emsley 2004). Importantly, the asymmetric unit contains a complete 24mer assembly (24 *Ks*HDH chains or eight *Ks*HDH trimers).

Most surprisingly, twelve regions with extended extra electron density appeared in the asymmetric unit, which were initially built as poly-alanine chains (~88 amino acids; corresponding to a 9-10 kDa protein). The overall quality of the electron density map was significantly improved by density modification using DM (Cowtan 1999) by the application of 24-fold averaging for each chain of *Ks*HDH and additional 12-fold averaging for the smaller protein molecules found in the density during building and refinement (see below). Iterative model building and refinement cycles were performed using COOT (Emsley 2004) and REFMAC (Murshudov 1997), respectively. During refinement, non-crystallography symmetry restraints were applied separately for the *Ks*HDH monomers and the small protein, respectively. Care was taken to define the test set in thin resolution shells because of the high non-crystallographic symmetry (this resulted in a test site size of 5.0 %).

Another native data set from an identically grown crystal was collected at an X-ray wavelength of 0.9918 Å and processed up to a resolution limit of 2.8 Å using XDS. The *Ks*HDH model obtained from the previous data set was refined against the new data and further model building and refinement cycles were carried out as described above. After the small protein partner of *Ks*HDH was identified as the gene product of kustc1130 (without its signal sequence) using Edman sequencing (see section 3.2.9), the poly-alanine chain was replaced by the Kustc1130 sequence and the corresponding side chains were built into the 2.8 Å resolution electron density map.

The refinement of this model converged at a working R-factor of 23.4 % and R_{free} of 24.7 %, which indicates good agreement of the refined model with the experimental data. Because high non-crystallographic symmetry was expected from the outset of structure determination, the test set was defined in thin resolution shells. Thus, the small difference between R and R_{free} is unlikely to be due to contamination of the test set but rather to the enormous observation-to-parameter ratio caused by the large unit cell in combination with the use of non-crystallographic symmetry restraints. The validity of the model was analyzed by MOLPROBITY (Davis 2007) resulting in good Ramachandran statistics and stereochemical parameters. X-ray data and refinement statistics for the 2.8 Å dataset are given in table 3.1.

Table 3.1 X-ray data statistics of Native *Ks*HDH

Data set	**Native *Ks*HDH**
Data collection	
Strategy	Native, 1 dataset (total 1,200 images)
Space group	$P3_1$
Unit cell dimensions	
a, b, c (Å)	212.7, 212.7, 397.1
α, β, γ (°)	90, 90, 120
Wavelength (Å)	0.99186
Resolution range (Å) [a]	950.0-2.8 (2.9-2.8)
Reflections measured [a]	984,312 (103,296)
Reflections unique [a]	476,130 (48,761)
Completeness (%) [a]	96.6 (98.8)
Redundancy N [a]	2.0 (2.1)
I/σI [a]	6.67 (1.17)
R_{merge} (%) [a, b]	11.1 (74.5)
R_{meas} (%) [a, c]	14.7 (99.4)
$CC_{1/2}$ (%) [a, d]	98.9 (45.7)
CC* (%) [a, e]	99.7 (79.2)
Refinement	
Resolution range in refinement (Å)	184.9-2.8
Number of reflections in refinement	452,090
R_{work}/ R_{free} (%) [f]	23.4/ 24.7
Protein residues	15,039
(no. of atoms)	(118,913)
Water molecules	1,365
Overall B-factor (Å^2)	64.1
Rmsd bonds (Å)	0.0073
Rmsd angles (°)	1.3345
Ramachandran plot [g]	
Most favoured (%)	95.3
Additionally allowed (%)	4.6
Disallowed (%)	0.1

Legend to table 3.1

a) Values of the highest resolution shell are given in brackets.

b) $R_{merge} = \sum_h \left| \langle I_h \rangle - I_{h,i} \right| / \sum_h \sum_i^{n_h} I_{h,i}$, where I_i is the intensity of a reflection and $\langle I_h \rangle = \frac{1}{n_h} \sum_i^{n_h} I_{h,i}$ is the mean value of that reflection and the summations are over all reflections h.

c) $R_{meas} = \sum_h \sqrt{\frac{N}{N-1}}\ R_{merge}$ Redundancy-independent merging R factor (Diederichs 1997).

d) $CC_{1/2} = \sum_{i=1}^{n} \left(\left(x_i - \bar{x} \right) \left(y_i - \bar{y} \right) \right) \Big/ \sqrt{\sum_{i=1}^{n} \left(x_i - \bar{x} \right)^2 \sum_{i=1}^{n} \left(y_i - \bar{y} \right)^2}$ Pearson's correlation coefficient between merged intensity estimates $I_{h,i}$ (x_i, y_i) and $\langle I_h \rangle$ ($\bar{x}$, $\bar{y}$) from half data sets x and y.

e) $CC^* = \sqrt{\frac{2CC_{1/2}}{1+CC_{1/2}}}$ Estimated correlation coefficient of the merged dataset against the true (usually unmeasurable) intensities (Karplus 2012).

f) $R_{work} = \sum_h |F_{obs} - F_{calc}| / \sum_h F_{obs}$ (working set, no σ cut-off applied) R_{free} is calculated the same way as R_{work}, but for a reflection test set with 5.0 % of the reflections excluded from refinement.

g) Ramachandran analysis was performed using COOT (Emsley 2004).

3.2.3 Overall Structure of the *Ks*HDH 24mer in Complex with Kustc1130

As mentioned in section 3.2.2, *Ks*HDH crystallizes as an octamer of trimers (or 24mer) along with twelve copies of a ~10 kDa protein which was identified as Kustc1130. Although the octameric assembly of *Ks*HDH was known before through its biophysical characterization (Maalcke 2016), the presence of Kustc1130 as *Ks*HDH binding partner was unanticipated.

This overall octamer assembly with twelve copies of Kustc1130 results in a complex with a molecular mass of 1,725 kDa. The 2.8 Å overall structure of the *Ks*HDH 24mer looks like a cube where the *Ks*HDH trimers are located at each corner with their apexes pointing outwards. The three-fold rotational axis of each trimer passes through the center of the cube (Fig 3.6). Each monomer from a given trimer makes contacts with a monomer from one of the three neighboring trimers. In the 24mer assembly, all trimers have their entrances to the active site tunnel well exposed (Fig 3.6).

Kustc1130 is an elongated molecule present along the length of each possible 12 edges of the 24mer *Ks*HDH cube. Therefore, there are 12 molecules of Kustc1130 each of which is present between two neighboring trimers (for more details see section 3.2.6).

The particle size of the 24mer assembly along the diagonal through center of the cube is 250 Å and along each face of the cube is ~200 Å. The size of each of the 12 edges is ~138 Å. This gigantic assembly contains a high solvent content which is evident from a very big solvent cavity present in the center of the octamer of HDH trimers (Fig 3.6).

An analysis using PDBePISA (Krissinel 2007) (section 3.2.8) shows that only few residues of *Ks*HDH are involved in interactions between any two trimers in the octameric assembly. The side chains of the residues which contribute significantly in these interactions are Ile112, Phe116, Gln120, Ala123, Cys124, Val127 and Met128. Interestingly, most of these residues are either conserved or substituted by similar amino acids in *Ks*HOX which only exists as trimer. However, Ile112 and Met128 of *Ks*HDH are substituted by more hydrophilic residues namely Thr107 and Gln123, respectively, in *Ks*HOX (see sequence alignment Fig 3.17). Ala123 of *Ks*HDH is substituted by Leu118 in *Ks*HOX. Although both amino acids are hydrophobic in nature, the presence of Leu in place of Ala would lead to a clash between Leu118 and Val122 in *Ks*HOX (Val127 in *Ks*HDH) when assuming a similar trimer-trimer assembly for *Ks*HOX as observed for *Ks*HDH. All the mentioned residues of *Ks*HDH

involved in Van-der-Waals contacts align with the corresponding residues of *Ks*HOX both at the structural (not shown) and the sequence level (Fig 3.17). Significant hydrophobic trimer-trimer interactions (Van-der-Waals contacts) are summarized in table 3.2 and can also be corroborated with the results from PDBePISA. Thus, the octameric assembly of trimers (24mer) is held together by hydrophobic interactions. As mentioned, the trimer-trimer contact area is surprisingly small (~389 $Å^2$) with very few interacting residues. Kustc1130, however, interacts with any two neighboring trimers at the same time, hence working as a clip between them. The interactions between *Ks*HDH and Kustc1130 primarily involve hydrogen bonds and salt bridges (section 3.2.6).

Table 3.2 Hydrophobic interactions at the trimer-trimer junctions in the 24meric *Ks*HDH structure

Interacting residues (chain)	Atoms involved	Distance (Å)
Phe109 (E)—Val122 (G)	CE1—CG1	3.8
Phe109 (E)—Met128 (G)	CZ—SD	4.0
Ile112 (E)—Met128 (G)	CG2—CE	4.0
Ile112 (E)—Ile112 (G)	CD1—CD1	3.8
Met128 (G) —Phe109 (E)	SD—CZ	4.0
HEM600 (G)—Met128 (E)	CMC—CE	3.4
Ala123 (G)—Val127 (E)	CB—CG	3.4
Ala123 (E)—Val127 (G)	CB—CG	3.4
HEM600 (G)—HEM600 (E)	CBC—CBC	3.5
Val127 (E)—Glu120 (G)	CG1—CG	3.5
Val127 (G)—Glu120 (E)	CG1—CG	3.5

No hydrophilic interactions could be observed. However, between some of the trimers interfaces (e.g. the chain P and L containing trimer interface), Lys117 (P) binds a bridging sulfate ion which interacts with Arg303 (L) and Arg337 (L). In some cases Lys117 interacts with a neighboring trimer *via* a bridging water molecule. HEM600 corresponds to heme 1.

(Figure on next page)

Figure 3.6 Overall X-ray Structure of the *Ks*HDH 24mer in complex with Kustc1130
The left column shows a cartoon representation of 24meric HDH in different orientations, each trimer is represented in different colors. *Ks*HDH trimers are primarily α-helical. Kustc1130 (shown in grey), which has a 7-stranded β-sheet structure, is located in between two trimers. The right column represents surface views; again each trimer is represented in different colors with Kustc1130 in grey. The overall structure looks like a cube with the *Ks*HDH trimers present at the corner of the cube. The apex of each trimer is pointing outwards in the direction of the cube's corner. The distances along the diagonal through the center of the cube (250 Å, red), along each face of the cube (200 Å) and the size of each of the 12 edges (138 Å) are shown by scale bars. The red circles at the top surface representation of the 24meric *Ks*HDH assembly show the entrances to the active site tunnels. Each trimer has three of such tunnels (only one of them is indicated).

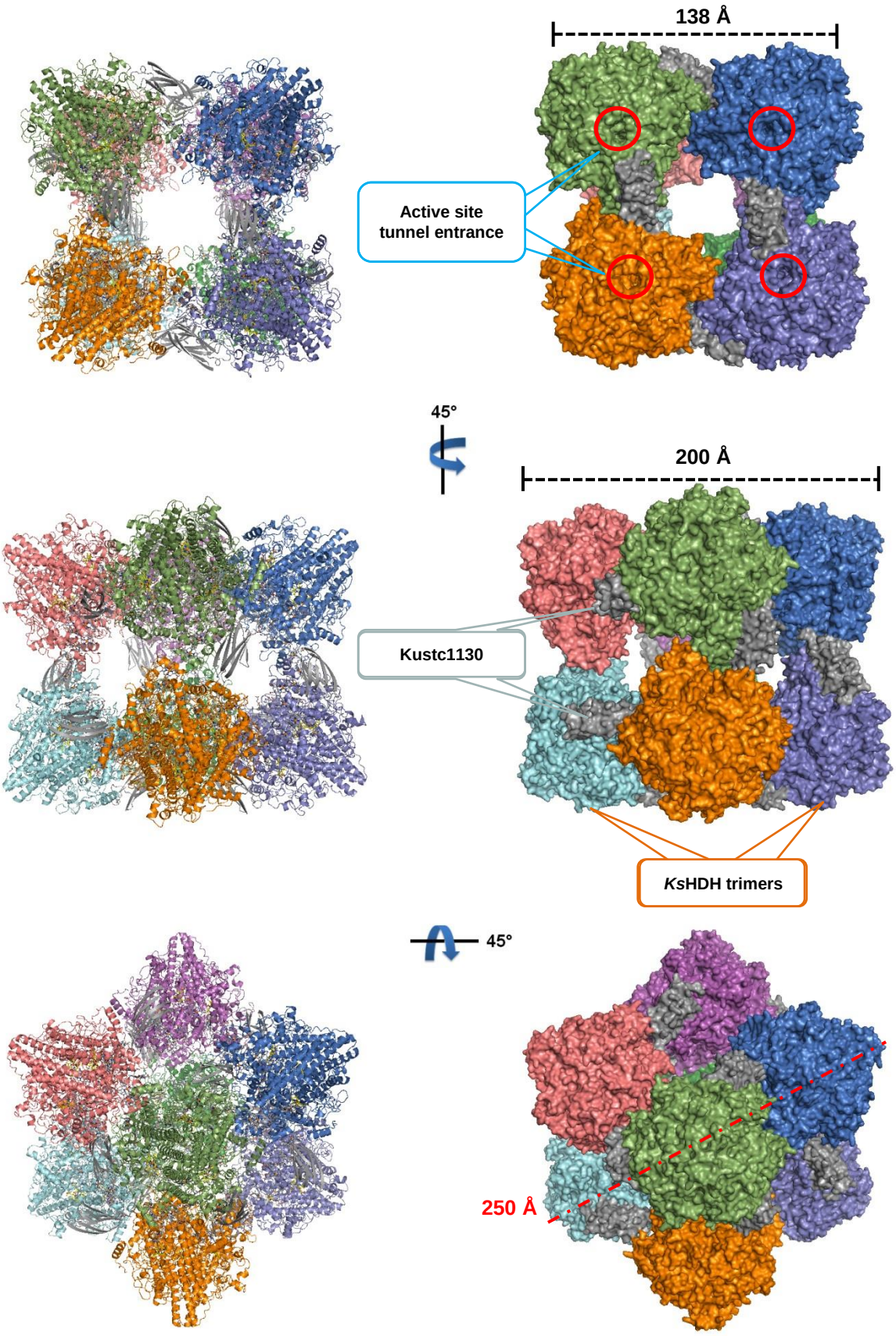
138 Å
Active site
tunnel entrance
45°
200 Å
Kustc1130
KsHDH trimers
45°
250 Å

The eight heme cofactors in the monomers of *Ks*HDH and *Ks*HOX superimpose almost perfectly (Fig 3.7). The ring-like heme arrangement in the *Ks*HDH trimer (Fig 3.8 a), as expected, is fully superimposable with that in trimeric *Ks*HOX in terms of the distances between the hemes as well as their relative orientations. The heme ring from one trimer interacts with that of three neighboring trimers *via* hydrophobic interaction between heme 1 (table 3.2). The equivalent heme has been suggested to be the electron exit site in case of *Ks*HOX (Maalcke 2014) and *Ne*HAO (Igarashi 1997). The edge-to-edge (atom to atom) distance between two heme 1 cofactors from neighboring trimers is 3.5 Å (Fig 3.8 b), which is close enough for efficient electron transfer. Figure 3.8 summarizes possible routes for flowing electron within the heme ring of one trimer and between two heme rings from adjacent trimers. Each heme ring makes three contacts to the heme rings of neighboring HDH trimers which are all mediated by their heme 1 (Figure 3.8 b shows one such interaction and all the possible heme ring interactions are visualized in the right column of figure 3.9).

The complex of the *Ks*HDH 24mer with 12 molecules of Kustc1130 shows an interesting electrostatic surface potential distribution (Fig 3.10). The complex is highly negatively charged especially around its 24 active site tunnels. The negatively charged surface extends from the active site tunnel in one trimer to the exposed surface of Kustc1130 and further continues to the next trimer and also surrounds the active site tunnel (Fig 3.10 a and b). This charge distribution is the same for all the 12 edges of the cubic assembly. The negatively charged patches are surrounded by discretely distributed positively charged areas.

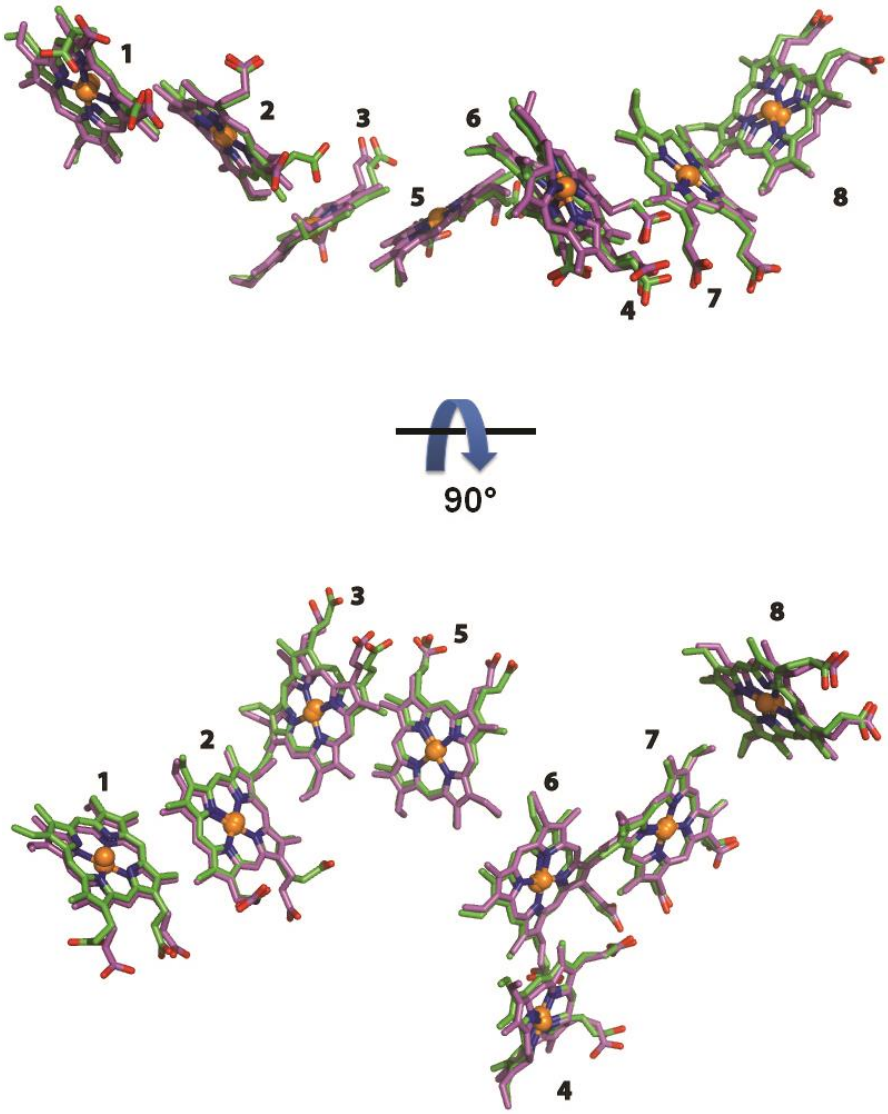

Figure 3.7 Conservation of the heme arrangement between *Ks*HDH and *Ks*HOX (PDB id: 4N4J). The eight hemes colored in magenta and green are from the monomers of *Ks*HDH and *Ks*HOX, respectively. The numbers indicate the heme position according to their appearance along the sequence of the respective monomer. Heme 4 is the active site P460 cofactor. The positions and relative orientations of all the hemes are highly conserved among both proteins.

(Figure on next page)

Figure 3.8 Heme Arrangements in the X-ray Structures of a single *Ks*HDH trimer and two adjacent trimers in the 24mer
The protein structure is rendered as a semi-transparent surface representation with the heme cofactors as stick models. The hemes are colored according to the subunits they belong, except for the active site hemes 4 which is colored in yellow. **a)** Heme arrangement in a *Ks*HDH trimer. The hemes belonging to each HDH monomer are numbered as they appear along the sequence of each monomer. The heme arrangement is conserved with respect to *Ks*HOX (PDB id: 4N4J) (Maalcke 2014). Red lines show possible flow paths which electrons (obtained from the oxidation of hydrazine) could take to exit. **b)** In the *Ks*HDH 24mer two trimers are brought together closely enough such that electrons can be exchanged between the ring-like heme assemblies in each trimer *via* their hemes 1.The red line show possible directions of the electron flow. This arrangement is equal for each equivalent contact sites of two HDH trimers in the 24mer assembly.

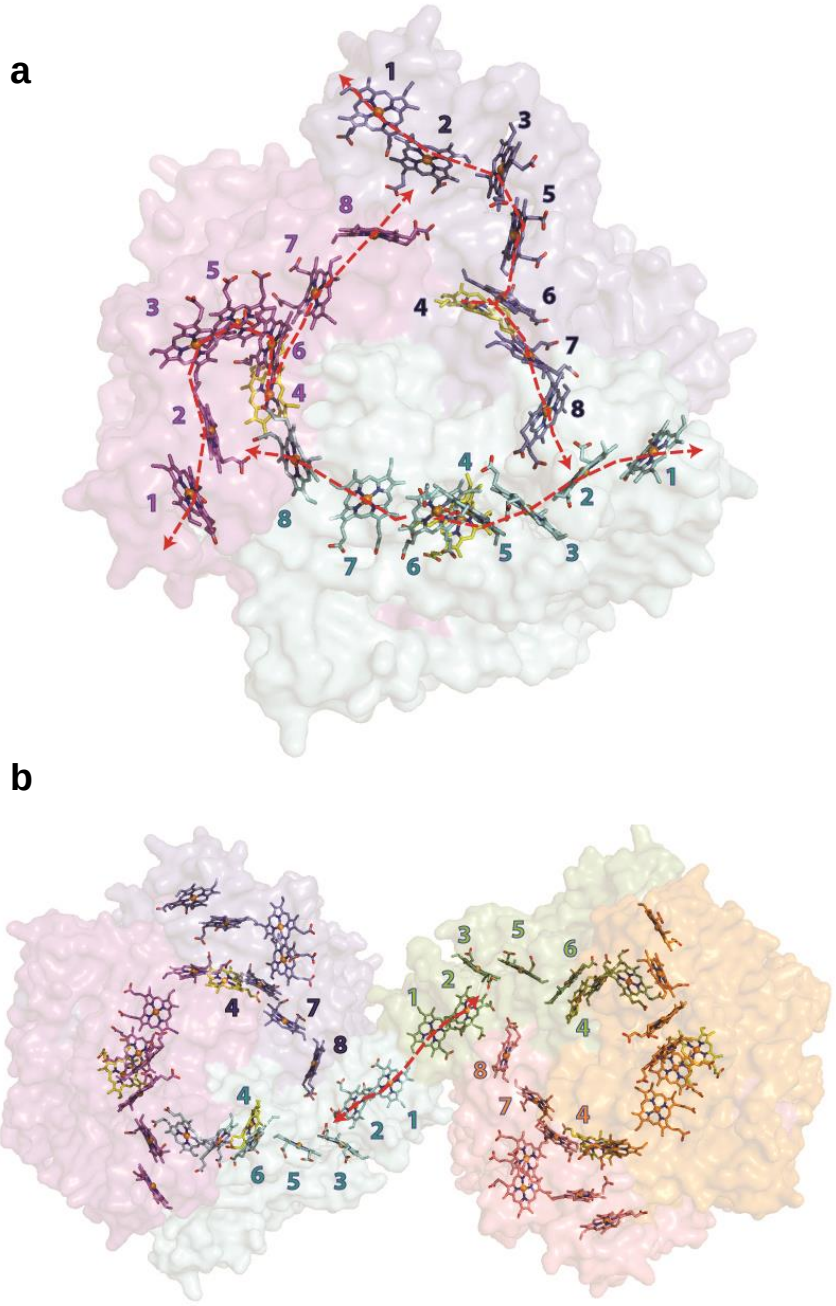

(Figure on next page)

Figure 3.9 The Heme Arrangement in the X-ray Structure of the *Ks*HDH 24mer
The left column shows a partially transparent surface representation in different orientations, with each trimer rendered in different colors. Each trimer possesses 24 hemes making a ring-like arrangement.
The octamerization of HDH trimers causes the heme 1 cofactors from adjacent heme rings of neighboring HDH trimers to come closer making an extended 192 hemes network. The right column shows only the network of hemes as stick models present in the 24mer *Ks*HDH structure in the corresponding orientation. The carbon atoms of the active site hemes 4 (P460 cofactor) are colored in yellow whereas those in the other hemes are colored grey. At bottom right, the red arrows indicate three contact sites at which the heme rings from neighboring HDH trimers interact *via* their heme 1 cofactors.

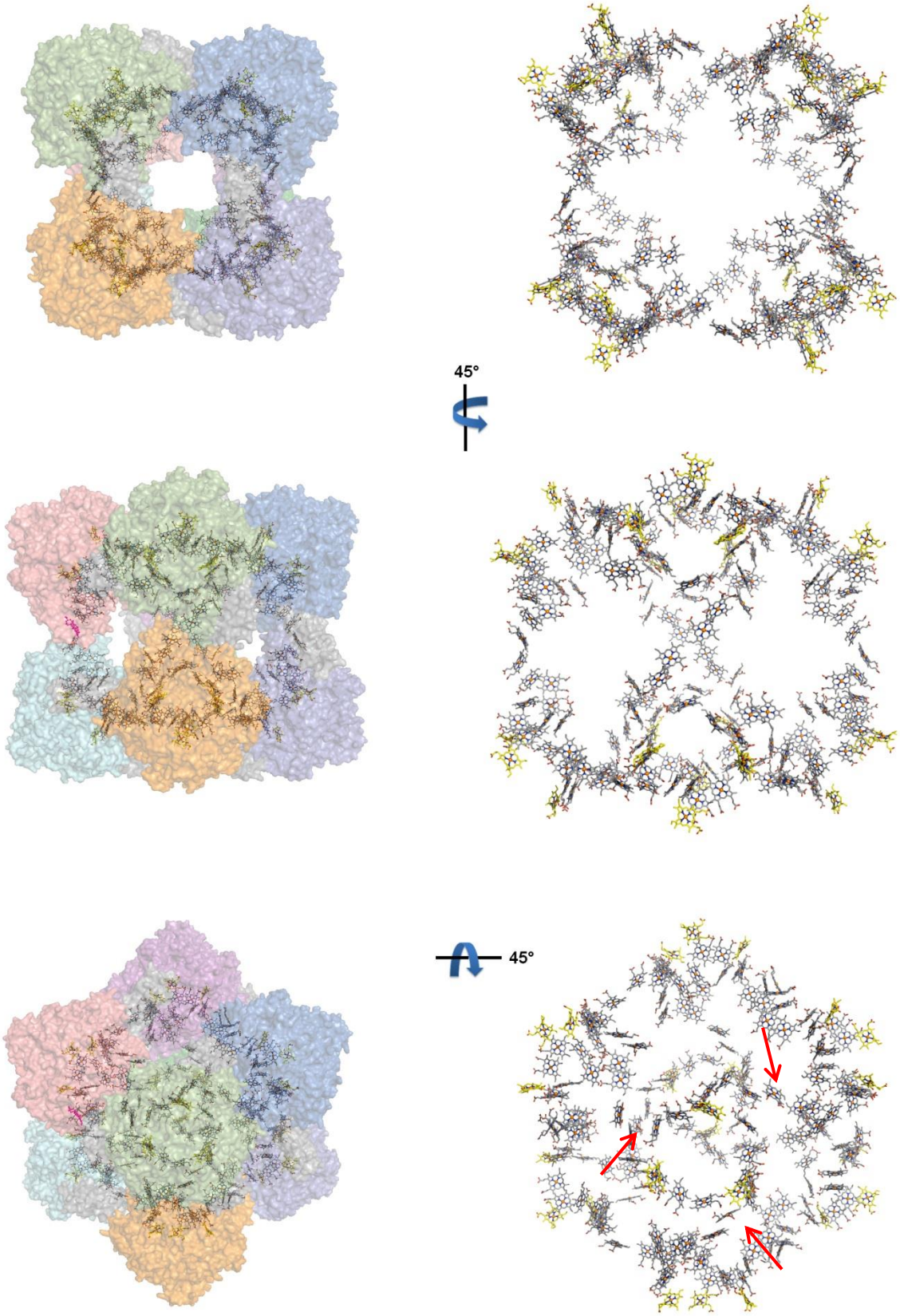
45°
45°

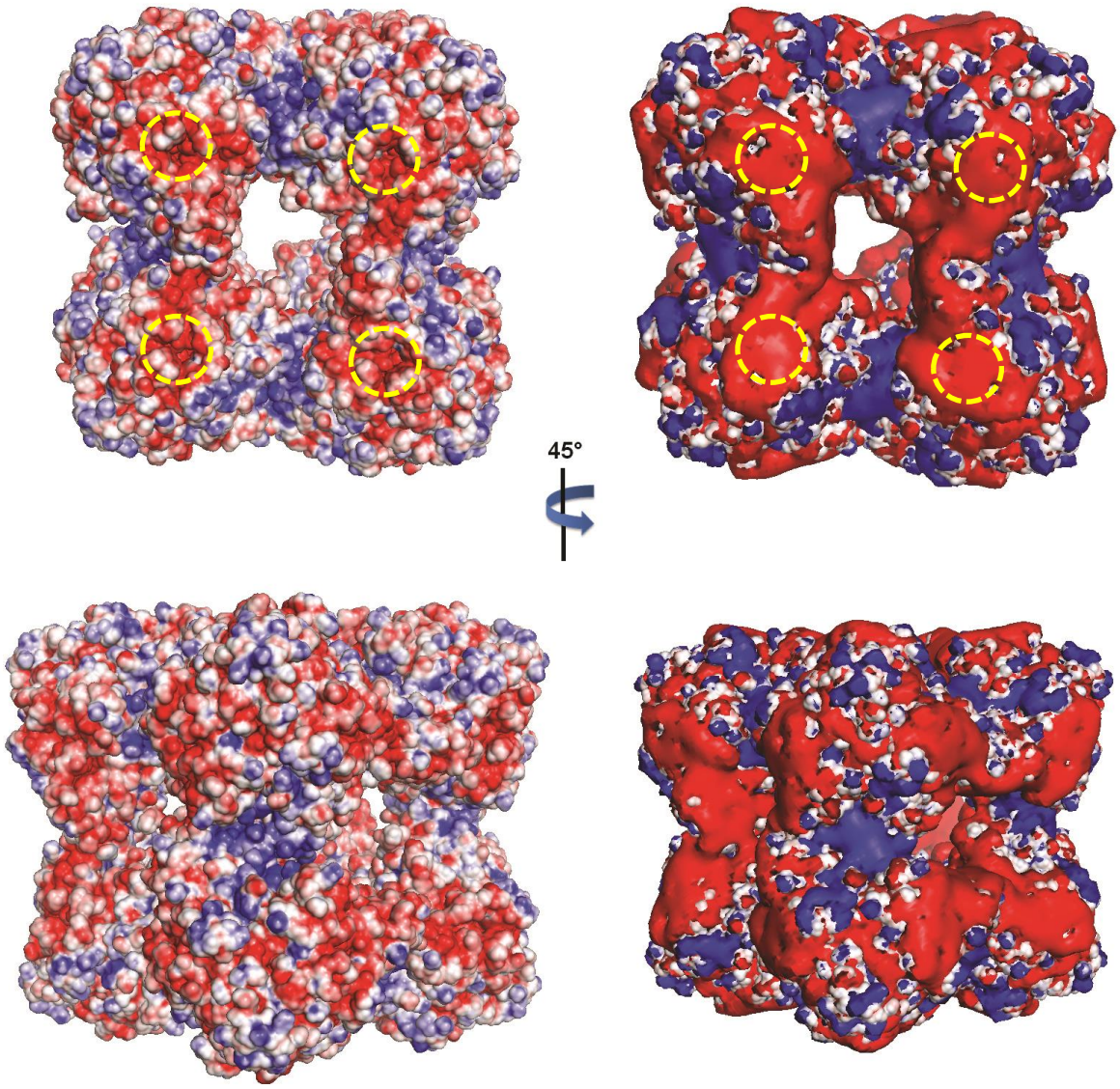

Figure 3.10 Electrostatic Surface of the X-ray structure of the 24mer *Ks*HDH Complex
The left panel shows the surface potentials (at -5 and +5 kT/e), red and blue colors indicate negative and positive potentials, respectively. The right panel shows the positive (blue) and negative (red) iso-surfaces at contour levels of +1 kT/e and -1 kT/e, respectively. The yellow circles indicate the entrance to the active site tunnel which is surrounded by a negative electrostatic environment. The pink arrow shows the position of Kustc1130; the equivalent positions in the figures in the right panel also include Kustc1130. As it can be observed, the continuous negative surface surrounding the active site tunnel on one trimer extends through the bridging Kustc1130 molecule and continues to the next trimer again surrounding the active site tunnel on that trimer. This continuous negative surface is surrounded by big patches of positively charged surface. This charge distribution creates a negative and positive potential separation in the 24mer *Ks*HDH complex. The electrostatic surface potentials were calculated using the APBS tool (Unni 2012) in Pymol (DeLano 2002). The atomic charge and radii of the heme cofactors were based on the values for comparable residues in the PARSE force field.

3.2.4 The Structure of the *Ks*HDH Trimer

The trimer forms the functional unit in all HAO-like octaheme c-type cytochromes. The overall structure of the *Ks*HDH trimer is highly similar to that of *Ks*HOX (PDB id: 4N4J) (Maalcke 2014). The two structures can be superimposed with root mean square positional deviations of 1.3 Å for 438 C_α-atoms. However, there are also some very important differences which might account for the specificity of *Ks*HDH towards hydrazine (section 3.2.5). The similarities and differences between the trimeric structures of these two closely related proteins are described here. In the *Ks*HDH trimer, each subunit is covalently attached to a neighboring subunit *via* two bonds between Tyr462 and heme 4 of an adjacent subunit (the P460 cofactor), respectively. At 2.8 Å resolution, however, it is difficult to judge whether Tyr462 is bound to the P460 heme by one or two bonds, but the proximity of the tyrosine hydroxyl group to the heme makes the one-bond model extremely unlikely. Therefore, this structure assumes the far more likely two-bond model from the homologous *Ne*HAO and *Ks*HOX high resolution structures which have been discussed by Cedervall *et al*. (2013) and Maalcke *et al*. (2014). The overall structure of the trimer appears as a closed tulip bulb with an apex and a flat base with three lateral faces forming approximately a triangle when looking through the base (Fig 3.8 a, Fig 3.11 a). The height of the trimer from the base to the apex is ~75 Å while the edge-to-edge distances at the triangular base are ~80 Å.

The *Ks*HDH structure is primarily α-helical as mentioned before. In each monomer there are 24 α-helices out of which three (α17, α18 and α19) are relatively long and run almost parallel to the three-fold axis in the trimer (see Fig 3.11 a and sequence alignment Fig 3.17). Therefore, a total of nine out of 72 α-helices surround the central cavity of the trimer which is occupied by solvent molecules.

(Figure on next page)

Figure 3.11 Comparisons of the Overall Structures of trimeric *Ks*HDH, *Ks*HOX and *Ne*HAO
The trimers are rendered as cartoon. In the left column, side views and in the right column, top views of the trimers are shown. The three subunits are shown in green, light blue and grey, the N-terminus and C-terminus in case of **a** and **b** are shown in dark blue and red colors, respectively, while in **c** only the N-terminus is shown in dark blue. **a)** In a representative trimer from the *Ks*HDH 24mer complex, the C-terminal α-helix (α24) seems to come out of rest of the structure. **b)** Trimeric structure of *Ks*HOX (PDB id: 4N4J). **c)** *Ne*HAO trimeric structure (PDB id: 4FAS) with its binding partner Ne1300 (shown in orange). The overall structure of HDH looks highly similar to *Ks*HOX (structural rmsd 1.3 Å) and *Ne*HAO (structural rmsd 1.5 Å) including three long α-helices from each subunit surrounding the central cavity which runs through the three-fold axis of the trimer. However, major differences can be observed at the termini.

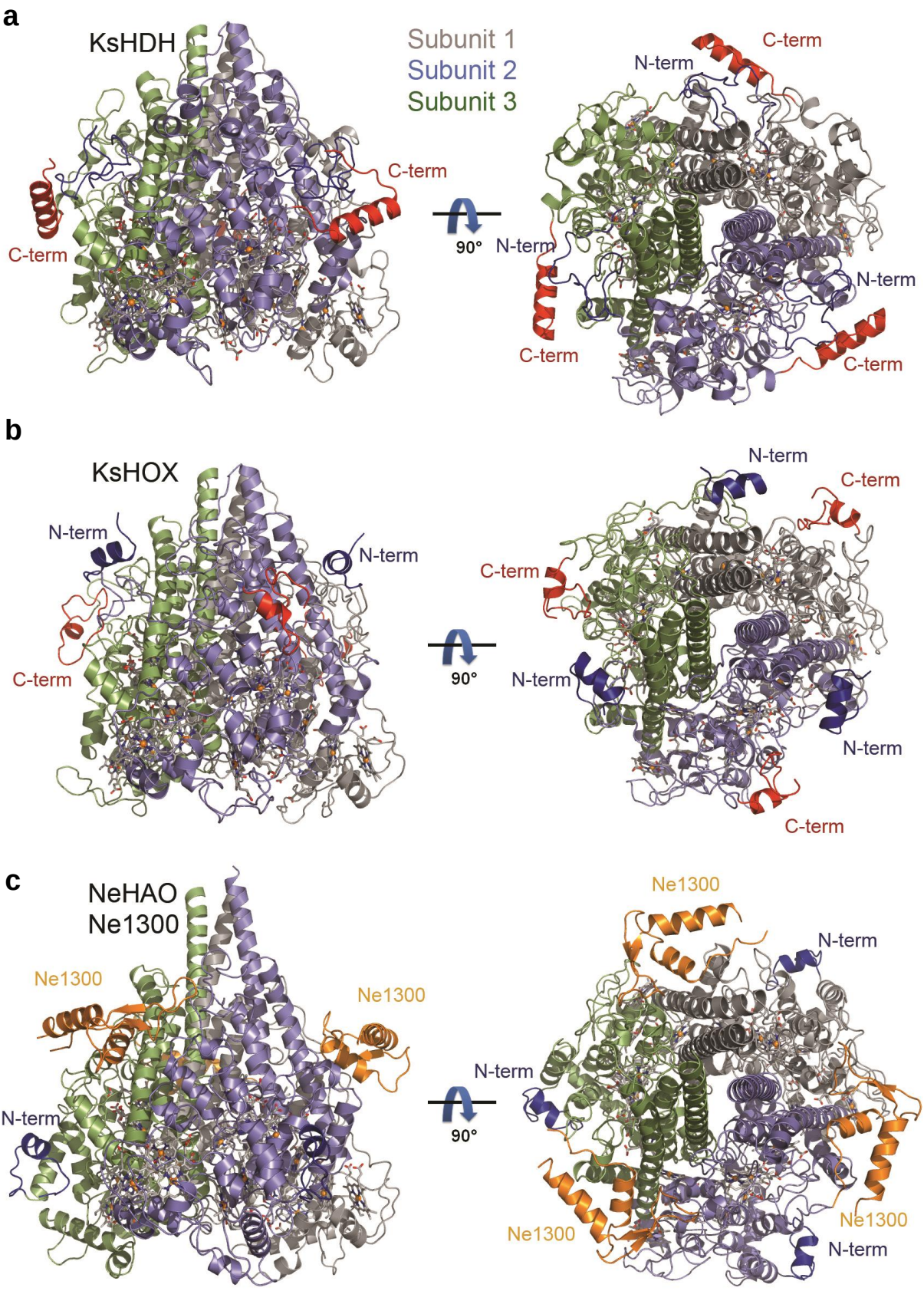
a
KsHDH
Subunit 1
Subunit 2
Subunit 3
C-term
C-term
90°
N-term
C-term
N-term
N-term
C-term
b
KsHOX
N-term
N-term
C-term
90°
N-term
C-term
C-term
N-term
N-term
C-term
c
NeHAO
Ne1300
Ne1300
Ne1300
N-term
90°
N-term
Ne1300
N-term
Ne1300
Ne1300
N-term

Maalcke *et al.* (2014) described four domains in *Ks*HOX namely N1 and N2 domains, a central domain and a C-terminal domain. The N1 and C-terminal domains, however, are not present in the *Ne*HAO structures (Maalcke 2014; Igarashi 1997; Cedervall 2013). The *Ks*HDH monomer possesses all four domains described for *Ks*HOX. In *Ks*HDH, the N1 domain comprises amino acid 33 to 80, the N2 domain residues 81 to 256, the central domain residues 257 to 494 and finally the C-terminal domain amino acids 495 to 563 (Fig 3.12 c). However, it is still questionable whether these are real protein domains for both *Ks*HOX and *Ks*HDH. As described for *Ks*HOX (Maalcke 2014), the N1 domain of *Ks*HDH also has an inwardly located positively charged patch which interacts with a negatively charged patch from the neighboring chain in the trimer (not shown).

As mentioned earlier, the heme arrangement is conserved when compared with *Ks*HOX both in terms of orientation and relative distances (Fig 3.7) and leads to a ring-like arrangement in the trimer (Fig 3.8). As in the case of the *Ks*HOX trimer, heme 2 in *Ks*HDH occupies a position such that it can accept electrons coming from both heme 3 and 5 of the same subunit and from heme 7 and 8 of a neighboring subunit (Fig 3.8 a). Both in *Ks*HOX and *Ks*HDH all hemes are *bis*-His coordinated, except for the P460 heme cofactor. However, in *Ks*HDH heme 3 is unique, as it is attached *via* a non-canonical CX_4CH (**C**GTAE**CH**) heme binding motif (for more details see section 3.2.7).

Additionally, there are differences in the N1 and C-terminal domains between the *Ks*HOX and *Ks*HDH structures (and also in the environment of heme 3; described in section 3.2.7). In *Ks*HOX, the entire N1 domain is exposed at the surface and interacts with a neighboring subunit in the trimer. In the *Ks*HDH trimer this domain also interacts with the neighboring subunit. However, the N1 domain of *Ks*HOX comprises a small α-helix (Phe41 to Phe49) whereas in *Ks*HDH it forms an entirely random coiled structure. A 27 amino acid long part of the N1 domain starting from Val53 in *Ks*HOX is superimposable with that of *Ks*HDH from Glu50 onwards. The regions preceding these residues are oriented differently. Interestingly, in *Ks*HDH this region (Val33-Val52) is an extended piece of peptide chain which runs through the tunnel leading to the active site heme of a neighboring subunit positioning the side chain of the first residue Val33'' towards the distal pocket of the active site heme (Fig 3.13 and 3.15 a, c). This N1 domain loop comes from the subunit which is not involved in the Tyr462-heme crosslink to the heme where it interacts.

The differences in the C_α-positions of the C-termini in *Ks*HOX and *Ks*HDH start at Arg507 and Ile517, respectively. The C-terminal fragment following Arg507 in *Ks*HOX forms a random coil except for a short α-helical insertion (Val514 to Arg519) which finally ends at the opening of the channel leading to active site by folding in itself. It does not appear to interact with the neighboring subunits. In contrast, the C-terminal part of *Ks*HDH also primarily adopts a random coil conformation but contains a 14-amino acid long α-helix (Ala543 to Gly557; α24). This part seems extended and comes out of rest of the structure. Following helix α24 the chain takes a more than 90° turn and moves towards the opening of the active site channel (Fig 3.12 a). A few residues from this stretch interact with the N-terminus from a neighboring subunit which moves through the active site channel as previously discussed. The last 19 residues following His563 are not resolved in the *Ks*HDH X-ray structure. Helix α24 is also involved in interactions with Kustc1130 *via* hydrogen bonding and salt bridge interactions (discussed in detail in section 3.2.6).

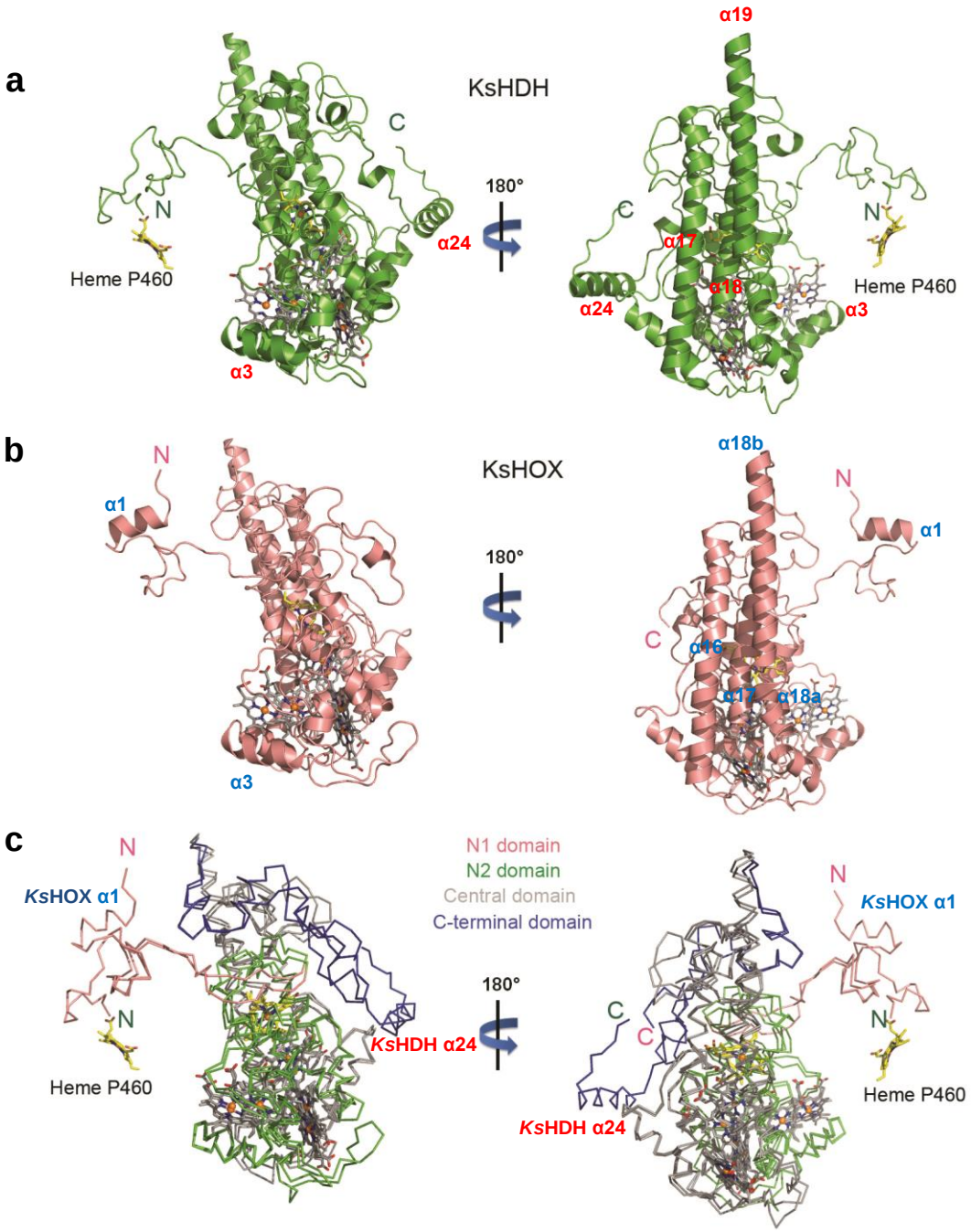

Figure 3.12 Domain Structures of *Ks*HDH and *Ks*HOX monomers
a) Monomer structure of *Ks*HDH shown as cartoon. Only few α-helices are marked for clarity. α17, α18 and α19 surround the central cavity in the trimer. α24 is located at the C-terminus which is markedly different when compared with *Ks*HOX. The N-terminus is shown which interacts with the active site heme P460 (in yellow) from a neighboring subunit. α3 interacts with the surrounding trimers in the 24mer *Ks*HDH structure.
b) Monomer structure of *Ks*HOX (PDB id: 4N4J) for comparison rendered as cartoon. In *Ks*HOX, α16, α17, α18a and α18b surround the central cavity in the trimer. The N-terminus contains an α-helix (α1).
c) The four domains of *Ks*HDH and *Ks*HOX are shown in ribbon representation. The N1, N2, central and C-terminal domains of *Ks*HOX are formed by amino acids 38-80, 81-263, 264-484 and 285-534, respectively, and that of *Ks*HDH are made of residues 33-80, 81-256, 257-494 and 495-563, respectively. The N-terminal domain of *Ks*HDH is completely random coiled whereas *Ks*HOX contains an α-helix (α1).

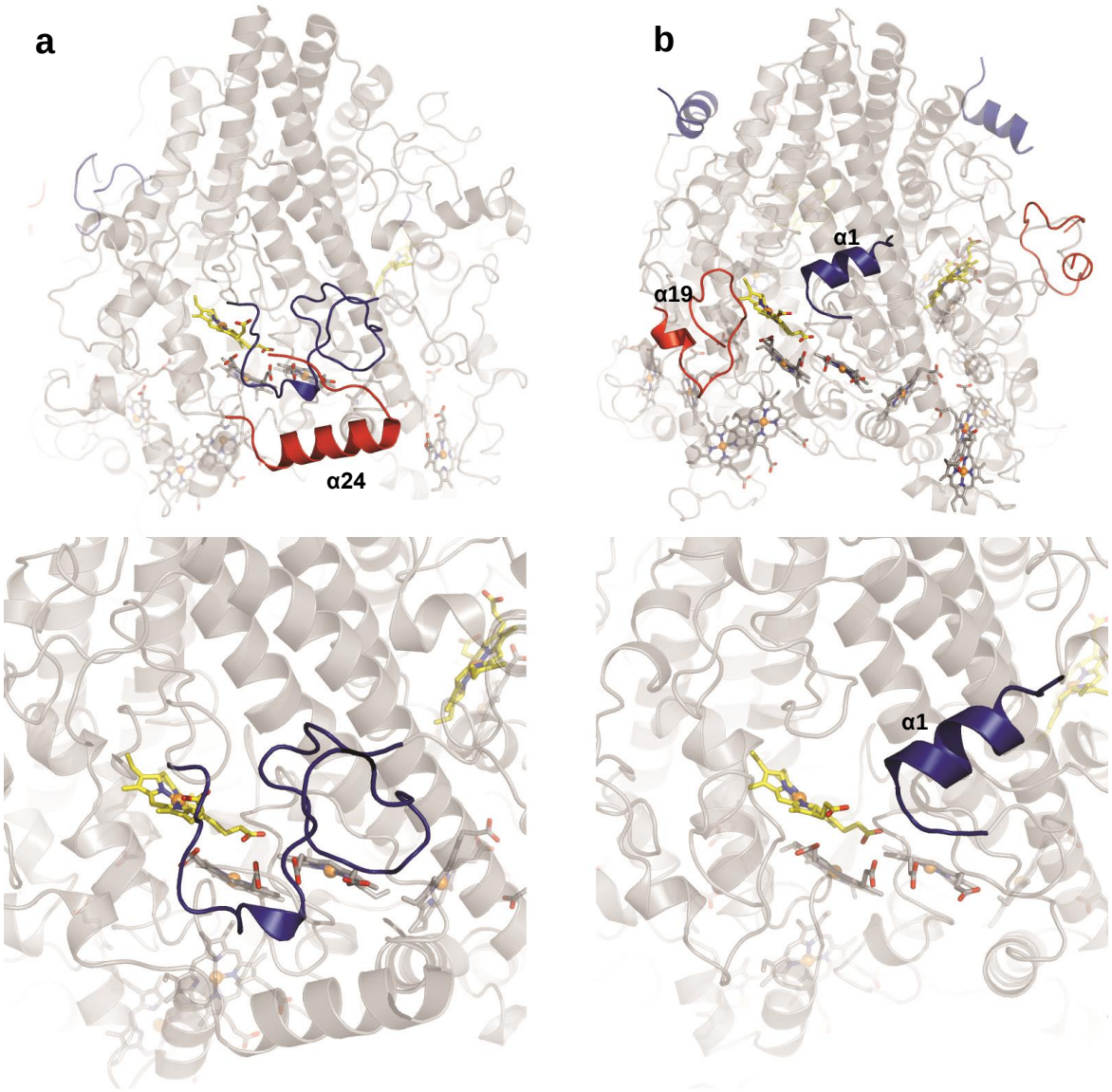

Figure 3.13 Comparison of N- and C-termini of the *Ks*HDH and *Ks*HOX Trimers
The structures are rendered as cartoons. The left panel shows the structure of *Ks*HDH and right panel shows the structure of *Ks*HOX (PDB id: 4N4J). The upper row shows the view of the trimers and lower row shows the zoomed in view of the tunnel to the active site. The active site heme (P460) is shown in yellow.
a) In *Ks*HDH the N-terminus (33-65, shown in blue) is a random coil which moves through the tunnel to the active site where the side chain of the terminal residue Val33'' contributes to the heme environment. Although the last 19 residues were missing in the structure, the remaining C-terminus (540-563, shown in red) forms an α-helix (α24: 543-557) and the last loop moves towards the tunnel and ends at its entry site close to His42 of the N-terminus.
b) In the *Ks*HOX trimer (PDB id: 4N4J) the N-terminus (38-52, shown in blue) shows a small α-helix (α1: 41-49) pointing away from the active site entrance. The C-terminus (513-534, shown in red) is a random loop with a small helix (514-519) at the beginning. The loop ends towards the active site entrance, the last two amino acids are missing in the structure.

Comparative surface potential analyses of *Ks*HDH, *Ks*HOX and *Ne*HAO trimers (figure 3.14) show some intriguing features. Both *Ks*HDH and *Ne*HAO trimers possess highly negatively charged surface potentials especially around the active site tunnel and also at the bottom (Fig 3.14 a & c). In *Ks*HDH, as already mentioned in section 3.2.3, the negatively charged area around the active site tunnel is surrounded by sporadic positively charged patches. However, in *Ne*HAO the side and upper part of the trimer are entirely negatively charged while the bottom is moderately positively charged (Fig 3.14 c). Interestingly, the *Ks*HOX trimer is comparatively highly positively charged especially at the bottom and also at the active site tunnel entrance (Fig 3.14 b). The tunnel in *Ks*HOX is positively charged, however, few negatively charged patches can be seen surrounding the tunnel entrance (Fig 3.14 b).

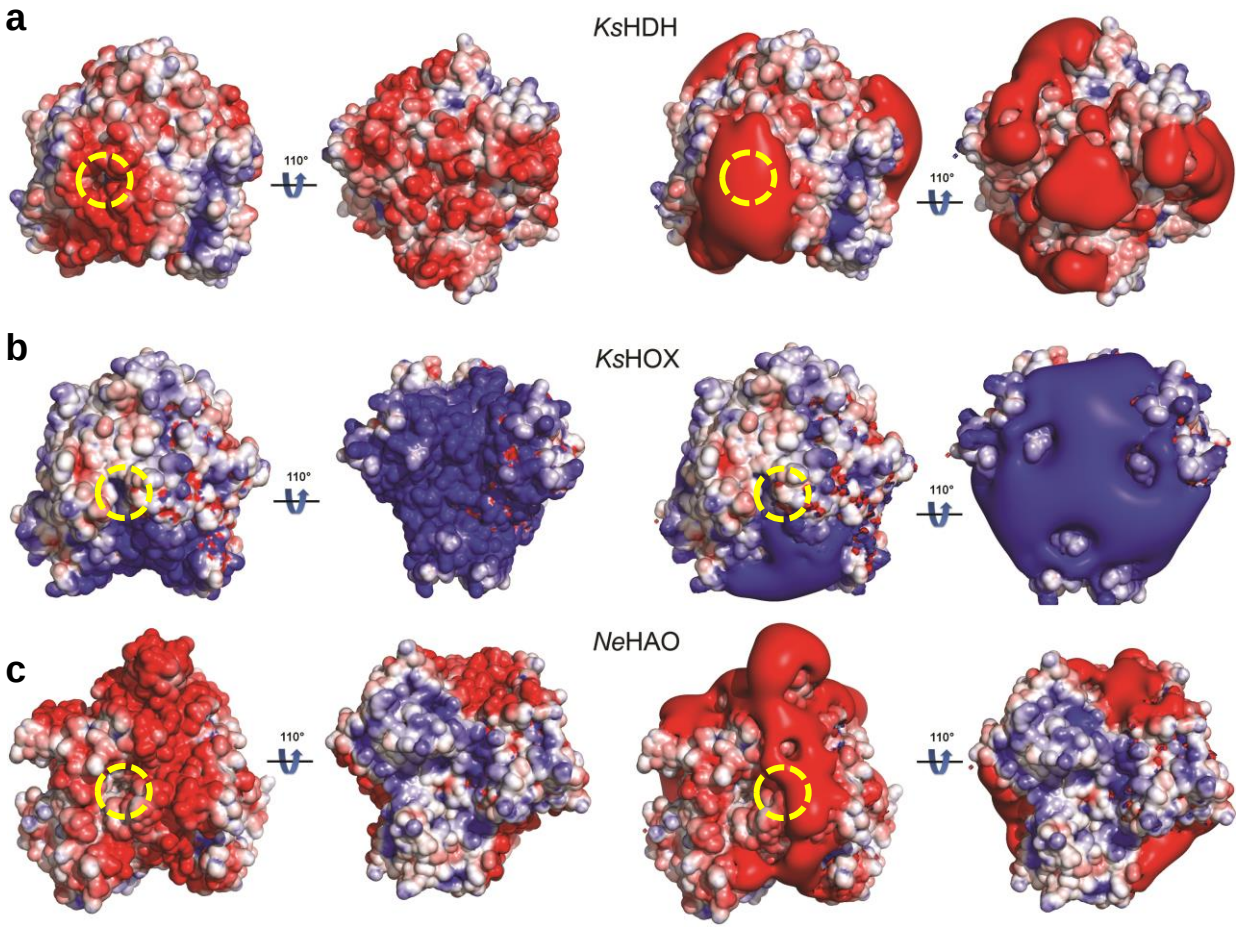

Figure 3.14 Comparison of the Electrostatic Surface of *Ks*HDH, *Ks*HOX and *Ne*HAO trimers
The left panel shows the surface potentials (at +4 and -4 kT/e) in red (negative) and blue (positive) for two different orientations of the trimers. The right panel shows the iso-surfaces at contour levels of +4 kT/e and -4 kT/e, respectively. Yellow circles indicate the entrances to active site tunnels. Atomic charges and radii of atoms were calculated using the PDB2PQR server (http://nbcr-222.ucsd.edu/pdb2pqr_2.1.1/). The surface potentials were generated using the ABPS plugin (Unni 2012) and PyMol (DeLano 2002). The two views shown in the left and right panels represent the side view showing the active site tunnel entrance and a 110° rotated bottom view of each trimer, respectively.
a) One of the trimers from the *Ks*HDH 24mer X-ray structure.
b) *Ks*HOX trimer (PDB id: 4N4J; Maalcke 2014).
c) *Ne*HAO trimer with its binding partner Ne1300 (PDB id: 4FAS; Cedervall 2013).

3.2.5 The *Ks*HDH Active Site and its Comparison with *Ks*HOX

The active sites of *Ks*HDH and *Ks*HOX look similar at first glance with most of the common features; however, there are also significant differences (Fig 3.15 and 3.16). The active site heme 4 (P460) is bound by a canonical heme binding motif (**C**TF**CH** in HDH). As in case of *Ks*HOX and also mentioned before (section 3.2.4), Tyr462' is covalently bound to the P460 heme *via* two covalent bonds between the heme *meso* carbon C5 and Tyr462' Cε1 as well as heme C4 and Tyr462' Oη (the bonds are assigned according to Maalcke *et al.*, 2014). When discussing the active site in a subunit, the residues of the subunit harboring the active site heme under consideration will be denoted without any suffix (X). Residues from the subunit forming the covalent tyrosine crosslink to the active site heme will be denoted X', and those of the third subunit X''.

The tyrosine crosslink causes pronounced ruffling of the active site heme 4 plane to a similar extent as heme 4 of *Ks*HOX. The distal coordination site of the P460 heme was found to be probably occupied by a water molecule. A characteristic aspartate-histidine pair (Asp255 and His256 in *Ks*HDH; Asp262 and His263 in *Ks*HOX) is present in the same orientation as in *Ks*HOX. A methionine residue (Met319 in *Ks*HDH and Met323 in *Ks*HOX) points towards the active site which in case of *Ks*HOX was proposed to act in restricting water molecules to enter the reaction center when reaction intermediates are bound (Maalcke 2014). During the oxidation of hydroxylamine and hydrazine, three and four protons (H^+), respectively, are released which have to be transported out of the active site environment. In *Ks*HOX, Tyr432 and Tyr447' are proposed to play a role in proton transport, while in *Ks*HDH the equivalent positions are occupied by Tyr443 and Asn458', respectively, which could both perform the same function. A tunnel leading from the active site to the protein surface is also present, as mentioned, which possesses a highly negatively charged surface (Fig 3.14 a).

Despite all these similarities in the active sites of *Ks*HDH and *Ks*HOX, hydrazine dehydrogenase is highly specific for hydrazine turnover while hydroxylamine and NO (which are substrate and product of *Ks*HOX, respectively) are strong inhibitors. In order to account for this specificity, some differences existing at the active sites between the two proteins need to be considered.

Immediately apparent is the presence of an extra crosslink between the active site heme carbon C2 and a cysteine Sγ (Cys202). This additional covalent bond might modulate the heme redox potential hence the specificity of the active site. Indeed, it was reported that the redox potential of the active site heme of *Ks*HDH is -420 mV whereas in *Ks*HOX it is -300 mV (Maalcke 2016). In addition, the N-terminal residue Val33'' of a neighboring subunit points its side chain towards the P460 heme. The N-terminal amino group of Val33'' is located ~3.8 Å away from the plane of Trp204 and thus appears to interact through an amino-aromatic interaction (Perutz 1986; Burley 1986). In *Ks*HOX (PDB id: 4N4J), Phe209 occupies the position at the same side (but not exactly the same position) of heme P460 as Val33'' in *Ks*HDH. In addition to a methionine residue (Met323 in *Ks*HOX and Met319 in *Ks*HDH), Val33'' (*Ks*HDH) and Phe209 (*Ks*HOX) might increase the hydrophobicity of the active site to prevent water molecules from entering the cavity. In general, both *Ks*HOX and *Ks*HDH possess several aromatic-hydrophobic residues around their active sites. These include Phe457', Trp211, Phe416, Leu427, Met325, Tyr320 and Met259 in *Ks*HOX (PDB id: 4N4J) while the corresponding positions are occupied by residues Phe467', Trp204, Met427, Phe425, Met321, Tyr316 and Trp252 in *Ks*HDH, respectively. In addition, Phe438 is located near the *Ks*HDH active site. All the mentioned residues are conserved in all HDH homologues (sequence alignment figure 3.17). Moreover, most of the residues mentioned for *Ks*HOX are conserved but few of them are also substituted with similar (hydrophobic) amino acids (Phe457' and Trp211 are fully conserved in all the homologues; Phe416 is substituted by methionine in the *Scalindua brodae* orthologue; Leu427 is substituted by valine in the *S. brodae* orthologue and by phenylalanine in the paralogues; Tyr320 is conserved in all orthologues but substituted by asparagine in all the corresponding paralogues; both Met259 and Met325 are conserved in all the orthologues but are substituted by threonine in all the corresponding paralogues).

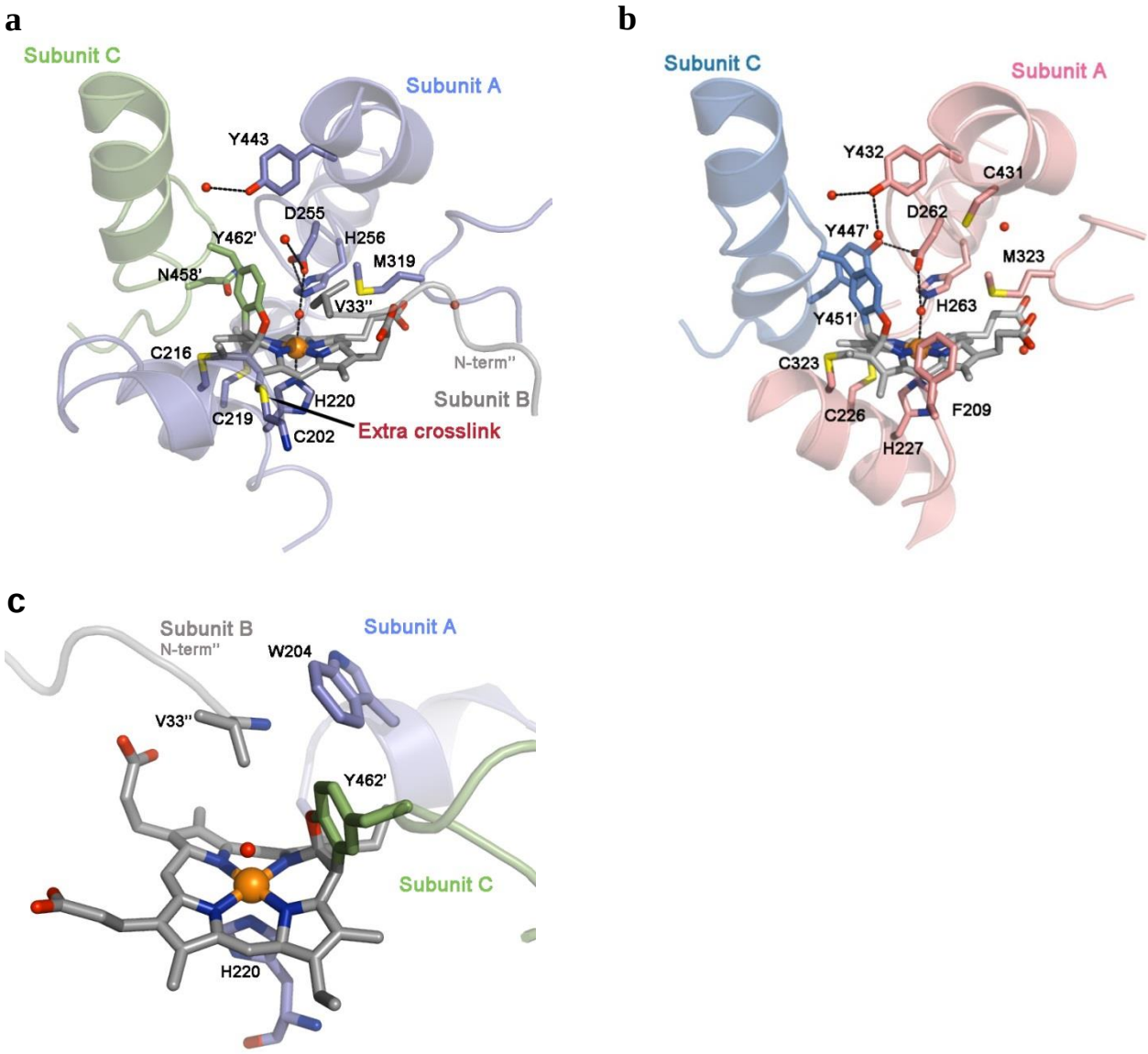

Figure 3.15 Active site Heme Environment of *Ks*HDH compared to *Ks*HOX
Cartoon and stick model of the active site hemes of *Ks*HDH and *Ks*HOX (PDB id: 4N4J). **a)** & **b)** Show the active site heme environments of *Ks*HDH and *Ks*HOX, respectively. In *Ks*HDH all three subunits of the trimer contribute to the heme environment while in *Ks*HOX only two chains are involved. The characteristic tyrosine crosslink to the active site heme 4 is formed *via* two bonds between heme *meso* carbon C5 and Tyr462' Cε1 and heme C4 and Tyr462' Oη in *Ks*HDH and between the corresponding atoms of Tyr451' and heme 4 of *Ks*HOX. A highly conserved Asp-His pair (Asp255-His256 in *Ks*HDH and Asp262-His263 in *Ks*HOX) is present in both active sites. Met319 and Met323 are also conserved in HDH and HOX, respectively. This methionine residue was proposed to prevent water molecules from entering the distal active site cavity (Maalcke 2014). Tyr432 in *Ks*HOX was proposed to work as proton transporter. The corresponding position in the *Ks*HDH structure is occupied by Tyr443, which forms hydrogen bonds to nearby water molecules. However, Tyr447' of *Ks*HOX, which was also proposed to be involved in proton transfer, is substituted by Asn458' in *Ks*HDH. The most prominent difference is the presence of an extra thioether crosslink between Cys202 and the heme 4 methyl group (C2). The *Ks*HDH Val33'' side chain also points towards the heme, while in *Ks*HOX the exact position is vacant. However, Phe209 is located close to that position. In both cases strong ruffling of the heme was observed to similar extents.
c) The N-terminal amino group of Val33'' interacts with the aromatic plane of Trp204. The distance between the aromatic plane and the amino group is ~3.8 Å**.**

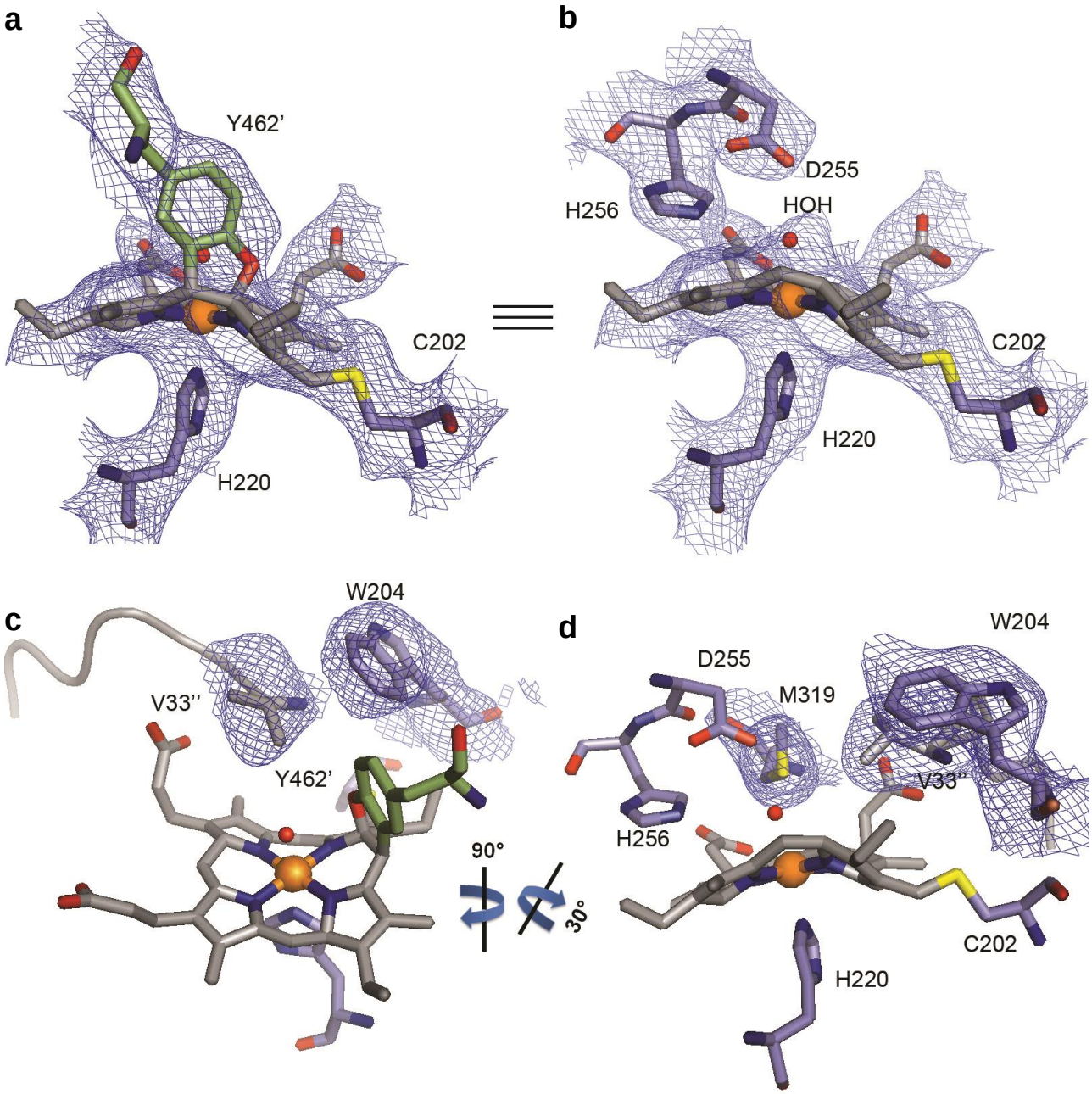

Figure 3.16 Active Site Heme Environment of *Ks*HDH
The active site environment of *Ks*HDH (rendered as a stick model) is overlaid with the 2*m*F_o-*D*F_c simulated annealing composite omit map (blue mesh) at a contour level of 1 σ. The map was calculated using PHENIX for the entire structure. **a)** The active site heme shows two crosslinks; the common P460 crosslink with Tyr462 (in green) and a unique extra thioether crosslink with Cys202 (in blue). The proximal heme ligand His220 is also shown. **b)** Same view as in a). The highly conserved Asp-His pair is shown (in blue). Extra electron density at the distal face of the heme iron indicates the coordination of a small ligand which was modelled as a water molecule (red sphere).**c)** The N-terminus (33-38) and Val33'' from a neighboring subunit is shown along with Trp204 which interacts with the amino terminus of Val33''. **d)** Met319 along with Trp204 and Val33'' are shown making this side of the active site hydrophobic.

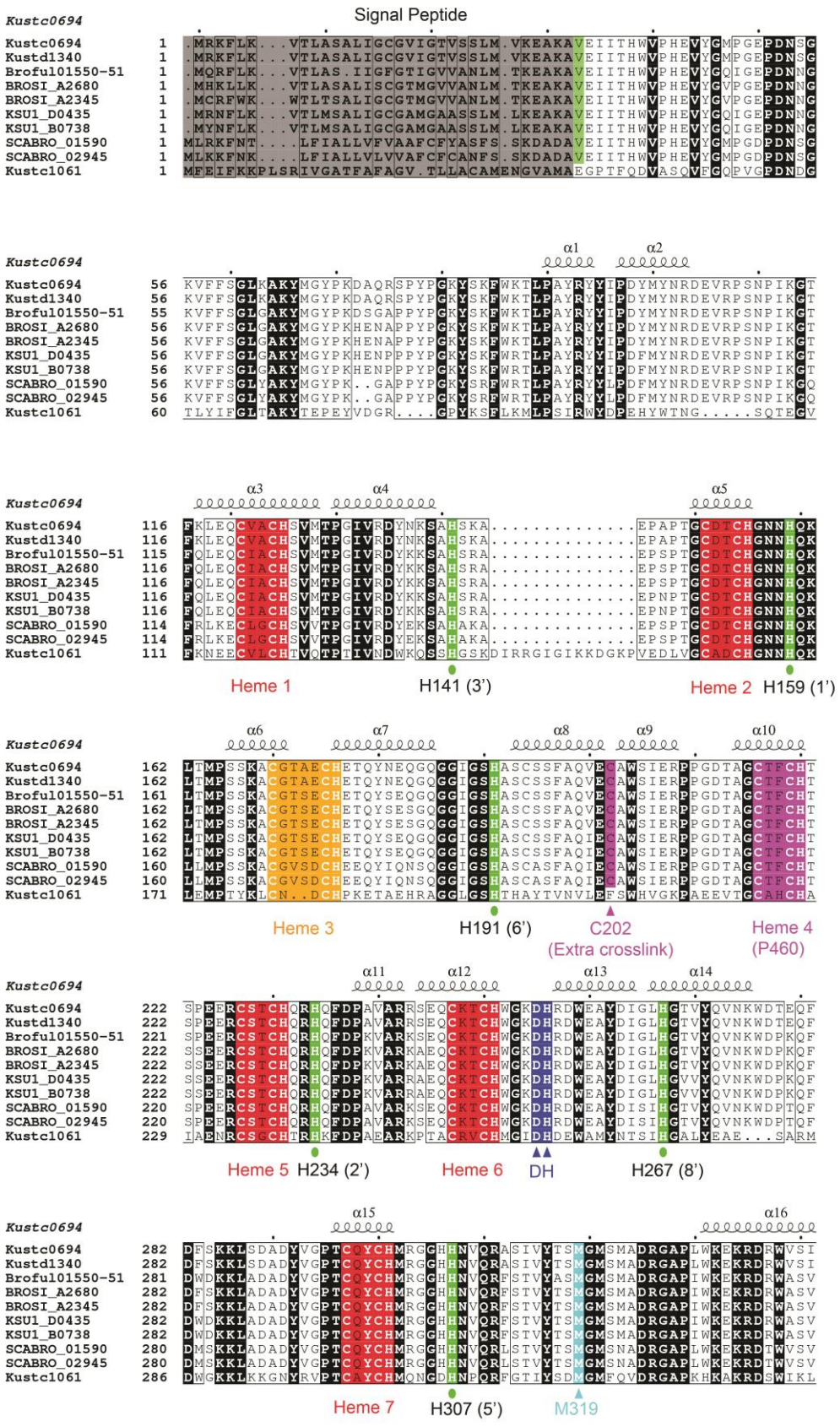
Signal Peptide
α1
α2
α3
α4
α5
α6
α7
α8
α9
α10
α11
α12
α13
α14
α15
α16
Heme 1
H141 (3')
Heme 2
H159 (1')
Heme 3
H191 (6')
C202
(Extra crosslink)
Heme 4
(P460)
Heme 5
H234 (2')
Heme 6
DH
H267 (8')
Heme 7
H307 (5')
M319

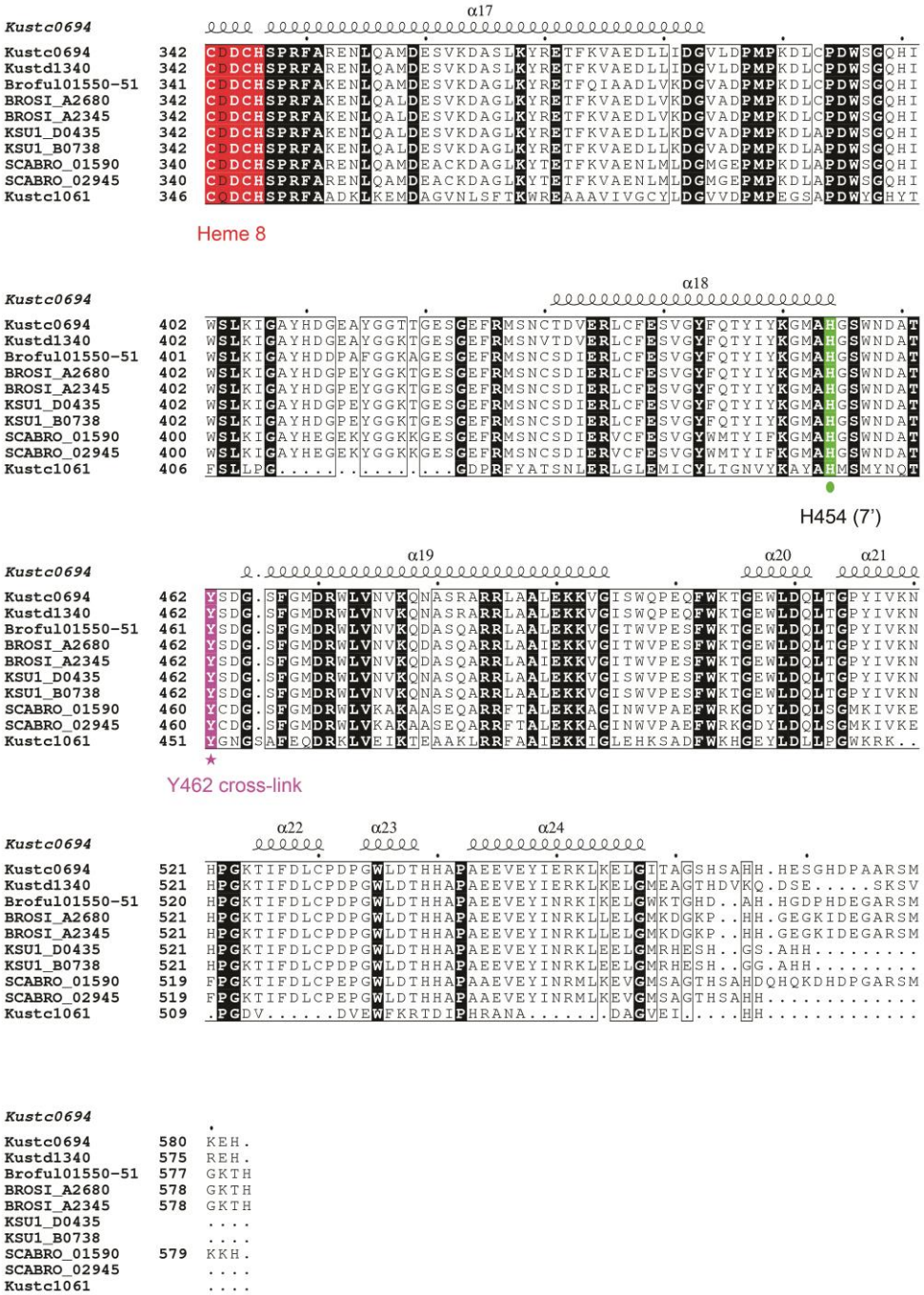
α17
Kustc0694
Kustc0694 342 CPDCHSPRFARENLQAMDESVKDASLKYRETFKVAEDLLIDGVLDPMPKDLCPDWSGQHI
Kustd1340 342 CPDCHSPRFARENLQAMDESVKDASLKYRETFKVAEDLLIDGVLDPMPKDLCPDWSGQHI
Brofu101550-51 341 CPDCHSPRFAKENLQAMDESVKDAGLKYRETFQIAADLVKDGVADPMPKDLCPDWSGQHI
BROSI_A2680 342 CPDCHSPRFAKENLQALDESVKDAGLKYRETFKVAEDLVKDGVADPMPKDLCPDWSGQHI
BROSI_A2345 342 CPDCHSPRFAKENLQALDESVKDAGLKYRETFKVAEDLVKDGVADPMPKDLCPDWSGQHI
KSU1_D0435 342 CPDCHSPRFAKENLQALDESVKDAGLKYRETFKVAEDLLKDGVADPMPKDLAPDWSGQHI
KSU1_B0738 342 CPDCHSPRFAKENLQALDESVKDAGLKYRETFKVAEDLLKDGVADPMPKDLAPDWSGQHI
SCABRO_01590 340 CPDCHSPRFARENLQAMDEACKDAGLKYTETFKVAENLMLDGMGEPMPKDLAPDWSGQHI
SCABRO_02945 340 CPDCHSPRFARENLQAMDEACKDAGLKYTETFKVAENLMLDGMGEPMPKDLAPDWSGQHI
Kustc1061 346 CQDCHSPRFAADKLKEMDAGVNLSFTKWREAAAVIVGCYLDGVVDPMPEGSAPDWYGHYT
Heme 8
α18
Kustc0694
Kustc0694 402 WSLKIGAYHDGEAYGGTTGESGEFRMSNCTDVERLCFESVGYFQTYIYKGMAHGSWNDAT
Kustd1340 402 WSLKIGAYHDGEAYGGKTGESGEFRMSNVTDVERLCFESVGYFQTYIYKGMAHGSWNDAT
Brofu101550-51 401 WSLKIGAYHDDPAFGGKAGESGEFRMSNCSDIERLCFESVGYFQTYIYKGMAHGSWNDAT
BROSI_A2680 402 WSLKIGAYHDGPEYGGKTGESGEFRMSNCSDIERLCFESVGYFQTYIYKGMAHGSWNDAT
BROSI_A2345 402 WSLKIGAYHDGPEYGGKTGESGEFRMSNCSDIERLCFESVGYFQTYIYKGMAHGSWNDAT
KSU1_D0435 402 WSLKIGAYHDGPEYGGKTGESGEFRMSNCSDIERLCFESVGYFQTYIYKGMAHGSWNDAT
KSU1_B0738 402 WSLKIGAYHDGPEYGGKTGESGEFRMSNCSDIERLCFESVGYFQTYIYKGMAHGSWNDAT
SCABRO_01590 400 WSLKIGAYHEGEKYGGKKGESGEFRMSNCSDIERVCFESVGYWMTYIFKGMAHGSWNDAT
SCABRO_02945 400 WSLKIGAYHEGEKYGGKKGESGEFRMSNCSDIERVCFESVGYWMTYIFKGMAHGSWNDAT
Kustc1061 406 FSLLPG.....H.....GDPRFYATSNLERLGLEMICYLTGNVYKAYAHMSMYNQT
H454 (7')
α19
α20
α21
Kustc0694
Kustc0694 462 YSDG.SFGMDRWLVNVKQNASRARRLAALEKKVGISWQPEQFWKTGEWLDQLTGPYIVKN
Kustd1340 462 YSDG.SFGMDRWLVNVKQNASRARRLAALEKKVGISWQPEQFWKTGEWLDQLTGPYIVKN
Brofu101550-51 461 YSDG.SFGMDRWLVNVKQDASQARRLAALEKKVGITWVPESFWKTGEWLDQLTGPYIVKN
BROSI_A2680 462 YSDG.SFGMDRWLVNVKQDASQARRLAALEKKVGITWVPESFWKTGEWLDQLTGPYIVKN
BROSI_A2345 462 YSDG.SFGMDRWLVNVKQDASQARRLAALEKKVGITWVPESFWKTGEWLDQLTGPYIVKN
KSU1_D0435 462 YSDG.SFGMDRWLVNVKQNASQARRLAALEKKVGISWVPESFWKTGEWLDQLTGPYIVKN
KSU1_B0738 462 YSDG.SFGMDRWLVNVKQNASQARRLAALEKKVGISWVPESFWKTGEWLDQLTGPYIVKN
SCABRO_01590 460 YCDG.SFGMDRWLVKAKAASEQARRFTALEKKAGINWVPAEFWRKGDYLDQLSGMKIVKE
SCABRO_02945 460 YCDG.SFGMDRWLVKAKAASEQARRFTALEKKAGINWVPAEFWRKGDYLDQLSGMKIVKE
Kustc1061 451 YGNGSAFEQDRKLVEIKTEAAKLRRFAALEKKIGLEHKSADFWKHGEYLDLLPGWKRK..
Y462 cross-link
α22
α23
α24
Kustc0694
Kustc0694 521 HPGKTIFDLCPDPGWLDTHHAPAEEVEYIERKLKELGITAGSHSAHH.HESGHDPAARSM
Kustd1340 521 HPGKTIFDLCPDPGWLDTHHAPAEEVEYIERKLKELGMEAGTHDVKQ.DSE.....SKSV
Brofu101550-51 520 HPGKTIFDLCPDPGWLDTHHAPAEEVEYINRKIKELGWKTGHD..AH.HGDPHDEGARSM
BROSI_A2680 521 HPGKTIFDLCPDPGWLDTHHAPAEEVEYINRKLLELGMKDGKP..HH.GEGKIDEGARSM
BROSI_A2345 521 HPGKTIFDLCPDPGWLDTHHAPAEEVEYINRKLLELGMKDGKP..HH.GEGKIDEGARSM
KSU1_D0435 521 HPGKTIFDLCPDPGWLDTHHAPAEEVEYINRKLEELGMRHESH..GS.AHH.........
KSU1_B0738 521 HPGKTIFDLCPDPGWLDTHHAPAEEVEYINRKLEELGMRHESH..GG.AHH.........
SCABRO_01590 519 FPGKTIFDLCPEPGWLDTHHAPAAEVEYINRMLKEVGMSAGTHSAHDQHQKDHDPGARSM
SCABRO_02945 519 FPGKTIFDLCPEPGWLDTHHAPAAEVEYINRMLKEVGMSAGTHSAHH............
Kustc1061 509 .PGDV......DVEWFKRTDIPHRANA......DAGVEI.....HH............
Kustc0694
Kustc0694 580 KEH.
Kustd1340 575 REH.
Brofu101550-51 577 GKTH
BROSI_A2680 578 GKTH
BROSI_A2345 578 GKTH
KSU1_D0435 ....
KSU1_B0738 ....
SCABRO_01590 579 KKH.
SCABRO_02945 ....
Kustc1061 ....

Figure 3.17 Sequence Alignment of *Ks*HDH Homologues
Kuenenia stuttgartiensis Kustc0694 or *Ks*HDH (CAJ71439.1) and its paralogue Kustd1340 (CAJ72085.1) were aligned to their orthologues from *Jettenia caeni* (Planctomycete KSU-1) KSU1_D0435 (HzoB, WP_040544494.1) and KSU1_B0738 (HzoA, WP_007220714.1), *Brocadia sinica* JPN1 BROSI_A2680 (WP_052564202.1) and BROSI_A2345 (WP_052563890.1) as well as *Scalindua brodae* SCABRO_01590 (KHE92657.1) and SCABRO_02945 (KHE91265.1). The sequence of the *Brocadia fulgida* homologue (*Bf*HDH) was composed of the partial sequences of Broful_01550 (KKO19737) and Broful01551 (KKO19738) which were further completed and confirmed by Sanger sequencing. For comparison the sequence alignment also includes the sequence of *Kuenenia stuttgartiensis* Kustc1061 or *Ks*HOX (CAJ71806.1) (40 % sequence identity to *Ks*HDH).The sequence identities to Kustc0694 are 97 % for Kustd1340, 89 % for KSU1_D0435 and KSU1_B0738, 87 % for *Bf*HDH (Broful01550-51), BROSI_A2680 and BROSI_A2345, 79 % for SCABRO_01590 and SCABRO_02945. Alignments were performed using ClustalO (Sievers, 2011) and secondary structure elements were manually assigned based on the *Ks*HDH structure. Fully conserved peptide sequences are marked black. The CXXCH c-type heme binding motifs are highlighted in red, the CX_4CH motif (heme 3) in orange, the active site heme 4 (P460 cofactor) in pink. The predicted signal peptides are highlighted in grey. The distal histidine ligands of the hemes (x', green circles), the conserved Asp-His pair (DH, blue triangles), the conserved tyrosine involved in subunit crosslinking (Tyr462, pink star), a cysteine residue making an extra crosslink with the active site heme (Cys202, pink triangle) and the first residue valine contributing to active site heme environment (Val33, highlighted in green) are also indicated. Moreover, a methionine residue at the distal face of the active site heme (Met319, cyan triangle) is conserved. The figure was prepared using ESPript (Gouet 1999).

3.2.6 Kustc1130 – The Small Binding Partner of *Ks*HDH

Kustc1130 is a ~9.4 kDa protein (89 amino acids long without its signal peptide) which shows a 7-stranded β-sandwich structure and was found without any cofactors. The two sheets of the β-sandwich are made up of three parallel-antiparallel (β1, β4 and β7) and four anti-parallel (β2, β3, β5 and β6) β-strands (Fig 3.18). Kustc1130 possesses a disulphide bond which is oriented towards the inner face of the *Ks*HDH octamer where one of the entrances to the large cavity in the 24mer *Ks*HDH complex is located (section 3.2.3). The two disulphide-forming cysteines (Cys56-Cys64) are conserved in all orthologues from fresh water anammox genera (*Kuenenia, Brocadia* and *Jettenia*) but are absent in the marine anammox genus *Scalindua* (Fig 3.19).

A query for structurally similar protein folds using the Dali server (Holm 2010) suggests that this fold is similar to the C-terminal 7-stranded β-sandwich domain of carboxypeptidase D domain II or CPD II (PDB id: 1H8L; z score=11.0; rmsd=2.7 Å and identity=24 %). This domain is reported to be similar to transthyretin (pre-albumin) and sugar binding proteins (Gomis-Rüth 1999), however, no functional significance of the domain has been defined so far. Interestingly, another hit was the carboxypeptidase M (CPM) C-terminal β-sandwich domain (PDB id: 1UWY; z-score= 9.6; rmsd= 2.0 Å and identity= 22 %). CPM is an extracellular glycosylphosphatidyl-inositol (GPI) anchored membrane glycoprotein (Reverter

2004). Many of the other significant hits are cell-adhesion proteins such as the CNA_2 domain (rmsd = 1.9 Å and identity only 13%) of the pilus component BcpA from *Bacilllus cereus* (Budzik 2007; Budzik 2009) and the fibronectin-adhesion protein Fba-B (rmsd = 1.9 Å and identity only 13%) responsible for invasion of endothelial cells by *Streptococcus pyogenes* (Amelung 2011). No features related to any type of membrane protein (integral or peripheral) could be located on the Kustc1130 sequence.

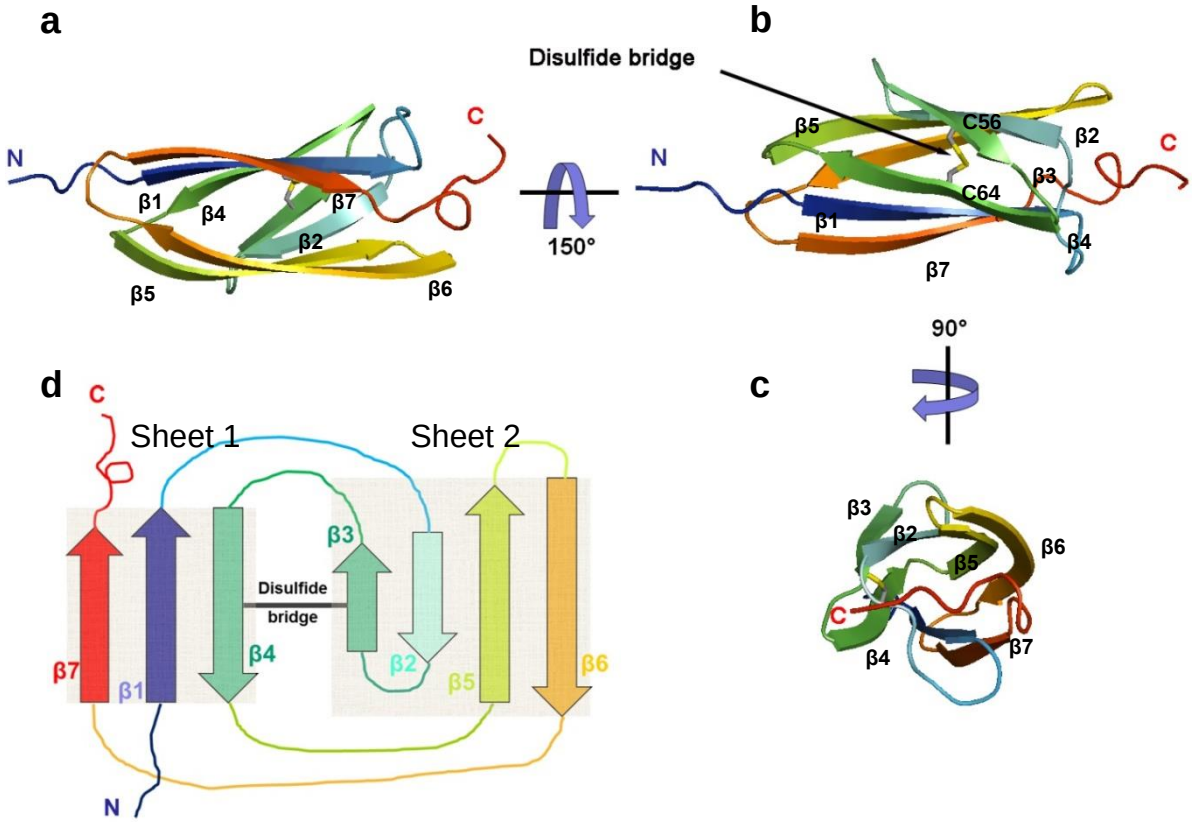

Figure 3.18 The Overall Structure of Kustc1130
a) Side view of the 7-bladed β-sandwich structure of Kustc1130. The two sheets of the sandwich are visible, the N- and C-termini are on opposite ends and both extend out of the rest of the structure. **b)** A view rotated by 150° about the x-axis with respect to figure **a** showing the disulfide bond between Cys56 and Cys64 which are located at β3 and β4, respectively. **c)** A view rotated by 90° about the y-axis with respect to figure **b** showing a β-barrel-like appearance. **d)** Topology diagram of Kustc1130. The arrows represent the β-strands in the two sheets. Sheet 1 is made up of three parallel-antiparallel strands (β1, β4 and β7) and sheet 2 is made up of four anti-parallel strands (β2, β3, β5 and β6). The relative sizes of the arrows signify the lengths of the strands relative to each other whereas the lengths of the loops are not drawn to scale. The disulfide bond is shown between strands β3 and β4.

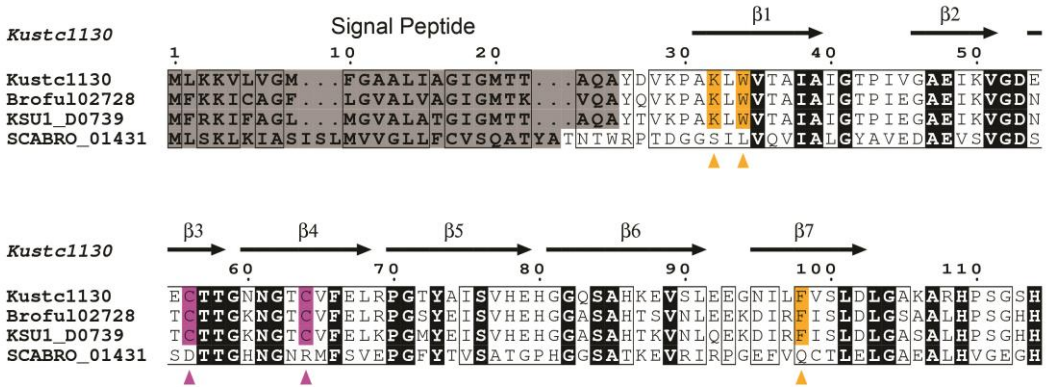

Figure 3.19 Multiple Sequence Alignment of Kustc1130 with its Homologues
Kuenenia stuttgartiensis Kustc1130 (CAJ71875.1) is aligned with its homologues from *Brocadia fulgida* Broful02728 (KKO18580.1), *Jettenia caeni* (previously called Planctomycete KSU-1) KSU1_D0739 (WP_007223131.1) and from *Scalindua brodae* SCABRO_01431 (KHE92823.1). Yellow triangles indicate the residues which are either interacting with or located close to *Ks*HDH heme 3. The pink triangles indicate the two cysteine residues which are involved in disulphide bond formation. Broful02728 and KSU1_D0739 are 74 % identical to Kustc1130 while SCABRO_01431 is only 33 % identical to Kustc1130.

Since this query did not yield any functionally significant hits, the most likely function of Kustc1130 appears to mediate interactions of *Ks*HDH (Fig 3.20). The N-terminal part of Kustc1130 (Tyr26 to Pro30) protrudes out of the core structure and its terminal amino group (of Y26) forms a salt bridge with Glu182 Oε of *Ks*HDH. In this region, few further salt bridges or hydrogen bonding interactions between Kustc1130 and *Ks*HDH are feasible as judged by the distances between interacting groups and also analyzed by the PDBePISA interface and assemblies analysis server (Krissinel 2007). These interactions include: Glu93 Oε with Arg311 NH; Thr72 (or Ser90) with Arg551 NH; Pro70 O with Glu544 Oε and Thr72 with Glu547 Oε (the first residue is part of Kustc1130 and the second one of the same *Ks*HDH single subunit). The residues involved in these interactions are conserved in *Ks*HDH, however, the corresponding residues are not conserved in the Kustc1130 homologues except for Pro70 (Fig 3.19). Interestingly, Arg551, Glu544 and Glu547 are located on the last helix α24 of *Ks*HDH. The mentioned interactions are formed with an HDH monomer of the trimer with which Kustc1130 shares minor interaction surface (interface area is 287 Å^2). However, the interaction surface of Kustc1130 with a *Ks*HDH monomer from a neighboring trimer is much larger (1,206 Å^2). These interactions include predominantly hydrogen bonds and salt bridges, but also some hydrophobic interactions. The most interesting interactions include a salt bridge/hydrogen bond between Kustc1130 Lys32 and *Ks*HDH Glu174. The latter residue is part of the non-canonical heme binding motif (CGTA**E**CH) at heme 3 (for details see

section 3.2.7). Figure 3.20 describes the minor and major interaction modes of Kustc1130 with the 24mer assembly of *Ks*HDH.

When looking at the electrostatic surface of Kustc1130, the side which interacts with two trimers shows patches of prominent positive charge while the opposite side possesses a continuous stretch of negative charge, which has been already mentioned in section 3.2.3. Figure 3.21 describes the interactions between *Ks*HDH and Kustc1130 through surface charge and also the surface structure complementation (presence of clefts and grooves).

(Figure on next page)

Figure 3.20 Arrangement of Kustc1130 on the *Ks*HDH Trimers in the 24mer Assembly
a) The 24mer X-ray structure is shown; Kustc1130 is shown as cartoons in rainbow colouring (blue N-terminus to red C-terminus), each trimer of *Ks*HDH as transparent surface and the hemes as sticks. In total twelve Kustc1130 molecules are visible.
b) Only the twelve Kustc1130 molecules from the 24mer *Ks*HDH complex structure are shown. Same view as in figure **a**.
c) & **d)** depict the two neighboring trimers with three molecules of Kustc1130 on each trimer. As it can be seen in figure **c,** the Kustc1130 molecules interact with their N-termini at their pointed face leading to a small interface surface area. In figure **d**, Kustc1130 interacts with its flat face including its C-terminus with neighboring HDH trimers. Here a significantly larger surface area of Kustc1130 is in contact with the HDH trimer.
e) Top view of the Kustc1130 arrangement as described in figure **c.** In addition, three possible neighboring trimers are shown.
f) The top view of the Kustc1130 arrangement as described in figure **d**, showing three additional neighboring trimers.

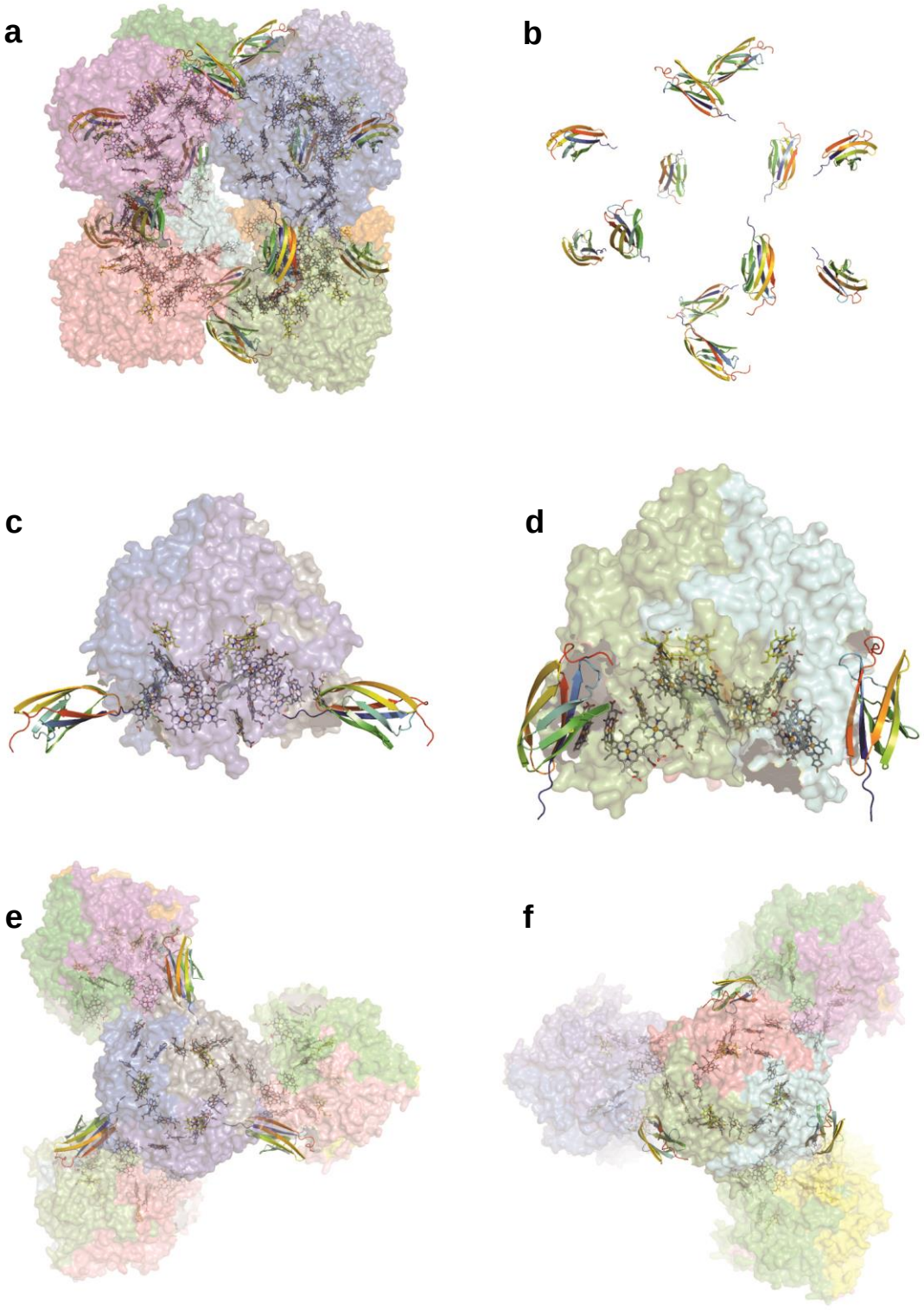
a
b
c
d
e
f

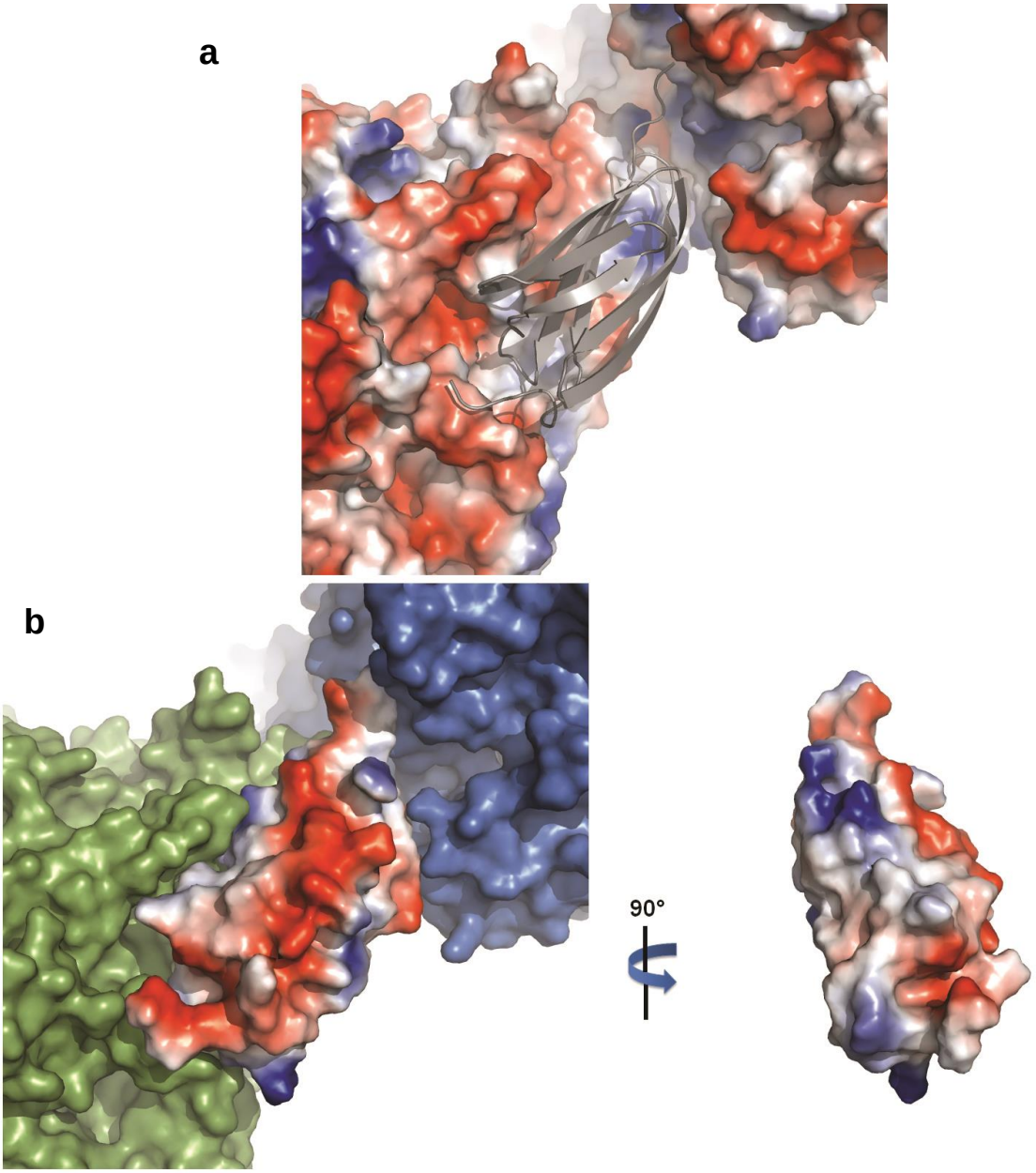

Figure 3.21 Electrostatic Interactions between Kustc1130 and Two Trimers of *Ks*HDH
a) The surface representation depicts the vacuum electrostatic potential of two neighboring trimers from the 24mer *Ks*HDH X-ray structure. The trimer on the left hand side shows patches of negative surface potential.
b) & c) The vacuum electrostatic potential of Kustc1130 present between two HDH trimers. With the trimer on the left side it shares major interaction surface as described in figure 3.20. The exposed surface of Kustc1130 has a continuous stretch of negative surface potential. The right panel shows the interaction surface of Kustc1130, which has primarily patches of positive potential. Therefore, charge complementation between *Ks*HDH and Kustc1130 is the most important factor for interaction.

3.2.7 Heme 3 in the *Ks*HDH 24mer X-ray Structure

A unique feature of heme 3 of *Ks*HDH is that it binds to the protein through a rare CX_4CH heme binding motif (**C**GTAE**CH**), which is considered to be a diagnostic feature of all known HDHs (Maalcke 2016; Shimamura 2007; Oshiki 2017). Now, the current X-ray structure sheds light on the intriguing architecture of this feature. When compared to *Ks*HOX and *Ne*HAO, heme 3 of *Ks*HDH is much more exposed to the solvent. As it can be seen in figure 3.22 a, an extended loop and an α-helix is shielding heme 3 in *Ks*HOX (PDB id: 4N4J) and in *Ne*HAO (PDB id: 1FGJ), respectively, making heme 3 less exposed to the solvent in both cases. The residues forming the heme 3 environment are derived from the loop (*Ks*HOX) and the α-helix (*Ne*HAO) and are hydrophobic (Ile145 and Ile147 in *Ks*HOX, Val123 and Lys120 in *Ne*HAO). The polar end of Lys120 in *Ne*HAO seems to move away from heme 3 only allowing the aliphatic part of its side chain to contribute to the heme environment (not shown). In fact, another HAO, the supposed nitrite reductase Kustc0458 from *K. stuttgartiensis* (PhD thesis Andreas Dietl, 2016) also possesses an α-helix shielding heme 3 with Ile153 and Lys149 contributing to the heme environment in the same manner as mentioned for *Ne*HAO. This extra loop represents the distal side of the heme. The proximal side which contains the **C**GTAE**CH** motif in *Ks*HDH protrudes out as a bulge when compared with the *Ks*HOX and *Ne*HAO structures because of the two extra amino acids in the heme binding motif.

As mentioned in the previous section (3.2.6), there are two kinds of trimers in the octamer, the ones to which Kustc1130 interact *via* a small number of residues including the N-terminus and the ones with larger interaction surface area at the C-terminal end of Kustc1130. The N-terminus of Kustc1130 is close to heme 5 of the minorly interacting trimer and to heme 3 of the majorly interacting trimer. Interestingly, in case of the majorly interacting *Ks*HDH trimer, Lys32 of Kustc1130 interacts with Glu174 from the heme 3 binding motif (CGTA**E**CH) *via* a salt bridge/hydrogen bond. This interaction brings two aromatic amino acids Trp34 (~4.3 Å away from the heme 3 edge) and Phe98 (~6.3 Å away from the heme 3 edge and directly stacking on Trp34 with a distance of 3.5 Å) close to heme 3. However, these residues from Kustc1130 are at different positions compared to that of the hydrophobic residues from the extra loop of *Ks*HOX as described above. This still keeps heme 3 solvent exposed when compared with *Ks*HOX and *Ne*HAO. However, none of the heme 3 cofactors in the minorly interacting HDH trimers interact with Kustc1130 which makes these hemes 3

even slightly more solvent exposed. Therefore, in a 24mer *Ks*HDH-Kustc1130 complex there are twelve heme 3 cofactors which interact with Kustc1130 and twelve which do not.

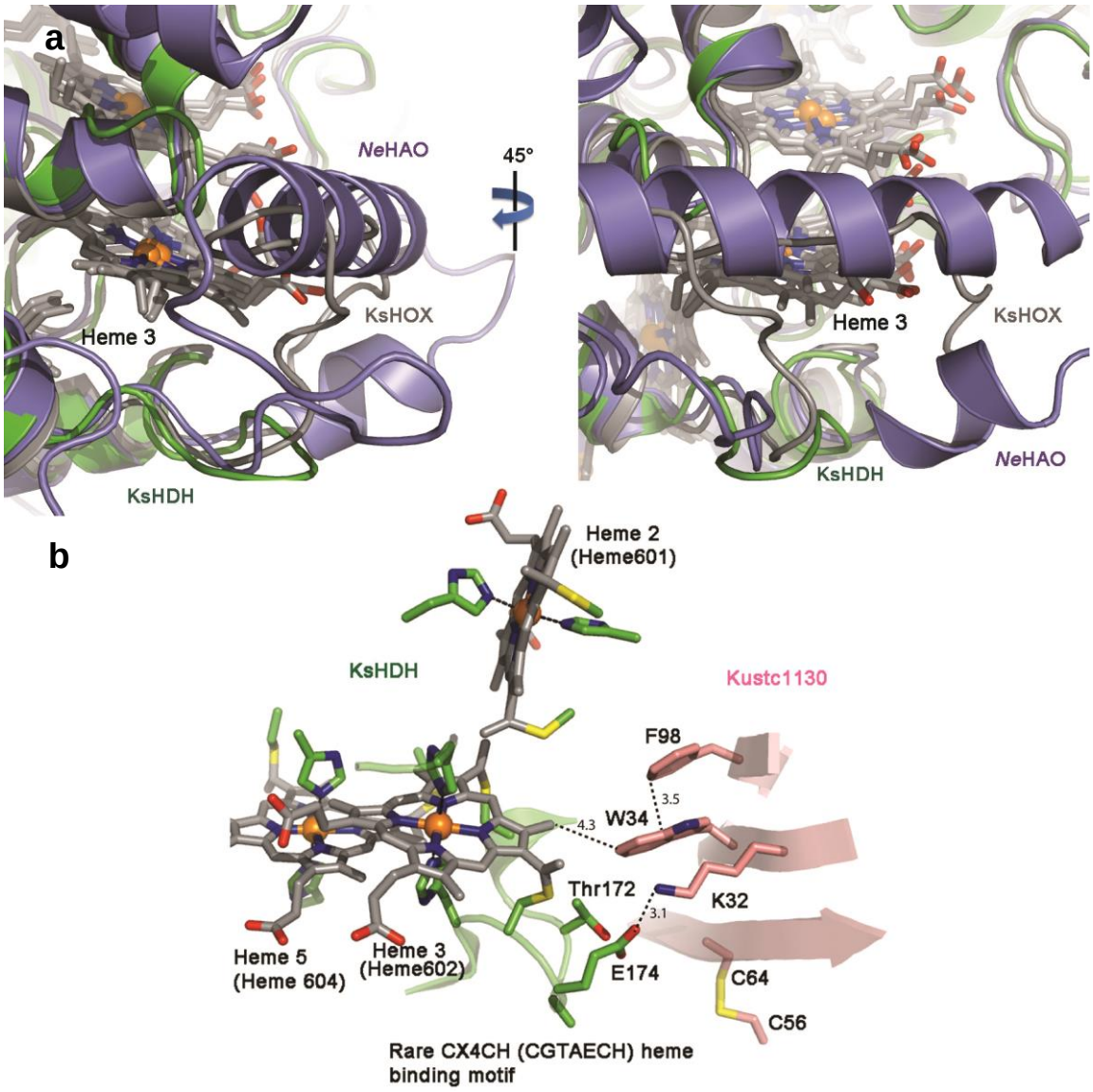

Figure 3.22 *Ks*HDH Heme 3 and its Interaction with Kustc1130
a) The figure shows a cartoon-stick model of *Ks*HDH (green) heme 3 and its surroundings including nearby hemes 2 and 5. **b)** Heme 3 is *bis*-His ligated and attached to the protein *via* a rare heme binding motif CGTAECH. A part of Kustc1130 is shown in pink. Lys32 from Kustc1130 interacts with Glu174 of the Heme 3 binding motif *via* a salt bridge/hydrogen bonding interaction. This interaction brings Trp34 close to heme 3 (~4 Å). Phe98 stacks with Trp32 perhaps *via* aromatic-aromatic interactions (the distance between the planes is ~3.5 Å).

3.2.8 Comparison of the 24mer X-ray structure with the 24mer and 30mer *Ks*HDH Cryo-EM structures

Cryo-EM sample preparation, image acquisition and 3D reconstruction were performed by Kristian Parey and Simone Prinz at the MPI of Biophysics, Frankfurt. The stable oligomerization of *Ks*HDH for cryo-EM analyses was achieved by either high salt (300 mM KCl) or by crosslinking using glutaraldehyde (Maalcke 2016). In both cases there were 24mer and 30mer assemblies present, however, the 30mer assembly represented a minor fraction. The high salt 24mer structure was obtained using 3,246 particles to yield a map with a final resolution of 5.0 Å. From crosslinked samples three dimensional maps of the 24mer and 30mer were obtained after 2D and 3D classification from 4,235 and 2,017 particles and refined to overall 5.2 Å and 6.1 Å resolution, respectively (Fig 3.23 b shows the crosslinked *Ks*HDH 30mer; the 24mer structure from crosslinked *Ks*HDH is not shown). The overall X-ray 24mer structure is identical to the cryo-EM high salt as well as the crosslinked 24mer structure (Fig 3.23 a). However, the small protein Kustc1130 was neither visible in high salt nor crosslinked 24mer cryo-EM structures. The absence of the small protein was also confirmed when no symmetry operations were applied in 3D reconstructions (personal communication from Kristian Parey) in order to eliminate the possibility of averaging out the occupancies of Kustc1130 molecules in case if only few positions were occupied by Kustc1130. However, the arrangement of *Ks*HDH trimers was highly identical to the 24mer X-ray structure including the interaction surface between two trimers. An astonishing continuous network of 192 and 240 hemes are present in both the 24mer and 30mer *Ks*HDH structures, respectively (Fig 3.24).

Based on geometrical considerations, there are expected differences between the 24mer and 30mer assemblies as they represent cubic and pentagonal prism-like shapes, respectively. The 30mer *Ks*HDH cryo-EM structure represents a sandwich of two pentagonal rings of *Ks*HDH trimers. The interactions between the trimers within each pentagonal ring are different compared to those between trimers from the two pentagonal rings (Fig 3.25 b & c). Indeed, the distance between the apexes of two trimers from within the same pentagonal ring on average is ~129 Å (Gly494-Gly494 distance; all the possible distances were measured), while the apex-to-apex distance between two trimers belonging to different pentagonal rings on average is ~138 Å (Fig 3.25). Both cryo-EM and X-ray 24mer cubic assemblies possess an average edge length of ~138 Å (Gly494-Gly494 distances). This indicates that the interaction

surfaces in the 30mer cryo-EM structure between the trimers from the two mentioned scenarios would be different. One would be exactly identical to that in the 24mer assemblies and the other one would slightly differ.

It is difficult to comment on the precise differences in the interactions based on the structure itself as the resolution of the *Ks*HDH 30mer structure is limited to 6.1 Å. However, it can be observed that those regions which are close enough for hydrophobic interactions in case of the X-ray 24mer structure are also in interaction range with few shifts in the cryo-EM 30mer structure. The overall shift also resulted in the positioning of the residues which are involved in the interactions with Kustc1130 in case of the X-ray 24mer structure to 5-10 Å shifted positions (Fig 3.25). Despite the shift at the shorter edge, the continuous network of 240 hemes in the 30mer is not disrupted.

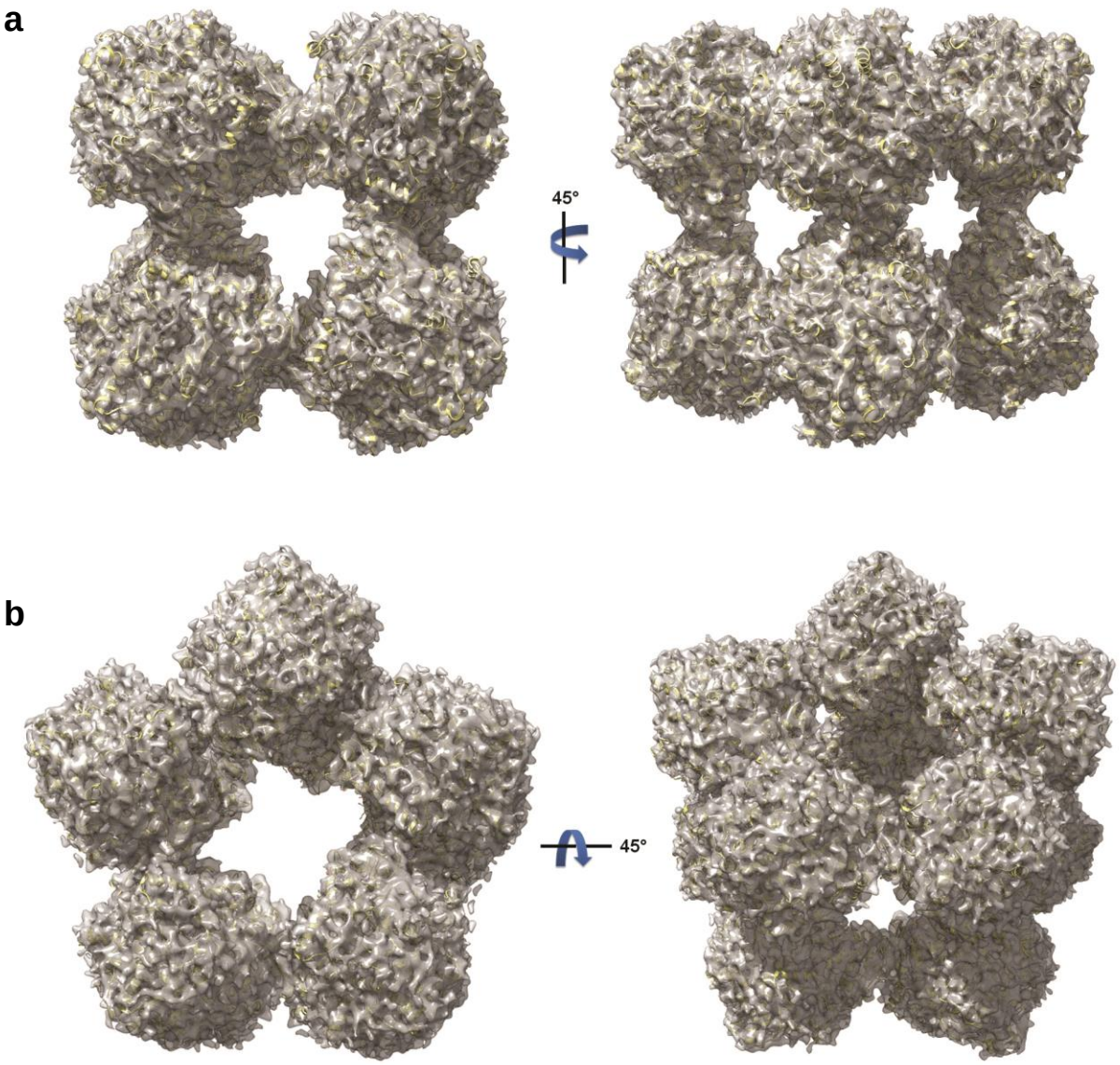

Figure 3.23 Cryo-EM Density Maps with Fitted Models of 24mer and 30mer Assemblies of *Ks*HDH
The figures were made using UCSF chimera (Pettersen 2004). The *Ks*HDH monomer model from the X-ray 24mer structure was fitted to the cryo-EM density maps by superimposition onto the real space refined *Ks*HDH model (obtained by Kristian Parey, MPI of Biophysics, Frankfurt) and performing rigid body refinement in COOT (Emsley 2004). The models are shown as ribbon (yellow).
a) Views of the cube-like 24mer assembly of *Ks*HDH at 5.0 Å obtained from high salt conditions.
b) Top and side views of the pentagonal prism-like 30mer assembly of *Ks*HDH at 6.1 Å obtained from glutaraldehyde crosslinked particles.

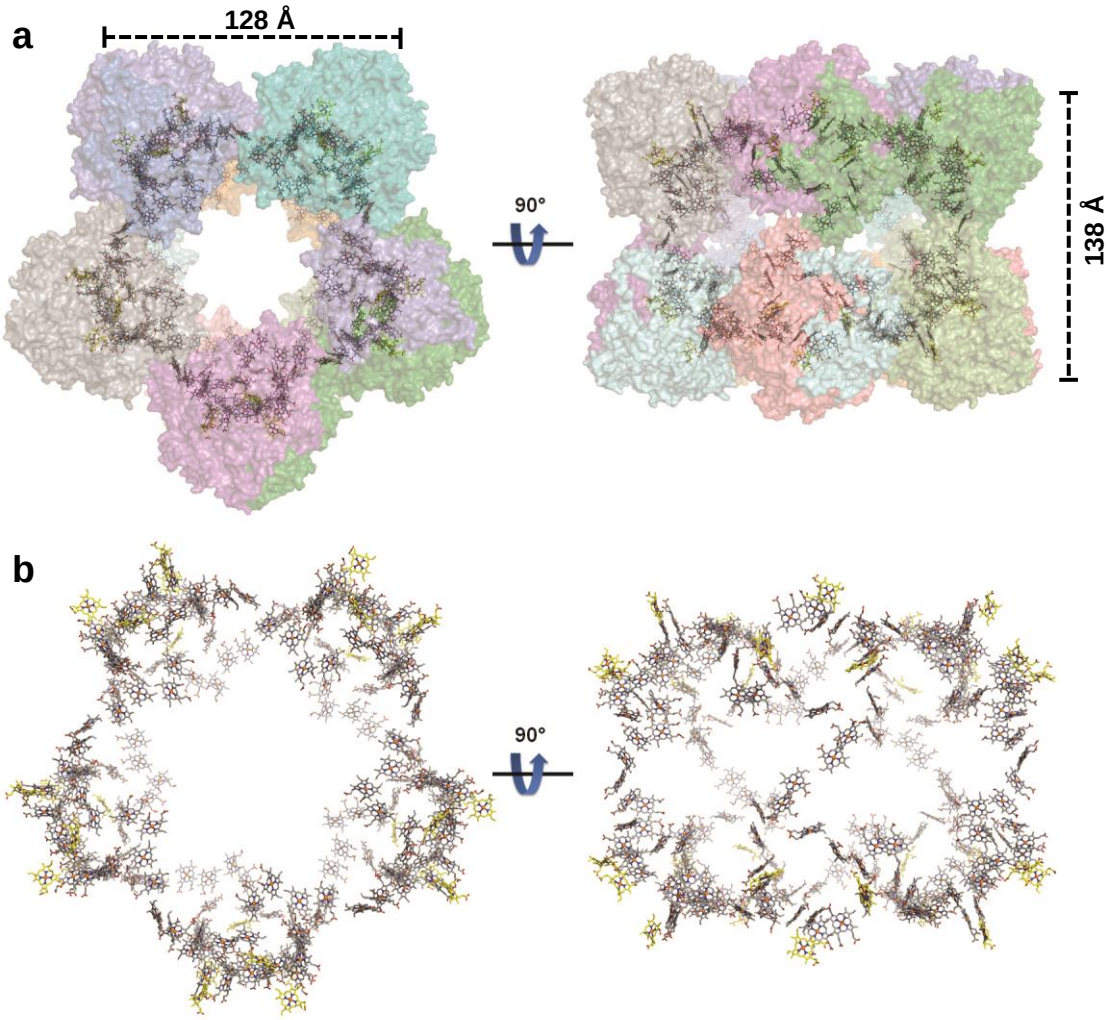

Figure 3.24 Cryo-EM Structure of the *Ks*HDH 30mer showing a network of 240 Hemes
a) Transparent surface representations of the pentagonal prism-like *Ks*HDH cryo-EM 30mer structure. The top view at the left shows five trimers, the distance between the apexes of two trimers is shown (128 Å). Similarly, the side view at the right side shows the distance (138 Å) between the apexes of two trimers from the two pentagonal rings of *Ks*HDH trimers in the 30mer. The distance of 138 Å is also present in the 24mer structures obtain by both Cryo-EM and X-ray crystallography for all the possible apex-to-apex distances.
b) Top and side views of the 240 hemes network present in the 30mer cryo-EM structure. The hemes are shown as stick models. The carbons of the active site P460 hemes are shown in yellow.

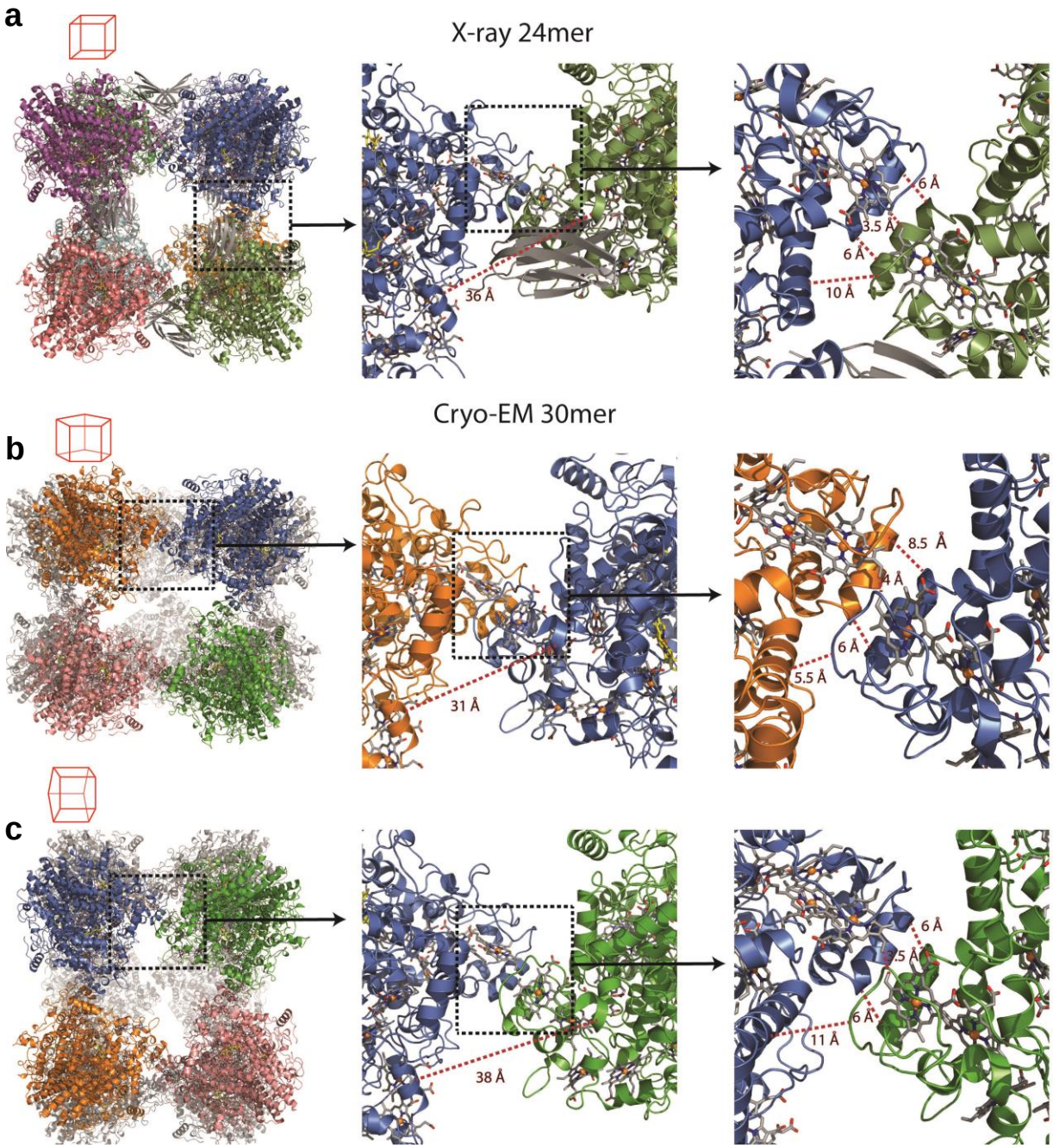

Figure 3.25 A Comparison of 24mer and 30mer *Ks*HDH Trimer-trimer Interfaces
The numbers represent the distances in Å between Cα-atoms of amino acid residues (red dashed lines). The left column indicates representative *Ks*HDH assemblies and their orientations (red pictograms), the middle column represents the zoomed-in view of the trimer-trimer interface showing the distances between Asp98 (right trimer) and Glu182 (left trimer). The right column shows further zoomed-in views of the trimer-trimer junction showing the distances between two edges of interacting α3-helices (at one end between Gln120 and Val127 and at the other the end in converse order between Val127 and Gln120), between hemes 1 and between Asp336 (from helix-α16 of the left trimer) and Gly114 (from loop α2-α3 of the right trimer). **a)** 24mer X-ray structure with Kustc1130 shown in grey. In the 24mer X-ray and Cryo-EM structures all the 12 sides are equivalent as they truly represents a cube (each side 138 Å). **b)** Trimer-trimer interface within one of the two pentagonal rings in the 30mer *Ks*HDH assembly. **c)** Interface of KsHDH trimers belonging to two different pentagonal rings in the 30mer *Ks*HDH assembly. Comparing figure **b)** and **c)** note that the distance change from 38 Å (figure **b**; middle column) to 31 Å (figure **c**; middle column). Similarly, note the differences between figure **b** and **c** (right columns). The distances in figure **c** are similar to that in **a**.

3.2.9 Expression and Purification of Kustc1130 and Broful02728

SDS-PAGE analyses of *Ks*HDH protein preparations from *Kuenenia stuttgartiensis* biomass (>95 % pure) revealed a prominent protein band at a molecular weight of around ~10 kDa in addition to the bands observed for the *Ks*HDH trimer at ~200 kDa (Fig 3.26). The absence of a band in a heme-stained gel indicated that the small co-purified protein was not a c-type cytochrome. Initial trials to identify the ~10 kDa protein by MALDI-MS peptide mass fingerprinting from a gels slice and also by direct analysis of the protein solution using ESI mass spectrometry failed. However, the first ten residues at the N-terminus could be sequenced using Edman's degradation method (Proteome factory, Berlin, Germany) (Edman 1950) yielding the sequence **YDVKPAKLXV** where "X" represents the 9th position in the sequence which could not be unambiguously determined. An NCBI-BLAST search of this sequence against the *Kuenenia stuttgartiensis* genome resulted in an unambiguous match for Kustc1130. As mentioned in section 3.2.2, the twelve extra molecules in the electron density maps of the *Ks*HDH 24mer could be satisfactorily explained with Kustc1130. Moreover, homologues of Kustc1130 could be detected in all known anammox genomes (Fig 3.19).

A homologue of *Ks*HDH, called *Bf*HDH could be purified from *Brocadia fulgida* cells obtained from DEMON® sludge (chapter 5). Therefore, *Bf*HDH was also used in parallel for biochemical and biophysical studies since the available amount of *Ks*HDH protein was limited. As it can be observed on SDS-PAGE gels (Fig 3.26), *Bf*HDH preparations lack a protein band near ~10 kDa. However, as already mentioned, the *Brocadia fulgida* genome encodes a close Kustc1130 homologue called Broful02728. The lack of Broful02728 in *Bf*HDH preparation gives us the attractive advantage to check its effect on the biophysical and biochemical properties of *Bf*HDH most importantly its effect on HDH oligomerization. Therefore, not only Kustc1130 but also Broful02728 were heterologously expressed and purified. As discussed in section 3.2.6, the N-terminal amino group of Kustc1130 interacts with Glu128 of *Ks*HDH *via* a salt bridge as observed in the X-ray structure of the 24mer complex. The possibility that this interaction is important was taken into account during the design of the expression constructs in order to make sure that the N-terminal residue after signal peptide cleavage would be a tyrosine (Tyr26 in both Broful02728 and Kustc1130) as in the case of the native proteins. For this purpose, the native N-terminal signal sequence was included in the constructs (Fig 3.27). The constructs were cloned into pET24d vectors (section 2.2.3.4) and expressed in *Escherichia coli* BL21. This expression host was chosen

since *E. coli* is known to apply a similar secretory machinery to transport proteins to the periplasm as the anammox bacterium *K. stuttgartiensis* uses for protein import to the anammoxosome (Ferousi 2013; Huston 2007). The expression of both constructs followed by a two-step purification procedure using Ni-NTA affinity chromatography and gel filtration (section 2.2.3.4) yielded pure and homogenous protein preparations (Fig 3.26). Total protein masses and sequences were confirmed by MALDI-MS and ETD-ESI-MS indicating that indeed the starting residue after signal peptide cleavage was tyrosine (Tyr26).

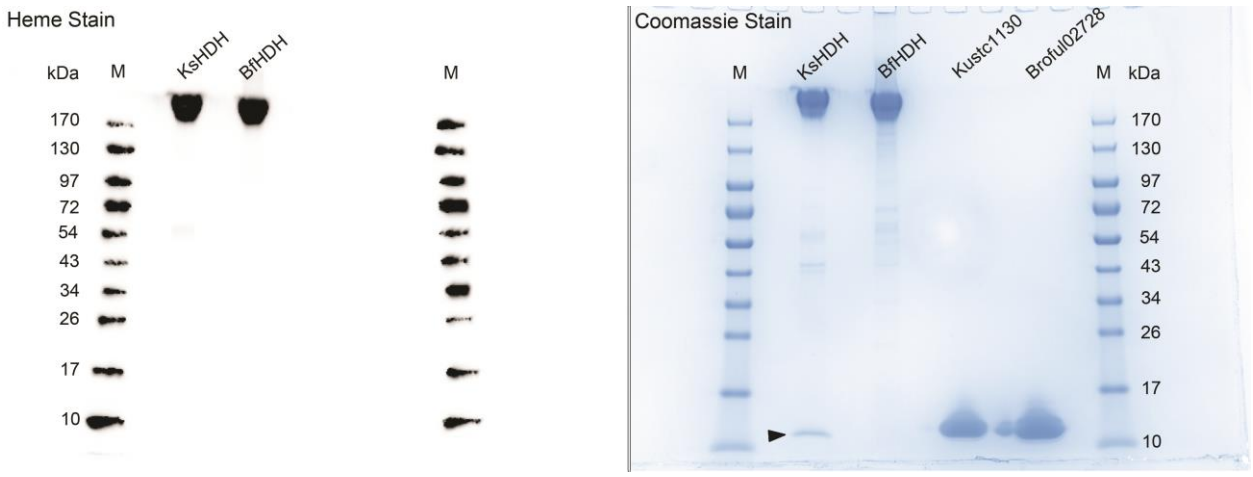

Figure 3.26 4-20 % Tris-glycine SDS-PAGE Analysis of *Ks*HDH, *Bf*HDH, Kustc1130 and Broful02728
3-5 µg of each protein samples were loaded on a Precast Mini-PROTEAN®TGX™ 4-20 % gradient gel (Bio-Rad, USA).The abbreviation M indicates PageRuler pre-stained protein ladder (Thermo Scientific, Darmstadt, Germany). For heme and Coomassie staining methods see section 2.2.4.2 and 2.2.4.3. Heme staining was used to detect c-type heme-containing proteins and the prestained protein marker was marked by luminescent paint. The gel shows *Ks*HDH and *Bf*HDH purified from *Kuenenia stuttgartiensis* biomass (obtained from J. Reimann, Radboud University, Nijmegen, the Netherlands) and from DEMON® sludge (purification see section 2.2.3.3), respectively. Kustc1130 and Broful02728 were overexpressed as described in section 2.2.3.4 with C-terminal 6xHis tags. In the Coomassie-stained image a black arrow indicates Kustc1130 (confirmed by Edman's N-terminal protein sequencing,and also by mass spectrometry). As can be seen there is no band in the native *Bf*HDH sample corresponding to the position of Kustc1130/Broful02728.

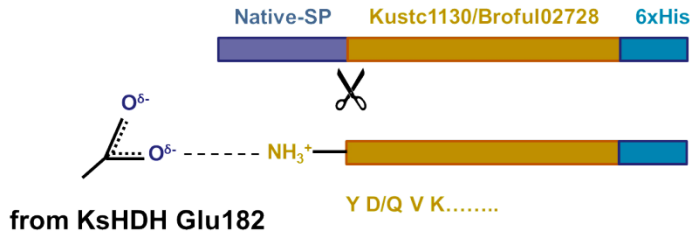

Figure 3.27 Expression Constructs for Kustc1130 and Broful02728
The native signal peptide (Native-SP) was used which was cleaved off after expression by the host (*E. coli* BL21) as confirmed by mass spectrometry (section 2.2.5.5). In the *Ks*HDH 24mer X-ray structure the N-terminal amino group from tyrosine Y26 interacts with Glu182.

3.2.10 Effects of Salt and Broful02728 on *Bf*HDH Oligomerization

HDH can exist in multiple oligomeric states as already shown previously (Maalcke 2016). However, the regulatory forces which are responsible for oligomerization have not been explored. This section describes the dependence of HDH (*Ks*HDH or *Bf*HDH) oligomerization on salt concentration and the presence or absence of its small binding partner (Kustc1130 or Broful02728, respectively). Based on the X-ray structure of the *Ks*HDH 24mer-Kustc1130 complex and the *Ks*HDH 30mer cryo-EM structure, homology models of the *Bf*HDH 24mer, 30mer and 24mer with 12x Broful02728 were computed (*Bf*HDH shares 87 % sequence identity with *Ks*HDH). The sedimentation coefficients for all the mentioned oligomeric states for both *Ks*HDH and *Bf*HDH were calculated using the software HYDROPRO (Ortega 2011). Owing to similar molecular mass and sequence conservation apparently all the oligomeric states of both *Ks*HDH and *Bf*HDH have nearly identical sedimentation coefficients. Analytical ultracentrifugation sedimentation velocity (AUC-SV) analyses of *Bf*HDH at different concentrations of potassium chloride (KCl) and with Broful02728 in the absence or presence of salt are shown in figure 3.28. Without any salt *Bf*HDH exist predominantly as trimers (α_3) which show a sedimentation coefficient of 9.7 Svedberg (S) corresponding to a $S_{w,\,20}$ of 9.9 S (Fig 3.28 and table 3.3) which is close to the value of 10.6 S calculated by HYDROPRO. An $S_{max}/S_{w,20}$ ratio of 1.25 (table 3.3) reflects that the *Bf*HDH trimers indeed possess a globular shape in the low salt conditions (0 mM KCl, 25 mM HEPES/KOH pH 7.5). With increasing KCl concentrations, the proportion of higher oligomeric forms (α_{24} and α_{30}) increases. For instance, at 50 mM KCl two peaks are visible at 10.7 S and 39.3 S representing trimers and higher oligomers with a proportion of 43 % and 57 %, respectively. Moreover, at 150 mM KCl the proportion further changes to 12 % and 88 % for trimer and higher oligomers, respectively (Fig 3.28 a). At 300 mM KCl it was even 6 % and 94 % (not shown), however, the change is not very significant when compared with 150 mM KCl. The peaks for α_{24} and α_{30} oligomeric states could not be resolved in AUC-SV experiments as the sedimentation coefficients of the two species are very close to each other as calculated using HYDROPRO (35.6 S and 40.4 S, respectively). However, the two forms were present at high salt concentrations (300 mM) as indicated by negative stain transmission electron microscopy (TEM) images (Fig 3.31 b).

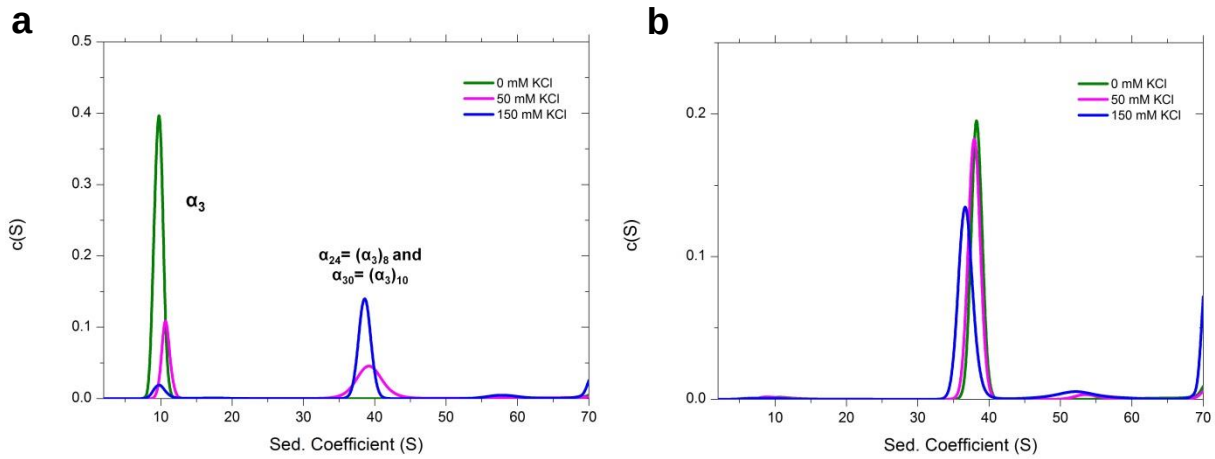

Figure 3.28 Analytical Ultracentrifugation Sedimentation Velocity (AUC-SV) Experiments of *Bf*HDH
AUC-SV experiments were performed at 20,000 rpm at 20 °C in a buffer containing 25 mM HEPES/KOH, pH 7.5 with different concentrations of KCl in the absence or presence of Broful02728. The absorption scans were recorded at 425 nm to avoid the absorbance from Broful02728 (at 280 nm) which was used at a concentration of ~100 µM (A_{280}^{1cm}~0.85). The absorptivity of *Bf*HDH at 425 nm is close to that at 280 nm. *Bf*HDH was diluted to A_{425}^{1cm} = 0.42. The proportions of the individual oligomeric species were determined by integration of the peak areas.
a) Sedimentation coefficient distribution c(S) of *Bf*HDH with different concentrations of KCl. Peaks at ~10 S represent *Bf*HDH trimers and at ~40 S represent probably both 24mer and 30mer assemblies of *Bf*HDH. As the concentration of KCl increases the proportion of 24mer and 30mer also increases.
b) The sedimentation coefficient distribution of *Bf*HDH samples including Broful02728 shows a major peak at ~40 S with a negligible trimers peak left at all KCl concentrations (0, 50, 150 mM). This indicates that Broful02728 promotes *Bf*HDH oligomerization. A detailed summary of probable oligomerization states and molecular weights derived from AUC-SV is given in table 3.3.

On the contrary, when Broful02728 was present during all salt concentrations there was only a single peak observed with an average sedimentation coefficient of 37.6 S (ranges from 36.8 to 38.2 S) corresponding to a $S_{w,20}$ of 38.5 S (Fig 3.28 b; table 3.3). The experimental values are close to the calculated value of 37.9 S using HYDROPRO for 24mer *Bf*HDH with 12x Broful02728 indicating that the peak might represent a complex of *Bf*HDH and Broful02728 in solution. This is expected to be reminiscent to the 24mer *Ks*HDH-Kustc1130 assembly observed in the X-ray structure and therefore this assembly most likely also represents the oligomeric state in solution. In all the individual salt conditions, this main peak represents 98-99 % of total protein present.

In the presence of salt only (50-300 mM KCl) the sedimentation coefficients of the *Bf*HDH higher oligomeric peaks in AUC-SV experiments are approximately 39 S corresponding to an $S_{w,\,20}$ of ~40 S. The calculated $S_{w,\,20}$ value for the *Bf*HDH 30mer is 40.4 S. As it is also shown by negative stain TEM images (Fig 3.31), the experimental values are most likely a result of a mixture of both 24mer and 30mer assemblies.

Interestingly, the ratio of S_{max}/S calculated with HYDROPRO for the BfHDH 24mer (also *Ks*HDH) with 12x Broful02728, the 24mer alone and 30mer are 1.37, 1.39 and 1.42, respectively. However, the experimental ratios of $S_{max}/S_{w,20}$ (1.35, 1.33 and 1.35) from the *Bf*HDH 24mer with 12x Broful02728 in all different salt conditions (see table 3.3) are very close to the calculated value (1.37).

Table 3.3 Characterization of different oligomeric forms of *Bf*HDH in different solution conditions

Experimental						
***Bf*HDH Conditions**	**Oligomer**	**Calculated Mw [kDa]**	**S_{max}**	**S**	**$S_{w,\,20}$**	**$S_{max}/S_{w,\,20}$**
0 mM KCl	α_3	200.73	12.38	9.69	9.91	1.25
0 mM KCl, +Broful02728	$(\alpha_3)_8$	1,605.91	49.51	38.19	38.37	1.29
	$(\alpha_3)_8$12xSBP	1,719.14	51.81	38.19	38.37	1.35
50 mM KCl	α_3	See above	12.38	10.71	11	1.13
	$(\alpha_3)_8$	See above	49.51	39.33	40.46	1.22
	$(\alpha_3)_{10}$	2007.3	57.45	39.33	40.46	1.42
50 mM KCl +Broful02728	$(\alpha_3)_8$	See above	49.51	37.90	39.00	1.27
	$(\alpha_3)_8$ 12xSBP	See above	51.81	37.90	39.00	1.33
150 mM KCl	α_3	See above	12.38	9.97	10.39	1.19
	$(\alpha_3)_8$	See above	49.51	38.59	40.18	1.23
	$(\alpha_3)_{10}$	See above	57.45	38.59	40.18	1.43
150 mM KCl +Broful02728	$(\alpha_3)_8$	See above	49.51	36.75	38.25	1.29
	$(\alpha_3)_8$ 12xSBP	See above	51.81	36.75	38.25	1.35
Calculated using HYDROPRO						
	α_3	See above	12.38	10.60	----	1.17
	$(\alpha_3)_8$ 12xSBP	See above	51.81	37.90	----	1.37
	$(\alpha_3)_8$	See above	49.51	35.60	----	1.39
	$(\alpha_3)_{10}$	See above	57.45	40.40	----	1.42

Sedimentation coefficients are given in Svedberg units (1 S = 10^{-13} s). $S_{w,\,20}$, sedimentation coefficients extrapolated to water at 20 °C; S_{max}, maximal sedimentation coefficients calculated as $S_{max} = 0.00361 \times M^{2/3}$ (Erickson 2009). The ratio of $S_{max}/S_{w,\,20}$ in the range of 1.2–1.3 indicates a globular shape of the particles. Mw indicates molecular mass. $(\alpha_3)_8$ 12xSBP represents the 24mer *Bf*HDH-12xBroful02728 complex (SBP=small binding partner). The S values using HYDROPRO (Ortega 2011) were calculated at 20 °C for 25 mM KCl and 25 mM HEPES/KOH pH 7.5 (viscosity η = 0.010194 g cm^{-1} s^{-1}, density ρ =1.00135 g cm^{-3} and partial specific volume 0.7300 mL/g). $S_{max}/S_{w,\,20}$ is $S_{max}/S_{HYDROPRO}$ for calculated section.

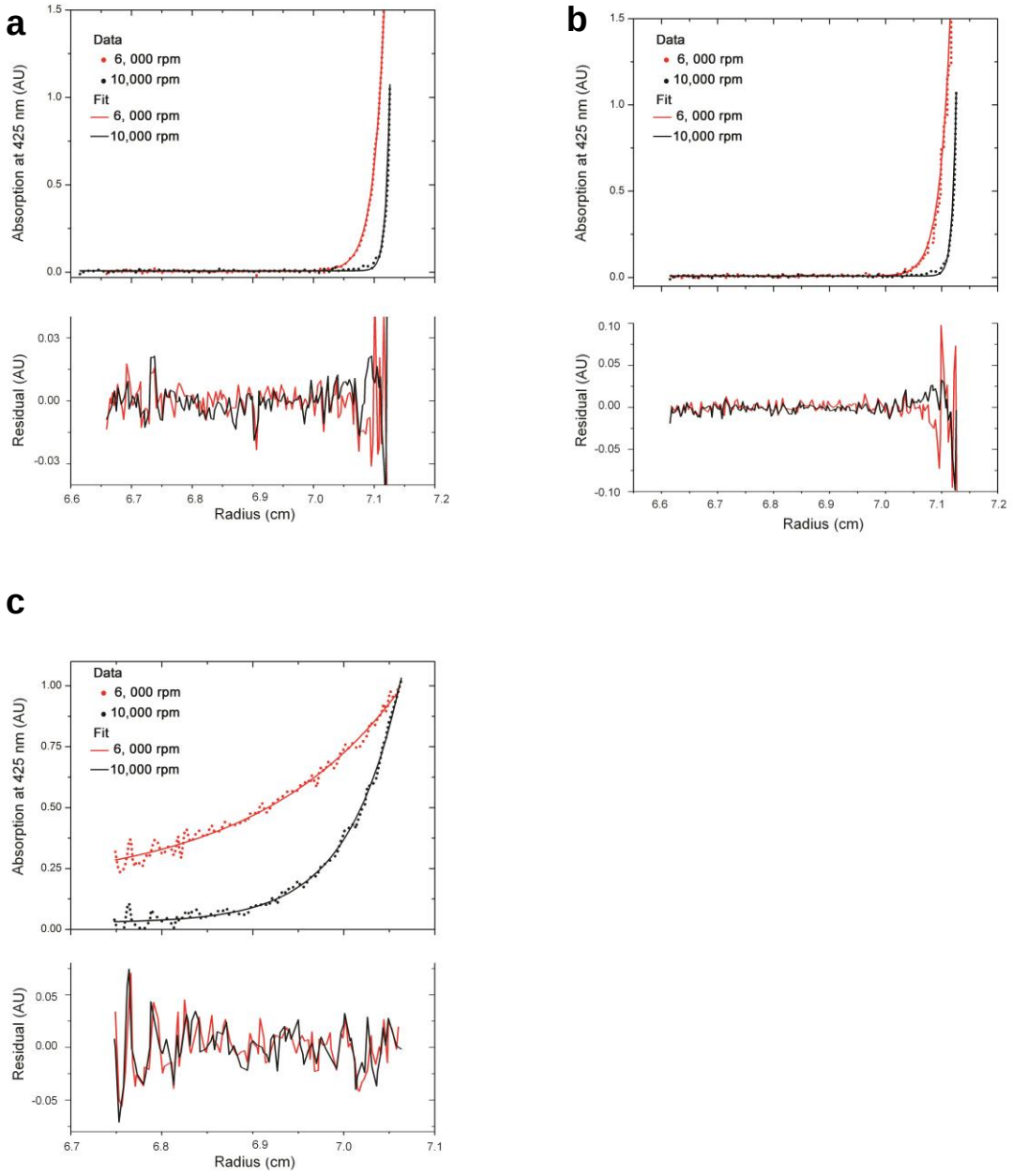

Figure 3.29 AUC-SE Experiments on *Bf*HDH
The samples used in Analytical Ultracentrifugation Sedimentation Equilibrium (AUC-SE) experiments were from AUC-SV experiment described before. The samples were gently homogenized and 200 µL of both samples and buffer were removed. Absorption scans were recorded at 425 nm. Sedimentation equilibrium curves were recorded after 22 h equilibration at a set speed at 20 °C. Three angular velocities (3,000, 6,000 and 10,000 rpm) were used to achieve equilibrium. In all cases, the scans from 3,000 rpm were not used in final calculations. Sedimentation equilibrium curves at 6,000 rpm (red) and 10,000 rpm (black) are shown. The data points were averaged from five individual scans at 425 nm and globally fitted assuming a model of discrete non-interacting species in SEDPHAT.
a) Sedimentation equilibrium curves of *Bf*HDH with Broful02728 and without additional potassium chloride. **b)** Sedimentation equilibrium curves of *Bf*HDH with Broful02728 and 150 mM KCl.
c) Sedimentation equilibrium curves of *Bf*HDH without additional KCl.

Table 3.4 Calculated *vs.* experimental molecular masses from AUC-SE

***Bf*HDH Conditions**	**Probable Oligomer**	**Calculated Mw [Da]**	**AUC-SE Mw [Da]**
No additional salt	α_3	200,739.4	199,849
No salt, Broful02728	$(\alpha_3)_8$+12xSBP	1,729,040.0	1,765,370
150 mM KCl, Broful02728	$(\alpha_3)_8$+12xSBP	1,729,040.0	1,727,007

The table shows the conditions used in the AUC-SE experiments (Figure 3.29). The calculated and experimental molecular masses assume a trimer or a 24mer *Bf*HDH-Broful02728 complex. The molecular mass is close to the calculated mass of 8x*Bf*HDH trimers and 12xBroful02728 complex (represented as $(\alpha_3)_8$+12xSBP). Mw is an abbreviation for molecular weight, SBP for small binding partner (here Broful02728).

Analytical ultracentrifugation sedimentation equilibrium (AUC-SE) analyses for *Bf*HDH samples either without salt (KCl) but including Broful02728 or with both salt and Broful02728 yielded nearly identical results (Fig 3.29 a and b) whereas *Bf*HDH alone without additional KCl clearly differed (Fig 3.29 c). For a *Bf*HDH sample with no additional salt (in 25 mM HEPES/KOH pH 7.5) but containing Broful02728, AUC-SE measurements yielded a molecular mass of 1,765.4 kDa. The closest molecular mass of 1,729.0 kDa can be calculated for a 24mer *Bf*HDH-Broful02728 complex (a complex of 8x *Bf*HDH trimers and 12x Broful02728-6xCHis). Similarly, the molecular mass for the *Bf*HDH sample with 150 mM KCl and Broful02728 was 1,727.0 kDa which is even closer to the calculated mass of the 24mer *Bf*HDH-Broful02728 complex.

As already mentioned from AUC-SV experiments, *Bf*HDH exists as trimers only when no additional salt or no Broful02728 is present. The AUC-SE experiments result in a molecular mass of 199.9 kDa which is very close to the calculated mass of 200.7 kDa (Fig 3.29 c and Table 3.4). AUC-SE experiments for *Bf*HDH in the presence of salt (50 mM, 150 mM and 300 mM KCl) but omitting its small binding partner did not yield meaningful results using the same model (discrete, non-interacting species) for fitting (data not shown).

The size exclusion chromatogram (SEC) of *Ks*HDH and *Bf*HDH and the molecular mass distribution obtained by multi-angle static light scattering (MALS) (section 2.2.5.3) are shown in figure 3.30. The salt concentration used in the experiment was 150 mM KCl. The chromatograms for *Ks*HDH and *Bf*HDH without their small binding partners were identical, showing two peaks at elution volumes of ~11 mL and ~15.8 mL. For *Bf*HDH a molecular mass of 2,022.0±179.9 kDa was obtained by MALS for the first peak and 217.4±19.2 kDa for the second peak. MALS analyses of the corresponding peaks for *Ks*HDH resulted in

molecular masses of 1,628.0±103.0 kDa and 121.3±7.6 kDa, respectively. In the presence of the respective small binding partners (Kustc1130 or Broful02728), however, the chromatograms of *Ks*HDH and *Bf*HDH looked different. In the presence of Kustc1130, the *Ks*HDH size exclusion chromatogram showed three peaks. Again the first peak was the largest but slightly shifted to 11.3 mL with a determined molecular mass of 1,638.0±162.7 kDa. A second new peak appeared at 15.1 mL with a molecular mass of 198.6±19.6 kDa, however, the peak at 15.8 mL can still be seen whose molecular mass was determined to be 176.1±17.4 kDa. The first peak for *Bf*HDH, however, was prominently shifted from 10.9 mL to 11.7 mL in presence of Broful02728. The first peak continued as a broad prominent shoulder with a maximum at around 13.7 mL. Contrary to *Bf*HDH alone, the peak at around 15.8 mL was absent in the presence of Broful02728. A prominent peak at ~19.3 mL was present in both *Ks*HDH and *Bf*HDH SEC-MALS runs with their respective small binding partner proteins. MALS analyses of these peaks resulted in molecular masses of ~10 kDa matching the mass of the small proteins (Kustc1130 or Broful02728).

The results from AUC-SV, AUC-SE and SEC-MALS for *Bf*HDH (and for *Ks*HDH in case of SEC-MALS) with and without their respective small binding partners were corroborated by negative stain transmission electron micrographs (negative stain TEM) (Fig 3.31). Uranyl acetate (pH 4.5) was applied to achieve negative staining in all cases. Both *Ks*HDH and *Bf*HDH at low ionic strength existed preferably as trimers (Fig 3.31 a) as it had also been shown by AUC-SV and –SE experiments for *Bf*HDH. With high concentration of salt (300 mM KCl), as expected, both *Ks*HDH and *Bf*HDH existed in higher oligomeric forms (24mers and 30mers) with a small amount of trimers present in addition (Fig 3.31 b). The higher oligomeric forms are the dominant species, however, a difference between *Ks*HDH and *Bf*HDH high salt conditions can be seen. In *Bf*HDH, 30mer assemblies contribute significant proportions while in *Ks*HDH they represent a minor population. Conversely, *Ks*HDH possesses 24mer assemblies in a significantly larger fraction than others while in *Bf*HDH both 24mer and 30mer are represented equally (Fig 3.31 b). With approximately three- to six-fold excess of their respective small binding proteins, both *Bf*HDH and *Ks*HDH form exclusively 24mer assemblies (Fig 3.31 c). However, in the case of *Bf*HDH a fraction of other states can be seen which mainly include dimers $(\alpha_3)_2$, trimers $(\alpha_3)_3$ and also probably tetramers $(\alpha_3)_4$ of HDH trimers (Fig 3.31 c).

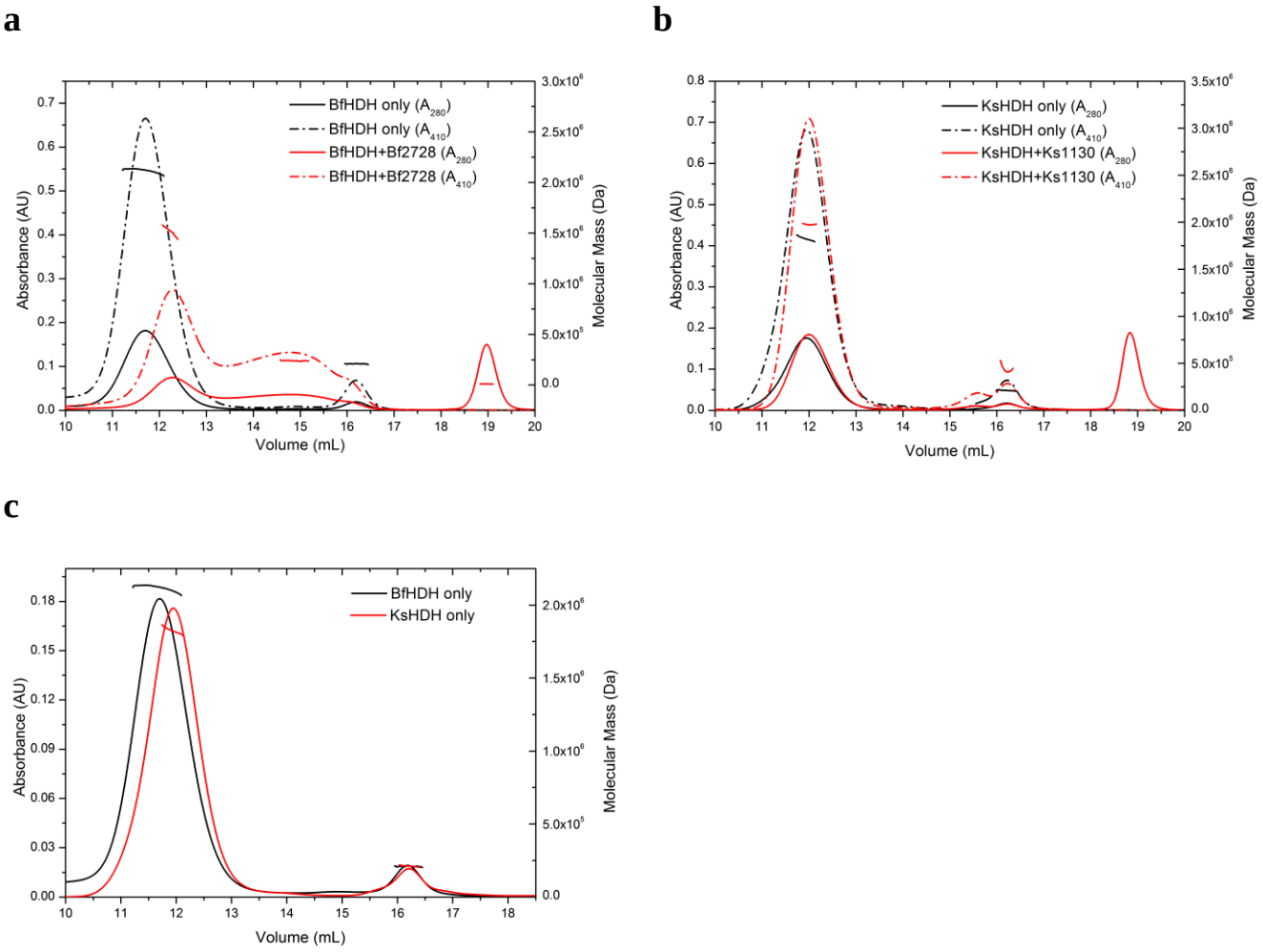

Figure 3.30 Analytical Size Exclusion Chromatograms and Molar Mass Distributions of *Bf*HDH and *Ks*HDH alone and with their Binding Partners
Approximately 150-200 µg of each samples were applied on a Superose 6 (10/300 Increase) gel filtration column (GE Healthcare, Uppsala, Sweden) at room temperature in a buffer containing 150 mM KCl, 50 mM HEPES/KOH, pH 7.5. The absorbance traces at 280 nm and 410 nm as well as the molar mass distribution determined by multi-angle static light scattering (MALS) are indicated. **a)** *Bf*HDH alone (black curves) and with its binding partner Broful02728 (indicated as Bf2728) in (red curves). **b)** *Ks*HDH alone (black curves) and with its binding partner Kustc1130 (indicated as Ks1130; red curves. **c)** Comparison of gel filtration elution profiles of *Bf*HDH (black curves) and *Ks*HDH (red curves) without their binding partners.

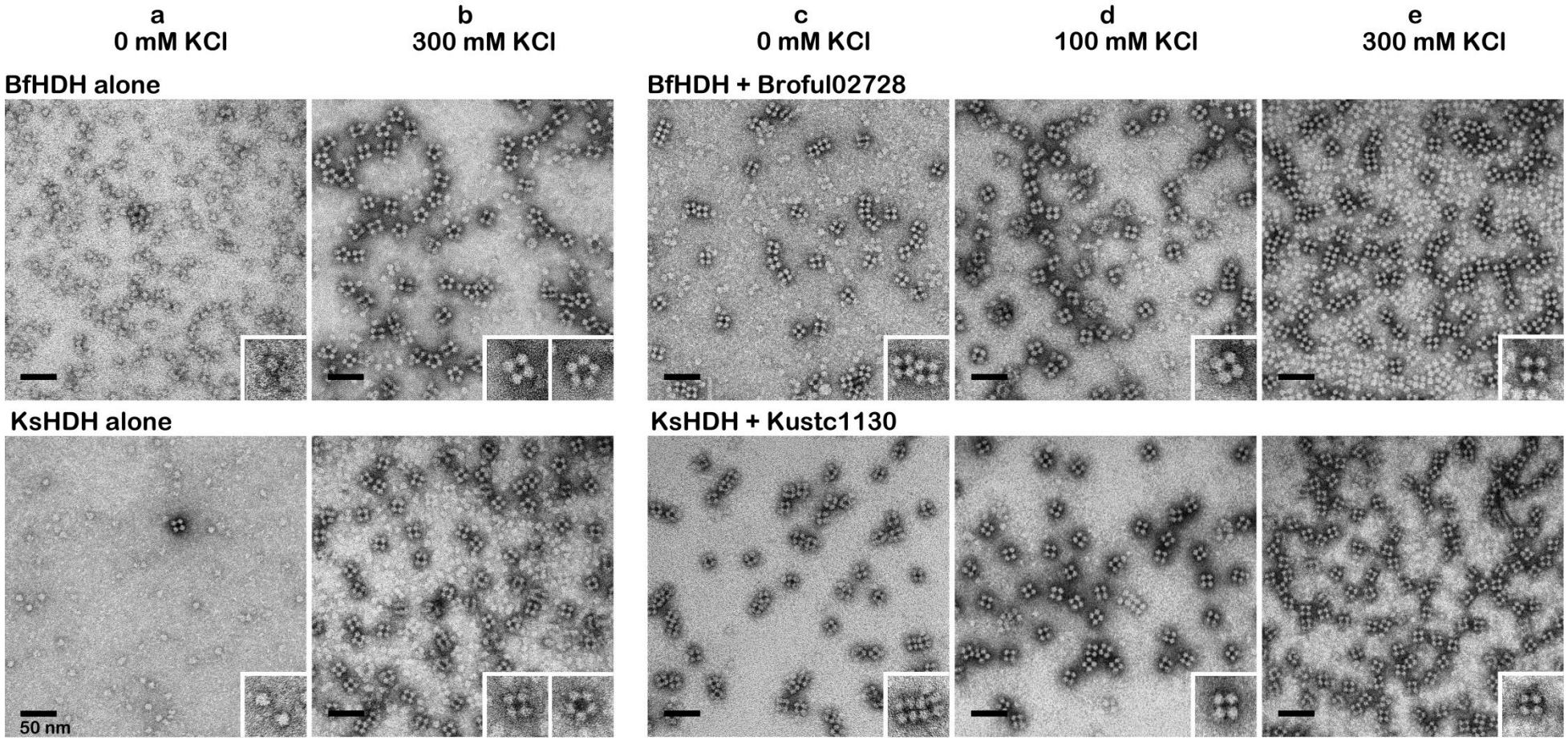

Figure 3.31 Negative Stain Transmission Electron Microscopy (TEM) Images of *Bf*HDH and *Ks*HDH in Different Conditions
The effect of ionic strength (from KCl in 25 mM HEPES/KOH, pH 7.5) and the presence of small binding partner (Broful02728 and Kustc1130) at different ionic strengths on the oligomerization of *Bf*HDH and *Ks*HDH were compared. *Bf*HDH or *Ks*HDH solutions were prepared with a final A_{280}^{1cm} of 1. The small binding partners were used up to 3-4 µM. Each black bar represents a length of 50 nm. The insets represent the oligomeric states found in each condition. The particles showing four-fold symmetry represent 24mers and the ones showing five-fold symmetry represent 30mers. **a)** Low ionic strength conditions (only 25 mM HEPES/KOH pH 7.5) showing mostly trimers. **b)** High ionic strength conditions (300 mM KCl) showing both 24mer and 30mer. **c)** Low ionic strength conditions (only 25 mM HEPES/KOH pH 7.5) with small binding partner. **d)** With medium ionic strength (100 mM KCl and 25 mM HEPES/KOH pH 7.5) and small binding partner **e)** High ionic strength (300 mM and 25 mM HEPES/KOH pH 7.5) with small binding partner**.** In column **c)**, **d)** and **e)** only 24mer assemblies can be observed as higher oligomers. For *Bf*HDH few dimers of trimers $(\alpha_3)_2$ and trimers of trimers $(\alpha_3)_2$ can also be seen probably representing intermediates between HDH trimers and 24mers. Sample preparation, image acquisition and analysis were kindly performed by Ulrike Mersdorf.

3.2.11 Biochemical Characterization

Hydrazine oxidation activities of *Bf*HDH were determined at different ionic strengths of various salts namely KCl, K_2SO_4 and potassium phosphate (K_2HPO_4/ KH_2PO_4; KPi) and are shown in Figure 3.32 a. The ionic strengths of KCl, K_2SO_4 and KPi (pH 7.2) are calculated as c, 3c and 4c, respectively, where c is the molar concentration of each salt. Figure 3.32 b shows 90° scattering intensities at a wavelength of 305 nm for the corresponding ionic strengths and ion types. Looking at the dependence of the *Bf*HDH activity as a function of the ionic strengths of different salts, a sigmoidal curve was observed in all cases. From 30-50 mM onwards *Bf*HDH activity started increasing and reached a plateau around 150-200 mM for KCl and KPi and around 100-120 mM for K_2SO_4. Similarly, the 90° scattering intensities indicating the degree of oligomerization of *Bf*HDH trimers also showed a sigmoidal trend when looking closely. Here, the saturation roughly started at an ionic strength of 120-150 mM. As mentioned earlier, AUC-SV experiments with 150 mM and 300 mM KCl yielded nearly similar amounts of higher oligomers (88 % and 94 %, respectively) and also dynamic light scattering (DLS) analyses showed only one peak corresponding to higher oligomers at ionic strengths above 100-150 mM of the three salts (data not shown). Therefore, the rising flanks of the curves from the 90° scattering intensities data are at the same position as those of the *Bf*HDH activity data.

It is now evident from the biophysical characterization of *Bf*HDH and *Ks*HDH that both of these homologues possess different oligomeric states which depend on the ionic strength of the medium as well as the presence of the small binding partner (Kustc1130 or Broful02728). Figures 3.32 c and d show the comparative effects of salt (KCl) and the small protein on the hydrazine oxidation activity of *Ks*HDH and *Bf*HDH. At low ionic strength the activity of *Bf*HDH remained lowest but when the small binding partner was added it was increased to almost twice (Fig 3.32 c). When increasing only the ionic strength, the activity also increased up to 100 mM after which it reached a plateau. However, when Broful02728 was present, the activity also increased further up to 100 mM KCl after which it started decreasing and reached the same level as with 300 mM KCl (Fig 3.32 a). The trend described for *Bf*HDH looked the same for *Ks*HDH. However, the activity differences at 0, 50 and 100 mM KCl with and without Kustc1130 appeared less significant. Around 150 mM KCl the activity was highest in the presence of Kustc1130, which was also only 1.3 times higher than at the corresponding KCl concentration without Kustc1130. At an ionic strength higher than 150 mM in the presence of Kustc1130, the activity decreased to reach an activity level similar to that at high

salt (300 mM KCl) only (Figure 3.32 b). The effects of ionic strength and the presence of the small protein in case of *Ks*HDH are much less pronounced when compared with *Bf*HDH.

The Michaelis-Menten kinetic parameters of *Bf*HDH also show that the catalytic turnover rate (k_{cat}) was highest in presence of Broful02728 at 100 mM KCl which was 3.5 times higher than the rate with no salt and without Broful02728 (Table 3.5). The catalytic efficiency (k_{cat}/K_M) also increased at high salt and further at 100 mM KCl together with Broful02728. However, the magnitude of increase between lowest and highest catalytic efficiency is 2.3 times which indicates that the increase in catalytic rate and efficiency are not linearly proportional. Interestingly, the apparent K_M values increased in presence of either high salt (300 mM) or medium salt (100 mM) and Broful02728.

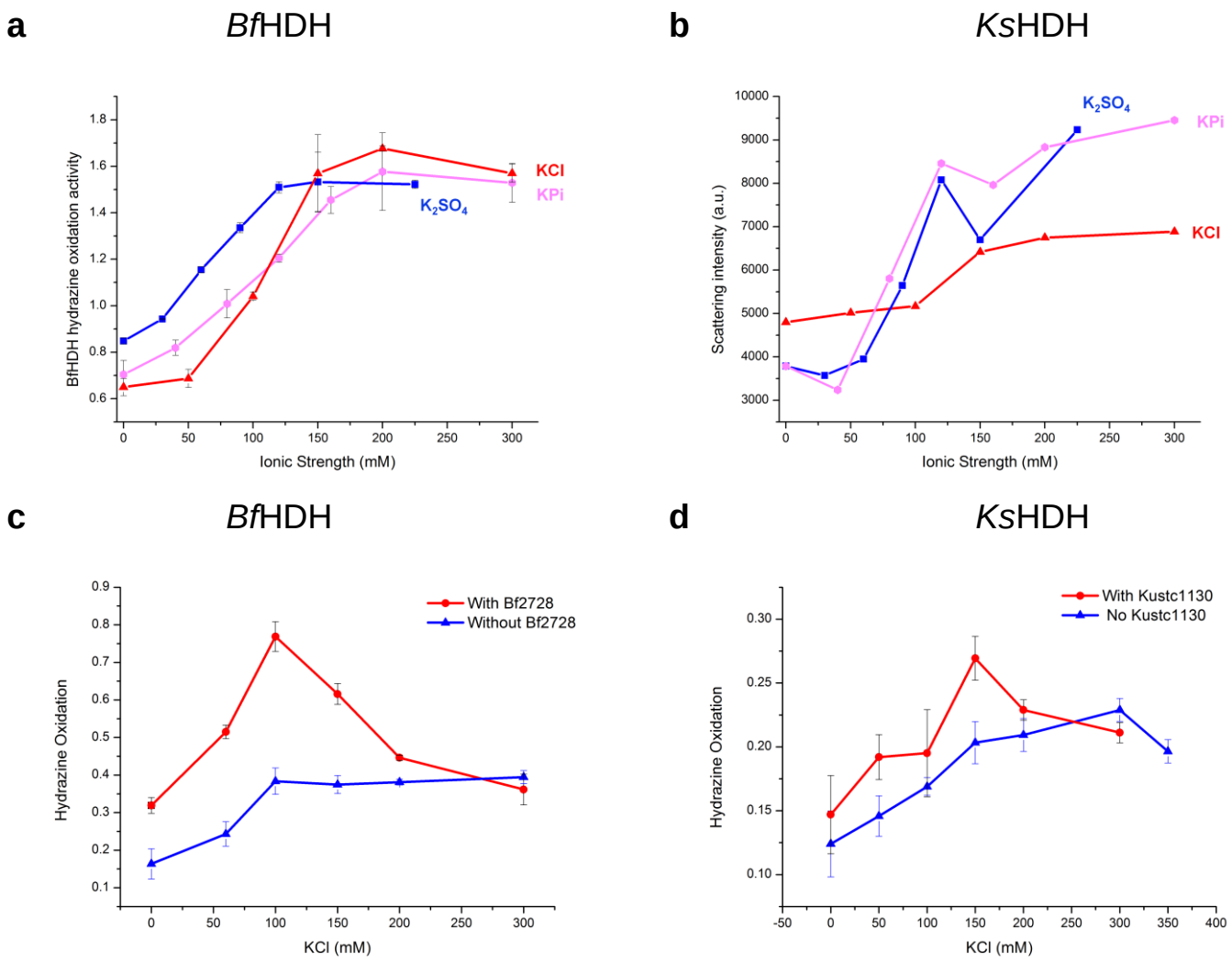

Figure 3.32 Correlation of HDH Activity, Oligomerization and Ionic Strength as well as the Effect of Small Binding Partner on HDH Activity

a) Effect of increasing ionic strengths of different types of salts on *Bf*HDH hydrazine oxidation activity. 10 µL *Bf*HDH stock (A_{280}^{1cm}=3) and bovine cyt c used as redox partner (~50 µM final concentration) were supplemented with an appropriate amount of the respective salt stock solution and diluted in buffer (25 mM HEPES/KOH pH 7.5) to reach a final reaction volume of 600 µL. The reaction was started by adding 100 µM of N_2H_4 (hydrochloride salt, pH=7) and the reduction of bovine cyt c was followed at 550 nm ($\Delta\varepsilon$=19,600 $M^{-1}cm^{-1}$) at 37 °C.

b) 90° scattering at 305 nm. The scattering signal correlates with the amount of higher oligomers present in the *Bf*HDH solution. The final reaction mixture (200 µL) was prepared in a buffer of 25 mM HEPES/KOH pH 7.5 supplemented with *Bf*HDH (final A_{280}^{1cm}=0.2), 100 µM of N_2H_4 (hydrochloride salt, pH=7) and an appropriate amount of the salt type in question. For figures **a** and **b,** the x-axis is normalized to ionic strengths of KCl, K_2SO_4 and KPi (K_2HPO_4/ KH_2PO_4). The ionic strengths for KCl, K_2SO_4 and KPi are c, 3c and 4c; where c is the molar concentration. The temperature was 37 °C

c) & d) show hydrazine oxidation activities of *Bf*HDH and *Ks*HDH, respectively, depending on KCl concentration and the presence of their respective binding partners (Broful02728 and Kustc1130). ~50 µM bovine cyt c was used as redox partner. 10 µL of each *Bf*HDH (stock A_{280}^{1cm}=0.1) and *Ks*HDH (stock A_{280}^{1cm}=0.03) were used in a final volume of 600 µL. The reaction was started by adding 100 µM of N_2H_4 (hydrochloride salt, pH=7) and the reduction of bovine cyt c was followed at 550 nm ($\Delta\varepsilon$=19,600 $M^{-1}cm^{-1}$) at 37 °C. The red curve shows *Bf*HDH activity from assays including the small protein binding partner and blue curve without it.

Table 3.5 Michaelis-Menten Kinetics of *Bf*HDH and *Ks*HDH under Different Conditions

Condition	V_{max} (µmol min^{-1} mg^{-1})	K_M (µM)	k_{cat} (s^{-1})	k_{cat}/K_M ($\mu M^{-1}s^{-1}$)
***Bf*HDH no salt**	0..92±0.03	49.52±6.57	1.03	0.021
***Bf*HDH + 300mM KCl**	2.26±0.03	73.04±11.05	2.54	0.035
***Bf*HDH + Bf2728 + 100 mM KCl**	3.15±0.03	71.13±10.56	3.50	0.049

1 µg of total *Bf*HDH enzyme was used with ~50 µM bovine cyt c as redox partner. The reaction was started by adding an appropriate amount of hydrazine (hydrochloride salt, pH=7) in a final volume of 600 µL made up by buffer (25 mM HEPES/KOH, pH 7.5). The reduction of bovine cyt c was followed at 550 nm ($\Delta\varepsilon$=19,600 $M^{-1}cm^{-1}$) at 37 °C.

3.2.12 *Bf*HDH Inhibition by Hydroxylamine and Organohydrazines

When incubated with 20 mM of methylhydrazine, phenylhydrazine or hydroxyethyl-hydrazine for over 30 min followed by complete removal of the excess compound by exhaustive buffer exchange, *Bf*HDH was rendered completely inactive (Fig 3.33 c).

Simultaneously, another aliquot of *Bf*HDH was also incubated with 20 mM hydroxylamine which, when present in the assay solution, inhibited the hydrazine oxidation activity of *Bf*HDH. After removal of hydroxylamine by buffer exchange, however, the enzymatic activity of *Bf*HDH could be rescued.

The UV-Vis spectra showed that hydroxyethylhydrazine partially reduced as-isolated (oxidized) *Bf*HDH, as does hydrazine (Fig 3.33 a). Incubation of as-isolated *Bf*HDH with hydroxylamine and methylhydrazine led to similar UV-Vis spectroscopic features. In both cases a small α-band at ~555 nm and a slight broadening of the Soret peak around 425 nm could be observed (Fig 3.33 b). There was no effect of phenylhydrazine on the UV-Vis spectra (Fig 3.33 b).

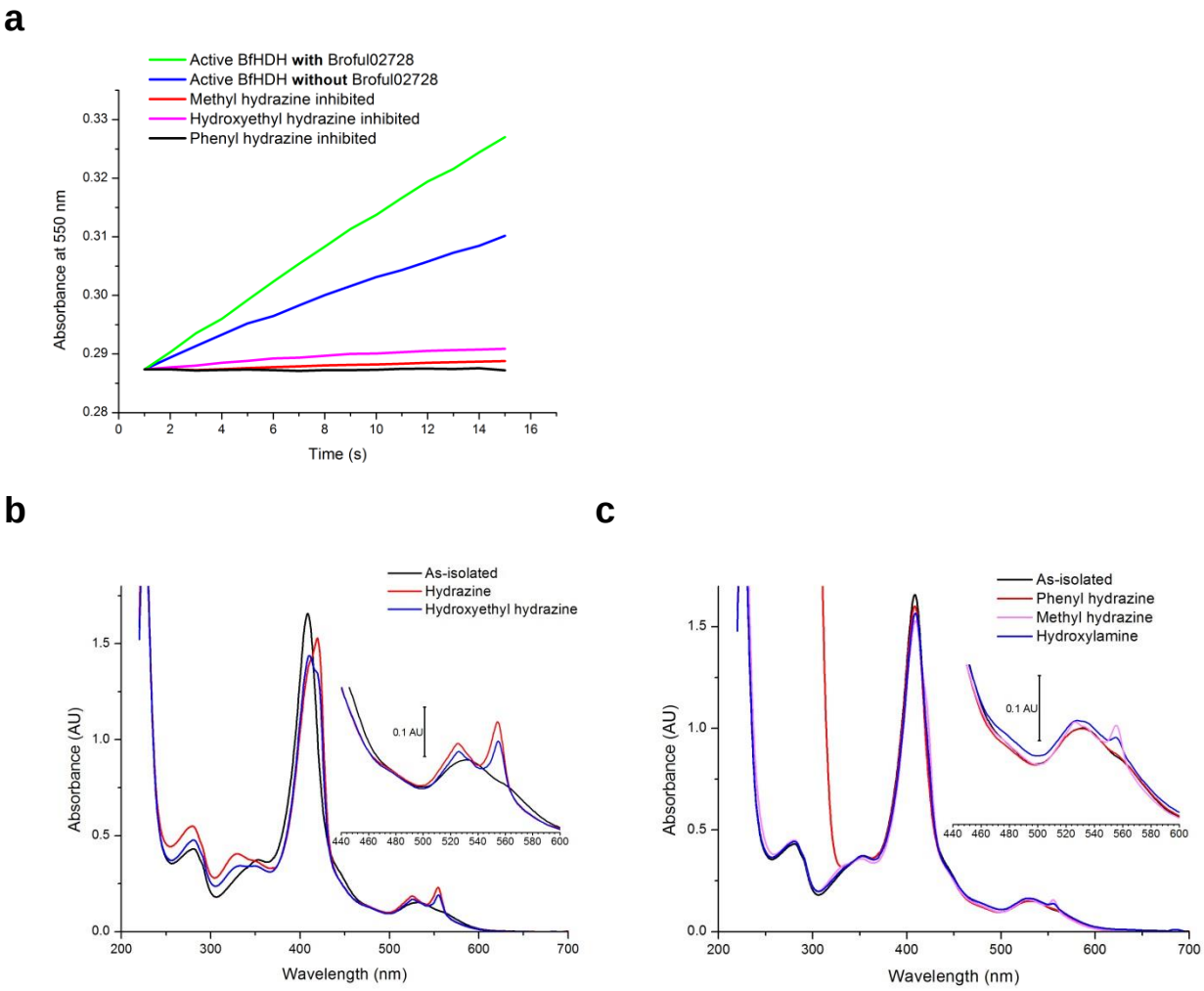

Figure 3.33 Inhibition of *Bf*HDH Activity and UV-Vis Spectra with Hydrazine Homologues
a) *Bf*HDH hydrazine oxidation activity is shown as the increase of absorption at 550 nm from reduced bovine cyt c ($\Delta\varepsilon$=19,600 $M^{-1}cm^{-1}$) at 25 °C. For activity inhibition, 5 µL *Bf*HDH stock (A_{280}^{1cm}=30, ~100 µM) was mixed with 20 mM methyl hydrazine, phenyl hydrazine or hydroxyethyl hydrazine and incubated for 30 min at room temperature. After that, the buffer was exchanged to completely remove excess methylhydrazine. A final stock at A_{280}^{1cm}=0.1 of both active and inactive enzymes were used for assays in 600 µL reaction mixture. The reaction was started by adding 100 µM hydrazine (hydrochloride, pH 7.0). The rate for inactive enzyme was close to zero for methylhydrazine and phenylhydrazine inhibited *Bf*HDH, however, some residual activity remained in hydroxyethylhydrazine inhibited enzyme.
b) and **c)** UV-Vis spectra of *Bf*HDH in the as-isolated state (oxidized) alone and with hydrazine and its homologues. Samples were prepared by mixing 75 µL of *Bf*HDH stock (A_{280}^{1cm}= 0.8) with 75 µL of buffer (25 mM HEPES/KOH pH 7.5) containing 20 mM of hydrazine or its homologues.
b) UV-Vis spectra with hydrazine (red), hydroxyethylhydrazine (blue) and as-isolated *Bf*HDH (black).
c) UV-Vis spectra with methylhydrazine (pink), phenylhydrazine (red), and hydroxylamine (blue) and as-isolated *Bf*HDH (black). Note that hydroxyethylhydrazine and hydrazine partially reduce the enzyme as evident by the appearance of α- and β-bands and a partial red shift of the Soret band (blue and green curves). Methyl hydrazine (red) also seems to reduce the enzyme but to a smaller extent. This feature (even less prominent) was also visible when incubated with hydroxylamine which reversibly inhibits *Bf*HDH (not shown) (Maalcke 2016).

3.3 Discussion

3.3.1 What is the Physiological Oligomeric State of HDH?

Through various biophysical methods, this study showed that both *Ks*HDH and *Bf*HDH can exist in multiple oligomeric states in solution such as covalently linked trimers (α_3), octamers ($(\alpha_3)_8$=24mers) and even decamers thereof ($(\alpha_3)_{10}$=30mers). Most importantly, the relative abundances of the mentioned oligomeric states were shown to be governed by at least two factors namely ionic strength and the presence of a small protein binding partner (SBP).

Negative stain electron micrographs (EM) and also AUC-SV and –SE analyses (in case of *Bf*HDH) showed that both *Bf*HDH and *Ks*HDH prefer to remain in their trimeric forms at lower ionic strengths. With increasing ionic strength, however, they started to form higher oligomers (both 24mers and 30mers). Increasing ionic strength of the medium is known to promote hydrophobic interactions (Zangi 2007). Indeed, the 24mer X-ray as well as cryo-EM structures confirmed that the interactions at a given trimer-trimer junction are hydrophobic in nature. Moreover, the fact that *Ks*HDH 24mer assemblies were obtained at high ionic strengths for structure determination by cryo-EM confirms this argument.

The other factor which promotes the oligomerization of both *Bf*HDH and *Ks*HDH is the presence of their small binding partners (Broful02728 and Kustc1130, respectively). Interestingly, in presence of the SBP oligomerization yields only 24mer assemblies for both HDH homologues as indicated by both negative stain EM and SEC-MALS analyses. In case of *Bf*HDH other smaller oligomers such as $(\alpha_3)_2$ and $(\alpha_3)_4$ were also observed which might represent intermediates between HDH trimers and 24mers. Moreover, addition of the respective small protein binding partners to both *Bf*HDH and *Ks*HDH resulted in nearly complete oligomerization to 24mer assemblies independent of ionic strength (0-300 mM KCl, 25 mM HEPES/KOH, pH 7.5).

Moreover, molecular mass determination by AUC-SE of *Bf*HDH in presence of its binding partner at low (0 mM KCl) and high (150 mM KCl) ionic strengths resulted in masses which correspond to the 24mer assembly with twelve molecules of SBP (HDH 24mer-12xSBP). This observation indicates that it is highly likely that a complex of a *Ks*HDH 24mer with 12 molecules of Kustc1130 as found in the X-ray structure might indeed represent the oligomeric assembly in solution. Furthermore, AUC-SE data obtained from high ionic strength

conditions in the absence of the small binding protein could not be appropriately fitted, most probably due to the presence of multiple oligomers.

In addition, the comparison of size exclusion chromatograms of as-isolated *Bf*HDH and *Ks*HDH at high ionic strength (150 mM KCl, 50 mM HEPES) showed differences in the positions of the peak corresponding to the higher oligomeric forms. This peak eluted later for *Ks*HDH than for *Bf*HDH indicating a lower molecular weight species for *Ks*HDH than for *Bf*HDH. Further addition of SBP to *Ks*HDH caused a very small change in the peak position compared to that of *Bf*HDH. These observations indicate that a large fraction of as-isolated *Ks*HDH exists as 24mers (bound to 12 molecules of Kustc1130) whereas *Bf*HDH predominantly forms 30mers under high ionic strength conditions. Indeed, the particles observed in negative stain-EM images were dominated by 30mers in case of *Bf*HDH whereas 24mers constituted the major species for *Ks*HDH. The difference in the oligomeric composition between *Ks*HDH and *Bf*HDH can surely be accounted for the presence of SBP in native *Ks*HDH preparations, whereas *Bf*HDH lacks it.

Altogether, these observations lead us to the following questions: What is the physiological oligomeric state of HDH? What is the functional significance of multiple oligomeric states of HDH and are they interconvertible under physiological conditions? Since *Ks*HDH was co-purified with Kustc1130 from *K. stuttgartiensis* as shown by SDS-PAGE followed by Edman's N-terminal sequencing and reconfirmed by the X-ray structure of the 24mer assembly, we can conclude that Kustc1130 is probably expressed in stoichiometric amounts compared to *Ks*HDH. This idea is further supported by metatranscriptomic data from *K. stuttgartiensis* (Kartal 2011). These data indicate that Kustc1130 is indeed highly expressed with an mRNA coverage of 88.7 compared to the average coverage of 6.9 of all genes (Fig 3.34). Moreover, the presence of an N-terminal signal sequence in Kustc1130 further indicates its localization in the anammoxosome where *Ks*HDH is also located as it has been shown by immunogold-labelling EM (Almeida 2015). Moreover, *Bf*HDH in the presence of its homologous SBP turned out to be the most active oligomeric state in enzymatic assays (discussed in section 3.3.6). Altogether, it can therefore be concluded that the HDH 24mer-12xSBP complex is likely the most physiologically relevant state of HDH.

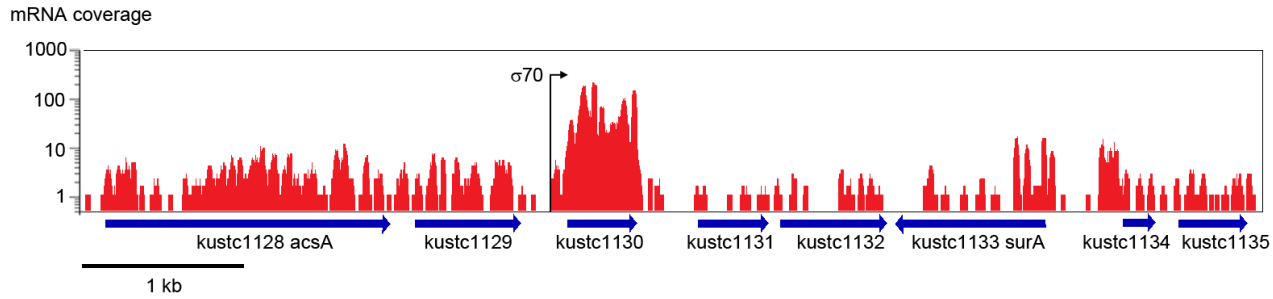

Figure 3.34 Transcription patterns of *K. stuttgartiensis* kustc1130 and its neighboring genes. mRNA reads from a metatranscriptome dataset (Gene expression omnibus GSE15408, SRR037687) were mapped against the *K. stuttgartiensis* reference genome. The graph shows the mRNA read coverage plotted on a logarithmic scale against the length of the genomic DNA and was prepared using the Integrative Genomics Viewer (Thorvaldsdottir 2013). A putative σ70 promotor site predicted using BPROM (Solovyev 2011) is indicated by a bent arrow. It can be seen that kustc1130 is highly expressed compared to the transcription levels of the neighboring genes. The average mRNA coverage (Kartal 2011) of the kustc1130 ORF is 88.7 which is about half of *Ks*HDH (188.7) and still above *Ks*HOX (55.9) and the average from all genes (6.9).

However, it is still questionable whether the HDH 24mer-12xSBP complex is the sole oligomeric state of HDH which could exist under physiological conditions. The answer would dependent upon the presence or absence of SBP in the anammoxosome along with HDH. If the expression of SBP is regulated *i.e.* non-constitutive, it might be possible that there are conditions when SBP is not expressed. In those supposed conditions, HDH might exist as trimers or as a mixture of both 24mers and 30mers depending upon the ionic strength of the environment. It is more likely that it would primarily exist as a mixture of 24mers and 30mers, since ionic strength inside bacterial cells is usually more than >100 mM (Spitzer 2011), though the ionic strength inside the anammoxosome is not known yet. Therefore, conceptually it might be possible that HDH interconverts between different oligomeric states given that the expression of SBP is regulated. The type of promotor for SBP could give hints about its expression. The implications of various oligomeric states of HDH on its activity are discussed in section 3.3.6.

3.3.2 Structures of *Ks*HDH Oligomers

3.3.2.1 The *Ks*HDH X-ray structure shows an HDH 24mer with 12 molecules of Kustc1130

In fact, the first indication that *Ks*HDH might possess a small protein binding partner (SBP) came from X-ray crystallographic data. The asymmetric unit of crystals obtained from *Ks*HDH purified from the anammox bacterium *Kuenenia stuttgartiensis* contains an HDH 24mer. Additional electron density, however, indicated the presence of twelve small non-heme protein molecules being bound to *Ks*HDH which were later assigned to Kustc1130. The

cube-like *Ks*HDH 24mer-12xSBP complex is unique in its overall architecture. Maalcke *et al*. (2016) suspected that a conserved 15 amino acids spanning stretch that is present near the C-terminus of *Ks*HDH (but absent in *Ks*HOX) might be responsible for HDH oligomerization. However, the current *Ks*HDH 24mer-12xSBP X-ray structure shows that interactions are formed by HDH trimers themselves which are only mediated by hydrophobic contacts between residues from helices α3, the loop connecting helices α3 and α4 as well as the heme 1 cofactors.

Furthermore, the arrangement of *Ks*HDH trimers with bound Kustc1130 molecules described in the 24mer X-ray structure might indeed represent the assembly in solution. This can be supported by the two following observations. Firstly, the 24mer cryo-EM structure obtained at high ionic strength (300 mM KCl, 25 mM HEPES pH 7.5) also shows exactly the same assembly of *Ks*HDH trimers as observed in the 24mer X-ray structure except for the absence of Kustc1130. Secondly, as discussed earlier, the molecular mass determined by AUC-SE of *Bf*HDH in presence of its small binding partner resulted in a value close to a *Bf*HDH 24mer-12x SBP complex.

However, no EM density for the small binding partner (Kustc1130) could be observed in both 24mer and 30mer *Ks*HDH cryo-EM structures. The presence of Kustc1130 was at least expected in case of the 24mer. From the biophysical characterization of both *Bf*HDH and *Ks*HDH, it is evident that even at high ionic strength (300 mM KCl, 25 mM HEPES/KOH pH 7.5) the small binding partner is able to bind HDH. In these experiments, however, the heterologously expressed small protein partner was additionally added in 5-10 fold excess which might have forced the equilibrium towards HDH 24mer-12xSBP assemblies. Contrarily, in cryo-EM grid preparation a natively purified *Ks*HDH sample was used. As evident from SDS-PAGE analysis this material contained a lower amount of Kustc1130 compared to HDH, presumably because of a partial loss of Kustc1130 during the purification from *K. stuttgartiensis* cells. Moreover, it might also be possible that Kustc1130 was lost during sample preparation for cryo-EM analysis. Therefore, probably only very few or none of the 24mer *Ks*HDH particles on the cryo-EM grid had Kustc1130 bound. Moreover, the occupancy of Kustc1130 in the X-ray structure was also partially poor for some of the total 12 molecules. In order to see Kustc1130 in cryo-EM 3D reconstructions (and possibly to obtain higher occupancies in the X-ray structure) it might therefore be necessary to supplement natively purified *Ks*HDH with recombinant Kustc1130 protein. This would be also beneficial

in terms of additionally promoting HDH oligomerization without the need of high ionic strength.

3.3.2.2 Differences between 24mer and 30mer Structures: Implications on Redox Partner Binding

To assess the differences between the two assemblies of *Ks*HDH (24mer and 30mer) we also determined the cryo-EM structure of the *Ks*HDH 30mer. In this structure ten HDH trimers are arranged in a pentagonal prism consisting of two pentagonal rings of five *Ks*HDH trimers sandwiched together. This geometrical change also results in altered molecular contacts at the interfaces of the HDH trimers compared to the cubic 24mer assembly. However, only the interactions between trimers within each pentagonal ring differ whereas those between trimers being located in the two distinct pentagonal rings are very similar to the ones between HDH trimers in the 24mer assembly. An apparent reason for this difference is the requirement to accommodate an extra trimer within each pentagonal ring which confines the space between each pair of trimers by 5-10 Å especially around heme 1.

Heme 1 has been supposed as a potential electron release site in other octaheme c-type cytochromes such as *Ne*HAO (Igarashi 1997) and hence a binding site for physiological redox partner proteins. In the HDH 24mer-12xSBP complex, which most likely represents the physiologically active oligomeric state, the surface provided by HDH near heme 1 including an additional surface formed by bound SBP might provide a docking site for a redox partner. Similar considerations have been drawn for the small, non-heme protein Ne1300 which forms a heterohexameric complex with *Ne*HAO (Cedervall 2013; Maalcke 2014). Molecular simulations indicated that Ne1300 could provide a docking platform for the tetraheme cytochrome c_{554}, the redox partner of *Ne*HAO (Cedervall 2013).

In case of the HDH 30mer assembly, however, the surface properties in the vicinity of heme 1 might be altered due to the mentioned spatial confinement between HDH trimers within the pentagonal rings. This would possibly prevent interactions of HDH and SBP and affect the interactions between HDH and its redox partner leading to suboptimal electron transfer.

As shown by biophysical analyses, the addition of SBP to HDH drives the formation of 24mer assemblies *i.e.* HDH 24mer-12xSBP complexes, whereas HDH 30mers are not obtained. This might provide indirect evidence that the altered orientation of HDH trimers within the pentagonal rings of the 30mer might prevent binding of SBP between the HDH trimers close

to heme 1. The implications of the geometrical constrains on the overall activity of HDH are discussed in section 3.3.6.

3.3.2.3 The X-ray Structure of the *Ks*HDH Trimer

Although the overall 24mer and 30mer structures of *Ks*HDH are unique, each *Ks*HDH trimer as a building block of the higher oligomers shares nearly an identical overall architecture with known hydroxylamine oxidoreductase structures such as *Ks*HOX (PDB id: 4N4J; Maalcke 2014) and *Ne*HAO (Igarashi 1997; Cedervall 2013; Maalcke 2014).

*Ks*HDH also possesses an N1-domain which has also been described for *Ks*HOX but is absent in *Ne*HAO (Maalcke 2014). This N1 domain is proposed to contribute in stabilizing the trimeric assembly. The most contrasting and unique features of *Ks*HDH are the structures of its N- and C-terminal parts.

The primarily random-coiled N-terminus of *Ks*HDH runs through the tunnel towards its active site eventually interacting with the P460 heme as opposed to the N-terminus of *Ks*HOX which contains an α-helix and remains close to the surface of the structure. Although the N1 domains in both *Ks*HOX and *Ks*HDH are involved in stabilizing the trimer, the N-terminus of *Ks*HDH might fulfill additional functions such as influencing the redox potential of the active site heme or to steer selectivity of the active site tunnel for the entrance of the substrate. However, the latter possibility seems unlikely, since both nitric oxide and hydroxylamine (Maalcke 2016) as well as organohydrazines are possibly able to enter through the tunnel to bind to the P460 heme, eventually inhibiting its activity (section 3.3.5).

Although the last 19 residues at the C-terminus of *Ks*HDH could not be resolved in the present structure, the remaining C-terminal part interacts with the N-terminus of a neighboring subunit. In *Ks*HOX, however, the C-terminal part does not interact with the neighboring subunit but is rather folded back towards the base of the monomer. Therefore, interactions mediated by the C-terminal part of *Ks*HDH might additionally stabilize the trimeric assembly.

3.3.3 Heme Arrangement and Electron Transfer

A unique feature of HAO-like proteins is the characteristic arrangement of the hemes, optimized for efficient electron transfer, which is evolutionarily conserved between *Ne*HAO, *Ks*HOX and *Ks*HDH monomers and also trimers. The presented *Ks*HDH structure corroborates the expected heme arrangement in the *Ks*HDH monomer based on homology as well as electron paramagnetic resonance (EPR) studies performed by Maalcke *et al.* (2016). In addition, this study suggests that heme 7 and 8 in *Ks*HDH are magnetically coupled, which was not observed in *Ks*HOX and *Ne*HAO. The suspected reason given for that is a slight change in the relative orientations of the imidazole ring planes of the histidine residues serving as axial heme ligands to each other and to the *meso* positions of the porphyrin ring, which might in turn affect the redox potential of the heme. Indeed, the distal histidine of *Ks*HDH heme 7 (His454) and the proximal histidine of heme 8 (His346) are rotated by 8-15° with respect to that of *Ks*HOX and *Ne*HAO along the nearly perpendicular axis to the porphyrin ring plane (Fig 3.35). In addition, several subtle changes in the environment of these hemes might further alter redox potentials compared to *Ks*HOX and *Ne*HAO accounting for coupling of heme 7 and 8 in *Ks*HDH.

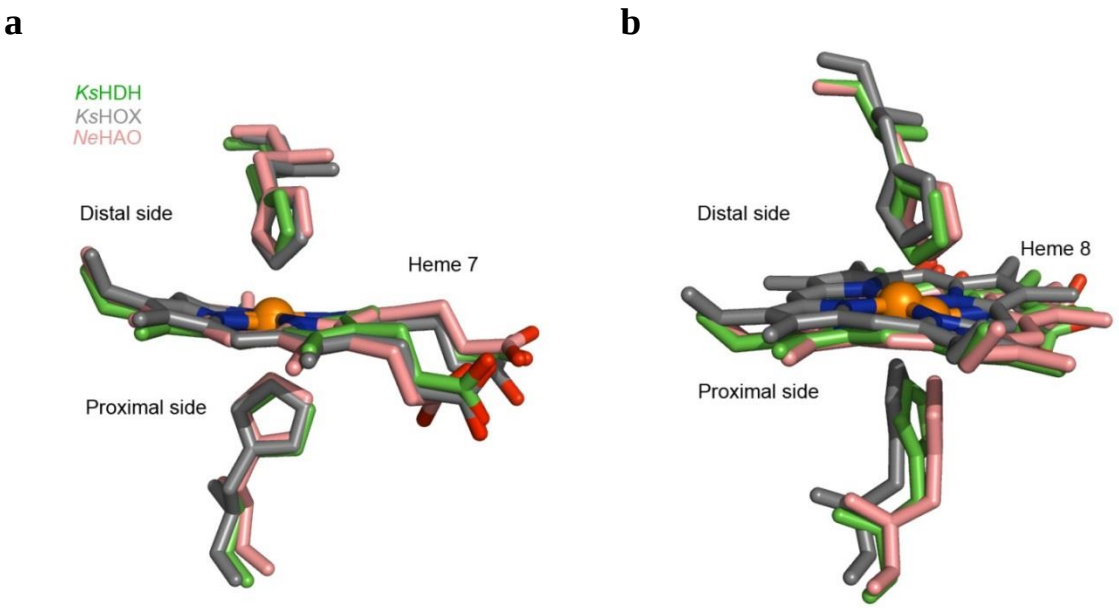

Figure 3.35 Imidazole Planes of the Distal and Proximal Histidine Ligands
The superposed heme cofactors including the axial histidine ligands are shown as stick models colored in green (*Ks*HDH), grey (*Ks*HOX) and salmon (*Ne*HAO).
a) The imidazole planes of the distal histidine ligands of *Ks*HDH heme 7 are rotated by 8-15° when compared to that of *Ks*HOX and *Ne*HAO.
b) Similarly, the proximal histidine ligand of *Ks*HDH heme 8 is rotated by 8-10° when compared to that of HAO and HOX. There are no changes in the orientations of the distal and proximal ligands of hemes 7 and 8 of *Ne*HAO and *Ks*HOX when compared to each other.

Generally, electron transfer (ET) between an electron donor and an acceptor site can either proceed by single-step quantum mechanical tunneling through space over short distances (<10 Å) or through multistep tunneling (so-called "electron hopping") between aromatic amino acids acting as high redox potential sites over long distances (> 20 Å) (Gray 2005). These aromatic amino acids including Trp, Tyr and His, temporarily form free radicals serving as electron hopping intermediates. However, in case of the *Ks*HDH monomer, all eight hemes including the penta-coordinated catalytic heme c and the seven *bis*-His ligated hemes are close enough (edge-to-edge distance <6 Å) to allow rapid electron transport through space.

Spectropotentiometric titrations of *Ne*HAO enabled the determination of redox potentials of its individual heme sites (Collins 1993). Later, the redox potentials of the hemes in *Ne*HAO were computationally simulated *ab initio* using continuum electrostatics calculations based on the *Ne*HAO crystal structure (Kurnikov 2005). This enabled the assignment of experimentally determined redox potentials to the individual heme sites of *Ne*HAO. A scheme of electron transfer within the *Ne*HAO trimer and electron release to a redox partner was proposed based on the redox potentials of the individual heme sites. According to this scheme, *Ne*HAO heme 2 is proposed to possess the highest redox potential. It would therefore act as electron sink and would probably stayed reduced during the entire catalytic cycle. The first two electrons generated from the four-electron oxidation of hydroxylamine at the active site heme P460 would pass through heme 6 and further flow *via* hemes 5 and 7 to hemes 3 and 8, respectively. At this stage, hemes 2, 3 and 8 are already reduced, therefore the next two electrons can only be transferred to hemes 3 and 8, which show similar redox potentials (Fig 3.36 a). Moreover, the significantly higher redox potential of heme 2 compared to the solvent exposed heme 1 was proposed to create an electrostatic lock. It was further proposed that the binding of the physiological redox partner cyt c_{554} to *Ne*HAO would desolvate the partially solvated heme 1 which would result in an increase of its redox potential by nearly 100 mV. In addition, the redox potential of heme 2 decreases when hemes 3 and 8 are reduced. Both desolvation of heme 1 and reduction of heme 2 would cause a decrease in the potential barrier between hemes 1 and 2, which would therefore result in a release of electrons to cyt c_{554} (Fig 3.36 b) (Arciero 1991).

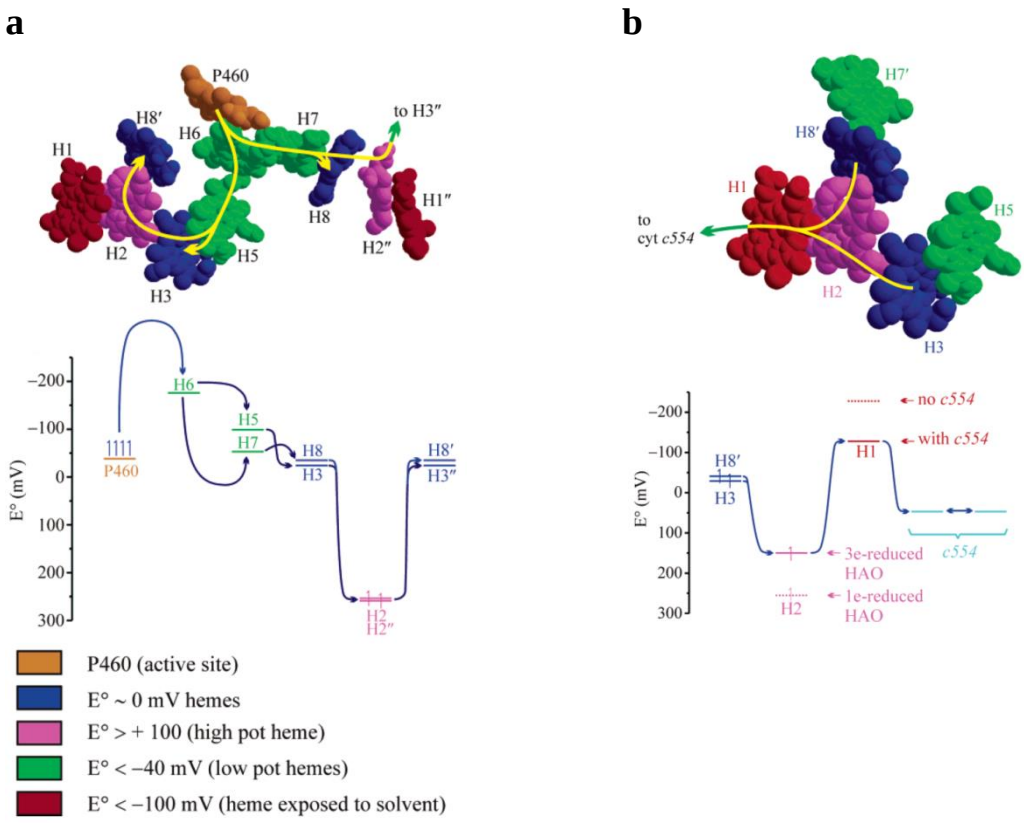

Figure 3.36 Model of the electron transfer in *Ne*HAO and to cytochrome c_{554}
a) Possible pathways for electrons extracted from the substrate at the P460 cofactor. The lower part shows the energy barriers to the electron flow in *Ne*HAO if only heme 2 is reduced. The hemes are color coded according to their redox potentials. **b)** Electron efflux pathway *via* hemes 2 and 1 to the tetraheme cytochrome c_{554} as electron acceptor. The lower part shows a redox potential diagram for the oxidation of reduced *Ne*HAO by cytochrome c_{554}. The potential of the solvent exposed heme 1 is expected to be increased by approximately 100 mV upon binding of cyt c_{554} to HAO, primarily due to its desolvation. The potential of heme 2 becomes more negative when hemes 3 and 8 are reduced, which further lowers the energy barrier for ET from heme 2 to heme 1. Figure adopted from (Kurnikov 2005).

There are subtle and also some prominent differences in the environments of the eight hemes and the mode of their mutual interactions in *Ks*HDH compared to those of *Ne*HAO, which might cause differences in the redox potentials between the heme sets of these proteins. Indeed, different ranges of redox potentials were reported namely -70 mV to -420 mV for *Ks*HDH (Maalcke 2016) and +288 mV to -412 mV (*vs.* SHE) for *Ne*HAO (Collins 1993). However, the effect of oligomerization of HDH on redox potential was not taken into account in those measurements.

Since oligomerization of *Ks*HDH modifies the environment of several heme cofactors, which might in turn influence their redox properties, the heme redox potentials of HDH in the context of different oligomeric states need to be determined and assigned in order to realistically depict the electron transfer paths. For instance, oligomerization of HDH trimers to the 24mer assembly causes the desolvation of hemes 1 and Kustc1130 interacts with 12 out

of 24 hemes 3 and hemes 5 which might result in an altered electron flow compared to trimeric HDH. Similar to the oxidation of hydroxylamine to nitrite by *Ne*HAO, the oxidation of hydrazine to dinitrogen by *Ks*HDH releases four electrons that are probably also shuttled in two steps of two electrons. It is therefore tempting to speculate that *Ks*HDH applies a similar strategy to distribute these electrons as described for *Ne*HAO.

In addition to the option that electrons can be distributed within the ring-like arrangement of hemes in the HDH trimer, the unique ability of *Ks*HDH to form higher oligomers enables the formation of a network of eight such heme-rings in the 24mer. Since the distances between two heme 1 cofactors at the contact sites are small enough for ET through space (~4 Å edge-to-edge distance) a distribution of electrons to the three neighboring heme rings appears feasible (Fig 3.37).

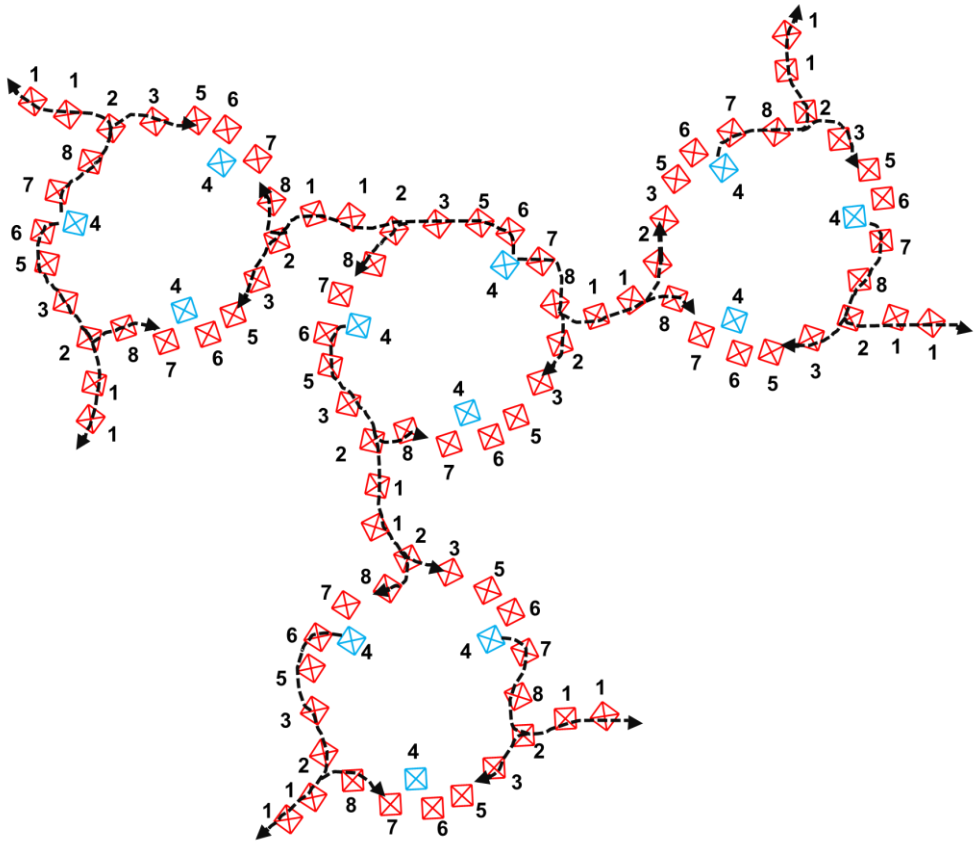

Figure 3.37 Possible Electron Distribution Pathways within the Heme Network of the HDH 24mer
The red and blue boxes represent *bis*-His coordinated hemes and active site hemes (P460), respectively. Each ring of hemes represents one trimer in the 24mer assembly. For simplicity only four out of eight trimers are shown. The number on each box shows the heme number in each monomer of HDH. Electron paths are shown with dashed black lines; the arrow head shows the direction of electron flow. Several electron paths are omitted for clarity, but the upper part in the middle ring shows all possible electron distribution paths.

However, *Ne*HAO exists as trimers only and is efficient in distributing four electrons produced from the oxidation of hydroxylamine to nitrite. Moreover, *Ne*HAO catalyzes the four-electron oxidation of hydrazine with a higher catalytic rate than HDH (Maalcke 2014; Maalcke 2016). It could be therefore supposed that the ring-like heme arrangement in the trimer should be sufficient to effectively distribute electrons in order to carry out efficient catalysis. This raises the question why HDH evolved towards the formation of higher oligomers enabling an extended heme network.

In order to release electrons, HDH needs an electron acceptor, which could be a soluble redox partner protein such as a small cytochrome c. The supposed soluble redox partner needs to be specific for binding to and receiving electrons from HDH and specifically delivering them to a yet unknown integral membrane protein complex. This complex is putatively involved in further transfer of electrons to the (mena)quinone pool and proton-motive force generation (Kartal 2013). If the proposed soluble redox partner were too promiscuous, it could potentially transfer electrons to other proteins or protein complexes such as hydrazine synthase (HZS) (Kartal 2011) or nitrite reductase (NIR) which would result in unproductive cycling of electrons (Figure 3.38 a).

Interestingly, the small binding partner (SBP, Kustc1130) of *Ks*HDH possesses a β-sandwich fold, which often occurs in protein domains involved in interactions with either membranes directly or other proteins (see section 3.2.6).

Therefore, two alternative models of electron release from HDH can be proposed. The first possibility would be a direct interaction of HDH with the anammoxosome membrane. However, binding of the HDH 24mer-12xSBP complex through one of its four faces to the membrane would lead to two complications. Firstly, the highly negatively charged area around the active site tunnel which continues through the exposed surface of SBP would be repelled by the negatively charged head groups of the membrane phospholipids. Secondly, in such a direct interaction, the heme 1 electron release site would be more than 25 Å away from the membrane surface. Therefore, it would not be feasible to transfer electrons directly to the quinone molecules sitting inside the membrane bilayer.

Alternatively, the SBP as part of the HDH 24mer-12xSBP complex could directly interact with the quinone-reactive integral membrane protein (QRP) complex such that electrons could be transferred (Figure 3.38 b). However, the interactions between HDH and the unknown membrane protein complex would most likely occur at one or two sites, possibly located at a docking site around hemes 1 and the SBP close to the trimer-trimer interfaces on one face of the cubic HDH complex. The HDH 24mer-12xSBP assembly brings all 192 hemes into a closed network. Having a direct interaction model between HDH and QRP in mind, the function of this extended heme network might not just be the temporary distribution of electrons to neighboring trimers but rather the provision of a path for electrons produced at one active site to travel through the entire network. Since the redox potentials of the heme centers would define the directionality of the electron flow as discussed for *Ne*HAO (Kurnikov 2005), their redox potentials should be modulated in order to allow electron flow through the entire heme circuit of the HDH 24mer-12xSBP assembly. This modulation might possibly occur *via* the interaction of HDH with SBP as already discussed.

Based on these considerations, one might conclude that the extended heme network could serve to transport electrons released at an arbitrary active site in the HDH 24mer to the site where the 24mer-12xSBP assembly interacts with the quinone-reactive integral membrane complex.

a

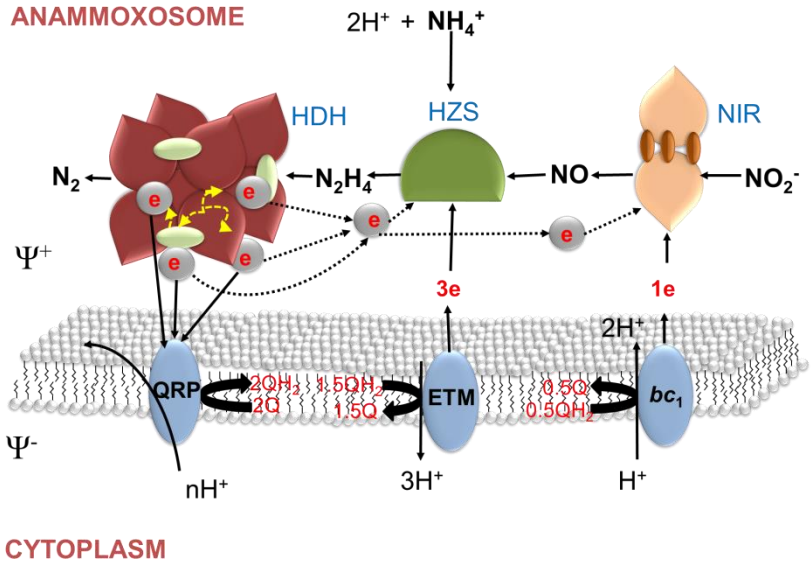

b

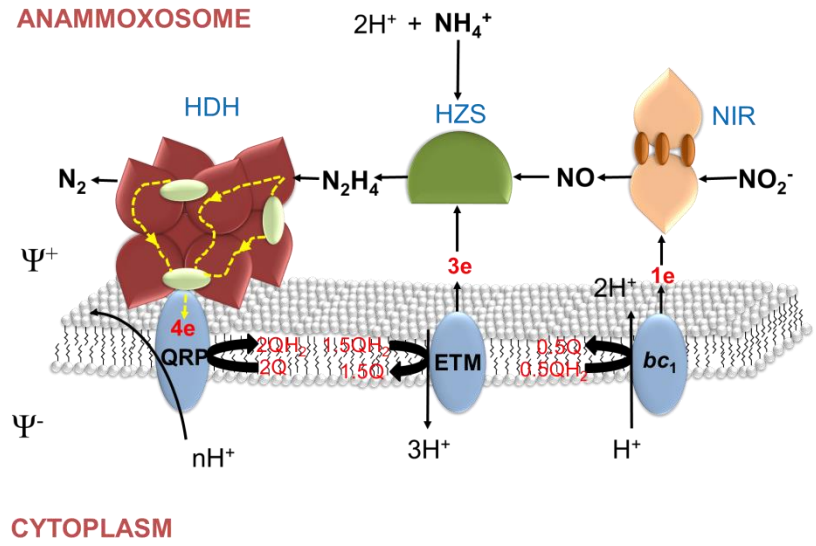

Figure 3.38 Hypothetical Models of the Anammox Pathway Assuming Different Scenarios of Electron Release from HDH

The anammox pathway models shown are based on the concept given by (Kartal 2011; Kartal 2013). The abbreviations are HDH for hydrazine dehydrogenase, HZS for hydrazine synthase, NIR for nitrite reductase, ETM for electron transport module, bc_1 for cytochrome bc_1 complex, QRP for quinone-reactive membrane protein, Q for quinone pool and e for electrons. For the sake of clarity only three small binding protein (SBP) molecules (bound to HDH) and no heme sites are shown.

a) Model involving a soluble redox partner (in grey) of HDH which supposedly transfers electrons (shown by solid arrows) to a yet unknown quinone-reactive membrane protein (QRP) complex. However, the putative promiscuity of such a soluble redox partner would result in a loss of electrons (shown by dashed arrows) to other complexes such as HZS or NIR. The yellow dashed lines with arrow head show the distribution of four electrons within the trimer and also to neighboring trimers.

b) Model assuming direct electron transport from HDH to the QRP complex. In this model, the integral membrane complex (in light blue) would interact directly with HDH at one or possibly two trimer-trimer interfaces. Electrons released from an arbitrary active site in the HDH 24mer could reach to the contact site *via* the heme network made by the HDH 24mer-12xSBP assembly (the electron path is shown by yellow dashed lines with arrow heads showing the direction of the electron flow).

3.3.4 Structural Basis of *Ks*HDH Hydrazine Oxidation Specificity

Both *Ks*HOX and *Ne*HAO have been shown to catalyze the oxidation of hydrazine to dinitrogen (Maalcke 2014), in addition to their physiological reactions *i.e.* the oxidation of hydroxylamine to NO and nitrite, respectively. *Ks*HDH, however, is highly specific to only hydrazine and is even competitively inhibited by hydroxylamine (Kartal 2011; Maalcke 2016). There could be several reasons for this specificity.

The first might be the interesting surface charge potential of the 24mer *Ks*HDH-Kustc1130 complex which shows highly negatively charged areas around the active site tunnel that are further surrounded by discrete positively charged patches. Therefore, electrostatic substrate guidance to the active site might probably play a role in substrate specificity. Nevertheless, the surface potential of trimeric *Ne*HAO is also highly negatively charged including its active site tunnel whereas that of the *Ks*HOX trimer is positively charged. Both *Ne*HAO and *Ks*HOX oxidize hydroxylamine (NH_2OH) as their common substrate but they also catalyze the oxidation of hydrazine (N_2H_4). Surprisingly the hydrazine oxidation rate of *Ne*HAO turned out to be even higher than of *Ks*HDH (Maalcke 2014).

The ionic nature of the substrates might provide some clues to explain this observation. The pKa values of $N_2H_5^+/N_2H_4$ and $N_2H_6^{2+}/N_2H_5^+$ are around 8 and -1 (Hinman 1958), respectively and that of NH_3^+OH/NH_2OH is 5.9 (Robinson 1961; Mollin 1975). Therefore, at the physiological pH of the anammoxosome of ~6.3 (van der Star 2010), N_2H_4 would obviously exist mostly as $N_2H_5^+$ while NH_2OH would be neutral with a minor protonated (NH_3^+OH) fraction. Perhaps positively charged hydrazinium ($N_2H_5^+$) ions are guided to the active site by electrostatic interactions with the negatively charged surface on *Ks*HDH as well as on *Ne*HAO. The active sites of both enzymes are also lined by many aromatic amino acids which can interact with protonated ammonium compounds such as $H_2N\text{-}NH_3^+$ *via* cation-π interactions (Dougherty 2013). This kind of electrostatic substrate guidance to the active site has also been described for acetylcholinesterase (Ripoll 1993), Cu-Zn superoxide dismutase (SOD) (Getzoff 1992) as well as electrostatic substrate channeling in bifunctional thymidylate synthase-dihydrofolate reductase (TS-DHFR) (Wheeldon 2016).

However, electrostatic substrate guidance does not explain why *Ks*HDH can only oxidize hydrazine whereas hydroxylamine and nitric oxide (NO) act as competitive inhibitors (Kartal 2011; Maalcke 2016) since all of these compounds could apparently reach the *Ks*HDH active site. In addition, it has also been observed that both NH_2OH and NO instantaneously oxidize

reduced *Ks*HDH (Maalcke 2016). The active site structure might provide some hints to explain these observations. The active sites of both *Ks*HOX and *Ks*HDH are fairly similar comprising a conserved tyrosine-heme crosslink (P460), an Asp-His pair for proton transfer and a methionine residue proposed to refrain water molecules from the active site pocket during catalysis (Maalcke 2014). However, the *Ks*HDH X-ray structure suggests an extra thioether crosslink between Cys202 and the methyl group at the C2 carbon of the P460 heme. Although there is no effect on the extent of heme ruffling when compared with *Ks*HOX, the extra crosslink could modulate the redox potential of the P460 heme. In addition, the N-terminal valine from a neighboring subunit (Val33'') of *Ks*HDH points its side chain towards the active site. Along with Met323 and Trp204, Val33'' might provide additional hydrophobicity to the active site and perhaps could further affect the redox potential (Kassner 1973). Indeed, the reported redox potential of the P460 heme in *Ks*HDH is -420 mV (Maalcke 2016) which is >100 mV lower than that of *Ks*HOX (-300 mV) (Maalcke 2014) and *Ne*HAO (-260 mV) (Collins 1993). Therefore, the specificity of *Ks*HDH towards hydrazine might result from the redox potential difference and also from the mode of active site binding of NH_2OH and N_2H_4. Both of these factors are further discussed in section 3.3.7.

3.3.5 Inhibition of *Bf*HDH by Hydroxylamine and Organohydrazines

As mentioned before, hydroxylamine and nitric oxide (NO) have been reported to inhibit the hydrazine oxidation activity of *Ks*HDH (Kartal 2011; Maalcke 2016). However, no other inhibitors were proposed so far. In this study, methylhydrazine, hydroxyethylhydrazine and phenylhydrazine were shown to inhibit *Bf*HDH activity. Enzymatic activity could not be rescued, even after exhaustive removal of the mentioned organohydrazine compounds by buffer exchange, indicating an irreversible inhibition of *Bf*HDH. Conversely, removal of excess NH_2OH from hydroxylamine-inhibited *Bf*HDH recovered its full activity, which is in line with the reported competitive inhibition of *Ks*HDH by hydroxylamine (Maalcke 2016). It is interesting to note that though phenylhydrazine inhibited *Bf*HDH, it did not show any effect on the UV-Vis spectrum of as-isolated *Bf*HDH. However, the incubation time in this experiment might have been insufficient. Phenylhydrazine has been shown to bind to the active site heme of *Ks*HOX (Maalcke 2014). All of the three investigated organohydrazines have also been shown to inactivate *Ne*HAO (Logan 1995).

The appearance of a split Soret band with two peaks located around 410 nm and 420 nm accompanied by the appearance of α- and β- bands indicated that hydroxyethylhydrazine

might interact with *Bf*HDH in a similar manner as hydrazine. Moreover, UV-Vis spectra of *Bf*HDH in presence of methylhydrazine or hydroxylamine showed similar features namely a shoulder around 419 nm and a small α-band around 555 nm. These features indicate their interactions with the heme iron. However, according to a previous study on *Ks*HDH (Maalcke 2016), hydroxylamine does not interact with oxidized *Ks*HDH but instantly oxidizes reduced *Ks*HDH. Studies performed in our lab (Dietl 2016) showing a similar alteration of the spectrum of oxidized *Ks*HDH in the presence of hydroxylamine as observed for *Bf*HDH contradict these findings. Hydroxylamine was also shown to interact with as-isolated (oxidized) HDH from *Jettenia caeni* (Shimamura 2007).

3.3.6 Factors Affecting the Hydrazine Oxidation Activity of HDH

Both *Bf*HDH and *Ks*HDH trimers form higher oligomers with increasing ionic strength and in presence of their small binding partners (SBP). Therefore, the effect of these two factors on hydrazine oxidation activity of *Bf*HDH and *Ks*HDH were tested, in order to eventually understand the effect of oligomerization on enzyme activity.

Both *Bf*HDH oligomerization and hydrazine oxidation activity showed sigmoidal behavior when the ionic strengths of the buffer provided by different salts such as KCl, K_2SO_4 and KPi was increased (0-300 mM). Therefore, it is highly likely that the increase in enzymatic activity is caused by oligomerization of *Bf*HDH. However, contributions from interactions of ions with the protein such as their influence on its overall surface potential might not be completely neglected.

Another important observation was made when hydrazine oxidation activities of both *Bf*HDH and *Ks*HDH were analyzed in the presence of their respective SBP (Broful02728 and Kustc1130, respectively) while ionic strength (KCl) was increased and compared with the activities without SBP at different ionic strengths. In the presence of Broful02728 the hydrazine oxidation activity of *Bf*HDH doubled compared to its absence (both at 0 mM KCl). The activity further increased up to a maximum at ~100 mM ionic strength. Further increase in ionic strength led to a decrease in activity until it reached the same level as in the absence of Broful02728. The highest activity in the presence of Broful02728 was two-fold higher than the activity without SBP at the same ionic strength (100 mM). Similar trends were also observed for *Ks*HDH when corresponding activity assays were performed (highest activity at 150 mM). However, the differences between the activities with and without Kustc1130 at different ionic strengths were not as pronounced as for *Bf*HDH. This might be due to the fact

that native *Ks*HDH preparations already contained low amounts of Kustc1130 which might have contributed to the increase in activity already when no additional Kustc1130 was added.

In conclusion, 100-150 mM ionic strength represents optimal conditions at which HDH reaches its maximal activity in the presence of its small binding partner. It is, however, difficult to comment on the factors which govern this behavior. At low ionic strength, *i.e.* in 25 mM HEPES buffer (pH 7.5) in the absence of additional salt, *Bf*HDH exists only as trimers which, however, oligomerize to the 24mer assembly as soon as Broful02728 is added (section 3.3.1). At this point the activity also increases by a factor of two as mentioned before. There could be two probable reasons. Firstly, the oligomerization to the 24mer which most probably provides additional options to distribute electrons to the hemes of neighboring trimers. Secondly, the binding of Broful02728 at the trimer-trimer interface (adjacent to heme 1) which might modulate the binding of the redox partner. However, in the current studies bovine cyt c was used as an artificial redox partner, which probably transfers electrons by random collision with HDH. Owing to that, the second reason might not be valid in the first place. Both possibilities could therefore only be compared if the physiological redox partner of HDH as well as precise redox potentials of the hemes in the HDH 24mer assembly bound to its small binding partner were known. Moreover, the first reason would only be valid if electron release were the rate limiting step in the overall reaction mechanism of HDH.

If only oligomerization induced by Broful02728 were responsible for the increase in HDH activity then the activity should have already reached a maximum before increasing ionic strength since the small binding partner would have caused nearly complete oligomerization of HDH even at low ionic strength. Therefore, the observed further increase in the activities of *Ks*HDH and *Bf*HDH up to a maximal point upon increasing ionic strength must be an effect of ionic strength itself. For instance, increased ionic strength might affect the interaction of HDH with its artificial redox partner (bovine cyt c) or might modify the surface charge distribution of HDH and thereby influence the interaction with its charged substrate ($N_2H_5^+$).

Finally, the decrease in hydrazine oxidation activity of HDH in the presence of its SBP after increasing ionic strength beyond the activity optimum might be likely explained by an abrogation of hydrophilic interactions between HDH and SBP under high salt conditions. Since HDH activity reaches to the same level as observed under high ionic strength without SBP, it could be speculated that the loss of SBP leads to the formation of both 24mers and 30mers at high ionic strength that are supposed to be less active than the HDH 24mer-12xSBP

complex. On the contrary, negative stain TEM of HDH in the presence of its SBP at 300 mM KCl showed only 24mer assemblies, which might hint at still intact interactions between HDH and its SBP. The interactions between these two proteins, however, need to be further investigated by techniques which can be applied to protein solutions such as isothermal titration calorimetry (ITC).

Given the different spatial arrangements of HDH trimers in the 24mer and 30mer states, one might expect differences in hydrazine oxidation activities of these two assemblies, too. As already discussed, the space between each pair of trimers within the pentagonal rings of the 30mer assembly is confined by 5-10 Å especially around the supposed electron release site at heme 1. As a consequence, the interactions between the HDH 30mer assembly and a redox partner might be poor or even disrupted, which would render the 30mer less active than the 24mer. In order to experimentally compare the activities of HDH 24mers and 30mers one of these species need to be isolated. Since the two assemblies are likely in equilibrium this approach must fail, however.

3.3.7 Reaction Mechanism

During refinement of the *Ks*HDH crystal structure a positive difference electron density appeared at the distal side of the P460 heme iron (Fig 3.39 a) which could be explained by a water molecule. This is consistent with the structures of *Ne*HAO (Cedervall 2013) and *Ks*HOX (Maalcke 2014), where also a water molecule has been proposed as the distal ligand of the active site heme in the resting state of the enzyme. This water molecule is close enough to Asp255 to form a hydrogen bond (~3.8-4.0 Å in all the 24 active sites of the *Ks*HDH 24mer). However, it does not seem to be close enough to the second residue of the conserved Asp-His pair (His256) to form another hydrogen bond. In *Ks*HOX, however, the corresponding histidine (His263) is close enough (~2.9 Å). Indeed, a slight shift in the position of His256 in *Ks*HDH was observed compared to the aligned *Ks*HOX structure (PDB id: 4N4J). This shift, however, might not be very significant in changing the properties of the active site. Moreover, in close homologs, the loop containing the Asp-His pair is flexible as evident from the comparison of hydroxylamine and hydrazine soaked structures of *Ks*HOX (Fig 3.39 b & c). This loop was also not resolved in the 3.3 Å structure of BfHOX (chapter 5) most probably because of its flexible nature. In line with the *Ks*HDH crystal structure, the absence of a clear high spin EPR signal in as-isolated *Ks*HDH indicates the coordination of a

small ligand such as a water molecule to the distal coordination site of the P460 heme in *Ks*HDH (Maalcke 2016).

The first step in the catalytic cycle of hydrazine oxidation by HDH (Fig 3.39 d) would be the displacement of the heme-bound water molecule by N_2H_4. Hydrazine would obviously coordinate to the heme iron *via* one of its two nitrogen atoms while the other (distal) $–NH_2$ group would interact with the Asp-His pair. Owing to the similar architecture of the active sites of *Ks*HOX and *Ks*HDH, N_2H_4 would bind in the same manner as described by Maalcke *et al.* (2014) for a structure obtained from a hydrazine-soaked *Ks*HOX crystal. Here, a diatomic ligand is observed at the active site heme whose distal group forms only one hydrogen bond to the histidine of the Asp-His pair while the aspartate rotates away (Fig 3.39 c). The bound diatomic species in *Ks*HOX could be either interpreted as a coordinated hydrazine molecule or a diazene (HN=NH) species which is the two-electron oxidation product of N_2H_4 after abstraction of two protons. The oxidation of N_2H_4 to HN=NH constitutes the second step in catalysis. At this stage two H^+ would be shuttled away from the active site by a proton conduit (such as Asn458', Tyr443, Asp255 and His256) and one of the two electrons would reduce the heme Fe^{III} to Fe^{II}. The other electron would be temporarily stored by the crosslinked tyrosine radical (Tyr462') as proposed earlier (Maalcke 2014). The sequence of proton and electron transfer is so far a matter of debate. However, for the oxidation of hydroxylamine by *Ne*HAO which possess similar active site architecture as that of *Ks*HOX and *Ks*HDH, Attia *et al.* (Attia 2014) proposed the transfer of two protons followed by the transfer of two electrons as the most favorable sequence based on quantum chemical calculations on the Density Functional Theory (DFT) level. Similar investigations are needed for hydrazine oxidation to diazene and eventually to N_2 in the *Ks*HDH active site environment.

In support of the Tyr462' radical formation, EPR spectra of *Ks*HDH revealed an unusual signal with at a g-value of 2.009 without hyperfine structure which decreased up to three-fold in intensity in the presence of hydrazine and relaxed rapidly. It has been proposed that this signal originates from a tyrosine radical specifically from the crosslinked Tyr462' (Maalcke 2016). The electrons stored by the tyrosine radical and the P460 Fe^{II} would eventually be transferred to the electron conducting hemes to recover the Fe^{III} state of the P460 heme. In the third step, the bound HN=NH would further lose two H^+ and two electrons to yield the final product N_2. Here, the electron storage and transfer strategy is expected to be same as already

described for the second step. The electrons would eventually leave the system after traveling through the chain of hemes if an appropriate redox partner is available.

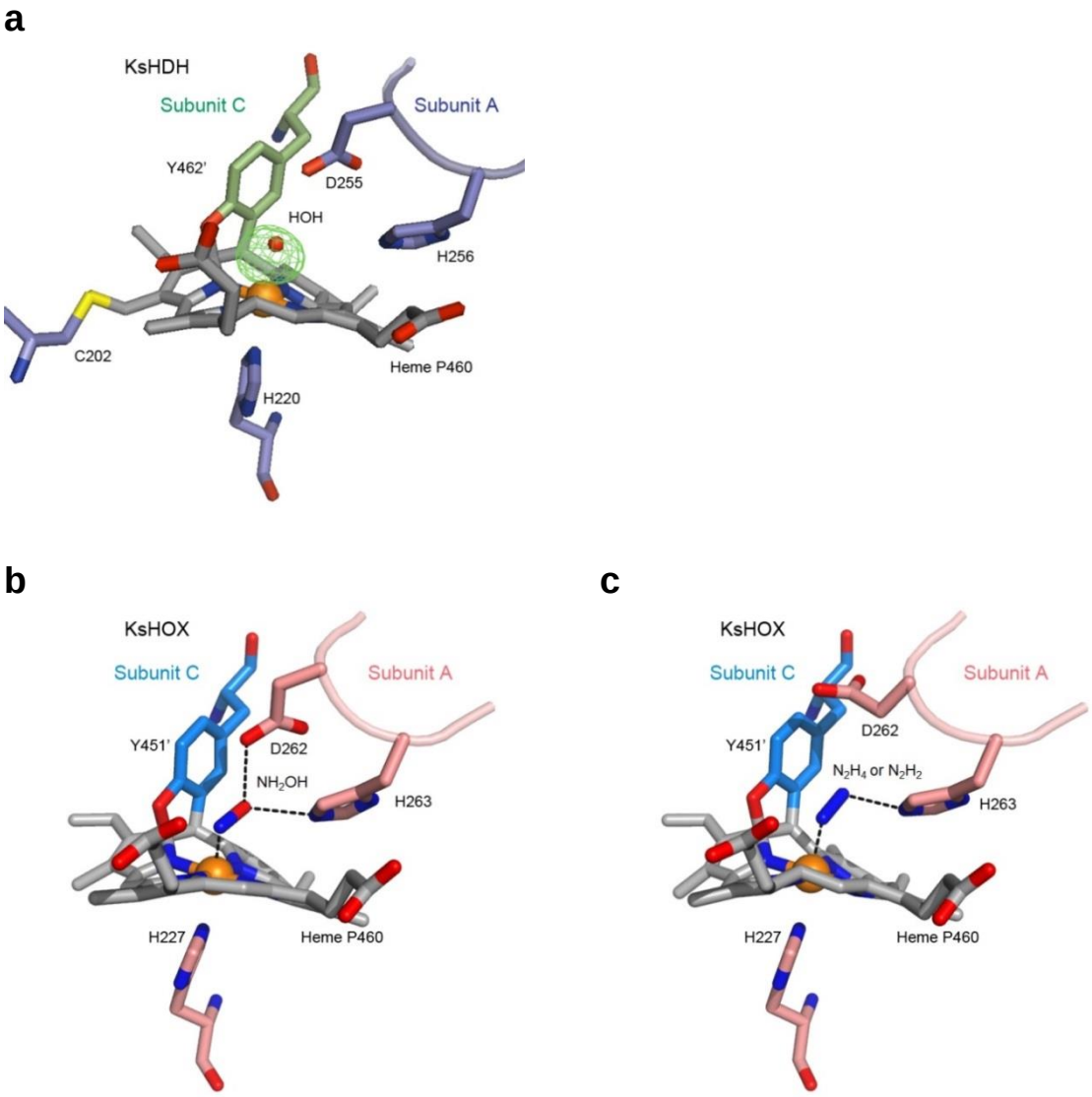

Figure 3.39 Reaction Mechanism of Hydrazine Oxidation by HDH and its Inhibition by Hydroxylamine
The active sites of *Ks*HDH and *Ks*HOX are shown as stick models.
a) Active site of *Ks*HDH before building the distal water molecule during the refinement. The mF_o-DF_c difference electron density map is shown as a green mesh at a contour level of 4 σ. The density could be explained by a water molecule. This species represents the resting state of *Ks*HDH.
b) The crystal structure of NH_2OH-soaked *Ks*HOX (PDB id: 4N4K) shows a diatomic species at the distal side of the active site heme iron presumably a coordinated hydroxylamine molecule (Maalcke 2014; Attia 2014). Note the two hydrogen bonds between the OH-group of hydroxylamine to aspartate and histidine.
c) The crystal structure of N_2H_4-soaked *Ks*HOX (PDB id: 4N4L) shows a diatomic species at the distal side of the active site heme iron presumably coordinated hydrazine (H_2N-NH_2) or a diazene (HN=NH) intermediate (Maalcke 2014). There is only one hydrogen bond between hydrazine and histidine while the aspartate rotates away. Histidine also slightly adjusts its position when compared to the hydroxylamine-bound *Ks*HOX structure.

d

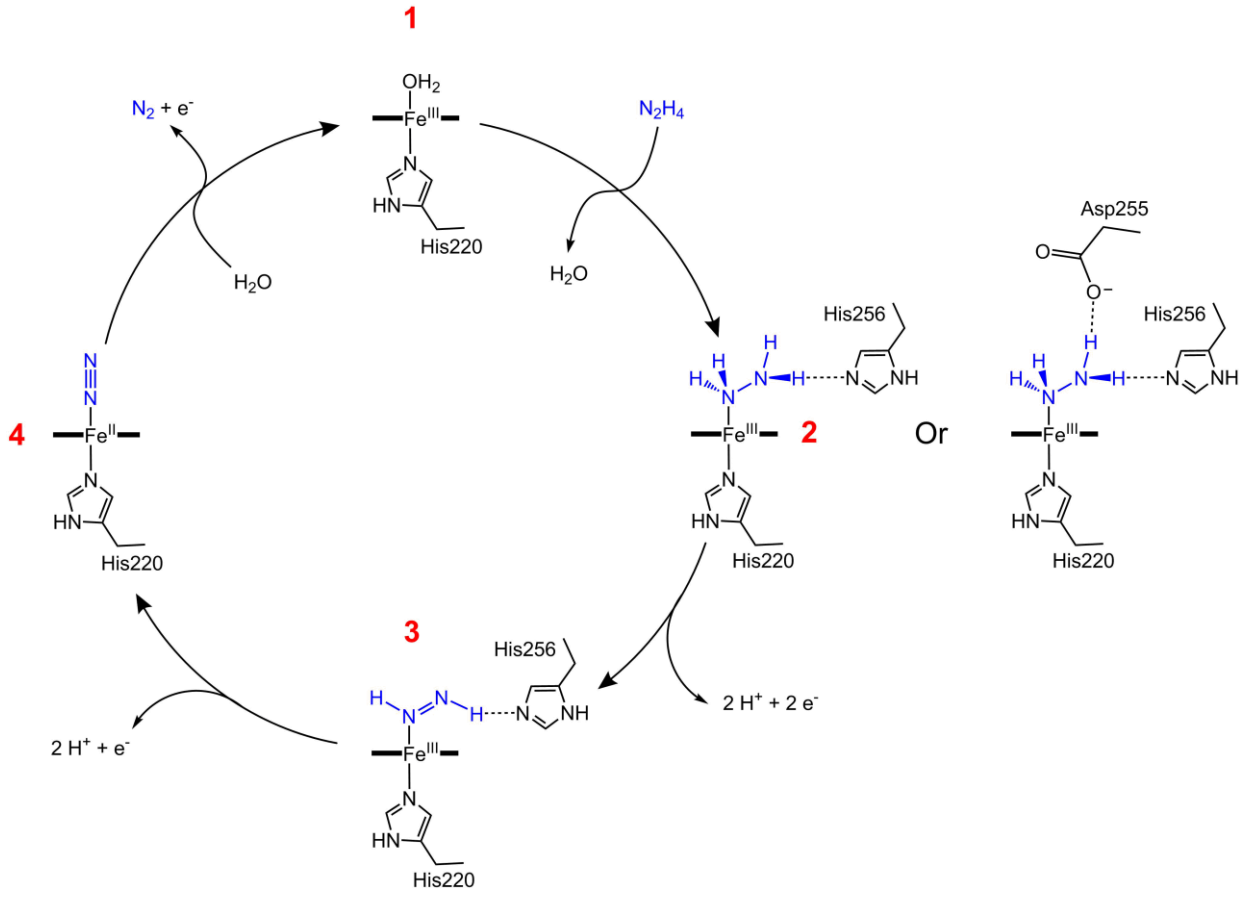

Figure 3.39 (continued)
d) Proposed catalytic cycle of hydrazine oxidation by HDH (modified acoording to Maalcke 2016). In state 2, the hydrogen atoms of the distal $–NH_2$ group of N_2H_4 are shown pointing downwards to avoid the less favorable eclipsed conformation. The hydrogen atoms of the iron bound $-NH_2$ group would always be pointing upwards due to steric hindrance. Likewise the hydrogen atoms of the diazene molecule (HN=NH) would most likely be in *trans* conformation. HN=NH would be formed after removal of two protons (H^+) and two electrons (e^-) from N_2H_4 (state 3). The water bound resting state (state 1) would be recovered after the removal of two H^+ and two e^- from diazene to form the final product N_2. A hypothetical iron(II)-dinitrogen intermediate (state 4) is postulated.

EPR spectra showed that incubation of *Ks*HDH with hydrazine resulted in 70 % reduction of magnetically coupled hemes 3 and 5 and 55 % of heme 1 with 3.2±0.5 electrons per *Ks*HDH monomer. Three different signals were also observed for heme 2 which is assumed as a sink for electrons coming from two different monomers (from heme pairs 7-8 and 3-5) (Maalcke 2014; Maalcke 2016). Interestingly, the authors report that the heme 7-8 pair remained fully oxidized. The electron produced from the oxidation of hydrazine would travel through the heme network of the HDH 24mer-12xSBP assembly eventually releasing them to the proposed quinone-reactive membrane protein (section 3.3.3)

Chapter 4
Structural and Functional Studies of Small c-type Cytochromes from Anammox Bacteria

4. Structural and Functional Studies of Small c-type Cytochromes from Anammox Bacteria

4.1 Introduction

A vast number of studies have been performed on small c-type cytochromes, especially on monoheme cytochromes c. Most of them play essential roles as electron transport proteins in a large variety of both aerobic and anaerobic electron transport chains such as mitochondrial respiration, nitrogen- and sulfur metabolism or photosynthesis (Bertini 2006; Pettigrew 1987). Owing to their key function in biological energy conversion, examples of monoheme cytochromes c are known from all domains of life *i.e.* eubacteria, archaea and eukarya (both plants and animals).

Based on their tertiary structures and their mode of heme binding, small c-type cytochromes have been divided into two major classes and several subclasses. As already mentioned in chapter 1, class I c-type cytochromes are low molecular weight proteins (~10 kDa) possessing a low spin heme which is often His/Met coordinated. The CXXCH heme binding motif is located near the N-terminus and the amino acid serving as distal heme ligand is located near the C-terminus. Class II c-type cytochromes usually possess a high spin (but occasionally low spin) heme which is bound to a heme binding motif located near the C-terminus, whereas the distal heme ligand is provided by a residue near the N-terminus of the protein (reviewed by Bowman 2008). Both class I and class II c-type cytochromes possess distinct diagnostic protein folds, the cytochrome c- and the four-helix bundle fold, respectively. Furthermore, based on phylogeny, amino acid sequence similarity and physiological function, at least six subclasses of single domain, low spin c-type cytochromes in prokaryotes have been described by Bertini *et al.* (2006), all belonging to what was originally termed Ambler's class I (Ambler 1991). These subclasses include cytochromes c_2, c_5, and c_6 as well as cytochromes c_{551}/c_{552}, c_{553} and c_{552}/c_{554}.

Almost all of the characterized class II cytochromes c can be further assigned to subclass IIa, whose members possess a penta-coordinated high spin heme (5c-heme) and are denoted as cytochrome c'. Bacterial cytochromes c' have been enigmatic so far with regard to their function since their first isolation in the 1950s (Elsden 1953). In these proteins, histidine serves as proximal ligand while the distal side remains vacant. The majority of cytochromes c' are homodimers (~14 kDa per subunit). However, *Rhodopseudomonas palustris* cytochrome c' is monomeric in solution (Cusanovich 1971; Shibata 1998) and ligand-induced dissociation of the dimer has been reported for the cytochromes c' from *Allochromatium vinosum* (Evers

2007; Motie 1991) and *Rhodobacter capsulatus* (Tsan 2000). The representative structural features of cytochromes c' include a solvent exposed proximal heme pocket around the proximal histidine heme ligand as well as a conserved positively charged residue (arginine or lysine) four residues succeeding the CXXCH motif. On the contrary, the distal heme pocket is usually crowded by hydrophobic residues.

The remaining class II c-type cytochromes belong to class IIb, whose members are characterized by a hexa-coordinated low spin heme and also possess a four-helix bundle protein fold (Hough 2015). The only structurally characterized representative from this subclass is cytochrome c-556 from *Rhodopseudomonas palustris* (Bertini 2004) which possesses histidine and methionine as proximal and distal heme ligands, respectively. There are also examples where the axial heme ligation is sensitive to the oxidation state of the Fe-center. Cytochrome c'' from the aerobic methylotrophic bacterium *Methylophilus methylotrophus*, for instance, exhibits a *bis*-His coordination in the ferric state (Fe^{III}) and is *mono*-His coordinated in the ferrous state (Fe^{II}) (Quintas 2011; Berry 1990) with spectroscopic features of the ferrous species similar to class IIa cytochrome c'.

Almost all known class IIa cytochromes c' bind diatomic gases such as carbon monoxide (CO) and nitric oxide (NO). The first structures of *Alcaligenes xylosoxidans* cytochrome c' (AXCP) bound to these diatomic gases showed that CO binds to the vacant distal heme coordination site whereas NO surprisingly binds at the proximal side of the heme, replacing the endogenous histidine ligand and forming a state referred to as 5cNO (5-coordinate NO) adduct (Lawson 2000). Based on the spectroscopic and kinetic studies of AXCP, it was proposed that the final proximal binding of NO proceeds *via* a distal NO-heme (referred as 6cNO adduct) and a putative dinitrosyl intermediate (George 2001; Lawson 2003; Pixton 2009). The eukaryotic heme *b* NO receptor domain of soluble guanylate cyclase (sGC) also binds NO in a manner reminiscent to that of cytochrome c' (Hough 2015). Proximal NO binding has also been shown in the crystal structure of the bacterial NO-sensor protein H-NOX from *Shewanella oneidensis*, where 6cNO (6-coordinate NO) and dinitrosyl intermediates have also been proposed (Herzik 2014). Despite extensive research in this field the function of several cytochromes c' has remained speculative.

The genome of the anammox bacterium *K. stuttgartiensis* codes for 63 c-type cytochromes. A list of mono-, di-, tri- and tetraheme cytochromes c from this anammox model organism is presented in table 4.1. There are several small class I and class II monoheme c-type cytochromes. Except for Kuste4313, all of them possess an N-terminal signal peptide which implies that they are transported into the anammoxosome where they would co-localize with

the multienzyme complexes involved in the central anammox energy metabolism (Almeida 2015). Since the anammox process is based on redox reactions, it is likely that some of those small cytochromes might work as redox partners of the major enzyme complexes such as hydrazine dehydrogenase (HDH), hydroxylamine oxidase (HOX) and hydrazine synthase (HZS). Besides class I and class II cytochromes c, there are also unclassified monoheme proteins as well as di-, tri- and tetraheme c-type cytochromes encoded by the *K. stuttgartiensis* genome. Some of those might also act as redox partners, but the number and diversity of the cytochromes mentioned in table 4.1 indicate that they might also possess other, yet unknown functions such as enzyme catalysis. For instance, Kuste2860 and Kuste2861 (both diheme c-type cytochromes) represent two of the three subunits of HZS (Dietl 2015).

Some of the cytochromes c mentioned in table 4.1 show significantly higher transcription levels compared to the average level of most others genes. Moreover, several small cytochromes are so highly expressed at the protein level that they could easily be purified from anammox biomass (Cirpus 2005).

Among the genes encoding monoheme c-type cytochromes in *K. stuttgartiensis*, kusta0087 and kusta0088 show the highest transcription levels (Table 4.1). Both genes are co-transcribed as a single mRNA (Figure 4.1 a) and the corresponding proteins have recently been purified as a stable complex from their source organism (Joachim Reimann, Radboud University, Nijmegen). The homologues of Kusta0087 and Kusta0088 from *Jettenia caeni* (formerly known as *Planctomycete* KSU-1) called NaxL and NaxS, respectively, were also purified as a heterodimeric complex (NaxLS) and spectroscopically characterized (Ukita 2010). Based on UV-Vis and electron paramagnetic resonance (EPR) spectroscopic analyses, the authors argued that the redox potential of the NaxLS complex is very low (below -400 mV). EPR spectroscopy also suggested a rare His/Cys axial heme ligation in both subunits. Both the Kusta0087/88 complex and NaxLS are the first examples of a complex between a class I and a class IIb c-type cytochrome, which make them attractive targets for structural studies.

The genes of two other class I monoheme cytochromes c, kustc0562 and kustc0563, from *K. stuttgartiensis* show fairly high transcriptional levels (Figure 4.1 b). Kustc0563 was the very first protein isolated from *K. stuttgartiensis* biomass (Cirpus 2005). This cytochrome was further heterologously expressed in *Escherichia coli* and its biochemical and spectroscopic characterization was performed (Huston 2007). Nevertheless, no structural studies of Kustc0563 have been performed which could help to understand the uncommon EPR

spectroscopic features of this protein. Most recently, the Kustc0563 homologue from *Jettenia caeni* (KSU1_B0428) was purified and spectroscopically characterized (Hira 2018).

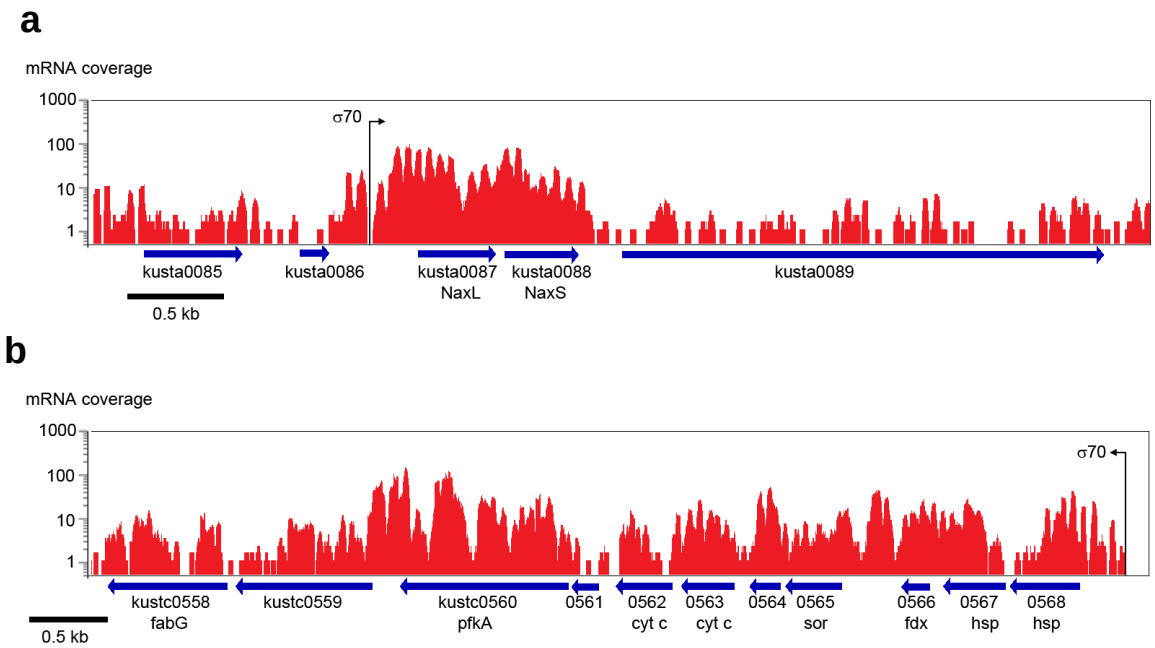

Figure 4.1 Transcription patterns of *K. stuttgartiensis* monoheme cytochromes c
a) kusta0087/88 and their neighbouring genes
b) kustc0562/63 and their neighbouring genes
The abbreviations are: NaxL, 25 kDa-heme protein complex large subunit; NaxS, 25 kDa-heme protein complex small subunit; fabG, 3-oxoacyl-[acyl-carrier-protein] reductase; pfkA, 6-phosphofructokinase; cytc, class I cytochrome c; sor, superoxide reductase; hsp, small heat shock protein. mRNA reads from a metatranscriptome dataset (Gene expression omnibus GSE15408, SRR037687) were mapped against the *K. stuttgartiensis* reference genome. The graph shows the mRNA read coverage plotted on a logarithmic scale against the length of the genomic DNA and was prepared using the Integrative Genomics Viewer (Thorvaldsdottir 2013). Putative σ70 promotor sites were predicted using BPROM (Solovyev 2011) and are indicated by bent arrows.

The objectives of this chapter include the structural and biophysical characterization of the Kusta0087/88 complex (hereafter called *Ks*NaxLS) by means of X-ray crystallography, analytical ultracentrifugation (AUC), size exclusion chromatography coupled to multi-angle static light scattering (SEC-MALS) and UV-Vis spectroscopy. Moreover, the *Ks*NaxLS complex, its separated components and several distal ligand mutants of the Kusta0087 and Kusta0088 subunits were prepared by heterologous expression in *Shewanella oneidensis* MR-1. Similarly, Kustc0563 as well as its close paralogue Kustc0562 were heterologously expressed and both proteins were structurally and biophysically characterized. The structural and preliminary biophysical characterization of Kustc0562 was performed by Josephine Bock, a lab rotation student.

Table 4.1 Mono-, di-, tri- and tetraheme c-type cytochromes in *K. stuttgartiensis*.

ORF	Peptides detected/peptides detectable (score)	mRNA coverage	Molecular weight (kDa)
Monoheme Class I			
Kusta0044	3/14 (117)	0.2	11.26
Kusta0088 (*Ks*NaxS)	3/9 (98)	32	11.46
Kustc0562	ND	ND	10.83
Kustc0563	4/15 (136)	13.5	10.12
Kustd1707	8/25 (270)	13.6	17.39
Kustc0397	ND	ND	17.61
Monoheme Class II			
Kusta0085	9/20 (318)	2.7	17.42
Kusta0087 (*Ks*NaxL)	6/14 (360)	38.3	12.93
Kustc1220	1/24 (60)	2.3	16.38
Kustd1686	4/21 (163)	2.7	16.40
Kustd1705	7/23 (394)	8.1	16.90
Kustd1955	3/24 (170)	0.3	17.60
Kustd1956	ND	ND	17.44
Kuste4313	8/20 (387)	19.1	20.55*
Unclassified monoheme			
Kustd1710	6/24 (236)	7.8	25.26
Kuste3440	1/18 (56)	11.2	17.24*
Kuste4137	ND	ND	17.24
Kuste4351	ND	ND	33.92
Diheme			
Kuste2860 (HZSγ)	20/41 (1173)	54.6	34.98
Kuste2905	1/33 (74)	4.5	36.63
Kustd1904	5/32 (245)	1.6	35.84
Kustc0457	13/34 (514)	8.3	29.01
Kustd1709	24/67 (1121)	14.1	57.45
Kustd1711	12/26 (539)	19.8	31.15
Kuste2474	ND	ND	32.04
Kuste2478	ND	ND	36.22
Kuste2861 (HZSα)	20/41 (1173)	52.6	87.62
Kuste4138	ND	ND	61.10
Kuste4347	1/56 (66)	0.6	50.50
Triheme			
Kuste4356	ND	ND	62.79
Tetraheme			
Kustc1170	ND	23.4	19.40
Kustc1045	ND	ND	41.47
Kustd1708	24/74 (1054)	7.3	52.97
Kuste2854	14/22 (500)	24.3	23.65
Kuste2461	ND	ND	48.43

Proteomic and transcriptomic data are from Kartal *et al.* (2011). Unless otherwise stated, the given molecular masses were calculated from the sequence without c-type hemes and signal peptides which were predicted using the SignalP 3.0 server (http://www.cbs.dtu.dk/services/SignalP-3.0/). *indicates that no signal peptide was detected in these sequences. Subunits of hydrazine synthase (HZS) are denoted as HZSα and HZSγ. Kusta0087 and Kusta0088 are named as *Ks*NaxL and *Ks*NaxS, respectively, and highlighted in blue. Kustc0563 and Kustc0562 are highlighted in green. Cytochromes above average transcription level (mRNA coverage > 6.9) are highlighted in grey.

4.2 Results

4.2.1 The *Ks*NaxLS Complex

4.2.1.1 Heterologous Expression and Purification of the *Ks*NaxLS complex and its Components

The expression constructs used for the recombinant production of the *Ks*NaxLS complex and its individual components are depicted in the figure 4.2. The kusta0087 (*Ks*NaxL) and kusta0088 (*Ks*NaxS) genes were cloned either individually or as a bicistronic operon into a pUC19-derived vector (Yanisch-Perron 1985). The native N-terminal signal peptides (in case of the bicistronic operon only for the upstream gene kusta0087) were replaced by the strong signal peptide from the small tetraheme cytochrome c (STC, SO2727) obtained from the expression host *Shewanella oneidensis* MR-1 (Ozawa 2001; Shi 2005). The cytochrome genes were constitutively expressed since IPTG-inducible expression strategies of similar cytochromes c had failed (Andreas Dietl, personal communication). The procedure for heterologous expression followed by purification *via* immobilized metal affinity chromatography (IMAC) and gel filtration (described in section 2.2.3.1 and 2.2.3.2) yielded proteins with C-terminal hexa-histidine tags from which signal peptides had been cleaved off. An analysis of samples from different stages of Ni-NTA purification by SDS-PAGE (section 2.2.4.1) followed by Coomassie staining (section 2.2.4.2) is shown in Figure 4.3 a. The size exclusion chromatograms of the purified *Ks*NaxLS complex, its individual components and mutants on a Superdex 75 (10/300 GL) column showed single, symmetrical peaks. The *Ks*NaxLS complex eluted around 11 mL while its components eluted at around 13 mL. The final yields of the proteins were 2-10 milligrams from 6 L of bacterial culture, sufficient for further biochemical and structural studies. A comparative Tris-tricine SDS-PAGE analysis is presented in figure 4.3 b, showing two separated bands corresponding to each component of the *Ks*NaxLS complex purified from its native source *K. stuttgartiensis* (Joachim Reimann, Radboud University, Nijmegen). The identity of the proteins was confirmed by MALDI-MS peptide mass fingerprinting. Total mass determination by ESI-MS confirmed the presence of a covalently bound c-type heme on both *Ks*NaxL and NaxS subunits.

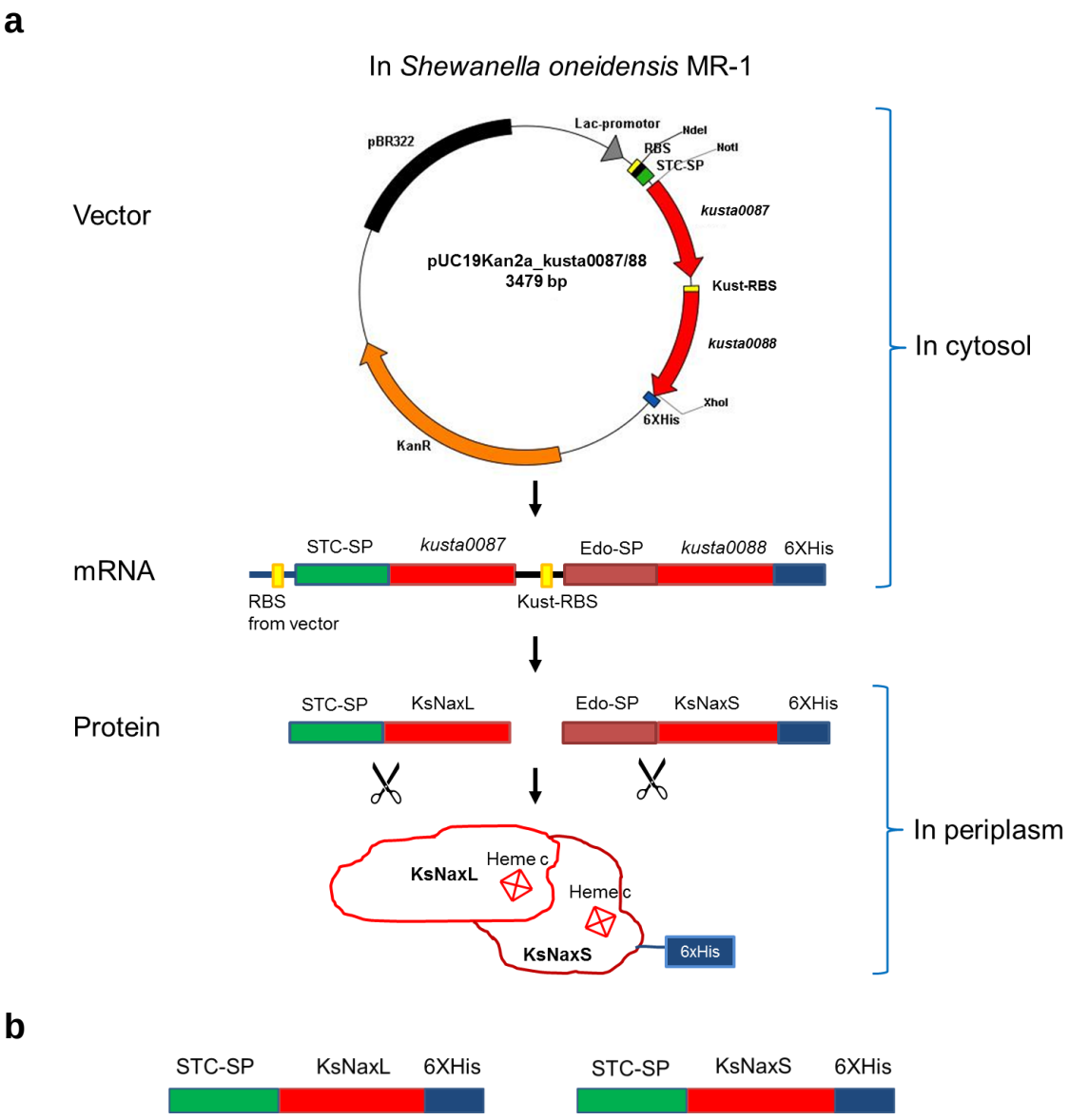

Figure 4.2 Bicistronic Heterologous Expression of the *Ks*NaxLS Complex in *S. oneidensis MR-1*
a) The pUC19 plasmid (Yanisch-Perron 1985) was modified by Andreas Dietl for constitutive expression of c-type cytochromes in *S. oneidensis MR-1* (section 2.2.3.1). The beta-lactamase gene (ampicillin resistance marker, Amp^R) was replaced by the neomycin phosphotransferase II gene (kanamycin resistance marker, Kan^R, orange). A periplasmic N-terminal signal peptide from the *S. oneidensis* tetraheme c-type cytochrome (STC-SP) was included (green). The kusta0087-kusta0088 bicistronic operon without its endogenous N-terminal signal peptide of kusta0087 but with that of kusta0088 (red-brown and indicated as Endo-SP) was cloned into the NotI/XhoI sites resulting in a 6xHis-tag at the C-terminus and the STC-SP at the N-terminus. The expressed proteins after N-terminal signal peptide cleavage and c-type heme attachment in the periplasm formed the mature *Ks*NaxLS complex with c-type hemes bound on each subunit. The complex was purified by Ni-NTA affinity chromatography using the C-terminal 6xHis-tag on the *Ks*NaxS subunit. RBS means ribosome-binding site (Shine-Dalgarno sequence)
b) For the expression of C-terminally His-tagged individual components of the *Ks*NaxLS complex, each corresponding gene (kusta0087 and kusta0088) without its endogenous N-terminal signal peptide was cloned separately into the pUC19kan2 vector using SacII/XhoI restriction sites. The STC-SP was used instead in both cases as shown in green.

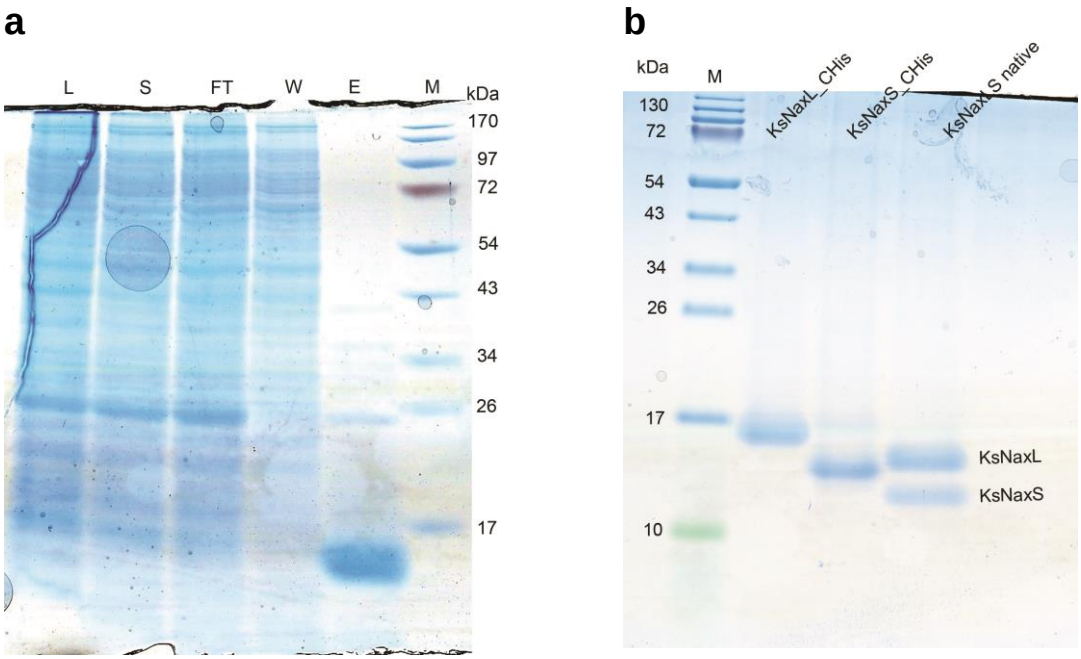

Figure 4.3 Tris-glycine and Tris-tricine SDS-PAGE Analyses
a) Purification of heterologously co-expressed *Ks*NaxL and NaxS subunits
A Coomassie-stained 15% SDS-PAGE shows different stages of the Ni-NTA affinity purification of the *Ks*NaxLS complex where only the *Ks*NaxS subunit is C-terminally His-tagged. For the purification procedure see section 2.2.3.2. L indicates lysate; S: supernatant; FT: flow through; W: wash; E: eluate and M: protein markers. The *Ks*NaxL and NaxS subunits are not well separated on Tris-glycine SDS-PAGE and form a broad band.
b) Tris-tricine SDS-PAGE Analysis. 12 % Tris-tricine SDS-PAGE (Schägger 1987) composition and electrophoresis procedure is described in section 2.2.4.1. The protein bands were stained by Coomassie blue. *Ks*NaxL_CHis and *Ks*NaxS_CHis represent overexpressed and metal-affinity purified C-terminally 6xHis-tagged *Ks*NaxL (Kusta0087) and *Ks*NaxS (Kusta0088), respectively. *Ks*NaxLS native represents the purified complex from *K. stuttgartiensis* biomass by Joachim Reimann (Radboud University, Nijmegen, the Netherlands). Although the difference in the molecular masses of *Ks*NaxL and *Ks*NaxS is only 1.5 kDa, Tris-tricine SDS-PAGE efficiently separated them into two distinct bands.

4.2.1.2 Oligomeric State of *Ks*NaxLS and its Reconstitution

The sedimentation coefficient distribution c(S) of the native *Ks*NaxLS complex (purified from *K. stuttgartiensis*) obtained by analytical ultracentrifugation sedimentation velocity (AUC-SV) resulted in a single symmetric peak at 2.68 S corresponding to a $S_{w,20}$ of 2.69 S (Figure 4.4 a). The ratio of the measured $S_{w,20}$ value and the maximum possible sedimentation coefficient $S_{max} \approx 0.00361 \times M^{2/3}$ (M in Da) (Erickson 2009) calculated for the *Ks*NaxLS heterodimer (24,397 Da) indicates a protein complex with a globular shape ($S_{max}/S_{w,20}$=1.11). Indeed, calculations of the sedimentation coefficient of the *Ks*NaxLS heterodimer found in the asymmetric unit of the crystal structure with HYDROPRO (Ortega 2011) resulted in 2.52 S, which is very close to the experimental value.

The sedimentation coefficient distribution c(S) of the individual components of the *Ks*NaxLS complex also resulted in single symmetric peaks corresponding to 1.8 S ($S_{w,20}$ of 1.8 S) and

1.71 S ($S_{w,20}$ of 1.72 S) for *Ks*NaxL and *Ks*NaxS, respectively (Figure 4.4 b). These values are close to the calculated values of 1.87 S and 1.64 S, respectively, obtained using HYDROPRO. The comparison of the measured $S_{w,20}$ values and the maximum possible sedimentation coefficients indicate that the components are globular and monomeric in solution ($S_{max}/S_{w,20}$ of 1.17 and 1.14 for *Ks*NaxL and *Ks*NaxS, respectively). AUC-SV of the reconstituted *Ks*NaxLS complex from its overexpressed subunits (both with C-terminal 6xHis-Tags) resulted in a sedimentation coefficient of 2.77 S ($S_{w,20}$ of 2.78 S), which is consistent with a heterodimeric complex of the NaxL and NaxS components with a $S_{max}/S_{w,20}$ ratio of 1.16 (Figure 4.4 b).

Moreover, analytical ultracentrifugation sedimentation equilibrium (AUC-SE) resulted in a molecular mass of 14.8 kDa for *Ks*NaxL and 12.8 kDa for *Ks*NaxS which are very close to the calculated values of 14.1 kDa and 12.7 kDa, respectively (Figure 4.4 c and d). AUC-SE of the native *Ks*NaxLS complex (Figure 4.4 e) resulted in a molecular mass of 23.9 kDa which also corresponds well to the calculated value of the heterodimer (24.4 kDa).

(Figure on next page)

Figure 4.4 Analytical Ultracentrifugation (AUC) of the *Ks*NaxLS complex and its Components
Sedimentation velocity (SV) experiments were performed at 30,000 rpm in a buffer containing 25 mM KCl, 25 mM HEPES/KOH pH 7.5 at 20 °C. The samples were diluted to A_{420}^{1cm}= ~0.42. Absorption scans were recorded at 420 nm. Sedimentation equilibrium (SE) experiments were performed using the same samples from the SV experiments but after removing 200 µL each of samples and buffer. SE curves were recorded after 22 h equilibration at 20 °C. Data points were averaged from five individual scans at 280 nm and globally fitted assuming a model of discrete non-interacting species in SEDPHAT.
a) Sedimentation coefficient distribution c(S) of native *Ks*NaxLS complex from *K. stuttgartiensis*.
b) Sedimentation coefficient distributions c(S) of the heterologously expressed *Ks*NaxL (CHis) and *Ks*NaxS (CHis) components and the reconstituted *Ks*NaxLS complex.
c) and **d)** SE curves of the *Ks*NaxL and *Ks*NaxS components at 30,000 rpm. The resulting molecular mass for *Ks*NaxL was 14,769 Da (calculated 14,067 Da) and for *Ks*NaxS 12,775 Da (calculated 12,671 Da).
e) SE curves of the native *Ks*NaxLS complex (as purified from *K. stuttgartiensis*) at 20,000 rpm (red) and 30,000 rpm (black). The fit resulted in a molecular mass of 23,863 Da (calculated 24,397 Da).

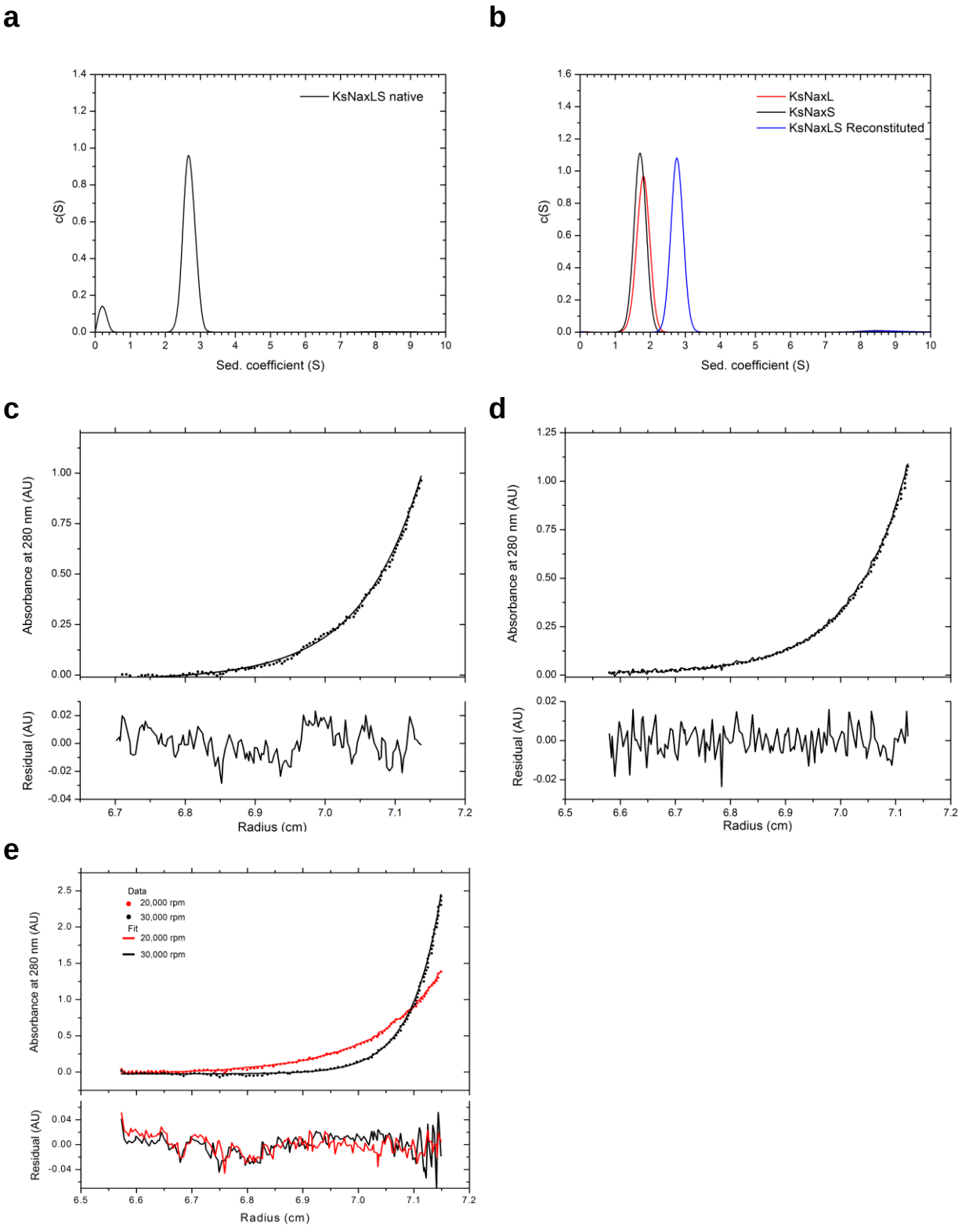

An analysis of the native *Ks*NaxLS complex and its heterologously expressed components by size exclusion chromatography (SEC) coupled to multi-angle static light scattering (MALS) is shown in figure 4.5. The size exclusion chromatograms of *Ks*NaxLS and its components *Ks*NaxL and *Ks*NaxS all showed single peaks at elution volumes of 11.9 mL, 13.1 mL and

13.2 mL, respectively (Figure 4.5 a and b). Using the calibration function fitted to five standard proteins (Figure 4.5 d) molecular masses of 26.3 kDa, 15.5 kDa and 15.0 kDa could be calculated for the *Ks*NaxLS complex, *Ks*NaxL and *Ks*NaxS, respectively. MALS analysis resulted in 20.4 kDa and 13.4 kDa for the *Ks*NaxLS complex and *Ks*NaxL, respectively. However, molecular mass determination failed for *Ks*NaxS by MALS. These results further corroborate the heterodimeric assembly of the *Ks*NaxLS complex, while *Ks*NaxL and *Ks*NaxS are present as monomers.

Moreover, when the *Ks*NaxL and *Ks*NaxS components were mixed in a 2:1 ratio, they could be reconstituted into a stable *Ks*NaxLS complex, with the excess of *Ks*NaxL remaining (Figure 4.5 c). MALS analysis of the reconstituted complex resulted in a molecular mass of 22.8 kDa.

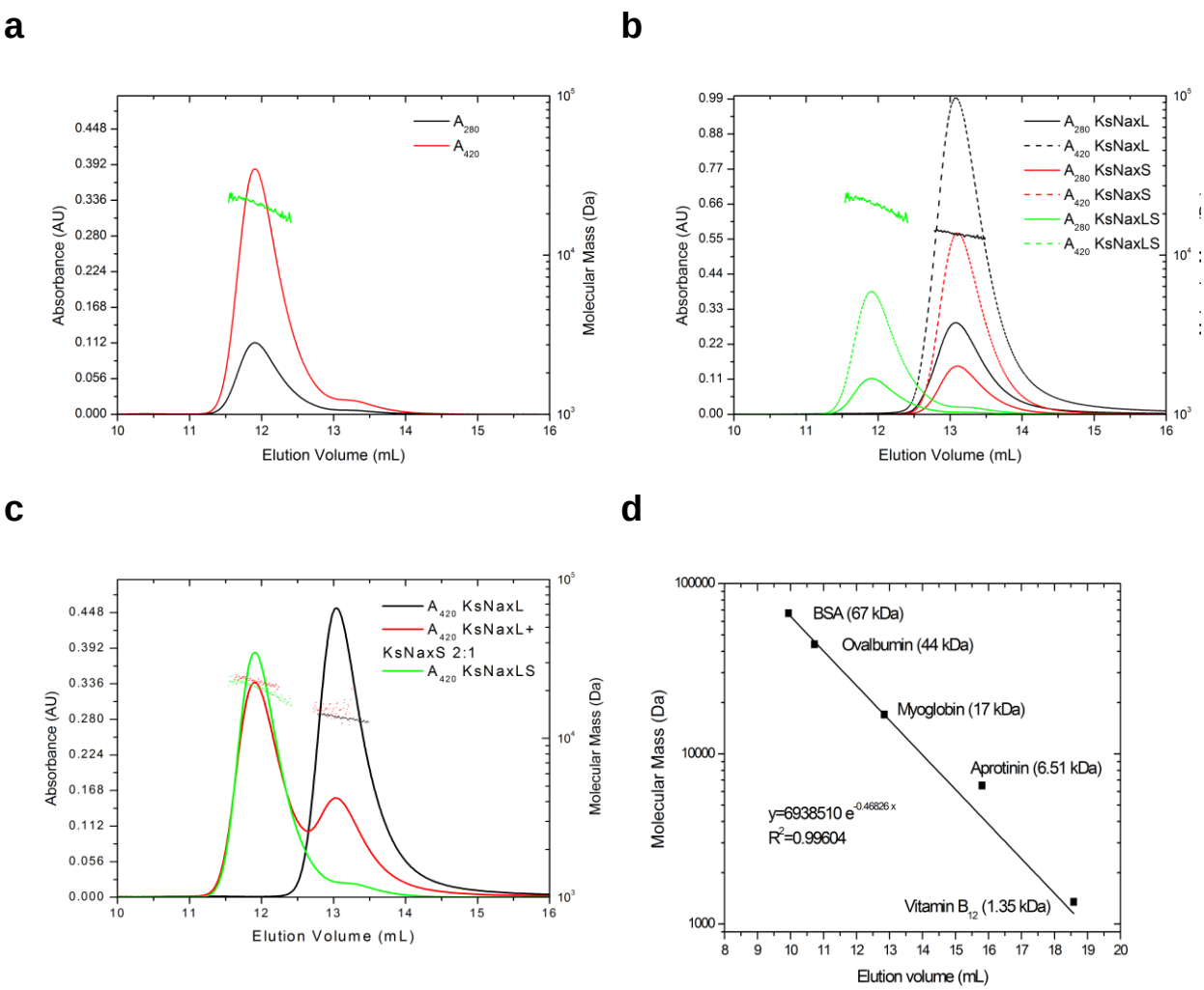

Figure 4.5 Analytical Size Exclusion Chromatograms and Molar Mass Distributions of Native *Ks*NaxLS, its Components and the Reconstituted Complex
Approximately 200-250 µg of each samples were applied on a Superdex 75 (10/300 GL) gel filtration column (GE Healthcare, Uppsala, Sweden) at room temperature in a buffer containing 150 mM KCl, 50 mM HEPES/KOH, pH 7.5. The absorbance traces at 280 nm and 420 nm as well as the molar mass distribution determined by multi-angle static light scattering (MALS) are indicated. **a)** Natively purified *Ks*NaxLS complex. **b)** Heterolgously expressed components with C-terminal His tags (*Ks*NaxL in black and *Ks*NaxS in red) and native *Ks*NaxLS (in green) for comparison. **c)** Reconstitution of the *Ks*NaxLS complex from its components (*Ks*NaxL was used in two-fold excess of *Ks*NaxS). **d)** Calibration curve obtained from the separation of five standard compounds (Bio-Rad, Hercules, USA). The calibration curve was fitted to the protein components only. In the given calibration function y is the molecular mass in Da, x the elution volume in mL.

4.2.1.3 UV-Vis Spectroscopy

The purified native *Ks*NaxLS complex and its overexpressed components appeared reddish brown in color. The UV-Vis spectra of the as-isolated, reduced and re-oxidized NaxLS complex as well as its components are shown in figure 4.6 a-c. In all of them the Soret band in the as-isolated state resides at 420 nm, which upon reduction with 1 mM Ti(III)citrate was blue-shifted with concomitant appearance of typical α- and β-bands at 553 nm (551 nm for *Ks*NaxS) and 523 nm, respectively. Interestingly, upon re-oxidation by sparging 1-2 mL of air through the sample the Soret band was further blue-shifted and reached to ~410 nm with simultaneous disappearance of α- and β-bands.

UV-Vis spectra of different distal ligand mutants in their as-isolated, reduced (by 1 mM Ti(III)citrate) and re-oxidized states (by sparging with air) are shown in figure 4.6 d-h. The Soret band in the as-isolated states of all these mutants reside around 412-415 nm. Upon reduction with Ti(III)citrate, a red shift of the Soret band to ~417 nm was observed in all mutants with appearance of α- and β-bands at around 553 nm and 523 nm. The Soret peak shifted back to around 408 to 410 nm upon re-oxidation by sparging air (except for the mutant *Ks*NaxL wt/ NaxS C101M, which had a Soret maximum at 416 nm in the re-oxidized state). The double methionine mutant *Ks*NaxL C32M/ NaxS C101M was isolated in a partially reduced state. Moreover, after full reduction the re-oxidation by air took more than 1 hour after which α- and β-bands were completely flattened. Although the mutants *Ks*NaxL wt/ NaxS C101G and *Ks*NaxL wt/ NaxS C101M were in their completely oxidized states after purification, re-oxidation after full reduction yielded still partially reduced species as evident from minor α- and β-bands (in these cases the spectra were measured immediately after sparging air). Conversely, the single mutants *Ks*NaxL C32G/ NaxS wt and *Ks*NaxL C32M/ NaxS wt which were isolated in their completely oxidized state were immediately fully re-oxidized by air starting from their completely reduced state.

a *Ks*NaxL

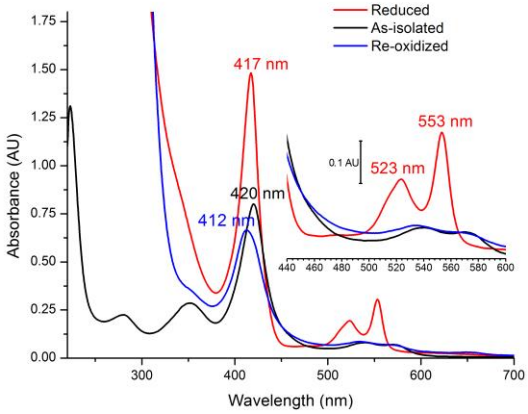

b *Ks*NaxS

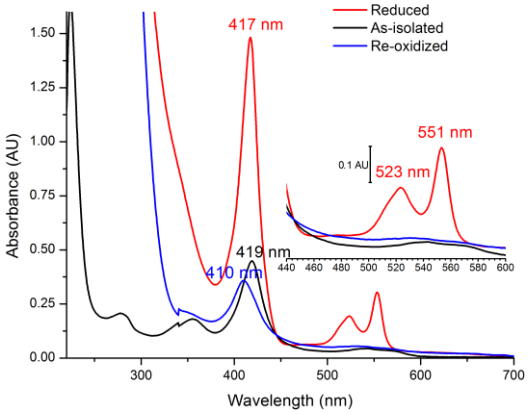

c *Ks*NaxLS complex

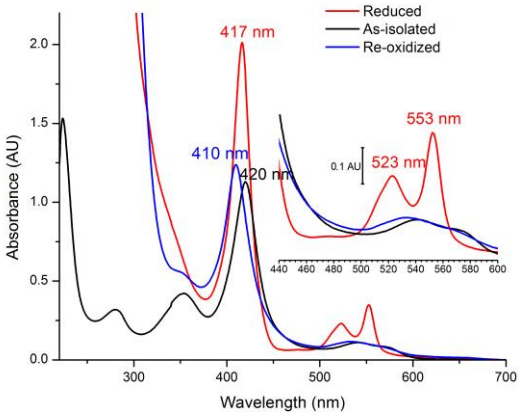

d *Ks*NaxL C32M/ NaxS C101M

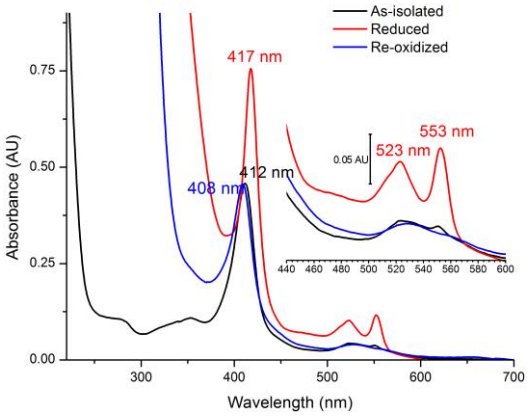

e *Ks*NaxL C32G/ NaxS wt

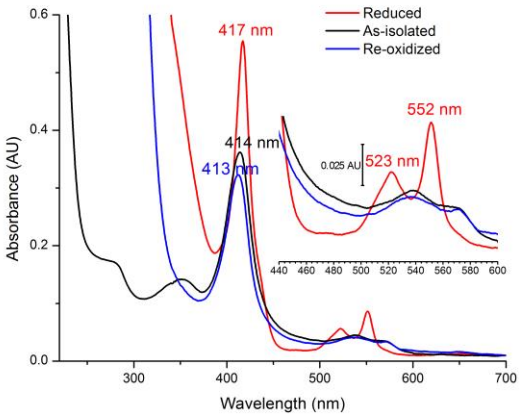

f *Ks*NaxL wt/ NaxS C101G

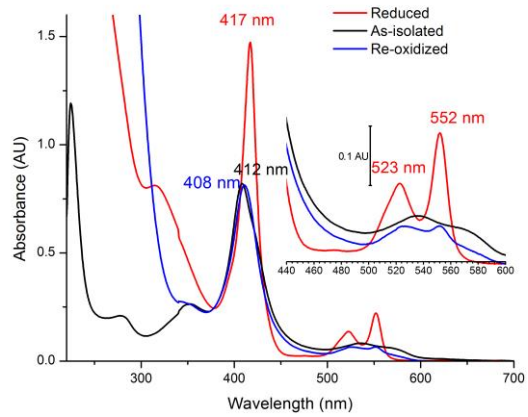

g *Ks*NaxL C32M/ NaxS wt **h** *Ks*NaxL wt / NaxS C101M

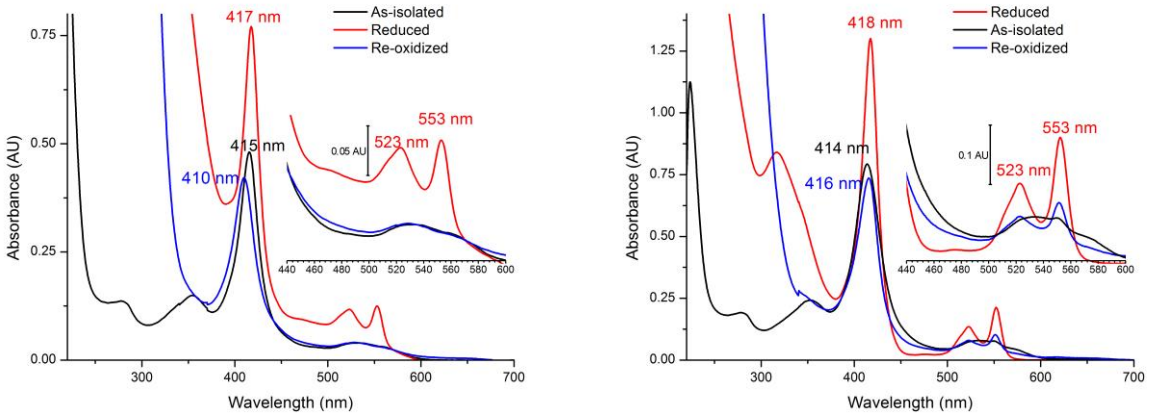

Figure 4.6 UV-Vis Spectroscopy of the *Ks*NaxLS complex, its Subunits and Distal Ligand Mutants.
The preparations of all samples for UV-Vis spectroscopy were carried out under a nitrogen atmosphere in a glove box. All buffers and solutions used were degassed under vacuum and sparged with argon. The quartz cuvettes containing the samples were closed with rubber stoppers to make them air tight. Spectra were collected using a Jasco V-650 spectrophotometer (Jasco Deutschland GmbH, Gross-Umstadt, Germany) outside of the glove box. Individual protein samples were diluted to a final A_{280}^{1cm}= 0.15-0.25 in their as-isolated states (black curves) in a buffer containing 25 mM KCl, 25 mM HEPES/KOH pH 7.5. Samples were reduced by 1 mM Ti(III)citrate (red curves) and re-oxidized (blue curves) by sparging 1-2 mL air using a 200 µL pipette.
a) & **b)** UV-Vis spectra of *Ks*NaxL and *Ks*NaxS. Both components possess Soret bands at 420 nm in their as-isolated states which are blue shifted to 417 nm upon reduction with the concomitant emergence of characteristic β-bands at 523 nm while the α-bands differed slightly. The α-band of *Ks*NaxL resided at 553 nm while that of *Ks*NaxS at was at 551 nm. Upon re-oxidation the Soret band of both components shifted to ~ 410 nm.
c) The UV-Vis spectra of the KsNaxLS complex showed identical behavior as described for its individual components, with the α-band at 553 nm in its reduced state
UV-Vis spectra of distal heme ligand mutants:
d) *Ks*NaxL C32M/ NaxS C101M **e)** *Ks*NaxL C32G/ NaxS wt **f)** *Ks*NaxL wt/ NaxS C101G
g) *Ks*NaxL C32M/ NaxS wt **h)** *Ks*NaxL wt/ NaxS C101M

4.2.1.4 Ligand Binding Studies

Different ligands such as nitric oxide (NO), carbon monoxide (CO), hydroxylamine (NH_2OH), hydrazine (N_2H_4), nitrite (NO_2^-), azide (N_3^-) and cyanide (CN^-) were tested for their abilities to bind to the *Ks*NaxLS complex. Among the tested ligands, NO and CO were found to coordinate to the c-type hemes in the complex as determined qualitatively by UV-Vis spectroscopy. Figures 4.7 and 4.8 show the effects of NO- and CO-binding, respectively, on the UV-Vis spectra of the *Ks*NaxLS wild type complex, its individual subunits and distal ligand mutants. Wild type *Ks*NaxLS in its as-isolated state could bind NO as was evident from both the increase in intensity and the blue shift of the Soret band from 420 nm to 417 nm (Fig 4.7 a). In the reduced state, *Ks*NaxLS showed a slight decrease in the overall intensity of the spectrum while the Soret band remained at the same position (417 nm) (Fig 4.7 b).

Moreover, in both the as-isolated and reduced state a slight tailing at around 400 nm was observed upon incubation with NO.

Both the as-isolated and reduced species of *Ks*NaxL showed a prominent shift of the Soret band to ~396 nm with a tail at ~415 nm upon incubation with NO, indicating coordination of the nitrosyl ligand to the heme iron in both ferric and ferrous states (Figure 4.7 c and d). *Ks*NaxS showed a different behavior than *Ks*NaxL upon incubation with NO. The Soret band in both as-isolated and reduced states of *Ks*NaxS shifted to 415 nm with a broad tailing at around 396 nm upon NO binding (Figure 4.7 e and f).

All the distal ligand mutants of *Ks*NaxLS in their reduced states showed similar changes in the UV-Vis spectra when being incubated with NO. The Soret band shifted from 417 to 415 nm (or 414 nm) with a prominent tailing at around 396 nm (Fig 4.7 h-l). The α- and β-bands disappeared in all cases. Interestingly, in the as-isolated state of all the mutants, the changes in the spectra with NO were not very significant at first glance. However, in the *Ks*NaxL C32M/ NaxS C101M mutant the small α- and β-bands in the as-isolated state were flattened with the appearance of slight tailing of the Soret band around 395 nm (Fig 4.7 g). The *Ks*NaxL C32M/ NaxS wt mutant showed a decreased intensity of the Soret band which remained at 415 nm compared to the as-isolated state (Fig 4.7 i). In both the mentioned mutants changes around the region from 440 to 600 nm were also observed. Interestingly, the *Ks*NaxL wt/ NaxS C101M mutant showed partial reduction when it was incubated with NO in its as-isolated state as evident from the red shift of the Soret band from 413 nm to 417 nm and the appearance of the α- and β-bands at 552 nm and 523 nm, respectively (Fig 4.7 k).

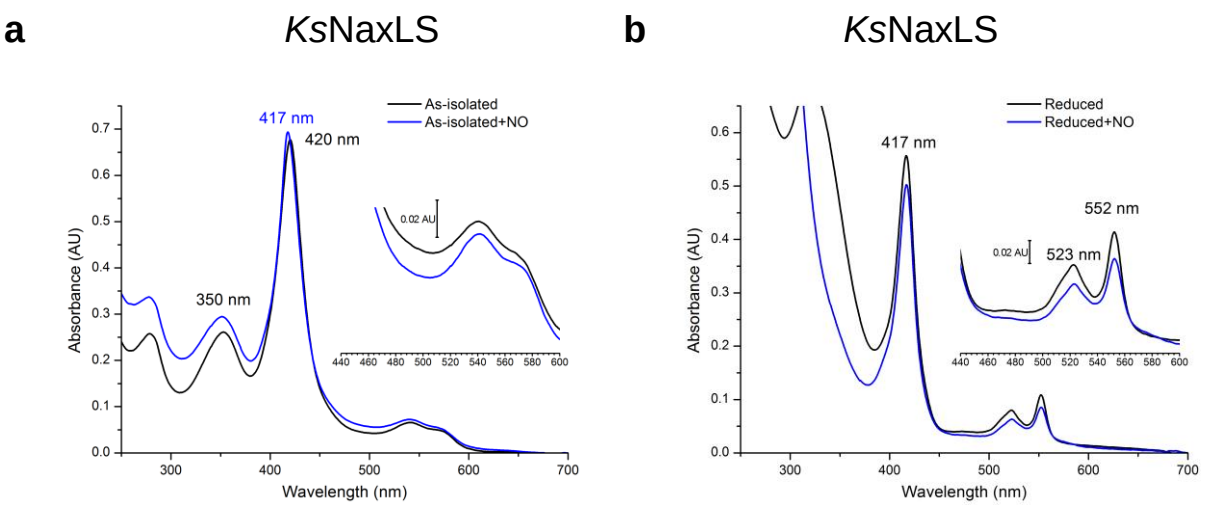

c *Ks*NaxL

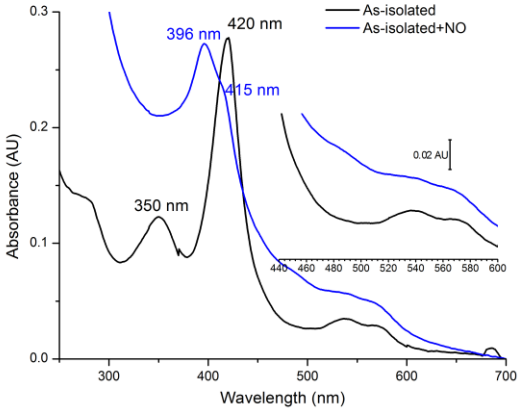

d *Ks*NaxL

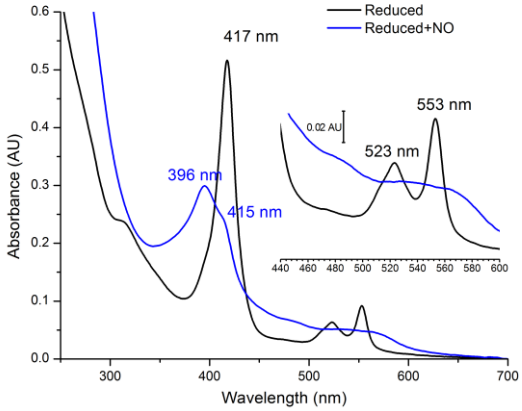

e *Ks*NaxS

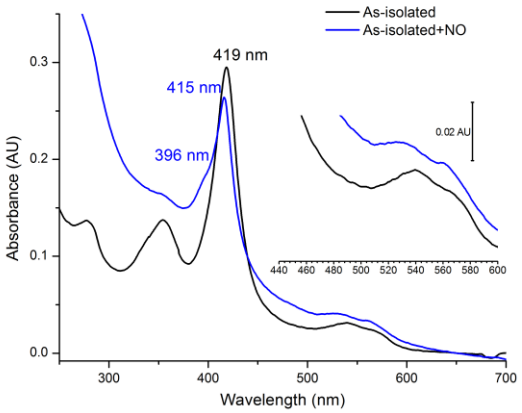

f *Ks*NaxS

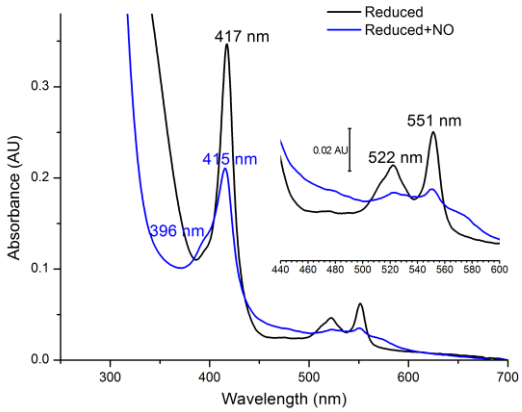

g KsNaxL C32M/ NaxS C101M

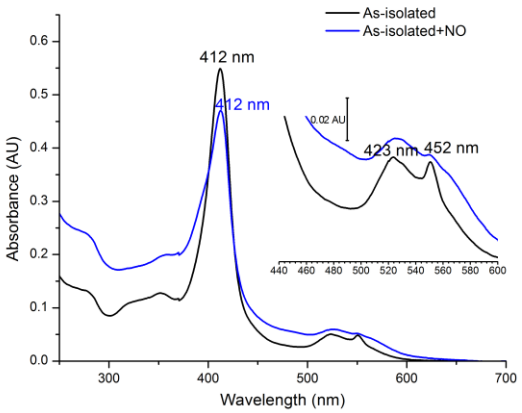

h *Ks*NaxL C32M/ NaxS C101M

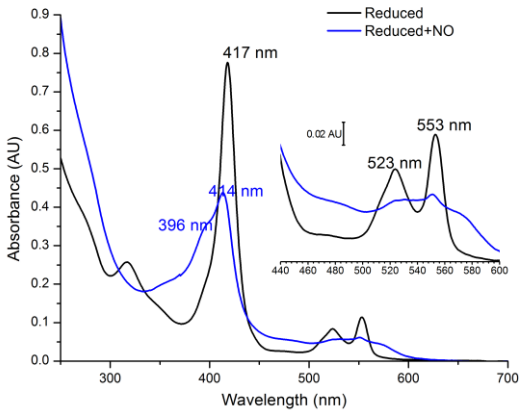

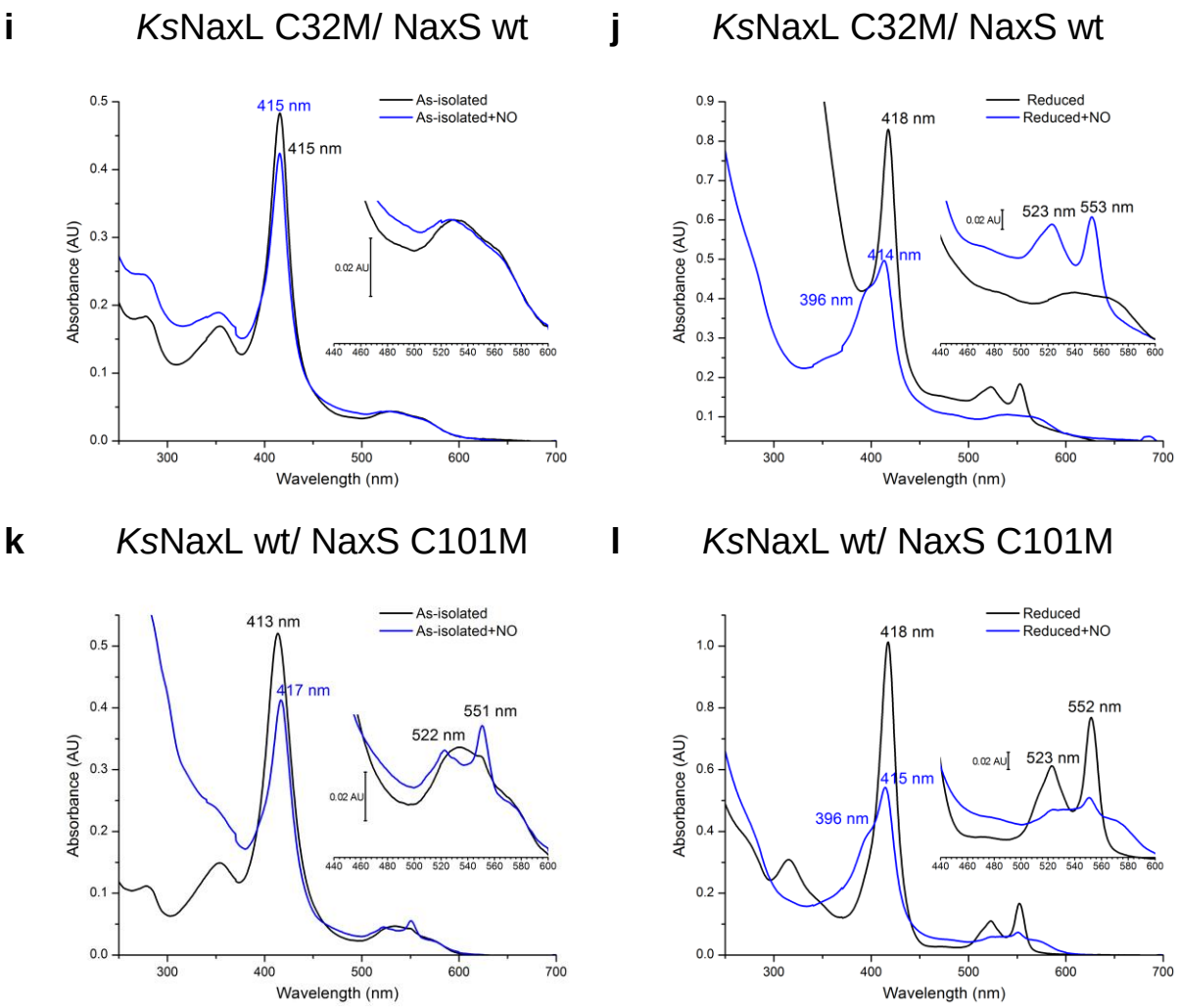

Figure 4.7 Nitric oxide (NO) Binding to the *Ks*NaxLS Complex, its Subunits and Distal Ligand Mutants Pure NO gas was prepared in a glove box under an N_2 environment according to (Lim 2005). 15-20 mL of freshly prepared NO was bubbled through 1 mL buffer containing 25 mM HEPES pH 7.5 and 25 mM KCl. The protein solutions were reduced with 1 mM Ti(III)citrate and buffer exchanged to 25 mM HEPES pH 7.5 and 25 mM KCl using a NAP-5 desalting column (GE Healthcare, Buckinghamshire, UK). Wild type *Ks*NaxLS complex and *Ks*NaxS stock solutions were kept in the presence 1 mM Ti(III)citrate, since they were highly sensitive to air-oxidation when the reducing agent was removed. 75 µL of protein stock solutions were mixed with 75 µL freshly prepared NO-saturated buffer in 1 cm path length quartz cuvettes (Hellma Analytics, Germany) and sealed using rubber stoppers. All samples were prepared under N_2 atmosphere in a glove-box. The spectra were collected using a Jasco V-650 spectrophotometer (Jasco Deutschland GmbH, Gross-Umstadt, Germany) outside of the glove box. In the figure, the left column shows spectra of the as-isolated proteins after reaction with NO and the right column shows spectra of the reduced proteins bound to NO. **a,b)** NaxLS wild type complex; **c,d)** *Ks*NaxL; **e,f)** NaxS; **g,h)** *Ks*NaxL C32M/ NaxS C101M; **i,j)** *Ks*NaxL C32M/ NaxS wt and **k,l)** *Ks*NaxL wt/ NaxS C101M.

a *Ks*NaxLS

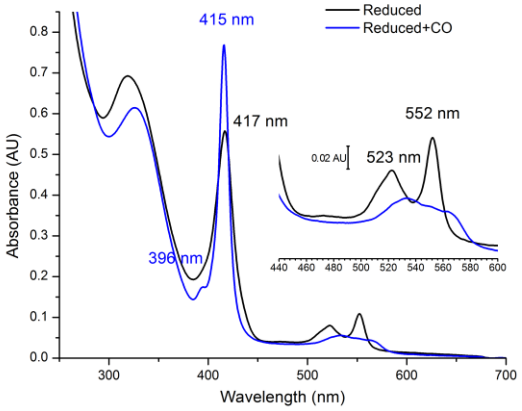

b *Ks*NaxL

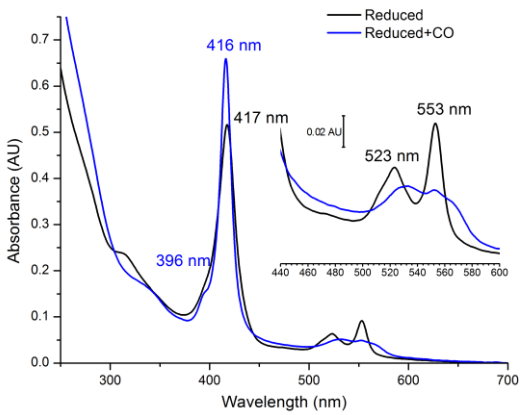

c *Ks*NaxS

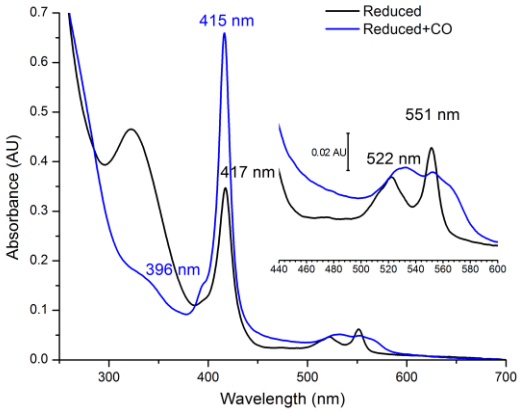

d *Ks*NaxL C32M/ NaxS C101M

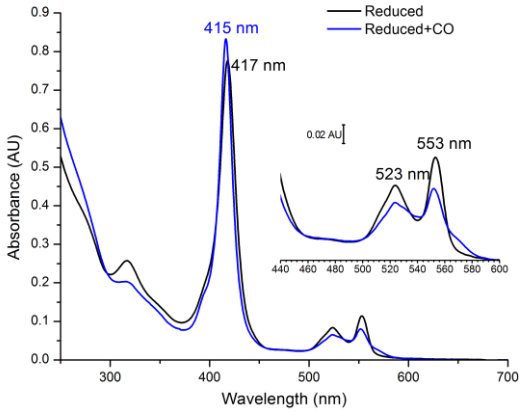

e *Ks*NaxL C32M/ NaxS wt

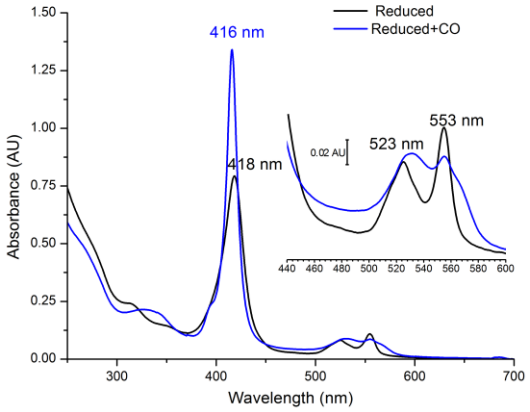

f *Ks*NaxL wt/ NaxS C101M

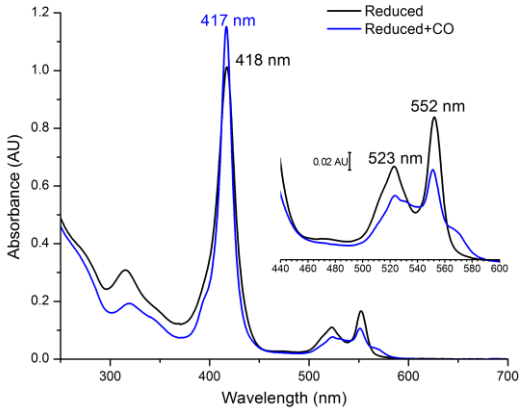

Figure 4.8 Carbon monoxide (CO) Binding to *Ks*NaxLS, its Subunits and Distal Ligand Mutants
Sample preparation was done in a glove box under N_2 atmosphere and spectra were measured essentially as performed for NO-treated samples. CO gas was transferred from a lecture bottle (AirLiquide, Ludwigshafen, Germany) into a balloon which was transferred into the glove box for further use. 1-2 mL buffer containing 25 mM HEPES pH 7.5 and 25 mM KCl was bubbled by several mL of CO. Protein solutions were reduced by 1 mM Ti(III)citrate and buffer exchanged to 25 mM HEPES pH 7.5 and 25 mM KCl using a NAP-5 desalting column (GE Healthcare, Buckinghamshire, UK). Wild type *Ks*NaxLS complex and *Ks*NaxS stock solutions were kept with 1 mM Ti(III)citrate, since they were highly sensitive to air-oxidation after the reducing agent was removed. 75 µL of protein stock solutions were mixed with 75 µL freshly CO-bubbled buffer in 1 cm path length quartz cuvettes (Hellma Analytics, Germany) and sealed using rubber stoppers.
a) NaxLS wild type complex; **b)** *Ks*NaxL; **c)** NaxS; **d)** *Ks*NaxL C32M/ NaxS C101M; **e)** *Ks*NaxL C32M/ NaxS and **f)** *Ks*NaxL wt/ NaxS C101M.

In order to investigate CO-binding, the *Ks*NaxLS complex, its components and distal ligand mutants were first reduced using 1 mM Ti(III)citrate and then incubated with buffer containing dissolved CO. As shown in figure 4.8, the Soret bands of the *Ks*NaxLS complex, its components and distal ligand mutants sharpened and increased in their intensities. The Soret band shifted from 417 nm to 415 nm in case of the *Ks*NaxLS complex, both its subunits and the *Ks*NaxL C32M/ NaxS wt mutant upon interaction with CO. Two broad bands around 540 nm and 570 nm also appeared, replacing the α- and β-bands in all cases (Fig 4.8 a, b, c and e). The sharpening and increase in the intensities of the Soret bands in case of the *Ks*NaxL C32M/ NaxS C101M and *Ks*NaxL wt/ NaxS C101M mutants were less pronounced when compared with others. Moreover, the α- and β-bands of these mutants did not completely disappear in both of these mutants upon interactions with CO (Fig 4.8 d and f).

4.2.1.5 Pull-down Assay

The C-terminally hexahistidine-tagged *Ks*NaxLS complex, *Ks*NaxL and *Ks*NaxS (section 4.2.1.1) as well as Kustc0563 (section 4.2.2.1) were used as "bait" proteins. Aliquots of 50 µL Ni-IDA beads were pre-saturated with the bait proteins in order to avoid unspecific binding (for detailed procedure see section 2.2.4.5). Ni-IDA beads without a bait protein were used as negative control. Ni-IDA beads loaded with the individual bait proteins were incubated with cleared lysate prepared from *Kuenenia stuttgartiensis* cells, followed by extensive washing and elution of the the bait proteins using an imidazole-containing buffer. SDS-PAGE analysis of the eluted bait proteins (Fig 4.9) followed by mass spectrometric analyses of the co-eluted protein bands showed that only *Ks*NaxLS was able to pull down all three subunits of the hydrazine synthase (HZS) complex. In addition, a protein band around 200 kDa in many lanes appeared which belonged to *Ks*HDH. However, *Ks*HDH was most probably bound non-specifically as it was also bound to the Ni-IDA beads without any bait protein. No additional

bands were observed for *Ks*NaxL, *Ks*NaxS and Kustc0563. Similar results were obtained when purified HZS protein solution was incubated with bait proteins loaded onto Ni-IDA beads.

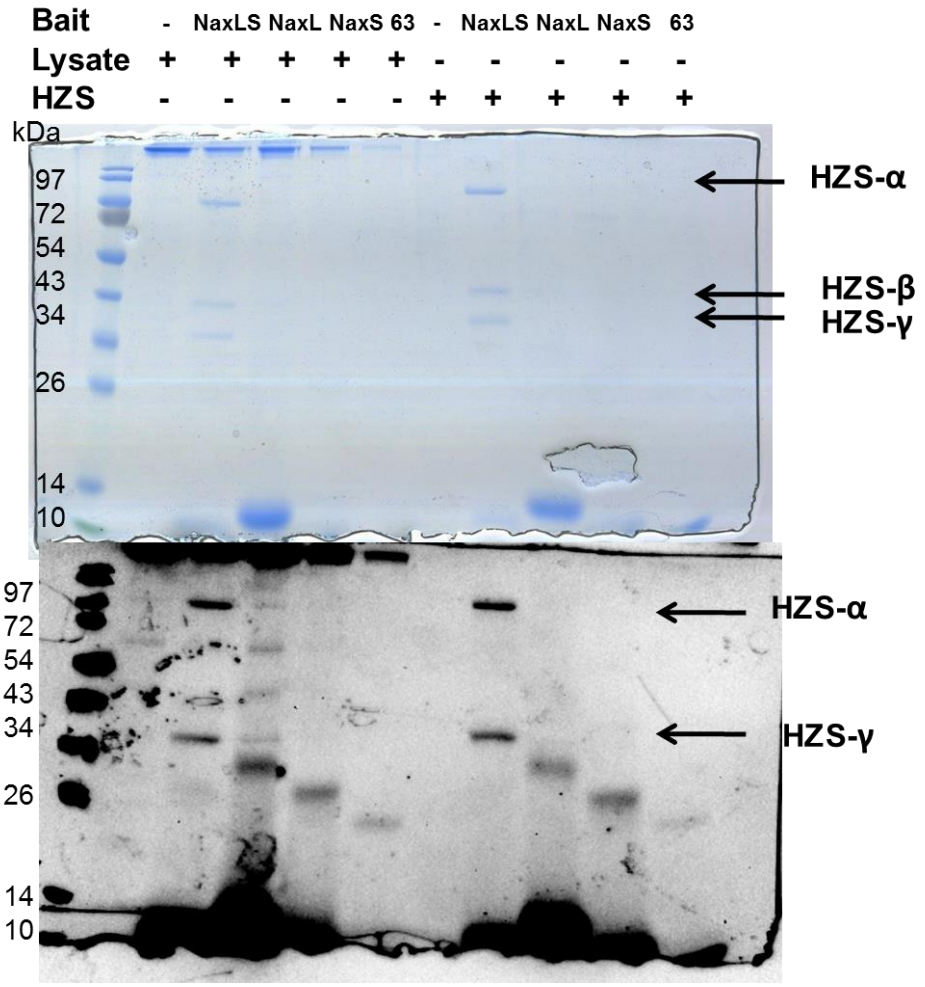

Figure 4.9 SDS-PAGE Analysis of Pull-down Assays using NaxLS and its Components as "Bait"
The eluted proteins from the pull-down assay were analyzed by 15 % SDS-PAGE. The upper and lower sections show Coomassie stained and heme stained gels, respectively. "**-**" and "**+**" indicate the absence and presence of certain components, respectively. "63" indicates Kustc0563. The lysate was prepared from a suspension of *Kuenenia stuttgartiensis* cells in a buffer containing 25 mM HEPES, pH 7.5, 150 mM NaCl and 0.4 % Triton X-100, followed by sonication, incubation on ice (15 min) and centrifugation (16,000 x g, 15-20 min, 4 °C). Triton X-100 was used in order to solubilize membrane proteins. Pure HZS solution was supplied in a buffer containing 50 mM HEPES pH 7.5 and 150 mM NaCl. The cleared lysate or HZS protein solution was incubated with Ni-IDA beads pre-loaded with bait proteins for 1.5-2.0 hours at 4 °C while rotating. The beads were washed with several fold excess of buffer (50 mM HEPES pH 7.5, 150 mM NaCl) and the bait proteins were eluted using elution buffer (50 mM TrisCl pH 8.0, 300 mM NaCl, 250 mM imidazole). Only the lane containing the *Ks*NaxLS complex showed all three subunits of HZS after Coomassie staining. In the heme stain of the same lane only the two c-type heme-containing diheme subunits (HZSα and HZSβ) were visble.

4.2.1.6 Crystallization of the *Ks*NaxLS Complex and its Mutants

Initial precipitant screening for the native *Ks*NaxLS complex and its recombinantly produced mutants (*Ks*NaxL C32G/ NaxS wt and *Ks*NaxL C32M/ NaxS C101M) resulted in several crystallization conditions containing PEG. For large scale hanging drop vapor-diffusion crystallization setups 1 µL *Ks*NaxLS (wild type complex or mutants) protein stock (A_{280}^{1cm}= 6–7 in 25 mM HEPES/KOH, pH 7.5, 25 mM KCl) was mixed with 1 µL precipitant solution containing 20–25 % (w/v) PEG 3000 and 0.1 M sodium citrate, pH 5.5 equilibrated against 800 µL reservoir solution in 24-well Linbro plates. Thin, light brown plates with a length of 300–600 µm appeared after one day at 20 °C (Figure 4.10) for wild type and mutant complexes. *Ks*NaxL C32M/ NaxS wt and *Ks*NaxL wt/ NaxS C101M could also be crystallized in the same conditions, whereas the *Ks*NaxL wt/ NaxS C101G mutant could not. There was only one condition (0.2 M zinc acetate and 20 % (w/v) PEG 3350) from initial screening in which crystals of this mutant could be obtained, which, unfortunately, could not be optimized further. All the crystals from wild type and mutant complexes were cryo-protected by short soaking in reservoir solution supplemented with 20 % (v/v) ethylene glycol followed by flash cooling in liquid nitrogen.

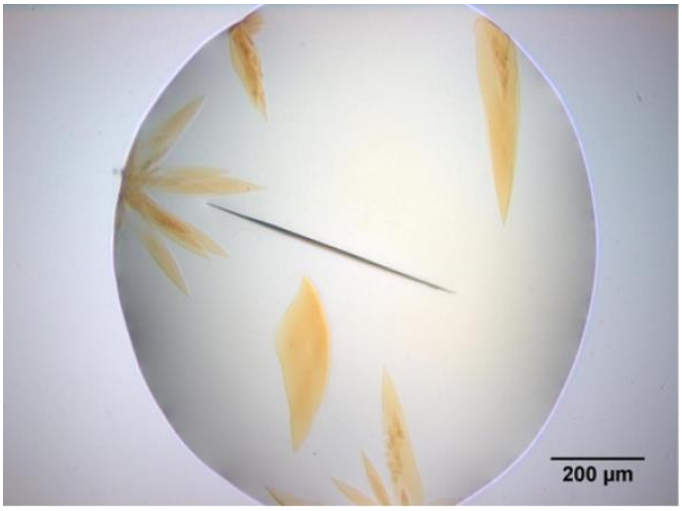

Figure 4.10 Crystallization of *Ks*NaxLS Wild Type and Mutant Complexes.
The figure shows a representative example of crystals from the wild type *Ks*NaxLS complex. Similarly shaped crystals were obtained from the mutants. The red-brown colored crystals were grown in 24-well hanging drop vapour diffusion setups at 20 °C. Droplets of 1 µL *Ks*NaxLS (wild type or mutants) stock at (A_{280}^{1cm} = ~7.0 and A_{420}^{1cm} = ~27, stored in 25 mM HEPES/KOH pH 7.5, 25 mM KCl) were mixed with 1 µL precipitant solution on glass cover slips, which were placed over reservoir wells containing 800 µL of precipitant solution. Both wild type and mutants crystals were grown in PEG 3000 (20-25 % w/v) and 50-100 mM of sodium citrate pH 5.5 within one day. In all cases crystals were very thin, semi-transparent plates.

4.2.1.7 Structure Determination and Refinement

Crystals of the natively purified *Ks*NaxLS complex displayed orthorhombic $P2_12_12$ space group symmetry with unit cell dimensions of a = 44 Å, b = 131 Å, c = 46 Å, α= γ = β = 90°. A native data set (λ = 1.000 Å) with a resolution limit of 1.7 Å as well as a highly redundant anomalous data set collected near the Fe K-edge (1.7433 Å, 7,112.0 eV) at a wavelength of 1.7 Å (Table 4.2) were processed with XDS (Kabsch 2010).

The phase problem was solved by the method of single anomalous dispersion (SAD) using the anomalous signal of the heme iron (anomalous scattering factor f'' = 3.770 electrons at λ = 1.7 Å; http://skuld.bmsc.washington.edu/cgi-bin/edgeplots). Phase determination was carried out by AutoSHARP (Vonrhein 2007). SHELXD (Schneider 2002) identified two heavy atom sites, which were used by SHARP for phasing, resulting in a figure-of-merit (FOM) of 0.297 before solvent flattening. Density modification with DM (Cowtan 1999) resulted in a readily interpretable electron density map into which protein main and side chains as well as the c-type heme cofactors could be manually built using COOT (Emsley 2004). The asymmetric unit contained a *Ks*NaxLS heterodimer with a solvent content of 38 % as calculated according to (Matthews 1968). Several cycles of maximum-likelihood refinement of the initial model against the 1.7 Å native data set using REFMAC (Murshudov 1997) and model building in COOT including the modelling of water molecules and potassium ions resulted in a working R-factor of 21.4 % (R_{free} = 23.8 %). A model of the *Ks*NaxL C32G/ NaxS wt complex was refined against the 1.9 Å data set followed by rebuilding in COOT. Phases for the 2.0 Å dataset of the *Ks*NaxL C32M/ NaxS C101M complex were obtained by molecular replacement using the structural coordinates from the wild type complex followed by refinement in REFMAC and model building in COOT. Iterative model building and refinement of *Ks*NaxL C32G/ NaxS wt and *Ks*NaxL C32M/ NaxS C101M resulted in R-factors of 20.2 % (R_{free} = 22.7 %) and 21.1 % (R_{free} = 26.5 %), respectively. The other two mutants *Ks*NaxL C32M/ NaxS wt and *Ks*NaxL wt/ NaxS C101M were also processed as described for *Ks*NaxL C32G/ NaxS wt, but there were no differences when compared with *Ks*NaxL C32M/ NaxS C101M. Therefore, they are not described here. Unfortunately, several peaks in the mF_o-DF_c difference Fourier map, likely representing partially ordered solvent components as well as a loop in the *Ks*NaxL subunit (Leu48 to Gly54) in all the structures could not be properly interpreted, which explains the elevated R-factors. The models displayed excellent stereochemistry as indicated by Ramachandran statistics and by analysis using MOLPROBITY (Davis 2007) as indicated in table 4.2.

Table 4.2 X-ray data statics of *Ks*NaxLS wild type and mutant complexes

Data set	***Ks*NaxLS wt Fe-SAD**	***Ks*NaxLS wt native**	***Ks*NaxL C32M/ NaxS C101M native**	***Ks*NaxL C32G/ NaxS wt native**
Data collection				
Space group	$P2_12_12$	$P2_12_12$	$P2_12_12$	$P2_12_12$
Unit cell dimensions				
a, b, c (Å)	44.11, 131.06, 46.08	44.30, 130.36, 45.37	44.68, 130.43, 45.66	44.24, 131.45, 45.33
α, β, γ (°)	90, 90, 90	90, 90, 90	90, 90, 90	90, 90, 90
Wavelength (Å)	1.700	1.000	1.000	1.000
Resolution range (Å) [a]	40.0-2.3 (2.4-2.3)	40.0-1.7 (1.8-1.7)	50.0-2.0 (2.1-2.0)	50.0-1.9 (2.0-1.9)
Reflections measured [a]	454,148 (47,909) [f]	184,876 (21,515)	116,845 (15,895)	182,263 (25,654)
Reflections unique [a]	22,941 (2,727) [f]	29,424 (4,287)	18,722 (2,465)	21,517 (2,996)
Completeness (%) [a]	100 (99.9) [f]	98.8 (93.4)	99.6 (99.4)	99.6 (99.5)
Redundancy N [a]	19.8 (17.6) [f]	6.3 (5.0)	6.2 (6.4)	8.5 (8.6)
I/σI [a]	28.1 (5.6) [f]	17.6 (2.2)	13.7 (2.0)	19.2 (3.0)
R_{merge} (%) [a, b]	8.4 (54.8) [f]	5.5 (54.7)	11.3 (67.7)	6.8 (90.4)
R_{meas} (%) [a, c]	8.6 (56.5) [f]	6.0 (61.0)	12.3 (73.6)	7.3 (96.0)
$CC_{1/2}$ (%) [d]	99.9 (98.3)	99.9 (91.8)	99.7 (91.7)	99.9 (91.7)
CC* (%) [e]	99.9 (99.5)	99.9 (97.8)	99.9 (97.8)	99.9 (97.8)
Refinement				
Resolution range in refinement (Å)	65.5-2.3	65.2-1.7	65.7-2.0	65.7-1.9
Number of reflections in refinement	11,843	27,973	17,722	20,436
R_{work}/ R_{free} (%) [g]	21.1/ 26.6	21.4/ 23.8	21.1/ 26.5	20.2/ 22.7
Protein residues	210 (1,823)	210 (18,77)	211 (1,824)	211 (1,847)
Ligands (no. of atoms)	2 heme (86)	2 heme (86)	2 heme (86)	2 heme (86)
Water molecules	119	162	113	136
Overall B-factor (Å^2)	37.3	30.7	37.4	35.1
Rmsd bonds (Å)	0.011	0.016	0.011	0.009
Rmsd angles (°)	2.300	1.546	1.421	2.089
Ramachandran plot [h]				
Most favoured (%)	96.1	96.5	96.6	97.6
Additionally allowed (%)	3.4	3.5	3.4	2.4
Disallowed (%)	0.5	0	0	0

Legend to Tables 4.2

a) Values of the highest resolution shell are given in brackets.

b) $R_{merge} = \sum_h \left| \langle I_h \rangle - I_{h,i} \right| / \sum_h \sum_i^{n_h} I_{h,i}$, where I_i is the intensity of a reflection and $\langle I_h \rangle = \frac{1}{n_h} \sum_i^{n_h} I_{h,i}$ is the mean value of that reflection and the summations are over all reflections h.

c) $R_{meas} = \sum_h \sqrt{\frac{N}{N-1}}\ R_{merge}$ Redundancy-independent merging R factor (Diederichs 1997).

d) $CC_{1/2} = \sum_{i=1}^{n} \left(\left(x_i - \bar{x} \right) \left(y_i - \bar{y} \right) \right) \Big/ \sqrt{\sum_{i=1}^{n} \left(x_i - \bar{x} \right)^2 \sum_{i=1}^{n} \left(y_i - \bar{y} \right)^2}$ Pearson's correlation coefficient between merged intensity estimates $I_{h,i}$ (x_i, y_i) and $\langle I_h \rangle$ ($\bar{x}$, $\bar{y}$) from half data sets x and y.

e) $CC^* = \sqrt{\frac{2CC_{1/2}}{1+CC_{1/2}}}$ Estimated correlation coefficient of the merged dataset against the true (usually unmeasurable) intensities (Karplus 2012).

f) Considering Friedel mates as individual reflections.
g) $R_{work} = \sum_h |F_{obs} - F_{calc}| / \sum_h F_{obs}$ (working set, no σ cut-off applied) R_{free} is calculated the same way as R_{work}, but for a reflection test set with 5 % of the reflections excluded from refinement.
h) Ramachandran analysis was performed using COOT (Emsley 2004).

4.2.1.8 Overall Structure of the *Ks*NaxLS Complex

The 1.7 Å resolution X-ray structure of the *Kuenenia stuttgartiensis* NaxLS complex contains one heterodimer consisting of one *Ks*NaxL and one *Ks*NaxS subunit in the asymmetric unit (Figure 4.11). The overall complex is Mauser pistol-shaped (Fig 4.11 a and b) where *Ks*NaxL forms the 'barrel' of the pistol and *Ks*NaxS the 'handle'. The *Ks*NaxL subunit is an elongated four-helix bundle belonging to the class II c-type cytochrome family (Fig 4.12 a). *Ks*NaxS possesses a typical class I cytochrome c fold consisting of six small- to medium-sized α-helices (Fig 4.12 b).

The two subunits in the complex interact mostly *via* hydrogen bonds and salt bridges. The contact surface between the two subunits is formed by regions Asp82 to Tyr92 and Arg115 to Thr129 of *Ks*NaxL as well as Glu29 to Gly61 and Val119 to Lys126 of *Ks*NaxS. A large, buried surface area of 2,120 $Å^2$ (out of in total 10,950 $Å^2$) is made upon complex formation. This assembly keeps the two hemes at an edge-to-edge distance of 18 Å (Fig 4.11 c).

The electrostatic surface of the *Ks*NaxLS complex shows highly positively charged areas surrounded by negatively charged patches. The heme in *Ks*NaxL is completely surrounded by a big positively charged patch which continues at the opposite side of the molecule (when rotating along the length of the 'barrel') which is surrounded by negatively charged areas (Fig 4.13 a). On the contrary, the heme site in *Ks*NaxS is also surrounded by a positively charged area but only at one side (towards the distal heme face; Fig 4.13 b), while the other side is neutral or negatively charged (proximal heme face).

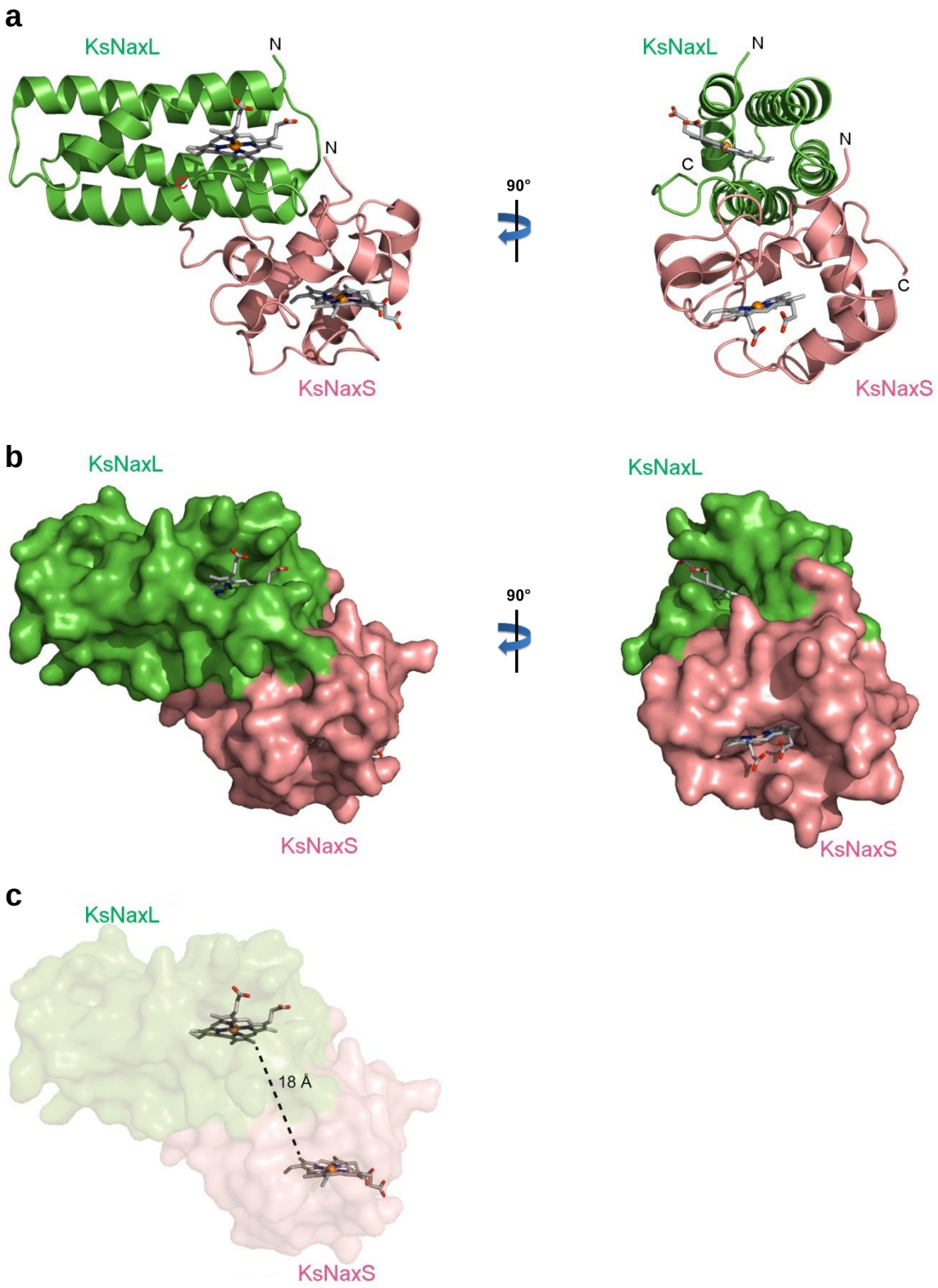

Figure 4.11 Overall structure of the *Ks*NaxLS wild type complex at 1.7 Å resolution
a) Cartoon representation of the complex. **b)** Surface representation of the complex, the hemes in both subunits are exposed. **c)** Semi-transparent surface representation and edge-to-edge distance between the two c-type hemes which is 18 Å. *Ks*NaxL is colored in green, *Ks*NaxS in salmon.

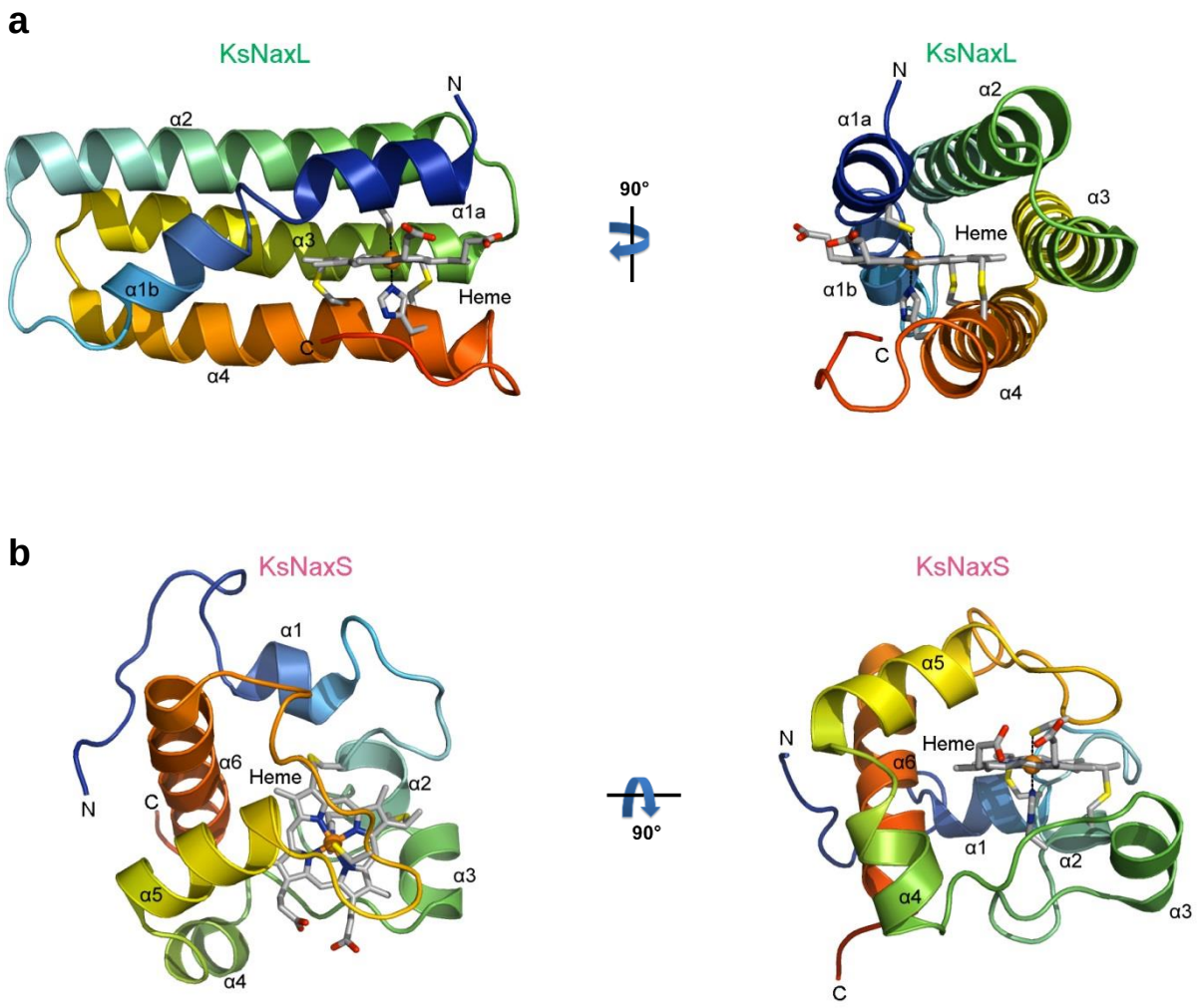

Figure 4.12 Structures of the Individual *Ks*NaxL and *Ks*NaxS Subunits
The molecules are rendered as cartoons and are rainbow-colored from their N-terminus (blue) to their C-terminus (red). **a)** *Ks*NaxL possesses all characteristics of a class II c-type cytochrome such as a four-helix bundle fold, a C-terminal heme binding motif and a distal ligand derived from a residue near the N-terminus. **b)** *Ks*NaxS displays a typical class I cytochrome c fold and a heme binding motif located near the N-terminus while its distal ligand is provided by an amino acid close to the C-terminus.

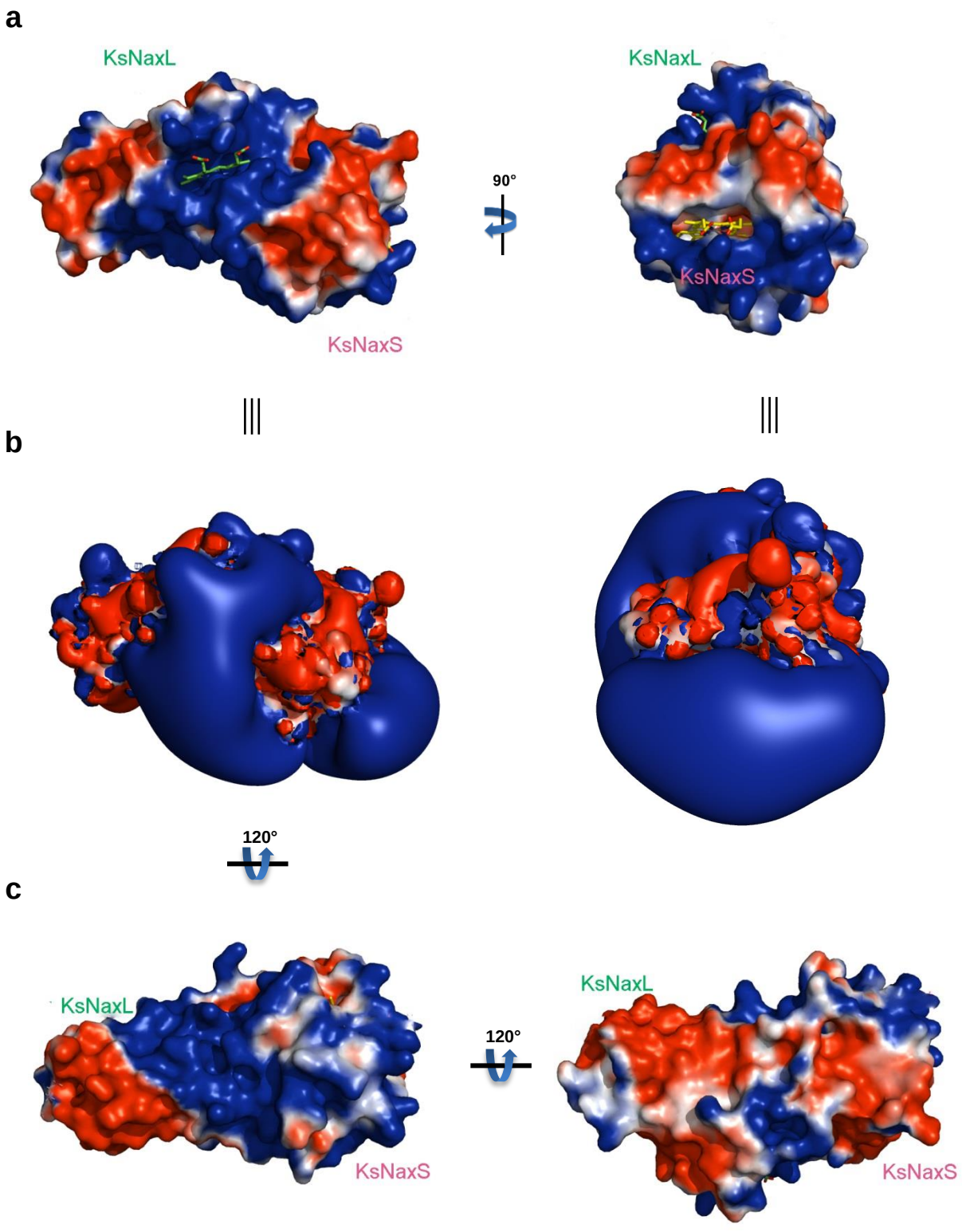

Figure 4.13 Surface Electrostatics of the *Ks*NaxLS Complex
Figure a and c represent surface electrostatic potentials of the *Ks*NaxLS complex in different orientations. Positive potentials are shown in blue and negative potentials are shown in red. Figure b represents electrostatic isosurfaces at contour levels of +1 kT/e and -1 kT/e for positive and negative potentials, respectively.

4.2.1.9 C-type Heme Sites in *Ks*NaxL and *Ks*NaxS

The c-type hemes in both subunits are highly solvent exposed (Fig 4.11 b and 4.14) and hexa-coordinated with histidines serving as proximal ligands and cysteines as distal ligands. In *Ks*NaxL the heme binding motif ($C^{120}RNCH^{124}$) is located near the C-terminus of the protein sequence whereas the distal cysteine (Cys32) ligand originates from the N-terminal part (Fig 4.17 a). The opposite scenario is true for *Ks*NaxS where the heme binding motif ($C^{54}YYCH^{58}$) is located close to the N-terminus and the distal cysteine ligand (Cys101) is harbored near the C-terminus (Fig 4.17 b). The distal environment of the *Ks*NaxL heme is lined by many hydrophilic residues (Gln28, Ser73, Tyr83 and Asn87) on one side (where the propionate groups of the hemes are located) and hydrophobic residues (Met35, Trp36 and Val70) on the opposite side. The environment at the proximal face of the heme is formed by C-terminal residues namely Leu133, Val134 and the terminal Pro135 residue (Fig 4.14 a, 4.15 c). The heme in *Ks*NaxS is surrounded by several aromatic amino acids (such as Tyr43, Phe71, Phe76, Phe81, His93 and Tyr104) as well as other hydrophobic residues such as Met35, Val73 and Ile94 at both distal and proximal sides (Fig 4.14 d, 4.15 a). All of these residues make the *Ks*NaxS heme pocket more hydrophobic when compared with that of *Ks*NaxL.

The distal ligand mutants *Ks*NaxL C32G/ NaxS wt and *Ks*NaxL C32M/ NaxS C101M do not change the heme environment radically. Mutation of Cys32 to methionine in *Ks*NaxL causes Gln28 to move away whereas in the wild type it points towards the iron-center of the heme (Fig 4.14 b, 4.15 d). This movement causes helix α1 to move slightly upwards compared to the wild type. On the contrary, the *Ks*NaxL C32G crystal structure does not show evidence for any conformational change. However, a water molecule occupies the vacant distal heme site (Fig 4.14 c, 4.15 e). Upon mutation of Cys101 to methionine in *Ks*NaxS, a histidine residue (His93), which is commonly bound *via* a hydrogen bond to a nearby water molecule in the wild type, rotates away and the water molecule is displaced (Fig 4.14 e, 4.15 b).

There were no changes observed in the overall structures of *Ks*NaxL C32G/ NaxS wt and *Ks*NaxL C32M/ NaxS C101M complexes compared with wild type complex (Fig 4.16).

a *Ks*NaxL wild type

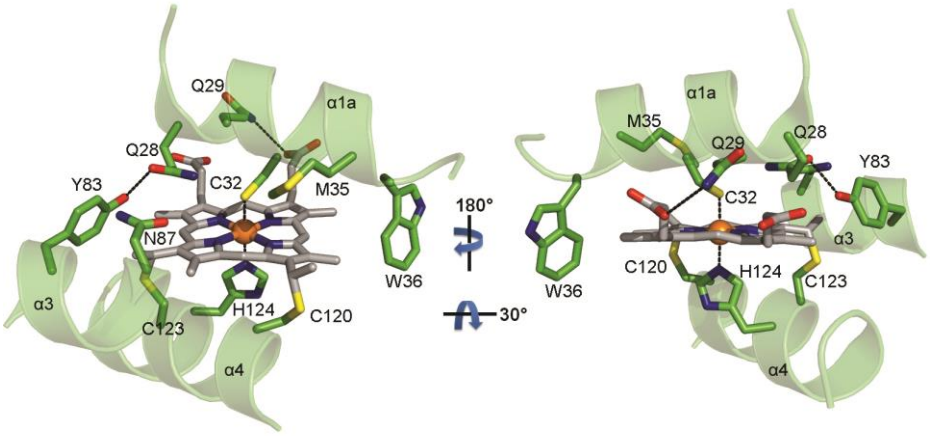

b *Ks*NaxL C32M

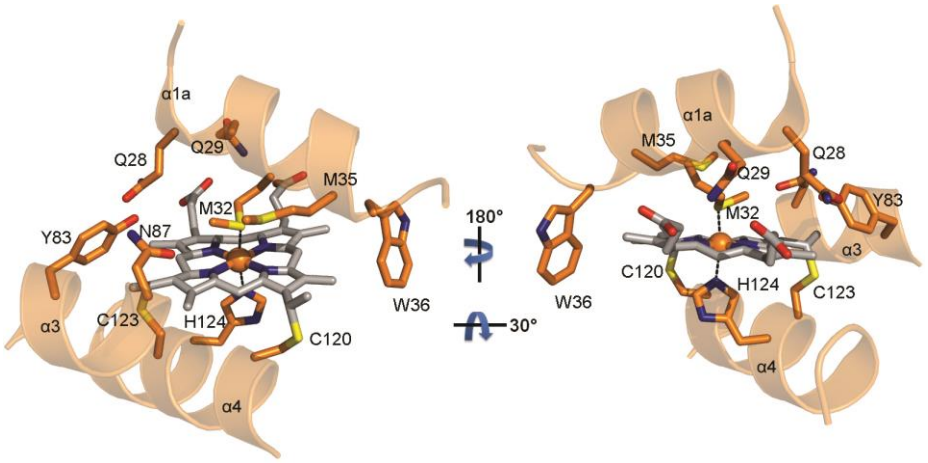

c *Ks*NaxL C32G

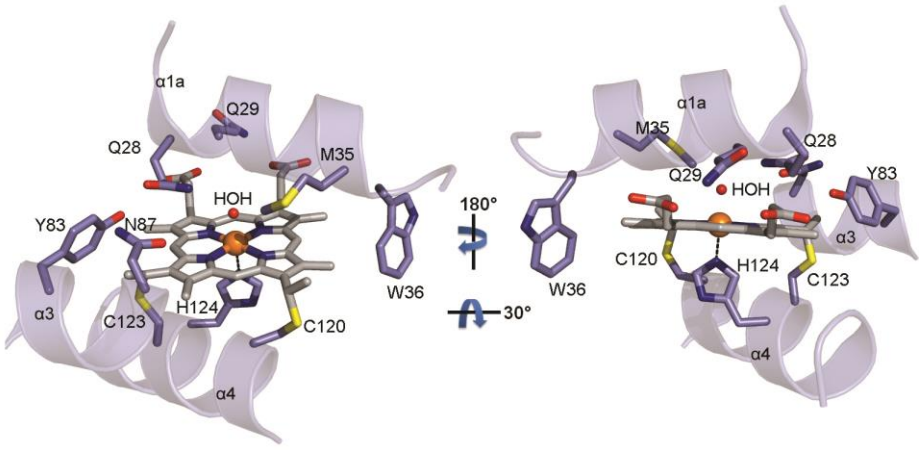

d *Ks*NaxS wild type

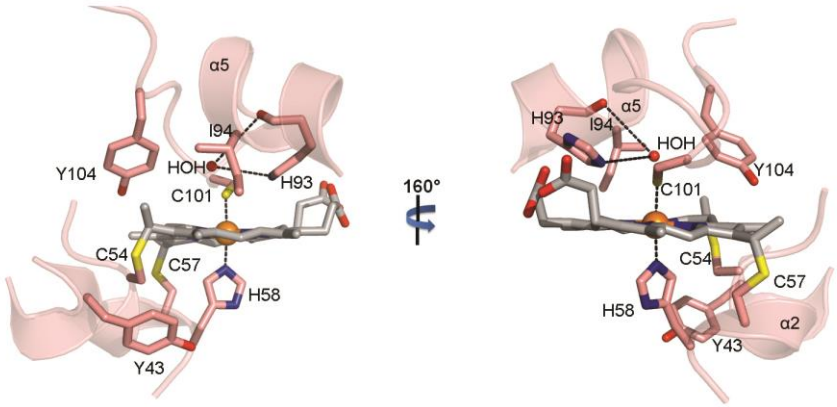

e *Ks*NaxS C101M

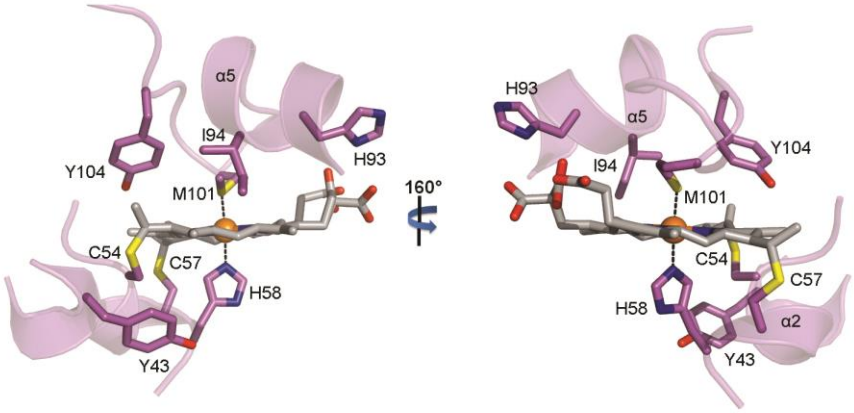

Figure 4.14 Heme Environments of *Ks*NaxL and *Ks*NaxS Wild Type and distal ligand Mutants within the *Ks*NaxLS Complex.
The figures are rendered as cartoon and stick model. Only the residues in close vicinity of the heme are shown. **a)** *Ks*NaxL wild type heme site. **b)** *Ks*NaxL C32M mutant heme site. Note the relative orientations of residues Q28 and M35 with respect to their orientations in figure a. The side chains of Q28 and M35 rotate away from the heme center. **c)** *Ks*NaxL C32G mutant heme site. The distal site of the heme is now occupied by a water molecule while the side chains of the other residues in the vicinity are in the same orientation compared to the wild type (figure a). **d)** *Ks*NaxS wild type heme site. **e)** *Ks*NaxS C101M mutant showing methionine as the distal ligand. The side chain of H93 rotates away and a water molecule in the distal heme pocket is displaced compared to the wild type (figure d).

a *Ks*NaxS wild type

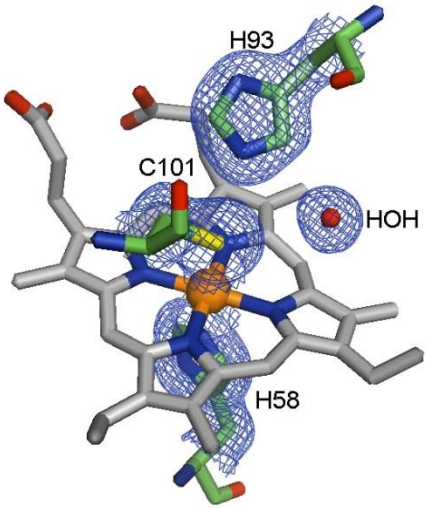

b *Ks*NaxS C101M

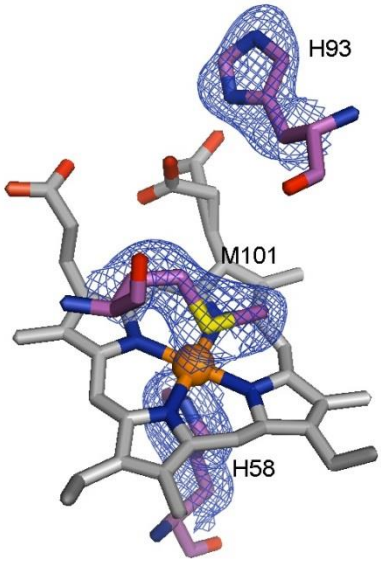

c *Ks*NaxL wild type

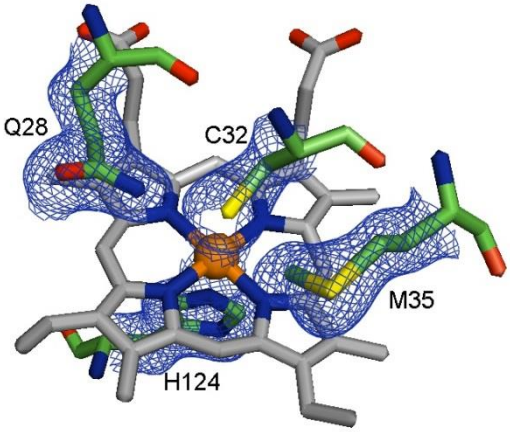

d *Ks*NaxL C32M

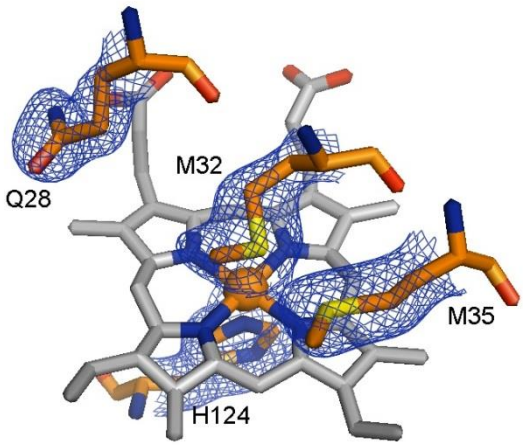

e *Ks*NaxL C32G

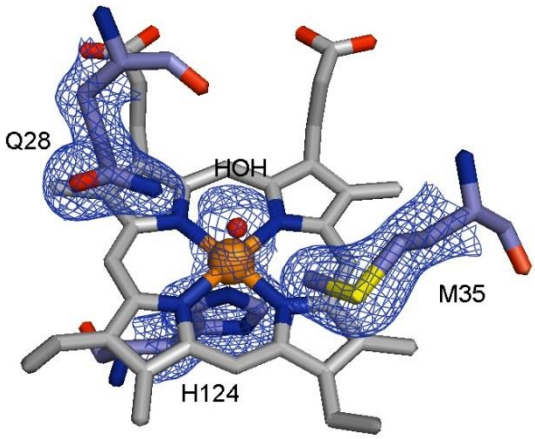

Figure 4.15 Heme Environments of *Ks*NaxL and *Ks*NaxS Wild Type and Distal Ligand Mutants within the *Ks*NaxLS Complex
The individual heme sites of *Ks*NaxLS wild type and mutants are shown as stick model overlaid with $2mF_o$-DF_c maps (blue mesh) at a contour level of 1 σ. For clarity, the electron density maps were drawn only around selected amino acid residues, not around the heme. **a)** The distal cysteine (C101) residue, a water molecule and nearby histidine (H93) residue of the NaxS wild type heme site. **b)** H93 turns away while the water molecule is displaced in the NaxS C101M heme site of the NaxL C32M/ NaxS C101M complex. **c)** Heme site of the NaxL subunit in the wild type complex with distal cysteine (C32), methionine (M35) and glutamine (Q28) residues. **d)** Q28 and M35 rotate away when cysteine is substituted by methionine in the NaxS C32M heme site within the *Ks*NaxL C32M/ NaxS C101M complex. **e)** Heme site of *Ks*NaxL C32G within the *Ks*NaxL C32G/ NaxS wt complex. The vacant distal site is occupied by a water molecule. There were no further changes observed in the positions of the side chains of nearby residues.

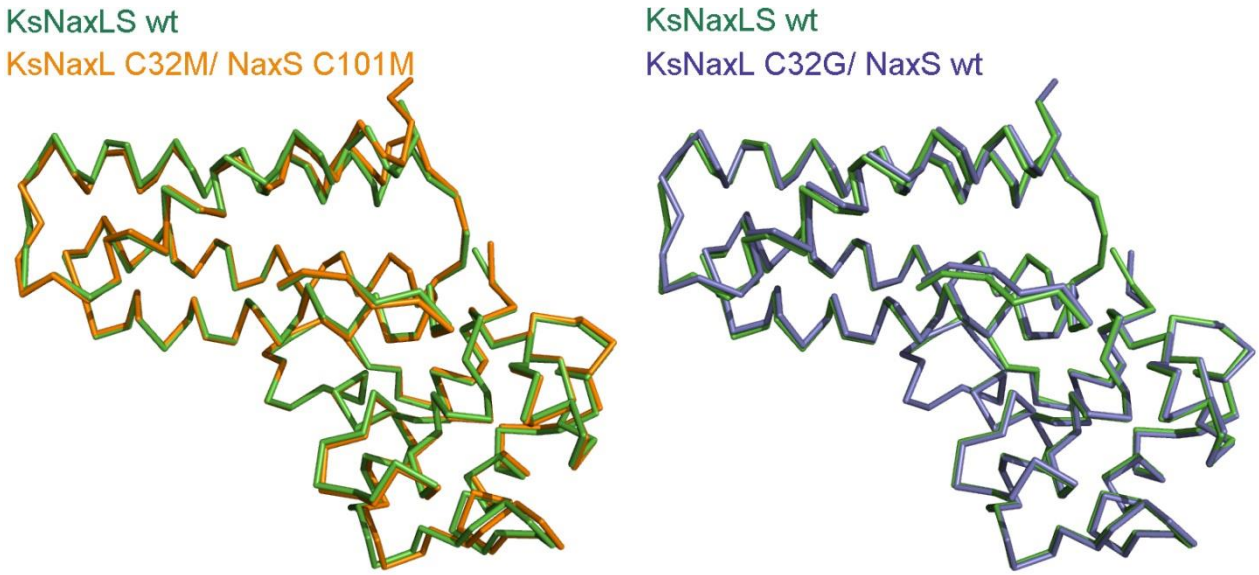

Figure 4.16 Structural Superposition of *Ks*NaxLS Wild Type and Mutants
The molecules are rendered as Cα traces. Both *Ks*NaxL C32M/ NaxS C101M and *Ks*NaxL C32G/ NaxS wt mutants show no difference in their overall structure as compared with the *Ks*NaxLS wild type (wt) complex (structural rmsd 0.6 Å and 0.4 Å for 210 residues each, respectively).

a

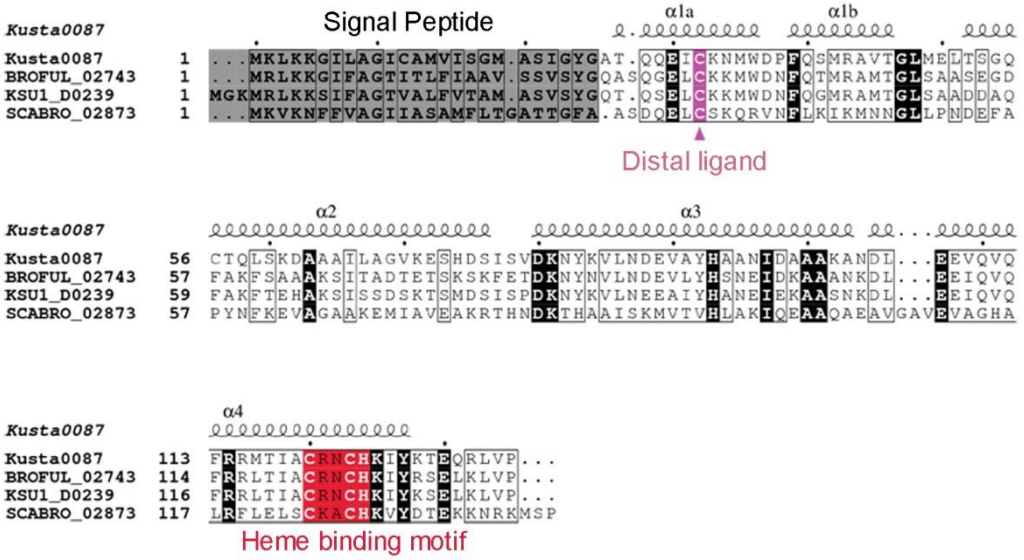

b

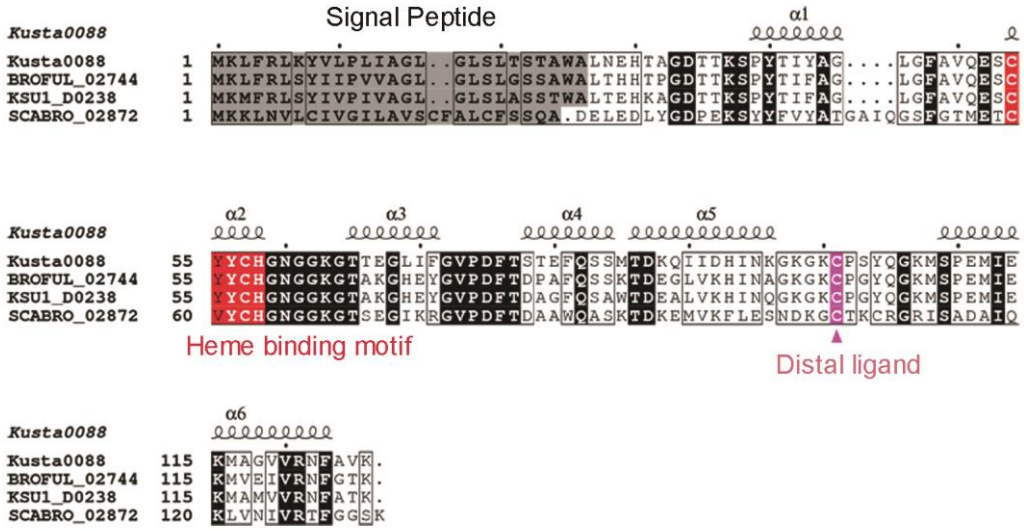

Figure 4.17 Sequence alignments of *Ks*NaxL and *Ks*NaxS homologues.
a) The protein sequence of *Kuenenia stuttgartiensis* NaxL (Kusta0087; WP_099326125.1) was aligned to its orthologues from *Brocadia fulgida* BROFUL_02743 (KKO18555.1), *Jettenia caeni* (Planctomycete KSU-1) KSU1_D0239 (WP_007222634.1) as well as *Scalindua brodae* SCABRO_02873 (KHE91380.1).The sequence identities to Kusta0087 are 55 % for BROFUL_02743, 58 % for KSU1_D0239 and 26 % for SCABRO_02873.
b) Similarly, *Kuenenia stuttgartiensis* NaxS (Kusta0088; WP_099326126.1) was also aligned to its homologues. It shares 75 % sequence identity each with BROFUL_02744 (KKO18556.1) and KSU1_D0238 (WP_007222633.1) and 38 % sequence identity with SCABRO_02872 (KHE91379.1). Alignments were performed using ClustalO (Sievers 2011) and secondary structure elements were manually assigned based on the *Ks*NaxLS complex structure. Fully conserved sequences are marked black. The CXXCH c-type heme binding motifs are highlighted in red. The predicted signal peptides are highlighted in grey (but experimentally confirmed in case of both *Ks*NaxL and *Ks*NaxS). The distal cysteine ligands of the hemes are highlighted in pink (with pink triangle). The figure was prepared using ESPript (Gouet 1999).

4.2.2 The Monoheme Cytochromes c Kustc0563 and Kustc0562

4.2.2.1 Expression and Purification

Both C- and N-terminally hexahistidine-tagged Kustc0563 constructs were cloned in pUC19 based vectors. The construct with a C-terminal His-tag was cloned in a similar way as described for the individual subunits of *Ks*NaxL and *Ks*NaxS (section 4.2.1.1). The N-terminally His-tagged construct was cloned into a pUC19 derivative with some further modifications. The final construct contained the *Shewanella oneidensis* MR-1 small tetraheme cytochrome c signal peptide (STC-SP) followed by a hexahistidine-tag, a TEV protease cleavage site and the kustc0563 gene without its endogenous signal peptide (appendix 1). Both C- and N-terminally His-tagged Kustc0563 proteins were constitutively expressed in *Shewanella oneidensis* MR-1. Purification by Ni-NTA affinity and gel filtration chromatography yielded sufficient amounts (7-8 mg protein per litre of *S. oneidensis* culture) of homogenous protein preparations of both constructs (Fig 4.18) for structural and biophysical studies. The N-terminal His-tag was removed using TEV protease (purification not shown). C-terminally His-tagged Kustc0563 is termed as Kustc0563_CHis whereas tag-free protein obtained by cleavage of the N-terminal His-tag by TEV-protease is denoted as Kustc0563nt or simply Kustc0563. Similarly, tag-free Kustc0562 (by TEV protease cleavage of N-terminally 6xHis-tagged protein) was successfully expressed and purified by Josephine Bock.

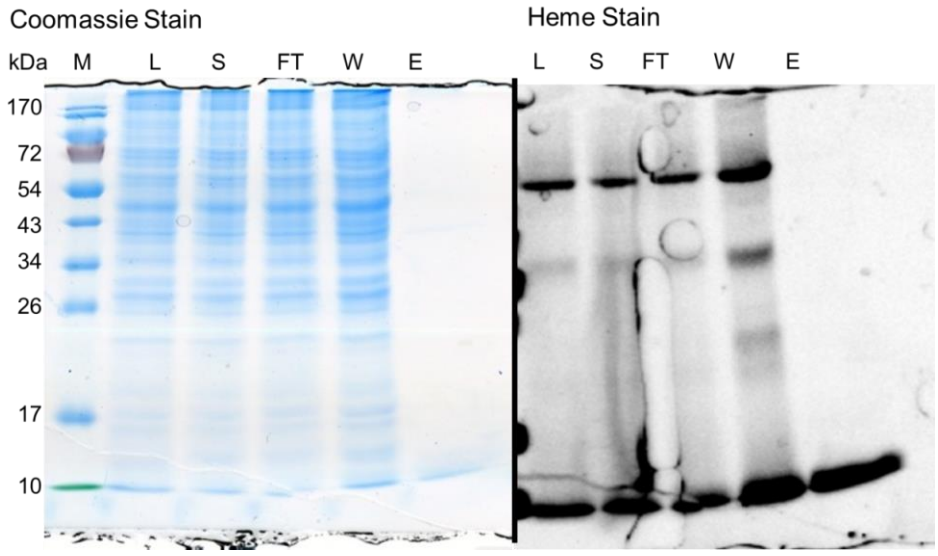

Figure 4.18 15 % SDS-PAGE Analysis of the Kustc0563_CHis Purification
Kustc0563_CHis was purified by affinity chromatography using Ni-NTA beads followed by gel filtration. The first step is shown in the figure. The following abbreviations are used: M: marker; L: lysate; S: supernatant; FT: flow through; W: wash and E: Ni-NTA eluate (for details see section 2.2.3.2). The eluate was pooled, concentrated and applied to a Superdex 75 (10/300) gelfiltration column (GE healthcare, Uppsala, Sweden).

4.2.2.2 UV-Vis Spectroscopy

The UV-Vis spectra of as-isolated, oxidized and reduced Kustc0563 showed similar behavior to that described by (Huston 2007). The spectrum of as-isolated Kustc0563 indicated that the protein remained partially reduced with the Soret peak at 413 nm and α- and β-bands at 551 nm and 523 nm, respectively. The α- and β-bands readily disappeared when few grains of ammonium persulphate ($(NH_4)_2S_2O_8$) were added which was accompanied by a shift of the Soret band to 409 nm. The intensities of both α- and β-bands increased and the Soret band was further red-shifted to 416 nm when sodium dithionite was added to as-isolated Kustc0563 indicating that the protein was completely reduced (Fig 4.19 a). According to Huston *et al.* (2007) heterologously purified Kustc0563 showed distinct UV-Vis spectroscopic features under high and low salt conditions. At low salt concentrations Kustc0563 showed well defined α- and β-bands which became relatively broad under high salt conditions (400 mM NaCl). However, as shown in figure 4.19 b, no difference(s) in the spectra recorded in high and low salt buffers could be observed in the present study.

The as-isolated form of Kustc0562 was also partially reduced as was evident from the presence of α- and β-bands at 553 nm and 523 nm, respectively. When 100 mM imidazole was added to the as-isolated protein, the Soret band shifted from 416 nm to 406 nm accompanied by the disappearance of the α- and β-bands which indicated binding of imidazole at the heme site. Moreover, when imidazole was removed by buffer exchange, Kustc0562 retrieved its as-isolated state, as evident from the superposition of spectra of as-isolated and buffer-exchanged Kustc0562 (Fig 4.19 c). On the contrary, imidazole had no influence on the spectrum of Kustc0563 (Fig 4.19 d).

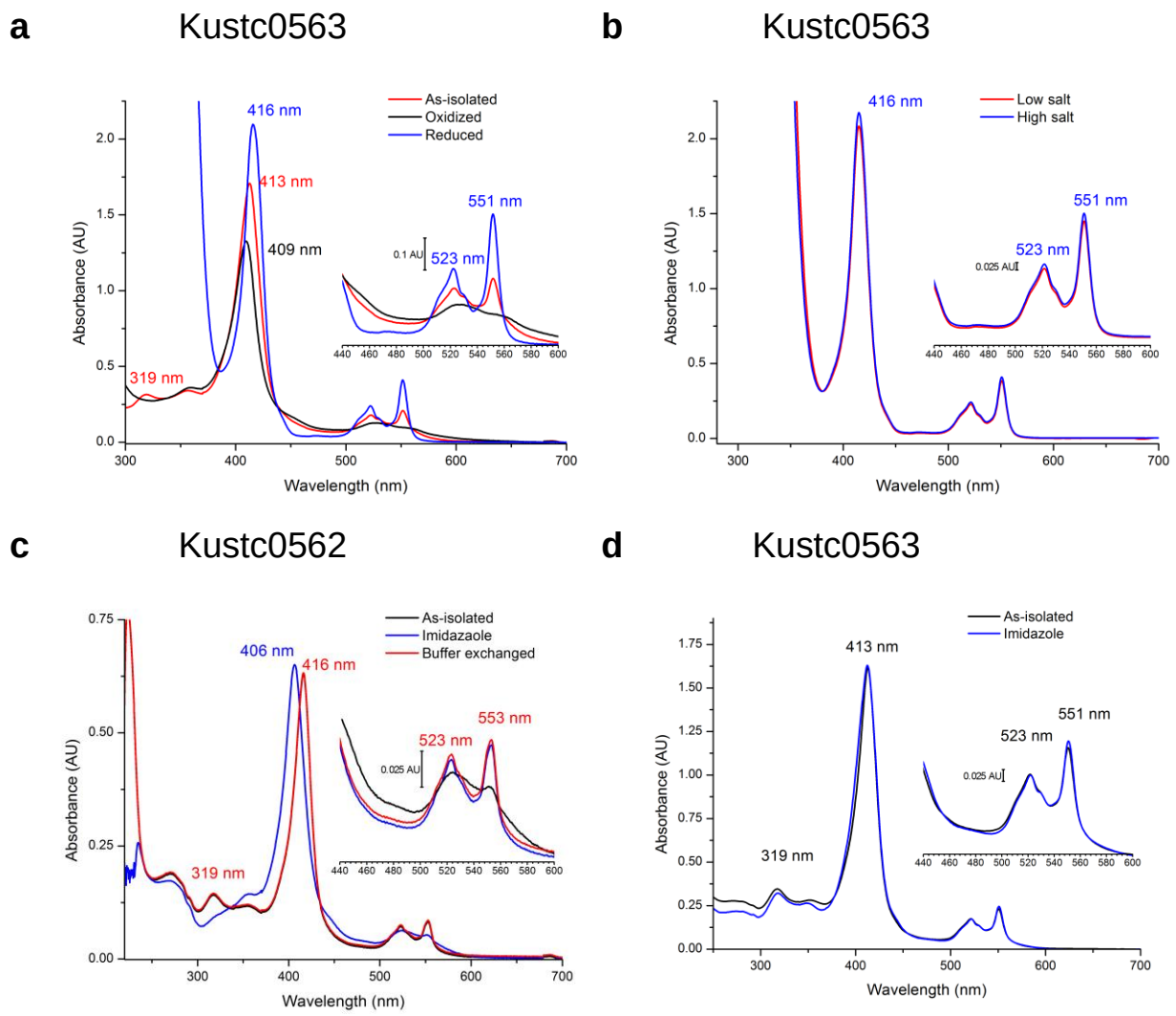

Figure 4.19 UV-Vis Spectroscopy of Kustc0563 and Kustc0562
Individual protein samples were diluted to a final A_{280}^{1cm}= 0.2-0.3 in their as-isolated states in a buffer containing 25 mM KCl, 25 mM HEPES/KOH pH 7.5. **a)** Kustc0563 UV-Vis spectra. The partially reduced as-isolated sample (red curve) was fully reduced by adding few grains of sodium dithionite (blue curve) and oxidized by few grains of ammonium persulphate (black curve). **b)** Comparison of the UV-Vis spectra of fully reduced (by sodium dithionite) Kustc0563 at low salt (25 mM NaCl, red curve) and high salt (500 mM NaCl, blue curve) conditions. No differences between the spectra could be observed contradictory to (Huston 2007). **c)** The UV-Vis spectra of Kustc0562 show the effect of imidazole binding to the protein. In presence of 100 mM Imidazole pH 8.0, the Soret peak shifted from 416 nm to 406 nm while the α- and β-bands nearly completely disappeared. The as-isolated state was partially reduced as it is clear from the presence of α- and β-bands, which further intensify in the presence of sodium dithionite and disappear in the presence of ammonium persulphate (not shown). **d)** The UV-Vis spectra of Kustc0563 show no effect of imidazole binding to the protein.

4.2.2.3 Redox Activity of Kustc0563 and Kustc0562

Spectropotentiometric redox potential determinations of both Kustc0562 and Kustc0563 resulted in very similar values of +242 and +269 mV (*vs.* SHE), respectively (Fig 4.20). These mid-point redox potentials are similar to that of bovine mitochondrial cytochrome c (cyt c) which is +262 mV (Raphael 1991). The previously reported redox potential of Kustc0563 was +230 mV (Huston 2007).

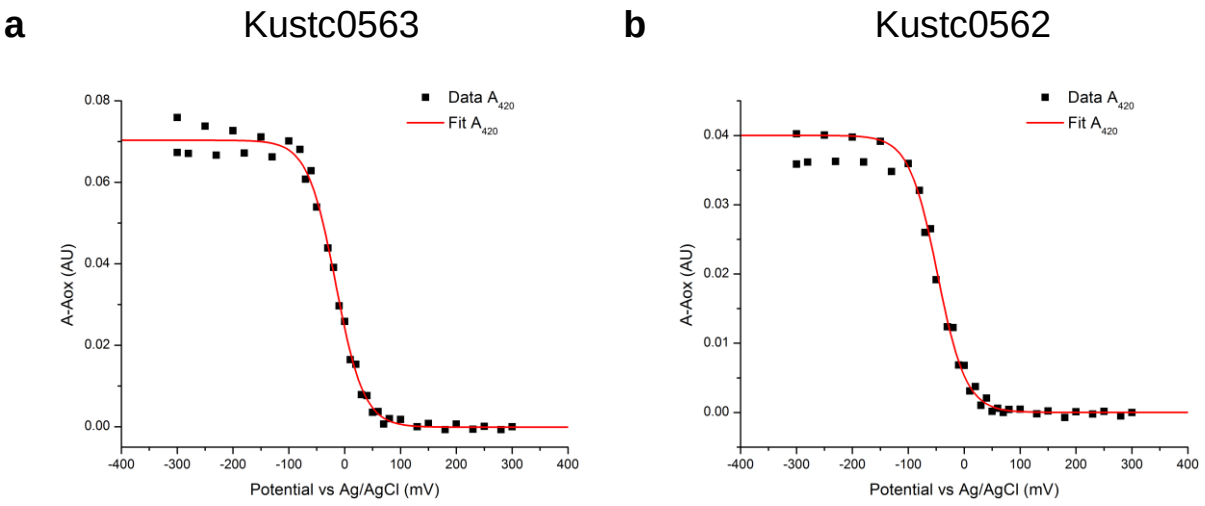

Figure 4.20 Spectroelectrochemistry of Kustc0563 and Kustc0562
UV-Vis spectra were recorded over a wavelength range of 350–700 nm at potentials between +300 mV and -300 mV in both directions. Samples of untagged Kustc0562 and Kustc0563 were buffer exchanged to 10 mM MOPS/KOH (pH 7.0), 100 mM KCl. Kustc0563 was supplemented with a mixture of 10 redox mediators (final concentration of 10 µM each). A final A_{280}^{1cm} of 12 and 14 was used for Kustc0562 and Kustc0563, respectively. The procedure for spectroelectrochemistry is described in section 2.2.5.8. The absorbance difference to the fully oxidized state (+300 mV) at 420 nm is plotted against the potential. **a)** The spectropotentiometric titration of Kustc0563 resulted in a mid-point potential of -16 mV *vs.* Ag/AgCl/100 mM KCl electrode. Correction of this value resulted in a redox potential of +269 mV *vs.* SHE. **b)** The spectropotentiometric titration of Kustc0562 resulted in -42 mV *vs.* Ag/AgCl/100 mM KCl electrode. Correction of this value resulted in a redox potential of +242 mV *vs.* SHE.

A comparison of the redox activities of Kustc0563, Kustc0562, Kuste2854 and bovine cyt c in enzymatic assays with *K. stuttgartiensis* hydroxylamine oxidase (*Ks*HOX) and hydrazine dehydrogenase (*Ks*HDH) is shown in figure 4.21 a and b (the tetraheme c-type cytochrome Kuste2854 was provided by Christina Ferousi, Radboud University, Nijmegen). Comparing initial rates, Kustc0563 was reduced eight times faster than bovine cytochrome c (Fig 4.21 a) by electrons derived from the three-electron oxidation of hydroxylamine by *Ks*HOX (Maalcke 2014). However, the reduction rate using bovine cyt c was nearly two times faster than that using Kustc0563 when electrons were derived from the four-electron oxidation of hydrazine by *Ks*HDH (Maalcke 2016). Kuste2854 showed no redox activity with either enzyme. Interestingly, Kustc0562 showed redox activity in a hydrazine oxidation assay with *Ks*HDH

with the same initial rate (first 10-15 seconds) as shown for Kustc0563 (Fig 4.21 b). However, it remained inactive in a hydroxylamine oxidation assay with *Ks*HOX in (Fig 4.21 a). A comparison of the Michaelis-Menten kinetic parameters of *Ks*HDH and *Ks*HOX using either Kustc0563 or bovine cyt c as redox partners are presented in table 4.3. To measure the substrate oxidation activities of *Ks*HDH and *Ks*HOX, the amount of substrate (hydroxylamine or hydrazine) was varied while keeping the redox partner (Kustc0563 or bovine cyt c) at a constant concentration (50 µM).

The apparent Michaelis-Menten constants for hydroxylamine oxidation ($K_M^{NH_2OH}$) by *Ks*HOX in presence of Kustc0563 or bovine cyt c as redox partners were similar. However, the catalytic rate (k_{cat}) was six times higher when Kustc0563 was used as redox partner compared to bovine cyt c. This also translates into different catalytic specificities (k_{cat}/K_M) which were nearly eight-fold higher when Kustc0563 was used as redox partner compared to bovine cyt c. Interestingly, the Michaelis-Menten constant, catalytic rate and specificity were in similar ranges for both Kustc0563 and cyt c as redox partners in a hydrazine oxidation assay with *Ks*HDH.

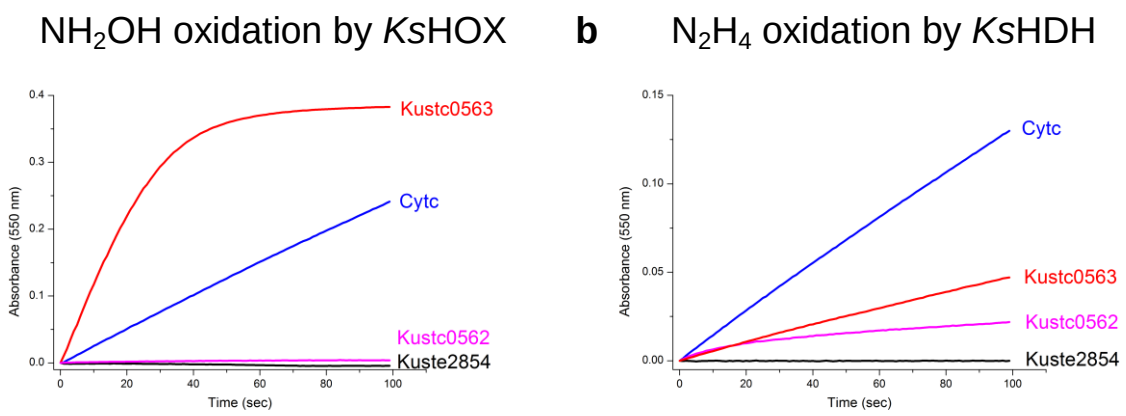

Figure 4.21 Comparison of the Substrate Oxidation Activity of *Ks*HOX and *Ks*HDH in presence of different redox partners.
1 mL reaction mixtures containing 1 µg of *Ks*HDH or 1.15 µg of *Ks*HOX as well as approximately 50 µM of each redox partner (Kustc0563, Kustc0562 and bovine heart cyt c) or 20 µM Kuste2854 in 20 mM potassium phosphate buffer pH 7.0 were prepared. The reaction was started by adding 100 µM of substrate (hydroxylamine for *Ks*HOX and hydrazine for *Ks*HDH; both neutralized to pH 7.0) and the reduction of the redox partners was followed at 550 nm at 37 °C. The progress curves show the increase in absorbance at 550 nm *versus* time indicating the reduction of the redox partners when substrates are oxidized by the respective enzyme (the reactions were started by substrate addition at 0 s).

Table 4.3 Michaelis-Menten Kinetics for the Substrate Oxidation Activity of *Ks*HOX and *Ks*HDH in presence of Kustc0563 or Bovine cyt c.

Redox partner	V_{max} (µmol min^{-1} mg^{-1})	K_M (µM)	k_{cat} (s^{-1})	k_{cat}/K_M ($\mu M^{-1}s^{-1}$)
With KsHOX				
Kustc0563	0.32±0.02	1.64±0.42	0.33	0.20
Cyt c	0.06±0.01	1.23±0.89	0.05	0.05
With KsHDH				
Kustc0563	0.40±0.05	9.29±1.49	0.48	0.05
Cyt c	0.34±0.01	9.35±0.71	0.40	0.04

50 µM of each Kustc0563 ($\Delta\varepsilon_{551}$=19,100 $M^{-1}cm^{-1}$) and bovine heart cyt c ($\Delta\varepsilon_{550}$=19,600 $M^{-1}cm^{-1}$) were used. 1 µg of *Ks*HDH was used in each experiment. 0.5 µg of *Ks*HOX was used with Kustc0563 as redox partner, whereas 1.5 µg were used with bovine cyt c. The reaction was started by adding an appropriate amount of hydrazine or hydroxylamine (hydrochloride salt, pH=7.0) for *Ks*HDH or *Ks*HOX, respectively, in a final volume of 1 mL made up by buffer (20 mM potassium phosphate, pH 7.0).
The reduction of bovine cyt c was followed at 550 nm and that of Kustc0563 was followed at 551 nm at 37 °C.

4.2.2.4 Crystallization

Only few crystallization conditions were obtained from initial screening of Kustc0563_CHis. All of the initial crystals failed to diffract. Therefore, crystallization optimization using a detergent screen (Hampton Research, Aliso Viejo, CA, USA) was performed. The reservoir contained 15 % (w/v) PEG 6000, 0.5 M LiCl and 0.1 M sodium cacodylate pH 6.5. Crystallization drops were set in hanging drop vapor diffusion setups, containing 1 µL reservoir, 1 µL protein (A_{280}^{1cm} = 6-7) and 0.2 µL of detergent solution (final 1 x CMC) at 20 °C. Well-diffracting, bipyramidally shaped crystals were obtained with several detergents. Crystals grown in the presence of CHAPS (3-[(3-Cholamidopropyl)dimethylammonio]-1-propanesulfonate) were chosen for final diffraction data collection (Fig 4.22 a). Crystals of Kustc0563 with cleaved N-terminal His-tag were obtained in sitting drop 96-well vapor diffusion setups. These crystals were grown in a drop containing 100 nL protein solution and 100 nL reservoir solution composed of 20 % (w/v) PEG 3350 and 0.2 M zinc acetate. These crystals also showed a bipyramidal shape (Fig 4.22 b). All the crystals were cryoprotected in artificial mother liquors containing 20-25 % ethylene glycol and were flash-cooled in liquid nitrogen.

Initial crystallization screening hits for untagged Kustc0562 were obtained in sitting drop vapor diffusion setups using a precipitant consisting of 30 % (w/v) PEG 8000, 0.2 M NaCl, 0.1 M imidazole pH 8.0. Needle-like crystals appeared within one to two days at 20 °C. These crystals were optimized using detergent screens 1 and 2 (Hampton research, Aliso Viejo, CA, USA) in hanging drop vapor diffusion setups with protein and precipitant volumes of 1 µL

each and 0.2 µL (final 1 x CMC) of the respective detergent stock and were equilibrated against 800 µL precipitant solution containing 0.2 M NaCl, 30 % (w/v) PEG 8000, 0.1 M imidazole pH 8.0. Crystals grown in the presence of 277 µM Cyclohexylethanoyl-N-hydroxyethylglucamide (C-HEGA-8) became more plate-like and reached dimensions of up to 400 µm in length. Crystals were cryoprotected in a solution consisting of 33 % (w/v) PEG 8000, 0.2 M NaCl, 0.1 M imidazole pH 8.0 and 25 % (v/v) ethylene glycol or 25 % (v/v) glycerol and were then flash-cooled in liquid nitrogen.

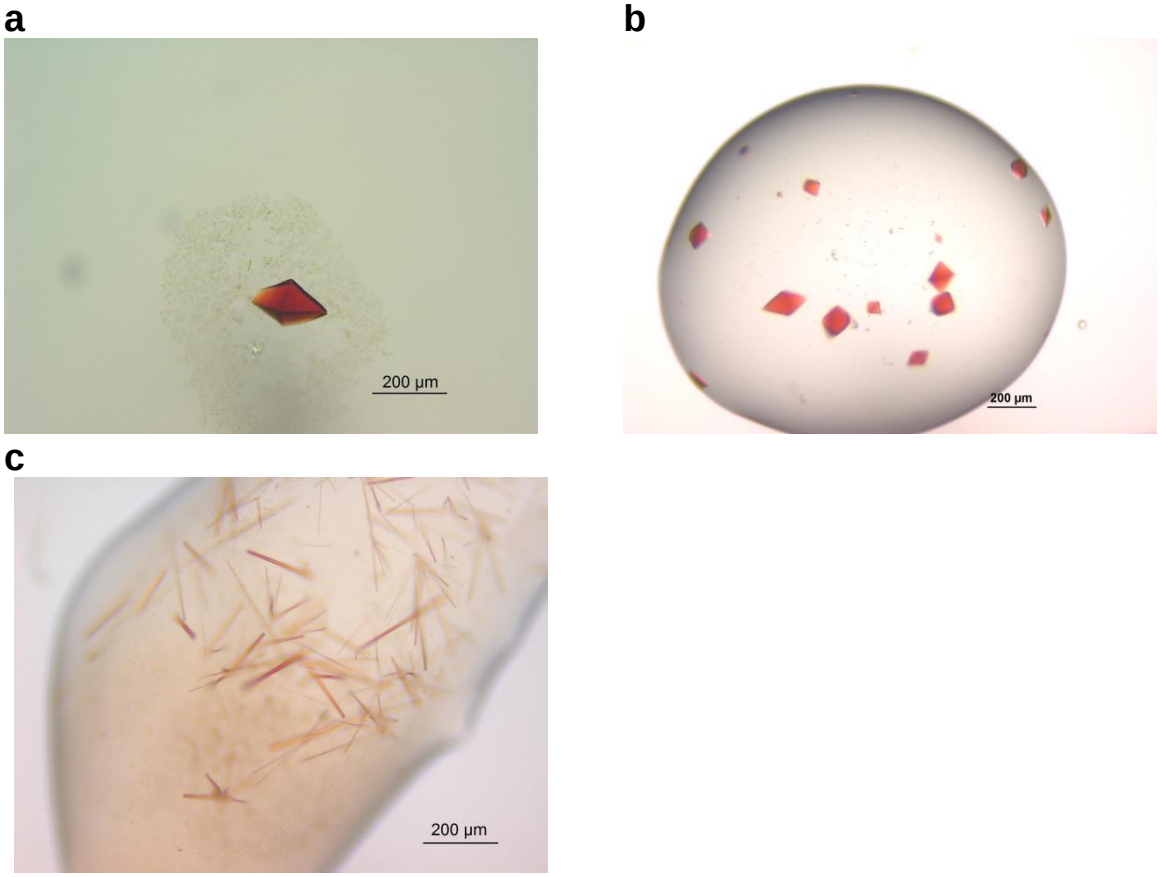

Figure 4.22 Crystallization of Kustc0563_CHis, Kustc0563nt and Kustc0562nt.
a) Red colored Kustc0563_CHis crystals were grown in 24-well hanging drop vapor diffusion setup at 20 °C. Droplets of 1 µL Kustc0563_CHis stock (A_{280}^{1cm}~7.0, stored in 25 mM HEPES/KOH pH 7.5, 25 mM KCl) were mixed with 1 µL precipitant solution (15 % (w/v) PEG 6000, 0.5 M LiCl and 0.1 M sodium cacodylate pH 6.5) and 0.2 µL CHAPS detergent solution (final 1 x CMC) on cover slips, which were placed over reservoir wells containing 800 µL of precipitant solution.
b) Kustc0563nt crystals were also grown at A_{280}^{1cm}~7.0 stored in the same buffer. Crystallization was performed in sitting drop 96-well plates using a reservoir solution containing 20 % (w/v) PEG 3350 and 0.2 M zinc acetate.
c) Kustc0562nt crystals were grown at A_{280}^{1cm}~18.0 stored in the buffer described in figure a. Crystallization was performed in sitting drop 96-well plates using a reservoir solution containing 30 % (w/v) PEG 8000, 0.2 M NaCl and 0.1 M imidazole pH 8.0.

4.2.2.5 Data Collection and Refinement

The optimized crystals of Kustc0563_CHis displayed orthorhombic $P2_12_12_1$ space group symmetry with unit cell dimensions of a = 85 Å, b = 49 Å, c = 253 Å, α= β = γ = 90°. A moderately redundant anomalous data set near the Fe K-edge (1.7433 Å, 7,112.0 eV) at a wavelength of 1.736 Å was collected and processed with XDS (Kabsch 2010) up to 2.7 Å final resolution. The phase problem was solved by the method of single anomalous dispersion (SAD) using the anomalous signal of the heme iron (anomalous scattering factor f'' = 3.952 electrons at λ = 1.736 Å; http://skuld.bmsc.washington.edu/scatter/AS_index.html). Phase determination was carried out by Phenix AutoSol (Terwilliger 2009) which identified six Fe sites with good occupancies (>1). The program also built six poly-alanine chains into the initial density. This result is consistent with an analysis according to (Matthews 1968) indicating six protein molecules and hence six heme moieties in the asymmetric unit (solvent content 47 %). The poly-alanine chains were replaced by the sequence of Kustc0563_CHis. Then iterative model building and refinement were carried out using COOT (Emsley 2004) and REFMAC (Murshudov 1997), respectively, applying non-crystallographic symmetry operations for the six molecules in the asymmetric unit. Further, a native dataset of a Kustc0563_CHis crystal was collected at a wavelength of 1.000 Å resulting in a resolution limit of 2.3 Å and was processed with XDS. Then the Kustc0563_CHis model was refined against this native data set. Further model building and refinement of Kustc0563_CHis finally resulted in a working R-factor of 24.0 % and R-free of 27.8 %.

Moreover, a native data set of Kustc0563nt was collected at a wavelength of 1.000 Å and processed to a final resolution of 1.9 Å using XDS (Kabsch 2010). The Kustc0563nt crystal showed tetragonal $P4_32_12$ space group symmetry with unit cell dimensions of a = b = 48 Å, c = 100 Å, α= γ = β = 90°. According to the Matthews volume (Matthews 1968), one molecule per asymmetric unit was present (solvent content 58 %). The structure was solved by molecular replacement with PHASER (McCoy 2007) using one protein molecule from the 2.3 Å structure of Kustc0563_CHis including its heme Fe-atom as the search model. The structure was iteratively modeled using COOT (Emsley 2004) and refined in REFMAC (Murshudov 1997) resulting in working and free R-factors of 19.8 % and 22.9 %, respectively. The final Kustc0563nt model displayed excellent stereochemistry as indicated by the Ramachandran statistics and by analysis using MOLPROBITY (Davis 2007). Statistics of data collection and refinement are summarized in table 4.4.

A data set from a Kustc0562 crystal was collected using a rotating copper anode X-ray source (Rigaku MicroMax 007HF) at the Cu Kα wavelength (1.5418 Å). Raw diffraction data were processed to a diffraction limit of 3.0 Å with XDS (Kabsch 2010). The crystals displayed hexagonal $P6_4$ space group symmetry with unit cell dimensions of $a = b = 101.7$ Å, $c = 28.3$ Å, $\alpha = \beta = 90°$ and $\gamma = 120°$. A single molecule of Kustc0562 was present in the asymmetric unit. The structure was solved by molecular replacement in PHASER (McCoy 2007) using the Kustc0653nt structure as the search model. Kustc0562 shares 55 % sequence identity with Kustc0563. Since the protein crystals contained large amounts of solvent (68 % according to (Matthews 1968), solvent flattening was performed using DM (Cowtan 1999) to enhance the electron density map. Amino acid residues that differed from the Kustc0563 search model sequence were replaced for the actual residues in Kustc0562 and could be well fitted into the electron density map. Iterative cycles of rebuilding with COOT (Emsley 2004) and model refinement using REFMAC (Murshudov 1997) were performed. During the refinement process, additional electron density at the distal face of the heme appeared. This additional density could be fitted best by an imidazole molecule coordinating the heme iron. Imidazole was present in the crystallization condition (section 4.2.2.4) and its coordination to the heme was also supported by UV-Vis spectroscopy (section 4.2.2.2). The refinement resulted in a final model with working and free R-factors of 19.3 % and 24.9 %, respectively. Nine out of the expected 89 amino acids are missing at the N-terminus in the model. The final model of Kustc0562 displayed excellent stereochemistry as indicated by the Ramachandran statistics and by analysis using MOLPROBITY (Davis 2007). Statistics of data collection and refinement of Kustc0562 are summarized in table 4.4.

Table 4.4 X-ray data statics of Kustc0563_CHis, untagged Kustc0563 and Kustc0562

Data set	Kustc0563_CHis Fe-SAD	Kustc0563_CHis native	Kustc0563nt native (pdb 5MXY)	Kustc0562nt native
Data collection				
Space group	$P2_12_12_1$	$P2_12_12_1$	$P4_32_12$	$P6_4$
Unit cell dimensions				
a, b, c (Å)	84.9, 49.2, 253.3	84.9, 49.2, 253.3	47.8, 47.8, 99.9	101.7, 101.7, 28.3
α, β, γ (°)	90, 90, 90	90, 90, 90	90, 90, 90	90, 90, 120
Wavelength (Å)	1.736	1.000	1.000	1.5418
Resolution range (Å) [a]	40.0-2.7 (2.8-2.7)	50.0-2.3 (2.5-2.3)	50.0-1.9 (2.0-1.9)	40-3.0 (3.1-3.0)
Reflections measured[a]	378,921 (17,857)[f]	179,508 (40,876)	65,768 (9,202)	8,066 (608)
Reflections unique [a]	32,168 (3,169) [f]	52,082 (11,545)	9,541 (1,329)	3,395 (252)
Completeness (%) [a]	99.3 (94.6) [f]	99.4 (99.8)	97.7 (98.7)	95.8 (90.6)
Redundancy N [a]	11.8 (5.6) [f]	3.4 (3.5)	6.9 (6.9)	2.4 (2.1)
I/σI [a]	15.5 (2.07) [f]	9.0 (2.25)	12.2 (1.54)	6.5 (2.7)
R_{merge} (%) [a, b]	10.3 (54.3) [f]	7.9 (55.0)	8.1 (278.6)	16.6 (3.7)
R_{meas} (%) [a, c]	10.7 (59.8) [f]	9.4 (64.9)	8.8 (301.1)	17.4 (4.1)
$CC_{1/2}$ (%) [d]	99.8 (86.6)	99.4 (74.2)	99.9 (82.3)	97.3 (74.5)
CC* (%) [e]	99.9 (96.3)	99.8 (92.2)	99.9 (95.0)	99.3 (92.4)
Refinement				
Resolution range in refinement (Å)		126.0-2.3	43.0-1.9	40.0-3.0
Number of reflections in refinement		28,152	9,040	3,390
R_{work}/ R_{free} (%) [g]		24.0/ 28.1	19.8/ 22.9	19.2/ 24.9
Protein residues		547 (4,239)	83 (773)	80 (654)
Ligands (no. of atoms)		6 heme (258)	1 heme (43)	1 heme (43),1 imd (5)
Water molecules		34	68	2
Overall B-factor (Å^2)		40.1	49.1	33.0
Rmsd bonds (Å)		0.012	0.009	0.013
Rmsd angles (°)		2.570	2.290	0.361
Ramachandran plot [h]				
Most favoured (%)		94.3	93.8	92.4
Additionally allowed (%)		5.1	6.2	7.6
Disallowed (%)		0.6	0.0	0.0

Legend to Tables 4.4

a) Values of the highest resolution shell are given in brackets.

b) $R_{merge} = \sum_h \left| \langle I_h \rangle - I_{h,i} \right| / \sum_h \sum_i^{n_h} I_{h,i}$, where I_i is the intensity of a reflection and $\langle I_h \rangle = \frac{1}{n_h} \sum_i^{n_h} I_{h,i}$ is the mean value of that reflection and the summations are over all reflections h.

c) $R_{meas} = \sum_h \sqrt{\frac{N}{N-1}}\ R_{merge}$ Redundancy-independent merging R factor (Diederichs 1997).

d) $CC_{1/2} = \sum_{i=1}^{n} \left(\left(x_i - \bar{x} \right) \left(y_i - \bar{y} \right) \right) \Big/ \sqrt{\sum_{i=1}^{n} \left(x_i - \bar{x} \right)^2 \sum_{i=1}^{n} \left(y_i - \bar{y} \right)^2}$ Pearson's correlation coefficient between merged intensity estimates $I_{h,i}$ (x_i, y_i) and $\langle I_h \rangle$ ($\bar{x}$, $\bar{y}$) from half data sets x and y.

e) $CC^* = \sqrt{\frac{2CC_{1/2}}{1+CC_{1/2}}}$ Estimated correlation coefficient of the merged dataset against the true (usually unmeasurable) intensities (Karplus 2012).

f) Considering Friedel mates as individual reflections.
g) $R_{work} = \sum_h |F_{obs} - F_{calc}| / \sum_h F_{obs}$ (working set, no σ cut-off applied) R_{free} is calculated the same way as R_{work}, but for a reflection test set with 5 % of the reflections excluded from refinement.
h) Ramachandran analysis was performed using COOT (Emsley 2004).

4.2.2.6 Overall Structures of Kustc0563 and Kustc0562

As mentioned in section 4.1 both Kustc0563 and Kustc0562 belong to class I c-type cytochromes based on the position of their heme binding motifs near the N-terminus of the sequence (Fig 4.27). The structures of both proteins confirm this (Fig 4.23). The distal methionine ligands (Met91 in Kustc0563 and Met94 in Kustc0562) in both structures are located close to the C-terminus of the sequence and are part of the loop connecting helices α5 and α6. However, in case of Kustc0562 the distal methionine ligand (Met94) is replaced by an imidazole molecule present in the crystallization condition (Fig 4.23 b). Both structures show typical cytochrome c folds containing six α-helices (Fig 4.23). The α-helices in both structures are four to thirteen amino acids long. Helices α1, α5 and α6 contain nine, eleven and thirteen residues whereas helices α2, α3 and α4 are made up by four, six and seven amino acids, respectively. The α5-α6 loop carrying the distal methionine ligand is relatively long with a length of thirteen residues (Fig 4.23 a and b).

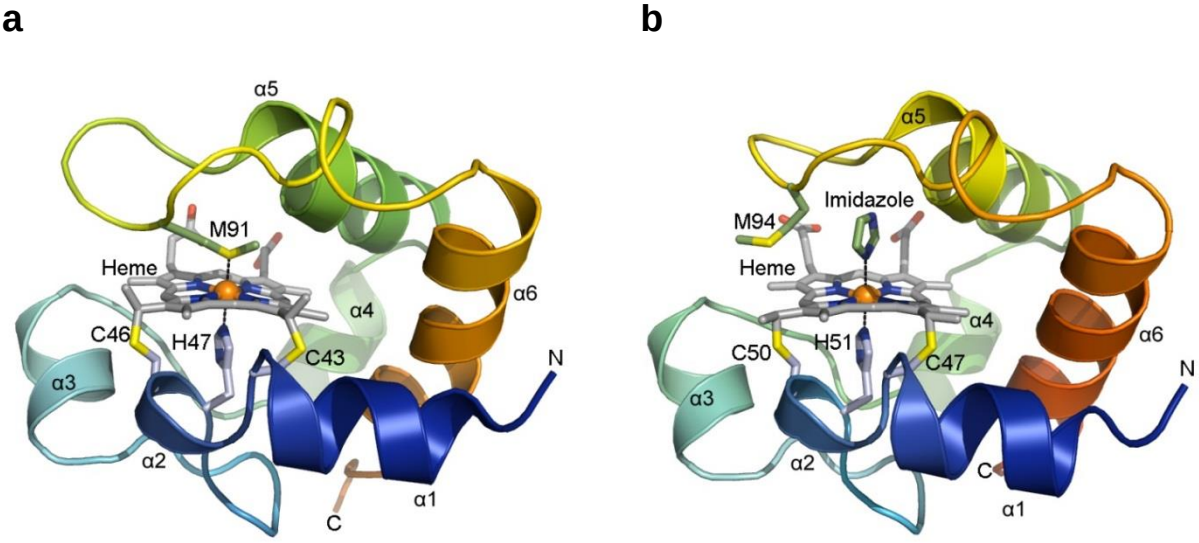

Figure 4.23 Overall Structures of Kustc0563 and its Paralogue Kustc0562
The structures are rendered as cartoon and colored as rainbow spectrum. **a)** Kustc0563 and **b)** Kustc0562. Both structures show all α-helical, typical class I c-type cytochrome folds. In Kustc0563 the heme is coordinated by His/Met. In Kustc0562, however, the supposed distal methionine (M94) is replaced by an imidazole molecule.

The overall structures of Kustc0563 and Kustc0562 are highly similar with a structural rmsd of 1.2 Å for 81 C_α-atoms (Fig 4.24). However, owing to the binding of an imidazole molecule at the distal site of the Kustc0562 heme, the supposed coordination bond between Met94 and the heme iron is broken and Met94 is rotated away. As a consequence, the entire α5-α6 loop in Kustc0562 containing Met94 moves towards the side of the heme where its propionate groups are located when compared with the same loop of Kustc0563. This also leads to a slight movement of helix α5 (Fig 4.24).

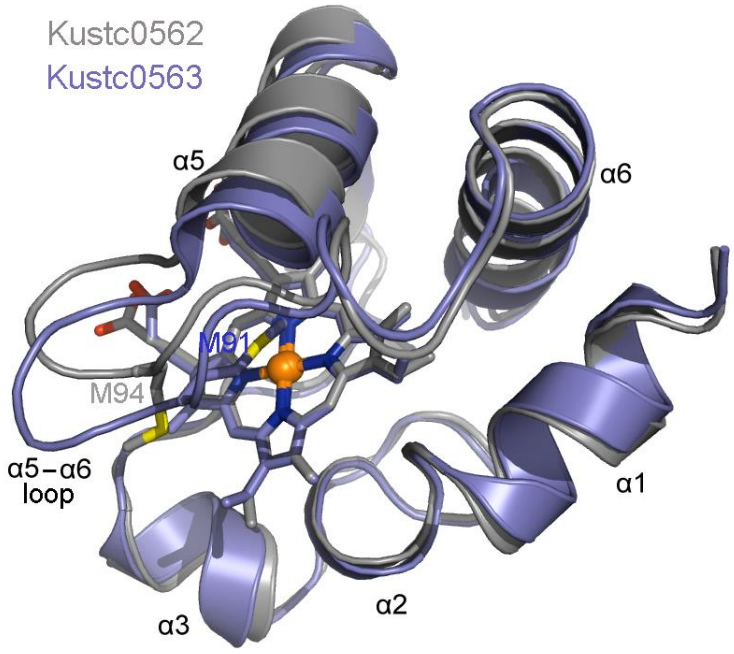

Figure 4.24 Structural superposition of Kustc0563 and Kustc0562.
The structures are shown as cartoon. Kustc0562 and Kustc0563 are colored in grey and blue, respectively. The structures were superposed at a structural rmsd of 1.2 Å for 81 C_α-atoms. The overall structures are highly similar except for the comparative positions of their distal ligands and the positions of the α5-α6 loops. A slight change in the position of helix α5 of Kustc0562 can also be observed.

Despite highly similar overall structures, there are striking differences in the electrostatic surface potential comparing Kustc0562 and Kustc0563. The two tunnels leading to the heme pocket in Kustc0563 are highly negatively charged except for few positively charged patches near the heme propionate groups (Fig 4.25 a). Conversely, the heme tunnels in Kustc0562 are surrounded by highly positively charged areas (Fig 4.25 b). In both cases, however, the oppositely charged surfaces are present at the opposite side of the molecules (positively charged in Kustc0563 and negatively charged for Kustc0562). The overall charge on Kustc0563 is -2.00 electrons compared with +3.00 electrons on Kustc0562 at pH 7.0 (determined by the PDB2PQR server; http://nbcr-222.ucsd.edu/pdb2pqr_2.1.1/).

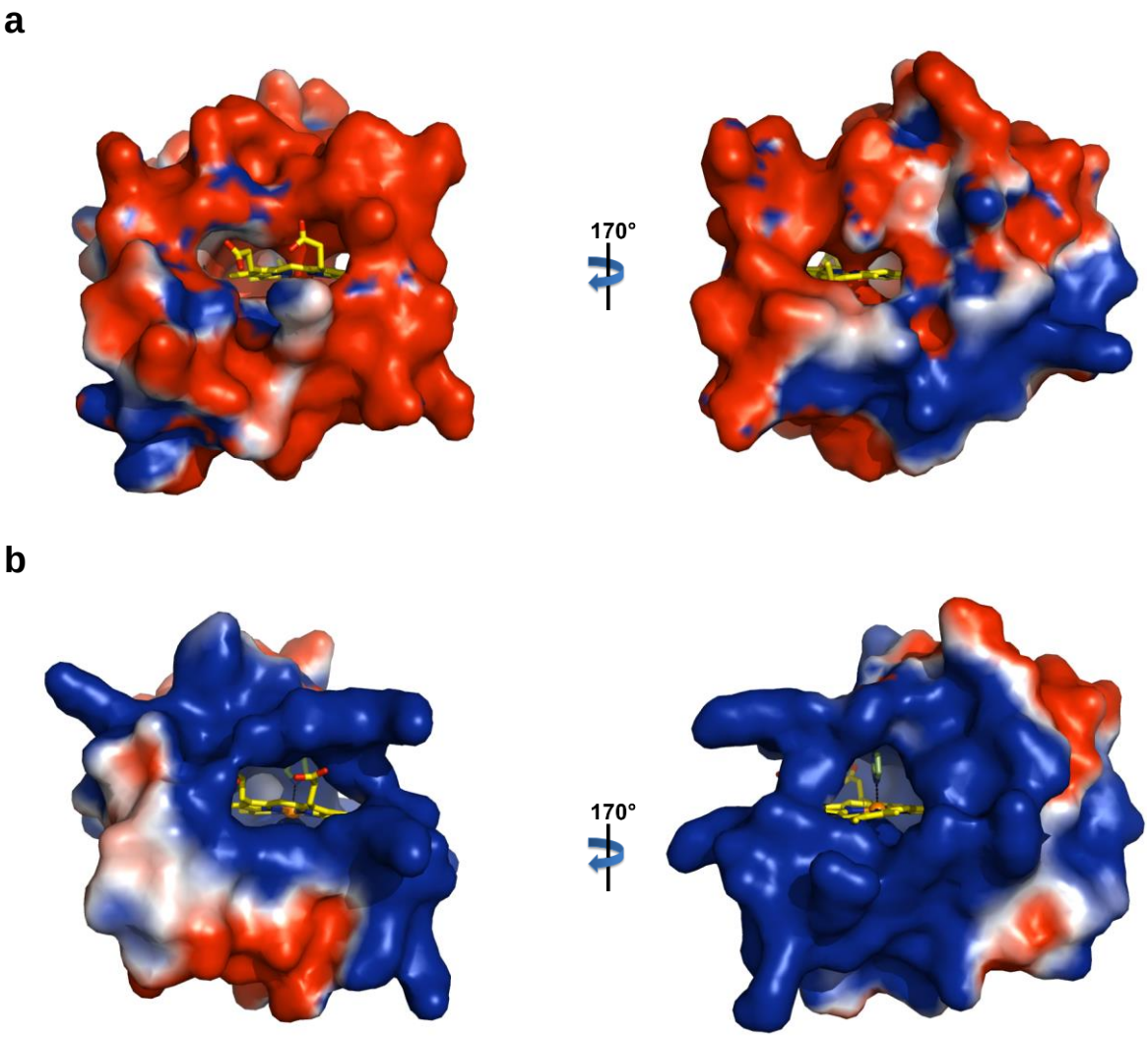

Figure 4.25 Surface Electrostatic Representation of Kustc0563 and Kustc0562
The blue surface shows positive charge while red represents negative charge. **a)** Kustc0563 and **b)** Kustc0562. The hemes in both Kustc0562 and Kustc0563 are exposed to the solvent *via* two tunnels. The heme environment in Kustc0563 is primarily negatively charged with some small positively charged patches. The electrostatic surface around the heme in Kustc0562, however, is highly positively charged.

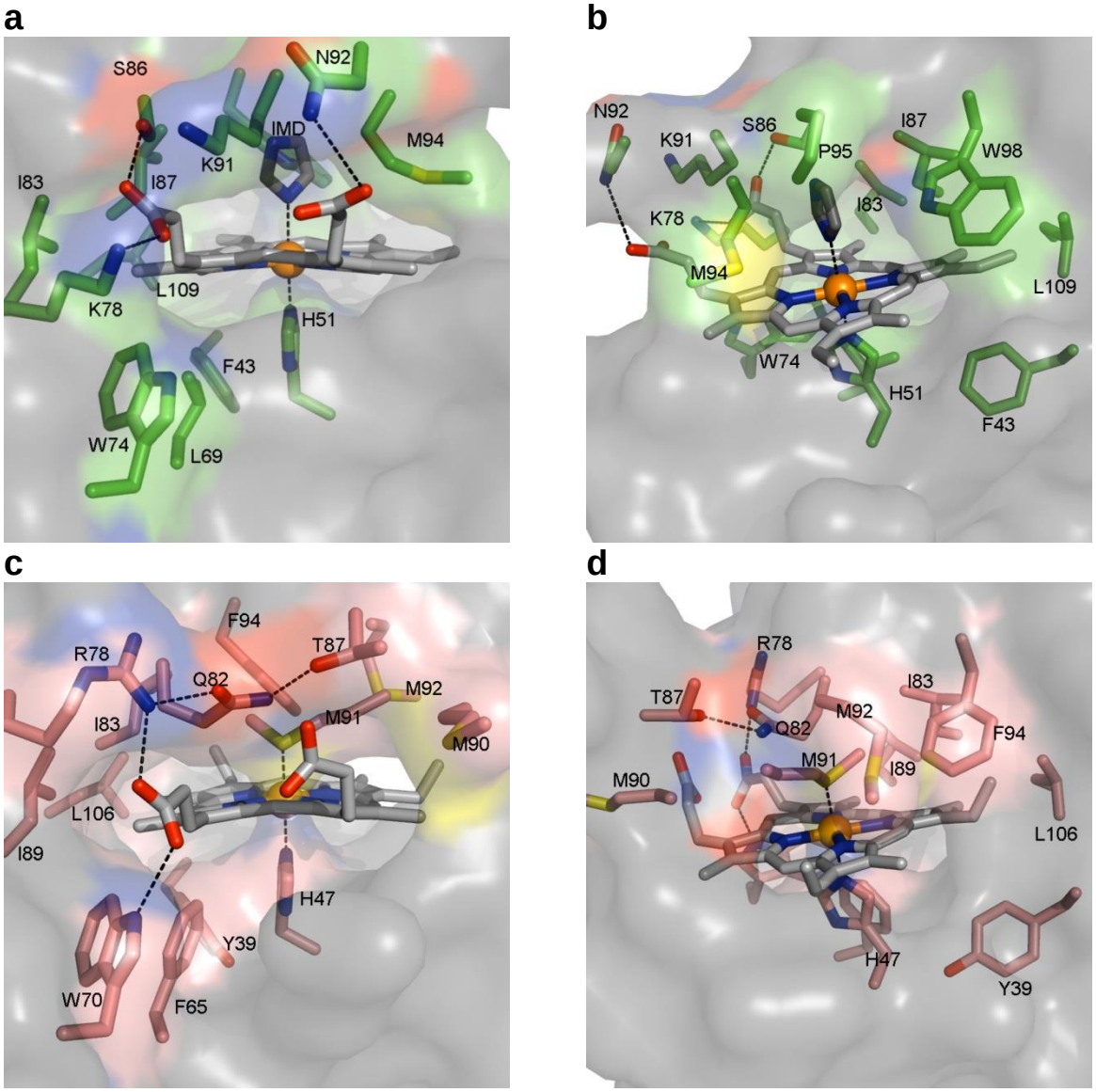

Figure 4.26 Heme Environments of Kustc0563 and Kustc0562
The structures are shown as semi-transparent surfaces. The residues forming the heme environment are shown as sticks. **a)** and **b)** Kustc0562; **c)** and **d)** Kustc0563. The exposed faces of the heme pockets are shown in figures a and c. The buried faces of the heme pockets (figures b and d) are surrounded by mostly hydrophobic residues in both structures. The propionate groups of both heme sites are surrounded by hydrophilic residues, making few hydrogen bonding interactions.

The c-type hemes in both structures are largely planar. They are highly solvent exposed *via* two entrances (Fig 4.26). The heme environment in both cytochromes is mostly hydrophobic. Most of these residues reside at the buried faces of the heme pocket and are at Van-der-Waals distances to the heme (Fig 4.26 b and d). The heme pocket entrances near the propionate groups of the hemes in both Kustc0563 and Kustc0562 are surrounded by hydrophilic residues. As shown in figure 4.26 a and c, the heme propionate groups are at hydrogen bonding distances to several hydrogen bonding donor/acceptor groups. Therefore, the entrance to the exposed face of the heme pocket is hydrophilic while the entrance to the buried face is hydrophobic. In Kustc0562, the distal side of the heme is slightly less crowded when compared with Kustc0563, since Met92 is replaced by a Pro95 in Kustc0562 (Fig 4.26 b and d). Met92 of Kustc0563 is either conserved or substituted by phenylalanine in all its orthologues (Fig 4.27). In Kustc0562, Pro95 is fully conserved (Fig 4.27).

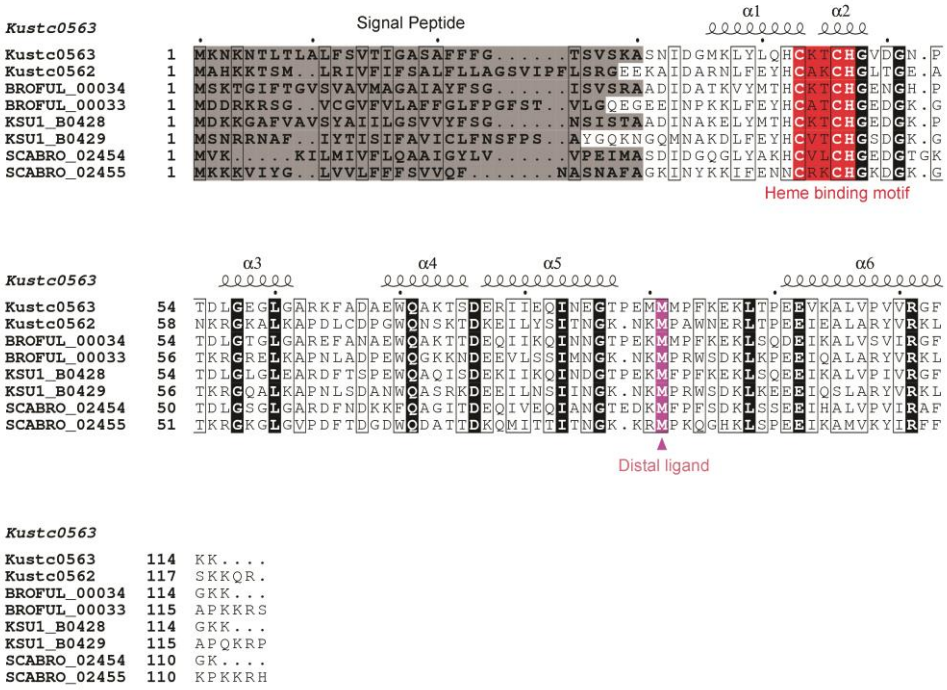

Figure 4.27 Sequence alignments of Kustc0563 and Kustc0562 homologues.
Kuenenia stuttgartiensis Kustc0563 (CAJ71308.1) and its paralogue Kustc0562 (CAJ71307.1) were aligned to their orthologues from *Brocadia fulgida* BROFUL_00034 (KKO21239.1), BROFUL_00033 (KKO21238.1), *Jettenia caeni* (Planctomycete KSU-1) KSU1_B0428 (WP_007220410.1), KSU1_B0429 (WP_040543216.1) as well as *Scalindua brodae* SCABRO_02454 (KHE91815.1) and SCABRO_02455 (KHE91816.1). The sequence identities to Kustc0563 are 55 % for Kustc0562, 62 % for BROFUL_00034, 34 % BROFUL_00033, 56 % for KSU1_B0428, 33 % for KSU1_B0429, 49 % for SCABRO_02454 and 37 % for SCABRO_02455. Alignments were performed using ClustalO (Sievers 2011) and secondary structure elements were manually assigned based on the Kustc0563 structure. Fully conserved sequences are marked black. The CXXCH c-type heme binding motifs are highlighted in red. The predicted signal peptides are highlighted in grey. The distal methionine heme ligands are highlighted in pink (with pink triangle). The figure was prepared using ESPript (Gouet 1999).

4.3 Discussion

4.3.1 The *Ks*NaxLS Complex

4.3.1.1 *Ks*NaxLS – A Heterodimer of Class I and IIb Cytochromes c

The purification of *Ks*NaxLS from *Kuenenia stuttgartiensis* biomass (Joachim Reimann, Radboud University, Nijmegen) as well as its orthologues from *Jettenia caeni* (Ukita 2010) as stable heterodimeric complexes indicate that this oligomeric state is indeed physiologically relevant. Moreover, it could be shown in this study that the individual components *Ks*NaxL and *Ks*NaxS readily assemble into the heterodimer *in vitro* (by mixing individually expressed subunits) and *in vivo* (by heterologous co-expression of the subunits from a bicistronic operon in *Shewanella oneidensis* MR-1). Biophysical characterization of the *Ks*NaxLS complex and its components in solution by AUC and SEC-MALS further corroborated that *Ks*NaxLS exists as a heterodimer and its individual subunits as monomers. Furthermore, the *Ks*NaxLS complex crystallized as one heterodimer per asymmetric unit containing each of *Ks*NaxL and KsNaxS components. Consequently, it can be concluded that the heterodimeric assembly found in the crystal structure indeed represents the oligomeric state in solution.

Strikingly, the X-ray structure of *Ks*NaxLS at 1.7 Å resolution provides the first molecular model of a complex between class I and class II c-type cytochromes. Moreover, based on its hexa-coordinated low spin heme iron along with its four-helix bundle fold NaxL can be assigned to subclass IIb of monoheme c-type cytochromes. Consequently, *Ks*NaxL is the first crystal structure of a member belonging to this subclass. The only other structurally characterized example from class IIb is the His/Met ligated cytochrome c-556 from *Rhodopseudomonas palustris* whose three-dimensional structure was modelled and validated by NMR spectroscopy (Bertini 2004). Its four-helix bundle fold is well superimposable with *Ks*NaxL showing a structural rmsd of 3.0 Å for 97 C_{α}-atoms.

4.3.1.2 *Ks*NaxL and NaxS possess a Rare His/Cys Heme Ligation

The presented X-ray structure confirms that the c-type hemes in both *Ks*NaxL and *Ks*NaxS are coordinated by proximal histidine and distal cysteine ligands. Previously, EPR spectroscopy of the *Jettenia caeni* NaxLS (*Jc*NaxLS) complex resulted in low spin signals originating from two hexa-coordinated hemes (Ukita 2010). Combined with sequence analyses, Ukita *et al.* had already proposed a rare His/Cys axial ligation of both heme irons.

So far, there are relatively few known examples of c-type cytochromes with His/Cys axial heme ligation reported. Several of them are involved in sulfur metabolism such as the SoxAX complex which shows thiosulphate oxidation activity (Cheesman 2001; Reijerse 2007; Bamford 2002), DsrJ which is part of the DsrMKJOP transmembrane complex involved in sulphur respiration (Pires 2006; Grein 2010) and the thiosulphate dehydrogenase TsdA (Denkmann 2012). Other examples include the triheme cytochrome PufC (part of a photosynthetic reaction centre; (Alric 2004), GHP (putatively involved in heat shock response in some proteobacteria; (Van Driessche 2006), PsbV2 (a small class I c-type cytochrome from *Thermosynechoccus elongates;* (Suga 2013) and the recently described c-type heme protein TII0287 proposed to be associated with photosystem II of *T. elongatus* (Motomura 2017).
Including the *Ks*NaxLS complex, there are in total only five three-dimensional structures known so far containing c-type hemes with His/Cys ligation, many of them have been reported fairly recently. These structures include the SoxAX complex (Bamford 2002; Kilmartin 2011), TsdA (Brito 2015), PsbV2 (Suga 2013) and TII287 (Motomura 2017). However, neither *Ks*NaxL nor *Ks*NaxS show any homology to the mentioned proteins with His/Cys ligation considering both their primary and tertiary structures.

4.3.1.3 His/Cys Heme Ligation Causes a Lower Redox Potential

The exact function of the His/Cys heme c ligation is unknown, however, it is a general consensus that the thiolate group of cysteine acts as a strong σ-donor. This results in a very low redox potential of the heme by stabilizing the ferric state. For example, the M80C mutant of mitochondrial cytochrome c exhibits a redox potential of -390 mV *vs.* SHE which is nearly 600 mV lower than the wild type (+262 mV, His/Met) (Raphael 1991). Other examples include the His/Cys ligated monoheme protein TII0287 with -255 ± 20 mV (pH 7.5) and the heme c of the SoxA component of the *Starkeya novella* diheme SoxAX complex (Kappler 2008) with -479 ± 10 mV (pH 7.0).
Sodium dithionite (redox potential about -400 mV (Mayhew 1978) could not completely reduce the *Jc*NaxLS complex whereas Ti(III) citrate (-800 mV; Reijerse 2007) could. As a result, it was expected that the redox potential of the NaxLS complex should also be in the range of at least -400 mV (Ukita 2010). In the present study, the mutant *Ks*NaxL C32M/ NaxS C101M was isolated in a partially reduced state as evident from the presence of an α-band at 553 nm in the UV-Vis spectrum. This indicates an increase in the redox potential of the heme center(s). Similarly, the spectra of the *Ks*NaxL wt/ NaxS C101M and *Ks*NaxL wt/

NaxS C101G mutants where only the distal cysteine in *Ks*NaxS was substituted by methionine and glycine, respectively, also showed a small α-band. All three mutant complexes where only *Ks*NaxS was mutated could not be immediately re-oxidized as opposed to the NaxLS complexes with a mutated distal ligand in *Ks*NaxL which underwent immediate re-oxidation.

Based on these results, two conclusions can be drawn. Firstly, that the cysteine axial heme ligand causes a lowered redox potential of the *Ks*NaxLS complex. Secondly, it is likely that there might be an appreciable difference between the redox potentials of the two hemes in the *Ks*NaxLS complex and that the redox potential of the heme belonging to *Ks*NaxL is higher than that of *Ks*NaxS. In order to reach unambiguous conclusions, precise redox potentials need to be determined. Although spectropotentiometric titrations of *Ks*NaxLS and its mutants were tried and two distinct transitions in the titration curves were visible, the heme mid-point potentials could not be reproducibly determined probably due to sluggish electron transfer to the working electrode.

4.3.1.4 Effects of His/Cys Heme Ligation on UV-Vis Spectra

The distal cysteine ligation is supposed to be responsible for the unique red-shifted Soret band maximum at 420 nm in the *Ks*NaxLS wild type complex as well as its individual components in their as-isolated state representing the ferric form of the heme iron. In contrast to His/Met ligated cytochromes, the Soret band is blue-shifted to 417 nm upon reduction *i.e.* in the ferrous state of the heme.

In the present study, mutation of the distal cysteines to either methionine or glycine in either one or both subunits of the *Ks*NaxLS complex led to blue-shifted Soret bands (412-415 nm in the as-isolated state) with respect to the wild type complex. Moreover, in all the mutants a red shift to 417 nm was observed upon reduction. These observations indicate that the unique position of the Soret band indeed originates from the His/Cys ligation in the *Ks*NaxLS complex.

Interestingly, further re-oxidation of the *Ks*NaxLS wild type complex and its individual components by air yields spectra with further blue-shifted Soret maxima (~410 nm) including the expected disappearance of α- and β-bands. As mentioned before, the partially reduced as-isolated state of the *Ks*NaxL C32M/ NaxS C101M mutant possessed a Soret band at 412 nm, which further blue shifted to 408 nm upon complete re-oxidation. This might imply that either reduction or re-oxidation of the wild type *Ks*NaxLS complex triggers either dissociation of

the distal cysteine ligands, replacement by other ligands or a mixture of both. In either case, dissociation of both Cys ligands is required, since the dissociation of the distal cysteine in only one subunit would lead to a Soret peak that is more red-shifted than the peak at 408 nm as can be observed in the spectra of the as-isolated single distal cysteine mutants. Moreover, both individual components also show a Soret band around 410 when being re-oxidized, which unambiguously indicates that both components respond identically to reduction and re-oxidation. Surprisingly, once reduced and re-oxidized the Soret maximum does not get back to 420 nm again. This implies that if there were any dissociation or replacement of the distal cysteine it would be irreversible. However, under physiological, hence anaerobic, conditions re-oxidation might yield different results than when it is achieved by exposing to oxygen (air). Nevertheless, it can be concluded that the distal cysteine ligands in both components of the *Ks*NaxLS complex are flexible. However, UV-Vis spectroscopic studies of the oxidized, reduced and re-oxidized distal cysteine mutants of *Ks*NaxLS alone cannot prove that this flexibility is inherent to cysteine as distal ligand only. This is due to the fact that methionine as distal ligand produces the same UV-Vis spectra as when it is putatively removed upon re-oxidation. UV-Vis spectra of the distal glycine mutants support this view. Here the vacant distal heme site is occupied by a water molecule as can be seen in the structure of *Ks*NaxLS wt/ NaxS C101G. However, the flexibility of the cysteine distal ligand can be compared with that of methionine by analyzing how they bind to exogenous gaseous ligands as discussed further in the next section (section 4.3.1.5).

The structures of the reduced and re-oxidized NaxLS complex might shed further light on the heme ligation state under these conditions. However, structure determination by X-ray crystallography has to be combined with single-crystal UV-Vis microspectrometry since photoreduction by X-rays can alter the oxidation state of metal centers such as the heme iron (Beitlich 2007). The thin crystals of the *Ks*NaxLS complex would be particularly suitable for microspectrometry due to their low optical density. Electron paramagnetic resonance (EPR) spectroscopy would also be an option to determine the ligation state in solution.

4.3.1.5 Exogenous Ligand Binding

Binding of different exogenous ligands such as nitric oxide (NO) and carbon monoxide (CO) to class I (Nicholls 1996) and class II (Hough 2015) c-type cytochromes is well known. NO can bind to both ferrous and ferric forms of the heme iron, whereas CO exclusively binds to the ferrous form. UV-Vis spectroscopic features of NO-bound ferrous and ferric NaxL and NaxS were reminiscent to the respective ferrous and ferric complexes of various pentacoordinated heme-containing proteins. Such proteins include eukaryotic and prokaryotic NO-sensors such as soluble guanylate cyclase (sGC) (Stone 1994) and H-NOX (Boon 2006), respectively. They also include cytochrome c' from *Rhodobacter sphaeroides* (Choi 2005) and Nitrophorins (Ding 1999; Andersen 2000) both of which are NO-shuttling proteins. The observed UV-Vis features of NaxL and NaxS give implications for the formation of 6cNO and 5cNO adducts upon NO binding. A depiction of 5cNO and 6cNO heme adducts is presented in figure 4.28 (according to the concepts reviewed by Hough *et al.* 2015). According to previous studies, the broadening of the Soret band around 395-400 nm has been associated with the formation of 5cNO adducts, whereas a Soret maximum at ~415 nm has been related to 6cNO adducts of cytochromes c' (Andrew 2002; Andrew 2005; Yoshimura 1996; Manole 2015). The proportion of 6cNO and 5cNO adducts varied in those reports. In most cases, however, the 5cNO adduct by far dominated while the 6cNO species was either reported to be transient or occurred only in a small fraction (10-40 %). However, in several other studies, the 6cNO adduct has been reported as the dominant form (Hespen 2016).

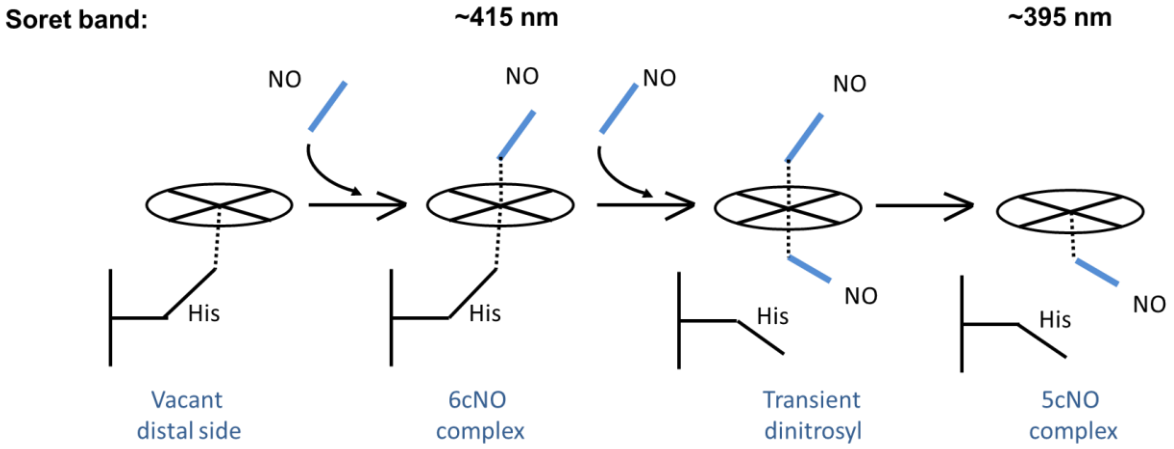

Figure 4.28 Binding of Nitric Oxide (NO) to Heme
The 6cNO adduct is characterized by the presence of a Soret peak around 415 nm, whereas a typical feature of the 5cNO adduct is a broad Soret band around 395-400 nm. The heme cofactor (circle) is shown proximally coordinated by a histidine. The concepts are reviewed by Hough *et al.* (2015).

Considering similar notions for NO binding to the ferrous NaxL and NaxS subunits, it can be inferred that both ferrous NaxL and NaxS subunits can bind NO and both can form 5cNO and 6cNO adducts. The 5cNO species, however, seems to be the final state for NaxL, whereas the 6cNO species dominates for NaxS. Moreover, NO binding to the ferric form of both subunits also shows similar spectral changes and proportions of 6cNO and 5cNO complexes.

The dissimilar NO binding preferences of NaxL and NaxS could perhaps be explained by the differences in the heme environments. Recent studies suggested that a decrease in the steric hindrance at the distal heme pocket of *Alcaligenes xylosoxidans* cytochrome c' (AXCP) could stabilize the 6cNO adduct (Kekilli 2017). However, the heme environment at the proximal side does not affect the NO binding behavior in various cytochromes c' (Hough 2011). In case of NaxL and NaxS, the formation of a 6cNO adduct would result in a replacement of the distal cysteine ligand and could be modulated by the surrounding residues in the distal heme pocket. The *Ks*NaxLS structure revealed a glutamine (Gln28) and methionine (Met35) in the distal heme pocket of *Ks*NaxL as well as a histidine (His93) residue in NaxS in close proximity to the heme iron. Such different distal heme environments might therefore account for dissimilar NO binding behaviors between *Ks*NaxL and *Ks*NaxS. Moreover, as will be discussed for Kustc0563 in the next section, the α5-α6 loop in NaxS is significantly flexible. This flexibility might provide additional movability to the distal cysteine ligand compared to that of NaxL, thereby promoting formation of the 6cNO adduct.

Interestingly, the *Ks*NaxLS complex shows a different behavior upon NO binding than its isolated components. Upon incubation with NO, the as-isolated (ferric state) of *Ks*NaxLS showed a shift of the Soret peak from 420 nm to 417 nm with a concomitant increase in its intensity indicating formation of a 6cNO adduct, while no features of a 5cNO adduct could be observed. Contrarily, it is difficult to assess NO binding to the ferrous state of *Ks*NaxLS, since the position of the Soret peak would remain the same *i.e.* at 417 nm upon NO binding. Moreover, spectra of NO-incubated samples showed no changes at the α- and β-band positions except for a decrease in their intensities. This decrease in intensity might be due to partial re-oxidation of *Ks*NaxLS. Therefore, NO binding to ferrous *Ks*NaxLS cannot be unambiguously deduced from the current results and will be a matter of further investigations.

Why does the *Ks*NaxLS complex exclusively prefer the formation of the 6cNO adduct with no sign of the 5cNO species as opposed to the preferences observed for the isolated subunits? The answer might be the interaction between the NaxL and NaxS subunits upon complex formation which might prevent proximal NO binding by rendering the proximal histidines

less flexible. Indeed few interactions can be observed in the *Ks*NaxLS structure such Van-der-Waals contacts between Ile126 of *Ks*NaxL with Phe123 and Tyr40 of *Ks*NaxS as well as a hydrogen bond between the backbone C=O of Ile126 in *Ks*NaxL and the backbone N-H of Asn60 in *Ks*NaxS. Moreover, *Ks*NaxL Lys125 interacts with *Ks*NaxS Ala44 *via* hydrogen bonding as well as hydrophobic interaction. *Ks*NaxL Lys125 possibly also makes hydrophobic interactions with *Ks*NaxS Tyr55. The residues Lys125, Ile126 of *Ks*NaxL and Asn60 of *Ks*NaxS are close to the respective proximal histidine residues *Ks*NaxL His124 and *Ks*NaxS His58, respectively (Fig 4.29).

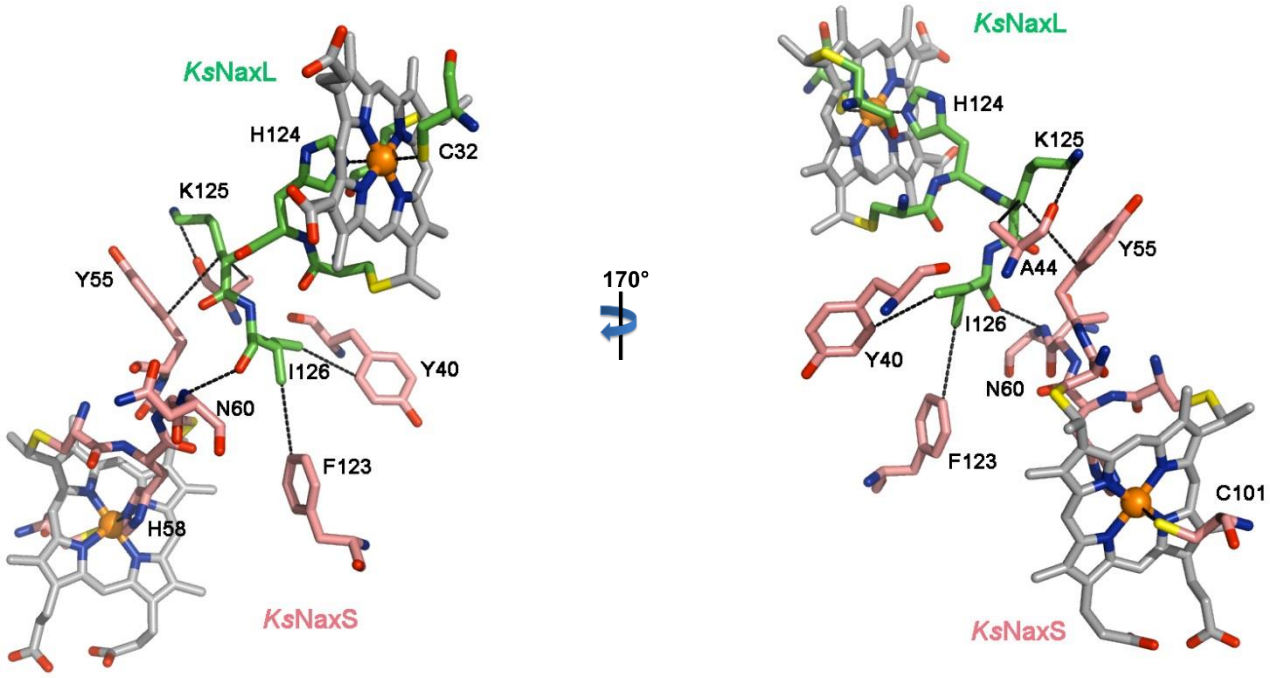

Figure 4.29 Interactions between NaxL and NaxS near the Proximal Histidines
The figure shows various hydrophobic (Van-der-Waals contacts) and hydrophilic interactions (black dashed lines) between residues from the *Ks*NaxL and *Ks*NaxS subunits in the KsNaxLS complex. These interactions are between residues close to the proximal histidine ligands (H124 and H58) of *Ks*NaxL and *Ks*NaxS and might prevent replacement of the proximal histidines by NO to form 5cNO adducts.

However, different observations were made for NO binding to the distal cysteine mutants (*Ks*NaxL wt/ NaxS C101M, *Ks*NaxL C32M/ NaxS wt and *Ks*NaxL C32M/ NaxS C101M), which contradict the above argument. Similar to the wild type complex, the mutant complexes in their ferric (as-isolate) states seemed to exclusively form 6cNO adducts. In their ferrous states, however, they showed a mixture of both 6cNO and 5cNO species as opposed to the wild type complex where no NO binding was observed. Therefore, along with the interactions between the subunits in the *Ks*NaxLS complex, the distal cysteine ligand might also contribute to the exclusive formation of 6cNO adducts by ferric wild type *Ks*NaxLS.

The UV-Vis spectroscopic features of CO-bound *Ks*NaxLS, its components and mutants (Soret band around 415-417 nm with increased intensity and flattening of α- and β-bands) are similar to the ferrous 6cCO adducts of other cytochromes (reminiscent to their 6cNO species) (Hough 2015). This again implies that the distal cysteine ligand is flexible enough to move out enabling distal CO binding. Although the mutant *Ks*NaxL C32M/ NaxS shows similar CO binding when compared to the wild type complex, the *Ks*NaxL wt/ NaxS C101M and *Ks*NaxL C32M/ NaxS C101M mutant complexes show lowered affinity for CO as could be judged from the mitigated relative increase in the intensity of the Soret band. This implies that the distal methionine ligand in the *Ks*NaxS subunit of the mutant complexes might resist distal binding of CO, whereas the cysteine ligand in the wild type protein allows it.

Since *Ks*NaxLS exists as a heterodimer under physiological conditions with cysteines as distal ligands, only 6cNO and 6cCO *Ks*NaxLS complexes are possible. Since nitric oxide is an intermediate in the anammox pathway, only the 6cNO adduct might be a physiologically relevant form among adducts of diatomic gases bound to *Ks*NaxLS. This conclusion brings us to a possible functional implication of the *Ks*NaxLS 6cNO adduct in anammox cells which will be discussed in the next section.

4.3.1.6 Functional Implications

Both nitric oxide (NO) and hydroxylamine (NH_2OH) completely inhibit the activity of hydrazine dehydrogenase (HDH), the final enzyme in the anammox pathway oxidizing hydrazine to dinitrogen (Maalcke *et al.* 2016). The inhibitory effects of both NO and NH_2OH are very similar as can be judged from the reported inhibitory constants (K_i^{NH2OH} = 7.9 ± 1.8 μM and K_i^{NO} = 2.5 ± 0.9 μM). In the physiological context of the anammox cells, NH_2OH has been proposed as an intermediate of the reaction catalyzed by hydrazine synthase (HZS; Dietl 2015). Leakage of NH_2OH from HZS would therefore be detrimental to the activity of HDH. Another highly abundant enzyme, hydroxylamine oxidase (HOX) (Maalcke 2014), was therefore supposed to oxidize NH_2OH to NO in order to mitigate the inhibitory effect of NH_2OH on HDH and to recycle nitric oxide as a substrate for HZS. However, NO produced by HOX would again inhibit the activity of HDH such that the proposed detoxification mechanism of HOX is not completely fulfilled.

Therefore, another protein would be needed to scavenge nitric oxide produced by HOX as well as by nitrite reductase (Nir) and perhaps to shuttle it to HZS. This protein needs to be present in large amounts in the anammoxosome, since NO is a highly diffusible compound and can easily penetrate lipid bilayers. The NaxLS complex satisfies many of the discussed criteria to act as an NO-scavenging and -shuttling protein. Ukita *et al.* reported that the NaxLS complex from *Jettenia caeni* represents approximately 10 % of the total molar protein content in the cell, which is similar to the molar content of HDH and HOX. Indeed, *Kuenenia stuttgartiensis* NaxLS is highly expressed as well, as indicated by transcriptomic data (Kartal 2011) and its ready purification from anammox biomass. In addition, the current study shows that NaxLS forms a 6cNO adduct upon NO binding similar to other NO-shuttling proteins (section 4.3.1.5). Moreover, pull-down assays indicate that NaxLS might interact with HZS maybe to transfer NO. However, there should also be an NO-releasing mechanism at the target site. Since the ferrous state of the *Ks*NaxLS complex does not seem to bind NO, the redox state change of *Ks*NaxLS might be a possible mechanism to release NO at its target site. Further research in this direction might give a concrete answer.

4.3.2 The Monoheme Cytochromes c Kustc0563 and Kustc0562

As already mentioned in section 4.1, the anammox pathway can only be productive if the electrons released from the oxidation of hydrazine to dinitrogen by hydrazine dehydrogenase (HDH) are shuttled to membrane complexes where they are involved in proton motive force generation. Finally, they have to be transported back to the soluble nitrite reductase (Nir) as well as hydrazine synthase (HZS) complexes where they are consumed for the reduction of nitrite to NO and the synthesis of hydrazine from NO and ammonium, respectively (Kartal 2013). Small c-type cytochromes, especially class I cytochromes c, are primarily known for their electron transport function between soluble and membrane-bound enzyme complexes in both eukaryotes and prokaryotes. The small class I c-type cytochrome Kustc0563 and its paralogue Kustc0562 were studied here as candidate redox partners of anammox enzyme complexes.

Kustc0563 has been reported to be highly expressed in *Kuenenia stuttgartiensis* on both mRNA and protein levels (Kartal 2011) and could even be purified from anammox biomass (Cirpus 2005). Moreover, its orthologue (KSU1_B0428) was recently purified from *Jettenia caeni* alongside with another monoheme cytochrome c (KSU1_C0855) possessing an unusual distal 3,4-dihydroxyphenylalanine (DOPA) ligand (Hira 2018). Expression of Kustc0562, however, has neither been reported in transcriptomic nor proteomic data (Kartal 2011). However, re-analysis of transcription profiles indicated that the kustc0562 and kustc0563 genes are transcribed at comparable levels (section 4.1).

Crystallization of Kustc0563 was strongly dependent on the presence of a hexahistidine-tag used for affinity purification. A construct with a C-terminal His-tag crystallized with orthorhombic space group symmetry ($P2_12_12$) with six molecules in the asymmetric unit. A construct where the N-terminal His-tag has been removed by TEV-protease, however, showed $P4_32_12$ symmetry with only one molecule in the asymmetric unit. Since Kustc0563_CHis comprises 94 amino acids, the His-tag already constitutes 6 % of its total sequence. Hence, there is a high chance that the His-tag could affect the crystallization outcome of such a small protein. The crystal structures of Kustc0563 and Kustc0562 determined at 1.9 Å and 3.0 Å resolution, respectively, both show a typical all helical class I cytochrome c fold (Bertini 2006). Despite possessing 55 % sequence identity and nearly identical tertiary structures the two proteins differ significantly in their biochemical properties.

4.3.2.1 Flexibility of the α5-α6 loop in Kustc0563 and Kustc0562

Fully oxidized Kustc0563, for instance, was reported to bind nitric oxide (NO) and cyanide (CN^-) (Huston 2007) whereas Kustc0562 did not bind any of them. Kustc0562 was bound to imidazole as evident both from its structure and from spectroscopic studies while imidazole binding was not observed for Kustc0563. The two methionine residues flanking the distal methionine ligand (Met91) in Kustc0563 are at Van-der-Waals distance from the heme. In Kustc0562, one of those flanking methionines (Met90) is substituted by lysine and the other one (Met92) by proline (Fig 4.30).

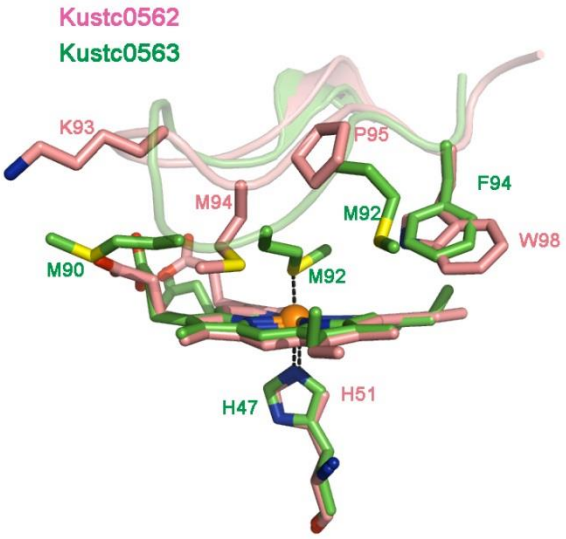

Figure 4.30 Differences at the α5-α6 Loops of Kustc0562 and Kustc0563 Modulating Loop Mobility
The α5-α6 loops of Kustc0562 (salmon) and Kustc0563 (green) are shown. Hydrophobic interactions from methionine 90 (M90) and 92 (M92) to the heme might stabilize the α5-α6 loop of Kustc0563. Both of these residues are substituted by lysine 93 (K93) and proline 95 (P95) in Kustc0562. Even if Cα-atoms of Kustc0562 P95 and Kustc0563 M92 superposed, P95 would be unable to make hydrophobic interactions with the heme, since it would still be more than 5 Å apart.

A hypothetical superposition of the Cα-atoms of Kustc0562 Lys93 and Pro95 to the respective Cα-atoms of the methionine residues Met90 and Met92 in Kustc0563 would be possible assuming Met94 as distal heme ligand of Kustc0562. In this case the carbon atoms of Kustc0562 Pro95 might not be close enough to the heme to form hydrophobic interactions. The polar residue Lys93, however, might possibly interact with the negatively charged heme propionate groups. The overall additional hydrophobicity provided by the methionine residues in Kustc0563 might explain the lower flexibility of its α5-α6 loop compared to Kustc0562. Mutational studies involving the respective residues in the α5-α6 loop might provide indications on their role in modulating loop mobility.

4.3.2.2 Kustc0563 as Putative Redox Partner of *Ks*HOX

Differences in functional properties were also reflected by comparative redox activities of Kustc0562 and Kustc0563 in assays with *Ks*HOX and *Ks*HDH. Kustc0562 showed no redox activity with *Ks*HOX while Kustc0563 showed significant activity which was even six to eight times higher than bovine cytochrome c and could be saturated. With *Ks*HDH, however, both Kustc0562 and Kustc0563 showed comparative initial activities.

Interactions between redox-active enzymes and their small electron transfer partners are generally transient involving low geometrical complementarity and loose packing to ensure fast dissociation (Crowley 2003; Crowley 2004). The surface of redox-active enzymes can possess multiple encounter sites where redox partners can bind and the ease of electron transfer can depend on the orientation of the enzyme and the electron transfer partner to one another (Nyola 2008; Volkov 2015). Despite having similar structures and redox potentials, Kustc0562 and Kustc0563 possess very different electrostatic surface potentials. Kustc0562 possesses a highly positively charged area around the heme pocket while the surface around the corresponding region in Kustc0563 is negatively charged. This dichotomy in charge distribution might dictate the nature of transient interactions between Kustc0562/ Kustc0563 with *Ks*HOX/ *Ks*HDH and might hence influence the rate of electron transfer.

Both Kustc0562 and Kustc0563 possess an N-terminal signal peptide. Therefore, both of these proteins are likely targeted to the anammoxosome of *K. stuttgartiensis* cells, co-localizing with the enzymes involved in the anammox pathway. Moreover, transcriptomic data showed that both Kustc0562 and Kustc0563 were expressed above average level (Kartal 2011) (section 4.1). Additionally, the current study shows that Kustc0563 is able to perform electron transport reactions with both *Ks*HOX and *Ks*HDH, and Kustc0562 with *Ks*HDH. As mentioned before, Kustc0563 shows higher redox activity with *Ks*HOX when compared with the tested redox partners. It might be therefore possible that Kustc0563 acts as physiological redox partner of *Ks*HOX. However, since this study included only few of the available small cytochromes from *K. stuttgartiensis* for comparison, there might be other cytochromes which would show even better activity with *Ks*HOX than Kustc0563. Therefore, the identity of the redox partner of Kustc0563 cannot be unambigously concluded. However, it is clear that both Kustc0563 and Kustc0562 can perform electron transport.

Chapter 5

Purification, Biochemical, Biophysical and Structural Characterization of Anammox Proteins from DEMON® Granular Sludge

5. Purification, Biochemical, Biophysical and Structural Characterization of Anammox Proteins from DEMON® Granular Sludge

5.1 Introduction

From the discovery of the anammox process (Mulder 1995) and the identification of the first anammox species, *Brocadia anammoxidans* (Strous 1999), to the purification of the first proteins from *Kuenenia stuttgartiensis* (Cirpus 2005) and finally the biochemical, biophysical and structural characterization of anammox protein complexes (Kartal 2011; Maalcke 2014; Maalcke 2016; Dietl 2015) more than two decades passed. Indeed, despite efforts by several groups, our understanding of some unique aspects of anammox bacteria such as the biochemistry of the anammox pathway itself or the biosynthesis of ladderane lipids is still limited. A main reason for the slow progress in this research field has been the failure to obtain c-type multiheme-containing proteins and protein complexes using heterologous expression systems. Thus, anammox proteins must typically be purified from anammox biomass which has been commonly obtained from laboratory scale enrichment cultures that are difficult to set up. These difficulties include the extremely slow growth of these bacteria and their tendency to form biofilms coexisting with several other unrelated bacteria. Moreover, protein purification from such material can be extremely challenging (Cirpus 2006).

The slow growth rate of anammox bacteria is obviously due to their long doubling times between 7 to 21 days. Therefore, it takes 180-260 days to enrich an anammox species up to ~80 % and even 350-400 days to obtain ~95 % enrichment (Kartal 2013). Moreover, bacterial cultivation over such a long time span requires sophisticated feeding and monitoring capacities.

Most anammox enrichment techniques such as the sequencing batch reactor (SBR; Strous 1998) are based on the formation of biofilms *i.e.* bacterial cell aggregates which are embedded in a matrix of extracellular polymeric substances (EPS) mostly consisting of polysaccharides and proteins. The cell paste prepared from SBR biomass was reported as sticky, and gelling of EPS components at low temperatures made it extremely troublesome to purify proteins for further biochemical studies (Cirpus 2006). However, this problem could be relieved by enrichment of planktonic anammox bacterial cells in a membrane bioreactor (MBR) (van der Star 2008b). This improvement enabled successful purification, biochemical

and structural characterization of several soluble anammox proteins and protein complexes (Kartal 2011; Maalcke 2014; Maalcke 2016; Dietl 2015). Nevertheless, bioreactor-based, long-term laboratory scale cultures of anammox bacteria are still technically very demanding and yield only limited amounts of bacterial biomass. Owing to these obstacles, an alternative, easily accessible source of anammox biomass for research purposes would be highly desirable.

Anammox sludge from large-scale reactors used in waste water treatment plants (WWTPs) could be an alternative source of anammox bacterial biomass for biochemical studies. In recent times, the anammox process has been extensively applied as a cost effective and environmentally friendly solution for nitrogen removal from municipal waste water. Since the first full-scale anammox-based WWTP in Rotterdam (2002), the number of such plants has grown to fifteen in 2011 and currently to more than 110 worldwide (Mao 2017; Ni 2013) (Figure 5.1).

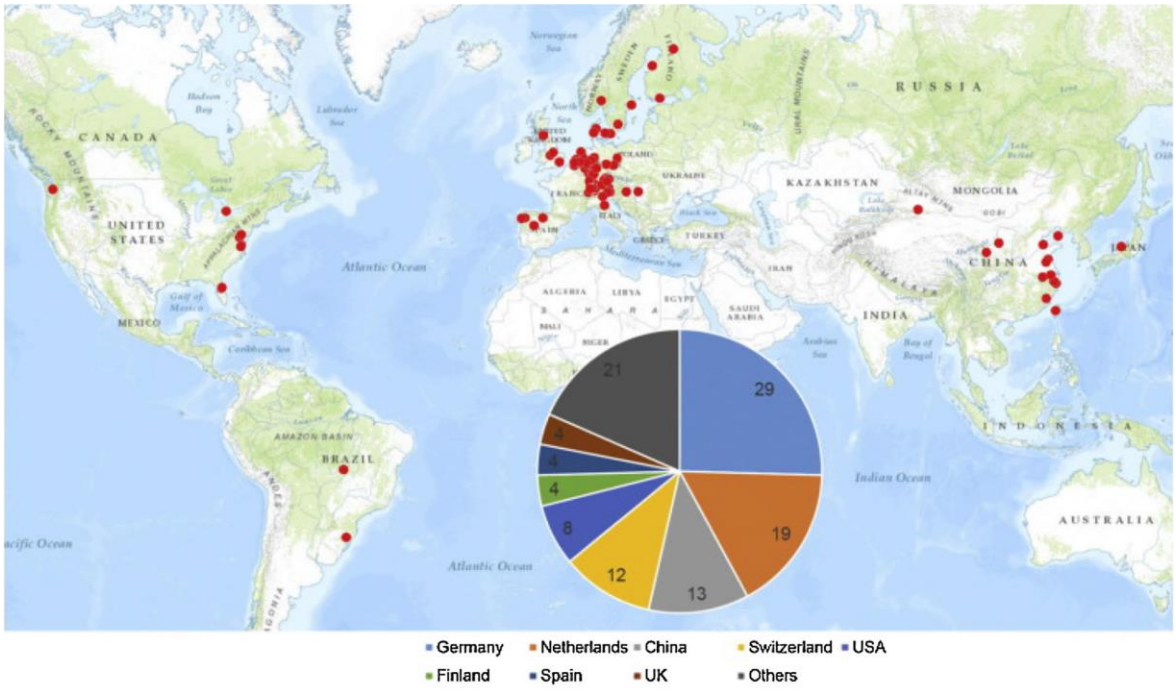

Figure 5.1 Worldwide distribution of anammox-based waste water treatment plants (WWTPs)
The red dots on the world map show the location of each WWTP. The pie chart shows the total number of anammox-based WWTPs present in each country. Germany leads with 29 of such plants (figure adapted from (Mao 2017)).

In general, anammox-based ammonium-nitrogen removal systems combine a partial nitrification step, which converts a part of the ammonium into nitrite, with anammox to turn ammonium and nitrite into molecular nitrogen (N_2). There are two principle ways to make these processes work in concert. The two steps can be either separated in two distinct reactors *e.g.* the SHARON-ANAMMOX® system (van Dongen 2001); SHARON stands for **S**ingle reactor system for **H**igh activity **A**mmonium **R**emoval **O**ver **N**itrite) or are both carried out in a single reactor. Such one-stage systems include **C**ompletely **A**utotrophic **N**itrogen removal **O**ver **N**itrite (CANON®) (Third 2001), **S**ingle stage **N**itrogen removal using **A**nammox and **P**artial nitritation (SNAP®) (Furukawa 2006), **P**artial **N**itrification and **A**nammox (PN/A) (Mulder 2003) and **DE**am**MON**ification (DEMON®) (Wett 2006). All of the mentioned systems represent sequencing batch reactors (SBRs) which work by settling of biomass, decanting effluent and again replenishing influent (culture medium). This cycle is periodically repeated and selects for the formation of bacterial biofilms (Kartal 2013).

Although one-stage single reactor systems are more cost-efficient, they require the coexistence of both aerobic and anaerobic ammonium-oxidizing bacteria (AOB and anammox). In order to maintain the interaction of the two different groups of bacteria in a common biofilm, precise regulation of the level of dissolved oxygen (DO) is required.
In case of the DEMON® process, a sequencing batch reactor is intermittently aerated in a pH-controlled manner (Wett 2006). Aeration of the reactor promotes nitrification but (reversibly) inhibits anammox activity. Therefore, during each aeration period ammonium is partially oxidized to nitrite by AOB, a process releasing protons and therefore decreasing pH. If pH decreases below an allowed change ($\Delta pH=0.01$), aeration is stopped, AOB consume residual oxygen such that the reactor turns anaerobic and anammox activity is resumed. During this anaerobic period anammox bacteria turn ammonium and nitrite into N_2 which is accompanied by a pH increase. When pH increases by 0.01, aeration is started concomitantly resuming nitrification activity. This cycle of tightly pH-controlled intermittent aeration is repeated for six hours followed by a two-hour period of settling bacterial biomass, decanting ammonium-depleted effluent and subsequent filling with ammonium-loaded influent (Figure 5.2 a) (Innerebner 2007).

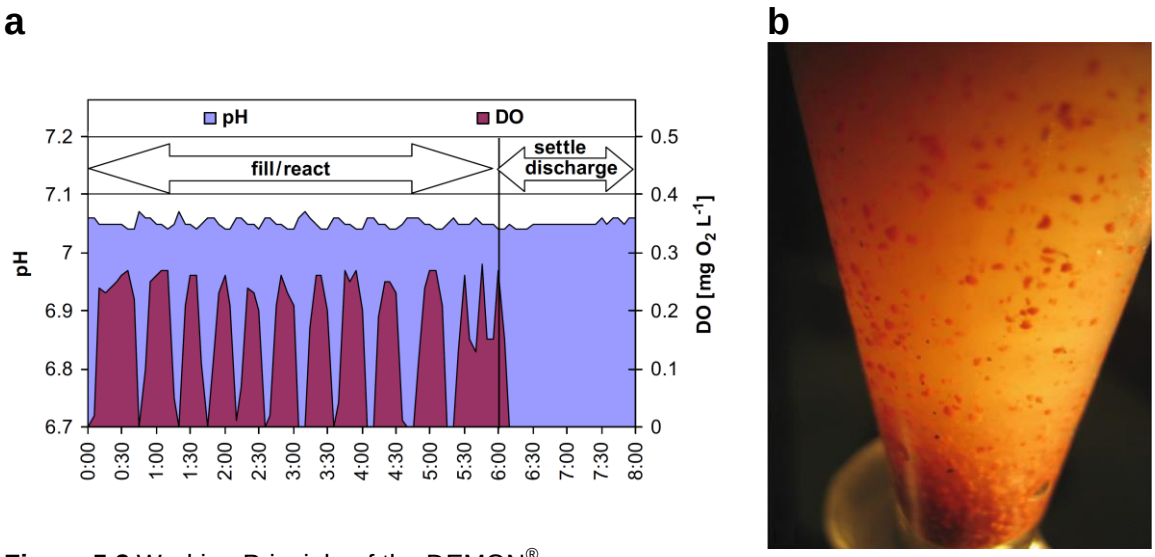

Figure 5.2 Working Principle of the DEMON® process
a) Tightly pH-controlled (ΔpH=0.01) intermittent aeration is used for the regulation of aerobic and anaerobic ammonium oxidation activity within a single-stage sequencing batch reactor. DO is the level of dissolved oxygen. The figure is taken from (Innerebner 2007).
b) The DEMON® process is carried out in a single-stage reactor with both aerobic and anaerobic ammonium-oxidizing bacteria enriched in the biomass. The image shows a sludge sample from a full-scale DEamMONification (DEMON®) reactor in Strass, Austria. Red, settling granules are separated from floating floccules in a separatory funnel. The figure is taken from (Innerebner 2007).

The bacterial biomass in DEMON® and other reactor types can be divided into granular and floccular sludge particles (Innerebner 2007). Sludge granules are usually dense and have a steep oxygen gradient with an anaerobic core and a micro-aerobic outer layer (Nielsen 2006). The smaller, less dense floccules, however, are less likely to possess an anaerobic core (Speth 2016; Vlaeminck 2010). Therefore, the core of the dense granules is the home of the anammox bacteria (Hao 2005).

Figure 5.2 b shows the separation of dense, settling, red DEMON® sludge granules from less dense, floating floccules in a separatory funnel (Innerebner 2007). Granules are composed of microoorganisms belonging to various bacterial phyla including aerobic and anaerobic ammonium oxidizers, other chemoautrophs such as *Nitrospira* as well as some heterotrophic bacteria *e.g. Chlorobi* which are all embedded in a common EPS matrix (Figure 5.3) (Innerebner 2007; Lawson 2017). However, the abundance of members from each bacterial phylum in a granule depends upon its size. The bigger the size of a granule, the larger the fraction of anammox bacteria which can vary from less than 10 % to more than 90 % (Luo 2017; Bagchi 2016; Lawson 2017; Persson 2017).

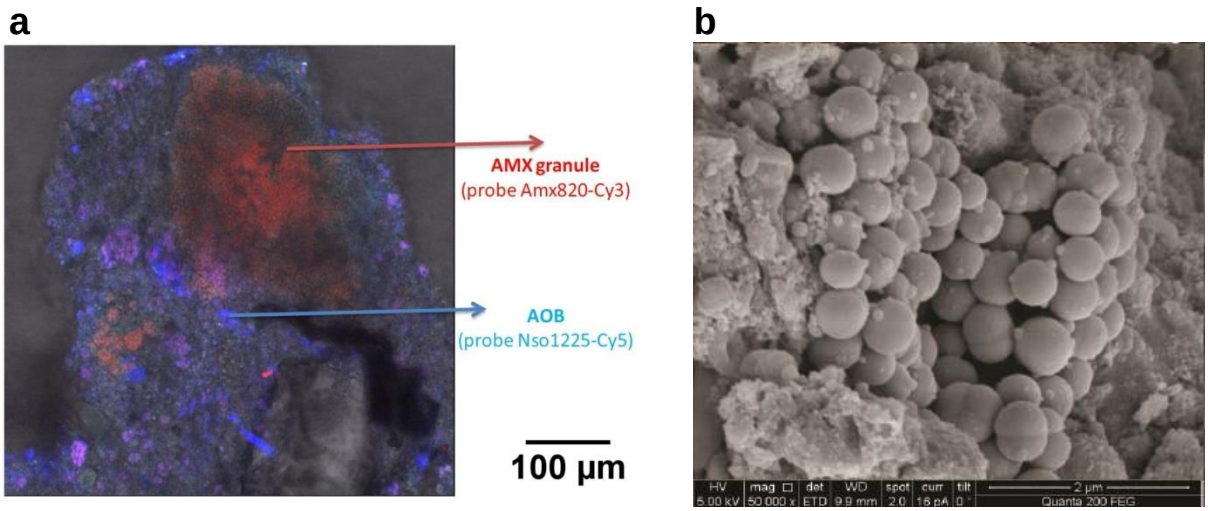

Figure 5.3 Bacteria in Sludge Granules
a) FISH image of a DEMON® granule sample from the WWTP in Strass, Austria. Anammox bacteria were hybridized with the 16S rDNA probe Amx820-Cy3, which targets both *Candidatus* "Brocadia" and "Kuenenia". AOB were detected using probe Nso1225-Cy5. The figure is adapted from (Wett 2013). **b)** The Scanning Electron Microscopic (SEM) image of a granule from a laboratory scale SBR culture shows coccoid anammox bacteria embedded in EPS. The figure is taken from (Bagchi 2016).

In this chapter the possibility to purify anammox proteins and protein complexes from granular sludge obtained from a DEMON® reactor at a local WWTP in Heidelberg, Germany was explored. The microbial biodiversity of the collected biomass was assessed using PCR-bases genetic phylomarkers. Since it was found that only a single anammox species (*Brocadia fulgida*) was present in the sludge, the purification of central anammox c-type cytochrome complexes namely hydrazine synthase (*Bf*HZS), hydrazine dehydrogenase (*Bf*HDH) and hydroxylamine oxidase (*Bf*HOX) was pursued. The proteins were purified to homogeneity and were biochemically and biophysically analyzed. Finally, it was studied whether the purified proteins were suitable for crystallization and subsequent structural characterization of *Bf*HOX by X-ray crystallography was carried out.

5.2 Results

5.2.1 Collection and Processing of DEMON® Sludge Granules

The biomass used in this study was collected from a full-scale deammonification (DEMON®) facility in Heidelberg, Germany (49°26'7.96" N, 8°38'33.83" E) in August 2015. This plant was installed in 2008 and consists of two 550 m^3 sequencing batch reactors with an operational capacity of 320 m^3d^{-1}. It is used for the treatment of effluents from activated sludge dehydration (1,050 mg L^{-1} and < 150 mg L^{-1} ammonium nitrogen in influent and effluent, respectively). Granular sludge samples were taken underneath a hydrocyclone for sludge separation from liquid effluents. Brownish sludge granules settled by gravity within 15 minutes followed by removal of the supernatant. The remaining liquid was drained through a piece of cotton cloth while pressing out the liquid. 50 L of DEMON® sludge yielded 17 kg of granules (wet-weight). Granules were frozen in liquid nitrogen and stored at -20 °C until use.

5.2.2 Biodiversity Analysis

The gene encoding the α-subunit of the hydrazine synthase (HZS) complex served as an anammox-specific phylomarker (Harhangi 2012). PCR amplification using the degenerated primers hzsA 526F/1829R (Harhangi 2012) resulted in a part of the HZSα gene (~1.4 kb). The obtained DNA sequence was 99.7 % identical to the HZSα gene from *Brocadia fulgida* followed by orthologous gene sequences from other anammox species (Figure 5.4 a).

Moreover, the amplification and sequencing of a 16S rDNA fragment using specific primers for *Planctomycetes* (PLA46F/1393R; Neef 1998; van der Star 2008b) resulted in three clones which showed nearly 100 % identity to the 16S rDNA from *Brocadia fulgida*. Four additional clones clustered with certain uncultured bacteria and one with an uncultured *Chloroflexi* species (Fig 5.4 c). Based on the genetic analyses of both HZSα and 16S rDNA sequences it can be concluded that *Brocadia fulgida* is probably the only dominant anammox species present in the analyzed DEMON® granules. However, there might also be other bacteria distinct from anammox present belonging to the phylum of *Planctomycetes*.

A part of the hydroxylamine oxidoreductase (HAO) gene sequence was amplified as a phylomarker for aerobic ammonium-oxidizing bacteria (AOB). The used primers were specifically targeted to β-proteobacterial HAO. All of the sequenced clones either clustered with *Nitrosomonas europaea* or *N. eutropha* (Fig 5.4 b) as representatives of the AOB community in the analyzed DEMON® sludge sample.

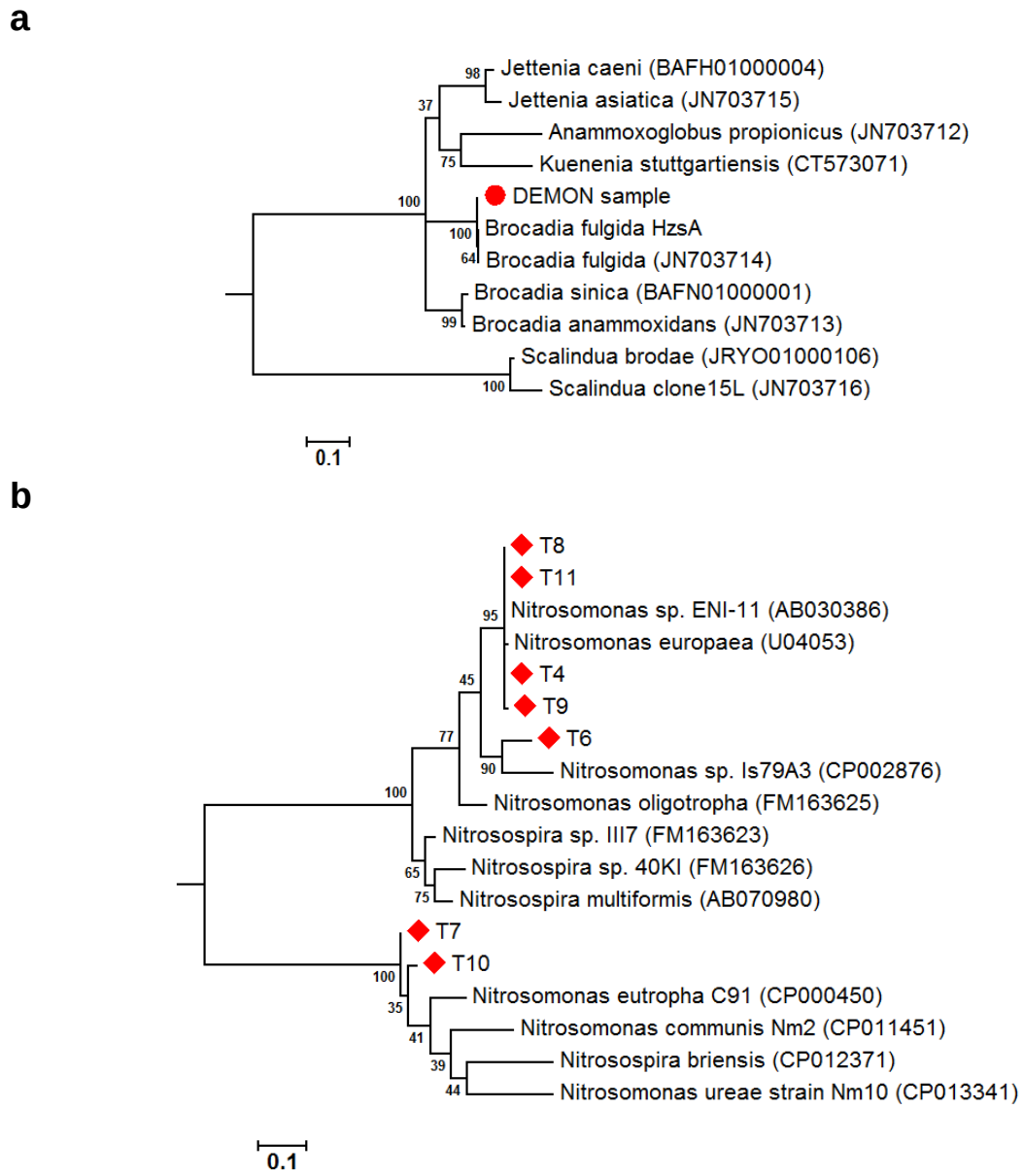

Figure 5.4 Biodiversity of DEMON® granules
Genomic DNA was extracted from sludge granules and unique marker genes from both anammox and aerobic ammonium-oxidizing bacteria (AOB) as well as 16S rRNA genes from *Planctomycetes* were amplified by PCR, cloned and sequenced. Comparative sequences were retrieved from the National Center for Biotechnology Information (NCBI). GenBank accession numbers are given next to the species names. Phylogenetic trees were generated by the Phylogeny.fr server (Dereeper 2008) using multiple sequence alignment in MUSCLE and tree reconstruction by the maximum-likelihood method in PhyML using 100 bootstrap replicates (confidence values are indicated on the branch points). The scale bar represents 0.1 substitutions per nucleotide position.
a) Hydrazine synthase alpha (HZSα) as a phylomarker for anammox bacteria was amplified using primers hzsA 526F/1829R (Harhangi 2012). A single consensus HZSα sequence was obtained from the DEMON® sample (red dot) which showed 99.7 % sequence identity to *Brocadia fulgida.*
b) Hydroxylamine oxidoreductase (HAO) as an AOB phylomarker. A fragment of the HAO gene was amplified using custom primers (appendix 2). The obtained clones cluster either with *Nitrosomonas europaea* or *N. eutropha.*

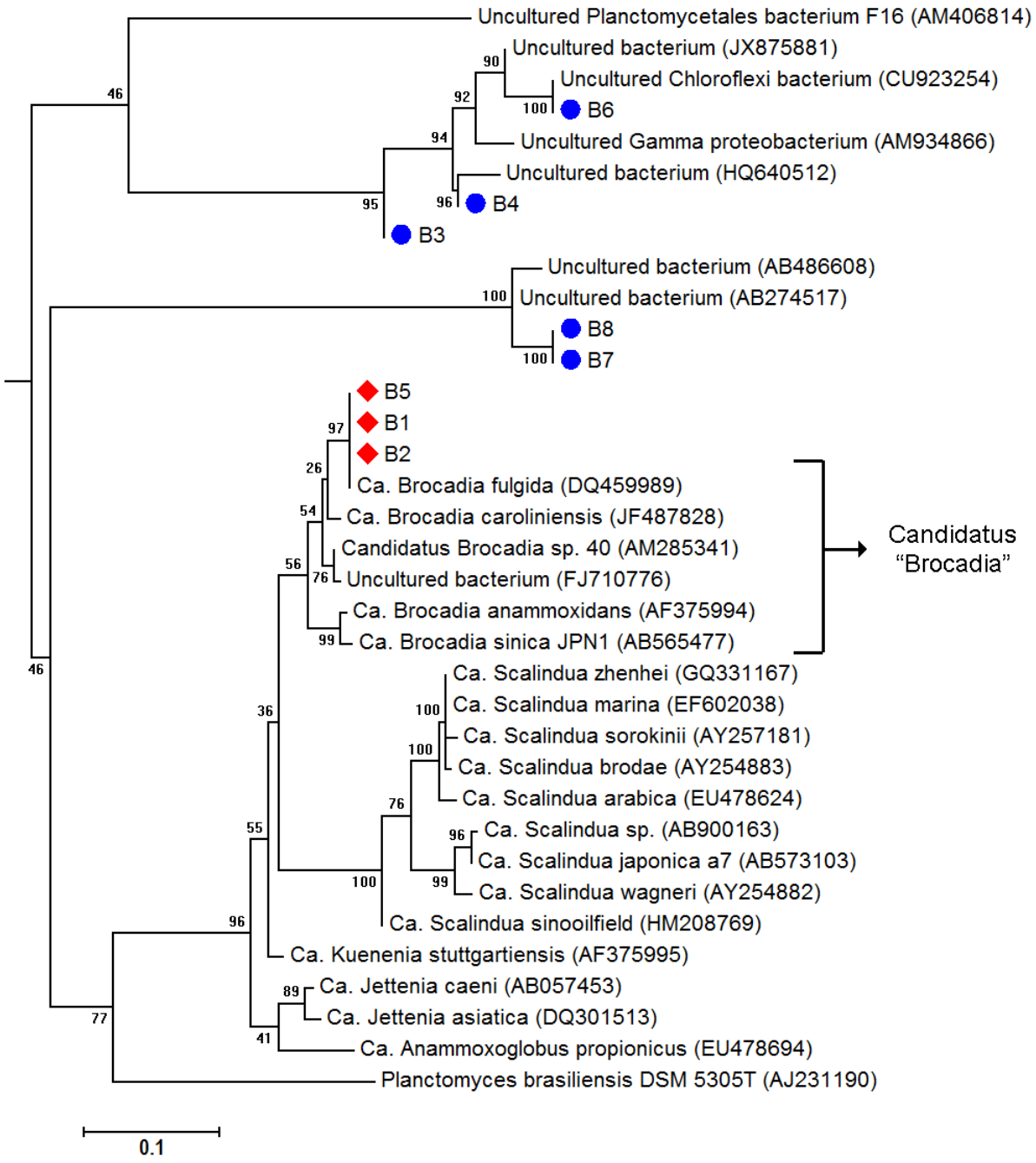

Figure 5.4 Biodiversity of DEMON® granules (continued)
c) Planctomycetes 16S rDNA as a phylomarker for all *Planctomycetes*. A fragment of the 16S rRNA gene was amplified using primers PLA46F/1393R (Neef 1998, Ferris 1996). Clones B1, B2 and B5 (red diamonds) cluster with *B. fulgida* with sequence identities of 99% (B1 and B5) and 91% (B2). The residual clones (blue dots) cluster with other uncultured bacteria belonging to the *Planctomycetes* phylum distinct from anammox.

5.2.3 Purification of *Bf*HDH, HOX and HZS from Sludge Granules

The detailed purification procedure of *Brocadia fulgida* c-type cytochrome complexes from DEMON® sludge granules is described in section 2.2.3.3. Homogenization of 200 g DEMON® granules (Fig 5.5 a and b) as the first step resulted in a thick paste-like suspension (Fig 5.5 c). Following cell lysis by sonication and ultracentrifugation, a red-colored cell-free extract was obtained indicating the presence of cytochromes (Fig 5.5 d).

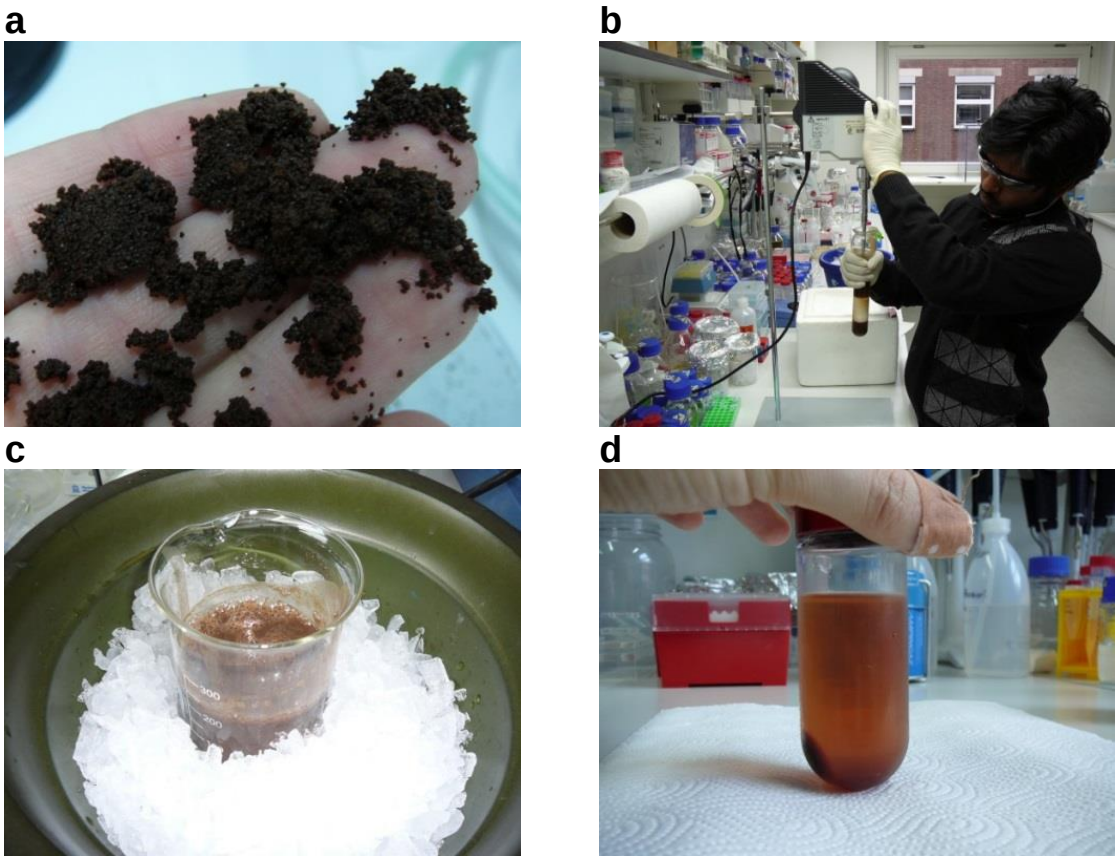

Figure 5.5 Preparation of a cell-free extract from DEMON® granules
a) Reddish-brown DEMON® granules collected from a local WWTP in Heidelberg, Germany.
b) The granules were homogenized using a Dounce homogenizer with a motor-driven Teflon pestle at 1,000-1,400 rpm in a buffer containing 20 mM TrisCl pH 8.0.
c) Granule suspension after homogenization.
d) The cell debris from the crude, sonicated lysate was removed by centrifugation at 17,696 x g. The supernatant from the first centrifugation step was further subjected to ultracentrifugation at 158,420 x g. The figure shows the red colored, cytochrome-containing supernatant after ultracentrifugation. The obtained cell-free extract was used for the three-step chromatographic purification of anammox protein complexes.

The obtained cell-free extract was subjected to a three-step chromatographic separation. The crude extract after ultracentrifugation was loaded onto a Q-Sepharose anion exchange column. After washing, elution with an NaCl gradient from 0 to 800 mM in 10 column volumes (CV) resulted in two peaks. The first peak at 320-390 mM NaCl was dominated by *Brocadia fulgida* hydrazine synthase (*Bf*HZS) whereas the second peak at 440-530 mM NaCl mainly contained octaheme c-type cytochromes (OCCs). Fractions corresponding to the two peaks were pooled separately and loaded onto a hydroxyapatite column which was eluted with an increasing concentration of potassium phosphate (KPi) pH 7.0. This resulted in two overlapping peaks around 220 mM KPi and 290 mM KPi, respectively. The fractions from both peaks were pooled separately and subjected to gel filtration chromatography (Superose 6, 10/300 column). The pool collected at 220 mM KPi resulted in two peaks at 11 mL and 16 mL elution volume. The peak at 16 mL was significantly higher in absorbance at 280 nm (15 times) than the peak at 11 mL and was confirmed to be pure hydroxylamine oxidase (*Bf*HOX) by SDS-PAGE and mass spectrometry. The gel filtration peak eluting at 11 mL contained pure hydrazine dehydrogenase (*Bf*HDH). The pool eluting at 290 mM KPi from the hydroxyapatite column also resulted in two peaks in gel filtration at the same positions. In this case, however, the peak at 16 mL was only about 3 times higher in absorbance at 280 nm than the peak at 11 mL. The 11 mL peak contained *Bf*HDH, whereas the 16 mL peak consisted of a mixture of both *Bf*HOX and *Bf*HDH.

The Q-Sepharose fractions corresponding to *Bf*HZS were also pooled and subjected to hydroxyapatite column chromatography resulting in a single asymmetric peak eluting at around 250 mM KPi. Gel filtration of this material resulted in a single peak around 15.9 mL. An SDS-PAGE analysis of purified *Bf*HOX, *Bf*HDH and *Bf*HZS is presented in figure 5.6.

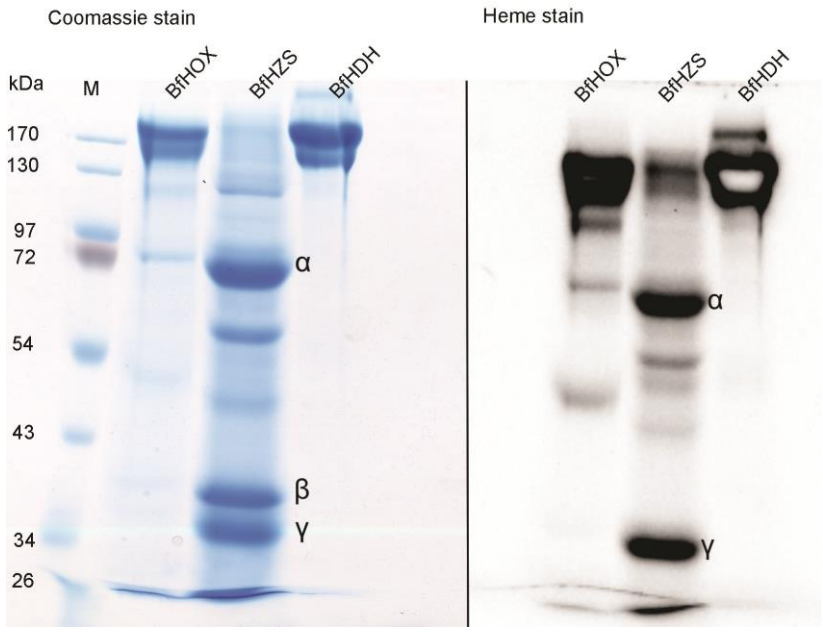

Figure 5.6 Tris-glycine 4-20 % Gradient SDS-PAGE Analysis of *Bf*HOX, *Bf*HZS and *Bf*HDH Purified from DEMON® Granules
3-5 µg of each protein sample was loaded. M: PageRuler pre-stained protein ladder (Thermo Scientific, Darmstadt, Germany). The three subunits of *Bf*HZS are indicated as α, β and γ. Since the α- and γ-subunits of *Bf*HZS are diheme c-type cytochromes, the corresponding bands are visible with heme staining.

5.2.4 UV-Vis Spectroscopy

The UV-Vis spectra of *Bf*HDH and *Bf*HOX (Figure 5.7 a and b) in their as-isolated state showed a Soret peak around 408-409 nm with a broad band in the region of 530 nm. Upon reduction with sodium dithionite the Soret maximum of both *Bf*HDH and *Bf*HOX was red-shifted to 420 nm accompanied by an increase in its absorbance. The spectra of both proteins in their reduced state also showed α- and β-bands at 555 and 525 nm, respectively. Additionally, the spectrum of fully reduced *Bf*HDH and *Bf*HOX showed a small peak at 473 and 468 nm, respectively, which is a diagnostic feature for OCCs containing a tyrosine-linked heme cofactor (Maalcke 2014).

The potential substrates hydrazine (N_2H_4) and hydroxylamine (NH_2OH) partially reduced *Bf*HOX as indicated by the appearance of α- and β-bands as well as a shoulder of the Soret peak around 420 nm. In case of *Bf*HDH, however, only hydrazine caused reduction as evident from the presence of α- and β-bands and a double Soret peak (at 408 nm and 420 nm). Nevertheless, hydroxylamine addition to *Bf*HDH also caused a very small peak in the spectrum at the position of the α-band.

The UV-Vis spectrum of as-isolated *Bf*HZS showed a Soret peak at 406 nm (Figure 5.7 c). Upon dithionite reduction, the Soret band was red-shifted to 420 nm with concomitant appearance of α- and β-bands at 554 and 524 nm, respectively. Both hydrazine and hydroxylamine did not cause any change in the spectra.

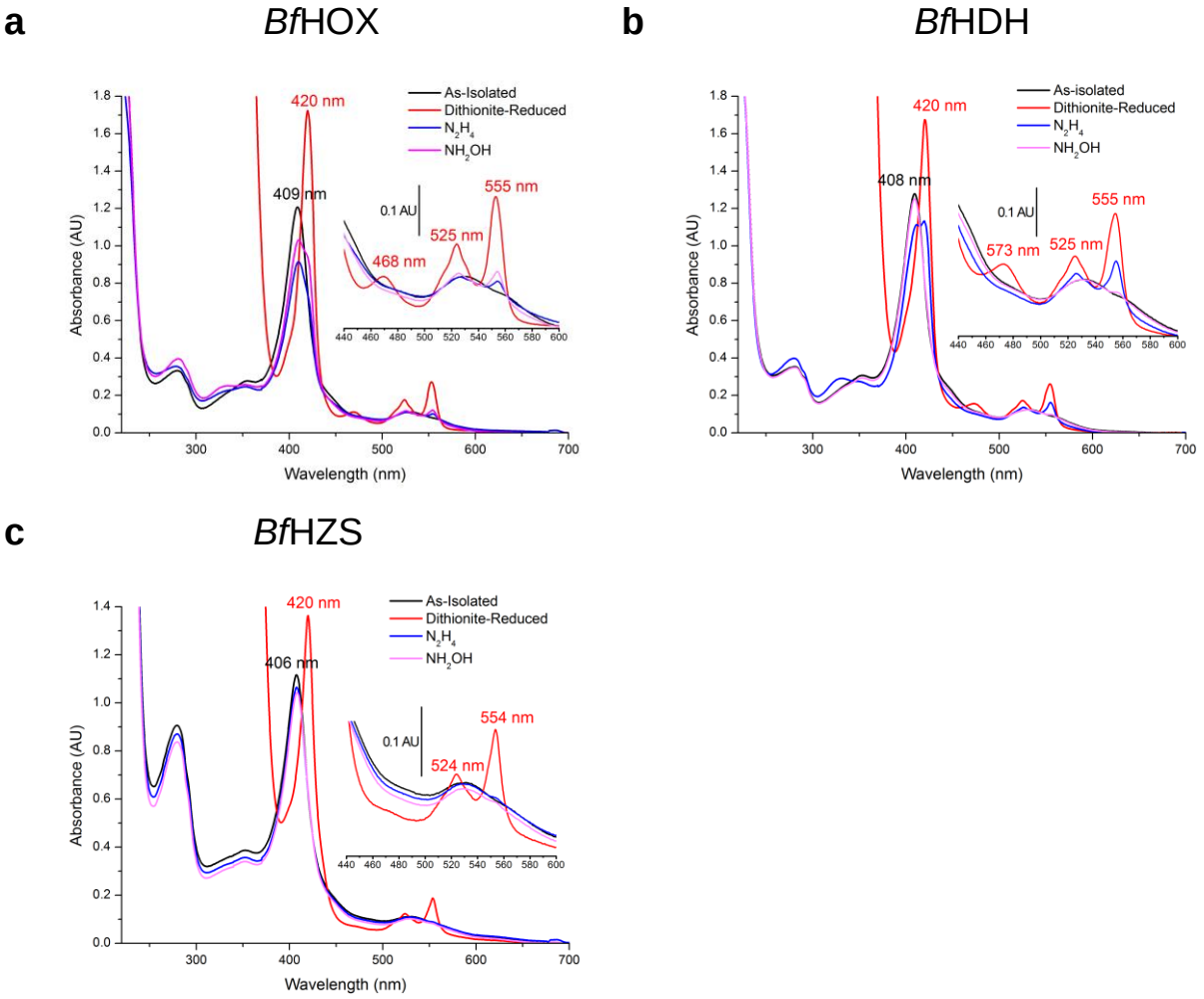

Figure 5.7 UV-Vis Spectroscopy of *Brocadia fulgida* hydroxylamine oxidase (*Bf*HOX), hydrazine dehydrogenase (*Bf*HDH) and hydrazine synthase (*Bf*HZS)
Individual as-isolated protein samples were diluted to an absorbance of ~1.2 at their Soret maximum in a buffer containing 25 mM KCl, 25 mM HEPES/KOH pH 7.5. A few grains of sodium dithionite were used to fully reduce the proteins. 10 mM of either hydrazine (N_2H_4) (as hydrazinium sulphate, pH=7.0) or hydroxylamine (NH_2OH) (as hydrochloride salt, pH=7.0) were used.
a) *Brocadia fulgida* hydroxylamine oxidase (*Bf*HOX)
b) Hydrazine dehydrogenase (*Bf*HDH)
c) Hydrazine synthase (*Bf*HZS)
The Soret band maxima of the spectra in the as-isolated (black line) and fully reduced state (red line) are indicated. The peaks at 468 nm and 473 nm in the spectra of fully reduced *Bf*HOX and *Bf*HDH, respectively, are indicative of a tyrosine-heme crosslink (Maalcke 2014). Both N_2H_4 and NH_2OH caused partial reduction of *Bf*HOX as indicated by the presence of weak α- and β-bands and a partially red-shifted Soret peak. However, only N_2H_4 caused partial reduction of *Bf*HDH, whereas NH_2OH only resulted in a very small peak at the α-band position.

5.2.5 Activity Assays

The catalytic rate ($k_{cat}^{NH_2OH}$) and the catalytic efficiency ($k_{cat}/K_M^{NH_2OH}$) of hydroxylamine oxidation by *Bf*HOX were similar to the values determined for their homologues (Table 5.1). Likewise, the catalytic rate ($k_{cat}^{N_2H_4}$) and the catalytic efficiency ($k_{cat}/K_M^{N_2H_4}$) of hydrazine oxidation by *Bf*HDH were also comparable to the orthologues of the enzyme. These results indicate that both *Bf*HOX and *Bf*HDH were purified in an optimally active state.

Table 5.1 Michaelis-Menten Kinetics of *Bf*HOX and *Bf*HDH Compared with their Homologues

Organism	***Brocadia fulgida***	***Jettenia caeni***	***Kuenenia stuttgartiensis***	***Brocadia anammoxidans***
		HOX Kinetics		
Locus tag	**Broful00019 (*Bf*HOX)**	**KSU1_D0438 (JcHOX)**	**Kustc1061 (KsHOX)**	**BaHOX**
***V*$_{max}$ NH_2OH (µmol min^{-1} mg^{-1})**	1.71	9.6	4.8±0.2	21
***k*$_{cat}$ NH_2OH (s^{-1})**	16	19	15	64
***K*$_M$ NH_2OH (µM)**	20	33	4.4±0.9	26
***k*$_{cat}$/*K*$_M$ NH_2OH (s^{-1}µM^{-1})**	0.8	0.58	3.4	2.5
Total Size (kDa)	184	174*	184	183
Subunit size (kDa)	61	58	61.5	58
Subunit Composition	α_3	α_3*	α_3	α_3
P460 heme optical maximum (nm)	468	468	468	468
Reference	This study	(Shimamura 2008)	(Maalcke 2014)	(Schalk 2000)
		HDH Kinetics		
Locus tag	**Broful01550-51 (*Bf*HDH)**	**KSU1_B0738 (JcHDH A) KSU1_D0435 (JcHDH B)**	**Kustc0694 (KsHDH)**	**BaHDH**
***V*$_{max}$ N_2H_4 (µmol min^{-1} mg^{-1})**	0.51	6.2	11±1.2	ND
***k*$_{cat}$ N_2H_4 (s^{-1})**	5.7	13.4	36	ND
***K*$_M$ N_2H_4 (µM)**	7.6	5.5	10±2.2	ND
***k*$_{cat}$/*K*$_M$ N_2H_4 (s^{-1} µM^{-1})**	0.75	2.4	3.5	ND
Total Size (kDa)	200.7 (~1600)	186*	201.5 (~1600)	ND
Subunit size (kDa)	66.9	62	67.2	ND
Subunit Composition	$\alpha_3((\alpha_3)_8)$	α_3*	$\alpha_3((\alpha_3)_8)$	ND
P460 heme optical maximum (nm)	473	472	473	ND
Reference	This study	(Shimamura 2007)	(Maalcke 2016)	

A reaction mixture of 1 mL in a buffer containing 20 mM potassium phosphate pH 7.0 was prepared containing 1 µg of either *Bf*HOX or *Bf*HDH. 50 µM of bovine heart cyt c ($\Delta\varepsilon_{550}$=19,600 $M^{-1}cm^{-1}$) was used as redox partner. The reaction was started by adding an appropriate amount of hydroxylamine (hydrochloride salt, pH=7.0) or hydrazine (as hydrazinium sulphate, pH=7.0) for *Bf*HOX or *Bf*HDH, respectively. The reduction of bovine cyt c was followed at 550 nm at 37°C. *) The oligomeric states of *Jc*HOX (Shimamura 2008) and *Jc*HDH (Shimamura 2007) were originally assigned as dimers based on analytical gel filtration using calibration with standard proteins. Using the same method, *Ks*HOX and *Bf*HOX were also assigned as dimers. However, given the fact *Ks*HOX and *Bf*HOX unambiguously formed trimers as concluded from biophysical analyses (AUC and SEC-MALS), the previously assigned oligomers of *Jc*HOX and *Jc*HDH are probably incorrect.

5.2.6 Crystallization

Precipitant screening using the sitting drop vapor diffusion method resulted in a few conditions where red colored crystals of *Bf*HDH and *Bf*HOX appeared, whereas crystallization of *Bf*HZS failed. Tiny, cube-like *Bf*HDH crystals were visible after one day, whereas pyramid-shaped *Bf*HOX crystals grew after several months at 20 °C. *Bf*HDH crystals (Figure 5.8 a) were grown in a precipitant solution containing 0.2 M magnesium chloride, 0.1 M sodium cacodylate pH 6.5 and 10 % (w/v) PEG 3000. *Bf*HOX crystals (Figure 5.8 b) grew in a condition containing 0.1 M ammonium sulfate, 0.3 M sodium formate, 0.1 M sodium cacodylate pH 6.5, 3 % (w/v) γ-PGA (sodium polyglutamic acid, low molecular weight polymer) and 20 % (v/v) 2-methyl-2,4-pentanediol (MPD). All crystals were flash frozen using 25 % (v/v) ethylene glycol as cryo-protectant. *Bf*HOX crystals diffracted to a resolution limit of 3.3 Å, while *Bf*HDH crystals diffracted only to a maximum resolution of 30 Å. Further optimization of the initial *Bf*HDH crystallization condition did not yield bigger or better diffracting crystals.

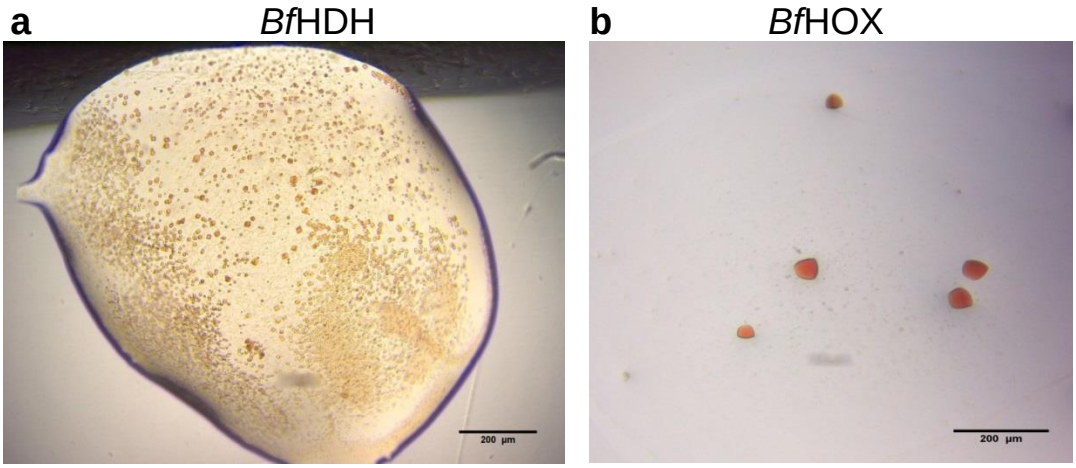

Figure 5.8 Crystallization of Purified Proteins
Crystallization screening was performed in sitting drop vapor diffusion setups.
The crystallization drops contained 100 nL of protein (A_{280}^{1cm} ~20.0) and 100 nL precipitant solution.
a) *Bf*HDH crystals were observed after 1 day in a precipitant solution containing 0.2 M magnesium chloride, 0.1 M sodium cacodylate pH 6.5 and 10 % (w/v) PEG 3000.
b) *Bf*HOX crystals after several months at 20 °C. The precipitant solution contained 0.1 M ammonium sulfate, 0.3 M sodium formate, 0.1 M sodium cacodylate pH 6.5, 3 % (w/v) γ-PGA (sodium polyglutamic acid, low molecular weight polymer) and 20 % (v/v) 2-methyl-2,4-pentanediol (MPD).

Batch crystallization of *Bf*HDH using a 1:1 (v/v) ratio of protein and precipitant (0.2 M NaCl, 0.1 M TrisCl pH 8.0 and 15-17 % (w/v) PEG 6000) at 20 °C yielded potato-shaped microcrystals (size ~10 µm, not shown) without any defined edges. A slurry of these microcrystals was used for a test diffraction experiment at the X-ray free-electron laser (XFEL) located at the Linac Coherent Light Source (Stanford Linear Accelerator Center, SLAC; Menlo Park, CA, USA). However, these microcrystals did not diffract.

5.2.7 Data Collection and Refinement

*Bf*HOX crystals obtained from the initial screen (Fig 5.8 b) displayed cubic $P2_13$ space group symmetry with unit cell dimensions of a = 124.6 Å, b = 124.6 Å, c = 124.6 Å, $\alpha = \gamma = \beta = 90°$. A native data set at a wavelength of 0.977 Å was collected and processed with XDS (Kabsch 2010) up to 3.3 Å final resolution. According to (Matthews 1968), one molecule (monomer) per asymmetric unit was present (solvent content 53.4 %). The phases were solved by molecular replacement with PHASER (McCoy 2007) using the structure of the *Ks*HOX monomer (PDB id: 4N4J, 1.8 Å resolution) as search model including its eight heme Fe-atoms. The structure was iteratively modeled using COOT (Emsley 2004) and refined in REFMAC (Murshudov 1997) resulting in working and free R-factors of 23.0 % and 26.3 %, respectively. The final *Bf*HOX model displayed good stereochemistry as indicated by the Ramachandran statistics and by analysis using MOLPROBITY (Davis 2007). Statistics of data collection and refinement are summarized in table 5.2.

Table 5.2 X-ray data statistics of *Bf*HOX

Data set	***Bf*HOX native**
Data collection	
Space group	$P2_13$
Unit cell dimensions	
a, b, c (Å)	124.6, 124.6, 124.6
α, β, γ (°)	90, 90, 90
Wavelength (Å)	0.9774
Resolution range (Å) [a]	999.0-3.3 (3.4-3.3)
Reflections measured [a]	194,523 (15,214)
Reflections unique [a]	18,802 (1,404)
Completeness (%) [a]	100.0 (100.0)
Redundancy N [a]	10.3 (10.8)
I/σI [a]	11.3 (1.8)
R_{merge} (%) [a, b]	17.5 (156.0)
R_{meas} (%) [a, c]	18.4 (164.2)
$CC_{1/2}$ (%) [d]	99.8 (65.3)
CC* (%) [e]	99.9 (88.9)
Refinement	
Resolution range in refinement (Å)	88.0-3.3
Number of reflections in refinement	9,487
R_{work}/ R_{free} (%) [f]	23.0/ 26.3
Protein residues	439 (3,483)
Ligands (no. of atoms)	8 heme (344)
Water molecules	0
Overall B-factor (Å^2)	27.7
Rmsd bonds (Å)	0.019
Rmsd angles (°)	2.050
Ramachandran plot [g]	
Most favoured (%)	94.2
Additionally allowed (%)	5.3
Disallowed (%)	0.5

Legend to Tables 5.2

a) Values of the highest resolution shell are given in brackets.

b) $R_{merge} = \sum_h \left| \langle I_h \rangle - I_{h,i} \right| / \sum_h \sum_i^{n_h} I_{h,i}$, where I_i is the intensity of a reflection and $\langle I_h \rangle = \frac{1}{n_h} \sum_i^{n_h} I_{h,i}$ is the mean value of that reflection and the summations are over all reflections h.

c) $R_{meas} = \sum_h \sqrt{\frac{N}{N-1}}\ R_{merge}$ Redundancy-independent merging R factor (Diederichs 1997).

d) $CC_{1/2} = \sum_{i=1}^{n} \left(\left(x_i - \bar{x} \right) \left(y_i - \bar{y} \right) \right) \Big/ \sqrt{\sum_{i=1}^{n} \left(x_i - \bar{x} \right)^2 \sum_{i=1}^{n} \left(y_i - \bar{y} \right)^2}$ Pearson's correlation coefficient between merged intensity estimates $I_{h,i}$ (x_i, y_i) and $\langle I_h \rangle$ ($\bar{x}$, $\bar{y}$) from half data sets x and y.

e) $CC^* = \sqrt{\frac{2CC_{1/2}}{1+CC_{1/2}}}$ Estimated correlation coefficient of the merged dataset against the true (usually unmeasurable) intensities (Karplus 2012).

f) $R_{work} = \sum_h \left| F_{obs} - F_{calc} \right| / \sum_h F_{obs}$ (working set, no σ cut-off applied) R_{free} is calculated the same way as R_{work}, but for a reflection test set with 5 % of the reflections excluded from refinement.

g) Ramachandran analysis was performed using COOT (Emsley 2004).

5.2.8 The Structure of *Bf*HOX

The overall trimeric structure of *Bf*HOX is almost identical to that of *Ks*HOX (PDB id: 4N4J; (Maalcke 2014) with a structural rmsd of 0.57 Å for 436 residues (Fig 5.9 a-c). Moreover, these proteins share very high sequence identity (87 %, Fig 5.10). As shown in figure 5.9 a, the overall structure of *Bf*HOX is predominantly α-helical and looks like a tulip-shaped bulb. Three helices from each subunit run parallel to the three-fold rotational axis of the trimer and surround a central solvent filled cavity (Fig 5.9 a).

A part of the N1-domain in *Ks*HOX (Maalcke 2014) as well as two loops (Gln314-Lys334 and Gly260-His263) are not resolved in the *Bf*HOX structure (Fig 5.9 b and c). These parts are located around the active site tunnel in *Ks*HOX. Since the overall structures of *Bf*HOX and *Ks*HOX are nearly identical, it could be assumed that corresponding structural elements would also be present at similar positions in the *Bf*HOX structure. The unresolved loop in the *Bf*HOX structure corresponding to *Ks*HOX Gly260-His263 harbors the conserved Asp-His pair in the distal pocket of the active site heme (Fig 5.9 c, Fig 5.10).

The active site heme 4 (P460) is crosslinked to a conserved tyrosine (Tyr449) residue (Fig 5.9 c, Fig 5.10) and is proximally coordinated by histidine His225 whereas its distal face appears vacant. The other seven c-type hemes in the *Bf*HOX monomer are *bis*-His ligated. The 24 hemes in the *Bf*HOX trimer form a ring-like structure (Fig 5.9 d). The positions and arrangement of the hemes both in the trimer (Fig 5.9 d) and the monomer (Fig 5.9 e) are highly identical to those in *Ks*HOX.

(Figure on next page)

Figure 5.9 The Structure of *Bf*HOX and its Comparison with *Ks*HOX
Both *Bf*HOX and *Ks*HOX (PDB id: 4N4J) are rendered as cartoon and their hemes as sticks models. *Bf*HOX crystallized as one monomer per asymmetric unit. The trimer was constructed using two other monomers as crystallographic symmetry mates.
a) Overall structure of *Bf*HOX possessing a tulip bulb-like structure similar to that of *Ks*HOX. Three helices (α17, α18 and α19) from each monomer run parallel surrounding a central cavity.
b) Structural superposition of *Bf*HOX (pink) with *Ks*HOX (green) rendered as ribbons. Note that a part of the N1 domain (*Ks*HOX G38-K69) is unresolved in the *Bf*HOX structure.
c) Three loops in the *Ks*HOX structure (blue, green and salmon) are not resolved in the molecular model of *Bf*HOX. The loop *Ks*HOX G260-H263 (salmon) contains the conserved active site Asp-His pair which takes part in catalysis.
d) Superposition of the ring-like heme arrangement in the *Bf*HOX and *Ks*HOX trimers. The active site heme 4 (P460) is highlighted in yellow.
e) Heme superposition in the *Bf*HOX and *Ks*HOX monomers.

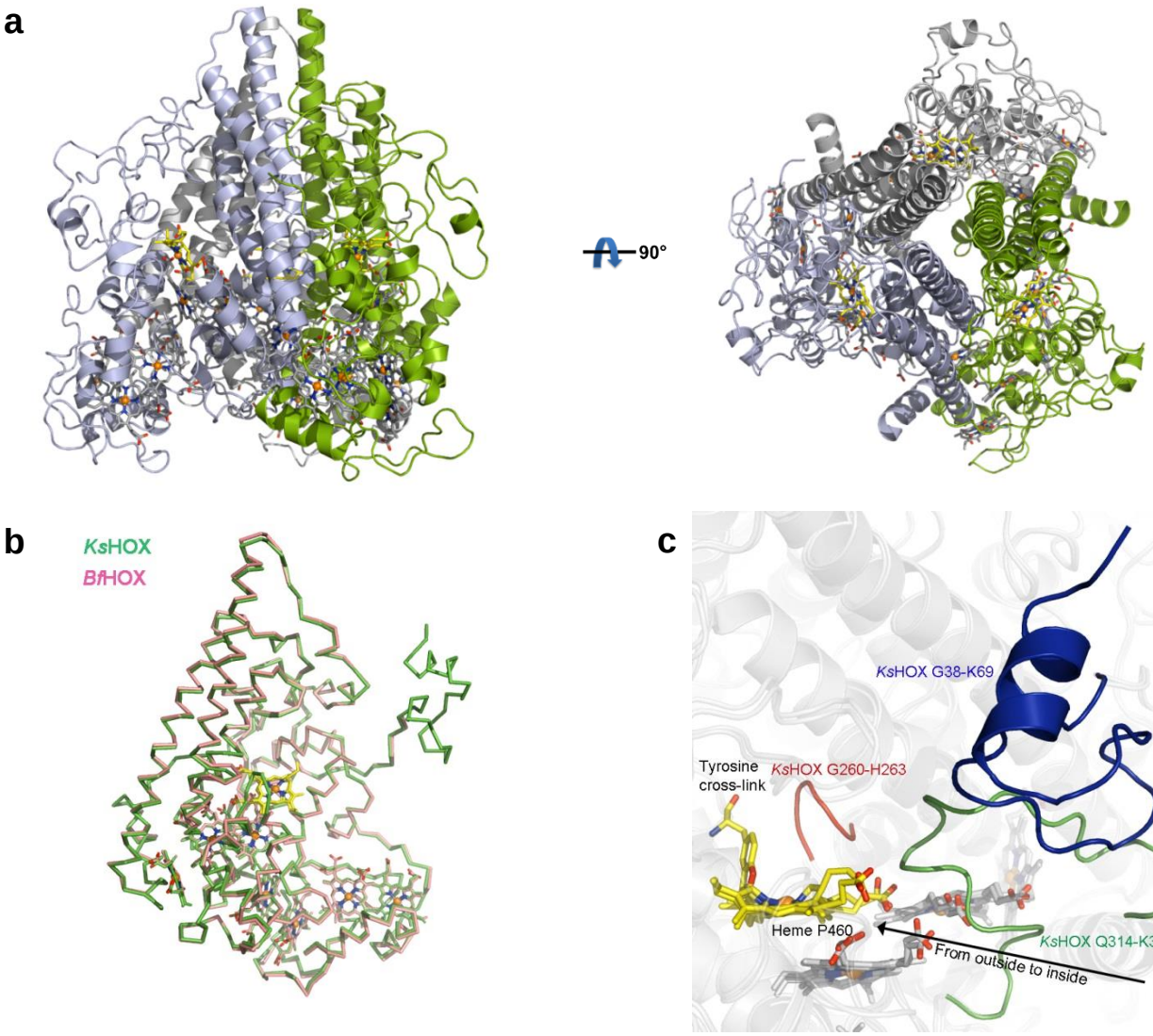
a
90°
b
KsHOX
BfHOX
c
KsHOX G38-K69
Tyrosine cross-link
KsHOX G260-H263
Heme P460
KsHOX Q314-K334
From outside to inside
d
e
KsHOX
BfHOX
1
2
3
4 (P460)
5
6
7
8

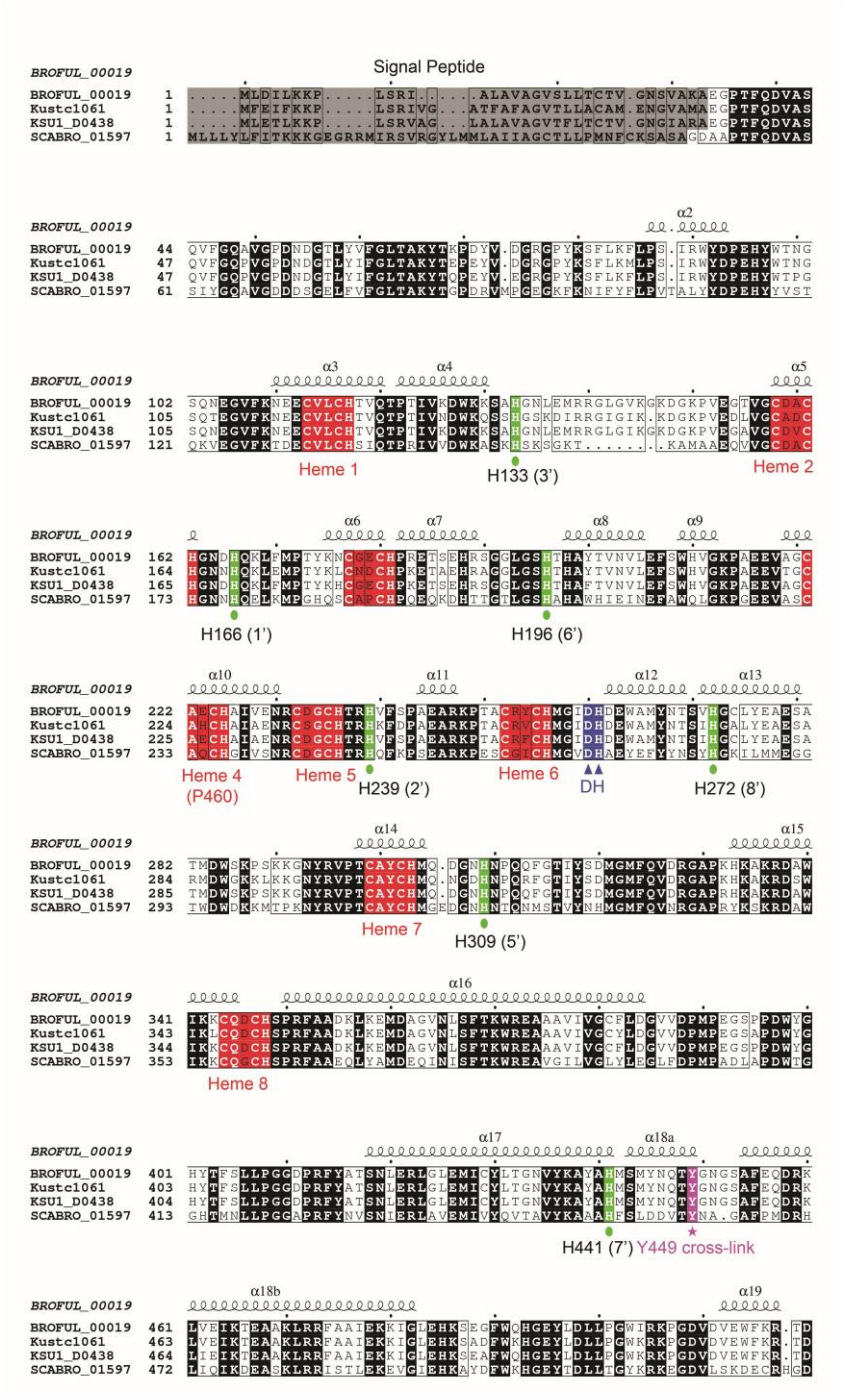

Figure 5.10 Sequence alignment of *Bf*HOX to its orthologues.
The sequence of *Brocadia fulgida* HOX (BROFUL_00019, KKO21247.1) was aligned to its orthologues from *Kuenenia stuttgartiensis* Kustc1061 (CAJ71806.1), *Jettenia caeni* (Planctomycete KSU-1) KSU1_D0438 (WP_007222832.1) as well as *Scalindua brodae* SCABRO_01597 (KHE92664.1). The sequence identities to Kustc1061 are 87 %, 94 % for KSU1_D0438 and 54 % for SCABRO_01597. Alignments were performed using ClustalO (Sievers 2011) and secondary structure elements were manually assigned based on the *Bf*HOX structure. Fully conserved sequences are marked black. The CXXCH c-type heme binding motifs are highlighted in red. The predicted signal peptides are highlighted in grey. The distal heme ligands are highlighted in green and marked with a dot. The tyrosine residue involved in the crosslink to heme 4 is highlighted in pink and marked with a star. The figure was prepared using ESPript (Gouet 1999).

5.3 Discussion

5.3.1 Abundance of Anammox Bacteria in DEMON® Granules and Protein Purification

This study describes the first successful attempt to purify and characterize anammox proteins from granular sludge obtained from a full-scale reactor. This might pave the way to take advantage in the growing number of anammox WWTPs as an opportunity to provide material for biochemical and biophysical studies.

In this study it has been shown that the single, dominant anammox species in granular sludge obtained from a DEamMONification (DEMON®) reactor in Heidelberg is *Brocadia fulgida.* Several other studies on the biodiversity of engineered ecosystems also reported *Brocadia* as the only dominant genus of anammox bacteria (Lawson 2017; Speth 2016; Luo 2017; Gonzalez-Martinez 2018). Likewise, the community of aerobic ammonium-oxidizing bacteria (AOB) in the analyzed DEMON® granules is represented by *Nitrosomonas europaea* and *N. eutropha* which is also consistent with previous studies. Although the relative abundance of each bacterial group present in the granules was not determined, the multi-milligram yields of anammox proteins (*e.g.* 25-35 mg of *Bf*HDH per 200 g of granular sludge wet-weight) indicate that anammox bacteria constitute a significant proportion of the biomass.

The cleared lysate obtained from the DEMON® granules did not show any gelling effect at low temperatures, despite the fact that neither reducing nor chelating agents (EDTA) or high salt conditions were used in lysate preparation. This is in contrast to the observations described earlier during the protein purification procedure from *Kuenenia stuttgartiensis* biomass enriched in a sequencing batch reactor (Cirpus 2006). One explanation for this difference could be that the lysate prepared from DEMON® granular sludge might possess a different composition of polysaccharides and other potential gelling agents compared to the lysate from *K. stuttgartiensis* cell aggregates. The EPS matrix of *B. fulgida*, for instance, was shown to contain autofluorescent components (Kartal 2008), which were absent in *K. stuttgartiensis* biomass obtained from SBR culture. Another explanation could also be the difference in the biodiversity of *B. fulgida*-containing granular sludge and *K. stuttgartiensis* cell aggregates. Recent studies on the nature of the interactions between autotrophic *Brocadia* sp. and heterotrophic *Chlorobi* bacteria in granular sludge from a PN/A reactor indicated that the *Chlorobi* bacteria consumed peptides present in EPS as their carbon source (Lawson 2017). Therefore, different types of interactions between different bacterial populations might

affect the composition of EPS. Nevertheless, purification of proteins from DEMON® granules provides a clear advantage over purification from *K. stuttgartiensis* SBR biomass due to its accessibility and absence of gelling effects.

Among other components, the EPS matrix usually consists of large amounts of differently charged polysaccharides which are likely also present in the lysate prepared from DEMON® granules. However, most negatively charged polysaccharides might have already been removed by the first anion exchange chromatography step using Q-Sepharose. They might bind more strongly to the anion exchanger and are therefore eluted at higher salt concentrations than the proteins of interest. The positively charged and neutral polysaccharides would not bind to the anion exchanger and would therefore be removed in the flow-through and washing steps. For this reason, a strong anion exchanger column such as Q-Sepharose is a vital step in removing different types of polysaccharides during protein purification from granular sludge. An alternative approach to further remove persistent polysaccharides might be the application of concanavalin A beads which bind sugars, glycoproteins and glycolipids. However, in the presented purification procedure this step was omitted since the final protein preparation appeared of sufficient purity even for crystallization experiments.

The three anammox proteins (*Bf*HDH, *Bf*HOX and *Bf*HZS) purified in this study were pure and homogenous as shown by mass spectrometry and analytical gel filtration. *Bf*HZS could be well separated from octaheme c-type cytochromes (OCCs) by anion-exchange chromatography using Q-Sepharose whereas the weaker anion exchanger DEAE-Sepharose did not result in a satisfactory resolution of the *Bf*HZS and OCC peaks.

Furthermore, as shown in chapter 3, *Bf*HDH forms higher oligomeric assemblies (1.6 MDa and 2.0 MDa) at high salt conditions. Therefore, *Bf*HDH is very efficiently separated from *Bf*HOX during gel filtration chromatography which otherwise would not have been possible since both proteins are around 200 kDa in their covalently linked trimeric states.

5.3.2 The Purification Yielded Active Proteins

A detailed biophysical characterization of *Bf*HDH is presented in chapter 3. A diagnostic UV-Vis spectroscopic characterization of all purified cytochromes showed that the spectral features of all three protein complexes were similar to the ones described before for their respective homologues (Shimamura 2007; Shimamura 2008; Maalcke 2014; Maalcke 2016; Dietl 2016). Reduction by sodium dithionite yielded a peak around 468 nm for *Bf*HOX and at 473 for *Bf*HDH, indicating the presence of a tyrosine crosslink with the P460 heme. The tyrosine link in *Bf*HOX was confirmed by its X-ray structure (section 5.2.8) whereas that of *Bf*HDH is consistent with the structure of its homolog from *Kuenenia stuttgartiensis Ks*HDH (chapter 3).

Other unique UV-Vis spectroscopic features of *Bf*HOX and *Bf*HDH could be observed in the presence of their potential substrates hydrazine and hydroxylamine. Both compounds partially reduced *Bf*HOX similarly as described for *Ks*HOX (Maalcke 2014). However, only hydrazine was able to partially reduce *Bf*HDH, whereas hydroxylamine only caused a small feature in the α-band region, possibly indicating an interaction with the active site heme not leading to an effective reduction. The implications of this observation have been already discussed in chapter 3.

Michaelis-Menten kinetics indicated that the catalytic rates (k_{cat}) and catalytic efficiencies (k_{cat}/K_M) of *Bf*HOX and *Bf*HDH were comparable to those of their respective homologues. This implies that both *Bf*HOX and *Bf*HDH were optimally active even when purified from granular sludge. These results further substantiate that the purification from granular sludge does not harm the quality of proteins. Therefore, granular biomass could be used for the purification of other proteins as well, such as small c-type cytochromes, which might play a role as electron transport partners in the anammox pathway.

5.3.3 The Structure of *Bf*HOX

The crystallization of both *Bf*HDH and *Bf*HOX as well as the successful structural characterization of *Bf*HOX altogether prove that proteins purified from granular sludge can also be used for their structural characterization.

Owing to its high sequence homology (~87 %), it was already expected that the structure of *Bf*HOX would be similar to *Ks*HOX which is indeed the case. However, three loops were unresolved in the structure of *Bf*HOX. Considering its high sequence similarity with *Ks*HOX, the missing regions in the *Bf*HOX structure are also expected to structurally align with those of *Ks*HOX. This raises the question why those loops are not resolved. There might be two possible reasons, namely high mobility of the loops or their proteolytic cleavage. Considering that the crystals which were used for diffraction experiments grew for more than six months, the second possibility appears more likely. However, it might also be possible that proteolytic cleavage occurred during purification. This possibility is however rather unlikely, since a cocktail of several protease inhibitors was added to the crude lysate. Therefore, protease cleavage during crystallization seems to be more probable at least for the two exposed parts at the active site tunnel entrance (the parts which correspond to *Ks*HOX Gly38-Lys69 and Gln314-Lys334). The loop containing the Asp-His pair, however, is probably too deep inside the *Bf*HOX structure to be available for cleavage by proteases. Moreover, it is evident that this loop can adopt different conformations as described in chapter 3 for *Bf*HDH and reported previously for a *Ks*HOX structure obtained from phenylhydrazine soaked crystals (Maalcke 2014). Therefore, the reason why the loop containing the Asp-His pair was not resolved might be its flexibility rather than proteolytic cleavage.

Chapter 6
Conclusions and Outlook

6. Conclusions and Outlook

Several aspects of anammox research have seen considerable growth in the last two decades (Zhang 2014). However, most of this research has been focused on the application of anammox in waste water treatment systems. Importantly, our group performed pioneering work in the field of structural biology of the anammox pathway. This led to the structural characterization of several intriguing multienzyme complexes such as *K. stuttgartiensis* hydrazine synthase (*Ks*HZS) (Dietl 2015), hydroxylamine oxidase (*Ks*HOX; Maalcke 2014) and a putative octaheme c-type cytochrome nitrite reductase (ONR, Kustc0457/58; unpublished). Two of these enzymes are proposed to be directly involved in the central anammox metabolism. Nitrite reductases such as NirS, NirK or ONR, which are involved in the first step of the pathway, catalyze the one-electron reduction of nitrite (NO_2^-) to nitric oxide (NO). The next step, the condensation of NO and ammonium (NH_4^+), is catalyzed by HZS using three electrons to produce the unusual and highly reactive compound hydrazine (N_2H_4). This reaction is proposed to occur *via* the intermediate hydroxylamine (NH_2OH) which is thought to be shuttled within the HZS complex. Since hydroxylamine is a strong inhibitor of hydrazine dehydrogenase (HDH), which catalyzes the last step in the anammox metabolism, its leakage from the HZS complex would be detrimental. However, hydroxylamine oxidase (HOX) is proposed to act as a detoxification system converting hydroxylamine back to NO, the substrate of HZS. Hydrazine dehydrogenase (HDH) catalyzes the four-electron oxidation of hydrazine to dinitrogen gas (N_2) which completes the anammox pathway. The four electrons released in this reaction are fed into an electron transport chain setting up a proton-motive force and replenishing the electrons used for nitrite reduction and hydrazine synthesis.

The structural characterization of HDH had failed in previous trials (Dietl 2016) although it was known from biophysical investigations that the protein could exist in various oligomeric states (Maalcke 2016). In addition, the identity and molecular structures of the proteins which might act as redox partners of the central enzyme complexes have been unknown so far. Therefore, this study focused on the structural, biophysical and biochemical characterization of HDH as well as several small c-type cytochromes as putative candidate redox partners.

6.1 Hydrazine Dehydrogenase – A Missing Link in Anammox Structural Biology

The most important outcome of this study is definitely the structural characterization of *Ks*HDH by both X-ray crystallography and cryo-electron microscopy (cryo-EM). This study also included the biophysical and biochemical characterization of *Ks*HDH as well as its homologue from *Brocadia fulgida* (*Bf*HDH). The 2.8 Å resolution X-ray structure of *Ks*HDH revealed a cubic assembly of eight HDH trimers (*i.e.* a 24mer) bound to twelve molecules of a previously unanticipated small binding partner (SBP). The arrangement of eight HDH trimers in a 24mer allows the formation of an intriguing closed electronic network of 192 hemes with contact sites at their heme 1 cofactors. The binding partner of *Ks*HDH was identified as Kustc1130, a ~10 kDa non-heme protein, which is located between each pair of HDH trimers in the *Ks*HDH 24mer-12xSBP assembly. Since transcriptomic data have shown that Kustc1130 is highly expressed in *K. stuttgartiensis* cells (it is in fact the second most highly transcribed gene after *Ks*HDH; Kartal 2011) and the protein has been co-purified as a complex with *Ks*HDH, it appears highly likely that Kustc1130 is constitutively expressed in stoichiometric amounts with *Ks*HDH. Moreover, Kustc1130 orthologues are also conserved in other anammox genera. Interestingly, native *Bf*HDH protein preparations did not contain a Kustc1130 homologue (Broful02728) as their small binding partner, putatively because of its dissociation from HDH during purification due to weaker protein-protein interactions.

An equivalent arrangement of eight HDH trimers could also be found in the 5.0 Å resolution cryo-EM structure of the HDH 24mer. However, Kustc1130 was absent in this structure probably due to its loss during EM grid preparation. Particle classification in cryo-EM by our collaborators, also allowed the determination of the structure of the HDH 30mer assembly at 6.1 Å resolution. The molecular model of the *Ks*HDH 30mer shows a pentagonal prism consisting of a sandwich of two rings, each of which containing five HDH trimers. As in the 24mer, the contact sites between the trimers in this assembly are located between their heme 1 cofactors creating a closed electronic network of 240 hemes. In each pentagonal ring the trimers are arranged to accommodate an additional trimer compared to the 24mer assembly. Thereby, the space between the trimers is squeezed by 5-10 Å especially around heme 1. Since heme 1 is supposed to be the electron release site where redox partner proteins are supposed to bind, it can be proposed that the closer packing of HDH trimers within each pentagonal ring of the 30mer might prevent redox partner binding. Since the interactions between HDH trimers belonging to two distinct pentagonal rings in the 30mer are identical to the 24mer assembly, these sites might still be available for redox partner binding. The overall

number of redox partner interaction sites, however, would be smaller in the 30mer assembly compared to the 24mer which might account for a lower enzymatic activity of the 30mer.

The effect of the discovered small binding partner as well as ionic strength on the oligomerization and enzymatic activity of both *Ks*HDH and *Bf*HDH were further investigated by biophysical methods (AUC and SEC-MALS), negative stain EM and enzymatic assays. Both *Ks*HDH and *Bf*HDH are capable to form at least three stable oligomeric states in solution namely trimers (α_3), 24mers ($(\alpha_3)_8$) and 30mers ($(\alpha_3)_{10}$). Both *Ks*HDH and *Bf*HDH predominantly exist as trimers at low ionic strength (up to 25-50 mM of KCl), whereas at high ionic strength the equilibrium is shifted towards 24mers and 30mers. This is consistent with the fact that the interactions between HDH trimers in the higher oligomers are mainly hydrophobic in nature. Addition of the respective small binding partners to *Ks*HDH and *Bf*HDH caused oligomerization to form exclusively 24mer assemblies independent of ionic strength (0-300 mM of KCl).

Enzymatic assays with *Bf*HDH showed a clear effect of both its small binding partner (SBP, Broful02728) and ionic strength on hydrazine oxidation activity. In the absence of the SBP, enzymatic activity showed a sigmoidal behavior with a plateau starting around 100-150 mM upon increasing ionic strength. By contrast, the optimal activity in the presence of the SBP was nearly two-fold higher than the highest activity in its absence at high ionic strength (100-150 mM). As evident from biophysical studies and negative stain EM, the presence of the SBP promotes the formation of exclusively 24mer assemblies (as HDH 24mer-12xSBP complexes) whereas high ionic strength in the absence of the SBP results in formation of both 24mers and 30mers. Therefore, the lower overall activity of HDH in the absence of the SBP might result from a mixed population with HDH 30mers that might be less active compared to the 24mers, possibly due to worse redox partner interactions as discussed above.

Altogether, based on these structural, biophysical and biochemical findings it can be proposed that the HDH 24mer-12xSBP assembly is most likely the physiologically relevant oligomeric state of hydrazine dehydrogenase.

However, several aspects related to HDH such as the identity of its redox partner (soluble or membrane-bound), the mechanism of electron transfer towards the quinone-pool in the membrane or the functional significance of different HDH oligomers still need further investigation.

A possible approach to identify soluble redox partners of HDH might be pull-down assays of immobilized HDH with lysates from whole anammox cells or even purified anammoxosomes (Neumann 2014). Bound interaction partners could then be analyzed by SDS-PAGE and

identified by mass spectrometry. This method, however, would be rather problematic if the interaction with a soluble redox partner was transient or if HDH interacted directly with its proposed terminal electron acceptor, a quinone-reactive integral membrane protein (QRP). In these cases, careful chemical crosslinking of protein complexes in lysates followed by their separation and identification by gel electrophoresis and mass spectrometry, respectively, might be a feasible alternative approach.

Another aspect which could be further explored is the drop of HDH activity in the presence of SBP when ionic strength is increased beyond a certain optimum. One hypothesis could be that at high ionic strength the SBP might dissociate from the HDH 24mer-12xSBP complex which would result in the formation of a mixture of HDH 24mer and 30mer assemblies in solution. Since the 30mer assemblies are expected to be less active than the 24mer assemblies, this would explain the decrease in HDH activity. However, negative stain EM images exclusively show 24mer assemblies in the presence of SBP even at high ionic strength (300 mM of KCl). However, these results might not be entirely conclusive since the staining process during EM grid preparation might introduce artifacts. Techniques than can be applied to proteins in solution such as analytical ultracentrifugation (AUC) or isothermal titration calorimetry (ITC) might be more appropriate to analyze these oligomerization and complex formation equilibria. Another hypothesis to explain the HDH activity drop at high ionic strength could be altered protein-protein interactions between the redox partner (in the assay bovine cytochrome c) and the HDH 24mer-12xSBP complex being affected by ionic strength as such. Owing to the binding of SBP near heme 1 in the HDH 24mer-12xSBP assembly, the supposed redox interaction site near heme 1 is dissimilar from the interaction site in the HDH 24mer without SBP. This dissimilarity might be reflected in the redox interactions between HDH and its redox partner at different ionic strengths. Nevertheless, bovine cytochrome c used in the assays is an artificial redox partner such that conclusive results on the redox interactions of HDH depending on ionic strength could only be drawn after identification of its physiological redox partner.

If the redox partner of HDH were a soluble protein as suggested in previous studies (Kartal 2011; Kartal 2013), it would have to be highly specific in interacting with HDH since otherwise electrons would be transferred to other protein complexes such as hydrazine synthase (HZS) (Kartal 2011) resulting in physiologically unproductive electron cycling. An attractive hypothetical model omitting a soluble redox partner would be direct electron transfer from the HDH 24mer-12xSBP assembly to the yet unknown quinone-reactive integral membrane complex (QRP). This model implies that the network of 192 hemes in the HDH

24mer-12xSBP might provide an electric circuit to conduct electrons released at an arbitrary active site of HDH towards one or two interaction sites of the HDH 24mer-12xSBP assembly with the integral membrane complex. However, it is difficult to test this model. One experimental proof could be the identification of the mentioned membrane-bound complex by chemical crosslinking and mass spectrometry. Subsequently, a biochemical assay might be designed using the HDH 24mer-12xSBP assembly together with the quinone-reactive integral membrane complex solubilized in detergent micelles. The reduction of (mena)quinone molecules could then be assayed spectrophotometrically.

A hypothetical anammox pathway model integrating the proposed concept of direct electron transfer from the HDH 24mer-12xSBP assembly to the quinone-reactive integral membrane complex along with other complexes is depicted in figure 6.1.

6.2 *Ks*NaxLS – A Potential Nitric Oxide (NO) Scavenging Complex

The 1.7 Å resolution X-ray structure of *Ks*NaxLS provides the first molecular model of a complex between class I and class II c-type cytochromes. This study provides further evidence that it indeed exists as a heterodimer based on biophysical methods, reconstitution of the complex from its individually isolated components and its purification as a complex when the components were co-expressed. The structural analysis confirms that *Ks*NaxL belongs to class II c-type cytochromes (more specifically class IIb) with a typical four-helix bundle fold and a heme binding motif located near its C-terminus. *Ks*NaxS possesses a typical class I cytochrome c fold with its heme cofactor bound close to its N-terminus. Both subunits show a rare His/Cys heme axial ligation system with cysteine as distal ligand. There were no major effects on the overall structure of the *Ks*NaxLS complex when the distal ligand was mutated except for few changes in the orientation of nearby residues.

An important spectroscopic feature of this complex was the presence of a Soret band at 420 nm in the as-isolated state which was uniquely blue shifted to around 417 nm upon reduction accompanied by the appearance of typical α- and β-bands. The individually expressed components of the *Ks*NaxLS complex also showed similar UV-Vis spectra in both their as-isolated and reduced states. When the distal cysteine ligand was mutated to methionine or glycine in either one or both subunits, the Soret band in their as-isolated states were blue-shifted to a position around 410-414 nm and red-shifted when being reduced. This behavior is typical of His/Met, His/His and His/H_2O ligated c-type hemes. Therefore, it can be concluded that the unique Soret peak position and its blue-shift upon reduction of the *Ks*NaxLS complex

is due to the His/Cys axial heme coordination. Another debated aspect of the His/Cys ligation is its effect on heme redox potential. It is generally considered that this ligation system drastically reduces the redox potential of the heme center. The double cysteine mutant (*i.e.* the distal cysteines in both NaxL and NaxS were mutated to methionines) along with the mutants where only the distal cysteine of *Ks*NaxS was mutated to either methionine or glycine showed a small α-band already in their as-isolated states. It can be concluded that the His/Cys ligation indeed caused lowering of the redox potential at least in the *Ks*NaxS subunit. However, when only the distal cysteine ligand of *Ks*NaxL was mutated to either methionine or glycine, no α-band was visible. This observation implies that the two heme sites might have significantly different redox potentials and that the redox potential of *Ks*NaxS is likely lower than that of *Ks*NaxL. However, precise redox potential determination of both sites is still needed.

Another interesting but not uncommon aspect of the *Ks*NaxLS complex is its ability to bind ligands such as nitric oxide (NO) and carbon monoxide (CO). The wild type complex, its components and also the distal ligand mutants were able to bind NO in both their as-isolated state (ferric or Fe(III) state) and in their reduced state (ferrous or Fe(II) state). However, there seems to be a difference in the mode of NO binding between the two components. The *Ks*NaxL component predominantly binds NO at the proximal heme site with its distal site being vacant (5cNO state) as indicated by a peak at 396 nm in the spectrum. A minor fraction of NO might be bound at its distal heme site (6cNO state) as indicated by a shoulder at 415 nm. The 6cNO complex might represent the intermediate between the His/Cys ligation state and the final 5cNO state. On the contrary, the *Ks*NaxS component showed a major peak at 415 nm accompanied by a small shoulder at 396 nm. This indicates that the *Ks*NaxS component primarily forms a 6cNO complex. A different scenario emerged when NO was bound to the *Ks*NaxLS complex. Here, the spectra showed a single Soret peak around 417 nm indicating the formation of probably the 6cNO state only. However, it is difficult to interpret which component contributes more to NO binding. This observation probably implies that in the NaxLS complex one or both of the components become less flexible such that they are no longer able to form multiple NO binding states compared to the separated subunits.

Ferrous *Ks*NaxLS, its individual components and mutants also bind carbon monoxide (CO). The UV-Vis spectroscopic features upon CO binding indicate that CO coordinates distally *i.e.* replacing the distal ligands (cysteine as well as methionine). It implies that both methionine and cysteine distal ligands are equally flexible to be replaced by an external ligand.

The function of *Ks*NaxLS could not be established so far. However, based on the expected low redox potentials of the heme centers, the homologous NaxLS complex from *Jettenia*

caeni (Ukita 2010) was suspected to be the redox partner of HDH which produces four low-potential electrons (-750 mV *vs.* SHE; Kartal 2011; Maalcke 2016). *Ks*NaxLS, however, did not show any redox activity with HDH (personal communication Joachim Reimann, Radboud University, Nijmegen). The UV-Vis spectroscopic features of NO- and CO-bound *Ks*NaxLS are similar to those of known CO and NO sensors which act either by direct gene transcription regulation (CooA; Shelver 1997; Reynolds 2000) or by signal transduction (sGC and H-NOX (Stone 1994; Boon 2006). The spectral features are also similar to NO storage and transport proteins such as nitrophorins (Andersen 2000; Ding 1999). Hence, it might be possible that *Ks*NaxLS might also possess one of these functions in anammox bacteria. Since *Ks*NaxLS is located in the anammoxosome while genomic DNA resides in the cytoplasm, it is highly unlikely that this complex can act as a direct gene expression regulator. However, it still might be considered that NaxLS acts as an NO-sensor within the anammoxosome sensing the level of NO as an important intermediate in anammox metabolism. Interaction of the NO-bound complex with a transmembrane signaling cascade might than transmit information on the anammoxosomal NO level to the cytosol where *e.g.* the transcription of key enzymes might be regulated. However, such signaling cascades in anammox bacteria are highly speculative.

Other possible functions of *Ks*NaxLS could be NO storage or transport. This raises the question why NO needs to be stored or transported in the anammoxosome, since it is freely diffusible in aqueous environments. The reason might be the proven toxicity of NO towards HDH activity (Maalcke 2016). The other potent HDH inhibitor, hydroxylamine, is proposed to be detoxified by *Ks*HOX (Maalcke 2014). Since NO is a substrate of HZS, NO has to be delivered to it while keeping it away from HDH. Preliminary pull-down assays suggested an interaction of *Ks*NaxLS with *Ks*HZS which might imply that *Ks*NaxLS probably feeds NO to HZS. In order to scavenge NO produced by nitrite reductase, NaxLS must be present in high amounts in the anammoxosome. Indeed, *Jettenia caeni* NaxLS was estimated to represent 10 % of the total molar protein content in cell lysates which is comparable to the molar content of HDH and HOX (Ukita 2010). Moreover, *Ks*NaxLS shows high expression at transcription level (Kartal 2011) and could readily be purified from *K. stuttgartiensis* as well.

Therefore, based on these initial findings it might be speculated that *Ks*NaxLS acts as an NO scavenging protein that might possibly transport NO to the HZS complex. This concept has also been depicted in figure 6.1.

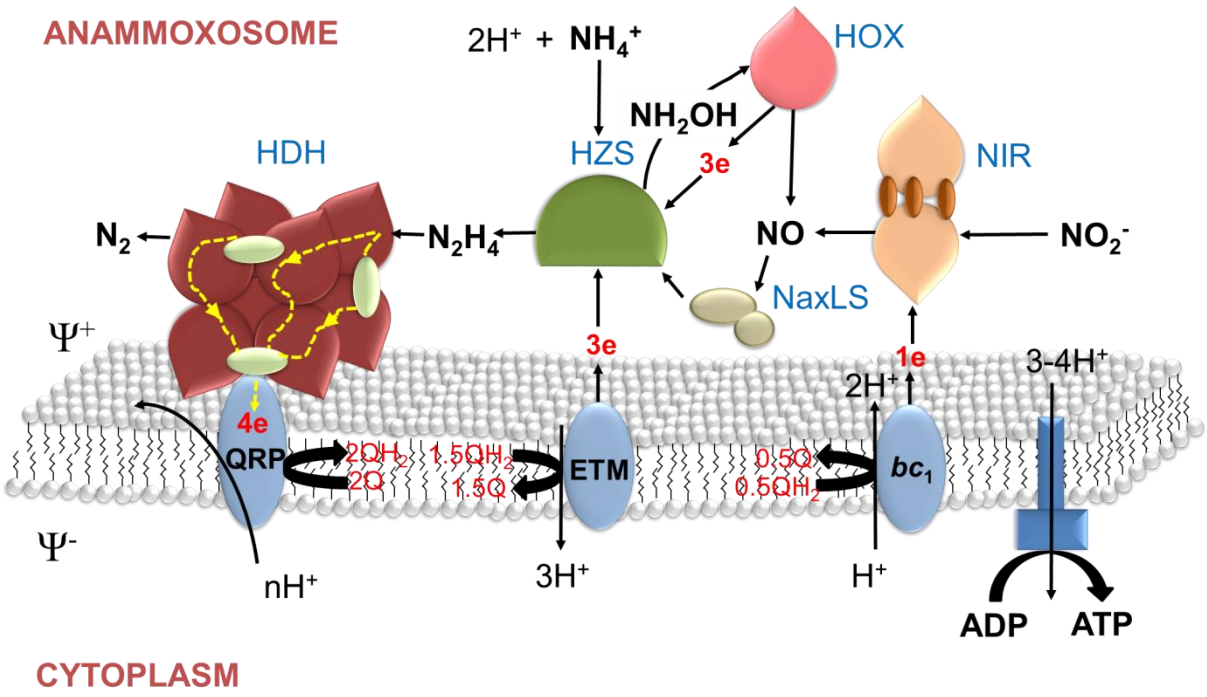

Figure 6.1 A New Hypothetical Model of the Anammox Pathway
The anammox pathway model shown is based on the concept given by (Kartal 2011; Kartal 2013). However, based on the current study and envisaged concepts, two new additions has been made, namely direct electron transport from HDH to a yet unknown quinone-reactive integral membrane complex (QRP) and scavenging and transport of nitric oxide (NO) to HZS by the NaxLS complex. In this model the proposed quinone-reactive membrane protein (in light blue) is shown to interact directly with the HDH 24mer (in red) at one or possibly two trimer-trimer interface sites (only one QRP molecule is shown). Electrons released from an arbitrary active site in the HDH 24mer could reach to the contact site *via* the heme network made by the HDH 24mer-12xSBP assembly (the path is shown by yellow dashed lines with arrow heads showing the direction of the electron flow). For the sake of clarity only three SBP molecules and no heme sites are shown. The abbreviation are: HDH for hydrazine dehydrogenase, SBP for small binding partner of HDH; HZS for hydrazine synthase, NIR for nitrite reductase, ETM for electron transport module, HOX for hydroxylamine oxidase, QRP for quinone-reactive integral membrane protein, Q for quinone pool and e for electrons.

Future studies could focus on further investigating the function of the NaxLS complex as NO transporter to the HZS complex. These might include HZS activity assays using ^{14}N-ammonium and ^{15}N-labelled NO-loaded NaxLS as starting substrates. Moreover, the dissociation constant (K_d) of NO binding to NaxLS as well as NO association and dissociation rate constants (k_{on} and k_{off}, respectively) might also give clues about the ability of NaxLS to scavenge and release NO. Experiments involving controlled NO binding and its photo-dissociation coupled with electron paramagnetic resonance (EPR) or UV-Vis spectroscopy could be used to determine $K_{d,}$ k_{on} and k_{off} values. In such assays, factors which might affect NO binding and release by NaxLS such as other proteins or ionic strength could also be explored. Co-crystallization of NaxLS and HZS in the presence or absence of NO could also be pursued to understand the nature of their interaction.

6.3 Kustc0563 – A Potential Physiological Redox Partner of *Ks*HOX

The X-ray structures of two other small c-type cytochromes, Kustc0563 and its paralogue Kustc0562 at 1.9 Å and 3.0 Å resolution, respectively, showed a typical class I cytochrome c fold with His/Met heme ligation. However, in case of Kustc0562 the distal methionine ligand was found to be replaced by an imidazole molecule. Imidazole binding could also be confirmed by UV-Vis spectroscopy. The as-isolated states of both Kustc0562 and Kustc0563 showed small α- and β-bands and a Soret peak around 413-414 nm indicating that they were already partially reduced. Further reduction led to intensified α- and β-bands with a concomitant red shift of the Soret band to around 416 nm. Adding ammonium persulphate to the as-isolated proteins led to a disappearance of the α- and β-bands and a blue shift of the Soret peak to 410 nm indicating that the proteins were fully oxidized.

Biochemical assays of Kustc0563 with *Ks*HOX and *Ks*HDH were carried out in order to investigate its ability to act as an electron transfer partner. *Ks*HOX showed at least 6-7 times faster rates of hydroxylamine oxidation in the presence of Kustc0563 compared to bovine cytochrome c, indicating enhanced electron transfer kinetics with Kustc0563. On the contrary, no hydroxylamine oxidation activity of *Ks*HOX in presence of Kustc0562 could be observed.

In hydrazine oxidation assays, however, *Ks*HDH showed nearly similar activities when Kustc0563, Kustc0562 or bovine cytochrome c served as redox partners. The redox potentials of both Kustc0562 and Kustc0563 are similar (+242 mV and +269 mV *vs.* SHE, respectively). Since redox partner interactions involve weak reversible encounters, a significant difference

in the surface charge potential between Kustc0562 and Kustc0563 might explain the difference in their redox activities.

It can be concluded that both Kustc0562 and Kustc0563 are able to transfer electrons. Moreover, since Kustc0563 is highly expressed in anammox cells (Kartal 2011), it is probable that Kustc0563 even serves as physiological redox partner of *Ks*HOX.

The transient nature of the encounters between redox-active enzymes and their electron transfer partner proteins poses problems in co-crystallization and eventually their structural characterization. Several trials to co-crystallize *Ks*HOX with Kustc0563 have already failed. Therefore, other techniques should be employed to further characterize redox interaction between KsHOX and Kustc0563 such as determination of electron transfer (ET) rates. The genomes of *Kuenenia stuttgartiensis* and other anammox bacteria encode a large variety of conserved small c-type cytochromes as well as copper proteins which could be tested for their ability to act as redox partners of various anammox complexes. Their redox potentials and ET rates could also be determined and compared in order to assign the physiological redox partners.

6.4 A New Source for Anammox Biomass

In order to obtain anammox proteins from a different organism than *Kuenenia stuttgartiensis*, granular sludge from a DEMON® reactor was explored as an unconventional source for protein purification. Phylogenetic analysis of granular sludge collected from a local waste water treatment plant (WWTP) in Heidelberg, Germany revealed *Brocadia fulgida* as the sole anammox species along with other bacterial groups such as aerobic ammonium-oxidizing bacteria (AOB) represented by *Nitrosomonas europaea* and *N. eutropha*. Anammox proteins such as hydrazine synthase (*Bf*HZS), hydroxylamine oxidase (*Bf*HOX) and hydrazine dehydrogenase (*Bf*HDH) could be purified in multi-milligram quantities from this granular sludge material (10-30 mg protein from 200 g biomass wet-weight). The purified proteins were of high quality as indicated by biochemical activity assays and their ability to form crystals. For instance, the crystals of *Bf*HOX diffracted up to 3.3 Å resolution and the protein structure was successfully solved. As expected, the structure of *Bf*HOX was nearly identical to that of *Ks*HOX (PDB id: 4N4J; Maalcke 2014).

During 1995-2012, out of total 1,059 articles published about any aspect of "anammox", only about 60 articles were related to the the field of biochemistry and molecular biology (Zhang 2014). One reason might be the scant availability of anammox biomass because of difficulties

in growing anammox bacteria at laboratory scale due their slow growth and sophisticated culture techniques. This study, however, proves that biomass from full-scale reactors such as DEMON® granular sludge can be can be used to purify and characterize proteins involved in vital metabolic processes in anammox bacteria. Hence, this study overcomes a long standing problem of anammox biomass availability for purification and biochemical characterization of anammox proteins.

6.5 General Outlook

As a short summary, this study contributes to the understanding of structural, biochemical and biophysical aspects of several important proteins involved in the anammox pathway directly or indirectly especially *Ks*HDH. Moreover, with this study our group has now completed the structural characterization of all supposed soluble enzyme complexes involved in the central anammox metabolism. However, our understanding of electron transfer proteins in the anammox pathway is still a stub and needs some more future attention. Along the same line, the characterization of other small c-type cytochromes such as the highly expressed small tetraheme c-type cytochrome, Kuste2854, which is the supposed redox partner of the hydrazine synthase complex, should be pursued.

Another fascinating aspect of anammox bacteria is the presence of unusual membrane lipids called ladderane lipids. Since these lipids contain multiple, fused, highly strained cyclobutane rings, they are considered as potential biofuels. The biosynthetic pathway for ladderane lipids is expected to differ from that of common straight or branched chain fatty acids. However, the current status of understanding this pathway is poor. Therefore, our group is steadily shifting its focus on the investigation of ladderane lipid biosynthesis. The study will include identification, structural, biophysical and biochemical characterizations of the enzymes involved in this pathway.

Appendix 1: Heterologously Expressed Protein Constructs

Table A1.1 PCR Primers used for cloning and mutagenesis.
All genes were amplified from *K. stuttgartiensis* gDNA or isolated DNA from DEMON® granules (contains *Brocadia fulgida*).

Name	Sequence 5'→ 3'	Length (nt)	Comments
KustA0087_F1	CGATTGGAGCGGCCGCAACACAACAAGAGATATG	34	Amplification of kusta0087, clone into pUC19kan3, NotI site
KustA0087_R1	GGAAATTAACGTAGGCATCTCGAGTTACGGAACG	34	Amplification of kusta0087, clone into pUC19kan3, XhoI site
KustA0087_F2	CGATTGGAGCCGCGGCAACACAACAAGAGATATG	34	Amplification of kusta0087, clone into pUC19kan2, SacII site
KustA0087_R	GGAAATTAACGTAGGCATTTTCTCGAGCGGAACG	34	Amplification of kusta0087, clone into pUC19kan2, XhoI site
KustA0088_F1	CAAGCACAGCGGCCGCTTTGAATGAACAC	29	Amplification of kusta0088, clone into pUC19kan3, NotI site
KustA0088_R1	CCCGATAGCCTCGAGTTACTTTACAGC	27	Amplification of kusta0088 clone into pUC19kan3, XhoI site
KustA0088_F2	CAAGCACAGCCGCGGCTTTGAATGAACAC	29	Amplification of kusta0088, clone into pUC19kan2, SacII site
KustA0088_R2	CCCGATAGCGAGCTCGAGCTTTACAGC	27	Amplification of kusta0088, clone into pUC19kan2, XhoI site
NotA0087_C32G_F	TGCGGCCGCAACACAACAAGAGATAGGTAAGAATATGTGGGATCC	45	Mutagenesis of kusta0087 C32G in pUC19Kan2a_KustA87-88
NotA0087_C32G_R	GGATCCCACATATTCTTACCTATCTCTTGTTGTGTTGCGGCCGC	44	Mutagenesis of kusta0087 C32G in pUC19Kan2a_KustA87-88
NotA0087_C32M_F	TGCGGCCGCAACACAACAAGAGATAATGAAGAATATGTGGGATCC	45	Mutagenesis of Kusta0087 C32M in pUC19Kan2a_KustA87-88
NotA0087_C32M_R	GGATCCCACATATTCTTCATTATCTCTTGTTGTGTTGCGGCCGC	44	Mutagenesis of kusta0087 C32M in pUC19Kan2a_KustA87-88
C0562_F1	CCTTTTCTTGCGGCCGCGGAAGAAAAGGCCATAGACG	37	Amplification of kustc0562, clone into pUC19kan2a, NotI site
C0562_R1	GCAATGGCGTCTCGAGCCGTTGCTTTTTTGATAATTTC	38	Amplification of kustc0562, clone into pUC19kan2a, XhoI site
C0563_F1	TCTGTTTCAGCGGCCGCGAACATTGATGGT	30	Amplification of kustc0563, clone into pUC19kan2a, NotI site
C0563_R1	CAGCACCTCGAGCTTTTTAAACCCTCTGA	29	Amplification of kustc0563, clone into pUC19kan2a, XhoI site

C0562_R2	CAATGGCTCGAGTCACCGTTGCTTTTTTGATAATTTCC	38	Amplification of kustc0562, clone into pUC19kan3, XhoI site, stop codon
C0563_R2	TTTCAGCTCGAGTTACTTTTTAAACCCTCTGAC	33	Amplification of kustc0563, clone into pUC19kan3, XhoI site, stop codon
K-1130fw	CAACTACTTCACGTTGGCGAAGGTCATCTCGAGCACC	37	Amplification of kustc1130, clone into pET24d, NcoI site
K-1130rev	GGTGCTCGAGGTGGCTCCCTGAAGGATGAC	31	Amplification of kustc1130, clone into pET24d, XhoI site
B-2728fw	GAAGTACCATGGCATTTAAGAAGATATGTGCAGG	34	Amplification of Broful02728, clone into pET24d, NcoI site
B-2728rev	GGTGCTCGAGGTGATGTCCGCTTGGATGAAG	31	Amplification of Br02728, clone into pET24d, XhoI site

pUC19kan2_A0087

ATQQEICKNMWDPFQSMRAVTGLMELTSGQCTQLSKDAAAILAGVKESHDSISVDK
NYKVLNDEVAYHAANIDAAAKANDLEEVQVQFRRMTIACRNCHKIYKTEQRLVP**LE**
HHHHHH

118 Amino acids
mW = 13381.11 pI = 6.07 (estimated)
ext= 10220.00 abs=0.764 (1g/l), assuming ALL Cys residues appear as half cystines
ext= 9970.00 abs=0.745 (1g/l), assuming NO Cys residues appear as half cystines
Negative (Asp + Glu): 15 Positive (Arg + Lys): 13

pUC19kan2_A0088

ALNEHTAGDTTKSPYTIYAGLGFAVQESCYYCHGNGGKGTTEGLIFGVPDFTSTEFQS
SMTDKQIIDHINKGKGKCPSYQGKMSPEMIEKMAGVVRNFAVK**LEHHHHHH**

109 Amino acids
mW = 11984.44 pI = 6.06 (estimated)
ext= 7637.00 abs=0.637 (1g/l), assuming ALL Cys residues appear as half cystines
ext= 7450.00 abs=0.622 (1g/l), assuming NO Cys residues appear as half cystines
Negative (Asp + Glu): 11 Positive (Arg + Lys): 10

pUC19Kan2a_KustA87-88

Kusta0087:
AATQQEICKNMWDPFQSMRAVTGLMELTSGQCTQLSKDAAAILAGVKESHDSISVD
KNYKVLNDEVAYHAANIDAAAKANDLEEVQVQFRRMTIACRNCHKIYKTEQRLVP

111 Amino acids
mW = 12387.07 pI = 6.01 (estimated)
ext= 10220.00 abs=0.825 (1g/l), assuming ALL Cys residues appear as half cystines
ext= 9970.00 abs=0.805 (1g/l), assuming NO Cys residues appear as half cystines
Negative (Asp + Glu): 14 Positive (Arg + Lys): 13

Kusta0088:
LNEHTAGDTTKSPYTIYAGLGFAVQESCYYCHGNGGKGTTEGLIFGVPDFTSTEFQSS
MTDKQIIDHINKGKGKCPSYQGKMSPEMIEKMAGVVRNFAVK**LEHHHHHH**

108 Amino acids
mW = 11913.36 pI = 6.06 (estimated)
ext= 7637.00 abs=0.641 (1g/l), assuming ALL Cys residues appear as half cystines
ext= 7450.00 abs=0.625 (1g/l), assuming NO Cys residues appear as half cystines
Negative (Asp + Glu): 11 Positive (Arg + Lys): 10

Total Molecular Weight of Kusta0087/88: 24300.43 Da

pUC19Kan3_KustC0563

Before TEV Cleavage:

ADHHHHHHGSGSENLYFQGAAANIDGMKLYLQHCKTCHGVDGNPTDLGEGLGAR
KFADAEWQAKTSDERIIEQINEGTPEMMMPFKEKLTPEEVKALVPVVRGFKK

106 Amino acids
mW = 11780.24 pI = 6.04 (estimated)
ext= 8605.00 abs=0.730 (1g/l), assuming ALL Cys residues appear as half cystines
ext= 8480.00 abs=0.720 (1g/l), assuming NO Cys residues appear as half cystines
Negative (Asp + Glu): 16 Positive (Arg + Lys): 12

After TEV Cleavage:

GAAANIDGMKLYLQHCKTCHGVDGNPTDLGEGLGARKFADAEWQAKTSDERIIEQI
NEGTPEMMMPFKEKLTPEEVKALVPVVRGFKK

88 Amino acids
mW = 9688.11 pI = 6.04 (estimated)
ext= 7115.00 abs=0.734 (1g/l), assuming ALL Cys residues appear as half cystines
ext= 6990.00 abs=0.722 (1g/l), assuming NO Cys residues appear as half cystines
Negative (Asp + Glu): 14 Positive (Arg + Lys): 12

pUC19Kan2a_C0563

AANIDGMKLYLQHCKTCHGVDGNPTDLGEGLGARKFADAEWQAKTSDERIIEQINE
GTPEMMMPFKEKLTPEEVKALVPVVRGFKK**LE<u>HHHHHH</u>**

94 Amino acids
mW = 10625.09 pI = 6.11 (estimated)
ext= 7115.00 abs=0.670 (1g/l), assuming ALL Cys residues appear as half cystines
ext= 6990.00 abs=0.658 (1g/l), assuming NO Cys residues appear as half cystines
Negative (Asp + Glu): 15 Positive (Arg + Lys): 12

pUC19kan2a_C0562

AAEEKAIDARNLFEYHCACHGLTGEANRGKALKAPDLCDPGWQNSKTDKEILYSITN
GKNKMPAWNERLTPEEIEALARYVRKLSKKQR**LE<u>HHHHH</u>**

99 Amino acids
mW = 11423.92 pI = 6.37 (estimated)
ext= 15657.00 abs=1.371 (1g/l), assuming ALL Cys residues appear as half cystines
ext= 15470.00 abs=1.354 (1g/l), assuming NO Cys residues appear as half cystines
Negative (Asp + Glu): 14 Positive (Arg + Lys): 18

pUC19Kan3_KustC0562

<u>Before TEV cleavage:</u>

112 Amino acids
mW = 12650.15 pI = 6.28 (estimated)
ext= 17147.00 abs=1.355 (1g/l), assuming ALL Cys residues appear as half cystines
ext= 16960.00 abs=1.341 (1g/l), assuming NO Cys residues appear as half cystines
Negative (Asp + Glu): 15 Positive (Arg + Lys): 18

AAD<u>HHHHHH</u>GSGS<u>ENLYFQ</u>GAAAEEKAIDARNLFEYHCAKCHGLTGEANKRGKA
LKAPDLCDPGWQNSKTDKEILYSITNGKNKMPAWNERLTPEEIEALARYVRKLSKKQ
R

<u>After TEV Cleavage:</u>

93 Amino acids
mW = 10486.94 pI = 6.32 (estimated)
ext= 15657.00 abs=1.493 (1g/l), assuming ALL Cys residues appear as half cystines
ext= 15470.00 abs=1.475 (1g/l), assuming NO Cys residues appear as half cystines
Negative (Asp + Glu): 13 Positive (Arg + Lys): 18

GAAAEEKAIDARNLFEYHCAKCHGLTGEANKRGKALKAPDLCDPGWQNSKTDKEIL
YSITNGKNKMPAWNERLTPEEIEALARYVRKLSKKQR

pET24d_Broful02728

YQVKPAKLWVTAIAIGTPIEGAEIKVGDNTCTTGKNGTCVFELRPGSYEISVHEHGGA
SAHTSVNLEEKDIRFISLDLGSAALHPSGHH**LEHHHHHH**

97 Amino acids
mW = 10502.69 pI = 6.08 (estimated)
ext= 8605.00 abs=0.819 (1g/l), assuming ALL Cys residues appear as half cystines
ext= 8480.00 abs=0.807 (1g/l), assuming NO Cys residues appear as half cystines
Negative (Asp + Glu): 11 Positive (Arg + Lys): 7

pET24d_Kustc1130

YDVKPAKLWVTAIAIGTPIVGAEIKVGDEECTTGNNGTCVFELRPGTYAISVHEHGGQ
SAHKEVSLEEGNILFVSLDLGAKARHPSGSH**LEHHHHHH**

97 Amino acids
mW = 10448.64 pI = 6.04 (estimated)
ext= 8605.00 abs=0.824 (1g/l), assuming ALL Cys residues appear as half cystines
ext= 8480.00 abs=0.812 (1g/l), assuming NO Cys residues appear as half cystines
Negative (Asp + Glu): 12 Positive (Arg + Lys): 7

Appendix 2: Phylogenetic Analysis of DEMON® Granular Sludge

Table A2.1 Degenerate PCR Primers used for phylogenetic analyses of isolated DNA from DEMON® sludge granules. Y=C/T , D=A/G/T , R=A/G.

Name	Sequence 5'→ 3'	Comments	Reference
Pla46F	GGATTAGGCATGCAAGTC	16S rDNA analysis of *Planctomycetes*	(Innerebner 2007; Neef 1998)
1392R	ACGGGCGGTGTGTAC	16S rDNA analysis of *Planctomycetes*	(Ferris 1996)
DegHaoF	GCGCTGGTCAAGCGTTACAAGG	Degenerate HAO primers specific for *N. europaea, communis, eutropha*	This work
DegHaoR	GCTTACGCTTGCGCCAGCC	Degenerate HAO primers specific for *N. europaea, communis, eutropha*	This work
hzsA526F	TAYTTTGAAGGDGACTGG	Degenerate HZSα forward primer	(Harhangi 2012)
hzs1829R	TCATACCACCARTTGTA	Degenerate HZSα reverse primer	(Harhangi 2012)

Table A2.2 PCR Conditions

Amplifcation	Primers	Melting Temperature (°C)	Elongation time (min)
Planctomycetes 16S rDNA	Pla46F/1392R	58	1.5
AOB HAO*	DegHaoF/DegHaoR	65	1
HZSα	hzsA526F/hzs1829R	57	1.5

*Primers were specific for *Nitrosomonas europaea, commmunis, eutropha*
Rest of the PCR conditions are similar to those describe in section 2.2.2.3.

Abbreviations

2D	Two-dimensional
3D	Three-dimensional
Å	Ångström, 1 Å = 10^{-10} m
aa	Amino acid
anammox	Anaerobic ammonium oxidation
AOB	Aerobic ammonium-oxidizing bacteria
APBS	Adaptive Poisson-Boltzmann Solver
APS	Ammonium peroxodisulfate
ATP	Adenosine-5-triphosphate
AU	Absorbance unit
AUC	Analytical Ultracentrifugation
$A_{xxx}^{1\ cm}$	Absorbance at xxx nm wavelength and a path length of 1.0 cm
bp	Base pair
BROFUL	*Brocadia fulgida* locus tag
BROSI	*Brocadia sinica* locus tag
BSA	Bovine serum albumine
BSI	Brine-seawater interface
Ca.	*Candidatus*
CANON	Completely Autotrophic Nitrogen removal Over Nitrite
CAPS	N-cyclohexyl-3-aminopropanesulfonic acid
CCD	Charge-coupled device
CHAPS	3-[(3-Cholamidopropyl)dimethylammonio]-1-propanesulfonate
C-HEGA-8	Cyclohexylethanoyl-N-hydroxyethylglucamide
CL	Chemiluminescence
CoA	Coenzyme A
Comammox	Complete ammonia oxidation
conc.	Concentration
CTAB	Cetyltrimethylammonium bromide
CTF	Contrast transfer function
CV	Column volume
Da	Dalton
ddH2O	Doubly distilled water, here: "ELGA" water
DEAE	Diethylaminoethyl
DEMON	DEamMONification
DFT	Density functional theory
DLS	Dynamic light scattering
DMSO	Dimethylsulfoxide
DNA	Desoxyribonucleic acid
DNRA	Dissimilatory nitrite reduction to ammonium
DO	Dissolved Oxygen
DOPA	3,4-dihydroxyphenylalanine
DTE	Dithioerythritol
DTP	4,4'-dithiodipyridine
DTT	Dithiothreitol
E. coli	*Escherichia coli*
E°'	Standard redox potential at 25 °C, 1 bar and physiological pH (pH 7)
EDTA	Ethylenediaminetetraacetate
EG	Ethylene glycol

EPR	Electron paramagnetic resonance
EPS	Extracellular polymeric substances
eq.	Equation
ESI	Electrospray ionization
ET	Electron transfer
ETM	Electron transfer module (of HZS)
FISH	Fluorescence *in situ* hybridization
FOM	Figure-of-merit
GTP	Guanosine-5-triphosphate
h	Hour
HAO	Hydroxylamine Oxidoreductase
HDH	Hydrazine dehydrogenase
HEPES	(N-2-Hydroxyethyl)-piperazin-N'-ethanesulfonic acid
HMM	Hidden Markov Model
HOX	Hydroxylamine oxidase
HZS	Hydrazine Synthase
ICM	Intracytoplasmic membrane
IDA	Imminodiacetae
IPTG	Isopropyl β-D-1-thiogalactopyranoside
ISD	In-source-decay
ITC	Isothermal titration calorimetry
kb	Kilobase
k_{cat}	Enzyme turnover rate (in s^{-1})
K_D	Dissociation constant
kDa	Kilodalton
K_m	Michaelis Menten constant
KPi	Potassium phosphate buffer
KSU1	*Jettenia caeni* (Planctomycete KSU1) locus tag
Kust	*Kuenenia stuttgartiensis* locus tag (starting with a capital letter refers to proteins, starting with a small letter refers to genes)
LB	Lysogeny Broth
MALDI	Matrix-assisted laser desorption ionization
MALS	Multi-angle static light scattering
MBR	Membrane bioreactor
min	Minute
MOPS	3-(*N*-morpholino)propanesulfonic acid
MPD	2-methyl-2,4-pentanediol
MR	Molecular replacement
mRNA	Messenger ribonucleic acid
MS	Mass spectrometry
MWCO	Molecular weight cutoff
NA	Not applicable
NCBI	National Center for Biotechnology Information
NCS	Non-crystallographic symmetry
ND	Not determined
N-DMAO	Nitrite-driven anaerobic methane oxidation
*Ne*HAO	Hydroxylamine oxidoreductase from *Nitrosomonas europaea*
NirK	Copper-containing nitrite:nitric oxide oxidoreductase
NirS	Cytochrome cd_1 nitrite:nitric oxide oxidoreductase
NMR	Nuclear magnetic resonance

NNM	Neural Network Model
NTA	Nitrilotriacetate
Nxr	Nitrite:nitrate oxidoreductase
OCC	Octaheme c-type cytochrome
OD_{600}	Optical density at 600 nm (1 OD_{600} equals approximately 10^9 bacteria/mL)
OM	Outer membrane
OMP	Outer membrane porin
OMZ	Oxygen minimum zone
ONR	Octaheme cytochrome c nitrite reductase
ORF	Open reading frame
OTR	Octaheme cytochrome c tetrathionate reductase
OTTLE	Optically transparent thin-layer electrochemical
P460	Tyrosine-heme crosslinked cofactor in the active site of HAO enzymes
PAGE	Polyacrylamide gel electrophoresis
PBS	Phosphate-buffered saline
PCR	Polymerase chain reaction
PDB	Protein data bank
PEG	Polyethylene glycol
PGA	γ-Polyglutamic acid
pKa	Negative logarithm of the acid dissociation constant (Ka)
PMF	Peptide mass fingerprints, also: proton-motive force
PN/A	Partial Nitrification and Anammox
PTFE	Polytetrafluoethylene (Teflon ®)
PVC	Planctomycetes–Verrucomicrobia–Chlamydiae superphylum
PVDF	Polyvinylidene fluoride
Q	Quinone
QRP	Quinone-reactive Protein
rDNA	rRNA coding DNA
rmsd	Root mean square deviation
rpm	Revolutions per minute
rRNA	Ribosomal ribonucleic acid
RT	Room temperature
s	Second, also: sedimentation coefficient (unit: seconds)
S	Svedberg unit (1 S = 10^{-13} s), also: sedimentation coefficient (unit: Svedberg units)
SAD	Single wavelength anormalous dispersion
SAM	S-adenosylmethionine
SBP	Small binding partner protein (of HDH)
SBR	Sequencing batch reactor
SCABRO	*Scalindua brodae* locus tag
SDS	Sodium dodecyl sulfate
SE	Sedimentation equilibrium
SEC	Size exclusion chromatography
Sec	Secretory
SHARON	Single reactor system for High activity Ammonium Removal Over Nitrite
SHE	Standard hydrogen electrode
S_{max}	Maximal sedimentation coefficient (for compact spheres)
SMRT	Single-Molecule Real-Time
SMU	Source measure unit
SNAP	Single-stage nitrogen removal using anammox and partial nitritation

SP	Signal peptide
STI	Standard-I-nutrients
SV	Sedimentation velocity
TAE	Tris-acetate-EDTA buffer
TCEP	Tris(2-carboxyethyl)phosphine
TEM	Transmission electron microscopy
TEMED	N,N,N',N'-Tetramethylethylendiamine
TEV	Tobacco etch virus
T_m	Melting temperature
TMH	Transmembrane helix
TOF	Time-of-flight
Tris	Tris-(hydroxymethyl)-aminomethane
UV	Ultraviolet
v/v	Volume per volume
vers.	Version
Vis	Visible
w/v	Weight per volume
w/w	Weight per weight
wt	Wild type
WWTP	Water treatment plant
$\Delta_r G_m^\circ$	Standard Gibbs free molar reaction energy under standard conditions (25 °C, 1 bar)
ε_{xxx}	Molar extinction coefficient at a wavelength of xxx nm

Nucleotides:

A	adenosine
T	thymidine
G	guanosine
C	cytidine

Amino Acids:

alanine	Ala	A
arginine	Arg	R
asparagine	Asn	N
aspartate	Asp	D
cysteine	Cys	C
glutamine	Gln	Q
glutamate	Glu	E
glycine	Gly	G
histidine	His	H
isoleucine	Ile	I
leucine	Leu	L
lysine	Lys	K
methionine	Met	M
phenylalanine	Phe	F
proline	Pro	P
serine	Ser	S
threonine	Thr	T
tryptophan	Trp	W
tyrosine	Tyr	Y
valine	Val	V

References

Afonine, Pavel V, Grosse-Kunstleve, Ralf W, Echols, Nathaniel, et al. 2012. Towards automated crystallographic structure refinement with phenix.refine, *Acta Crystallographica Section D Biological Crystallography*, 68: 352-67.

Ali, Mohamed Fauzi Haroon, Yuko Narita, Lei Zhang,cDario Rangel Shaw, Satoshi Okabe, Pascal E. Saikaly. 2016. Draft Genome Sequence of the Anaerobic Ammonium-Oxidizing Bacterium "*Candidatus Brocadia sp. 40*", *Genome Announcements*. 4: e01377-16

Ali, Muhammad, and Okabe, Satoshi. 2015a. Anammox-based technologies for nitrogen removal: Advances in process start-up and remaining issues, *Chemosphere*, 141: 144-53.

Ali, Muhammad, Oshiki, Mamoru, Awata, Takanori, et al. 2015b. Physiological characterization of anaerobic ammonium oxidizing bacterium *'Candidatus Jettenia caeni*', *Environmental Microbiology*, 17: 2172-89.

Allgeier, Peterson W. H., JudayC., and E. A. Birge. 1932. The Anaerobic Fermentation of Lake deposits, *International Review of Hydrobiology*: 26: 444-461.

Almeida, Naomi M de, Neumann, Sarah, Mesman, Rob J, et al. 2015. Immunogold Localization of Key Metabolic Enzymes in the Anammoxosome and on the Tubule-Like Structures of *Kuenenia stuttgartiensis*, *Journal of Bacteriology*, 197: 2432-41.

Alric, J., Tsukatani, Y., Yoshida, M., et al. 2004. Structural and functional characterization of the unusual triheme cytochrome bound to the reaction center of *Rhodovulum sulfidophilum*, *J Biol Chem*, 279: 26090-7.

Ambler, RP. 1991. Sequence variability in bacterial cytochromes c, *Biochimica et Biophysica Acta (BBA) - Bioenergetics*, 1058: 42-47.

Amelung, S., Nerlich, A., Rohde, M. Spellerberg, B., Cole, Jason N., Nizet, V., Chhatwal, Gursharan S., Talay, Susanne R. 2011. The FbaB-type fibronectin-binding protein of *Streptococcus pyogenes* promotes specific invasion into endothelial cells, *Cellular Microbiology*, 13:1200-11.

Andersen, John F., Ding, Xiao D., Balfour, Celia, et al. 2000. Kinetics and Equilibria in Ligand Binding by Nitrophorins 1−4: Evidence for Stabilization of a Nitric Oxide−Ferriheme Complex through a Ligand-Induced Conformational Trap, *Biochemistry*, 39: 10118-31.

Andrew, Colin R., George, Simon J., Lawson, David M., et al. 2002. Six- to Five-Coordinate Heme−Nitrosyl Conversion in Cytochrome c' and Its Relevance to Guanylate Cyclase, *Biochemistry*, 41: 2353-60.

Andrew, Colin R., Kemper, Lenord J., Busche, Tammy L., et al. 2005. Accessibility of the Distal Heme Face, Rather than Fe−His Bond Strength, Determines the Heme-Nitrosyl Coordination Number of Cytochromes c': Evidence from Spectroscopic Studies, *Biochemistry*, 44: 8664-72.

Aragao, D., Frazao, C., Sieker, L., et al. 2003. Structure of dimeric cytochrome c3 from *Desulfovibrio gigas* at 1.2 A resolution, *Acta Crystallogr D Biol Crystallogr*, 59: 644-53.

Arciero, D M, Balny, C, and Hooper, A B. 1991. Spectroscopic and rapid kinetic studies of reduction of cytochrome c554 by hydroxylamine oxidoreductase from *Nitrosomonas europaea*, *Biochemistry*, 30: 11466-72.

Arp, Daniel J, Sayavedra-Soto, Luis A, and Hommes, Norman G. 2002. Molecular biology and biochemistry of ammonia oxidation by *Nitrosomonas europaea*, *Archives of microbiology*, 178: 250-55.

Arrigo, Kevin R. 2005. Marine microorganisms and global nutrient cycles., *Nature*, 437: 349-55.

Atkinson, Sally J, Mowat, Christopher G, Reid, Graeme A, et al. 2007. An octaheme c-type cytochrome from *Shewanella oneidensis* can reduce nitrite and hydroxylamine, *FEBS Letters*, 581: 3805-08.

Attia, Amr A A, and Silaghi-Dumitrescu, Radu. 2014. Computational Investigation of the Initial Two-Electron, Two-Proton Steps in the Reaction Mechanism of Hydroxylamine Oxidoreductase, *Journal of Physical Chemistry B*, 118: 12140-45.

Bagchi, Samik, Lamendella, Regina, Strutt, Steven, et al. 2016. Metatranscriptomics reveals the molecular mechanism of large granule formation in granular anammox reactor., *Scientific Reports*, 6: 28327.

Bamford, Vicki A, Bruno, Stefano, Rasmussen, Tim, et al. 2002. Structural basis for the oxidation of thiosulfate by a sulfur cycle enzyme, *The EMBO Journal*, 21: 5599-610.

Beitlich, Thorsten, Kuhnel, Karin, Schulze-Briese, Clemens, et al. 2007. Cryoradiolytic reduction of crystalline heme proteins: analysis by UV-Vis spectroscopy and X-ray crystallography, *Journal of Synchrotron Radiation*, 14: 11-23.

Bendtsen, Jannick Dyrløv, Nielsen, Henrik, Heijne, Gunnar von, et al. 2004. Improved prediction of signal peptides: SignalP 3.0, *Journal of Molecular Biology*, 340: 783-95.

Berry, M J, George, S J, Thomson, A J, et al. 1990. Cytochrome c″ isolated from *Methylophilus methylotrophus*. An example of bis-histidine-co-ordinated Fe^{3+} haem, with near-perpendicular orientation of the ligands, *Biochemical Journal*, 270: 413-17.

Bertero, Michela G, Rothery, Richard A, Palak, Monica, et al. 2003. Insights into the respiratory electron transfer pathway from the structure of nitrate reductase A, *Nature structural biology*, 10: 681-87.

Bertini, I, Cavallaro G, Rosato A. 2006. Cytochrome c: occurrence and functions, *Chem Rev*, 106: 90-115.

Bertini, Ivano, Faraone-Mennella, Jasmin, Gray, Harry B., et al. 2004. NMR-validated structural model for oxidized *Rhodopseudomonas palustris* cytochrome c 556, *JBIC Journal of Biological Inorganic Chemistry*, 9: 224-30.

Boedeker, Margarete Schüler, Greta Reintjes, Olga Jeske, Muriel C. F. van Teeseling, Mareike Jogler, Patrick Rast, Daniela Borchert, Damien P. Devos, Martin Kucklick, Miroslava Schaffer, Roberto Kolter, Laura van Niftrik, Susanne Engelmann, Rudolf Amann, Manfred Rohde, Harald Engelhardt & Christian Jogler. 2017. Determining the bacterial cell biology of *Planctomycetes*, *Nature Comminications*.

Boon, E. M., Davis, J. H., Tran, R., et al. 2006. Nitric oxide binding to prokaryotic homologs of the soluble guanylate cyclase beta1 H-NOX domain, *J Biol Chem*, 281: 21892-902.

Borin, Sara, Mapelli, Francesca, Rolli, Eleonora, et al. 2013. Anammox bacterial populations in deep marine hypersaline gradient systems, *Extremophiles : life under extreme conditions*, 17: 289-99.

Boumann, Henry A, Longo, Marjorie L, Stroeve, Pieter, et al. 2009a. Biophysical properties of membrane lipids of anammox bacteria: I. Ladderane phospholipids form highly organized fluid membranes, *Biochimica et biophysica acta*, 1788: 1444-51.

Boumann, Henry A, Stroeve, Pieter, Longo, Marjorie L, et al. 2009b. Biophysical properties of membrane lipids of anammox bacteria: II. Impact of temperature and bacteriohopanoids, *Biochimica et biophysica acta*, 1788: 1452-57.

Bowman, Sarah E J, and Bren, Kara L. 2008. The chemistry and biochemistry of heme c: functional bases for covalent attachment., *Natural product reports*, 25: 1118-30.

Bradford, M M. 1976. A rapid and sensitive method for the quantitation of microgram quantities of protein utilizing the principle of protein-dye binding, *Analytical Biochemistry*, 72: 248-54.

Brito, J. A., Denkmann, K., Pereira, I. A., et al. 2015. Thiosulfate dehydrogenase (TsdA) from *Allochromatium vinosum*: structural and functional insights into thiosulfate oxidation, *J Biol Chem*, 290: 9222-38.

Broda, E. 1977. Two kinds of lithotrophs missing in nature, *Zeitschrift für allgemeine Mikrobiologie*, 17: 491-93.

Budzik, J.M., Poor, C.B., Faull, K.F., Whitelegge, J.P., He, C., Schneewind, O. 2009. Intramolecular amide bonds stabilize pili on the surface of bacilli, *Proc.Natl.Acad.Sci.USA*, 106: 19992-97.

Budzik, JM, Marraffini LA, Schneewind O. 2007. Assembly of pili on the surface of *Bacillus cereus* vegetative cells, *Mol Microbiol*, 66: 495-510.

Burley, S.K. , G.A. Petsko. 1986. Amino-aromatic interactions in proteins, *FEBS Letters*, 203: 139-43.

Byrne, N, Strous, M, Crepeau, V, et al. 2009. Presence and activity of anaerobic ammonium-oxidizing bacteria at deep-sea hydrothermal vents, *The ISME Journal*, 3: 117-23.

Canfield, Donald E, Glazer, Alexander N, and Falkowski, Paul G. 2010. The evolution and future of Earth's nitrogen cycle., *Science*, 330: 192-6.

Castresana, J. 2000. Selection of conserved blocks from multiple alignments for their use in phylogenetic analysis, *Molecular biology and evolution*, 17: 540-52.

Cedervall, Peder, Hooper, Alan B, and Wilmot, Carrie M. 2013. Structural studies of hydroxylamine oxidoreductase reveal a unique heme cofactor and a previously unidentified interaction partner., *Biochemistry*, 52: 6211-8.

Chaban, Vitaly V, Nielsen, Morten B, Kopec, Wojciech, et al. 2014. Insights into the role of cyclic ladderane lipids in bacteria from computer simulations, *Chemistry and physics of lipids*, 181: 76-82.

Cheesman, M R, Little, P J, and Berks, B C. 2001. Novel heme ligation in a c-type cytochrome involved in thiosulfate oxidation: EPR and MCD of SoxAX from *Rhodovulum sulfidophilum*, *Biochemistry*, 40: 10562-69.

Chen, McMullan G, Faruqi AR, Murshudov GN, Short JM, Scheres SH, Henderson R. 2013. High-resolution noise substitution to measure overfitting and validate resolution in 3D structure determination by single particle electron cryomicroscopy, *Ultramicroscopy*, 135: 24-35.

Choi, P. S., Grigoryants, V. M., Abruna, H. D., et al. 2005. Regulation and function of cytochrome c' in *Rhodobacter sphaeroides*, *J Bacteriol*, 187: 4077-85.

Cirpus, Irina E Y, Been, Mark de, den Camp, Huub J M Op, et al. 2005. A new soluble 10kDa monoheme cytochrome c-552 from the anammox bacterium Candidatus "*Kuenenia stuttgartiensis*", *FEMS Microbiology Letters*, 252: 273-78.

Cirpus, Irina E Y, Geerts, Wim, Hermans, John H M, et al. 2006. Challenging protein purification from anammox bacteria, *International journal of biological macromolecules*, 39: 88-94.

Collins, M J, Arciero, D M, and Hooper, A B. 1993. Optical spectropotentiometric resolution of the hemes of hydroxylamine oxidoreductase. Heme quantitation and pH dependence of Em, *J Biol Chem*, 268: 14655-62.

Cowtan, K D, and Zhang, K Y. 1999. Density modification for macromolecular phase improvement, *Progress in biophysics and molecular biology*, 72: 245-70.

Cowton, K. 1994. 'dm': An automated procedure for phase improvement by density modification, *Joint CCP4 and ESF-EACBM Newsletter on Protein Crystallography*, 31: 34-38.

Crowe, Alexander H. Treusch , Michael Forth, Jiying Li, Cedric Magen,, and Donald E. Canfeld, Bo Thamdrup & Sergei Katsev. 2017. Novel anammox bacteria and nitrogen loss from Lake Superior, *Scientific Reports*, 7: 13757.

Crowley, Peter B, and Carrondo, Maria A. 2004. The architecture of the binding site in redox protein complexes: Implications for fast dissociation, *Proteins: Structure, Function, and Bioinformatics*, 55: 603-12.

Crowley, Peter B., and Ubbink, Marcellus. 2003. Close Encounters of the Transient Kind: Protein Interactions in the Photosynthetic Redox Chain Investigated by NMR Spectroscopy, *Accounts of Chemical Research*, 36: 723-30.

Cusanovich, Michael A. 1971. Molecular weights of some cytochromes c', *Biochimica et Biophysica Acta (BBA) - Protein Structure*, 236: 238-41.

Daims, Holger, Lebedeva, Elena V, Pjevac, Petra, et al. 2015. Complete nitrification by *Nitrospira* bacteria, *Nature*, 528: 504-09.

Davis, Ian W, Leaver-Fay, Andrew, Chen, Vincent B, et al. 2007. MolProbity: all-atom contacts and structure validation for proteins and nucleic acids, *Nucleic acids research*, 35: W375-83.

DeLano, W L. 2002. "The PyMOL Molecular Graphics System." San Diego, CA, USA: Schrödinger, L.L.C.

Denkmann, Kevin, Grein, Fabian, Zigann, Renate, et al. 2012. Thiosulfate dehydrogenase: a widespread unusual acidophilic c-type cytochrome, *Environmental Microbiology*, 14: 2673-88.

Dereeper, A, Guignon, V, Blanc, G, et al. 2008. Phylogeny.fr: robust phylogenetic analysis for the non-specialist, *Nucleic acids research*, 36: W465-9.

Diederichs, K, and Karplus, P A. 1997. Improved R-factors for diffraction data analysis in macromolecular crystallography, *Nature structural biology*, 4: 269-75.

Dietl, Andreas. 2016. Structural and Mechanistic Investigations of Proteins from Anaerobic Ammonium-Oxidizing Bacteria. PhD Thesis. Ruprecht-Karls-Universität Heidelberg.

Dietl, Andreas, Ferousi, Christina, Maalcke, Wouter J., et al. 2015. The inner workings of the hydrazine synthase multiprotein complex, *Nature*, 527: 394-97.

Ding, Xiao D., Weichsel, Andrzej, Andersen, John F., et al. 1999. Nitric Oxide Binding to the Ferri- and Ferroheme States of Nitrophorin 1, a Reversible NO-Binding Heme Protein from the Saliva of the Blood-Sucking Insect *Rhodnius prolixus*, *Journal of the American Chemical Society*, 121: 128-38.

Dougherty, Dennis A. 2013. The Cation−π Interaction, *Acc. Chem. Res.*, 46: 885–93.

Edgar, Robert C. 2004. MUSCLE: multiple sequence alignment with high accuracy and high throughput, *Nucleic acids research*, 32: 1792-97.

Edman, P. Högfeldt, Erik, Sillén, Lars Gunnar; Kinell, Per-Olof. 1950. Method for determination of the amino acid sequence in peptides, *Acta Chem. Scand*, 4: 283–93.

Einsle, O., Messerschmidt, A., Stach, P., et al. 1999. Structure of cytochrome c nitrite reductase, *Nature*, 400: 476-80.

Elsden, S. R., Kamen, M. D., and L. P. Vernon. 1953. A new soluble cytochrome, *J. Am. Chem. Soc.*, 75: 6347–48.

Emsley, Paul, and Cowtan, Kevin. 2004. Coot: model-building tools for molecular graphics, *Acta Crystallogr D Biol Crystallogr*, 60: 2126-32.

Erickson, Harold P. 2009. Size and shape of protein molecules at the nanometer level determined by sedimentation, gel filtration, and electron microscopy, *Biological procedures online*, 11: 32-51.

Ettwig, Katharina F, Butler, Margaret K, Le Paslier, Denis, et al. 2010. Nitrite-driven anaerobic methane oxidation by oxygenic bacteria, *Nature*, 464: 543-48.

Ettwig, Katharina F, Shima, Seigo, van de Pas-Schoonen, Katinka T, et al. 2008. Denitrifying bacteria anaerobically oxidize methane in the absence of Archaea, *Environmental Microbiology*, 10: 3164-73.

Evers, Toon H., van Dongen, Joost L. J., Meijer, E. W., et al. 2007. Ligand-induced monomerization of *Allochromatium vinosum* cytochrome c′ studied using native mass spectrometry and fluorescence resonance energy transfer, *JBIC Journal of Biological Inorganic Chemistry*, 12: 919-28.

Ferousi, Christina, Speth, Daan R, Reimann, Joachim, et al. 2013. Identification of the type II cytochrome c maturation pathway in anammox bacteria by comparative genomics., *BMC microbiology*, 13: 265.

Ferris, M J, Muyzer, G, and Ward, D M. 1996. Denaturing gradient gel electrophoresis profiles of 16S rRNA-defined populations inhabiting a hot spring microbial mat community, *Applied and Environmental Microbiology*, 62: 340-46.

Frank, J., Lucker, S., Vossen, Rham, et al. 2018. Resolving the complete genome of *Kuenenia stuttgartiensis* from a membrane bioreactor enrichment using Single-Molecule Real-Time sequencing, *Sci Rep*, 8: 4580.

Fuerst, John a, and Sagulenko, Evgeny. 2011. Beyond the bacterium: planctomycetes challenge our concepts of microbial structure and function., *Nature reviews. Microbiology*, 9: 403-13.

Fuerst, John A, and Sagulenko, Evgeny. 2013. Nested bacterial boxes: nuclear and other intracellular compartments in planctomycetes, *Journal of molecular microbiology and biotechnology*, 23: 95-103.

Furukawa, K., Lieu, P. K., Tokitoh, H., et al. 2006. Development of single-stage nitrogen removal using anammox and partial nitritation (SNAP) and its treatment performances, *Water Science and Technology*, 53: 83-90.

Gao, Haichun, Barua, Soumitra, Liang, Yili, et al. 2010. Impacts of *Shewanella oneidensis* c-type cytochromes on aerobic and anaerobic respiration, *Microbial Biotechnology*, 3: 455-66.

George, Simon J., Andrew, Colin R., Lawson, David M., et al. 2001. Stopped-Flow Infrared Spectroscopy Reveals a Six-Coordinate Intermediate in the Formation of the Proximally Bound Five-Coordinate NO Adduct of Cytochrome c‘, *Journal of the American Chemical Society*, 123: 9683-84.

Getzoff, ED., Cabelli, DE., Fisher, CL., Parge, HE., Viezzoli, MS., Banci, L., & Hallewell, RA. 1992. Faster superoxide dismutase mutants designed by enhancing electrostatic guidance, *Nature*, 358: 347–51.

Gomis-Rüth, F X, Companys, V, Qian, Y, et al. 1999. Crystal structure of avian carboxypeptidase D domain II: a prototype for the regulatory metallocarboxypeptidase subfamily, *The EMBO Journal*, 18: 5817-26.

Gonzalez-Martinez, Alejandro, Muñoz-Palazon, Barbara, Rodriguez-Sanchez, Alejandro, et al. 2018. New concepts in anammox processes for wastewater nitrogen removal: recent advances and future prospects, *FEMS Microbiology Letters*, 365: doi: 10.1093/femsle/fny031.

Gori, Fabio, Tringe, Susannah Green, Kartal, Boran, et al. 2011. The metagenomic basis of anammox metabolism in *Candidatus* ‘Brocadia fulgida’, *Biochemical Society Transactions*, 39: 1799-804.

Gouet, P, Courcelle, E, Stuart, D I, et al. 1999. ESPript: analysis of multiple sequence alignments in PostScript, *Bioinformatics*, 15: 305-08.

Gray, Harry B, and Winkler, Jay R. 2005. Long-range electron transfer, *Proceedings of the National Academy of Sciences of the United States of America*, 102: 3534-39.

Grein, Fabian, Venceslau, Sofia S., Schneider, Lilian, et al. 2010. DsrJ, an Essential Part of the DsrMKJOP Transmembrane Complex in the Purple Sulfur Bacterium *Allochromatium vinosum*, Is an Unusual Triheme Cytochrome c, *Biochemistry*, 49: 8290-99.

Guindon, Stéphane, Dufayard, Jean-François, Lefort, Vincent, et al. 2010. New algorithms and methods to estimate maximum-likelihood phylogenies: assessing the performance of PhyML 3.0, *Systematic biology*, 59: 307-21.

Hamersley, Lavik, G, Woebken, D, et al. 2007. Anaerobic ammonium oxidation in the Peruvian oxygen minimum zone, *Limnology and Oceanography*, 52: 923-33.

Hao, X. D., Cao, X. Q., Picioreanu, C., et al. 2005. Model-based evaluation of oxygen consumption in a partial nitrification - Anammox biofilm process. In *Water Science and Technology*, 52: 155-60.

Harhangi, Harry R, Le Roy, Mathilde, van Alen, Theo, et al. 2012. Hydrazine synthase, a unique phylomarker with which to study the presence and biodiversity of anammox bacteria, *Applied and Environmental Microbiology*, 78: 752-58.

Heidelberg, John F, Paulsen, Ian T, Nelson, Karen E, et al. 2002. Genome sequence of the dissimilatory metal ion-reducing bacterium *Shewanella oneidensis*, *Nature biotechnology*, 20: 1118-23.

Hermann, Bianca, Kern, Melanie, La Pietra, Luigi, et al. 2015. The octahaem MccA is a haem c-copper sulfite reductase, *Nature*, 520: 706-09.

Herzik, Mark A., Jonnalagadda, Rohan, Kuriyan, John, et al. 2014. Structural insights into the role of iron–histidine bond cleavage in nitric oxide-induced activation of H-NOX gas sensor proteins, *Proceedings of the National Academy of Sciences*, 111: E4156-64.

Hespen, Charles W., Bruegger, Joel J., Phillips-Piro, Christine M., et al. 2016. Structural and Functional Evidence Indicates Selective Oxygen Signaling in *Caldanaerobacter subterraneus* H-NOX, *ACS Chemical Biology*, 11: 2337-46.

Heun, Lucas Binnenkade, Maximilian Kreienbaum, and Kai M. Thormann. 2012. Functional Specificity of Extracellular Nucleases of *Shewanella oneidensis* MR-1, *Applied and Environmental Microbiology*, 78: 4400-11.

Hinman, Richard 1958. Notes -Base Strengths of Some Alkylhydrazines, *J. Org. Chem.*, 23: 1587–88.

Hira, Daisuke, Kitamura, Ryuji, Nakamura, Teruya, et al. 2018. Anammox Organism KSU-1 Expresses a Novel His/DOPA Ligated Cytochrome c, *Journal of Molecular Biology*, 430: 1189-200.

Hira, Daisuke, Toh, Hidehiro, Migita, Catharina T, et al. 2012. Anammox organism KSU-1 expresses a NirK-type copper-containing nitrite reductase instead of a NirS-type with cytochrome cd1, *FEBS Letters*, 586: 1658-63.

Holleman, Arnold F, Wiberg, Egon, and Wiberg, Nils. 2007. Lehrbuch der anorganischen Chemie, *de Gruyter*.

Holm, Liisa, and Rosenström, Päivi. 2010. Dali server: conservation mapping in 3D, *Nucleic acids research*, 38: W545-9.

Hooper, A B, and Nason, A. 1965. Characterization of hydroxylamine-cytochrome c reductase from the chemoautotrophs *Nitrosomonas europaea* and *Nitrosocystis oceanus*, *J Biol Chem*, 240: 4044-57.

Hooper, A B, Vannelli, T, Bergmann, D J, et al. 1997. Enzymology of the oxidation of ammonia to nitrite by bacteria, *Antonie van Leeuwenhoek*, 71: 59-67.

Hough, Michael A., and Andrew, Colin R. 2015. Cytochromes c': Structure, Reactivity and Relevance to Haem-Based Gas Sensing, *Advances in microbial physiology*, 67: 1-84.

Hough, Michael A., Antonyuk, Svetlana V., Barbieri, Sonia, et al. 2011. Distal-to-Proximal NO Conversion in Hemoproteins: The Role of the Proximal Pocket, *Journal of Molecular Biology*, 405: 395-409.

Hu, Ziye, van Alen, Theo, Jetten, Mike S M, et al. 2013. Lysozyme and penicillin inhibit the growth of anaerobic ammonium-oxidizing planctomycetes, *Applied and Environmental Microbiology*, 79: 7763-69.

Huston, Wilhelmina M, Harhangi, Harry R, Leech, Andrew P, et al. 2007. Expression and characterisation of a major c-type cytochrome encoded by gene kustc0563 from *Kuenenia stuttgartiensis* as a recombinant protein in *Escherichia coli*, *Protein expression and purification*, 51: 28-33.

Igarashi, N, Moriyama, H, Fujiwara, T, et al. 1997. The 2.8 Å structure of hydroxylamine oxidoreductase from a nitrifying chemoautotrophic bacterium, *Nitrosomonas europaea*, *Nature structural biology*, 4: 276-84.

Innerebner, Gerd, Insam, Heribert, Franke-Whittle, Ingrid H., et al. 2007. Identification of anammox bacteria in a full-scale deammonification plant making use of anaerobic ammonia oxidation, *Systematic and Applied Microbiology*, 30: 408-12.

Jaeschke, Andrea, Op den Camp, Huub J M, Harhangi, Harry, et al. 2009. 16S rRNA gene and lipid biomarker evidence for anaerobic ammonium-oxidizing bacteria (anammox) in California and Nevada hot springs, *FEMS Microbiology Ecology*, 67: 343-50.

Jeske, Olga, Schüler, Margarete, Schumann, Peter, et al. 2015. Planctomycetes do possess a peptidoglycan cell wall, *Nature Communications*, 6: 7116.

Jetten, Mike S M, van Niftrik, Laura, Strous, Marc, et al. 2009. Biochemistry and molecular biology of anammox bacteria, *Critical reviews in biochemistry and molecular biology*, 44: 65-84.

Johnson , Rajagopalan. 2001. An Active Site Tyrosine Influences the Ability of the Dimethyl Sulfoxide Reductase Family of Molybdopterin Enzymes to Reduce S-Oxides, *Journal of Biological Chemistry*, 276: 13178-85.

Jormakka, M., Tornroth, S., Byrne, B., et al. 2002. Molecular basis of proton motive force generation: structure of formate dehydrogenase-N, *Science*, 295: 1863-8.

Kabsch, Wolfgang. 2010. XDS, *Acta Crystallogr D Biol Crystallogr*, 66: 125-32.

Kappler, U., Bernhardt, P. V., Kilmartin, J., et al. 2008. SoxAX cytochromes, a new type of heme copper protein involved in bacterial energy generation from sulfur compounds, *J Biol Chem*, 283: 22206-14.

Karlsson, Roger, Karlsson, Anders Ola Bäckman Bengt R. Johansson Stefan Hulth. 2014. Subcellular localization of an ATPase in anammox bacteria using proteomics and immunogold electron microscopy, *FEMS Microbiology Letters*, 354: 10-18.

Karplus, Kay Diederichs. 2012. Linking crystallographic model and data quality, *Science*, 336: 1030-33.

Kartal, B, Kuenen, J G, and van Loosdrecht, M C M. 2010. Engineering. Sewage treatment with anammox, *Science*, 328: 702-03.

Kartal, Boran, Almeida, Naomi M de, Maalcke, Wouter J, et al. 2013. How to make a living from anaerobic ammonium oxidation, *FEMS Microbiology Reviews*, 37: 428-61.

Kartal, B., and Keltjens, J. T. 2016. Anammox Biochemistry: a Tale of Heme c Proteins, *Trends Biochem Sci*, 41: 998-1011.

Kartal, Boran, Kuypers, Marcel M M, Lavik, Gaute, et al. 2007a. Anammox bacteria disguised as denitrifiers: nitrate reduction to dinitrogen gas via nitrite and ammonium, *Environmental Microbiology*, 9: 635-42.

Kartal, Boran, Maalcke, Wouter J, Almeida, Naomi M de, et al. 2011. Molecular mechanism of anaerobic ammonium oxidation., *Nature*, 479: 127-30.

Kartal, Boran, Rattray, Jayne, van Niftrik, Laura A., et al. 2007b. *Candidatus* "Anammoxoglobus propionicus" a new propionate oxidizing species of anaerobic ammonium oxidizing bacteria, *Systematic and Applied Microbiology*, 30: 39-49.

Kartal, Boran, Van Niftrik, Laura, Rattray, Jayne, et al. 2008. *Candidatus 'Brocadia fulgida'*: An autofluorescent anaerobic ammonium oxidizing bacterium, *FEMS Microbiology Ecology*, 63: 46-55.

Kassner, Richard J. . 1973. Theoretical model for the effects of local nonpolar heme environments on the redox potentials in cytochromes, *J. Am. Chem. Soc.*, 95: 2674–77.

Kekilli, Demet, Petersen, Christine A., Pixton, David A., et al. 2017. Engineering proximal vs. distal heme–NO coordination *via* dinitrosyl dynamics: implications for NO sensor design *Chemical Science*, 8: 1986-94.

Khramenkov, S V, Kozlov, M N, Kevbrina, M V, et al. 2013. A novel bacterium carrying out anaerobic ammonium oxidation in a reactor for biological treatment of the filtrate of wastewater fermented sludge, *Microbiology*, 82: 628-36.

Kilmartin, J. R., Maher, M. J., Krusong, K., et al. 2011. Insights into structure and function of the active site of SoxAX cytochromes, *J Biol Chem*, 286: 24872-81.

Kloer, Daniel P, Hagel, Corina, Heider, Johann, et al. 2006. Crystal structure of ethylbenzene dehydrogenase from *Aromatoleum aromaticum*, *Structure*, 14: 1377-88.

Klotz, M G, Schmid, M C, Strous, M, et al. 2008. Evolution of an octahaem cytochrome c protein family that is key to aerobic and anaerobic ammonia oxidation by bacteria, *Environmental Microbiology*, 10: 3150-63.

König, E, Schlesner, H, and Hirsch, P. 1984. Cell wall studies on budding bacteria of the *Planctomyces/Pasteuria* group and on a *Prosthecomicrobium sp*, *Archives of microbiology*, 138: 200-05.

Könneke, Martin, Bernhard, Anne E, de la Torre, José R, et al. 2005. Isolation of an autotrophic ammonia-oxidizing marine archaeon, *Nature*, 437: 543-46.

Krissinel, Evgeny, and Henrick, Kim. 2007. Inference of macromolecular assemblies from crystalline state, *Journal of Molecular Biology*, 372: 774-97.

Kucukelbir, Sigworth FJ, & Tagare HD. 2014. Quantifying the local resolution of cryo-EM density maps, *Nature Methods*, 11: 63-65.

Kurnikov, Igor V, Ratner, Mark A, and Pacheco, A Andrew. 2005. Redox equilibria in hydroxylamine oxidoreductase. Electrostatic control of electron redistribution in multielectron oxidative processes, *Biochemistry*, 44: 1856-63.

Kurokawa, Seno S, Matsuda H, Ying BW. 2016. Correlation between genome reduction and bacterial growth, *DNA Research*, 23: 517-25.

Kuypers, M M M, Sliekers, A O, Lavik, G, et al. 2003. Anaerobic ammonium oxidation by anammox bacteria in the Black Sea, *Nature*, 422: 608-11.

Kuypers, Marcel M M, Lavik, Gaute, Woebken, Dagmar, et al. 2005. Massive nitrogen loss from the Benguela upwelling system through anaerobic ammonium oxidation, *Proceedings of the National Academy of Sciences of the United States of America*, 102: 6478-83.

Laemmli, U K. 1970. Cleavage of structural proteins during the assembly of the head of bacteriophage T4, *Nature*, 227: 680-85.

Lam, Phyllis, and Kuypers, Marcel M M. 2011. Microbial nitrogen cycling processes in oxygen minimum zones, *Annual review of marine science*, 3: 317-45.

Lawson, C. E., Wu, S., Bhattacharjee, A. S., et al. 2017. Metabolic network analysis reveals microbial community interactions in anammox granules, *Nature Communications*, 8: 15416.

Lawson, D. M., Stevenson, C. E. M., Andrew, C. R., et al. 2003. A two-faced molecule offers NO explanation: the proximal binding of nitric oxide to haem, *Biochemical Society Transactions*, 31: 553.

Lawson, David M., Stevenson, Clare E. M., Andrew, Colin R., et al. 2000. Unprecedented proximal binding of nitric oxide to heme: implications for guanylate cyclase, *The EMBO Journal*, 19: 5661.

Li, Heng, and Durbin, Richard. 2009. Fast and accurate short read alignment with Burrows-Wheeler transform, *Bioinformatics*, 25: 1754-60.

Li, Xueming, Mooney, Paul, Zheng, Shawn, et al. 2013. Electron counting and beam-induced motion correction enable near atomic resolution single particle cryoEM, *Nature Methods*, 10: 584-90.

Lim, M. D., Lorković, I. M., and Ford, P. C. 2005. The preparation of anaerobic nitric oxide solutions for the study of heme model systems in aqueous and nonaqueous media: Some consequences of NOx impurities. *Methods in Enzymology*, 396: 3-17.

Lindsay, M R, Webb, R I, Strous, M, et al. 2001. Cell compartmentalisation in planctomycetes: novel types of structural organisation for the bacterial cell, *Archives of microbiology*, 175: 413-29.

Logan, M S, and Hooper, A B. 1995. Suicide inactivation of hydroxylamine oxidoreductase of *Nitrosomonas europaea* by organohydrazines, *Biochemistry*, 34: 9257-64.

Lonhienne, Thierry G A, Sagulenko, Evgeny, Webb, Richard I, et al. 2010. Endocytosis-like protein uptake in the bacterium *Gemmata obscuriglobus*, *Proceedings of the National Academy of Sciences of the United States of America*, 107: 12883-88.

Louche, A., Salcedo, S. P., and Bigot, S. 2017. Protein-Protein Interactions: Pull-Down Assays, *Methods Mol Biol*, 1615: 247-55.

Ludtke, SJ, Baldwin PR, Chiu W. 1999. EMAN: semiautomated software for high-resolution single-particle reconstructions, *Journal of Structural Biology*, 128: 82-97.

Luo, J., Chen, H., Han, X., et al. 2017. Microbial community structure and biodiversity of size-fractionated granules in a partial nitritation-anammox process, *FEMS Microbiology Ecology*, 93 doi: 10.1093/femsec/fix021.

Maalcke, Wouter J, Dietl, Andreas, Marritt, Sophie J, et al. 2014. Structural basis of biological NO generation by octaheme oxidoreductases, *J Biol Chem*, 289: 1228-42.

Maalcke, Wouter J., Reimann, Joachim, de Vries, Simon, et al. 2016. Characterization of anammox hydrazine dehydrogenase, a key N_2-producing enzyme in the global nitrogen cycle, *Journal of Biological Chemistry*: 291: 17077-92.

Manole, Andreea, Kekilli, Demet, Svistunenko, Dimitri A., et al. 2015. Conformational control of the binding of diatomic gases to cytochrome c′, *JBIC Journal of Biological Inorganic Chemistry*, 20: 675-86.

Mao, Nianjia, Ren, Hongqiang, Geng, Jinju, et al. 2017. Engineering application of anaerobic ammonium oxidation process in wastewater treatment, *World Journal of Microbiology and Biotechnology*, 33: 153.

Matthews, B W. 1968. Solvent content of protein crystals, *Journal of Molecular Biology*, 33: 491-97.

Mayhew, S G. 1978. The redox potential of dithionite and SO_2 from equilibrium reactions with flavodoxins, methyl viologen and hydrogen plus hydrogenase, *European journal of biochemistry*, 85: 535-47.

McCoy, Airlie J. 2007. Solving structures of protein complexes by molecular replacement with Phaser, *Acta Crystallogr D Biol Crystallogr*, 63: 32-41.

Medema, Marnix H, Zhou, Miaomiao, van Hijum, Sacha a F T, et al. 2010. A predicted physicochemically distinct sub-proteome associated with the intracellular organelle of the anammox bacterium *Kuenenia stuttgartiensis*, *BMC genomics*, 11: 299.

Mollin, J., Kasparek, F., Lassvsky J. 1975. On the basicity of hydroxylamine and its derivatives, *Chem. Zwesti.*, 29: 39-43.

Motie, Marjan, Kassner, Richard J., Meyer, Terrence E., et al. 1991. Cyanide-linked dimer-monomer equilibrium of *Chromatium vinosum* ferric cytochrome c′, *Biochimica et Biophysica Acta (BBA) - Protein Structure and Molecular Enzymology*, 1076: 97-102.

Motomura, T., Suga, M., Hienerwadel, R., et al. 2017. Crystal structure and redox properties of a novel cyanobacterial heme protein with a His/Cys heme axial ligation and a Per-Arnt-Sim (PAS)-like domain, *J Biol Chem*, 292: 9599-612.

Mowat, Christopher G, Rothery, Emma, Miles, Caroline S, et al. 2004. Octaheme tetrathionate reductase is a respiratory enzyme with novel heme ligation, *Nature structural and molecular biology*, 11: 1023-24.

Mulder, A. 1992. Anoxic Ammonia Oxidation. *United States Patent* US5078884A.

Mulder, A. 1995. Anaerobic ammonium oxidation discovered in a denitrifying fluidized bed reactor, *FEMS Microbiology Ecology*, 16: 177-83.

Mulder, A. 2003. The quest for sustainable nitrogen removal technologies. *Water Science and Technology*, 48: 67-75.

Murshudov, G N, Vagin, A A, and Dodson, E J. 1997. Refinement of macromolecular structures by the maximum-likelihood method, *Acta Crystallogr D Biol Crystallogr*, 53: 240-55.

Myer, Y P. 1978. Circular dichroism spectroscopy of hemoproteins, *Methods in enzymology*, 54: 249-84.

Myers, C R, and Myers, J M. 1997. Replication of plasmids with the p15A origin in *Shewanella putrefaciens* MR-1., *Letters in applied microbiology*, 24: 221-5.

Neef, A, Amann, R, Schlesner, H, et al. 1998. Monitoring a widespread bacterial group: in situ detection of *planctomycetes* with 16S rRNA-targeted probes, *Microbiology*, 144 (Pt 1: 3257-66.

Neumann, Sarah, Wessels, Hans J C T, Rijpstra, W Irene C, et al. 2014. Isolation and characterization of a prokaryotic cell organelle from the anammox bacterium *Kuenenia stuttgartiensis*, *Molecular microbiology*, 94: 794-802.

Ni, Shou-Qing, and Zhang, Jian. 2013. Anaerobic ammonium oxidation: from laboratory to full-scale application., *BioMed Research International*, 2013: 469360.

Nicholls, Peter. 1996. Cytochrome c: A Multidisciplinary Approach *Journal of the American Chemical Society*, 118: 9459-60.

Nielsen, Michael, Bollmann, Annette, Sliekers, Olav, et al. 2006. Kinetics, diffusional limitation and microscale distribution of chemistry and organisms in a CANON reactor, *FEMS Microbiology Ecology*, 51: 247-56.

Noel, War R, Ludwig, Wolfgang , Whitman, William , et al. 2010. *Bergey's Manual of Systematic Bacteriology: Volume 4* (Springer-Verlag New York).

Nouri, Dustin H, and Tantillo, Dean J. 2012. Attack of radicals and protons on ladderane lipids: quantum chemical calculations and biological implications, *Organic & biomolecular chemistry*, 10: 5514-17.

Nyola, Ajeeta, and Hunte, Carola. 2008. A structural analysis of the transient interaction between the cytochrome bc1 complex and its substrate cytochrome c, *Biochemical Society Transactions*, 36: 981-85.

Ortega, A, Amorós, D, and García de la Torre, J. 2011. Prediction of hydrodynamic and other solution properties of rigid proteins from atomic- and residue-level models, *Biophysical journal*, 101: 892-98.

Oshiki, Keisuke Mizuto, Zen-ichiro Kimura, Tomonori Kindaichi, Hisashi Satoh, Satoshi Okabe. 2017. Genetic diversity of marine anaerobic ammonium-oxidizing bacteria as revealed by genomic and proteomic analyses of '*Candidatus* Scalindua japonica', *Environmental Microbiology Reports*, 9: 550-561.

Oshiki, Mamoru, Shimokawa, Masaki, Fujii, Naoki, et al. 2011. Physiological characteristics of the anaerobic ammonium-oxidizing bacterium '*Candidatus* Brocadia sinica', *Microbiology*, 157: 1706-13.

Oshiki, Mamoru, Shinyako-Hata, Kaori, Satoh, Hisashi, et al. 2015. Draft Genome Sequence of an Anaerobic Ammonium-Oxidizing Bacterium, '*Candidatus* Brocadia sinica', *Genome Announcements*, 3: e00267-15.

Ozawa, K, Yasukawa, F, Fujiwara, Y, et al. 2001. A simple, rapid, and highly efficient gene expression system for multiheme cytochromes c, *Bioscience, biotechnology, and biochemistry*, 65: 185-89.

Park, Hongkeun, Brotto, Ariane C., van Loosdrecht, Mark C. M., et al. 2017. Discovery and metagenomic analysis of an anammox bacterial enrichment related to *Candidatus* "Brocadia caroliniensis" in a full-scale glycerol-fed nitritation-denitritation separate centrate treatment process, *Water Research*, 111: 265-73.

Penton, C Ryan, Devol, Allan H, and Tiedje, James M. 2006. Molecular evidence for the broad distribution of anaerobic ammonium-oxidizing bacteria in freshwater and marine sediments, *Applied and Environmental Microbiology*, 72: 6829-32.

Perkins, David N., Pappin, Darryl J. C., Creasy, David M., et al. 1999. Probability-based protein identification by searching sequence databases using mass spectrometry data, *Electrophoresis*, 20: 3551-67.

Persson, F., Suarez, C., Hermansson, M., et al. 2017. Community structure of partial nitritation-anammox biofilms at decreasing substrate concentrations and low temperature, *Microbial Biotechnology*, 10: 761-72.

Perutz, Max F., Giulio. Fermi, Donald J. Abraham, Claude. Poyart, and E. Bursaux. 1986. Hemoglobin as a receptor of drugs and peptides: X-ray studies of the stereochemistry of binding, *J. Am. Chem. Soc.*, 108: 1064–78.

Pettersen, Eric F, Goddard, Thomas D, Huang, Conrad C, et al. 2004. UCSF Chimera--a visualization system for exploratory research and analysis, *Journal of Computational Chemistry*, 25: 1605-12.

Pettigrew, Graham W., Moore, Geoffre. 1987. *Cytochromes c* (Springer).

Pires, Ricardo H., Venceslau, Sofia S., Morais, Francisco, et al. 2006. Characterization of the *Desulfovibrio desulfuricans* ATCC 27774 DsrMKJOP ComplexA Membrane-Bound Redox Complex Involved in the Sulfate Respiratory Pathway, *Biochemistry*, 45: 249-62.

Pixton, David A., Petersen, Christine A., Franke, Alicja, et al. 2009. Activation Parameters for Heme−NO Binding in *Alcaligenes xylosoxidans* Cytochrome c′: The Putative Dinitrosyl Intermediate Forms via a Dissociative Mechanism, *Journal of the American Chemical Society*, 131: 4846-53.

Poirel , Héritier C, Nordmann P. 2004. Chromosome-encoded ambler class D beta-lactamase of *Shewanella oneidensis* as a progenitor of carbapenem-hydrolyzing oxacillinase., *Antimicrobial Agents Chemotherapy*, 48: 348-51.

Polyakov, Konstantin M, Boyko, Konstantin M, Tikhonova, Tamara V, et al. 2009. High-resolution structural analysis of a novel octaheme cytochrome c nitrite reductase from the haloalkaliphilic bacterium *Thioalkalivibrio nitratireducens, Journal of Molecular Biology*, 389: 846-62.

Quan, Zhe-Xue, Rhee, Sung-Keun, Zuo, Jian-E, et al. 2008. Diversity of ammonium-oxidizing bacteria in a granular sludge anaerobic ammonium-oxidizing (anammox) reactor, *Environmental Microbiology*, 10: 3130-39.

Quintas, Pedro O., Catarino, Teresa, Todorovic, Smilja, et al. 2011. Highly Selective Ligand Binding by *Methylophilus methylotrophus* Cytochrome c″, *Biochemistry*, 50: 5624-32.

Ralston, G. 1993. Introduction to Analytical Ultracentrifugation.

Raphael, Adrienne L., and Gray, Harry B. 1991. Semisynthesis of axial-ligand (position 80) mutants of cytochrome c, *Journal of the American Chemical Society*, 113: 1038-40.

Reijerse, Edward J, Sommerhalter, Monika, Hellwig, Petra, et al. 2007. The unusal redox centers of SoxXA, a novel c-type heme-enzyme essential for chemotrophic sulfur-oxidation of *Paracoccus pantotrophus*, *Biochemistry*, 46: 7804-10.

Reverter, D., Maskos, K., Tan, F., et al. 2004. Crystal structure of human carboxypeptidase M, a membrane-bound enzyme that regulates peptide hormone activity, *J Mol Biol*, 338: 257-69.

Reynolds, M F, Parks, R B, Burstyn, J N, et al. 2000. Electronic absorption, EPR, and resonance raman spectroscopy of CooA, a CO-sensing transcription activator from *R. rubrum*, reveals a five-coordinate NO-heme, *Biochemistry*, 39: 388-96.

Richards, F A. 1965. Chemical Oceanography: (edited by Riley J., Skirrow G.).

Ripoll, Daniel R., Faerman,Carlos H., Axelsen,Paul H., Silmani, Israel, Sussman, Joel, L. . 1993. An electrostatic mechanism for substrate guidance down the aromatic gorge of acetylcholinesterase, *Proc Natl Acad Sci U S A*, 90: 5128-32.

Robinson, R A, and Bower, V E. 1961. Ionization Constant of Hydroxylamine, *Journal of Physical Chemistry*, 65: 1279-80.

Russ, Lina. 2015. Microbial nitrogen cycle interactions in laboratory-scale model systems. PhD Thesis. Radboud University, Nijmegen.

Russ, Lina, Kartal, Boran, Op den Camp, Huub J M, et al. 2013. Presence and diversity of anammox bacteria in cold hydrocarbon-rich seeps and hydrothermal vent sediments of the Guaymas Basin, *Frontiers in microbiology*, 4: 219.

Sagulenko, Evgeny, Morgan, Garry P, Webb, Richard I, et al. 2014. Structural studies of planctomycete *Gemmata obscuriglobus* support cell compartmentalisation in a bacterium, *PLoS One*, 9: e91344.

Sambrook, Joseph, and Russell, David W. 2001. Molecular cloning: A laboratory manual.

Sawayama, Shigeki. 2006. Possibility of anoxic ferric ammonium oxidation, *Journal of bioscience and bioengineering*, 101: 70-72.

Schägger, von Jagow G. 1987. Tricine-sodium dodecyl sulfate-polyacrylamide gel electrophoresis for the separation of proteins in the range from 1 to 100 kDa, *Analytical Biochemistry*, 166: 368-79.

Schalk, J, Vries, S de, Kuenen, J G, et al. 2000. Involvement of a novel hydroxylamine oxidoreductase in anaerobic ammonium oxidation, *Biochemistry*, 39: 5405-12.

Scheres, Sjors H.W. 2012. RELION: Implementation of a Bayesian approach to cryo-EM structure determination, *Journal of Structural Biology*, 180.

Schmid, M, Schmitz-Esser, S, Jetten, M, et al. 2001. 16S-23S rDNA intergenic spacer and 23S rDNA of anaerobic ammonium-oxidizing bacteria: implications for phylogeny and in situ detection, *Environmental Microbiology*, 3: 450-59.

Schmid, M, Twachtmann, U, Klein, M, et al. 2000. Molecular evidence for genus level diversity of bacteria capable of catalyzing anaerobic ammonium oxidation, *Systematic and Applied Microbiology*, 23: 93-106.

Schmid, Markus C, Maas, Bart, Dapena, Ana, et al. 2005. Biomarkers for in situ detection of anaerobic ammonium-oxidizing (anammox) bacteria, *Applied and Environmental Microbiology*, 71: 1677-84.

Schmid, Markus C., Risgaard-Petersen, Nils, van de Vossenberg, Jack, et al. 2007. Anaerobic ammonium-oxidizing bacteria in marine environments: widespread occurrence but low diversity, *Environmental Microbiology*, 9: 1476-84.

Schmid, Markus, Walsh, Kerry, Webb, Rick, et al. 2003. *Candidatus* "Scalindua brodae", sp. nov., *Candidatus* "Scalindua wagneri", sp. nov., Two New Species of Anaerobic Ammonium Oxidizing Bacteria, *Systematic and Applied Microbiology*, 26: 529-38.

Schneider, Thomas R, and Sheldrick, George M. 2002. Substructure solution with SHELXD, *Acta Crystallogr D Biol Crystallogr*, 58: 1772-79.

Schouten, Stefan, Strous, Marc, Kuypers, Marcel M M, et al. 2004. Stable carbon isotopic fractionations associated with inorganic carbon fixation by anaerobic ammonium-oxidizing bacteria, *Applied and Environmental Microbiology*, 70: 3785-88.

Schubert, Carsten J, Durisch-Kaiser, Edith, Wehrli, Bernhard, et al. 2006. Anaerobic ammonium oxidation in a tropical freshwater system (Lake Tanganyika), *Environmental Microbiology*, 8: 1857-63.

Schuck, P. 2000. Size-distribution analysis of macromolecules by sedimentation velocity ultracentrifugation and lamm equation modeling, *Biophysical journal*, 78: 1606-19.

Shelver, D., Kerby, R. L., He, Y., et al. 1997. CooA, a CO-sensing transcription factor from *Rhodospirillum rubrum*, is a CO-binding heme protein, *Proc Natl Acad Sci U S A*, 94: 11216-20.

Shevchenko, A., Tomas, H., Havlis, J., et al. 2006. In-gel digestion for mass spectrometric characterization of proteins and proteomes, *Nat Protoc*, 1: 2856-60.

Shi, Liang, Lin, Jiann-Trzwo, Markillie, Lye M, et al. 2005. Overexpression of multi-heme C-type cytochromes., *BioTechniques*, 38: 297-9.

Shibata, Naoki, Iba, Satoaki, Misaki, Shintaro, et al. 1998. Basis for monomer stabilization in *Rhodopseudomonas palustris* cytochrome c′ derived from the crystal structure, *Journal of Molecular Biology*, 284: 751-60.

Shimamura, Munetaka, Nishiyama, Takashi, Shigetomo, Hiroyuki, et al. 2007. Isolation of a multiheme protein with features of a hydrazine-oxidizing enzyme from an anaerobic ammonium-oxidizing enrichment culture, *Applied and Environmental Microbiology*, 73: 1065-72.

Shimamura, Munetaka, Nishiyama, Takashi, Shinya, Kazutaka, et al. 2008. Another multiheme protein, hydroxylamine oxidoreductase, abundantly produced in an anammox bacterium besides the hydrazine-oxidizing enzyme, *Journal of bioscience and bioengineering*, 105: 243-48.

Sievers, Fabian, Wilm, Andreas, Dineen, David, et al. 2011. Fast, scalable generation of high-quality protein multiple sequence alignments using Clustal Omega, *Molecular systems biology*, 7: 539.

Simoes, P., Matias, P. M., Morais, J., et al. 1998. Refinement of the three-dimensional structures of cytochrome c_3, from *Desulfovibrio vulgaris* Hildenborough at 1.67 Å resolution and from *Desulfovibrio desulfuricans* ATCC 27774 at 1.6 Å resolution, *Inorganica Chimica Acta*, 273: 213-24.

Simon, Jörg 2002. Enzymology and bioenergetics of respiratory nitrite ammonification, *FEMS Microbiology Reviews*, 26: 285-309.

Simon, Jörg, Kern, Melanie, Hermann, Bianca, et al. 2011. Physiological function and catalytic versatility of bacterial multihaem cytochromes c involved in nitrogen and sulfur cycling, *Biochemical Society Transactions*, 39: 1864-70.

Sinninghe Damsté, Jaap S, Rijpstra, W Irene C, Strous, Marc, et al. 2004. A mixed ladderane/n-alkyl glycerol diether membrane lipid in an anaerobic ammonium-oxidizing bacterium, *Chemical communications*, 22: 2590-91.

Sinninghe Damsté, Jaap S, Strous, Marc, Rijpstra, W Irene C, et al. 2002. Linearly concatenated cyclobutane lipids form a dense bacterial membrane, *Nature*, 419: 708-12.

Smith, David B. Nedwell, Liang F. Dong, A. Mark Osborn. 2007. Diversity and Abundance of Nitrate Reductase Genes (narG and napA), Nitrite Reductase Genes (nirS and nrfA), and Their Transcripts in Estuarine Sediments, *Applied and Environmental Microbiology*, 73: 3612-22.

Solovyev, Victor, and Salamov, Asaf. 2011. Automatic Annotation of Microbial Genomes and Metagenomic Sequences. In: Metagenomics and its Applications in Agriculture, Biomedicine and Environmental Studies (Ed. R.W. Li), pp. 61-78.

Speth, Daan R, Hu, Baolan, Bosch, Niek, et al. 2012a. Comparative genomics of two independently enriched *Candidatus* "Kuenenia Stuttgartiensis" anammox bacteria, *Frontiers in microbiology*, 3: 307.

Speth, Daan R, in 't Zandt, Michiel H., Guerrero-Cruz, Simon, et al. 2016. Genome-based microbial ecology of anammox granules in a full-scale wastewater treatment system, *Nature Communications*, 7: 11172.

Speth, Daan R, Russ, Lina, Kartal, Boran, et al. 2015. Draft Genome Sequence of Anammox Bacterium "*Candidatus Scalindua brodae*", Obtained Using Differential Coverage Binning of Sequencing Data from Two Reactor Enrichments, *Genome Announcements*, 4: 1-2.

Speth, Daan R, van Teeseling, Muriel C F, and Jetten, Mike S M. 2012b. Genomic analysis indicates the presence of an asymmetric bilayer outer membrane in planctomycetes and verrucomicrobia, *Frontiers in microbiology*, 3: 304.

Speth, Daan R., Lagkouvardos, Ilias, Wang, Yong, et al. 2017. Draft Genome of *Scalindua rubra*, Obtained from the Interface Above the Discovery Deep Brine in the Red Sea, Sheds Light on Potential Salt Adaptation Strategies in Anammox Bacteria, *Microbial Ecology*, 74: 1-5.

Spitzer, Jan. 2011. From Water and Ions to Crowded Biomacromolecules: In Vivo Structuring of a Prokaryotic Cell, *Microbiology and Molecular Biology Reviews*, 75: 491-506.

Stieglmeier, Michaela, Klingl, Andreas, Alves, Ricardo J E, et al. 2014. *Nitrososphaera viennensis* gen. nov., sp. nov., an aerobic and mesophilic, ammonia-oxidizing archaeon from soil and a member of the archaeal phylum *Thaumarchaeota*, *International journal of systematic and evolutionary microbiology*, 64: 2738-52.

Stone, James R., and Marletta, Michael a. 1994. Soluble Guanylate Cyclase from Bovine Lung: Activation with Nitric Oxide and Carbon Monoxide and Spectral Characterization of the Ferrous and Ferric States, *Biochemistry*, 33: 5636-40.

Strous, M, Fuerst, JA, and Kramer, EHM. 1999. Missing lithotroph identified as new planctomycete, *Nature*, 400: 446–449.

Strous, M, Heijnen, J J, Kuenen, J G, et al. 1998. The sequencing batch reactor as a powerful tool for the study of slowly growing anaerobic ammonium-oxidizing microorganisms, *Applied Microbiology and Biotechnology*, 50: 589-96.

Strous, M, Pelletier, E, Mangenot, S, et al. 2006. Deciphering the evolution and metabolism of an anammox bacterium from a community genome, *Nature*, 440: 790-94.

Strous, M, van Gerven, E, Kuenen, J G, et al. 1997. Effects of aerobic and microaerobic conditions on anaerobic ammonium-oxidizing (anammox) sludge, *Applied and Environmental Microbiology*, 63: 2446-48.

Studier, F W, and Moffatt, B A. 1986. Use of bacteriophage T7 RNA polymerase to direct selective high-level expression of cloned genes, *Journal of Molecular Biology*, 189: 113-30.

Suga, Michihiro, Lai, Thanh-Lan, Sugiura, Miwa, et al. 2013. Crystal structure at 1.5 Å resolution of the PsbV2 cytochrome from the cyanobacterium *Thermosynechococcus elongatus*, *FEBS Letters*, 587: 3267-72.

Tamura, Koichiro, Stecher, Glen, Peterson, Daniel, et al. 2013. MEGA6: Molecular Evolutionary Genetics Analysis version 6.0, *Molecular biology and evolution*, 30: 2725-29.

Taylor, R G, Walker, D C, and McInnes, R R. 1993. E. coli host strains significantly affect the quality of small scale plasmid DNA preparations used for sequencing, *Nucleic acids research*, 21: 1677-78.

Terwilliger, Thomas C, Adams, Paul D, Read, Randy J, et al. 2009. Decision-making in structure solution using Bayesian estimates of map quality: the PHENIX AutoSol wizard, *Acta Cryst*, 65: 582-601.

Third, K.A., Sliekers, A. Olav, Kuenen, J.G., et al. 2001. The CANON System (Completely Autotrophic Nitrogen-removal Over Nitrite) under Ammonium Limitation: Interaction and Competition between Three Groups of Bacteria, *Systematic and Applied Microbiology*, 24: 588-96.

Thorvaldsdottir, H, Robinson, J T, and Mesirov, J P. 2013. Integrative Genomics Viewer (IGV): High-performance genomics data visualization and exploration, *Briefings in Bioinformatics*, 14: 178-92.

Tourna, Maria, Stieglmeier, Michaela, Spang, Anja, et al. 2011. *Nitrososphaera viennensis*, an ammonia oxidizing archaeon from soil, *Proceedings of the National Academy of Sciences of the United States of America*, 108: 8420-25.

Tsan, Pascale, Hus, Jean-Christophe, Caffrey, Michael, et al. 2000. Rotational Diffusion Anisotropy and Local Backbone Dynamics of Carbon Monoxide-Bound *Rhodobacter capsulatus* Cytochrome c‘, *Journal of the American Chemical Society*, 122: 5603-12.

Ukita, Saki, Fujii, Takao, Hira, Daisuke, et al. 2010. A heterodimeric cytochrome c complex with a very low redox potential from an anaerobic ammonium-oxidizing enrichment culture, *FEMS Microbiology Letters*, 313: 61-67.

Unni, Samir, Yong Huang, Robert Hanson, Malcolm Tobias, Sriram Krishnan, Wilfred W. Li, Jens E. Nielsen, and Nathan A. Baker. 2012. Web servers and services for electrostatics calculations with APBS and PDB2PQR, *J Comput Chem*, 32: 1488-91.

Vagin, Alexei, and Teplyakov, Alexei. 1997. MOLREP: an Automated Program for Molecular Replacement, *J. Appl. Cryst*, 30: 1022-25.

van de Graaf, A A, Bruijn, P de, Robertson, L A, et al. 1996. Autotrophic growth of anaerobic ammonium-oxidizing micro-organisms in a fluidized bed reactor, *Microbiology*, 142: 2187-96.

van de Graaf, A A, Mulder, A, Bruijn, P de, et al. 1995. Anaerobic oxidation of ammonium is a biologically mediated process, *Applied and Environmental Microbiology*, 61: 1246-51.

van de Vossenberg, J, Rattray, J E, Geerts, W, et al. 2008. Enrichment and characterization of marine anammox bacteria associated with global nitrogen gas production, *Environmental Microbiology*, 10: 3120-29.

van de Vossenberg, Jack, Woebken, Dagmar, Maalcke, Wouter J, et al. 2013. The metagenome of the marine anammox bacterium '*Candidatus* Scalindua profunda' illustrates the versatility of this globally important nitrogen cycle bacterium., *Environmental Microbiology*, 15: 1275-89.

van der Star, W R L. 2008a. Growth and metabolism of anammox bacteria. PhD Thesis. TU Delft, Delft

van der Star, Wouter R L, Dijkema, Cor, Waard, Pieter de, et al. 2010. An intracellular pH gradient in the anammox bacterium *Kuenenia stuttgartiensis* as evaluated by 31P NMR, *Applied microbiology and biotechnology*, 86: 311-17.

van der Star, Wouter R L, Miclea, Andreea I, van Dongen, Udo G J M, et al. 2008b. The membrane bioreactor: a novel tool to grow anammox bacteria as free cells., *Biotechnology and bioengineering*, 101: 286-94.

van Dongen, U, Jetten, M S, and van Loosdrecht, M C. 2001. The SHARON-Anammox process for treatment of ammonium rich wastewater, *Water science and technology*, 44: 153-60.

Van Driessche, Gonzalez, Devreese, Bart, Fitch John, C., et al. 2006. GHP, a new c-type green heme protein from *Halochromatium salexigens* and other proteobacteria, *The FEBS Journal*, 273: 2801-11.

van Kessel, Maartje A H J, Speth, Daan R, Albertsen, Mads, et al. 2015. Complete nitrification by a single microorganism, *Nature*, 528: 555-59.

van Niftrik, Laura. 2008a. Cell biology of anaerobic ammonium-oxidizing bacteria. PhD Thesis. Radboud Universiteit, Nijmegen.

van Niftrik, Laura, Geerts, Willie J C, van Donselaar, Elly G, et al. 2008b. Linking ultrastructure and function in four genera of anaerobic ammonium-oxidizing bacteria: cell plan, glycogen storage, and localization of cytochrome c proteins, *Journal of Bacteriology*, 190: 708-17.

van Niftrik, Laura, Geerts, Willie J C, van Donselaar, Elly G, et al. 2009. Cell division ring, a new cell division protein and vertical inheritance of a bacterial organelle in anammox planctomycetes, *Molecular microbiology*, 73: 1009-19.

van Niftrik, Laura, Geerts, Willie J C, van Donselaar, Elly G, et al. 2008c. Combined structural and chemical analysis of the anammoxosome: a membrane-bounded intracytoplasmic compartment in anammox bacteria, *Journal of Structural Biology*, 161: 401-10.

van Niftrik, Laura, van Helden, Mary, Kirchen, Silke, et al. 2010. Intracellular localization of membrane-bound ATPases in the compartmentalized anammox bacterium '*Candidatus* Kuenenia stuttgartiensis', *Molecular microbiology*, 77: 701-15.

van Teeseling, Muriel C F, Almeida, Naomi M de, Klingl, Andreas, et al. 2014. A new addition to the cell plan of anammox bacteria: *Candidatus* Kuenenia stuttgartiensis has a protein surface layer as the outermost layer of the cell, *Journal of Bacteriology*, 196: 80-89.

van Teeseling, Muriel C F, Benz, Roland, Almeida, Naomi M. de, Jetten, Mike S.M., Mesman, Rob J., van Niftrik, Laura. 2018. Characterization of the first planctomycetal outer membrane protein identifies a channel in the outer membrane of the anammox bacterium *Kuenenia stuttgartiensis*, *Biochimica et Biophysica Acta (BBA) - Biomembranes*, 1860: 767-76.

van Teeseling, Muriel C F, Maresch, Daniel, Rath, Cornelia B, et al. 2016. The S-Layer Protein of the Anammox Bacterium *Kuenenia stuttgartiensis* Is Heavily O-Glycosylated, *Frontiers in microbiology*, 7: 1721.

van Teeseling, Muriel C F, Mesman, Rob J, Kuru, Erkin, et al. 2015. Anammox Planctomycetes have a peptidoglycan cell wall, *Nature Communications*, 6: 6878.

van Teeseling, Muriel C F, Neumann, Sarah, and van Niftrik, Laura. 2013. The anammoxosome organelle is crucial for the energy metabolism of anaerobic ammonium oxidizing bacteria, *Journal of molecular microbiology and biotechnology*, 23: 104-17.

Vlaeminck, S. E., Terada, A., Smets, B. F., et al. 2010. Aggregate size and architecture determine microbial activity balance for one-stage partial nitritation and anammox, *Applied and Environmental Microbiology*, 76: 900-09.

Volkov, Alexander N. 2015. Structure and Function of Transient Encounters of Redox Proteins, *Accounts of Chemical Research* 8: 3036-43.

Vonrhein, Clemens, Blanc, Eric, Roversi, Pietro, et al. 2007. Automated structure solution with autoSHARP, *Methods in molecular biology*, 364: 215-30.

Wett, B. 2006. Solved upscaling problems for implementing deammonification of rejection water, *Water Science & Technology*, 53: 121.

Wett, B, Nyhuis, G, Podmirseg, S, et al. 2013. Population dynamics at the limits of DEMON plant operations, *13th World Congress on Anaerobic Digestion*.

Wheeldon, Ian, Shelley D. Minteer, Scott Banta, Scott Calabrese Barton, Plamen Atanassov & Matthew Sigman. 2016. Substrate channelling as an approach to cascade reactions, *Nature Chemistry*, 8: 299–309.

Wilson, K. 2001. Preparation of genomic DNA from bacteria, *Current protocols in molecular biology / edited by Frederick M. Ausubel ... [et al.]*, Chapter 2: Unit 2.4.

Woebken, Dagmar, Fuchs, Bernhard M, Kuypers, Marcel M M, et al. 2007. Potential interactions of particle-associated anammox bacteria with bacterial and archaeal partners in the Namibian upwelling system, *Applied and Environmental Microbiology*, 73: 4648-57.

Wyatt, Philip J. 1993. Light scattering and the absolute characterization of macromolecules, *Analytica Chimica Acta*, 272: 1-40.

Yang, Wendy H, Weber, Karrie A, and Silver, Whendee L. 2012. Nitrogen loss from soil through anaerobic ammonium oxidation coupled to iron reduction, *Nature Geoscience*, 5: 538-41.

Yanisch-Perron, C., Vieira, J., and Messing, J. 1985. Improved M13 phage cloning vectors and host strains: nucleotide sequences of the M13mpl8 and pUC19 vectors, *Gene*, 33: 103-19.

Yonetani, T. 1965. Studies on cytochrome c peroxidase. II. Stoichiometry between enzyme, H_2O_2, and ferrocytochrome c and enzymic determination of extinction coefficients of cytochrome c, *J Biol Chem*, 240: 4509-14.

Yoshimura, Tetsuhiko, Fujii, Satoshi, Kamada, Hitoshi, et al. 1996. Spectroscopic characterization of nitrosylheme in nitric oxide complexes of ferric and ferrous cytochrome c′ from photosynthetic bacteria, *Biochimica et Biophysica Acta (BBA) - Protein Structure and Molecular Enzymology*, 1292: 39-46.

Zangi, Ronen, Hagen, Morten, and Berne, B. J. 2007. Effect of Ions on the Hydrophobic Interaction between Two Plates, *Journal of the American Chemical Society*, 129: 4678-86.

Zhang, K. 2016. Gctf: Real-time CTF determination and correction, *Journal of Structural Biology*, 193: 1-12

Zhang, Zuotao, and Liu, Sitong. 2014. Hot topics and application trends of the anammox biotechnology: a review by bibliometric analysis, *SpringerPlus*, 3: 220.